

School of Earth and Planetary Sciences

**Implications of Sedimentary Provenance and
Regional Tectonic Evolution on the Formation
Process of the South China Sea**

Yuchi Cui

**This thesis is presented for the collaborative Degree of
Doctor of Philosophy
of**

**Tongji University
and**

Curtin University

May 2024

Extended abstract of the thesis “Formation and Provenance Evolution of the South China Sea as a Western Pacific Marginal Basin” and its outcome

This thesis focuses on the Upper Mesozoic to Cenozoic stratigraphy framework in the northern South China Sea region. Based on the systematic collection and organization of previously published research results and data, combined with seismic profiles and the latest joint inversion results of gravity, magnetic, and seismic data in key areas of the basin, this study conducts petrographic, mineralogical, elemental geochemical, zircon U-Pb dating, and Lu-Hf isotopic analysis of drilling and outcrop samples in the South China continental margin, especially in the northern South China Sea. Through comprehensive tracing techniques of "source-to-sink" correlation, structural environment discrimination, and sedimentary environment reconstruction, this thesis reinterprets and systematically reveals the characteristics of the Mesozoic basement in the northern South China Sea. Based on this, it further explores the spatiotemporal evolution of the Mesozoic Andes-type active continental margin, clarifying the timing and mechanism of the transition of the South China continent from an active to a passive margin, providing deeper insights into the early Cenozoic magmatic activity and evolution characteristics in the northern South China Sea and its significance for the expansion of the South China Sea.

This thesis also systematically studies processes such as the provenance and evolution of the large ancient river systems of "Kontum-Ying-Qiong" on the western side of the South China Sea, the formation and development of the Pearl River Basin, the evolution of the Late Middle to Late Miocene central canyon system, and the formation of the accretionary wedge turbidite bodies in the Hengchun Peninsula of Taiwan. It is found that these sedimentary filling processes have important implications for the overall paleogeographic pattern of the South China Sea. Based on specific "source-to-sink" system reconstruction models and regional tectonic environments, as well as factors controlling provenance evolution, this thesis completes the reconstruction of paleohydrology and paleogeography from the Late Mesozoic to Cenozoic in the South China Sea region. The main objectives and achievements of this thesis are summarized as follows.

- 1) Typical active continental margins include Andean-type plate margins and Western Pacific-type plate margins. Andean-type margins feature the development of active continental arcs, which is in contrast with the Western Pacific-type margins that feature the development

of marginal oceanic basins. Andean-type plate margins are characterized by continental arc magmatism, both interplate and intraplate seismicity, fold and thrust belts, and foreland basins (e.g., Jahn et al., 1976; Klimetz, 1983; Lapierre, et al., 1997; Ramos, 1999; Zhou and Li, 2000). The collision of aseismic ridges or oceanic plateaus along such margins often causes flat-slab subduction where a segment with a magmatic gap forms in place of the normal magmatic arc (Ramos and Folguera, 2009; Kazuo and Teruyoshi, 2013). On the other hand, Western Pacific-type margins are generally characterized by an extensional tectonic environment. Therein, back-arc or marginal oceanic basins are produced that separate the continental margins from the oceanic arcs. However, several questions remain: 1) Was there ever an Andean-type continental margin along the Western Pacific? 2) When did the Western Pacific-type active margin start? 3) What tectonic process resulted in the switching of active margin types?

To the northwest of the Pacific Ocean, continental East Asia is an assemblage of the Siberia, Mongolia, North China, South China and Indochina cratons/continental blocks that developed an active continental margin along its border with the Paleo-Pacific Ocean (e.g., Metcalfe, 1996). An Andean-type active continental margin is widely believed to have developed along the southeastern margin of the South China Block between the Triassic – Jurassic and Middle Cretaceous. The existence of this convergent plate margin has been documented by the widespread development of a broad continental volcanic arc (e.g., Klimetz, 1983; Charvet et al., 1994; Zhou and Li, 2000; Zhou et al., 2006; Li and Li, 2007; Li et al., 2012b). However, the subduction of the Paleo-Pacific Plate could have initiated as early as the late Carboniferous or the early Permian, as indicated by geological records from the Japanese islands (Isozaki et al., 2010). The onset of the continental magmatic arc along southeastern South China is indicated by a middle Permian (ca. 265 Ma) arc pluton on Hainan Island (Li et al., 2006), and more recent work has suggested that the continental arc there could have started as early as 290–280 Ma (Li et al., 2012a; Zhang et al., 2019).

Li and Li (2007) and Li et al. (2012b) proposed that similar to the present-day Andean margin, coastal South China experienced an episode of flat-slab subduction during 250–200 Ma. They further speculated that once flat subduction was jammed by ca. 200 Ma, normal subduction was reinitiated along the coastal zone, based on both kinematic necessity and the reappearance of magmatic and volcanoclastic rocks along the coastal zone. Similarly, Xu et al. (2017) revealed arc-related magmatism in the Early Jurassic (198–195 Ma for magnesian granite and diorite, 187 Ma for granodiorite) in the NE South China Sea and the SW East China Sea basin areas. In addition, boreholes in the NE South China Sea basin have penetrated numerous Late Cretaceous granites, granodiorites, diorites and monzonites (Table 1; Qiu et al.,

1996; Li et al., 1999).

Similar metavolcanic rocks and granites have also been observed farther south and west in the Southeast Asia region, including Palawan, SE Vietnam, northern Borneo, and other areas along the Sundaland margin (e.g. Nguyen et al., 2004; Hennig et al., 2017; Shao et al., 2017; Shao et al., 2019). Nguyen et al. (2004) reported the initiation of arc magmatism in southern Vietnam on the basis of 112–88 Ma I-type calc-alkaline granitoid bodies. Hennig et al. (2017) interpreted the 130–80 Ma meta-igneous rocks in SW Borneo to have been formed during the Paleo-Pacific subduction beneath the Indochina-East Malaysia Block. Suggate et al. (2014) proposed that the late Cretaceous metasedimentary rocks of the Palawan Terrane were derived from the South China margin, and the terrane rifted away to the south during the subsequent opening of the South China Sea during early Cenozoic.

Mesozoic rocks underlying the Cenozoic basin of NW South China Sea have so far only been sporadically reported with limited geographic extent. Here, we report new age and geochemical data from granitic bodies and metasedimentary rocks penetrated by offshore hydrocarbon exploration drill holes along the continental margin of the northern South China Sea. By combining our new results with a regional data compilation and synthesis, we aim to systematically investigate 1) the initiation and evolution of the Andean-type active continental margin along this section of the Western Pacific margin and 2) the tectonic processes that might have caused the switch from an Andean-type to the Western Pacific-type convergent plate margin.

Summarized conclusions: integrated analyses of in situ zircon U-Pb ages and geochemistry were conducted on both granitic and metasedimentary borehole samples from immediately below the Cenozoic sedimentary cover of the northern South China Sea basin. Our work suggests that basement rocks of the South China Sea basin are not Proterozoic or Paleozoic rocks, as previously speculated based on gravity-magnetic inversion work. The analyzed metavolcaniclastic and metasedimentary rocks were likely deposited at or soon after ca. 145 Ma but prior to ca. 85 Ma. A nearby source in coastal South China is proposed based on the generally immature nature of the metasedimentary rocks and the lack of detritus from older basement rocks farther inland. The vast majority of the metavolcaniclastic samples have sparse ca. 250–190 Ma (particularly 200–190 Ma) zircons. This magmatic quiescence is consistent with the existence of a coastal magmatic gap to the east of Hainan Island during this time, previously interpreted as reflecting a period of flat-slab subduction. Metaclastic samples mostly exhibit a dominant ca. 180–120 Ma zircon population, indicating extensive magmatism along the coastal areas. This finding, together with previously reported ca. 190–180 Ma I-type

coastal granites and our newly dated ca. 115–98 Ma volcanic and granitic rocks under the western part of the South China Sea basin can best be interpreted by the former presence of an Andean-type continental arc during the Middle Jurassic – Early Cretaceous. Magmatism along this arc ceased soon after 90 Ma or before ca. 85 Ma, with its last pulse represented by a small group of ca. 100–85 Ma granitic intrusions in the eastern part of the northern South China Sea basin. The arc appears to have jumped toward the Western Pacific Ocean at or soon after 90 Ma, starting the development of the Western Pacific-type plate margin.

2) The South China Sea (SCS) is the largest marginal sea within the western Pacific. Extensive investigations have been conducted on the SCS, including scientific and industrial drilling, dredging, and multiple-channel seismic profiles. These surveys have significantly refined the understandings on the origin and subsequent opening of the SCS (Briais et al., 1993; Hsu et al., 2004; Franke et al., 2011; Barckhausen et al., 2014). In particular, recent International Ocean Drilling Program expeditions revealed that the northern SCS margin was neither completely “magma-rich” nor “magma-poor” identified in the other North Atlantic magmatism models (Larsen et al., 2018). Instead, the northern SCS is a representative of hyperextended margin, which is now considered as a missing link between “magma-rich” and “magma-poor” margins (Lei and Ren, 2016; Lei et al., 2019a). In order to precisely evaluate the Cenozoic tectonic evolution of the SCS, researches are also urged to be underpinned from the pre- Cenozoic framework and the geological processes which have greatly controlled the following Cenozoic evolutionary events. Beneath the Cenozoic sedimentary layer, the SCS Basin basement study is of crucial significance in structural geology and regional geodynamic reconstruction (Nissen et al., 1995a, 1995b; Braitenberg et al., 2006). However, ages and properties of the pre- Cenozoic basement still require accurate geological evidence to improve interpretation and integrated reviews of previous studies.

Antecedent attempted to illustrate the formation and composition of the SCS Basin basement were based on sketchy petrographic description as well as insufficient geochronological data. Particularly, the wide underlying components of Yinggehai Basin and Qiongdongnan Basin still were proved to be fairly problematic and poorly explored (Pigott and Ru, 1994; Braitenberg et al., 2006; Franke et al., 2011; Pichot et al., 2014). Their onshore continental margins were identified with Proterozoic schists and gneiss, Paleozoic and Mesozoic metaclastic rocks, carbonates and volcanic rocks (Sun et al., 2014). For the seaward extension, this offshore part is even harder to trace due to scarce borehole penetration and lacking of precise dating analyses. It was extrapolated that the Yinggehai and Qiongdongnan Basin basements might have generated similar lithological and tectonic features to the northern

Indochina Block margin (Nielsen et al., 1999). This assumption is in the light of basement consolidation during the collision and convergence between major continental blocks and scattered micro-terranes (Carter et al., 2001; Lepvrier et al., 2004; Li et al., 2006). According to previous studies, the onshore pre-Cenozoic meta-sedimentary strata and magmatic arc were likely to extend from land to sea. In some areas of Qiongdongnan Basin, the well-stratified formations are Mesozoic low-grade metamorphic sedimentary rocks (Nielsen et al., 1999). In the other sections, Precambrian metamorphic complexes were only restricted within continental shelf basement proximal to Vietnam (Hutchison, 1989; Dien, 1998). However, the low-resolution seismic profiles caused these considerations to remain uncertain. Upper Paleozoic carbonate platform deposits were also sporadically developed from the coastal region, such as the Beibu Gulf Basin and areas through the continental interior (Fyhn et al., 2018). Tectonically, this heterogeneous Paleozoic-Mesozoic basement surrounding the Hainan Island seems to be mainly controlled from a NW–SE fault system (Sun et al., 2014). These early discoveries have led to a series of questions on the overall assessment of the pre-Cenozoic SCS Basin basement regarding its physical properties and distribution patterns. Under which type of geodynamic background was the basement generalized? How did the basement control or influence the subsequent rifting of the Cenozoic SCS basins?

Along the South China Block southeastern margin, the broad distribution of granitic and granodioritic magmatic records show that an Andean-type active continental margin has already existed from late Triassic or early Jurassic, to Cretaceous (Zhou and Li, 2000; Li and Li, 2007; Yui et al., 2012; Faure et al., 2016; Xu et al., 2017). A drastic transformation from active to passive margin followed during the late Mesozoic (Li et al., 2012). The northern SCS Basin basement was considered as the southward extension of the South China Block, where thinned continental crust displays variable thicknesses (Hayes and Nissen, 2005; Lei and Ren, 2016; Lei et al., 2019a). According to Sun et al. (2014), lower-to-upper Paleozoic strata are supposed to be unevenly preserved in the Beibu Gulf Basin, western Zhujiang River Mouth Basin and Taixinan Basin (Fig. 1a). In early studies, sedimentary facies and seismic lines indicated that the pre-Cenozoic basement was divided into several separate sections and displayed an eastward trending of younger ages (Wang et al., 2002; Sun et al., 2014). The case lacking geochronological evidence has been changed until recent detrital zircon U-Pb dating results were obtained. Therein, two granite dredge samples were dated with magmatic ages varying from 159 Ma to 127 Ma in Nansha area (Yan et al., 2010). Additionally, Xisha area, to the southeast of Hainan Island, was previously postulated to be part of the Precambrian crystalline basement dated by Rb-Sr isochrones (Qin, 1987). Instead, the updated U-Pb age has

confirmed its late Jurassic amphibole plagiogneisses which was later intruded by Cretaceous magmatic bodies (Zhu et al., 2017). Therefore, it is questionable whether the Paleozoic or even Precambrian strata have ever been widely distributed beneath the Cenozoic northern SCS sediments? In addition, located in the conjunction of Yinggehai Basin, Qiongdongnan Basin and Zhujiang River Mouth Basin, the Hainan Island together with other dispersed micro-blocks were rifted from Gondwana supercontinent during the opening of the Palaeo-Tethys in the Devonian (Metcalf, 1996, 2011, 2013; Xu et al., 2008). Numerous researches show that the Hainan Island has recorded multiple thermal events and tectonic regime transitions since the late Paleozoic (Li et al., 2006; Jiang et al., 2015; Yao et al., 2017). As a key component of the SCS region, the Hainan Island as well as its surrounding areas still require further basement evaluation.

Principle of isostatic balance and gravity-field modeling are helpful in estimating the lateral density or thickness variations of the interior structure of the lithosphere (Braitenberg et al., 2006; Ebbing et al., 2006; Franke et al., 2011). These are essential methods and techniques in revealing lithospheric velocity anomalies. Another technique involves magnetic anomaly interpretations, which could reflect directions and speeds of the ridge spreading processes (Briaies et al., 1993; Hsu et al., 2004; Braitenberg et al., 2006; Li et al., 2008a, 2008b; Barckhausen et al., 2014). However, amplitudes of the basement features may be reduced in special cases where anomalies bend or two distinct directionalities meet. Moreover, due to the thick Cenozoic sedimentary blanket, the underlying flat-appearance structure might conceal different tectonic lineaments, tilted crustal highs, complicate-oriented ridges or faults. Therefore, ocean bottom topography not well charted could be very misleading in the crustal structure evaluation. Except for the weaknesses of the typical geophysical techniques, the subsequent rifting processes might also produce certain alteration onto the original pre-Cenozoic crustal structure (Nissen et al., 1995a, 1995b). In this case, the amount of crustal extension might be manifested in complicated manners in response to effective strengths, thicknesses, thermal structures and other rheological features according to disparate formation ages (Ebinger and Hayward, 1996; Clift and Lin, 2001; Qiu et al., 2001). For instance, the eastern SCS Basin basement generated widespread granite and sedimentary rocks during the late Mesozoic, where much extension is concentrated within younger, weaker and more ductile zones. Within the basement near eastern Hainan Island, on the other hand, the Paleozoic crust tends to be stretched in a similar degree to the more ancient Proterozoic crust (Hayes and Nissen, 2005). Hence, without constraints from any other supportive dating analyses, these geophysical parameters are likely to allow possible uncertainties.

Due to the limitation of the basal geological evidence and ongoing controversy over the formation of the pre-Cenozoic basement, this study aims to present a comprehensive interpretation by deriving a dense set of data, including petrographic identification, elemental geochemistry analysis, gravity-magnetic joint inversion and zircon U-Pb dating. Specifically, zircons are considered as a kind of widely formed and extremely stable minerals, which are resistant to chemical alteration by long-distance sedimentation and low- or medium-degree metamorphism. Since U-Pb isotopic system possesses the highest closure temperature, it is optimal to use U-Pb dating for the age determination of igneous or high-grade metamorphic rocks. Lithological combination characteristics and gravity-magnetic constraints are also instrumental in examining whether the results are internally consistent in this study. Questions remaining to be answered include: (1) what is the precise aging framework for the pre-Cenozoic SCS Basin basement? (2) what types of rock assemblages have been generalized with respect to different sections of the SCS Basin basement? (3) what tectonic events and geodynamic processes might have caused such distribution patterns of the answers to questions 1 and 2?

Summarized conclusions: the pre-Cenozoic northern South China Sea (SCS) Basin basement was supposed to exist as a complex of heterogeneous segments, divided by dozens of N-S faulting. Unfortunately, only the Hainan Island and the northeastern SCS region were modestly dated while the extensive basement remains roughly postulated by limited geophysical data. This study presents a systematic analysis including U-Pb geochronology, elemental geochemistry and petrographic identification on granite and meta-clastic borehole samples from several key areas. Constrained from gravity-magnetic joint inversion, this interpretation will be of great significance revealing the tectono-magmatic evolution along the southeastern margin of the Eurasian Plate. Beneath the thick Cenozoic sediments, the northern SCS is composed of a uniform Mesozoic basement while the Precambrian rocks are only constricted along the Red River Fault Zone. Further eastern part of the northern SCS below the Cenozoic succession was widely intruded by granites with Jurassic-to-early Cretaceous ages. Further western part, on the other hand, is represented by meta-sedimentary rocks with relatively sporadic granite complexes. To be noted, the western areas derived higher-degree and wider metamorphic zones, which is in contrast with the lower degree and narrower metamorphic belt developed in the eastern region. Drastic collisions between the Indochina Block and South China continent took place since at least late Triassic, resulting in large-scale suturing and deformation zones. At the westernmost part of the northern SCS, the intracontinental amalgamation with closure of the Meso-Tethys has caused fairly stronger and

broader metamorphism. One metamorphic biotite granite is located on the suturing belt and yields a Precambrian U-Pb age. It likely represents the relict from the ancient Gondwana supercontinent or its fringes. Arc-continental collision between the Paleo-Pacific and the southeast China Block, on the other hand, results in a relatively narrow NE–SW trending metamorphic belt during the late Mesozoic. Within the overall geological setting, the Cenozoic SCS oceanic basin was subsequently generated from a series of rifting and faulting processes along the collisional-accretionary continental margin.

3) We report zircon U-Pb geochronological, trace elemental geochemical and Lu-Hf isotopic results for drilling-penetrated plutonic rocks from the basement of the South and East China Sea basins and provenance analyses for metavolcaniclastic and meta-sedimentary rocks. Protoliths of our new metavolcaniclastic and meta-sedimentary samples, together with previously reported onshore and offshore records, commonly contain youngest zircon groups from ca. 145 Ma to ca. 85 Ma. The vast majority of the studied and compiled samples fall within the range of ca. 190–90 Ma (mostly between 180 Ma and 120 Ma), and are centralised around multiple age peaks, including ca. 175 Ma, 155 Ma, 150 Ma, 145 Ma, 120 Ma, etc. Minor populations of Proterozoic and Paleozoic detrital zircons do exist in a few samples, whereas extensive presence of immature meta-sedimentary rocks and paucity of older zircons from the crystalline basement farther inland preferentially indicate an in-situ or proximal provenance from the coastal South China (plus its seaward extension). It should be noted that the ancient Cathaysia crystalline basement might have been of broad extension during the Paleoproterozoic in contrast to its present scattered distribution as given by our singular ca. 1.84 Ga gneiss borehole sample with a variable Zircon $\epsilon\text{Hf}(t)$ range of -9.1–+3.9 from the ECS. Although further evidence is required, it likely to a certain degree constrains the origin and nature of late Mesozoic magma in the ECS.

Three granitic rock samples penetrating the Cenozoic successions yield zircon U-Pb ages of 103.3 ± 1.1 Ma, 115.1 ± 0.9 Ma and 163.5 ± 2.1 Ma. Zircon trace elemental geochemical results from both igneous and nearby-sourced clastic rock samples indicate arc-related tectonic setting. The corresponding $\epsilon\text{Hf}(t)$ values fall within the broad variations between -14 and +5.9 for SCS samples, and between -24.5 and +13.9 for ECS samples. Therefore, continual magmatic pulses along the South China margin are evidenced from the compiled ca. 190–180 Ma I-type coastal southeast China and northeast SCS–ECS granites, our newly dated ca. 165–100 Ma granites, and previously reported ca. 98–90 Ma volcanic and intrusive rocks from the western SCS and eastern Taiwan. It is thereby reasonable to suggest the existence of an Andean-type continental magmatic arc along the current continental shelf, from the outer

ECS, through eastern Taiwan to the east of Hainan Island during the Early Jurassic – Late Cretaceous.

Provenance analyses on the basis of compiled and studied samples reveal a low abundance of ca. 250–190 Ma zircons in the coastal belt, which is linked to the occurrence of flat-slab subduction with its magmatic front propagating craton-ward during Triassic–early Jurassic. This Andean-type arc magmatism largely became inactive soon after 90 Ma while episodic magmatic events remained ongoing in the northeastern SCS and ECS as evidenced by few ca. 85–80 Ma magmatic records and detrital zircons. After an oceanward retreat of the subduction system, the present continental shelf region was dominated by a Western Pacific-type plate margin with scattered ca. 70–60 Ma intrusions prior to experiencing the following drastic rifting processes during early Cenozoic.

4) Supercontinent cycles, characterized by amalgamation and dispersal of continental blocks/terranes, have exerted significant influence on the evolution of landmasses on Earth since at least early Proterozoic (Li et al., 2008a; Cawood et al., 2016; Li et al., 2023). The East and Southeast Asia lithosphere is a complex collage of multiple allochthonous continental fragments (e.g., the North China, South China, India, Indochina, Qiangtang, Sibumasu, Tarim and Lhasa blocks) with different Archean to Proterozoic crystalline basements (e.g., Metcalfe, 1996; Li et al., 2002b; Metcalfe, 2013). The role of those continental terranes in the Phanerozoic Gondwana and Pangea supercontinents is reasonably well-constrained, that most of them were once part of Gondwana during the early Palaeozoic before they gradually rifted separately and moved northward from the late Palaeozoic to Mesozoic (Metcalfe, 1996, 2013). However, discerning arrangement of those blocks and their components in the Proterozoic tectonics (Nuna and Rodinia supercontinent cycles) becomes a considerably greater challenge, which arises from the increasing paucity of reliable geological evidence when we delve further into Earth's ancient history (Cawood et al., 2018; Zhao et al., 2018).

Nuna (alternatively referred to as Columbia), is considered as the earliest recognized Precambrian supercontinent (Evans, 2013). It assembled during the Paleoproterozoic (ca. 2.0–1.6 Ga) with Laurentia occupying a central position of Nuna. Siberia and Baltica were situated to the east and southeast, respectively with present-day coordinates (e.g., Zhang et al., 2012; Evans, 2013; Pisarevsky et al., 2014; Li et al., 2019; Kirscher et al., 2021; Li et al., 2023). There are several cratonic blocks posited along the border of Laurentia, including East Antarctica (Moores, 1991; Hoffman, 1991; Goodge et al., 2008), Australia (Ross et al., 1992), North China (Hou et al., 2008), or the Cathaysia Block of South China (Li et al., 2008b; Zhang et al., 2012). The relative positions of those continents also generated substantial uncertainties

in the overall framework of the subsequent supercontinent, Rodinia (Li et al., 2023). It has been widely acknowledged that amalgamation and breakup of Rodinia supercontinent controlled numerous magmatic, sedimentary and tectono-thermal activities during the late Mesoproterozoic–Neoproterozoic (Cawood et al., 2013, 2016; Zhao et al., 2011). These geological events played a critical role in shaping the Earth's crust, hydrosphere, atmosphere as well as biosphere (Cawood et al., 2016). It is indicated that Earth's continental blocks were also largely involved in the Rodinia supercontinent cycle (Cawood et al., 2018; Li et al., 2008b). Nevertheless, configuration of Rodinia supercontinent remains hot debated (e.g., Evans, 2009; Li et al., 2008b), and in particular paleogeographic location of the South China Block stands as a key enigma (Cawood et al., 2013, 2018; Li et al., 2008b; Zhao and Cawood, 2012).

The South China Block is composed of Yangtze Block to the northwest and the Cathaysia Block to the southeast, and is regarded as one of the largest cratonic blocks in eastern Asia (Zhao and Cawood, 2012). By studying the internal constituents of the South China Proterozoic (as well as older) rock units, researchers have proposed various models for reconstructing the South China in Nuna and Rodinia supercontinents (Cawood et al., 2020; Liu et al., 2020). Paleo- and Mesoproterozoic basements from the northern and western Yangtze Block and Mesoproterozoic basement from the southwest Hainan Island were identified in previous studies (e.g., Yao et al., 2017; Zhang et al., 2019; Xu et al., 2020). Those Proterozoic rocks imply that the South China might have been involved in the assembly and breakup of Nuna. Unfortunately, precise position of South China remains poorly constrained with large ambiguity and uncertainty due to an extreme lack of geological records. Likewise, the placement of South China in the Rodinia supercontinent also remains controversial among different researchers despite more geological constraints (e.g., Li et al., 1995, 1999, 2002b, 2003; Zheng et al., 2007, 2008; Zhou et al., 2004, 2009; Zhao and Cawood, 2012; Wang et al., 2013, 2014b; Cawood et al., 2013, 2018; Zhang and Wang, 2016 and references therein). Consensus has not been reached yet whether the South China occupied in the core (Li, et al., 2002b, 2008b; Yao et al., 2017) or at the periphery (Cawood et al., 2013, 2018; Wang et al., 2013; Wang, et al., 2014b; Zhang and Wang, 2016, 2019; Zhao et al., 2011) within Rodinia supercontinent cycle. Although further evidence is required, the South China was recently suggested to have formed as an independent unit on a separate tectonic plate rather than a part of supercontinent (Merdith et al., 2017).

Hainan Island lies at the southern tip of South China and its basement plays an important role in paleogeographic reconstruction of the South China in supercontinent cycles (Li, et al., 2002b, 2008b; Liu et al., 2020; Xu et al., 2020; Yao et al., 2017; Zhang et al., 2018, 2019).

However, competing models still exist regarding the tectonic division and affiliation of Hainan Island. Some researchers divided Hainan into two fault-bounded terranes which contains a northerly unit attributed to South China and another southerly one attributed to Indochina or Australia (Xu et al., 2014; Yang et al., 1989; Yu et al., 1990). Unfortunately, precise delineation of position, structure and nature of the potential faults are hard to confirm due to isolated outcrops and thick tropical vegetation cover on Hainan Island. Other researchers divided Hainan into two Gondwana-affiliated terranes during the late Paleozoic including northwestern and southeastern units (Metcalf, 1994, 1996). There is another speculation that Hainan Island contains part of coastal continental block in the northwest (termed as “Huanan Block”), a Gondwana-derived terrane in the southeast (termed as “Dongnanya Block” and implied as eastern continuation of Sibumasu) (Hsü et al., 1990; Chen et al., 1992; Li et al., 2002a). Those researchers suggested a Mesozoic collision between those two aforementioned tectonic units and formation of “Shilu mélange” structure. However, this “Shilu mélange” was later identified to be Mesoproterozoic metasedimentary and metavolcanic rocks (Li et al., 2008b) and thus cast doubts on previous Mesozoic models.

It has been increasingly supported that Hainan basement became a southwestern continuation of Cathaysia Block after Proterozoic (e.g., GDBGMR, 1988; Shui, 1988; Zhang et al., 1990; Li et al., 2002b, 2008b). Sporadically cropping out in southwestern Hainan, the Baoban Complex consists of Mesoproterozoic metasedimentary and meta-igneous (formed at ca. 1.43 Ga) rock units. Presence of those Mesoproterozoic rocks were linked to the breakup of Nuna supercontinent in many previous studies (e.g., Xu et al., 2001; Li et al., 2008b; Yao et al., 2017; Zhang et al., 2018). Ca. 1.43 Ga igneous bodies of Hainan basement were coevally formed with the granite-rhyolite province in southern Laurentia (Li et al., 2002b, 2008b). Moreover, a group of ca. 1.6–1.5 Ga detrital zircons was detected in the Baoban Complex and Neoproterozoic sequences (Li et al., 2008b; Yao et al., 2017; Zhang et al., 2019), which seems to support correlative siliciclastic provenances between Hainan and Laurentia. These discoveries resulted in a widely-favoured interpretation that the Cathaysia might have lied adjacent to southwestern Laurentia prior to and during the assembly of Rodinia (ca. 1.5–1.35 Ga). By contrast, some researchers insist that the Hainan Island was not linked to the South China until the middle Paleozoic (Xu et al., 2020). In another word, the Mesoproterozoic Hainan record was unrelated to Cathaysia, and the South China largely lay outboard of western Laurentia during that time.

Therefore, more evidence of the composition, petrogenesis and tectonic evolution of the Hainan basement is required for a better constraint on the paleogeographic position in the

supercontinent cycles. In this study, we provide new geochronological and isotopic results from Mesoproterozoic offshore drilling samples to the southwest of Hainan Island for the first time. Combined with published dataset from both Hainan outcrops and possible adjoining continents, we aim to shed more lights on the Proterozoic tectonic setting of Hainan Island and unravel its paleogeographic relation with other continents during supercontinent cycles.

Summarized conclusions: located at the southwestern tip of South China Block, Hainan Island generated Proterozoic crystalline rocks which were included within the Cathaysia basement. Proterozoic tectonic evolution of Hainan Island has thus played a significant role in unravelling Nuna-Rodinia supercontinent cycles. Previous researchers conducted numerous studies on the Meso- to Neoproterozoic outcrops of Hainan basement. In this study, we collected offshore borehole samples for the first time which turn out to be southwestern extension of Hainan basement, and present new zircon U-Pb geochronological, trace elemental geochemical and Lu-Hf isotopic data for metamorphic biotite granites of Mesoproterozoic ages. Magmatic zircons from our drilling samples yielded a weighted mean $^{207}\text{Pb}/^{206}\text{Pb}$ age of 1454.8 ± 9.6 Ma, representing their crystallization ages. A large majority of our zircon $\varepsilon\text{Hf}(t)$ values are positive but range from -3.49 to +12.94, implying a dominant derivation from a juvenile source in addition to limited ancient crustal components. Our zircon geochemical and geochronological data, constrained by other regional geological evidence, commonly indicate that both onshore Baoban Complex (mainly consisting of 1.43 Ga igneous and metasedimentary rocks) and plutonic rocks of offshore SW Hainan basement largely formed in an anorogenic setting, and subsequently experienced metamorphism after ca. 1.3 Ga. Together with published data, our magmatic and provenance compilation among different continents confirms a unition of Tasmania, Cathaysia and Laurentia in the internal location of Nunasupercontinent during its breakup at ca. 1.45-1.43 Ga. During the following assemblage of Rodinia supercontinent, the Yangtze Block was amalgamated with Cathaysia by the Sibao orogeny up to ca. 1.3 Ga (part of Grenvillen-aged continental collision), pointing out the proximal affinity between Tasmania, Yangtze, Cathaysia and Laurentia landmasses.

5) Controversies on about the eastern margin of the Eurasia Plate, as a critical joint or collision zone of the Tethys and paleo-Pacific Ocean have never stopped (Ru and Pigott, 1986; Morley, 2012; Müller, et al., 2016). This region experienced ongoing, drastic subduction processes during the Mesozoic prior to the Cenozoic opening of the South China Sea (SCS) (Briais et al., 1993; Hall, 2002). Under this enormous geo-tectonic shifting from active to

passive continental margin, aside from the complexity and uncertainties of the southeast Asia drainage systems (e.g., Milliman and Farnsworth, 2013; Zheng et al., 2013), the reconstruction of early Cenozoic provenance evolution of the northern SCS has also been restricted to available bore-hole samples and scarce reliable dating results. Source-to-sink analysis is a promising tool to track erosional processes in the hinterland to the depocenters in adjacent sedimentary basins. Concerning the large quantities of sediments deposited in the sedimentary basins of the northwestern SCS during Cenozoic times, the Red River system was possibly responsible for the sediment supply from the Tibetan Uplift, although no precise timing constraint is available for the following drainage catchment (e.g., Clark et al., 2004; Clift, 2006a). Instead, the thick succession in the Yinggehai-Qiongdongnan Basin seems to be derived from the Central Vietnam area during the late Oligocene–Miocene attested by geochemical data (Zhao et al., 2015a; Yan et al., 2011). Consistently supported by NW–SE–oriented seismic profiles transecting the Qiongdongnan Basin, the fluvial drainage geometry, with incised channels and deltaic progradation structures since the early Miocene, indeed requires possible supplement from the continental Vietnamese margins (Wang et al., 2014; Zhong et al., 2013). The newly obtained seismic compilation even implies the presence of paleo-channels transporting detritus possibly dating back to the early Oligocene. Considering the complexity of proximal provenances, double- or multiple-contributor models were developed for regional depressions focusing on short time scales, particularly on post-Oligocene episodes (Yao et al., 2008). It was unraveled that the Central Canyon has been dumped with terrigenous sediments, from both Central Vietnam and Hainan Island, since the late Miocene (Cui et al., 2018). But hypotheses of long-time scales are still questionable due to the absence of independent geological evidence. Paucity of basin-scale provenance constraints also prevents the possibility of paleo-structure reconstruction.

To the east, increasing information on drainage-basin interactions has been extracted from Eocene–Oligocene sequences. Under the stepwise westward expansion of its drainage basin, the Pearl River is assumed to have gradually enlarged its influence on the SCS since the Oligocene (Ru and Pigott, 1986; Clift et al., 2006b; Shao et al., 2015; Cao et al., 2018). Contemporaneously, sediments were widely accumulated in the middle Zhu-II Depression during the late Oligocene thermal subsidence period (Pang et al., 2006). Previous provenance studies mainly focused on irregularly distributed sags or uplifts covering only short time intervals. Particularly, aside from the contributions of Mesozoic igneous rocks from the South China Block and the intra-basinal uplift zones, it is elusive when and how the Pearl River dominated the overall provenance pattern as a long-distance source (Liu et al., 2016). Also, a

neglected but essential provenance to the Zhu-II Depression in southern SCS, might somehow imply a vanished but once critical conduit, which is characterized by eastward or northeastward directed sediment transport from seismic data. Unfortunately, the limited number of integrated boreholes penetrating deep-sediment successions have restricted better understanding on this potential source.

Zircon U-Pb ages on bedrocks and sediments made great contributions in constraining age compositions in surrounding potential suppliers. Resistance to diagenesis and high closure temperature of U-Pb systems ensure the unchanged detrital zircon signatures of source rocks (Moecher and Samson, 2006; Dickinson and Gehrels, 2009; Clift, 2016). Source rock identification is supported by basic-acidic rock type differentiation derived from diagenetically stable rare earth elements (REE; McLennan, 1989). In particular Eu anomalies are ubiquitously utilized in provenance discrimination studies as mafic-ultramafic rocks are typically featured by positive values, contrary to the negative values of acidic-sedimentary samples. By comparing zircon ages and REE patterns separately, we are able to properly recognize the source-to-sink systems. However, due to possible sedimentary mixing effects from various end members, correlating sediments with potential terranes should be considered cautiously.

Employing powerful provenance tools, we aim to address the following problems based on new results from northern SCS basin samples: (1) when and how did the Pearl River influence the provenance pattern during the early Cenozoic and (2) did previous orogenic belts in Central Vietnam severely influence SCS sedimentary evolution?

Summarized conclusions: a combination of detrital zircon U-Pb geochronology and rare earth element geochemistry was employed to investigate the “source to sink” pathways of Eocene–lower Miocene strata in the northern South China Sea (SCS) taking into account the evolution of the surrounding drainage systems in comparison to the basin sediments. Drastic provenance transformation on the SCS sedimentary patterns has been first discovered that source of Central Vietnam was replaced by Pearl River networks. Rapidly changing local provenances of different source rocks were discerned during Eocene and early Oligocene times. Briefly, the Pearl River drainage system gradually evolved by regional tectonic processes into the present scale and exerted its influence on the northern SCS basins. During early Oligocene, only limited areas received sediments from Pearl River tributaries on the South China continent, while the majority of the southern areas were controlled by the Central Vietnam provenance before the late Oligocene. After the early Miocene, significant amounts of sediment from the inner South China continent were transported into northern SCS basins by the western Pearl River tributaries. Meanwhile, an impressive “Kontum-Ying-Qiong” river system (K-Y-Q) had

delivered huge amounts of sediments from Central Vietnam mafic-to- ultramafic source rocks to the regions farther east since the early Oligocene or even Eocene. This remarkable K-Y-Q traversing the whole Qiongdongnan Basin was gradually replaced by a transport system from the adjacent Hainan Island, in modern-day China, providing acidic detritus after the early Miocene. Admittedly, Tethyan subduction beneath Sundaland makes the paleo-reconstruction work tough and elusive. However, we laid the emphasis on possible basin depositions to unravel the mystery and our discovery of the impressive conduit from Central Vietnam of the Indochina Block, transferring abundant basic sediments derived from the Indosinian event, surely would be of remarkable significance on research of (1) paleo-geographical evolution by Tethys-southern Eurasia Plate collisional effects and (2) tectonic reconstruction for the entire southeastern margin of the Eurasian continent.

6) The Pearl River is one of the most important rivers along the South China continental margin. It has been transporting a large amount of sediments to the northern South China Sea since at least the mid-Cenozoic. As a result, large-scale deltas and submarine fans were formed throughout the Oligocene–Miocene in the Pearl River Mouth Basin (Peng et al., 2004; Pang et al., 2007; Wang et al., 2012); here many oil and gas reservoirs have been explored. Research on the evolution of the Pearl River is significant not only for systematically understanding ‘source-to-sink’ sedimentary processes in the SCS, but also for petroleum exploration in this region.

East Asia is known as the third pole on the planet, where the world's highest plateau and numerous fluvial systems all develop. During the Cenozoic, plate collision led to the uplift of the Xizang (Tibetan) Plateau, and East Asia experienced drastic topographic reversion from east-high–west-low to west-high–east-low. Accordingly, the development and reorganization of the river systems can directly reflect the general geomorphic evolution (e.g., Zheng et al., 2017). The Pearl River originates from the southeastern margin of the Xizang (Tibetan) Plateau, and its evolutionary process has been under direct control from the East Asian topography. Earlier research demonstrated that the Pearl River experienced stepwise evolution into its modern continental scale, in close relation to the multi- phase topographic inversion caused by the Xizang (Tibetan) uplift and SCS expansion (Wang, 2005). ODP site 1148 revealed that the northern SCS was influenced from different provenances across the Oligocene/Miocene boundary with unconformities possibly formed by regional tectonic events (Cliff et al., 2002; Li et al., 2003). Increasing lines of evidence confirm that the evolution of the northern SCS provenance has been closely linked with the continental-scale fluvial networks, such as the Pearl River (Shao et al., 2015, 2017, 2019a, b; Cao et al., 2018; Zhang et al., 2020). Apparently,

the coupling relationship between the Pearl River evolution and the Xizang (Tibetan) uplift is significant for restoring the East Asian topography–geomorphology evolution. In this paper, we use published data to make ‘source-to- sink’ provenance analyses with the aim of systematically deliberating the birth and evolutionary history of the Pearl River.

Summarized conclusions: as the link connecting the South China Continent and the northern South China Sea (SCS), the Pearl River is the focus of sedimentology and petroleum geology research. Its evolutionary process and controlling factors are of great significance in revealing the East Asian continental landscape reorganization during the Late Cenozoic. Based on published data, ‘source-to-sink’ provenance analyses allow systematic deliberation on the birth and evolutionary history of the Pearl River. Close to the Oligocene/Miocene boundary, an abrupt shift in the sedimentary composition indicates significant westward and northward expansion of the river’s watershed area, followed by the establishment of a near-modern fluvial network. This sedimentary change generally concurred with a series of regional geological events, including the onset of the Yangtze throughflow, large-scale development of the loess plateau, and formation of the northwestern arid zone and Asian Monsoon system. These major changes in the geology-climate-ecoenvironment system are in close response to the process of the Cenozoic Xizang (Tibetan) Plateau uplift. Consequently, the East Asian continental landscape and most of mid- Cenozoic drainage systems underwent critical reversion into east-tilting, or east-flowing networks.

7) Reservoir quality of sandstones is critically impacted with the clastic composition controlled by provenance distribution patterns. Therefore, potential sources and sedimentary transporting routes of the northern South China Sea (SCS) are of remarkable significance on hydrocarbon exploration as well as on geological information archive, such as paleo-environmental changes and tectonic evolution (Morton et al. 2001; Rossi et al. 2002). Nevertheless, it virtually remains further investigation due to the complexity of geological framework, limited borehole coverage and poorly dated stratigraphy in this region, particularly northwestern SCS area. Submarine canyons, which strongly dissect continental margins, are commonly regarded as significant conduits for sediment transfer from continental shelf into deep-sea basins (Popescu et al. 2004; Antobreh and Krastel 2006; Harris and Whiteway 2011). As important hydrocarbon reservoirs, these canyons or channels possess the potential of accumulating huge amount of sandy deposition, which have always attracted widespread interests all over the world (Mayall et al. 2006; Gong et al. 2011). Globally, sediments transported in canyon systems not only gathered voluminous oil and natural gas resources, but also kept high-quality record of regional structural evolution, environmental and climatic

change information (Hale et al. 2014; Bayliss and Pickering 2015; Flecker et al. 2015; Reimchen et al. 2016). Enhanced understanding of these geological structures on morphology, composition, evolution as well as depositional dynamics has been greatly generalized resulting from high-resolution seismic data and sequence stratigraphy (Arzola et al. 2008; Mountjoy et al. 2009; Jobe et al. 2011).

The present “S-shaped” Central Canyon is a large axial submarine system with an approximate length of 570 km and width of ~9–30 km, which lies paralleled to the shelf break and stretches with a NE–NEE orientation in the northwestern margin of the SCS (Fig. 1b). Due to its unique internal architecture and interplay of erosion and aggradation processes, forming mechanisms and sedimentary provenances of the Central Canyon area have long been in debate over the past 10 years (He et al. 2013). It has been implied that sufficient sediments for the initial growth of Central Canyon were provided by rapid and broad Tibetan Plateau uplift around 5.5 Ma (Gong et al. 2011). Meanwhile, the Red River Fault movement also induced high-energy gravity flows providing voluminous material (Yuan et al. 2009). By contrast, Li et al. (2017a) favored that eastern Vietnam has already delivered sufficient sediments with large-scale submarine fans stepwise developing in Central Canyon since 10.5 Ma. Based on further integration and compilation of 2D/3D seismic and well log profiles, provenance evolution was reconstructed for different segments in the Central Canyon source-to-sink system (Su et al. 2013; Li et al. 2017b). After describing morphological characteristics and dissecting internal architectures of the Central Canyon system, Su et al. (2013) developed multi-phases including initial, eroded infilling, tranquil infilling and rejuvenation period in order to reconstruct provenance evolution. On one hand, northern continental slope and major potential sources including Red River, eastern Vietnam or Hainan Island were dominant suppliers to the northwestern SCS, on the other hand, Qiongdongnan tectonic transformation was likely to constrain the evolution of Central Canyon eastern segment around 11.6 Ma (Xie et al. 2006, Su et al. 2014). However, due to lack of convincing evidence requested by source-to-sink system analysis, temporal and spatial variations of sediment composition patterns in Central Canyon area since late Miocene are still perplexing issues from the perspective of origination and infilling mechanisms, which seem even harder to be deeply interpreted by the complicated potential sources adjacent to Yinggehai–Qiongdongnan Basin illustrated in detail as follows. Although details on provenance of Red River remain controversial, its modern drainage system has been revealed as maximum discharge delivering high volumes of sediments into the northwestern SCS during the Neogene, likewise, the paleo–Red River was also presumed to be a significant source (Clift et al. 2006; Milliman and Farnsworth 2011; Zhao et al. 2015).

Seismic profiles initially indicated that progradational slope clinoforms were not largely generated in Hainan Island until the late Cenozoic (Van Hoang et al. 2010; Xie et al. 2008). Verified by U–Pb age dating, Hainan Island has already exerted its impact on sediment supply to its adjacent basins during Oligocene–Miocene (Shao et al. 2016; Yan et al. 2011). Additionally, eastward progradation from the Vietnamese margin into the western Qiongdongnan Basin and low degree of weathering conditions from geochemistry analysis together imply a Central Vietnam provenance since the Miocene, which is contrast to the speculation of little sediment delivery due to absorption of the Mekong River drainage basin (Ma et al. 2016). A series of intensive local mafic volcanic activities was also indicated by mineral assemblage of augite and olivine and positive Eu anomalies in the Qiongdongnan Basin during late Cenozoic (Fyhn et al. 2009; Zhao et al. 2015). Similarly, how exactly this suite of provenances influenced the Central Canyon's sedimentary evolution since its origination is scarcely systematically discussed and remains rather elusive.

Provenance studies of sedimentary sequences are critical to basin history analysis and natural resource exploration. It is ineffectively to interpret the source-to-sink system solely based on traditional petrography or heavy minerals particularly in the complicated source areas. Zircon is uniquely characterized by its mineral stability which can withstand mixed effects of weathering, erosion as well as thermal alteration processes (Kosler 2003). Due to its stable isotopic system under different pressure, temperature and fluid composition conditions (Moecher and Samson 2006), detrital zircon U–Pb age spectra dated by Laser Ablation Induction Coupled Plasma Mass Spectroscopy have been increasingly considered as a valuable tool in wide range of geological researches (Cao et al. 2018; Horton et al. 2008; Condie et al. 2009). In addition to zircon U–Pb geochronology, immobile trace elements, especially rare earth elements (REE) are also robust indicators of source rock geochemistry as these elements suffer minor modification from sorting, fractionation and diagenesis processes during transportation (Shao et al. 2017; McLennan 1989). Although detrital single-grain analysis has gained much popularity among provenance studying field, bulk rock geochemistry is still able to provide quantitative insights into siliciclastic sediments.

In this study, we aim to address the following problems by focusing on new results of detrital zircon U–Pb ages and geochemical analysis from Yinggehai Basin and Qiongdongnan Basin, in comparison with recalculation and integration on published or unpublished data from Central Vietnam, modern Red River, Hainan Island and SCS basement: (1) what exactly are the sediment contributors surrounding the SCS for the Central Canyon and what types of clastic materials did they provide? And (2) what is the sedimentary infilling history for the entire

Central Canyon during late Miocene–Pliocene?

Summarized conclusions: Provenance studies of the Central Canyon, Qiongdongnan Basin has provided significant insights into paleogeographic and sedimentology research of the South China Sea (SCS). A suite of geochemical approaches mainly including rare earth elemental (REE) analysis and detrital zircon U–Pb dating has been systematically applied to the “source-to-sink” system involving our upper Miocene–Pliocene Central Canyon sediments and surrounding potential source areas. Based on samples tracing the entire course of the Central Canyon, REE distribution patterns indicate that the western channel was generally characterized by positive Eu anomalies in larger proportion, in contrast to the dominance of negative values of its eastern side during late Miocene–Pliocene. Additionally, for the whole canyon and farther regions of Qiongdongnan Basin, the number of samples bearing negative Eu anomalies tended to increase within younger geological strata. On the other hand, U–Pb geochronology results suggest a wide Proterozoic to Mesozoic age range with peak complexity in Yanshanian, Indosinian, Caledonian and Jinningian periods. However in detail, age combination of most western samples displayed older-age signatures than the eastern. To make it more evidently, western boreholes of the Central Canyon are mainly characterized with confined Indosinian and Caledonian clusters which show great comparability with mafic-to-ultramafic source of Kontum Massif of Central Vietnam, while eastern samples largely bear with distinguishable Yanshanian and Indosinian peaks which more resemble with Hainan Island. Based on geochemistry and geochronology analyses, two significant suppliers and sedimentary infilling processes are generated: (1) the Indosinian collision orogenic belt in central-northern Vietnam, Indochina has ever played significant role in Central Canyon sedimentary evolution, (2) Hainan Island once as a typical provenance restricted within eastern Central Canyon, has been enlarging its influence into the whole channel, even into the farther western regions of Qiongdongnan Basin.

8) An accretionary prism is generally formed by frontal accretion in a subduction zone by scraping marine sediments off the downgoing oceanic slab or forearc underplating at convergent margins (e.g. Abbott et al., 1994; Brown and Spadea, 1999; Moore et al., 2001; Clift and Vannucchi, 2004). As a typical accretionary wedge, Taiwan Island is well known for its geodynamic processes associated with subduction and oblique collision between the Eurasian continent and the Philippine Sea Plate (PSP). After cessation of seafloor spreading at ca. 16 Ma, the South China Sea (SCS) began to subduct eastward beneath the northwest-moving PSP along the Manila Trench, generating the Hengchun accretionary prism and Luzon forearc basin (Briais et al., 1993; Huang et al., 1997; Sibuet and Hsu, 2004; Barckhausen et al.,

2014; Richter and Ali, 2015). The accretionary prism progressively increased in size, thickened and was then uplifted when the Luzon Arc of the PSP encroached upon the Eurasian continental margin (Huang et al., 2006; Lester et al., 2013). Since this collision takes place in an oblique direction to the convergent boundary, the orogenic belt has been propagating southward on Taiwan Island (Suppe, 1984). The Hengchun Peninsula is the most recently exposed part of Taiwan Island and preserves relatively intact upper Miocene deep-sea successions. Therefore, the Hengchun Peninsula represents a superb setting to address unresolved problems related to SCS sedimentology and plate motion histories.

Deep-marine turbidite sandstones have been documented on both sides of the Hengchun accretionary prism. However, many disputes remain regarding their provenances and transport routes. Based on paleocurrent measurements and geochemical analyses, the SE coastal South China Block was originally thought to have supplied sediments from the northwest but is currently hundreds of miles from the Hengchun Peninsula. In previous source-to-sink analyses, scholars attributed the Hengchun turbidites to the mainland of southern China via the paleo-Minjiang or Jiulongjiang River (e.g., Chen et al., 1990; Xu and Chen, 2010; Zhang et al., 2014, 2017). These interpretations are mostly supported by the speculation of seaward shifts in the SE China coastline and late Miocene monsoon intensification, which possibly facilitated sedimentary delivery from broad inland areas. Alternatively, these paleo-tributaries, such as paleo-Minjiang or Jiulongjiang River, were recently implied to be associated with short-distance runoff with confined drainage areas (Chen et al., 2018b). The sediments transported by these rivers and the Hengchun Peninsula turbidites actually show differences on their U–Pb spectra. In any case, regarding the mineral compositions and properties of the Hengchun turbidites, their depositional and hydrodynamic conditions seem less closely linked with the coastal SE South China Block as a dominant provenance. Contrasting paleocurrent directions (SE to NW) and tectonic rotation have further complicated the transport pathway of the Hengchun turbidites (Chang et al., 2003; Shan et al., 2013). The distinct transport routes were ascribed potentially to intense compression and rotation activities. Proto-Taiwan (or the Central Ridge), the Luzon Arc and the SCS or PSP oceanic lithosphere have also been suggested as minor sources (e.g., Page and Lan, 1983; Kirstein et al., 2010; Chen et al., 2019; Tian et al., 2019). However, previous interpretations do not provide convincing geological evidence for basinal paleo-uplift or active forearc contributions.

In addition to the prevalence of deep-marine sandstone deposits, the Hengchun Peninsula remarkably features abundant mafic rocks. These accreted mafic clasts exhibit different degrees of roundness and meta- morphism. Most scholars consider that Hengchun Peninsula contains

several ophiolite-bearing stratigraphic units, including the Kenting Melanges, Shihmen Conglomerate, the Cingwashih slump deposits and Lilungshan Sandstone. Of these igneous materials, rounded basalt and gabbro conglomerates are valuable sedimentary deposits for revealing the crustal properties of the convergent plates and were deposited synchronously within thick-bedded turbidite sandstones. According to previous research (e.g. Page and Lan 1983; Pelletier and Stephan, 1986), fragments of the SCS oceanic crust were incorporated into the accretionary wedge along the Manila Trench since the middle Miocene. The ophiolitic materials were possibly originated from a slice of Oligocene-lower Miocene SCS crust obducted upon the Chinese passive margin (Zhang et al., 2014). In those studies, dating of the mafic rocks resulted in ambiguous ages which are mostly based on biostratigraphy, structural analysis and regional geophysics. A recent study suggested that the overriding PSP possibly provided one source region of both normal and enriched mid-ocean ridge basalts (N-MORBs and E-MORBs, respectively) accreted onto the Hengchun Peninsula (Chen et al., 2018a). However, this model appears to neglect the significant role of the Gagua Ridge, which blocks any potential constituents from the PSP slab. Instead, Tian et al. (2019) attributed the E-MORBs to fragments of the Luzon volcanic arc or the Huatung Basin. Additionally, Hengchun ocean island basalts (OIBs), with later recycling and rounding, might represent the product of SCS seamount subduction under a submarine eruption environment (Lin et al., 2009; Tian et al., 2019). In summary, the age and origin of these mafic clasts remain controversial, with numerous models proposed to explain their separate emplacement mechanism. Mafic materials (N-MORBs and E-MORBs) from both subducting and overlying slabs were mixed with the fine-grained sediments, and were widely distributed in the Hengchun accretionary wedge (Kirstein et al., 2010; Zhang et al., 2014; Tian et al., 2019). In particular, the OIB-type rounded Shihmen Conglomerates were attributed to the gravity-driven collapse of seamounts. Mafic rocks dispersed in the Kenting Melanges and slump deposits in the Cingwashih area, on the other hand, might directly derive from the intensive tectonic shearing of the accretionary complex (Zhang et al., 2016). However, the presence of rounded mafic pebbles within the complete records of turbidite sequences is still problematic and thus remains a goal of further investigation. Namely, the mafic pebbles seem to have been uniquely and abundantly deposited as the bottom layers of the turbidites rather than subsequently mixing with exotic sedimentary clasts.

In this work, we combine field observations, petrography, geochemistry and U–Pb geochronology of Hengchun polygenetic blocks, and samples from International Ocean Discovery Program (IODP) 367/368 and commercial boreholes in the northern SCS to address

the following questions: 1) What are the precise ages of the mafic pebbles in the Hengchun turbidites? Are they derived from typical oceanic crust or submarine seamounts? 2) What is the dominant provenance of the thick-bedded turbiditic sandstones on the Hengchun Peninsula? 3) What mechanisms are responsible for the deposition of mafic pebbles as the Ta conglomerate layer (basal layer) within turbidite sequences? 4) Finally, what regional tectonic and geodynamic implications for the interacting SCS and PSP plates can be inferred from our sedimentary constraints?

Summarized conclusions: although plate motion models for the Philippine Sea Plate (PSP) are relatively well established, they remain to be confirmed by reliable geological records. Oblique convergence between Eurasia and the PSP has resulted in the uplift of Taiwan Island along the plate boundary. As the latest exposed portion of Taiwan, the Hengchun Peninsula features well-preserved deep-sea turbidites with rounded mafic conglomerate clasts. We apply an integrated source-to-sink analysis and broad field investigations to generate a reliable kinematic reconstruction linking the Hengchun turbidite outcrops with South China Sea (SCS) borehole sediments. Deposited in the lowermost turbidite layer, the Hengchun rounded gabbro and basalt clasts resemble the SCS oceanic crust based on our U–Pb geochronological (~23.6–25.4 Ma) and elemental geochemical results (normal mid-ocean ridge basalts), along with previous magnetic anomaly constraints. The multimodal U–Pb spectra of the matrix-supported sandstones suggest a mixed provenance including central Vietnam, the Pearl River tributaries and potential intrabasinal uplifts, which have not received prior consideration. During the late Miocene, abundant terrigenous sediments from the eastward-flowing “Kontum-Ying-Qiong River” and Pearl River were transported into the submarine environment. The extensive turbidity currents scoured and eroded the SCS mid-ocean ridges, which feature numerous low-angle detachment faults. These materials of various sources were transported eastwards for thousands of kilometers prior to their incorporation into the accretionary prism adjacent to the Manila Trench. From the late Miocene to Pleistocene, the PSP moved northwestward at estimated velocities of ~61–65 mm/yr, facilitating the final uplift and exposure of the accretionary prism.



A Mesozoic Andean-type active continental margin along coastal South China: New geological records from the basement of the northern South China Sea

Yuchi Cui^{a,b}, Lei Shao^{a,*}, Zheng-Xiang Li^b, Weilin Zhu^a, Peijun Qiao^a, Xiangtao Zhang^c

^aState Key Laboratory of Marine Geology, Tongji University, Shanghai 200092, China

^bEarth Dynamics Research Group, The Institute for Geoscience Research (TIGeR), School of Earth and Planetary Sciences, Curtin University, GPO Box U1987, Australia

^cResearch Institute of Shenzhen Branch, CNOOC, Shenzhen 518000, China

ARTICLE INFO

Article history:

Received 19 December 2020

Revised 14 June 2021

Accepted 26 June 2021

Available online 1 July 2021

Handling Editor: Y.J. Liu

Keywords:

Andean-type plate margin

South China Sea

Mesozoic

Magmatic arc

Flat-slab subduction

U-Pb ages

ABSTRACT

Integrated analyses of in situ zircon U-Pb ages and geochemistry were conducted on both granitic and metasedimentary borehole samples from immediately below the Cenozoic sedimentary cover of the northern South China Sea basin. Our work suggests that basement rocks of the South China Sea basin are not Proterozoic or Paleozoic rocks, as previously speculated based on gravity-magnetic inversion work. The analyzed metavolcaniclastic and metasedimentary rocks were likely deposited at or soon after ca. 145 Ma but prior to ca. 85 Ma. A nearby source in coastal South China is proposed based on the generally immature nature of the metasedimentary rocks and the lack of detritus from older basement rocks farther inland. The vast majority of the metavolcaniclastic samples have sparse ca. 250–190 Ma (particularly 200–190 Ma) zircons. This magmatic quiescence is consistent with the existence of a coastal magmatic gap to the east of Hainan Island during this time, previously interpreted as reflecting a period of flat-slab subduction. Metaclastic samples mostly exhibit a dominant ca. 180–120 Ma zircon population, indicating extensive magmatism along the coastal areas. This finding, together with previously reported ca. 190–180 Ma I-type coastal granites and our newly dated ca. 115–98 Ma volcanic and granitic rocks under the western part of the South China Sea basin can best be interpreted by the former presence of an Andean-type continental arc during the Middle Jurassic – Early Cretaceous. Magmatism along this arc ceased soon after 90 Ma or before ca. 85 Ma, with its last pulse represented by a small group of ca. 100–85 Ma granitic intrusions in the eastern part of the northern South China Sea basin. The arc appears to have jumped toward the Western Pacific Ocean at or soon after 90 Ma, starting the development of the Western Pacific-type plate margin.

© 2021 International Association for Gondwana Research. Published by Elsevier B.V. All rights reserved.

1. Introduction

Typical active continental margins include Andean-type plate margins and Western Pacific-type plate margins. Andean-type margins feature the development of active continental arcs, which is in contrast with the Western Pacific-type margins that feature the development of marginal oceanic basins. Andean-type plate margins are characterized by continental arc magmatism, both interplate and intraplate seismicity, fold and thrust belts, and foreland basins (e.g., Jahn et al., 1976; Klimetz, 1983; Lapierre, et al., 1997; Ramos, 1999; Zhou and Li, 2000). The collision of aseismic ridges or oceanic plateaus along such margins often causes flat-slab subduction where a segment with a mag-

matic gap forms in place of the normal magmatic arc (Ramos and Folguera, 2009; Kazuo and Teruyoshi, 2013). On the other hand, Western Pacific-type margins are generally characterized by an extensional tectonic environment. Therein, back-arc or marginal oceanic basins are produced that separate the continental margins from the oceanic arcs. However, several questions remain: 1) Was there ever an Andean-type continental margin along the Western Pacific? 2) When did the Western Pacific-type active margin start? 3) What tectonic process resulted in the switching of active margin types?

To the northwest of the Pacific Ocean, continental East Asia is an assemblage of the Siberia, Mongolia, North China, South China and Indochina cratons/continental blocks (Fig. 1) that developed an active continental margin along its border with the Paleo-Pacific Ocean (e.g., Metcalfe, 1996). An Andean-type active continental margin is widely believed to have developed along the southeast-

* Corresponding author.

E-mail address: lshao@tongji.edu.cn (L. Shao).

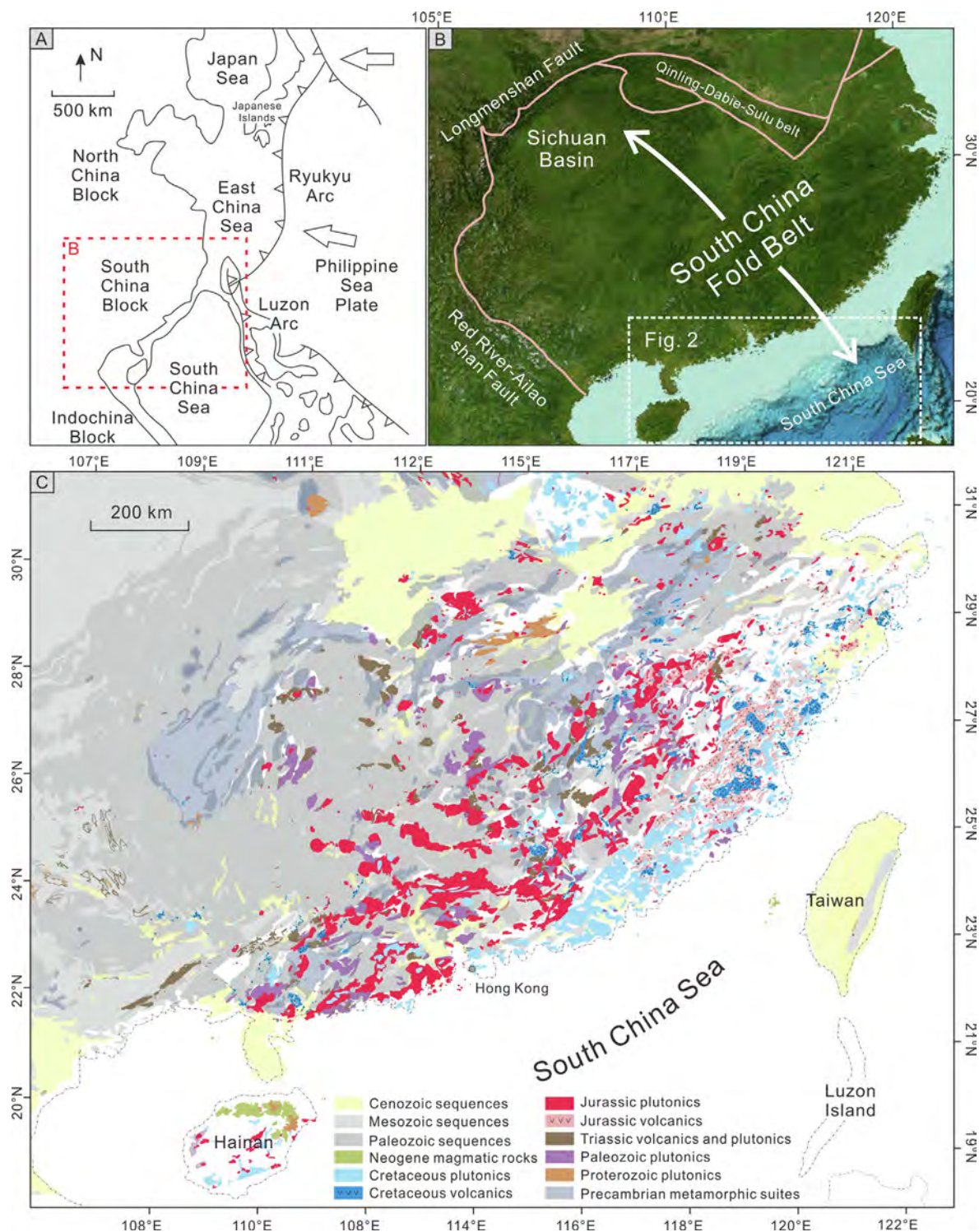


Fig. 1. A) Schematic map of Southeast Asia showing the major tectonic units; B) Digital topography of the South China Block (original data from the General Bathymetric Chart of the Oceans (GEBCO) [https://www.gebco.net/data_and_products/printable_maps/]) showing the width of the South China Fold Belt and major boundary faults; the position of our study area (see Fig. 2 for details) is also shown; C) A simplified geological map of South China.

ern margin of the South China Block between the Triassic – Jurassic and Middle Cretaceous. The existence of this convergent plate margin has been documented by the widespread development of a broad continental volcanic arc (e.g., Klimetz, 1983; Charvet et al., 1994; Zhou and Li, 2000; Zhou et al., 2006; Li and Li, 2007; Li et al., 2012b). However, the subduction of the Paleo-Pacific Plate could have initiated as early as the late Carboniferous or the early

Permian, as indicated by geological records from the Japanese islands (Isozaki et al., 2010). The onset of the continental magmatic arc along southeastern South China is indicated by a middle Permian (ca. 265 Ma) arc pluton on Hainan Island (Li et al., 2006), and more recent work has suggested that the continental arc there could have started as early as 290–280 Ma (Li et al., 2012a; Zhang et al., 2019).

Li and Li (2007) and Li et al. (2012b) proposed that similar to the present-day Andean margin, coastal South China experienced an episode of flat-slab subduction during 250–200 Ma. They further speculated that once flat subduction was jammed by ca. 200 Ma, normal subduction was reinitiated along the coastal zone, based on both kinematic necessity and the reappearance of magmatic and volcanoclastic rocks along the coastal zone. Similarly, Xu et al. (2017) revealed arc-related magmatism in the Early Jurassic (198–195 Ma for magnesian granite and diorite, 187 Ma for granodiorite) in the NE South China Sea and the SW East China Sea basin areas. In addition, boreholes in the NE South China Sea basin have penetrated numerous Late Cretaceous granites, granodiorites, diorites and monzonites (Table 1; Qiu et al., 1996; Li et al., 1999).

Similar metavolcanic rocks and granites have also been observed farther south and west in the Southeast Asia region, including Palawan, SE Vietnam, northern Borneo, and other areas along the Sundaland margin (e.g. Nguyen et al., 2004; Hennig et al., 2017; Shao et al., 2017; Shao et al., 2019). Nguyen et al. (2004) reported the initiation of arc magmatism in southern Vietnam on the basis of 112–88 Ma I-type calc-alkaline granitoid bodies. Hennig et al. (2017) interpreted the 130–80 Ma meta-igneous rocks in SW Borneo to have been formed during the Paleo-Pacific subduction beneath the Indochina-East Malaysia Block. Suggate et al. (2014) proposed that the late Cretaceous metasedimentary rocks of the Palawan Terrane were derived from the South China margin, and the terrane rifted away to the south during the subsequent opening of the South China Sea during early Cenozoic.

Mesozoic rocks underlying the Cenozoic basin of NW South China Sea have so far only been sporadically reported with limited geographic extent. Here, we report new age and geochemical data from granitic bodies and metasedimentary rocks penetrated by offshore hydrocarbon exploration drill holes along the continental margin of the northern South China Sea (Fig. 2). By combining our new results with a regional data compilation and synthesis, we aim to systematically investigate 1) the initiation and evolution of the Andean-type active continental margin along this section of the Western Pacific margin and 2) the tectonic processes that might have caused the switch from an Andean-type to the Western Pacific-type convergent plate margin.

2. Geological setting and sampling

The South China Block hosts three Permo-Triassic – Jurassic orogens: the Qinling-Dabie-Sulu orogen along its northern margin;

the Longmenshan Fault zone along its northwestern margin; and the northeasterly-trending South China Fold Belt over the southeastern half of the continental block (Fig. 1). In the South China Fold Belt, the ages of thrusting, metamorphism and synorogenic magmatism show a trend of younging toward the cratonic interior (Li and Li, 2007). Subduction-related calc-alkaline I-type granites were dated from ca. 265 Ma to ca. 190 Ma and were reported in both inland and coastal areas (Ding et al., 2006; Li et al., 2006; Li and Li, 2007). The resulting ~1300-km-wide South China Fold Belt also notably features the extensive occurrence of Jurassic – Cretaceous postorogenic magmatism (Fig. 1; e.g., Martin et al., 1994; Fu et al., 2004; Li and Li, 2007; Li et al., 2007; Li et al., 2012b; Wang et al., 2013). A coastward-younging distribution pattern was initially implied for post-150 Ma magmatism (e.g., Chen and Jahn, 1998; Zhou and Li, 2000). Some researchers linked this postorogenic magmatic activity with a retreating continental arc. In their models, the slab dip of Paleo-Pacific subduction increased from a low angle to a moderate angle during the process (e.g., Zhou and Li, 2000). However, later analyses demonstrated that the temporal-spatial distribution of the postorogenic magmatism is more complex. Early Mesozoic (ca. 180–150 Ma) magmatism propagated from the center of the orogen in a radiating fashion, and the rocks are not entirely arc-related; many are within-plate A-type granites (Li et al., 2007; Li and Li, 2007). Li and Li (2007) therefore proposed a flat-slab subduction model to explain the cratonward migration of the orogen during 250–200 Ma and invoked a center-first slab delamination and foundering process to explain the complex pattern and composition of the postorogenic magmatism. Li et al. (2012b) further speculated a ca. 190 Ma reinitiation of coastal normal subduction based on the discovery of ca. 190 Ma I-type granites and nearby sedimentary provenance data along the coastal zone.

The South China Block extends southward into the northern South China Sea basin. The extensively thinned continental crust varies from ~6 km to ~30 km thick (Hayes and Nissen, 2005). Based on gravity-seismic-magnetic inversion analyses, four lithospheric layers have been identified in the basement of the northern South China Sea basin, and they are assigned pre-Sinian, Sinian-early Paleozoic, late Paleozoic and Mesozoic ages (Sun et al., 2014). Extrapolation implied that the basement for the Cenozoic Qiongdongnan Basin and western Pearl River Mouth Basin east of Hainan Island is dominated by Paleozoic strata (Fig. 2; Liu et al., 2011; Sun et al., 2014; (Shao et al., 2019)). In particular, the basement of the Xisha area has a previously reported Precambrian Rb-Sr isochron

Table 1

Summary of published data of pre-Cenozoic South China Sea basin basement (refer to Fig. 2 for detailed sample locations).

No.	Sample	Depth (m)	Isotopic ages (Ma)	Analytical method	Lithology	References
1	XJ24-1-1X	3851–3851.5	84	K-Ar	granite	Li et al., 1999
2	HZ32-1-1	2791	88.5 ± 3.6	K-Ar	cataclastic granite	Li et al., 1999
3	YJ26-1-1	1700–1702	89.2 ± 1.58	K-Ar	rhyolite porphyry	Li et al., 1999
4	PY21-3-1	4068–4019.5	89.83 ± 1.32	K-Ar	cataclastic biotite granite	Li et al., 1999
5	LH11-1-1A	1836.5	90.62 ± 1.49	K-Ar	cataclastic granodiorite	Li et al., 1999
6	PY3-1-1	3192	90.7 ± 3.3	K-Ar	granite	Li et al., 1999
7	LF2-1A	2480–2483.5	100.38 ± 1.46 94.83 ± 1.89	K-Ar Rb-Sr	cataclastic dimicaceous granite	Li et al., 1999 Li et al., 1999
8	XJ24-3-1AX	4318–4319	98	K-Ar	cataclastic granite	Li et al., 1999
9	HZ25-2-1X	3196.4	99.8 ± 1.53	K-Ar	cataclastic granite	Qiu et al., 1996
10	EP18-1-1A	3448.25	100.5 ± 1.7	K-Ar	granite	Qiu et al., 1996
11	HZ35-1-1	2218.9	105	K-Ar	cataclastic quartz diorite	Li et al., 1999
12	HF28-2-1	3942–3943.6	109.25 ± 2.4	K-Ar	cataclastic granodiorite	Li et al., 1999
13	SH2-1-1	3641.2	118	K-Ar	Biotite-hornblende diorite	Li et al., 1999
14	PY27-1-1	3607–3609	118.9 ± 2.1	K-Ar	quartz monzonite	Li et al., 1999
15	PY4-1-1	3160	130 ± 5	K-Ar	granite	Qiu et al., 1996
16	KP9-1-1	1662–1774	153 ± 6	K-Ar	cataclastic granite	Li et al., 1999
17	LF354	2472.3	196.4 ± 1.4	U-Pb	granite	Xu et al., 2017
18	LF3521	2443.5	195 ± 2.2	U-Pb	diorite	Xu et al., 2017

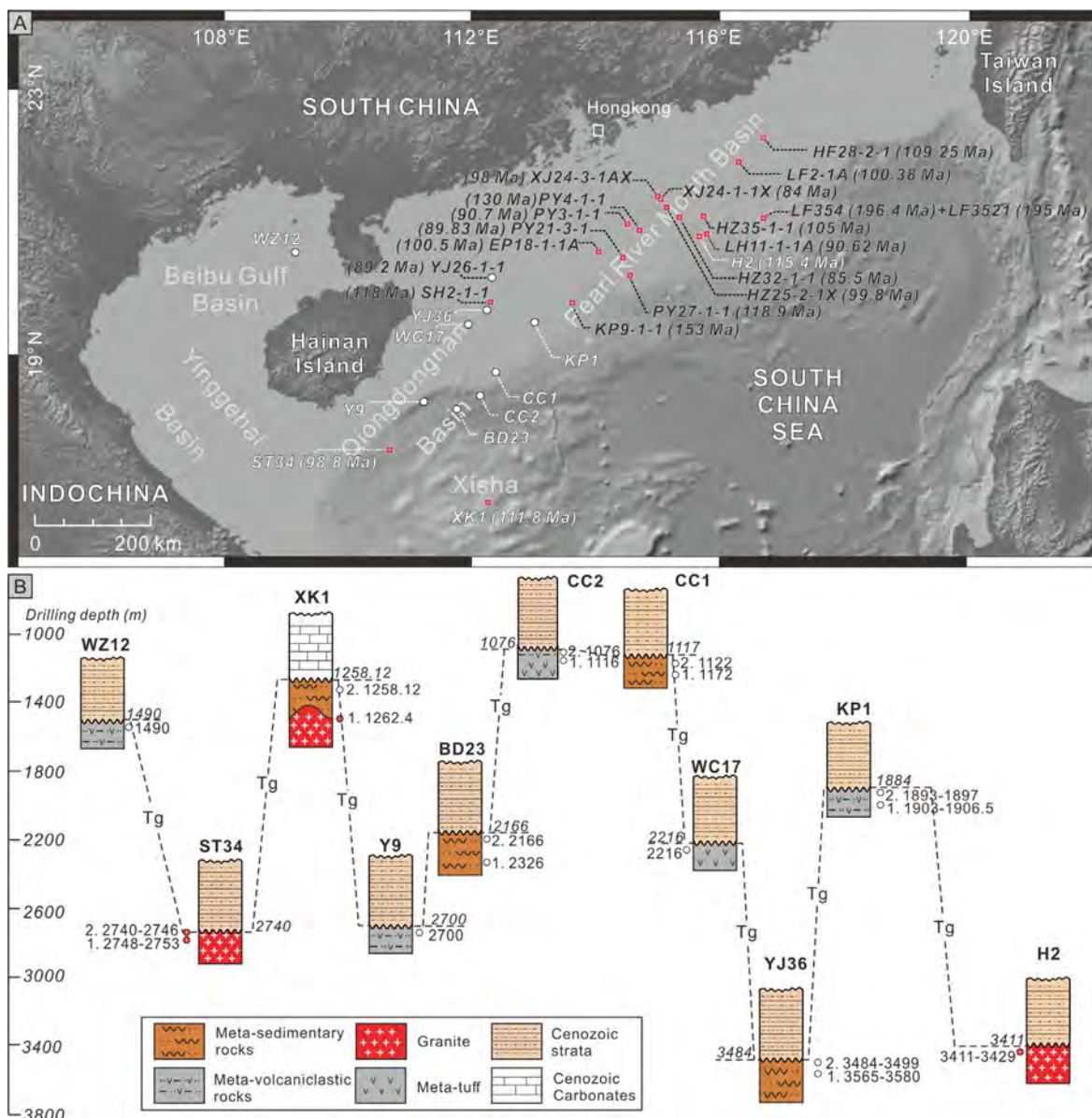


Fig. 2. A) Topographic map of the northern South China Sea basin showing the locations of borehole samples analyzed in this study (white borehole names) and reported in previous studies (black borehole names from Li et al. (1999), Qiu et al. (1996), and Xu et al. (2017)). Boreholes that penetrated granites are shown by filled red circles with dated magmatic ages given following the borehole names. Refer to Tables 1 and 2 for sampling and stratigraphic details, lithological characteristics, ages, analytical methods, and references of previously studied samples. B) Schematic stratigraphic columns of boreholes analyzed in this study; depth of the South China Sea basement (Tg) is shown in italic font. (For interpretation of the references to colour in this figure legend, the reader is referred to the web version of this article.)

age (Qin, 1987). However, recent U-Pb age determinations suggest a Late Jurassic amphibole plagiogneiss basement for the Xisha area, which was later intruded by Early Cretaceous plutons (Zhu et al., 2017b). Therefore, the question of whether the northern South China Sea basin is indeed floored by Paleozoic or even Precambrian rocks needs to be reevaluated.

Taiwan Island, located on the continental margin of the South China Block, holds significant relevance for this research because it is a lateral extension of the submarine continental margin in the northern South China Sea (Figs. 1, 2). Similar to the pre-Cenozoic South China Sea basin basement, outcrops in central and northern Taiwan display affinities with continental South China. The Tananao Metamorphic Complex represents the oldest rocks exposed on Taiwan Island (Jahn et al., 1992). They mainly consist of schists, marbles and granites. In addition to the late

Mesozoic (90–80 Ma) granitic intrusions (Jahn et al., 1986; Lo and Onstott, 1995; Li et al., 2012b), ca. 190 Ma I-type granites were reported by Yui et al. (2009), which were related to oceanic subduction beneath the eastern Eurasian continental margin.

Farther southwest near the western end of the South China continental margin, Hainan Island provides another anchor point outcrop due to the nature of this margin (Figs. 1, 2). The ubiquitous igneous rocks exposed on Hainan Island have mostly Triassic ages (Indosinian), and the remainder have Jurassic and Cretaceous ages (Yanshanian) (e.g., Wang et al., 1991). Some calc-alkaline I-type granites give precise SHRIMP (sensitive high-resolution ion microprobe) U-Pb ages of 267–262 Ma and have been interpreted to represent a continental arc during the late Permian (Li et al., 2006). The Late Jurassic – Early Cretaceous Yanshanian intrusive and volcanic rocks, on the other hand, appear to have been derived from a

subduction-modified mantle source through magma hybridization in an extensional environment (e.g., Wang et al., 2012; Zhu et al. 2014, 2017a; Jiang et al., 2015; Zhou et al., 2015).

To verify the nature and tectonic environment of the submerged continental margin in the northern South China Sea, we collected both igneous and metasedimentary borehole samples from this region (Fig. 2) for geochronological, geochemical and sedimentary provenance analyses. All samples were from the bottoms of hydrocarbon exploration boreholes drilled by the China National Offshore Oil Company, which penetrated the unconformity below the Cenozoic sedimentary basin sequence (the main exploration target). Our samples were thus all located immediately below this unconformity (see Table 2 for the depth of each sample). Samples WC17 and CC2-1 were from metatuff. Samples CC2-2, WZ12, Y9, KP1-1 and KP1-2 were from metavolcaniclastic rocks. Samples BD23-1 and BD23-2 were from meta-quartzose sandstones. Samples CC1-1 and CC1-2 were from metasandstones. Samples YJ36-1 and YJ36-2 were from metamudstones and metasiltsstones. These samples were intended for U-Pb zircon provenance analysis. We also collected four granitic samples and one gneissic sample for age determinations (Table 2): samples ST34-1, ST34-2 and XK1-1 represent granitic intrusions; sample H2, granodiorite; and sample XK1-2, amphibole plagiogneiss. In addition, the zircon trace elemental geochemistry of our granitic and gneissic samples was examined for petrogenetic discrimination purposes. For data interpretation, we also reviewed published work from both the inland and coastal South China continent and Hainan and Taiwan Islands.

3. Analytical procedures

In this study, zircon grains were separated from granite, metatuff, metavolcaniclastic and metasedimentary rocks using standard density and magnetic separation techniques at the laboratory of the Institute of Regional Geology and Mineral Resources, Langfang, China. Typically, more than 200 zircon grains from each sample

were randomly adhered to adhesive tape and then cast in an epoxy mount prior to the polishing process. Zircons were examined with cathodoluminescence (CL) images to determine their internal structures and microzonations. Measurements of U, Th and Pb isotopes were conducted at the State Key Laboratory of Marine Geology of Tongji University, China, using a Thermo Elemental X-Series ICP-MS (inductively coupled plasma-mass spectrometry) coupled with a New Wave 213 nm laser ablation system. Five-scan cycles were conducted for each analysis with spot diameters of 20–30 μm . The 91,500 external standard zircon (1065.4 ± 0.3 Ma) was interspersed with the tested samples to calculate isotopic ratios. The glass standard NIST 610 was used as an internal standard to optimize the machine. The accuracy of our analytical results was validated by the reference material Plešovice with an age of 337.1 ± 0.4 Ma (Sláma et al., 2008). Measured compositions were corrected for common Pb using the method of Andersen (2002). The $^{206}\text{Pb}/^{238}\text{U}$ and $^{207}\text{Pb}/^{206}\text{Pb}$ ages were finally adopted for zircons younger and older than 1000 Ma, respectively. The measured U-Pb isotope ratios and calculated ages for the individual spots are presented in Supplementary Data, Table S1. Uncertainties in individual U-Pb analyses are quoted at the 1σ level. Weighted mean ages of igneous rocks are plotted at either 2σ or 95% confidence levels. Age distributions in this study and other published documents are visualized as histograms and kernel density estimation plots (Vermeesch, 2012).

The measurements of trace elements in zircon were performed using an ICP-MS system in the State Key Laboratory of Marine Geology of Tongji University, China. Analyses were conducted on four granite samples and one gneiss sample. The results for individual spots are presented in Supplementary Data, Table S2. Trace element compositions of zircons were calibrated against multiple reference materials combined with the NIST 610 glass as an internal standard. The trace element contents of standard 91,500 were calibrated by Si in NIST 610 glass as an internal standard. The average results calibrated using element Si as an internal standard against NIST 610 glass are lower than the LA-ICP-MS working val-

Table 2
List of samples analyzed for Laser-ICP-MS detrital zircon U-Pb dating and trace element analyses (refer to Fig. 2 for detailed sample locations).

Borehole name	Depth of the South China Sea basement (m)/Tg	Sample name	Lithology	Sampling depth (m)	Igneous age (in bold) or youngest detrital zircon age (Ma)	U-Pb dating effective/total number of zircons analyzed	Geochemistry Sampling depth (m)
ST34	2740	ST34-2	Granite	2740–2746	98.4 ± 1.7	25/32	2740–2746
		ST34-1		2748–2753	98.6 ± 2.1	39/51	2748–2753
XK1	1258.12	XK1-2	Amphibole plagiogneiss	1258.12	151.8 ± 2.7	17/17	1258.12
		XK1-1	Granite	1262.4	111.8 ± 3.3	13/16	1262.4
H2	3411	H2	Granodiorite	3411–3429	115.4 ± 0.7	107/112	3411–3429
WC17	2216	WC17	Metatuff	2216	114.6 ± 4.7	101/112	–
CC2	1076	CC2-2	Metavolcaniclastic rock	1076	91.9 ± 8.2	111/112	–
		CC2-1	Metatuff	1116	138.3 ± 2.6	110/112	–
WZ12	1490	WZ12	Metavolcaniclastic rock	1490	98 ± 14	106/112	–
Y9	2700	Y9	Metavolcaniclastic rock	2700	111.9 ± 6.2	104/112	–
KP1	1884	KP1-2	Metavolcaniclastic rock	1893–1897	122.0 ± 7.5	228/252	–
		KP1-1		1903–1906.5	103.9 ± 9.0	106/120	–
BD23	2166	BD23-2	Meta-quartzose sandstone	2166	87.0 ± 4.2	91/107	–
		BD23-1		2326	122.7 ± 2.8	92/117	–
CC1	1117	CC1-2	Metasandstone	1122	101 ± 5	101/112	–
		CC1-1		1172	112.8 ± 7.5	95/105	–
YJ36	3484	YJ36-2	Metamudstone and metasiltsstone	3484–3499	88 ± 2	128/140	–
		YJ36-1		3565–3580	112 ± 3	113/147	–

ues recommended by Wiedenbeck et al. (2004) by factors of 0.16–6% for Er, Hf, Ta and U; 7.40–16.67% for Pr, Nd, Sm, Tb, Dy, Ho, Tm, Lu and Th; and 21.09–27.85% for Ce and Nb, while they are higher by factors of 0.31, 3.94, and 6.17% for Y, Yb, and Ti, respectively. The elements Eu and Gd calibrated using Si as an internal standard against NIST 610 glass are almost equal to the recommended working values. Based on the Si internal standard, La is much higher than the working value. Although there are no working values to compare with P and Sc, their concentrations are also calibrated using Si as an internal standard.

4. Results

4.1. U-Pb geochronology

Samples ST34-1, ST34-2, XK1-1 and H2 were all from borehole-penetrated granitoids below the Cenozoic northern South China Sea Basin sediments (Fig. 2; Table 2; Supplementary Data, Table S1). Samples ST34-1 and ST34-2 were from a medium-grained granite beneath the Qiongdongnan Basin southeast of Hainan Island. Thin sections show a granitic structure that comprises mainly plagioclase (20%), orthoclase (45%), quartz (30%) and a small amount (5%) of dark-colored minerals such as biotite. Th and U concentrations for sample ST34-1 range between 20.67 ppm and 599.50 ppm and between 38.88 ppm and 1069.61 ppm, respectively. Their Th/U ratios of 0.18–1.93 are consistent with a magmatic origin (Fig. 3). Zircon crystals commonly exhibit core-rim structures (Fig. 4). In total, 39 analyses yield $^{206}\text{Pb}/^{238}\text{U}$ ages between 246 Ma and 82 Ma. Thirty-five of these ages lie within the 111–82 Ma interval and give a weighted mean age of 98.6 ± 2.1 Ma (mean square weighted deviation (MSWD) = 1.8, probability = 0.003) (Fig. 4A). Duplicate sample ST34-2 from the same granite has Th and U concentrations varying between 47.80 ppm and 327.98 ppm and between 55.21 ppm and 407.99 ppm, respectively. Th/U ratios of 0.65–1.46 indicate a magmatic origin. Twenty-five effective analyses obtained on oscillatory magmatic rims or on needle-like homogeneous magmatic zircon grains from sample ST34-2 have $^{206}\text{Pb}/^{238}\text{U}$ ages all falling within the 107–93 Ma range and giving a weighted mean age of 98.4 ± 1.7 Ma (MSWD = 0.62, probability = 0.92) (Fig. 4B). As the ages of the two related samples are indistinguishable within errors, a com-

bined dataset gives an overall weighted mean $^{206}\text{Pb}/^{238}\text{U}$ age of 98.8 ± 1.1 Ma (MSWD = 1.06, probability = 0.34), which we take as the crystallization age of the granite. Two zircon cores from ST34-1 give older $^{206}\text{Pb}/^{238}\text{U}$ ages of 129 ± 5 Ma and 155 ± 8 Ma, which we interpret as ages of inherited zircons either from the source region or entrained from the wall rocks during magma ascent and crystallization. An older age of 170 ± 8 Ma might be caused by cracks in the analyzed spot. The oldest age of 246 ± 14 Ma from this sample is from zircon rims and possibly represents zircons entrained from the wall rocks.

Sample XK1-1 is a medium-grained granite from the southernmost region of the Qiongdongnan Basin. A typical granitic structure is observed in thin section (Fig. 4C). The Th and U contents in zircons range between 72.73 ppm and 1276.40 ppm and between 99.55 ppm and 1847.00 ppm, respectively. Th/U ratios vary between 0.39 and 1.01, indicating a magmatic origin. In total, 13 analyses give ages ranging between 132 Ma and 103 Ma. After a single analysis of 132 ± 2.5 Ma is rejected as an outlier (likely an inherited zircon), the remaining 12 analyses yield a weighted mean $^{206}\text{Pb}/^{238}\text{U}$ age of 111.8 ± 3.3 Ma (MSWD = 6.9) (Fig. 4C). Sample XK1-2 is an amphibole plagiogneiss from approximately 4 m above sample XK1-1. It consists mainly of plagioclase (45%), quartz (14%), K-feldspar (8%), hornblende (10%), and biotite (20%), as well as a small amount of accessory minerals, including epidote, apatite, sphene and zircon. All minerals exhibit an overall directional alignment. Thin sections also show hornblende and biotite chloritization and a high degree of plagioclase sericitization (Fig. 4D). XK1-2 has variable Th (81.61–1361.66 ppm) and U (214.78–2395.08 ppm) concentrations, and its Th/U ratios range between 0.37 and 0.88, confirming a magmatic origin (Fig. 3). In total, 17 analyses were conducted on oscillatory zircon zones with or without inherited cores. A single analysis of 137 ± 1.2 Ma is rejected as an outlier, and the remaining 16 analyses give a weighted mean $^{206}\text{Pb}/^{238}\text{U}$ age of 151.8 ± 2.7 Ma (MSWD = 10.5) (Fig. 4D). We interpret 111.8 ± 3.3 Ma as the crystallization age of the granite, which intruded the 151.8 ± 2.7 Ma protolith of the amphibole plagiogneiss.

Sample H2 is a medium- to fine-grained granodiorite from the basement of the Pearl River Mouth Basin (Fig. 2). The granodiorite porphyry (0.5–5 mm) consists of plagioclase (35%), K-feldspar (10%), quartz (20%), amphibole (10%) and biotite (10%) (Fig. 4E). Titanite, apatite and zircon are the common accessory minerals. Minerals in the groundmass (0.02–0.5 mm) are mainly plagioclase,

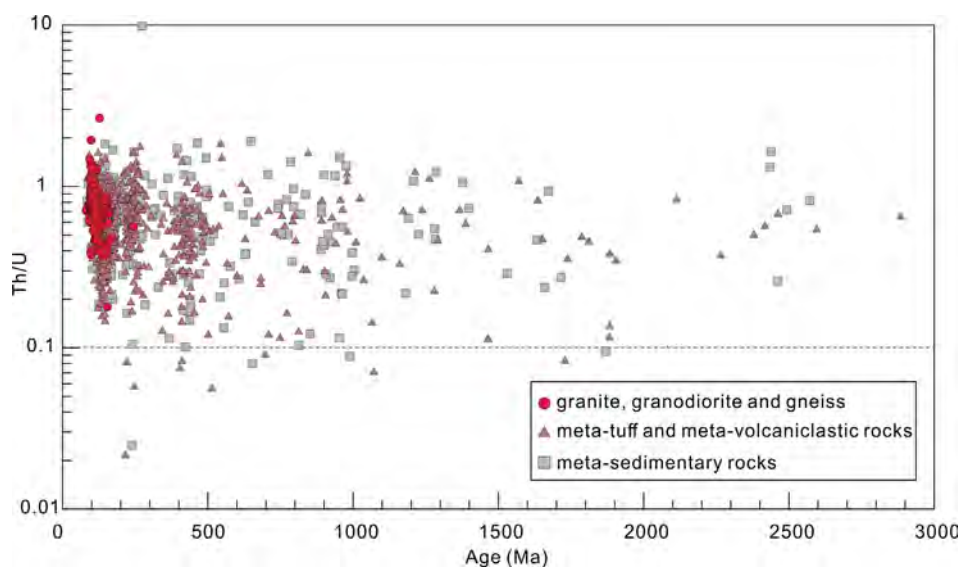


Fig. 3. Plots of Th/U ratios vs. U-Pb ages for all dated zircon grains.

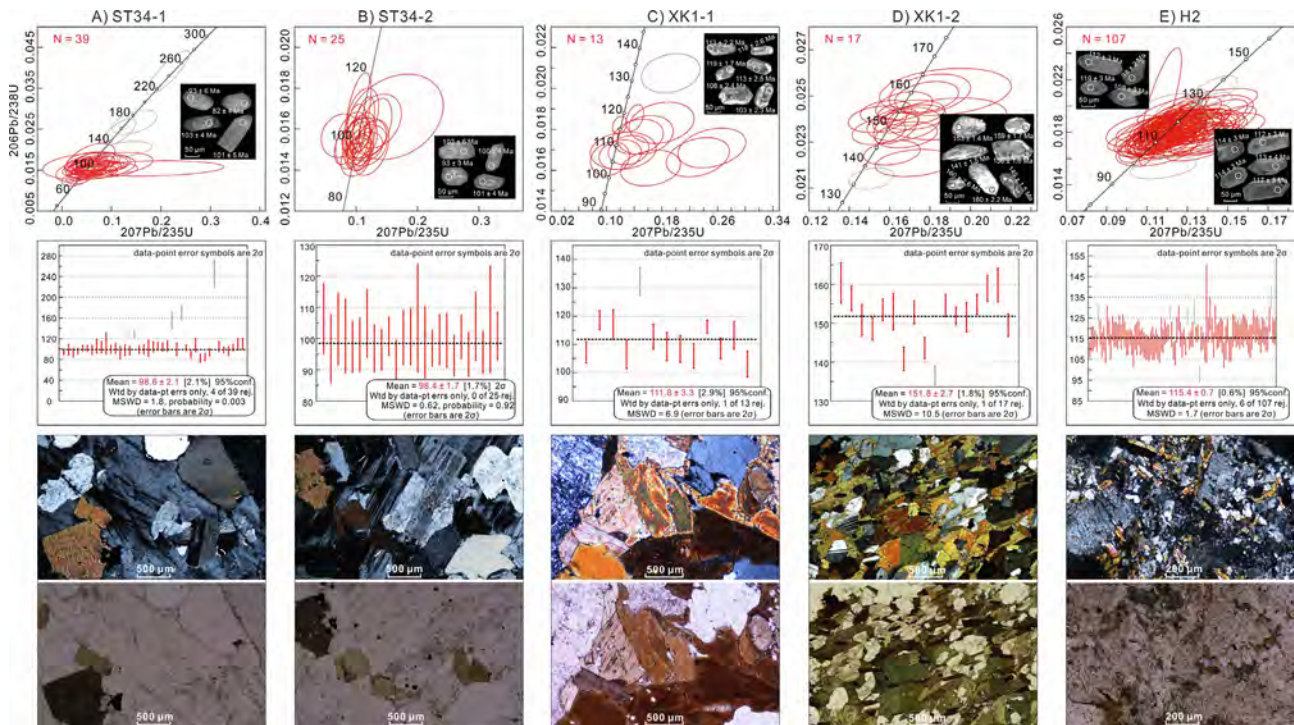


Fig. 4. LA-ICP-MS U-Pb concordia age plots, cathodoluminescence (CL) images of representative zircons, weighted mean ages and thin sections under cross/plane-polarized light of magmatic rocks. A) ST34-1: granite; B) ST34-2: granite; C) XK1-1: granite; D) XK1-2: amphibole plagiogneiss; E) H2: granodiorite. The term “N” denotes the total number of effective analyses for each sample. MSWD – mean square weighted deviations.

K-feldspar, quartz and minor amphibole, biotite, zircon, apatite and magnetite. Th and U concentrations in zircons vary between 65.42 ppm and 3865.52 ppm and between 117.29 ppm and 1463.05 ppm, respectively (Fig. 3). Th/U ratios range between 0.40 and 2.64, indicating a magmatic origin. Zircon grains feature clear core-rim structures. In total, 107 analyses were conducted on 107 crystal grains. One zircon core gives a $^{206}\text{Pb}/^{238}\text{U}$ age of 135 ± 3 Ma, indicating a possible inherited origin. Another five analyses were also rejected because they plot significantly away from the mean value (Fig. 4E). The remaining 101 analyses produce a weighted mean $^{206}\text{Pb}/^{238}\text{U}$ age of 115.4 ± 0.7 Ma (MSWD = 1.7) (Fig. 4E), interpreted as the magmatic crystallization age.

Samples WZ12, Y9, KP1-1, KP1-2 and CC2-2 are all metavolcaniclastic rocks (Fig. 2; Table 2; Supplementary Data, Table S1). Borehole WZ12 was drilled in the Beibu Gulf Basin to the northwest of Hainan Island. The zircon grains of sample WZ12 are mostly euhedral to subhedral in shape and commonly show concentric zoning (Fig. 5A). They have moderately high Th (~37–3048 ppm) and U (~106–4642 ppm) concentrations, with most Th/U ratios falling between 0.11 and 1.57 (Fig. 3). Six analyses ranging between 698 ± 17 Ma and 217 ± 4 Ma give Th/U ratios of 0.02–0.09, possibly reflecting a metamorphic origin. Of the 106 effective analyses, 86 analyses yield $^{206}\text{Pb}/^{238}\text{U}$ ages between 567 ± 10 Ma and 93 ± 2 Ma. The remainder are scattered between 2114 ± 106 Ma ($^{207}\text{Pb}/^{206}\text{Pb}$ age) and 601 ± 16 Ma (Fig. 7A). Three Cretaceous analyses (93 ± 2 Ma, 102 ± 2 Ma and 102 ± 4 Ma) give the youngest age of 98 ± 14 Ma (MSWD = 5.6). Permian – Triassic clusters consist of a single age peak of ca. 250 Ma, and spots between 567 ± 10 Ma and 340 ± 9 Ma form a prominent peak at ca. 420 Ma. The remainder are scattered ages between 2114 Ma and 601 Ma (Fig. 7A).

Zircon grains from sample Y9 have relatively high and variable Th (~66–3314 ppm) and U (~149–9662 ppm) concentrations. Their Th/U ratios vary between 0.30 and 1.78 (Fig. 3). In total, 104 spots were analyzed, all of which showed oscillatory zoning (Fig. 5B). Apart from one Neoproterozoic (957 ± 44 Ma) and two early Pale-

ozoic (467 ± 24 and 453 ± 17 Ma) grains, the remaining 101 analyses have Permian – Cretaceous ages between 290 ± 13 Ma and 108 ± 4 Ma (Fig. 7B). The youngest age group is 111.9 ± 6.2 Ma given by two zircons (108 ± 4 Ma and 118 ± 5 Ma), which is taken as the maximum depositional age of this volcanoclastic rock.

Samples KP1-1 and KP1-2 are from the same borehole at depths of 1903–1906.5 m and 1893–1897 m, respectively (Fig. 2; Table 2). Most of their zircon grains are euhedral to subhedral with clear internal core-rim structures (Fig. 6B, C). Totals of 106 and 228 effective analyses were obtained for the two samples, respectively. These analyses give Th/U ratios ranging between 0.08 and 1.63. In sample KP1-2, a single analysis of 222 ± 4 Ma gives a low Th/U of 0.08 (Fig. 3), possibly reflecting a metamorphic origin. Both samples are dominated by late Mesozoic age populations (Fig. 8B, C). For sample KP1-1, 106 analyses yield $^{206}\text{Pb}/^{238}\text{U}$ ages between 405 ± 7 Ma and 97 ± 2 Ma. There is only one pre-Mesozoic age of 405 ± 7 Ma. The remainder give 105 Jurassic – Cretaceous ages (Fig. 8C). Most zircons from this sample cluster around ca. 140 Ma, with a mean age of 103.9 ± 9.0 Ma given by the four youngest zircons (97 ± 2 Ma, 103 ± 4 Ma, 106 ± 2 Ma and 109 ± 2 Ma), defining the maximum depositional age. For sample KP1-2, eight pre-Mesozoic ages between 1173 Ma and 379 Ma account for only 3.5% of the 228 analyses. The remainder give two Triassic ages and 218 Jurassic – Cretaceous ages (Fig. 8B). KP1-2 has an age spectrum similar to that of KP1-1 in that the bulk of the analyses center around ca. 145 Ma. Because this sample is the shallower sample from the same borehole, if one assumes that the stratigraphy here has not been overturned, the depositional ages of both samples should be no older than the youngest age population of the lower sample at ca. 104 Ma.

Samples CC2-1 and WC17 are metatuffs from the basement of the Qiongdongnan Basin to the east of Hainan Island (Fig. 2; Table 2; Supplementary Data, Table S1). Sample CC2-1 is a low-grade metatuff. In total, 110 effective analyses were conducted on sample CC2-1 (Fig. 5D). Th and U concentrations are 87.35–

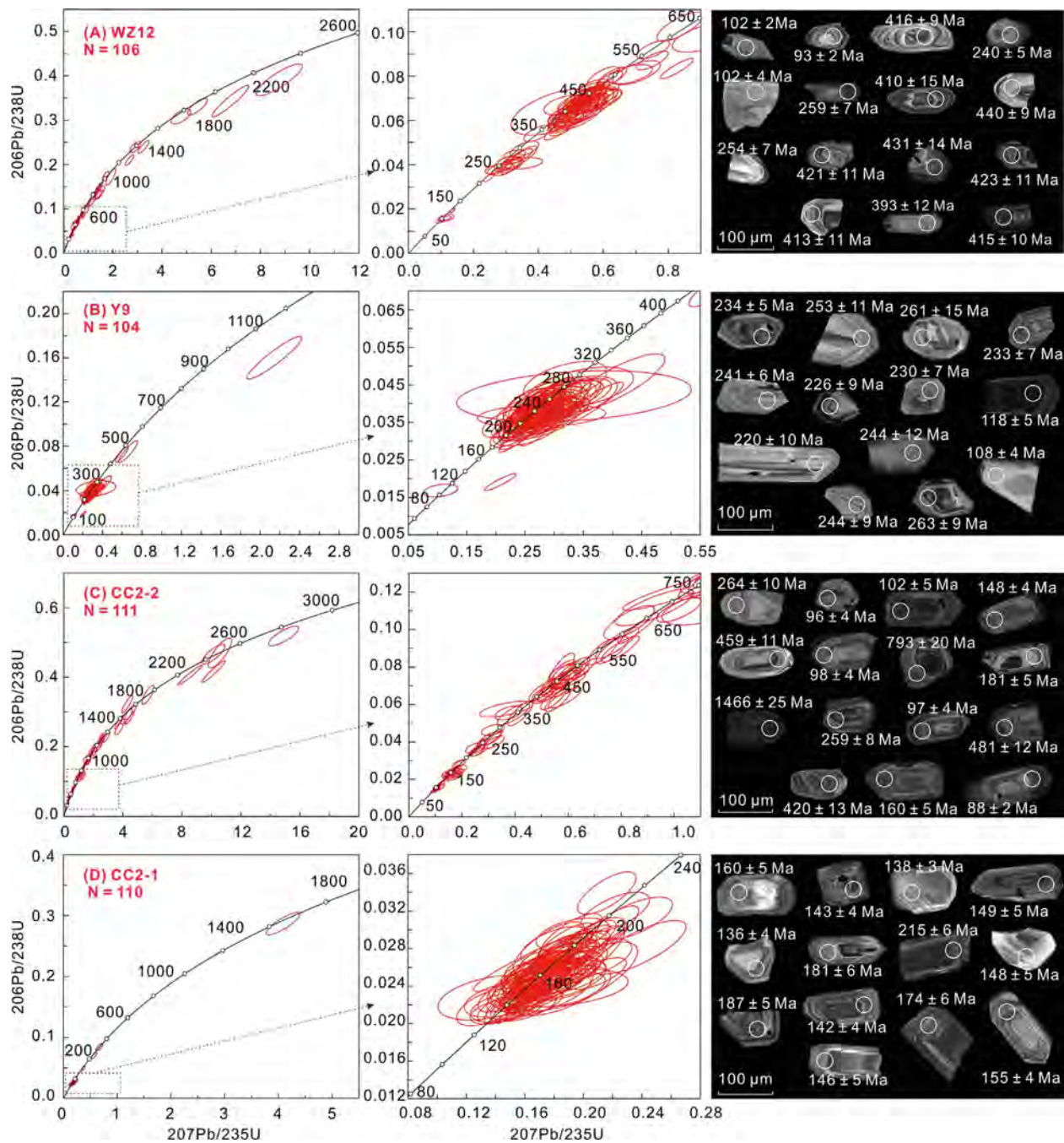


Fig. 5. LA-ICP-MS U-Pb concordia age plots and CL images of representative zircons from metatuffs and volcaniclastic rocks. (A) WZ12; (B) Y9; (C) CC2-2; (D) CC2-1. The term “N” denotes the total number of effective analyses for each sample.

1354.50 ppm and 129.38–2008.33 ppm, respectively. Their magmatic origin is suggested by their Th/U ratios between 0.39 and 1.01. All but four of the 110 measured ages fall within the Mesozoic ca. 215–136 Ma range, with the four outliers giving ages of 1652–306 Ma (Fig. 7D). The nine youngest grains (140 ± 4 – 136 ± 4 Ma) give a mean age of 138.3 ± 2.6 Ma, providing the maximum depositional age. Sample CC2-2, on the other hand, is from metavolcaniclastic rock 40 m above sample CC2-1. In total, 111 effective analyses were obtained (Fig. 5C). Most of these analyses give Th/U ratios ranging between 0.12 and 1.85, with only two exceptions of 0.07 and 0.08. All 111 measured ages form a broad ca. 2884–88 Ma range (Fig. 7C). The four youngest grains (88 ± 2 Ma, 96 ± 4 Ma, 97 ± 4 Ma and 98 ± 4 Ma) give a mean age of 91.9 ± 8 .

2 Ma, providing the maximum depositional age. Sample CC2-2 is dominated by age peaks centered at ca. 149 Ma and ca. 99 Ma, with minor age clusters of 492–344 Ma, 292–220 Ma, a spread of Proterozoic analyses between 2463 Ma and 545 Ma, and a few Archean grains.

Most zircon grains from sample WC17 retain their euhedral crystal shapes with magmatic growth zonation. Zircons from this sample show wide ranges of Th (56.70–2013.25 ppm) and U (118.61–3115.30 ppm) concentrations, producing Th/U ratios greater than 0.1 (Fig. 3). In total, 101 effective analytical spots were identified (Fig. 6A). The youngest mean age of 114.6 ± 4.7 Ma given by two grains (114 ± 4 Ma and 115 ± 3 Ma) (Fig. 8A) provides the maximum depositional age. Apart from one older zircon with an

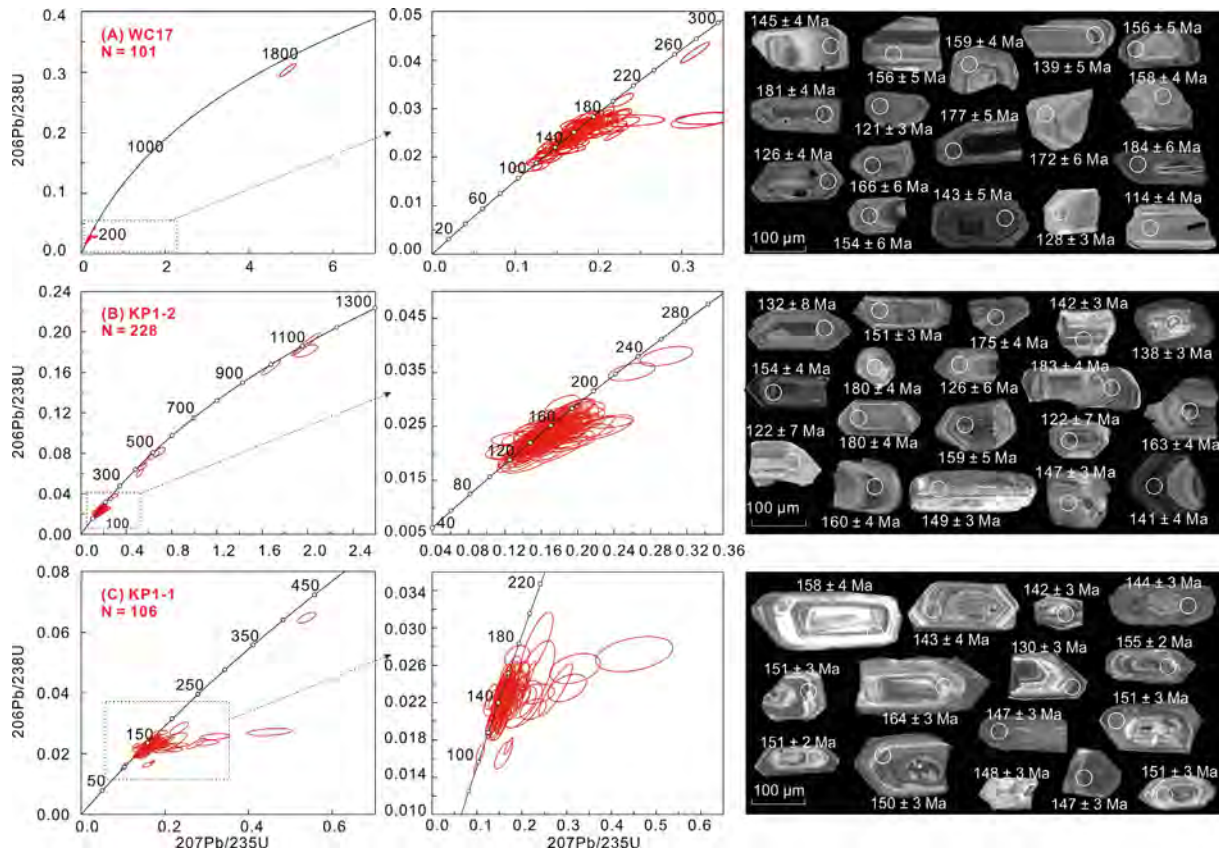


Fig. 6. LA-ICP-MS U-Pb concordia age plots and CL images of representative zircons from metatuffs and volcanoclastic rocks. (A) WC17; (B) KP1-2; (C) KP1-1. The term “N” denotes the total number of effective analyses for each sample.

age of 1884 ± 18 Ma, sample WC17 is dominated by a Mesozoic zircon group between ca. 184 Ma and 114 Ma, with two outlying analyses of 202 ± 5 Ma and 262 ± 9 Ma.

Samples BD23-1, BD23-2, CC1-1, CC1-2, YJ36-1 and YJ36-2 are all metaclastic sedimentary rocks penetrated near the bottoms of their respective boreholes (Fig. 2; Table 2; Supplementary Data, Table S1). Ninety-two and 91 concordant analyses were obtained for the low-degree meta-quartzose sandstone samples BD23-1 and BD23-2 from the same borehole, respectively. Most of the zircons are euhedral to subhedral, but a small proportion is modestly rounded (Fig. 9A, B). One single analysis of 1869 Ma in sample BD23-1 shows a low Th/U ratio of 0.09, indicating a likely metamorphic origin. The remainders of the two samples have Th/U ratios varying between 0.10 and 1.85 (Fig. 3). Sample BD23-1 yields a large age group between ca. 185 Ma and 120 Ma, with only two Proterozoic ages of 1869 Ma and 663 Ma (Fig. 10A). Its maximum depositional age of 122.7 ± 2.8 Ma is provided by the mean of the six youngest analyses (124 ± 4 – 119 ± 4 Ma). BD23-2, on the other hand, is dominated by a large age peak between ca. 185 Ma and 130 Ma, with minor age groups of 130–85 Ma, 250–200 Ma and 510–270 Ma, and six scattered Neoproterozoic grains (Fig. 10B). The mean age of the two youngest zircons (85 ± 3 and 89 ± 3 Ma) is 87.0 ± 4.2 Ma, which provides the maximum depositional age constraint.

Ninety-three and 101 effective analyses were obtained for metasandstone samples CC1-1 and CC1-2 from the same borehole, respectively. Most zircons are subhedral to euhedral (Fig. 9C, D). For sample CC1-1, Th and U concentrations vary from 18.20 to 1926.05 ppm and from 105.08 to 3890 ppm, respectively. Th/U ratios mostly fall between 0.12 and 1.71, with an outlier of 0.09 (Fig. 3). Sixty-nine of the 93 analyses range between 187 Ma and 112 Ma, mostly clustering at approximately 150 Ma, with thirteen

Paleozoic and thirteen Proterozoic zircons (accounting for 28.0% of the total analyses) scattered between 250 Ma and 990 Ma (Fig. 10C). The youngest age of 112.8 ± 7.5 Ma (mean of the two youngest zircons with ages of 112 ± 5 Ma and 114 ± 6 Ma) defines the maximum depositional age for the unit. Sample CC1-2 has Th and U concentrations ranging between 45.49 and 1630.02 ppm and between 71.97 and 2940.52 ppm, respectively. Most Th/U ratios exceed 1, with a single Th/U ratio of 0.08 at an age of 654 ± 26 Ma (Fig. 3). This sample shows a relatively broad U-Pb age spectrum compared to CC1-1. Twenty-nine of the 101 analyses form a narrow age range between 171 Ma and 101 Ma, with a maximum depositional age of 101 ± 5 Ma (a single analysis; Fig. 10D). Groups of older grains vary from 3323 Ma to 208 Ma, accounting for 77.4% of the total spots.

Zircon grains from low-degree metamudstone and metasiltstone samples YJ36-1 and YJ36-2, from the same borehole, are mostly subhedral to euhedral (Fig. 9E, F). Sample YJ36-1 has 113 effective analyses, and YJ36-2 has 128. Of the total 241 analyses for the two samples, Th (122.73–8349.25 ppm) and U (205.58–33224.03 ppm) concentrations are highly variable. Only a single analysis of 240 ± 6 Ma has a Th/U ratio of 0.02, with the remainder ranging between 0.11 and 1.24. Both samples are dominated by narrow age ranges between ca. 170 Ma and 110 Ma. Sample YJ36-1 has a youngest grain of 112 ± 3 Ma and only a few older grains of up to 348 Ma (Fig. 10E). Sample YJ36-2 has the youngest grain age of 88 ± 2 Ma, and scattered older grains range up to 1283 Ma (Fig. 10F).

4.2. Zircon trace elements of offshore igneous and gneissic rocks

To analyze the tectonic setting for the studied igneous rocks, we acquired trace element compositions for more than 200 zircons

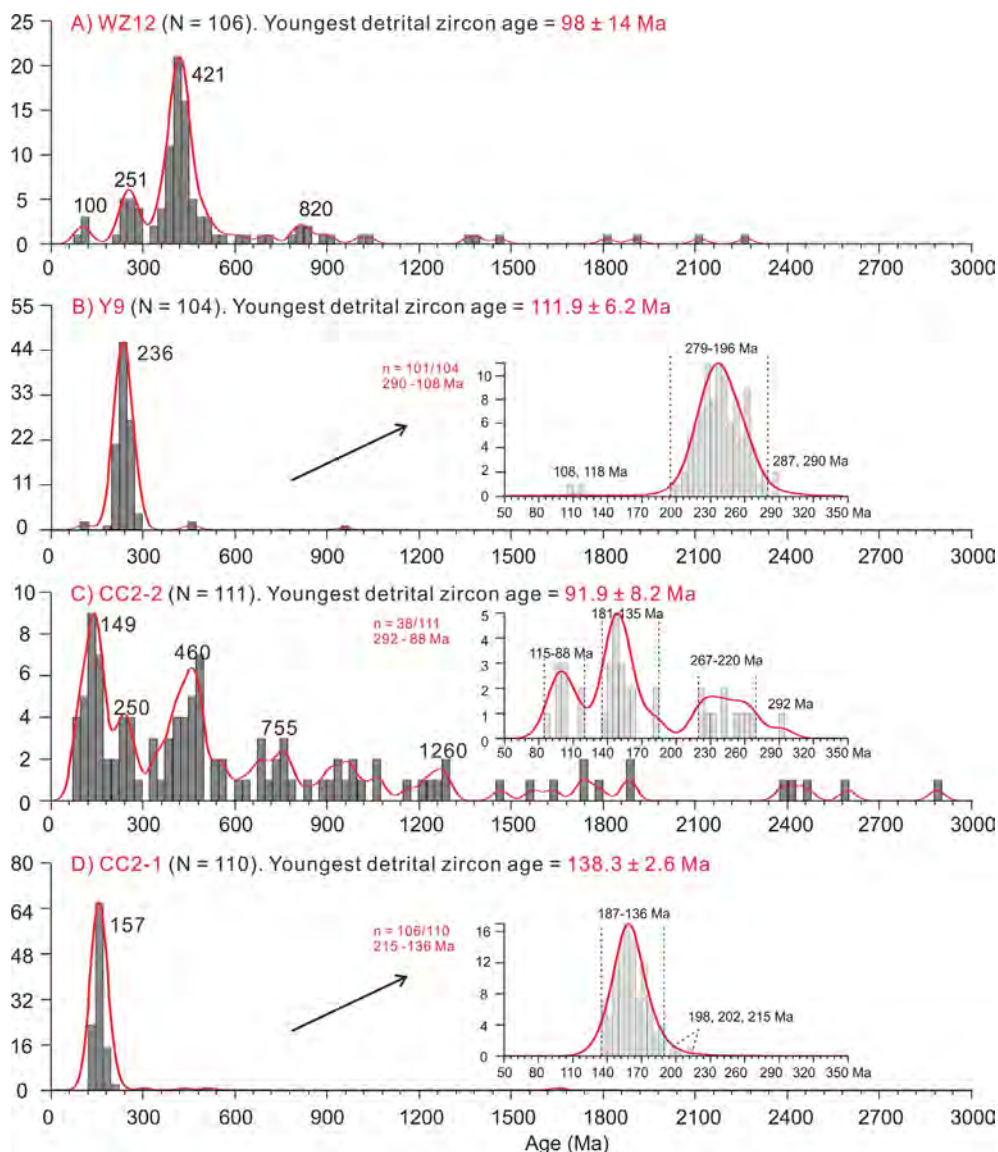


Fig. 7. Zircon U-Pb age spectra of metatuffs and volcaniclastic rocks. (A) WZ12; (B) Y9; (C) CC2-2; (D) CC2-1. The term “N” denotes the total number of effective analyses for each sample. Centralized age groups are also enlarged for samples Y9, CC2-2 and CC2-1. The term “n” denotes the ratio between the analytical number of enlarged age group and the total effective number.

from the four granitic and one gneissic samples: 39 grains for the 98.6 ± 2.1 Ma ST34-1 granite sample, 25 grains for the 98.4 ± 1.7 Ma ST34-2 granite sample, 13 grains for the 111.8 ± 3.3 Ma XK1-1 granite sample, 17 grains for the 151.8 ± 2.7 Ma XK1-2 amphibole plagiogneiss sample, and 107 grains for the 115.4 ± 0.7 Ma H2 granodiorite sample (Supplementary Data, Table S2). Chondrite-normalized rare earth element (REE) patterns for representative analyses are shown in Fig. 11. Most of the analyzed zircon grains display REE distribution patterns that increase steeply from La to Lu. They mostly feature pronounced positive Ce anomalies and negative Eu anomalies. However, seventeen zircon grains from sample H2 show flat light rare earth element (LREE) ($(Sm/La)_N \leq 1.45$) and steeply increasing heavy rare earth element (HREE) patterns, with small positive Ce anomalies ($Ce/Ce^* \leq 1.87$) (Fig. 11). Plagiogneiss sample XK1-2 also has one zircon exhibiting such a pattern. Eu/Eu^* ratios are commonly variable in samples H2 (0.04–0.55), XK1-1 (0.25–0.39), XK1-2 (0.16–0.74) and ST34-2 (0.44–0.82). Sample ST34-1 has two grains showing elevated Eu/Eu^*

ratios of 1.28 and 1.33, whereas the remainder vary between 0.09 and 0.76.

The Yb, Y, Hf and Nb contents of zircon grains are listed in Supplementary Data, Table S2. The Yb contents of samples H2 and XK1-2 range between 243.34 ppm and 2311.77 ppm and between 203.44 ppm and 1028.51 ppm, respectively. Samples XK1-1, ST34-1 and ST34-2 have relatively narrow variation ranges of 156.23–536.83 ppm, 41.98–538.93 ppm and 109.18–458.63 ppm, respectively. Similarly, the Y contents of samples H2 and XK1-2 show relatively wide ranges of 531.09–8413.27 ppm and 440.63–3252.58 ppm, respectively, whereas those of samples XK1-1, ST34-1 and ST34-2 fall in narrow ranges of 475.63–1691.49 ppm, 72.69–1748.14 ppm and 272.95–1474.17 ppm, respectively. The Hf contents of these samples are uniformly high, with ranges of 8114.13–14240.81 ppm (H2), 9579.00–12617.61 ppm (XK1-1), 6449.75–12005.61 ppm (XK1-2), 8697.88–14476.86 ppm (ST34-1) and 8562.98–14395.66 ppm (ST34-2). Nb contents are variable for zircons from samples H2 (0.65–24.06 ppm) and XK1-2 (0.53–

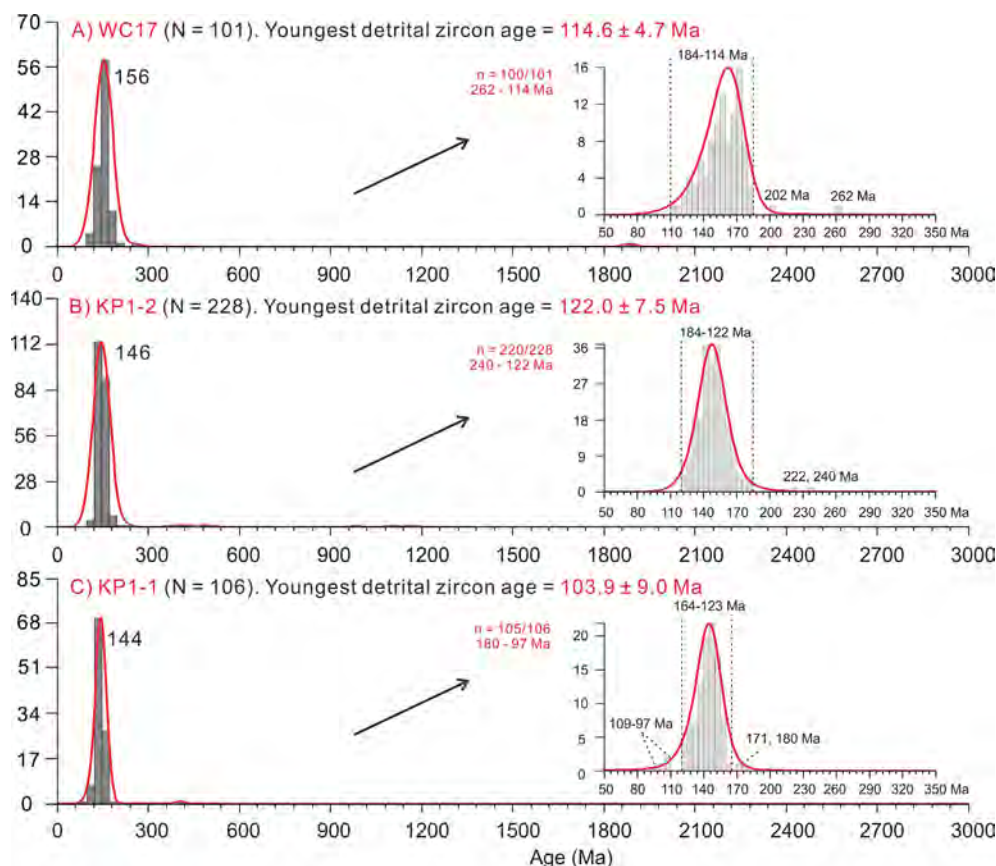


Fig. 8. Zircon U-Pb age spectra of metavolcaniclastic samples. (A) WC17; (B) KP1-2; (C) KP1-1. The term “N” denotes the total number of effective analyses for each sample. Centralized age groups are also enlarged. The term “n” denotes the ratio between the analytical number of enlarged age group and the total effective number.

18.17 ppm). Samples XK1-1, ST34-1 and ST34-2 have Nb content ranges of 0.55–9.53 ppm, 0.26–5.19 ppm, and 0.41–3.09 ppm, respectively.

5. Discussion

5.1. Ages and provenances of the offshore metatuff, metavolcaniclastic and metasedimentary rocks

Nonintrusive borehole samples from the basement of the Cenozoic northern South China Sea basins off the South China continent range from those displaying a singular Mesozoic age peak to those with wider age spectra. Several metatuff and metavolcaniclastic rocks record a single age cluster between ca. 185 Ma and ca. 120 Ma (Figs. 7 and 8). Two metatuff samples (CC2-1 and WC17) cluster at ca. 155 Ma (Fig. 7D, 8A), whereas metavolcaniclastic samples KP1-1 and KP1-2 cluster around ca. 145 Ma (Fig. 8B, C). Although it shows a multimodal pattern, metavolcaniclastic sample CC2-2 from forty meters above metatuff CC2-1 is characterized by prominent Cretaceous peak clustering at ca. 150 Ma (Fig. 7C). Metasedimentary rocks BD23-1, CC1-1 and YJ36-1 are all dominated by singular age peaks of ca. 150 Ma (individual analyses ranging between ca. 185 Ma and ca. 120 Ma) (Fig. 10A, C, E). Similar to metavolcaniclastic rock CC2-2, metaclastic samples BD23-2, CC1-2 and YJ36-2 from shallower depths also bear minor older zircon populations (Fig. 10B, D, F). Their dominant late Mesozoic (ca. 185–120 Ma) age peaks, relatively well-preserved zircon crystal morphology (Fig. 9) and geochemically immature rock texture suggest a local provenance off the South China continent. The youngest U-Pb ages of the metatuffs and metaclastic rocks are mostly

Middle to Late Cretaceous (120–90 Ma), among which BD23-2 and YJ36-2 have maximum depositional ages of ca. 90–85 Ma. Therefore, the protoliths of the South China continental margin were deposited around or soon after ca. 145 Ma but likely prior to ca. 85 Ma, which is the youngest plutonic age reported from the northern South China Sea basement (Fig. 2).

Small populations of older zircons are present in some metavolcaniclastic and metasedimentary samples. A few Paleoproterozoic (ca. 1900–1800 Ma) as well as Archean detrital zircon grains are found only in WZ12, CC2-2 and CC1-2 (Fig. 7A, 7C, 10D), indicating that at the time of deposition, little Cathaysian Paleoproterozoic crystalline basement (Xu et al., 2005, 2007; Yu et al., 2009; Li et al., 2014; Zhao et al., 2015) was exposed. The more prominent presence of early Paleozoic and Neo- to Mesoproterozoic zircon populations (Fig. 7A, 7C, 10B–D) suggests potential hinterland sources from (1) the late Mesoproterozoic to early Neoproterozoic Sibao orogen, i.e., the ca. 960–890 Ma Shuangxiwu arc and other ca. 1000–890 Ma rocks along the Sibao orogen between the Yangtze and Cathaysia blocks (e.g., Li et al., 2002; Li et al., 2009) and the ca. 850–750 Ma intracontinental plume and/or rifting magmatism (e.g., Li et al., 2003; Wang et al., 2007, 2009) and (2) the lower Paleozoic Wuyi-Yunkai orogen (e.g., Li et al., 2010; Wang et al., 2010, 2011; Xia et al., 2014). Based on the changes in provenance between samples from different depths in the same borehole (i.e., boreholes CC2, BD23, CC1 and YJ36) (Fig. 7C–D, 10A–F), there appears to be an increasing input from the Proterozoic–lower Paleozoic basement with time, possibly reflecting enhanced basement exposure during Cretaceous deposition in the study region.

In contrast to the samples discussed above with predominant late Mesozoic peaks, metavolcaniclastic sample WZ12 from the

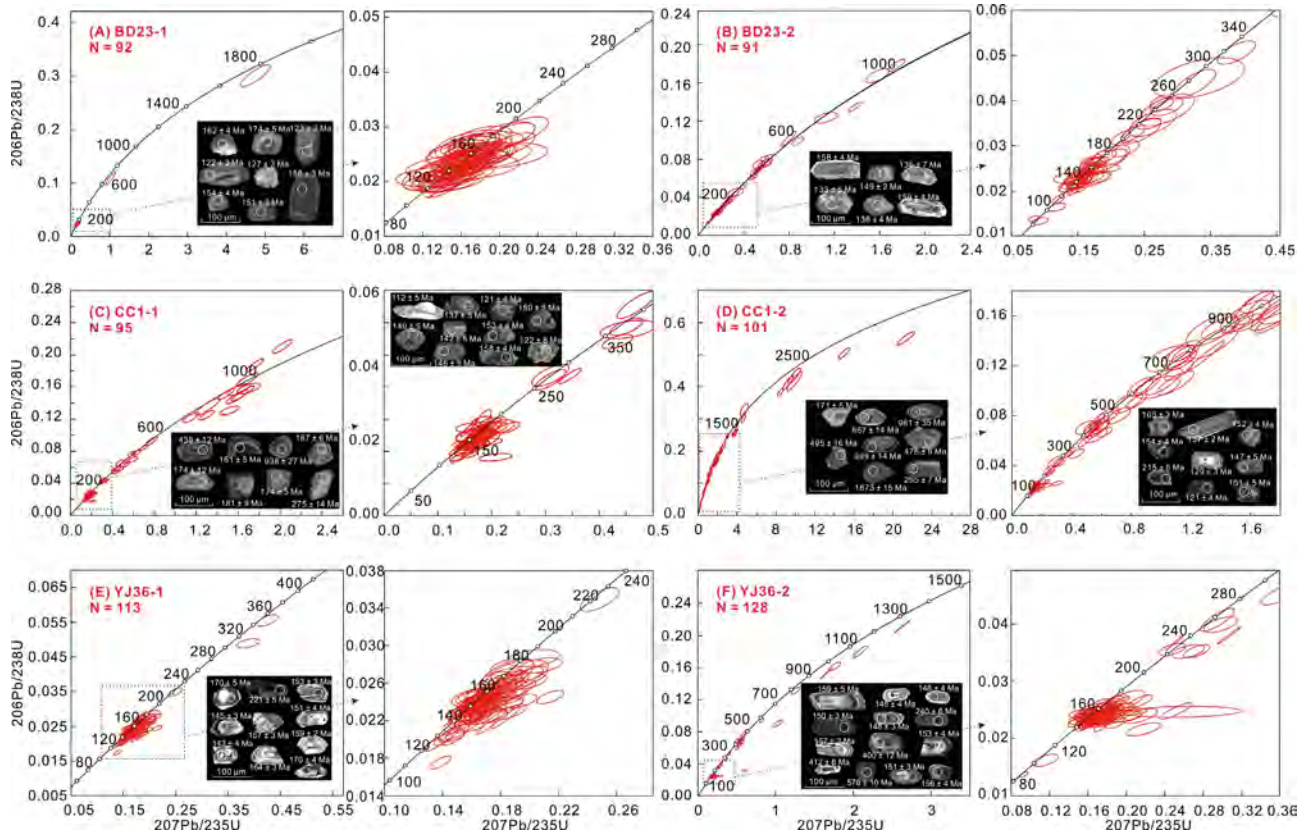


Fig. 9. LA-ICP-MS U-Pb concordia age plots and CL images of representative zircons from metasedimentary samples. (A) BD23-1; (B) BD23-2; (C) CC1-1; (D) CC1-2; (E) YJ36-1; (F) YJ36-2. The term “N” denotes the total number of effective analyses for each sample.

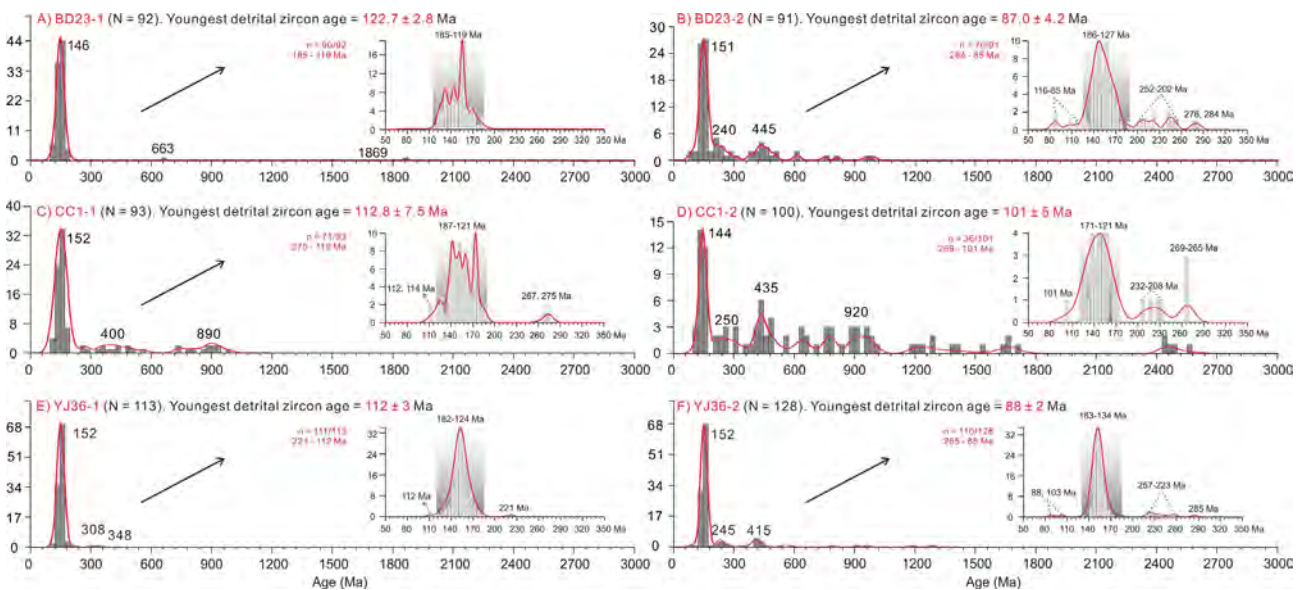


Fig. 10. Zircon U-Pb age spectra of metasedimentary samples. (A) BD23-1; (B) BD23-2; (C) CC1-1; (D) CC1-2; (E) YJ36-1; (F) YJ36-2. Centralized age groups are enlarged for all samples. The term “n” denotes the ratio between the analytical number of enlarged age group and the total effective number.

Beibu Gulf Basin (Fig. 2) is dominated by a large early Paleozoic cluster peaking at ca. 421 Ma (Fig. 7A). This sample also bears a secondary late Permian – Triassic cluster (centralized at ca. 250 Ma) plus a small ca. 820 Ma population. The dominance of ca. 420 Ma zircons here probably reflects their close affinity to the core of the lower Paleozoic Wuyi-Yunkai orogen where ca.

420 Ma granitic intrusions are widespread (e.g., Li et al., 2010; Liu et al., 2010). The ca. 250 Ma zircon peak in sample WZ12 (Fig. 7A) is echoed by the dominant peak of ca. 235 Ma in sample Y9 from SE of Hainan Island (Figs. 2 and 7B) and relatively small peaks in samples CC1-2, CC2-2 and BD23-2 from farther SE of Hainan Island (Figs. 2, 7C, and 10B, 10D). This relation is consistent

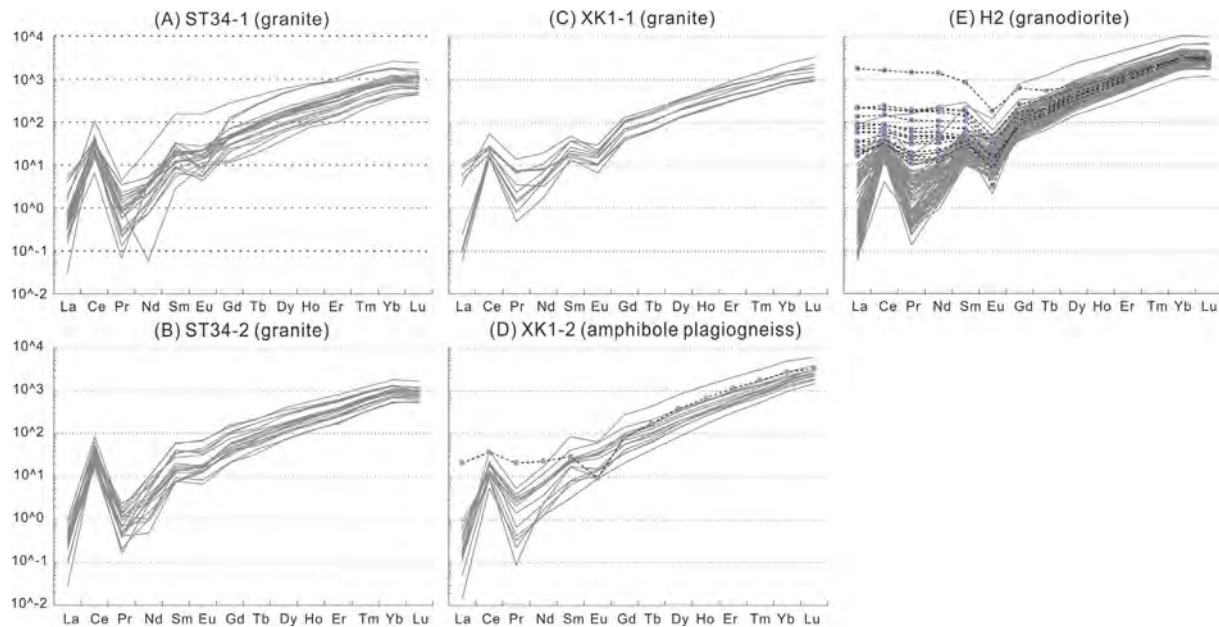


Fig. 11. Zircon rare earth element (REE) concentrations normalized to chondrites (Sun and McDonough, 1989) for igneous samples (A) ST34-1, (B) ST34-2, (C) XK1-1, (E) H2 and gneiss sample (D) XK1-2 from the northern South China Sea basin basement. Note that a few zircons from samples H2 and XK1-1 show flat LREE patterns (highlighted with purple dots and dashed lines).

with the close affinity of these sampling sites to Hainan Island, where arc magmatism is reported to have started from ca. 270 Ma (Li et al., 2006) and remained active during the Triassic (ca. 250–235 Ma) (Xie et al., 2005; Tang et al., 2013; Jiang et al., 2015) and possibly until the early Late Cretaceous (Wang et al., 2012) or even later, as suggested by Jiang and Li (2014).

5.2. Tectonic affinities of the offshore igneous rocks

Although a small proportion of the zircons from the studied igneous rocks possess flat LREE distribution patterns, implying a hydrothermal origin according to previous studies (Hoskin, 2005), the vast majority of them show pronounced positive Ce anomalies and negative Eu anomalies (Fig. 11), consistent with their magmatic origin. It has been suggested that zircon trace elements can be used to monitor the geochemical signatures of their host magmas (Grimes et al., 2015) and that their ratios can be used to determine tectonic affinities (Grimes et al., 2007). In Fig. 12, we plot our data from the igneous and plagiogneissic rocks on the diagnostic diagrams of U/Yb vs. Y, U/Yb vs. Hf and $\log_{10}(U/Yb)$ vs. $\log_{10}(Nb/Yb)$. The dashed lines in Fig. 12A and B mark the divides between zircons of continental and oceanic origins. Almost the entire dataset from the igneous and plagiogneissic rocks in this study plots within the field of “continental crust rock types”. The elevated U/Yb ratios (average 0.87) are also consistent with the whole-rock U/Yb ratio for the bulk continental crust (0.7; Rudnick and Gao, 2003). Fig. 12C further shows that zircons from the studied magmatic rocks generally plot within the continental arc field. In the Hf/Th vs. Th/Nb and Nb/Hf vs. Th/U diagrams (Fig. 13), zircons from these magmatic rocks plot dominantly within the arc-related orogenic field (Hawkesworth and Kemp, 2006; Yang et al., 2012).

Early Jurassic arc-related magmatism has previously been reported as suites of magnesian granite and diorite with ages of ca. 198–195 Ma in the NE South China Sea area (Xu et al., 2017). Onshore outcrops of I-type granites on southern Taiwan Island and in eastern Zhejiang have also been dated at ca. 190–180 Ma and ca. 90 Ma (Yui et al., 2009; Li et al., 2012b). Newly dated

arc-type granites penetrated by boreholes ST34, XK1 and H2 in the central-western section of the northern South China Sea, along with previously reported borehole granite ages (Qiu et al., 1996; Li et al., 1999; Shi et al., 2011; Xu et al., 2017), demonstrate the presence of a zone of Jurassic to Late Cretaceous arc granitoids under the northern South China Sea basin that formed from ca. 195 Ma until at least ca. 90 Ma (Fig. 2), consistent with the widespread occurrence of similar granitic intrusions onshore southeastern China (e.g., Zhou and Li, 2000; Li and Li, 2007; Li et al., 2012b) and on the islands of Taiwan and Hainan (Yui et al., 2009; Li et al., 2012b).

5.3. Tectonic implications: formation, duration and cessation of an Andean-type continental arc along the Western Pacific continental margin

The timing of subduction along the South China continental margin and of the change in the Western Pacific plate boundary from an Andean-type to the present-day Western Pacific type are questions of ongoing debate. The results of this study from samples penetrated by boreholes on the northwestern South China Sea continental margin shed new light on the lateral distribution and evolution of the arc system.

In Fig. 14, we use a model modified from Li and Li (2007) and Li et al. (2012b) to explain the new and existing results from the South China Sea basement. According to previous work, the Andean-type active margin started along coastal South China from ca. 280 Ma (Li et al., 2006, 2012a) (Fig. 14D). Our reported predominant ca. 270–205 Ma magmatic zircon clusters in the metavolcanic rocks, such as Y9 close to southeastern Hainan (Figs. 2 and 7B), imply a near-source provenance for this magmatic arc. According to the model of Li and Li (2007), this Andean-type active continental margin likely experienced flat slab subduction during the Triassic (ca. 250–200 Ma), featuring a predicted ~1000 km-wide coastal magmatic gap between the locations of Hong Kong and Shanghai once the reduced magmatic front had migrated to the cratonic interior by ca. 200 Ma (Fig. 14D, 250–200 Ma). In our results, such a coastal magmatic gap before and

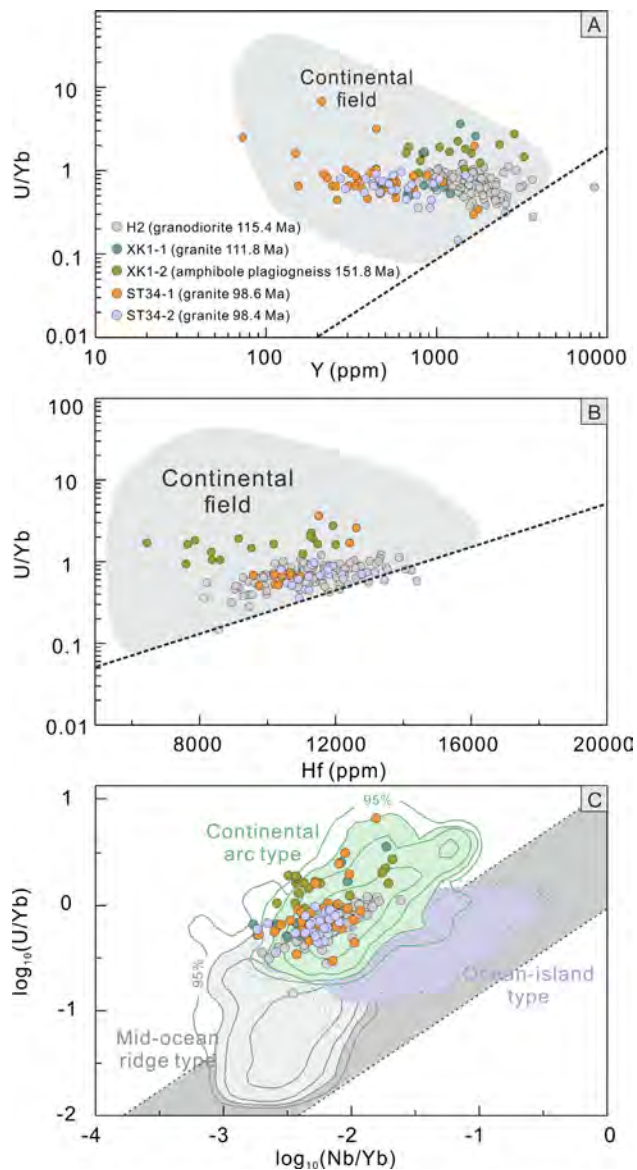


Fig. 12. Tectonic discrimination diagrams based on zircon trace elements. A) U/Yb vs. Y; B) U/Yb vs. Hf; C) $\log_{10}(U/Yb)$ vs. $\log_{10}(Nb/Yb)$. The lower boundary of the continental field is plotted by the dashed line on diagrams A and B (Grimes et al., 2007). In diagram C, the gray shaded fields are overlapping two-dimensional kernel density distributions for compiled datasets of “mid-ocean ridge-type”, “ocean island-type”, and “continental arc-type” zircons. The contours represent the density distribution of data from Grimes et al. (2015).

at approximately 200 Ma may be seen in the low number of detrital zircons at around 200 Ma in samples CC2-2, CC1-1 and YJ36-2 (Fig. 7C, 10C, 10F) and to a lesser degree in samples BD23-2 and CC1-2 (Fig. 10B, D). We interpret such a mixed signal to reflect the close affinity of these sites to Hainan Island, which is outside of the proposed flat-slab subduction segment.

Following the end of the flat-slab subduction phase, coastal arc magmatism appears to have restarted by ca. 190 Ma, interpreted to represent the resumption of normal subduction along the continental margin (Li et al., 2012b) (Fig. 14A–C). In our clastic samples from the basement of the northern South China Sea basins, post-200 Ma detrital zircon age peaks are commonly the most prominent (e.g., Figs. 7C–D, 8, and 9). The age spectra of these most samples between ca. 180 Ma and 120 Ma show no obvious gaps, but the signal obviously weakens toward ca. 90 Ma, implying almost continuous magmatic activity along the coastal region between 180 Ma

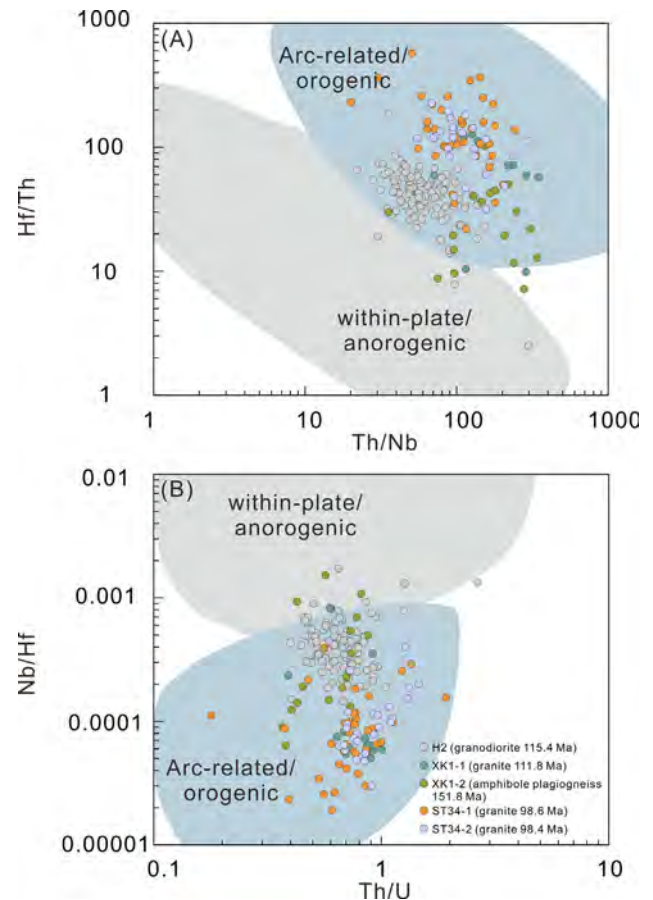


Fig. 13. Tectonic discrimination diagrams based on zircon trace elements. (A) Hf/Th vs. Th/Nb; (B) Nb/Hf vs. Th/U. The distinctly separated fields of the arc-related/orogenic environment and within-plate/anorogenic environment are from Hawkesworth and Kemp (2006) and Yang et al. (2012).

and 90 Ma but much weakened intensity after 120 Ma. This interpretation is consistent with results for Cretaceous metasedimentary rocks from Taiwan and implies an ongoing continental magmatic arc during this time interval.

As shown in Fig. 14A–B, 190–90 Ma plutonic arc magmatism spread from Hainan Island through the northern South China Sea to Taiwan, thus providing solid evidence for the presence of the continental arc along the present-day coastal and offshore continental shelf during this time. The lateral extent of this pre-90 Ma Andean-type plate boundary goes at least to the Korean Peninsula to the northeast (Sagong et al., 2005; Chough and Sohn, 2010), and to the Indochina block (Shellnutt et al., 2013) and Borneo (Hennig et al., 2017) to the south-west (Fig. 14E).

Although there are rare intrusive rocks within this belt dated as young as ca. 85 Ma (Fig. 2), the overall arc system appears to have stopped at or very soon after 90 Ma. Here we adopt the model of Li et al. (2012b) that the arc jumped oceanward soon after 90 Ma (Fig. 14D), marking the end of the Andean-type plate boundary and the beginning of the Western Pacific-type plate boundary based on observations in both East Asia and eastern Australia. However, exactly how this change of tectonic regime changed along the Western Pacific margin (e.g., Tapponnier et al., 1982; Biais et al., 1993; Hall, 2012; Huang et al., 2019) remain to be investigated. In addition, variable geochemical compositions from volcanic arc-related to within-plate signatures also imply a post-collisional or subduction-related environment, instead of being simply controlled by an oceanward subduction jump back event. It is possible that the actual history of the switching from

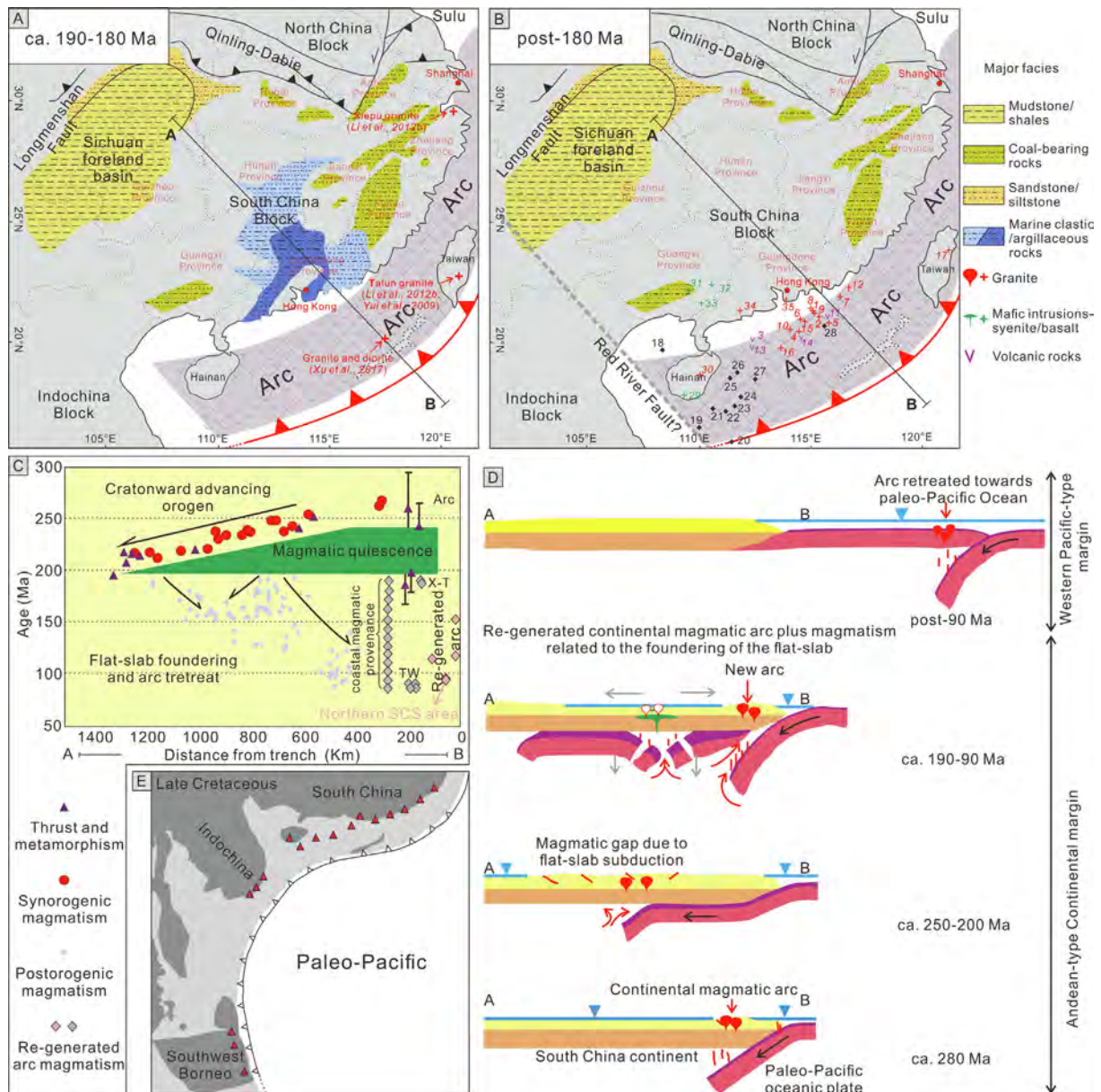


Fig. 14. A) Early Jurassic (ca. 190–180 Ma) paleogeography of the South China Block with a regenerated magmatic arc along the continental margin (after Li et al., 2012b). B) Post-180 Ma paleogeography of the South China Block (modified after Li et al., 2012b). Numbers in (B) mark the post-180 Ma magmatism within the South China Sea basin region, interpreted to represent the regenerated magmatic arc: 1–16 = granitoids and other igneous rocks in the South China Sea basement from Qiu et al. (1996) and Li et al. (1999) (refer to Table 1 for isotopic ages); 17 = 89–87 Ma granitoids from Tailuko valley, Taiwan Island, from Li et al. (2012b); 18–28 = granites, metatuffs, metavolcaniclastic rocks and metasedimentary samples in this study; 29 = basalt-andesite-rhyolite volcanic rocks on Hainan Island from Zhou et al. (2015); 30 = granodiorites and biotite granites on Hainan Island from Wang et al. (2012); 31–35 = mafic intrusions and granites within southern Guangxi and Guangdong Province from Li and Li (2007), and biotite granites therein. C) Time-space plot of magmatic rocks and thrust/metamorphic ages along cross-section A–B in A) and B), modified after Li and Li (2007) and Li et al. (2012b). “Coastal magmatic provenance” plotted as gray rhombuses = near-source provenance inferred from metatuff, volcanoclastic and metasedimentary rocks in this study and Tananao schist data from Li et al. (2012b). X–T = Xiepu and Talun granites that mark the onset of this regenerated arc (Yui et al., 2009; Li et al., 2012b). TW = ca. 89 Ma granites in eastern Taiwan Island from Li et al. (2012b). “Northern SCS basin” plotted as pink rhombuses = granites and granodiorites in the northern South China Sea basement. D) A cartoon illustrating the transformation from an active Andean-type continental margin to a passive Western Pacific-type continental margin, modified after Li et al. (2012b). E) A sketch of a reconstructed Late Cretaceous Andean-type arc along the South China and Sundaland margin, modified after Hall (2012). (For interpretation of the references to colour in this figure legend, the reader is referred to the web version of this article.)

Andean-type to Western Pacific-type subduction was fairly complicated. And this tectonic shifting subsequently led to even more enigmatic rifting events in southeastern Asia.

6. Conclusions

We report geochronological and geochemical results for borehole-penetrated plutonic rocks in the basement of the north-western South China Sea basins and provenance results for

metavolcaniclastic and metasedimentary rocks, which were previously believed to have Proterozoic or Paleozoic ages based on gravity-magnetic inversion. The protoliths of all the studied metaclastic samples (including metatuffs) contain youngest zircon populations between 140 Ma and 85 Ma and thus cannot be older than Cretaceous. Although a few samples contain prominent Proterozoic and Paleozoic detrital populations corresponding to local basement rock ages, the majority of the samples are dominated by ca. 180–120 Ma zircons with immature composition and relatively intact

zircon crystals, suggesting a nearby igneous provenance in coastal South China.

Three granites sampled through the boreholes that penetrated the metaclastic rocks give U-Pb zircon ages of 98.4 ± 1.7 Ma, 98.6 ± 2.1 Ma, 111.8 ± 3.3 Ma and 115.4 ± 0.7 Ma. Their geochemical data indicate an arc origin. Combined with previously discovered I-type granites both onshore and offshore eastern South China and on Hainan and Taiwan Islands, our new results support the presence of an Andean-type continental magmatic arc along the present-day continental shelf during 190–90 Ma. Our provenance data further support the previously proposed occurrence of a ca. 250–200 Ma episode of flat-slab subduction along this continental arc after the start of this arc system at ca. 280 Ma. The arc magmatism appears to have ceased soon after 90 Ma, interpreted as signaling an oceanward jump of the subduction system and the start of the present Western Pacific-type plate margin.

CRedit authorship contribution statement

Yuchi Cui: Conceptualization, Formal analysis. **Lei Shao:** Supervision, Visualization. **Zheng-Xiang Li:** Conceptualization, Validation, Writing - review & editing. **Weilin Zhu:** Project administration. **Peijun Qiao:** Methodology, Data curation. **Xiangtao Zhang:** Resources, Investigation.

Declaration of Competing Interest

The authors declare that they have no known competing financial interests or personal relationships that could have appeared to influence the work reported in this paper.

Acknowledgements

We thank China National Offshore Oil Corporation (CNOOC) for providing geological data and borehole samples from the northern South China Sea. This work was supported by the National Natural Science Foundation of China (grant numbers 42076066, 92055203 and 41874076), the National Science and Technology Major Project of China (grant number 2016ZX05026004-002), the National Key Research and Development Program of China (grant number 2018YFE0202400). Yuchi Cui acknowledges the China Scholarship Council and Curtin CIPRS and Research Scholarship for supporting her Joint PhD study at Curtin University. We thank Associate Editor Yongjiang Liu, Editor-in-Chief M. Santosh, reviewer Dr. Anne Briaies, and an anonymous reviewer for helpful comments on this manuscript.

Appendix A. Supplementary material

Supplementary data to this article can be found online at <https://doi.org/10.1016/j.gr.2021.06.021>.

References

Andersen, T., 2002. Correction of common lead in U-Pb analyses that do not report ^{204}Pb . *Chem. Geol.* 192, 59–79.

Briaies, A., Patriat, P., Tapponnier, P., 1993. Updated interpretation of magnetic anomalies and seafloor spreading stages in the South China Sea: implication for the tertiary tectonics of southeast Asia. *J. Geophys. Res.* 98, 6299–6328.

Charvet, J., Lapierre, H., Yu, Y., 1994. Geodynamic significance of the Mesozoic volcanism of southeastern China. *J. Asian Earth Sci.* 9 (4), 387–396.

Chen, J.F., Jahn, B.M., 1998. Crustal evolution of southeastern China: Nd and Sr isotopic evidence. *Tectonophysics* 284 (1–2), 101–133.

Chough, S.K., Sohn, Y.K., 2010. Tectonic and sedimentary evolution of a Cretaceous continental arc-backarc system in the Korean peninsula: New view. *Earth-Sci. Rev.* 101 (3), 225–249.

Ding, X., Chen, P., Chen, W., Huang, H., Zhou, X., 2006. Single zircon LA-ICPMS U-Pb dating of Weishan granite (Hunan, South China) and its petrogenetic significance. *Sci. China, Ser. D: Earth Sci.* 49 (8), 816–827.

Fu, J., Ma, C., Xie, C., Zhang, Y., Peng, S., 2004. The determination of the formation ages of the Xishan volcanic-intrusive complex in southern Hunan Province. *Acta Geosci. Sin.* 25 (3), 303–308.

Grimes, C.B., John, B.E., Kelemen, P.B., Mazdab, F.K., Wooden, J.L., Cheadle, M.J., Hanghøj, K., Schwartz, J.J., 2007. Trace element chemistry of zircons from oceanic crust: A method for distinguishing detrital zircon provenance. *Geology* 35 (7), 643–646.

Grimes, C.B., Wooden, J.L., Cheadle, M.J., John, B.E., 2015. “Fingerprinting” tectono-magmatic provenance using trace elements in igneous zircon. *Contrib. Mineral. Petrol.* 170, 46 (2015). <https://doi.org/10.1007/s00410-015-1199-3>.

Hall, R., 2012. Late Jurassic – Cenozoic reconstructions of the Indonesian region and the Indian Ocean. *Tectonophysics* 570–571, 1–14.

Hawkesworth, C.J., Kemp, A.I.S., 2006. Using hafnium and oxygen isotopes in zircons to unravel the record of crustal evolution. *Chem. Geol.* 226, 144–162.

Hayes, D.E., Nissen, S.S., 2005. The South China sea margins: Implications for rifting contrasts. *Earth Planet. Sci. Lett.* 237, 601–616.

Hennig, J., Breitfeld, H.T., Hall, R., Nugraha, A.M.S., 2017. The Mesozoic tectono-magmatic evolution at the Paleo-Pacific subduction zone in West Borneo. *Gondwana Res.* 48, 292–310.

Hoskin, P.W.O., 2005. Trace-element composition of hydrothermal zircon and the alteration of Hadean zircon from the Jack Hills. *Australia. Geochim. Cosmochim. Acta* 69, 637–648.

Huang, C.-Y., Wang, P., Yu, M., You, C.-F., Liu, C.-S., Zhao, X., Shao, L., Zhong, G., Yumul Jr, G.P., 2019. Potential role of strike-slip faults in opening up the South China Sea. *Natl. Sci. Rev.* 6, 891–901.

Isozaki, Y., Aoki, K., Nakama, T., Yanai, S., 2010. New insight into a subduction-related orogen: a reappraisal of the geotectonic framework and evolution of the Japanese Islands. *Gondwana Res.* 18, 82–105.

Jahn, B.M., Chen, P.Y., Yen, T.P., 1976. Rb-Sr ages of granitic rocks in southeastern China and their tectonic significance. *Geol. Soc. Am. Bull.* 86, 763–776.

Jahn, B.M., Martineau, F., Peucat, J.J., Cornichet, J., 1986. Geochronology of the Tananao schist complex, Taiwan, and its regional tectonic significance. *Tectonophysics* 125, 103–124.

Jahn, B.M., Chi, W.R., Yui, T.F., 1992. A Late Permian formation of Taowan (marbles from Chia-LiWell No.1): Pb-Pb isochron and Sr isotopic evidence, and its regional geological significance. *J. Geol. Soc. China* 35, 193–218.

Jiang, X.-Y., Li, X.-H., 2014. In situ zircon U-Pb and Hf-O isotopic results for ca. 73 Ma granite in Hainan Island: Implications for the termination of an Andean-type active continental margin in southeast China. *J. Asian Earth Sci.* 82, 32–46.

Jiang, X.-Y., Li, X.-H., Collins, W.J., Huang, H.-Q., 2015. U-Pb age and Hf-O isotopes of detrital zircons from Hainan Island: Implications for Mesozoic subduction models. *Lithos* 239, 60–70.

Kazuo, K., Teruyoshi, I., 2013. Spatiotemporal variations of Jurassic-Cretaceous magmatism in eastern Asia (Tan-Lu Fault to SW Japan): evidence for flat-slab subduction and slab rollback. *Terra Nova* 25, 414–422.

Klimetz, M.P., 1983. Speculations on the Mesozoic plate tectonic evolution of eastern China. *Tectonics* 2 (2), 139–166.

Lapierre, H., Jahn, B.M., Charvet, J., Yu, Y.W., 1997. Mesozoic magmatism in Zhejiang Province and its relation with the tectonic activities in SE China. *Tectonophysics* 274, 321–338.

Li, P.L., Liang, H.X., Dai, Y.D., Lin, H.M., 1999. Origin and tectonic setting of the Yanshanian igneous rocks in the Pearl River Mouth Basin. *Guangdong Geol.* 14 (1), 1–8 (in Chinese with English Abstract).

Li, X.-H., Li, Z.-X., Li, W.-X., Wang, Y.J., 2006. Initiation of the Indosinian Orogeny in South China: Evidence for a Permian Magmatic Arc on Hainan Island. *J. Geol.* 114 (3), 341–353.

Li, X.-H., Li, Z.-X., Li, W.-X., Liu, Y., Yuan, C., Wei, G., Qi, C., 2007. U-Pb zircon, geochemical and Sr-Nd-Hf isotopic constraints on age and origin of Jurassic I- and A-type granites from central Guangdong, SE China: A major igneous event in response to foundering of a subducted flat-slab?. *Lithos* 96, 186–204.

Li, X.-H., Li, W.-X., Li, Z.-X., Lo, C.H., Wang, J., Ye, M.F., Yang, Y.H., 2009. Amalgamation between the Yangtze and Cathaysia Blocks in South China: constraints from SHRIMP U-Pb zircon ages, geochemistry and Nd-Hf isotopes of the Shuangxiwu volcanic rocks. *Precambrian Res.* 174, 117–128.

Li, X.-H., Li, Z.-X., He, B., Li, W.-X., Li, Q.-L., Gao, Y., Wang, X.-C., 2012a. The Early Permian Active Continental Margin and Crustal Growth of the Cathaysia Block. In *Situ U-Pb, Lu-Hf and O Isotope Analyses of Detrital Zircons*. *Chem. Geol.* 328, 195–207.

Li, X.-H., Li, Z.-X., Li, W.-X., 2014. Detrital zircon U-Pb age and Hf isotope constrains on the generation and reworking of Precambrian continental crust in the Cathaysia Block, South China: A synthesis. *Gondwana Res.* 25, 1202–1215.

Li, Z.X., Li, X.H., Zhou, H.W., Kinny, P.D., 2002. Grenvillian continental collision in South China: New SHRIMP U-Pb zircon results and implications for the configuration of Rodinia. *Geology* 30 (2), 163–166.

Li, Z.-X., Li, X.-H., Kinny, P.D., Wang, J., Zhang, S., Zhou, H., 2003. Geochronology of Neoproterozoic syn-rift magmatism in the Yangtze Craton, South China and correlations with other continents: evidence for a mantle superplume that broke up Rodinia. *Precambrian Res.* 122, 85–109.

Li, Z.-X., Li, X.-H., 2007. Formation of the 1300-km-wide intracontinental orogen and postorogenic magmatic province in Mesozoic South China: a flat-slab subduction model. *Geology* 35 (2), 179–182.

Li, Z.-X., Li, X.-H., Wartho, J.A., Clark, C., Li, W.X., Zhang, C.L., Bao, C.M., 2010. Magmatic and metamorphic events during the early Paleozoic Wuyi-Yunkai orogeny, southeastern South China: new age constraints and pressure-temperature conditions. *Geol. Soc. Am. Bull.* 122, 772–793.

- Li, Z.-X., Li, X.-H., Chuang, S.-L., Lo, C.-H., Xu, X.S., Li, W.-X., 2012b. Magmatic switch-on and switch-off along the South China continental margin since the Permian: Transition from an Andean-type to a Western Pacific-type plate boundary. *Tectonophysics* 532–535, 271–290.
- Liu, H., Zheng, H., Wang, Y., Lin, Q., Wu, C., Zhao, M., Du, Y., 2011. Basement of the South China Sea area: tracing the Tethyan realm. *Acta Geol. Sin. (Engl. Ed.)* 83 (3), 637–655.
- Liu, R., Zhou, H.W., Zhang, L., Zhong, Z.Q., Zeng, W., Xiang, H., Jin, S., Lu, X.Q., Li, C.Z., 2010. Zircon U-Pb ages and Hf isotope compositions of the Mayuan migmatite complex, NW Fujian Province, southeast China: constraints on the timing and nature of a regional tectonothermal event associated with the Caledonian orogeny. *Lithos* 119, 163–180.
- Lo, C.H., Onstott, T.C., 1995. Rejuvenation of KAr systems for minerals in the Taiwan Mountain Belt. *Earth Planet. Sci. Lett.* 131 (1–2), 71–98.
- Martin, H., Bonin, B., Capdevila, R., Jahn, B.M., Lameyre, J., Wang, Y., 1994. The Kuiki peralkaline granitic complex (SE China) petrology and geochemistry. *J. Petrol.* 35 (4), 983–1015.
- Metcalfe, I., 1996. Gondwanaland dispersion, Asian accretion and evolution of eastern Tethys in Breakup of Rodinia and Gondwanaland and Assembly of Asia. *Aust. J. Earth Sci.* 43, 605–623.
- Nguyen, T.T.B., Satir, M., Siebel, W., Chen, F., 2004. Granitoids in the Dalat zone, southern Vietnam: age constraints on magmatism and regional geological implications. *Int. J. Earth Sci.* 93, 329–340.
- Qin, G.-Q., 1987. A preliminary study on foraminiferal assemblages of well 1 Xiyong, Xisha Islands and their coral reef formation. *Trop. Oceanol.* 6 (3), 10–20 (in Chinese with English Abstract).
- Qiu, Y.X., Li, P.L., Liang, H.X., 1996. Late Cretaceous–Cenozoic tectonic evolution and nature of continental margin in the northern South China Sea and Taiwan Strait. *Guangdong Geol.* 1 (3), 10–16 (in Chinese with English Abstract).
- Ramos, V.A., 1999. Plate tectonic setting of the Andean Cordillera. *Episodes* 22 (3), 183–190.
- Ramos, V.A., Folguera, A., 2009. Andean flat-slab subduction through time. *Geol. Soc. London, Spec. Publ.* 327 (1), 31–54.
- Rudnick R.L., Gao, S., 2003. Composition of the continental crust. In: Rudnick RL (ed) *The crust: Holland HD, Turekian KK (eds) Treatise on geochemistry, vol 3, Elsevier-Pergamon, Oxford, pp. 1–64.*
- Sagong, H., Kwon, S.-T., Ree, J.-H., 2005. Mesozoic episodic magmatism in South Korea and its tectonic implication. *Tectonics* 24, TC5002.
- Shao, L., Cao, L., Qiao, P., Zhang, X., Li, Q., van Hinsbergen, D.J.J., 2017. Cretaceous–Eocene provenance connections between the Palawan Continental Terrane and the northern South China Sea margin. *Earth Planet. Sci. Lett.* 477, 97–107.
- Shao, L., Cui, Y., Statteger, K., Zhu, W., Qiao, P., Zhao, Z., 2019. Drainage control of Eocene to Miocene sedimentary records in the southeastern margin of Eurasian Plate. *Geol. Soc. Amer. Bull.* 131 (3–4), 461–478.
- Shellnutt, J.G., Lan, C.-Y., Van Long, T., Usuki, T., Yang, H.-J., Mertzman, S.A., Iizuka, Y., Chung, S.-L., Wang, K.-L., Hsu, W.-Y., 2013. Formation of Cretaceous Cordilleran and post-orogenic granites and their microgranular enclaves from the Dalat zone, southern Vietnam: Tectonic implications for the evolution of Southeast Asia. *Lithos* 182, 229–241.
- Shi, H.S., Xu, C.H., Zhou, Z.Y., Ma, C.Q., 2011. Zircon U-Pb Dating on Granitoids from the Northern South China Sea and its Geotectonic Relevance. *Acta Geol. Sin. (Engl. Ed.)* 85 (6), 1359–1372.
- Sláma, J., Košler, J., Condon, D.J., Crowley, J.L., Gerdes, A., Hanchar, J.M., Horstwood, M.S.A., Morris, G.A., Nasdala, L., Norberg, N., Schaltegger, U., Schoene, B., Tubrett, M., Whitehouse, M.J., 2008. Plešovice zircon—A new natural reference material for U-Pb and Hf isotopic microanalysis. *Chem. Geol.* 249 (1–2), 1–35.
- Suggate, S.M., Cottam, M.A., Hall, R., Sevastjanova, I., Forster, M.A., White, L.T., Armstrong, R.A., Carter, A., Mojares, E., 2014. South China continental margin signature for sandstones and granites from Palawan, Philippines. *Gondwana Res.* 26 (2), 699–718.
- Sun, S.S., McDonough, W.F., 1989. Chemical and isotopic systematics of oceanic basalts: Implications for mantle composition and processes. *Geol. Soc. London, Spec. Publ.* 42, 313–345.
- Sun, X.M., Zhang, X.Q., Zhang, G.C., Lu, B.L., Yue, J.P., Zhang, B., 2014. Texture and tectonic attribute of Cenozoic basin basement in the northern South China Sea. *Sci. China Earth Sci.* 57 (6), 1199–1211.
- Tang, L.M., Chen, H.L., Dong, C.W., Yang, S.F., Shen, Z.Y., Cheng, X.G., Fu, L.L., 2013. Middle Triassic post-orogenic extension on Hainan Island: chronology and geochemistry constraints of bimodal intrusive rocks. *Sci. China Earth Sci.* 56, 787–793.
- Tapponnier, P., Peltzer, G., Le Dain, A.Y., Armijo, R., 1982. Propagating extension tectonics in Asia: new insights from simple experiments with plasticine. *Geology* 10, 611–616.
- Vermeesch, P., 2012. On the visualisation of detrital age distributions. *Chem. Geol.* 312–313 (3), 190–194.
- Wang, Q., Li, X.-H., Jia, X.-H., Wyman, D., Tang, G.-J., Li, Z.-X., Ma, L., Yang, Y.-H., Jiang, Z.-Q., Gou, G.-N., 2012. Late Early Cretaceous adakitic granitoids and associated magnesian and potassium-rich mafic enclaves and dikes in the Tunchang-Fengmu area, Hainan Province (South China): Partial melting of lower crust and mantle, and magma hybridization. *Chem. Geol.* 328, 222–243.
- Wang, X.C., Li, X.H., Li, W.X., Li, Z.X., 2007. Ca. 825 Ma komatiitic basalts in South China: first evidence for N1500C mantle melts by a Rodinian mantle plume. *Geology* 35, 1103–1106.
- Wang, X.C., Li, X.H., Li, W.X., Li, Z.X., 2009. Variable involvements of mantle plumes in the genesis of mid-Neoproterozoic basaltic rocks in South China: a review. *Gondwana Res.* 15, 381–395.
- Wang, X.F., Ma, D.Q., Jiang, D.H., Zhang, R.J., Zhang, Q.F., 1991. *Geology of Hainan Island (II): Magmatic Rocks*. Geological Publishing House, Beijing, p. 274 (in Chinese).
- Wang, Y.J., Zhang, F., Fan, W., Zhang, G., Chen, S., Cawood, P.A., Zhang, A., 2010. Tectonic setting of the South China Block in the early Paleozoic: resolving intracontinental and ocean closure models from detrital zircon U-Pb geochronology. *Tectonics* 29, TC6020.
- Wang, Y.J., Zhang, A.M., Zhao, G.C., Zhang, G.W., Zhang, Y.Z., Zhang, F.F., Li, S.Z., 2011. Kwangsiian crustal anatexis within the eastern South China Block: geochemical, zircon U-Pb geochronological and Hf isotopic fingerprints from the gneissoid granites of Wugong and Wuyi-Yunkai Domains. *Lithos* 127, 239–260.
- Wang, Y.J., Fan, W.M., Zhang, G.W., Zhang, Y.H., 2013. Phanerozoic tectonics of the South China Block: Key observations and controversies. *Gondwana Res.* 23, 1273–1305.
- Wiedenbeck, M., Hanchar, J.M., Peck, W.H., Sylvester, P., Valley, J., Whitehouse, M., Kronz, A., Morishita, Y., Nasdala, L., Fiebig, J., Franchi, I., Girard, J.P., Greenwood, R.C., Hinton, R., Kita, N., Mason, P.R.D., Norman, M., Ogasawara, M., Piccoli, P.M., Rhede, D., Satoh, H., Schulz-Dobrick, B., Skår, O., Spicuzza, M.J., Terada, K., Tindle, A., Togashi, S., Vennemann, T., Xie, Q., Zheng, Y.F., 2004. Further characterisation of the 91500 zircon crystal. *Geostand. Geoanal. Res.* 28 (1), 9–39.
- Xia, Y., Xu, X.S., Zou, H.B., Liu, L., 2014. Early Paleozoic crust–mantle interaction and lithosphere delamination in South China Block: evidence from geochronology, geochemistry, and Sr–Nd–Hf isotopes of granites. *Lithos* 184–187, 416–435.
- Xie, C.F., Zhu, J.C., Zhao, Z.J., Ding, S.J., Fu, T.A., Li, Z.H., Zhang, Y.M., Xu, D.M., 2005. Zircon SHRIMP U-Pb age dating of garnet-acmite syenite: constraints on the Hercynian–Indosinian tectonic evolution of Hainan Island. *Geol. J. Chin. Univ.* 11, 47–57 (in Chinese with English Abstract).
- Xu, C.H., Zhang, L., Shi, H.S., Brix, M.R., Huhma, H., Chen, L.H., Zhang, M.Q., Zhou, Z.Y., 2017. Tracing an early Jurassic magmatic arc from South to East China Seas. *Tectonics* 36 (3), 466–492.
- Xu, X., O'Reilly, Griffin, W.L., Deng, P., Pearson, N.J., 2005. Relict Proterozoic basement in the Nanling Mountains (SE China) and its tectonothermal overprinting. *Tectonics* 24, TC2003. <https://doi.org/10.1029/2004TC001652>.
- Xu, X.S., O'Reilly, S.Y., Griffin, W.L., Wang, X.L., Pearson, N.J., He, Z.Y., 2007. The crust of Cathaysia: age, assembly and reworking of two terranes. *Precambrian Res.* 158 (1–2), 51–78.
- Yang, J., Cawood, P.A., Du, Y., Huang, H., Huang, H., Tao, P., 2012. Large Igneous Province and magmatic arc sourced Permian–Triassic volcanogenic sediments in China. *Sediment. Geol.* 261–262, 120–131.
- Yu, J.-H., Wang, L., O'Reilly, S.Y., Griffin, W.L., Zhang, M., Li, C., Shu, L., 2009. A Paleoproterozoic orogeny recorded in a long-lived cratonic remnant (Wuyishan terrane), eastern Cathaysia Block, China. *Precambrian Res.* 174 (3–4), 347–363.
- Yui, T.F., Okamoto, K., Usuki, T., Lan, C.Y., Chu, H.T., Liou, J.G., 2009. Late Triassic–Late Cretaceous accretion/subduction in the Taiwan region along the eastern margin of South China evidence from zircon SHRIMP dating. *Int. Geol. Rev.* 51 (4), 304–328.
- Zhang, F.-Q., Wu, H.-X., Dilek, Y., Zhang, W., Zhu, K.-Y., Chen, H.-L., 2019. Guadalupian (Permian) Onset of Subduction Zone Volcanism and Geodynamic Turnover from Passive- to Active-Margin Tectonics in Southeast China. *Geol. Soc. Am. Bull.* 132 (1–2), 130–148.
- Zhao, L., Zhou, X., Zhai, M., Santosh, M., Geng, Y., 2015. Zircon U-Th-Pb-Hf isotopes of the basement rocks in northeastern Cathaysia block, South China: Implications for Phanerozoic multiple metamorphic reworking of a Paleoproterozoic terrane. *Gondwana Res.* 28, 246–261.
- Zhou, X.M., Li, W.X., 2000. Origin of Late Mesozoic igneous rocks in southeastern China: Implications for lithosphere subduction and underplating of mafic magmas. *Tectonophysics* 326, 269–287.
- Zhou, X.M., Sun, T., Shen, W.Z., Shu, L.S., Niu, Y.L., 2006. Petrogenesis of Mesozoic granitoids and volcanic rocks in South China: a response to tectonic evolution. *Episodes* 29, 26–33.
- Zhou, Y., Liang, X., Kroner, A., Cai, Y., Shao, T., Wen, S., Jiang, Y., Fu, J., Wang, C., Dong, C., 2015. Late Cretaceous lithospheric extension in SE China: Constraints from volcanic rocks in Hainan Island. *Lithos* 232, 100–110.
- Zhu, K.-Y., Li, Z.-X., Xu, X.-S., Wilde, S.A., 2014. A Mesozoic Andean-type orogenic cycle in Southeastern China as recorded by granitoid evolution. *Am. J. Sci.* 314, 187–234.
- Zhu, K.-Y., Li, Z.-X., Xia, Q.-K., Xu, X.-S., Wilde, S.A., Chen, H.-L., 2017a. Revisiting Mesozoic felsic intrusions in eastern South China: spatial and temporal variations and tectonic significance. *Lithos* 294–295, 147–163.
- Zhu, W.L., Xie, X.N., Wang, Z.F., Zhang, D.J., Zhang, C.L., Cao, L.C., Shao, L., 2017b. New insights on the origin of the basement of the Xisha Uplift, South China Sea. *Sci. China Earth Sci.* 60 (12), 2214–2222.

Formation of Hengchun Accretionary Prism Turbidites and Implications for Deep-water Transport Processes in the Northern South China Sea



CUI Yuchi^{1,2}, SHAO Lei^{1,*}, YU Mengming¹ and HUANG Chiyue¹

¹ State Key Laboratory of Marine Geology, Tongji University, Shanghai 200092, China

² Earth Dynamics Research Group, The Institute for Geoscience Research (TIGeR), School of Earth and Planetary Sciences, Curtin University, GPO Box U1987, Australia

Abstract: Located at the end of the northern Manila Trench, the Hengchun Peninsula is the latest exposed part of Taiwan Island, and preserves a complete sequence of accretionary deep-sea turbidite sandstones. Combined with extensive field observations, a ‘source-to-sink’ approach was employed to systematically analyze the formation and evolutionary process of the accretionary prism turbidites on the Hengchun Peninsula. Lying at the base of the Hengchun turbidites are abundant mafic normal oceanic crust gravels with a certain degree of roundness. The gravels with U-Pb ages ranging from 25.4 to 23.6 Ma are underlain by hundreds-of-meters thickness of younger deep-sea sandstone turbidites with interbedded gravels. This indicates that large amounts of terrigenous materials from both the ‘Kontum-Ying-Qiong’ River of Indochina and the Pearl River of South China were transported into the deep-water areas of the northern South China Sea during the late Miocene and further eastward in the form of turbidity currents. The turbidity flow drastically eroded and snatched mafic materials from the normal South China Sea oceanic crust along the way, and subsequently unloaded large bodies of basic gravel-bearing sandstones to form turbidites near the northern Manila Trench. With the Philippine Sea Plate drifting clockwise to the northwest, these turbidite successions eventually migrated and, since the Middle Pleistocene, were exposed as an accretionary prism on the Hengchun Peninsula.

Key words: IODP boreholes, source-to-sink analysis, submarine canyon, turbidite sandstones, Hengchun Peninsula, Taiwan

Citation: Cui et al., 2021. Formation of Hengchun Accretionary Prism Turbidites and Implications for Deep-water Transport Processes in the Northern South China Sea. *Acta Geologica Sinica (English Edition)*, 95(1): 55–65. DOI: 10.1111/1755-6724.14640

1 Introduction

Formation of large river systems always attracts much attention. Nowadays, global seafloor topographic maps are of great significance for the scientific observation of submarine canyons, such as the Taitung Canyon off the coast of eastern Taiwan Island and the submarine canyons in the Gulf of Mexico. Submarine canyons mostly originate from slope break zones of the continental shelf, and sediments are transported in mainly in the form of gravity flow (e.g. Callow et al., 2014; Hansen et al., 2015; Liu J et al., 2019; Liu B et al., 2020). However, integrated research on the deposition mechanism of submarine canyons is still lacking, and questions such as how they shape the seafloor landforms during transportation remain unknown. With the South China Sea (SCS) seafloor expansion during the Cenozoic, large topographic differences occurred along the continental margin and provided ideal conditions for submarine canyon evolution. Recent IODP 367/368 discovered a thick layer of well-rounded gravels of middle Miocene age at the northern SCS ocean–continent boundary (Stock et al., 2018; Sun et al., 2018), which implies that large submarine canyons had

possibly reached the then SCS deep basin. However, further researches about their transporting routes and depositional characteristics are still required for a better understanding of the deep-sea canyon process. Due to the collision between the Eurasian Plate (EP) and Philippine Sea Plate (PSP), the overall topography of the SCS area is west higher and east lower. As the deepest area of the SCS, the Manila Trench was first developed in the middle Miocene (Huang et al., 2018), and has since become an optimal receiver for voluminous sediments delivered by submarine canyons. The Hengchun Peninsula in the southern end of Taiwan is the latest exposed part of the Manila Trench accretionary wedge body (Fig. 1; Huang et al., 2018), and has rarely undergone transformation or destruction by subsequent tectonic movements. Therefore, the Miocene intact turbidite successions on the Hengchun Peninsula are promising to reveal the deep-sea sedimentary transport processes in canyons (Fig. 2).

Many controversies remain regarding the sedimentary sources and transportation routes of the Hengchun turbidite sandstones. According to the NW–SE paleocurrent measurement and elemental geochemical analysis, a large amount of sediments might have been delivered from the South China SE coastal area to the

* Corresponding author. E-mail: lshao@tongji.edu.cn

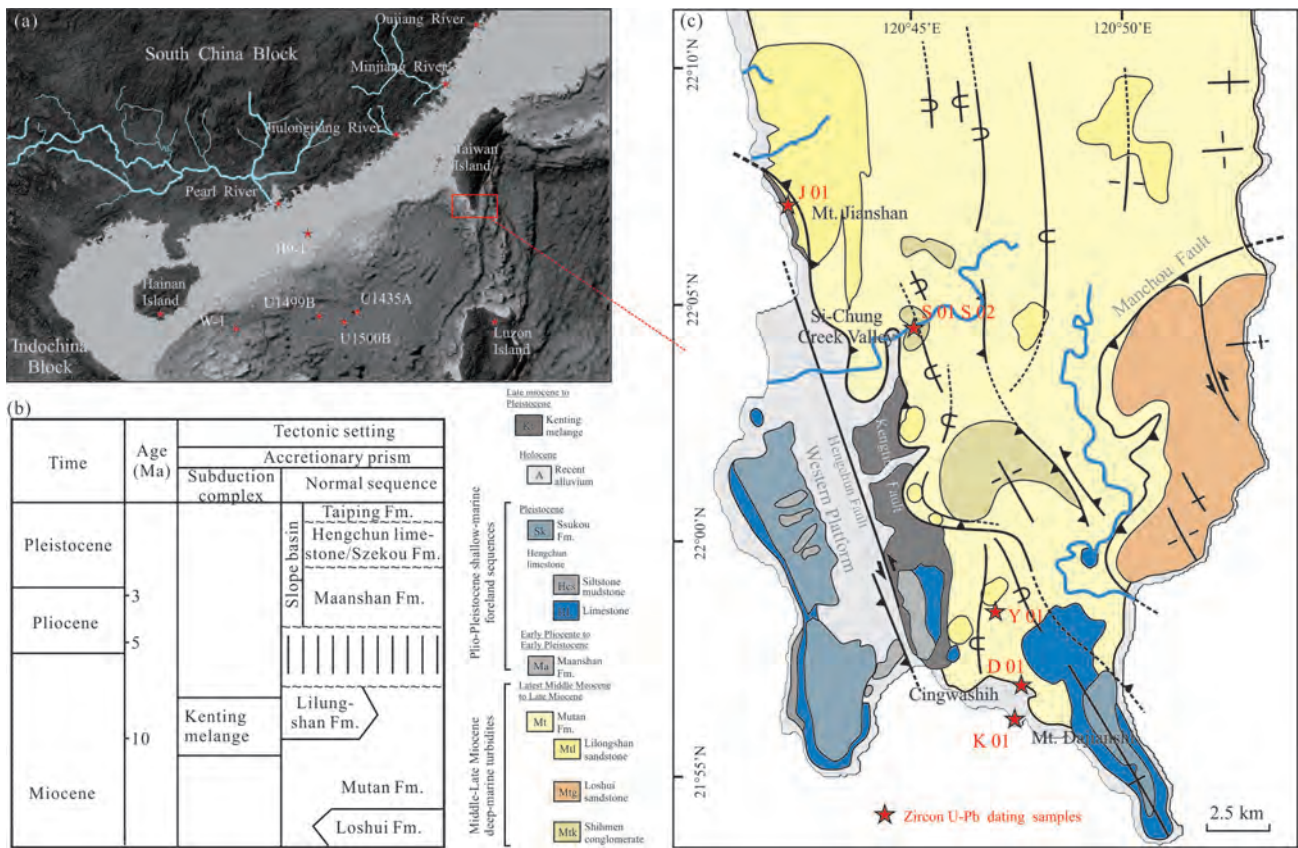


Fig. 1. Topographic and geologic maps of the northern South China Sea and surrounding areas. (a) Topographic map of Taiwan Island and its surrounds – studied samples and published data marked with red stars; (b) stratigraphic framework of the Hengchun Peninsula; (c) geological map of the Hengchun Peninsula (modified from Chang et al., 2003; Zhang et al., 2014); Studied samples for zircon U-Pb dating marked by red stars; J 01, S 01 and Y 01 are sandstones; S 02, K 01 and D 01 are gabbro gravels within turbidites.

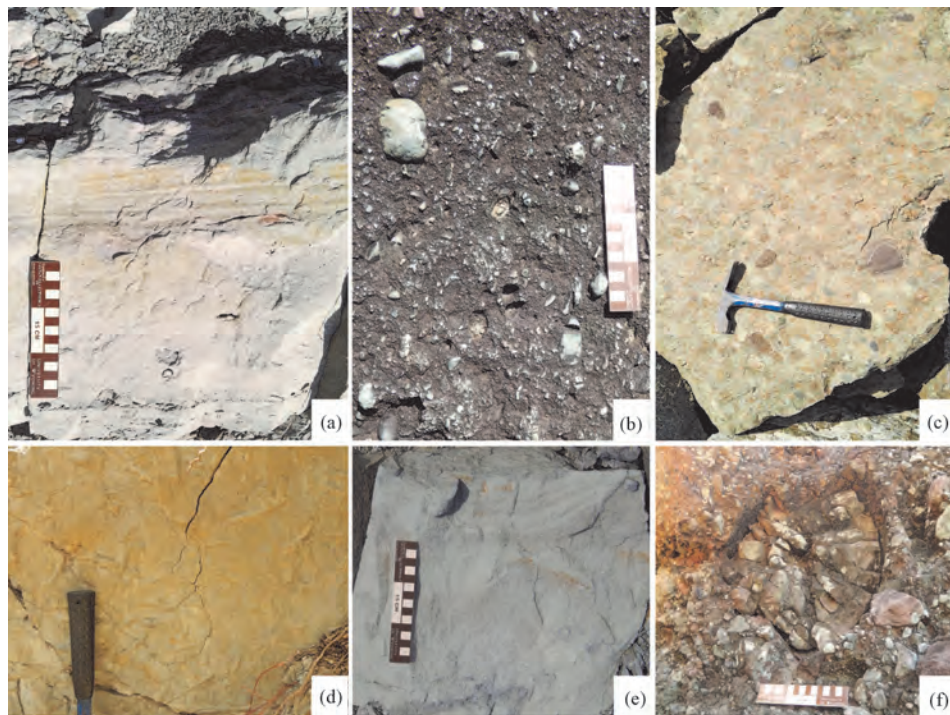


Fig. 2. Turbidite outcrops of Hengchun Peninsula, Taiwan. (a) Turbidites showing typical Bouma sequences; (b) basic rock gravels; (c) basic rock conglomerate layer forming grain-supported sedimentary structure; (d) trace fossils parallel to the sedimentary strata; (e) convolute beddings; (f) pillow basalt gravel.

Hengchun Peninsula via certain river networks, such as the Minjiang River and the Jiulongjiang River (Chen et al., 1990; Zhang et al., 2014, 2017). However, a SE–NW paleocurrent direction was also identified within the Hengchun turbidite sandstones (Chang et al., 2003; Shan et al., 2013). Apparently, for an accretionary prism with complex structural modifications, simply relying on paleo-flow direction measurements might cause serious misunderstanding about its provenance analysis. Also noteworthy is that the detrital zircon U–Pb age spectra show obvious differences between the Hengchun turbidites and the South China coastal river sediments. Combining with heavy mineral assemblage analyses, Chen X Y et al. (2018) implied that the Minjiang and Jiulongjiang rivers have long been of relatively confined fluvial networks with limited transport capacity. Therefore, the Hengchun Peninsula accretionary prism was most likely influenced from other provenances.

The Hengchun turbidite sequences are typified by abundant interbedded mafic gravels, such as basalts and gabbros. In addition to thick turbidite successions, the Hengchun accretionary prism also comprises a large number of basic gravel-bearing units, such as the Kenting mélange, the Shimen conglomerate, the Cingwashih slump deposits and the Lilungshan conglomerate (Page and Lan, 1983; Zhang et al., 2014, 2016). To be specific, the distinctive gravel or slumped layers were mainly formed by gravity flow, while well-rounded mafic gravels were deposited within the typical deep-sea turbidites. According to previous studies, these well-rounded gravels were sourced from the SCS broken oceanic crust, and were scraped off by the overlying slab of the Manila Trench during the SCS subduction (e.g. Page and Lan, 1983; Pelletier and Stephan, 1986; Zhang et al., 2014). These basic gravels commonly show geochemical characteristics of N-MORBs, E-MORBs and OIBs, which confirm their affinities to normal oceanic crust or seamounts (Chen H Y et al., 2018; Yu et al., 2018; Tian et al., 2019). It has been speculated that they were possibly sourced from the West PSP over the Manila Trench (Chen H Y et al., 2018; Tian et al., 2019), or the SCS downward plate (Yu et al., 2018; Tian et al., 2019). The ages of these basic rocks range mainly between the late Oligocene and early Miocene (Zhang et al., 2016; Tian et al., 2019). Therefore, they were more likely from the SCS subducting oceanic crust, with lesser possibility from the Huatung Basin of the PSP (Tian et al., 2019). Notably, the basic gravels within the Hengchun turbidites mostly exhibit good roundness (Fig. 2), and demonstrate features of long-distance transport and an abrasion process. Prior to the arc–continent collision on Taiwan Island, the SCS seamount subduction might have caused the Taiwan accretionary prism to experience a short exposure above sea level (Tian et al., 2019). Scraped off the SCS descending plate, the oceanic crustal fragments might have also undergone various exposure, transport and re-sedimentation processes, resulting in the mafic gravel layer within the accretionary turbidites. Yet, according to simulation results, the seamount subduction possibly cast limited influence on the uplift of the Hengchun ridge (Li et al., 2013). Although seamount subduction might significantly destroy the original

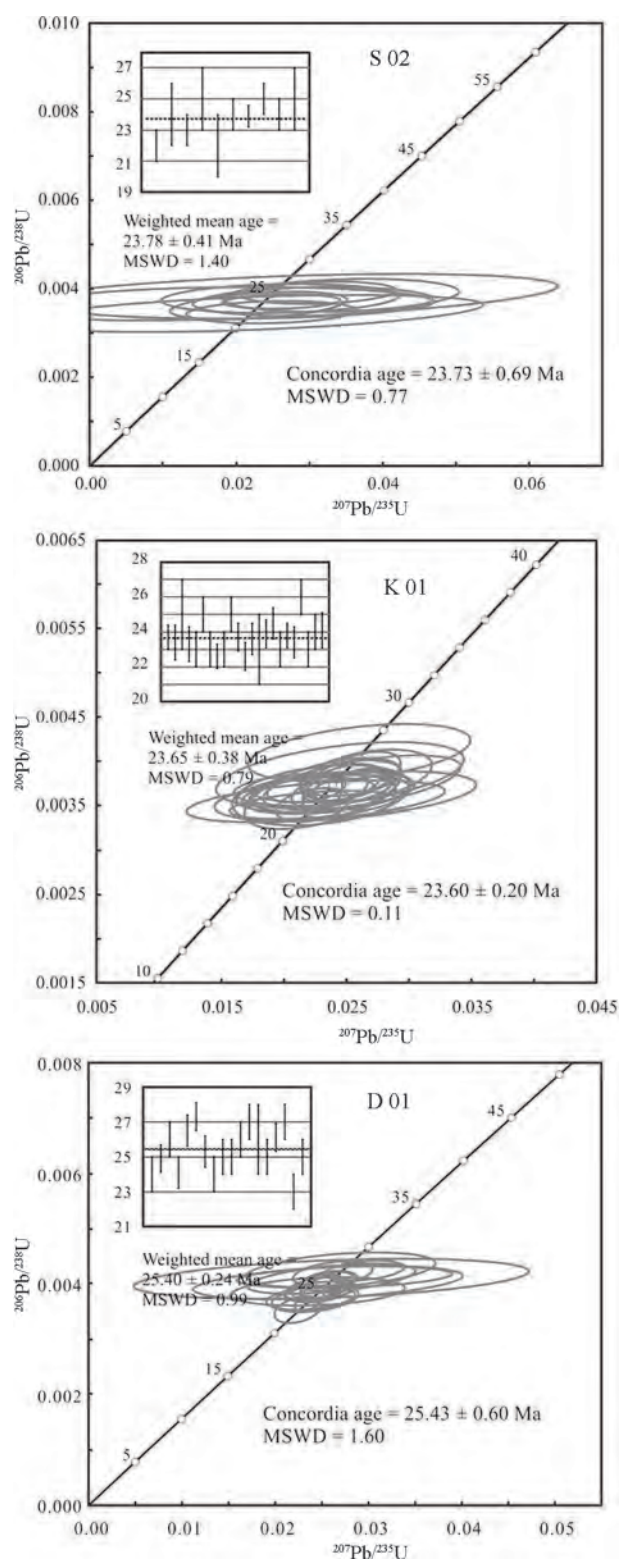


Fig. 3. Zircon U–Pb dating of the gabbro gravels within the Hengchun turbidite sequences. Both weighted mean ages and concordia ages are shown for samples S 02, K 01 and D 01. (data from Meng et al., 2020).

structure of the accretionary prism, this process is insufficient to interpret the existence of massive basic gravels within the normal turbidite successions. As a

consequence, provenances and formation of the Hengchun turbidite body as well as its unique mafic gravels require a more integrated explanation.

This paper combines field geological observations and detrital zircon U-Pb geochronology to reveal the sedimentary characteristics of the Hengchun accretionary turbidite sandstones. A source-to-sink comparative analysis has been conducted using data systematically compiled from Hainan Island, the Qiongdongnan Basin, the Pearl River Mouth Basin, the modern Pearl River Delta, IODP367/368 site U1499B/1500B, IODP349 site U1435A of the northern SCS, and the Jiulongjiang–Minjiang–Oujiang fluvial systems of the South China SE coastal areas, and the Luzon Volcanic arc. We aim to extrapolate the evolution of the Hengchun accretionary turbidite and to provide better comprehension of the sedimentary transport processes in the SCS deep-water basins.

2 Geological Background and Stratigraphic Framework

Taiwan Island is an arc-continent collision orogeny that still experiences ongoing enlargement. Since the middle Miocene, the SCS oceanic crust started to subduct eastward beneath the PSP. As a result, Luzon volcanic island arc and its accretionary prism to the west were gradually formed (Huang et al., 2006, 2018). Because of the PSP clockwise rotation to the northwest, the Luzon Arc collided obliquely with the Eurasian Plate at ca. 7–5 Ma. Consequently, the Cenozoic sedimentary strata of the South China continental margin, and the original accretionary wedge around the Manila Trench commonly suffered from strong deformation and uplift. Taiwan Island then started to form, and presently still experiences continual growth (e.g. Huang et al., 2006; Lee et al., 2006; Lin et al., 2009). Meanwhile, the PSP was also subducting northward under the Eurasian Plate. Younger strata of the southern Taiwan orogenic belt emerged and were uplifted while older strata to the north collapsed in turn and disappeared into the submarine environment (Teng, 1996; Sibuet and Hsu, 2004).

Located at the southernmost tip of Taiwan, the Hengchun Peninsula extends further north to the Central Range, and south to the Hengchun Ridge in the underwater setting (Fig. 1a). The Hengchun Peninsula represents the initial stage of the Taiwan collision and uplifting processes. Therefore, this part has preserved many oceanic crust basic conglomerates, normal deep-sea turbidite sequences, and subsequent shallow-marine sediments, which comprise the Kenting mélangé structure. The presence of these materials further allows the Hengchun Peninsula to serve as a natural laboratory for studying the formation and evolution of accretionary wedges (Pelletier and Stephan, 1986; Chang et al., 2003; Lester et al., 2013).

The Kenting mélangé comprises two sets of sedimentary sequences in the Hengchun Peninsula: 1) middle–Upper Miocene deep-sea turbidites, and 2) Pliocene–Pleistocene shallow-marine sediments (Fig. 1b). The Mutan Formation (Fm.) is the main stratigraphic unit of the accretionary turbidite sandstones. Together with

interbedded strata such as the Shihmen Conglomerate, the Loshui Sandstone, and the Lilungshan Sandstone, the Mutan Fm. reaches ca. 2000 m in thickness and is dominated by alteration of sandstones and siltstones interbedded with abundant lenticular gravels. According to planktonic foraminifera biostratigraphy, the Mutan Fm. was deposited around 11.6–6.4 Ma in a deep-sea canyon environment (Chang, 1964; Cheng et al., 1984; Chang et al., 2003). Basic conglomerates of the Mutan Fm. are widely distributed in the Si-chung Creek Valley, the Cingwashih and other areas (Fig. 1c). These gravels include mostly basalt, gabbro and diabase rocks, showing grain- or matrix-supported sedimentary structures and a high degree of roundness. Exposed in the eastern part of the Hengchun Peninsula, the Loshui Sandstone is ca. 1,000 m thick and dominated by thick layers of fine- to medium-grained sandstone. Planktonic foraminifera biostratigraphy indicates its deposition age of ca. 12 Ma, close to the frontal edge of a deep-water fan. The Lilungshan Sandstone, on the other hand, is mainly distributed on the western side of the Hengchun Peninsula. It is ca. 2,000 m in thickness, and features upward-coarsening sequences deposited at 11.6–6.4 Ma (Chang, 1964).

From the Pliocene to the Pleistocene, the Hengchun Peninsula was dominated by a shallow-marine sedimentary environment. The Maanshan Fm. is an Upper Pliocene–Lower Pleistocene neritic sequence (ca. 800-m thick) of ca. 3.7–1 Ma unconformably overlying the Upper Miocene deep-sea turbidite successions (Fig. 1b). Mainly exposed on the Western Platform of the Hengchun Peninsula, the Maanshan Fm. reaches an elevation of ca. 200–300 m, and represents the initial arc-continent collision in Taiwan. The Hengchun Pleistocene strata were deposited in less than 0.5 Ma, and are mainly distributed on the Western Platform's eastern slope. With the predominance of neritic reefal limestone and fluvial deposits, these younger Hengchun strata imply that the slope basin was initially uplifted and exposed above sea level during this period.

3 Field Observation of Hengchun Turbidites

The lower beds of the Hengchun turbidite successions mainly comprise basic gravels, which commonly form the A section of a typical Bouma sequence (Bouma, 1962). These gravels are dominated by basalts and gabbros, showing relatively good roundness and poor sorting. Metamorphic rock fragments have rarely been observed. Overall, the lowest sandstone layer of the Hengchun turbidites contains gravels, and develops obvious erosion boundaries. Parallel and cross bedding are common in the upper sandstones, which are followed by an uppermost mudstone with horizontal bedding (Fig. 2a). Mafic rock conglomerates are mainly accumulated within the turbidite A section (Fig. 2b), whereas other sections also bear basic rock gravels of extremely high content, and form conglomerate layers with 0.5 m to several meters in thickness. These conglomerates mostly show matrix- or grain-supported structures (Fig. 2c). Basalt gravels with pillow-shape are also observed (Fig. 2f). Presence of

imbricate arrangements within certain beds indicates paleo-current directions, deep-water trace fossils are frequently preserved parallel to the sedimentary strata (Fig. 2d). In addition, the sandstones commonly develop water-escape sedimentary structures, such as dish bedding (Fig. 2e).

Apparently, the basic rock gravels and thick sandstones were commonly deposited as deep-sea turbidite sequences in the form of gravity flows. In addition to the voluminous typical turbidity current deposits, the Hengchun Peninsula also has a large abundance of exposures of other gravity flow deposits, such as detrital flow and mud-rock flow sediments. Representative basic-ultrabasic rock gravels, such as gabbros and pillow-shaped lava, are shown in Fig. 2b and 2f.

4 Samples and Methodology

Zircon U-Pb dating analyses were carried out on the Hengchun turbidite sandstone and gabbro samples, the IODP 367/368 scientific drilling and the northern SCS commercial drilling samples. Zircon grain collection, mounting, cathodoluminescence (CL) imaging and LA-ICP-MS isotopic dating were all completed in the State Key Laboratory of Marine Geology, Tongji University, Shanghai. The laser ablation system is New Wave 213 nm, and the ICP-MS is Thermo Elemental X-Series. In the laser ablation process, helium gas is used as carrier gas, and argon gas is used as compensation gas to adjust sensitivity. Beam size of the laser spot is 30 μm , and the ablation frequency is 10 Hz. Each analysis includes a blank signal of 25 s and a sample signal of 50 s. U-Pb isotopic dating uses the international standard zircon 91500 (1065.4 ± 0.3 Ma) as an external standard, and uses zircon standard Plešovice (337.1 ± 0.4 Ma) to monitor the accuracy of the analysis results. U-Pb isotopic ratio and age calculations were completed using software ICPMSDataCal, and common Pb correction was performed following the method of Andersen (2002). According to Compston et al. (1995), calculated $^{206}\text{Pb}/^{238}\text{U}$ ages are adopted for zircons younger than 1000 Ma, whereas $^{207}\text{Pb}/^{206}\text{Pb}$ ages are adopted for those older than 1000 Ma.

5 Results

5.1 U-Pb ages of the Hengchun gabbros

Zircon CL images of the gabbro gravels within the Hengchun accretionary prism turbidites show that most grains develop clear oscillatory zoning structures. Th/U values are higher than 0.1 indicating a magmatic origin (Hoskin and Schaltegger, 2003). The concordia U-Pb age is 23.60 ± 0.20 Ma (MSWD = 0.11) for Sample K 01, 23.78 ± 0.41 Ma (MSWD = 1.40) for Sample S 02, and 25.40 ± 0.24 Ma (MSWD = 0.99) for Sample D 01, respectively (Fig. 3). Thus, we consider that the crystallization ages of the gabbro gravels are 25.4–23.6 Ma, in the late Oligocene.

5.2 Detrital zircon U-Pb age patterns of Hengchun turbidite sandstones

Detrital zircon U-Pb age spectra of the Hengchun

turbidite sandstones show that samples S 01, J 01, and Y 01 are characterized by broad multimodal patterns, including obvious Yanshanian (ca. 150–65 Ma), Indosinian (ca. 260–200 Ma), and Lvliangian (ca. 2500–1800 Ma) peaks plus a unique Cenozoic cluster. The minor age clusters include Caledonian (ca. 550–350 Ma) and Jinningian (ca. 1000–800 Ma) periods. To be noted, both samples S 01 and J 01 are featured by apparent Cenozoic peaks centralized at ca. 23 Ma, whereas sample Y 01 has peaks centralized at ca. 25 Ma of slightly lower proportion (Fig. 4a).

5.3 Detrital zircon U-Pb age patterns of northern South China Sea borehole samples

The upper Oligocene sandstone sample U1499 33R from drill site U1499B has a detrital zircon U-Pb age pattern characterized by a single prominent Yanshanian peak centralized at ca. 150 Ma. The upper Miocene turbidite sandstone samples U1500B 22R and U1500B 25R from site U1500B both feature dark gray sandstones with plentiful feldspar-quartz grains. Their detrital zircon U-Pb age patterns show broad spectra with obvious Yanshanian, Indosinian, and Caledonian populations, and secondary Jinningian and Archean peaks (Fig. 4b).

Sample W-1 taken from the Central Canyon of the Qiongdongnan Basin also shows a broad multimodal pattern in its detrital zircon U-Pb age spectrum. It is dominated by an obvious Yanshanian peak, with Indosinian, Caledonian and Jinningian periods as secondary clusters. Additionally, its Indosinian and Caledonian groups in the U-Pb age spectrum bear similar proportion (Fig. 4b).

6 Discussion

6.1 Origin of basic rock gravels within Hengchun accretionary prism turbidites

Previous scholars have conducted petrographic and geochemical analyses on the basic rock gravels of the Hengchun accretionary prism turbidites, indicating that the gravels include mainly basalts, gabbros, and amphibolites, with elemental and isotopic geochemical characteristics similar to N-MORBs, E-MORBs and OIBs (Chen H Y et al., 2018; Yu et al., 2018; Tian et al., 2019). The subduction of the SCS oceanic crust beneath the PSP was the key to generating the Hengchun Peninsula accretionary prism. Ocean drilling and dredge sampling have revealed that the SCS oceanic crust develops N-MORBs, E-MORBs and OIBs features (Tu et al., 1992; Zhang G L et al., 2018). These mafic materials from the normal oceanic crust are exactly the same rock assemblages as those in the basic rock gravels of Hengchun accretionary wedge turbidites. Therefore, the SCS normal oceanic crust is extremely likely the most important source area for the turbidites.

The western region of the PSP, including the Huatung Basin and Luzon Island, on the other hand, represent the overlying plates of the Manila Trench. The Huatung Basin develops an E-MORB type (Hickey-Vagar et al., 2008), and Luzon Island develops ophiolitic suites while volcanic island arcs exposed since the Late Mesozoic (Yu et al.,

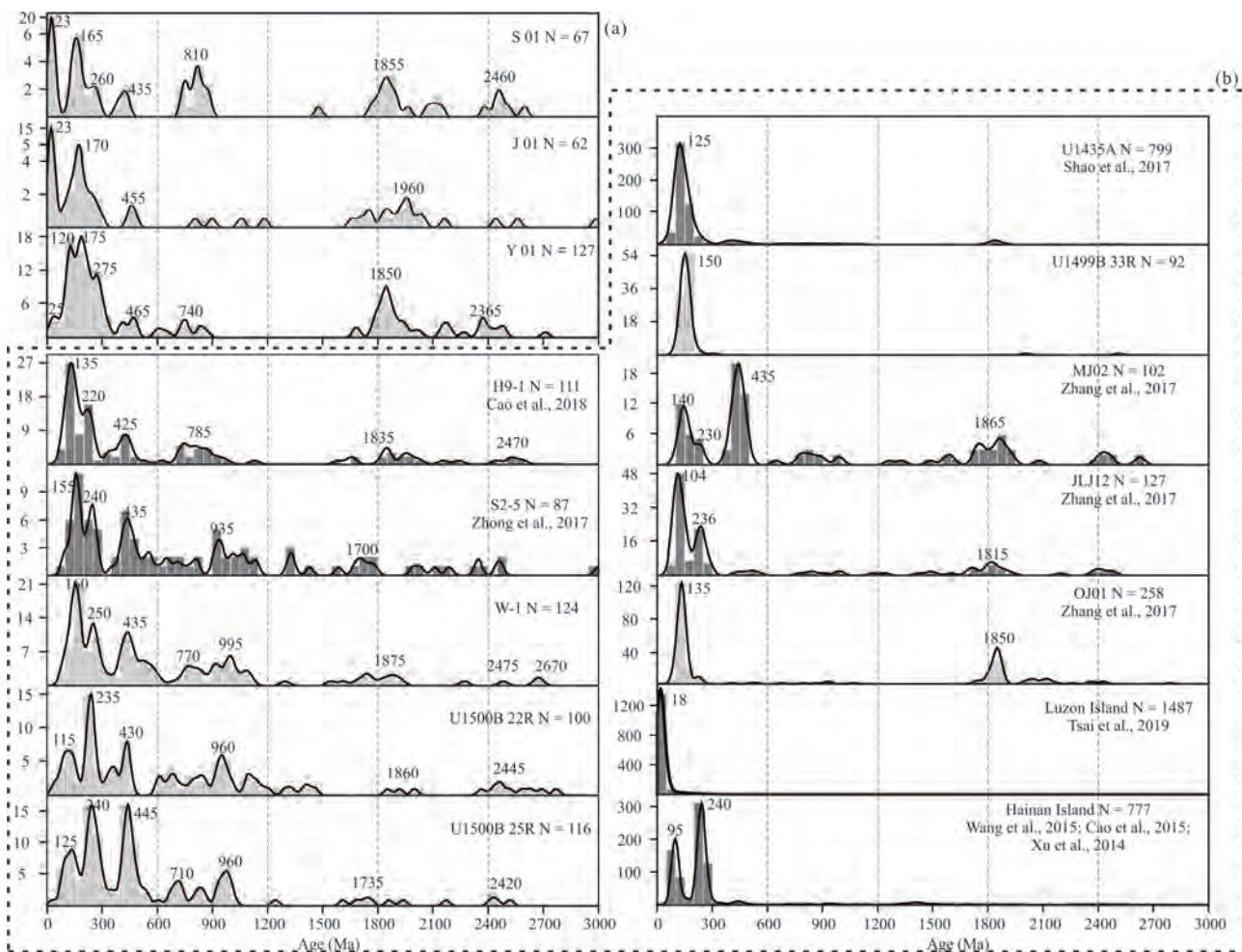


Fig. 4. Detrital zircon U-Pb age spectra.

(a) Hengchun turbidite sandstones; (b) samples within the northern South China Sea basin and surrounding provenance areas. Studied samples shaded light gray; published data shaded dark gray (modified from Meng et al., 2020; published data from Xu et al., 2014; Cao et al., 2015; Wang et al., 2015; Shao et al., 2017; Zhang et al., 2017; Zhong et al., 2017; Cao et al., 2018; Tsai et al., 2019).

2015). Both the Huatung Basin and Luzon Island register relatively complex rock components, which could also be the provenances for the accretionary wedge during the detachment of the trench front. However, the acidic volcanic rocks in the Luzon island arc are significantly different from the basic gravels within the Hengchun accretionary prism, implying that contributions from Luzon Island might have been limited. The Huatung Basin is distinct from the SCS especially in the age of the oceanic crust, the SCS being dated between ca. 33 Ma and 16.5 Ma (Li et al., 2015), whereas the Huatung Basin possibly formed during the Early Cretaceous (Deschamps et al., 2000; Huang et al., 2019).

In this study, zircon U-Pb ages of the basic rock gravels fall in the Late Oligocene–Early Miocene (ca. 25–23 Ma; Fig. 3), which is well within the age range of the SCS oceanic crust. Combined with published data (Chen H.Y. et al., 2018; Yu et al., 2018; Tian et al., 2019), these differences suggest that the basic rock gravels within the Hengchun accretionary prism were most likely derived from the SCS oceanic crust, other than from the Huatung Basin or other regions.

6.2 Provenances of Hengchun accretionary prism turbidite sandstones

As described above, the detrital zircon U-Pb age spectra of the Hengchun accretionary wedge turbidite sandstones display apparent Cenozoic peaks of ca. 23 Ma. The presence of these peaks is consistent with the crystallization ages of basalt and gabbro gravels in the accretionary wedge, and is clearly distinct from the ca. 18-Ma peak of the Luzon Island samples (Fig. 4). These lines of evidence confirm a major contribution from the SCS oceanic crust to the turbidite sequences in the Hengchun Peninsula. It can be envisaged that, as a result of drastic destruction, transportation and abrasion, a large number of basic fragments from the SCS oceanic crust, including well-rounded basalt and gabbro gravels, and finer clastic materials, were transported eastward in the form of a deep-sea gravity flow and subsequently accumulated within the accretionary wedge near the Manila Trench around 23 Ma.

Previous researchers indicated that the Hengchun Peninsula was mainly deposited with sediments from the Minjiang River or the Jiulongjiang River flowing across the southeast coast areas of the South China mainland during the Late Miocene (Zhang et al., 2017). As shown in

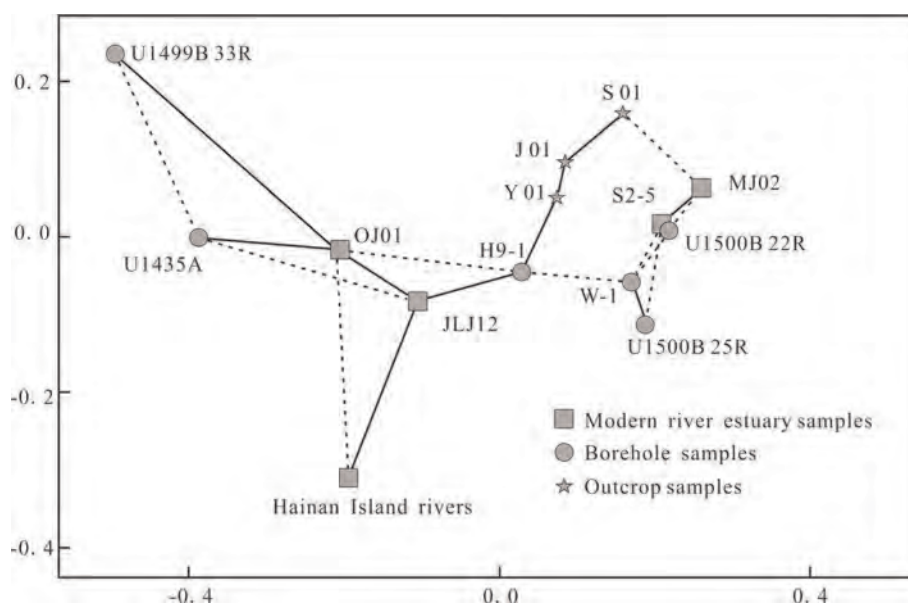


Fig. 5. Nonmetric multidimensional scaling (MDS) correlation analysis diagram for Hengchun turbidite sandstones and their surrounding potential provenances.

Fig. 4, the detrital zircon U-Pb age spectrum of the Minjiang River is dominated by a Caledonian (ca. 430 Ma) peak in addition to a secondary Yanshanian peak (ca. 143 Ma), and a small group of older aged zircon grains. However, the Hengchun turbidite sandstone samples exhibit many Cenozoic, Neoproterozoic and Mesoproterozoic zircons, with some Caledonian peaks proportionally lower than those Yanshanian clusters. These U-Pb age combination signatures have not been clearly identified within the Minjiang River sediments. Thus, the age-spectrum differences between the Hengchun turbidite sandstones and the Minjiang River cannot be overlooked. Moreover, on the nonmetric multidimensional scaling (MDS) correlation analysis diagram, samples from the Jiulongjiang River, the Ou River, and even Hainan Island, distance themselves markedly from the Hengchun Peninsula sections. All these provenances not only display narrow bimodal or single age patterns but also extremely minor content of Proterozoic zircons (Fig. 4). However, the Hengchun turbidite sandstones are more similar on the U-Pb combination to the samples from well W-1 in the Qiongdongnan Basin, H9-1 in the Pearl River Mouth Basin, and the site U1500B borehole. It is thus not surprising to see their close alignment on the MDS correlation analysis diagram (Figs. 4, 5).

According to previous studies, the western SCS region experienced complex stages of intense tectonic movements in the Cenozoic (Carter et al., 2001; Lepvrier et al., 2004). As an important potential provenance for other areas, the age combination pattern of the western SCS has increasingly attracted extensive attention (e.g. Fyhn et al., 2019; Wang et al., 2019); it features very clear Indosinian (ca. 250–210 Ma) and Caledonian (ca. 470–400 Ma) peaks, and a considerable number of older age groups, such as those of the Proterozoic. The recently discovered Central Canyon in the Qiongdongnan Basin allowed the transport of copious detrital materials from

both the Indochina Peninsula and Hainan Island during the Late Miocene in the form of turbidity current into the northwestern sub-basin of the SCS (e.g. Tang et al., 2014; Li et al., 2017; Ma et al., 2017; Mi et al., 2018; Cui et al., 2019; Lei et al., 2020). According to Shao et al. (2019a) and 2019(b), an ancient ‘Kontum–Ying–Qiong’ River developed prior to the Central Canyon. The river system began to deliver abundant sediments after the Late Eocene and stretched eastward for thousands of kilometers. With subsequent transgressions in the Oligocene–Miocene, the ‘Kontum–Ying–Qiong’ River was submerged below the sea surface, and finally gave way to the newly-born Central Canyon, which continued to transport sediments eastward since the late Miocene (Pang et al., 2018; Zhang et al., 2019). As shown in Figure 4, sample W-1 from the Qiongdongnan Basin and IODP U1500B samples from the COT zone share very similar U-Pb age combination features. The MDS correlation analysis diagram also confirms their close relationship (Fig. 5). Therefore, the ‘Kontum–Ying–Qiong’ River might have transported sediments further into the deep-water areas where site U1500 is located and probably even further east.

The Pearl River has evolved from a regional confined river into a continental-scale fluvial network with wide drainage area from the Oligocene to Miocene (Shao et al., 2001; Zhang G et al., 2010; Shao et al., 2016; Shao et al., 2017; Cao et al., 2018; Zhang G et al., 2018; Shao et al., 2019b). Since the Middle Miocene, the Pearl River tributaries have extended into the extensive Yunnan–Guizhou Plateau of the South China inland area, with a river network close to the modern drainage scale. Therefore, the Middle Miocene Paleo-Pearl River samples contain a large group of Caledonian and Proterozoic–Archaean zircons, in addition to the Yanshanian and Indosinian peaks (Fig. 4). Seismic profiles reveal that numerous large deep-water fans and submarine canyons were generated that stretched southward onto the northern

slope of the SCS. As a consequence, the Pearl River sediments were transported into the SCS deep-water basin in the form of a gravity flow (Pang et al., 2006; Shao et al., 2007; Zhang et al., 2015a; Zhang et al., 2015b; Lei et al., 2018). Borehole H9-1 is located in the Pearl River Delta and drilled into the upper Middle Miocene strata (Fig. 4). Its U-Pb age spectrum is dominated by Yanshanian and Indosinian peaks and weaker Caledonian and Jinningian clusters, which implies provenance influences from the South China inland and the Yangtze Block. The MDS correlation analysis diagram also demonstrates that boreholes H9-1 and U1500B are highly related (Fig. 5). Thus, it is suggested that the U1500B samples were possibly transported with the Pearl River sediments in addition to those from the provenance of the western SCS. In contrast, the U-Pb ages of U1435A and U1499B display a prominent single Cretaceous peak (Fig. 4), probably marking a local source of paleo-uplift (Shao et al., 2017). This Yanshanian age is consistent with the formation of a Mesozoic magmatic arc along the South China continental margin.

As a brief summary, the northern SCS deep-water area was likely a depocenter influenced by sediments from mixed provenances, including the ‘Kontum–Ying–Qiong’ River from the western SCS, the Pearl River from the north of the SCS, and the surrounding paleo-uplifts. During the Late Miocene, several hundred-meter thicknesses of turbidite successions were deposited in this area (Jian et al., 2019; Zhang et al., 2020).

6.3 Formation and evolution of Hengchun turbidites

The Upper Miocene deep-sea turbidites in the Hengchun Peninsula comprise a large number of well-rounded mafic gravels with affinities to the normal oceanic crust. The age of the examined gabbro gravels ranging from 25.40 to 23.60 Ma is consistent with the 26–23-Ma age peaks identified for the turbidite sandstones. All this strongly implies that the SCS oceanic crust were fragmented and eroded to provide mafic materials for the turbidite sequences during this period. The SCS is known to have spread between ca. 33 Ma and ca. 15 Ma. The

studied Cenozoic basic rock gravels are dated as Late Oligocene, indicating that only oceanic crust fragments with ages of the magnetic anomaly lineation C8–C6b (26.5–23.1Ma) were included within the Hengchun accretionary wedge turbidites.

Thus, we can envisage that, during the Miocene, both the Pearl River and the Kontum–Ying–Qiong River fluvial systems carried copious terrigenous clastic sediments, converging near the site U1500 locality, and charging further eastward under the submarine environment. This rapid-flowing turbidity current traveled along the magnetic anomaly strip C8–C6b (about 17°North), and strongly eroded the Upper Oligocene SCS oceanic crust. Both long-distance transport of terrigenous clastic sediments and basic oceanic crust materials were accumulated to form the accretionary prism turbidites near the Manila Trench. Due to the enhancement effect caused by negative geomorphology of the subducting trench, a large abundance of oceanic crust basic conglomerate layers and slump deposits were mixed with the typical turbidite sequences at the same time. With the clockwise northwestward drifting of the PSP, the original accretionary prism migrated and eventually was exposed to form the Hengchun Peninsula (Fig. 6).

7 Conclusions

In this paper, we combined data from field geological observation, elemental geochemistry, and zircon U-Pb geochronology to conduct a systematic ‘source-to-sink’ analysis on the Upper Miocene deep-sea turbidite sequences in the Hengchun Peninsula of Taiwan. Many well-rounded basic rock gravels in the Hengchun turbidites are derived from normal oceanic crust. Their crystallization age of 25.4–23.6 Ma is in line with the magnetic anomaly strip C8–C6b (about 17°N) during the South China Sea (SCS) spreading. Both the U-Pb age patterns and MDS correlation analysis diagram indicate that the northern SCS deep-water area was supplied with terrigenous clastic sediments transported by the ‘Kontum–Ying–Qiong’ River from the western SCS, and the Pearl

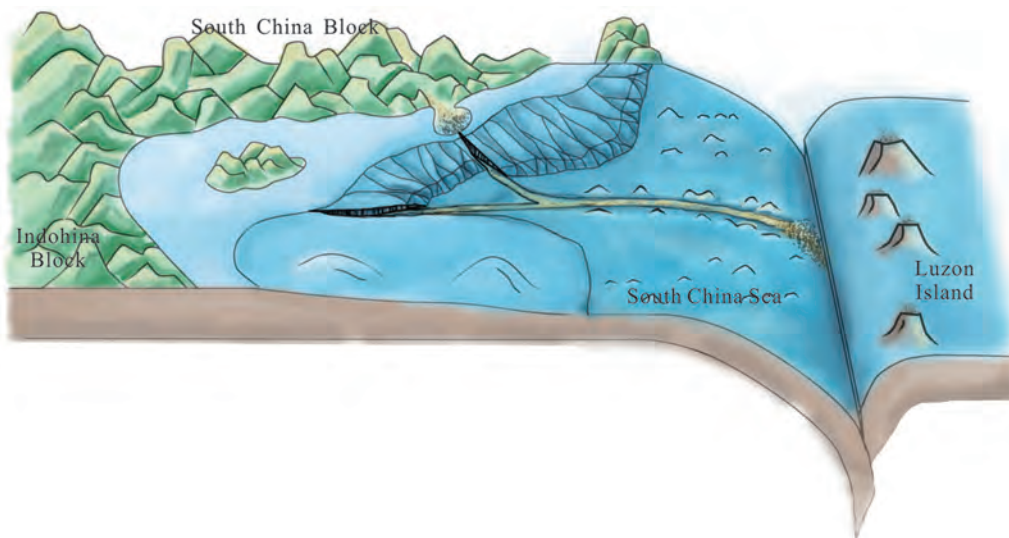


Fig. 6. Transport routes of the Hengchun accretionary prism turbidite sandstones.

River from the north during the Late Miocene, leading to the deposition of hundreds-of-meters thicknesses of turbidites in this region. Due to the overall ‘west-higher and east-lower’ topography of the SCS, sediments from these two river networks after their convergence traveled eastward in the form of turbidity currents. The turbidity transport system also strongly destroyed, wrecked and eroded the Upper Oligocene SCS normal oceanic crust prior to reaching the Manila Trench.

Together with other types of gravity flow sediments, the original accretionary prism was formed and accumulated around the subduction zone. As the Philippine Sea Plate was drifting to the northwest, this accretionary wedge was pushed, migrated, and finally exposed in the Hengchun Peninsula area.

Acknowledgements

We thank the China National Offshore Oil Corporation (CNOOC) for providing geological data and borehole samples from the northern South China Sea. Meng Xianbo, Ren Hailing and Zhou Junshen kindly provided us with help for the field trip. Constructive and careful reviews by two referees are gratefully appreciated. This work was supported by the National Natural Science Foundation of China (grant nos 42076066, 92055203 and 41874076), the National Science and Technology Major Project of China (grant no. 2016ZX05026004-002), the National Key Research and Development Program of China (grant no. 2018YFE0202400). Susan Turner (Brisbane) assisted with English language.

Manuscript received May 22, 2020
 accepted Nov. 27, 2020
 associate EIC: ZHANG Gongcheng
 edited by FEI Hongcai

References

- Andersen, T., 2002. Correction of common lead in U-Pb analyses that do not report ^{204}Pb . *Chemical Geology*, 192(1): 59–79.
- Bouma, A.H., 1962. *Sedimentology of some flysch deposits: A graphic approach to facies interpretation*. Elsevier, Amsterdam, 168.
- Callow, R.H.T., Kneller, B., Dykstra, M., and McIlroy, D., 2014. Physical, biological, geochemical and sedimentological controls on the ichnology of submarine canyon and slope channel systems. *Marine and Petroleum Geology*, 54: 144–166.
- Cao, L., Jiang, T., Wang, Z., Zhang, Y., and Sun, H., 2015. Provenance of Upper Miocene sediments in the Yinggehai and Qiongdongnan basins, northwestern South China Sea: evidence from REE, heavy minerals and zircon U-Pb ages. *Marine and Petroleum Geology*, 361: 136–146.
- Cao, L., Shao, L., Qiao, P., Zhao, Z., van Hinsbergen, D.J.J., 2018. Early Miocene birth of modern Pearl River recorded low-relief, high-elevation surface formation of SE Tibetan Plateau. *Earth and Planetary Science Letters*, 496: 120–131.
- Carter, A., Roques, D., Bristow, C.S., and Kinny, P., 2001. Understanding Mesozoic accretion in Southeast Asia: significance of Triassic thermos tectonism (Indosinian orogeny) in Vietnam. *Geology*, 29: 211–214.
- Chang, C.P., Angelier, J., Lee, T.Q., and Huang, C.Y., 2003. From continental margin extension to collision orogen: structural development and tectonic rotation of the Hengchun peninsula, southern Taiwan. *Tectonophysics*, 361: 61–82.
- Chang, L.S., 1964. A biostratigraphic study of the Tertiary in the Hengchun peninsula, Taiwan, based on smaller Foraminifera (I. Northern Part). *Proceedings of the Geological Society of China*, 7: 48–62.
- Chen, C.H., Jahn, B.M., Lee, T.P., Chen, C.H., and Jean, C., 1990. Sm-Nd isotopic geochemistry of sediments from Taiwan and implications for the tectonic evolution of southeast China. *Chemical Geology*, 88: 317–332.
- Chen, H.Y., Yang, H.J., Liu, Y.H., Huang, K.F., and Takazawa, E., 2018. Tectonic affinities of the accreted basalts in southern Taiwan. *Journal of Asian Earth Sciences*, 158: 253–265.
- Chen, X.Y., Huang, C.Y., and Shao, L., 2018. Characteristics of heavy minerals in modern sediments of Minjiang and Jiulongjiang Rivers, Fujian Province and their provenance implication. *Journal of Palaeogeography*, 20: 637–650 (in Chinese with English Abstract).
- Cheng, Y.M., Huang, C.Y., and Yen, J.J., 1984. The Loshui formation: Deeper-water sandstones on the Hengchun Peninsula, Southern Taiwan. *Acta Geologica Taiwanica*, 22: 100–117.
- Compston, W., Williams, I.S., Kirkschvink, J.L., Zhang, Z., and Guogan, M.A., 1992. Zircon U-Pb ages for the Early Cambrian time-scale. *Journal of the Geological Society*, 149: 171–184.
- Cui, Y., and Shao, L., Qiao, P., Pei, J., Zhang, D., and Tran, H., 2019. Upper Miocene-Pliocene provenance evolution of the Central Canyon in northwestern South China Sea. *Marine Geophysical Research*, 40: 223–235.
- Deschamps, A., Monié, P., Lallemand, S., Hsu, S.K., and Yeh, K.Y., 2000. Evidence for Early Cretaceous oceanic crust trapped in the Philippine Sea Plate. *Earth and Planetary Science Letters*, 179(3–4): 503–516.
- Fyhn, M.B.W., Thomsen, T.B., Keulen, N., Knudsen, C., Rizzi, M., Bojesen-Koefoed, J., Olivarius, M., Tran, V.T., Phung, V.P., Nguyen, Q.M., Abatzis, I., and Nielsen, L.H., 2019. Detrital zircon ages and heavy mineral composition along the Gulf of Tonkin – Implication for sand provenance in the Yinggehai-Song Hong and Qiongdongnan basins. *Marine and Petroleum Geology*, 101: 162–179.
- Hansen, L.A.S., Callow, R.H.T., Kane, I.A., Camberi, F., Rovere, M., Cronin, B.T., and Kneller, B., 2015. Genesis and character of thin-bedded turbidites associated with submarine channels. *Marine and Petroleum Geology*, 67: 852–879.
- Hickey-Vargas, R., Bizimis, M., and Deschamps, A., 2008. Onset of the Indian Ocean isotopic signature in the Philippine Sea Plate: Hf and Pb isotope evidence from Early Cretaceous terranes. *Earth and Planetary Science Letters*, 268(3–4): 255–267.
- Hoskin, P.W.O., and Schaltegger, U., 2003. The composition of zircon and igneous and metamorphic petrogenesis. *Reviews in Mineralogy and Geochemistry*, 53: 27–62.
- Huang, C.Y., Yuan, P.B., and Tsao, S.J., 2006. Temporal and spatial records of active arc-continent collision in Taiwan: A synthesis. *Geological Society of America, Bulletin*, 118: 274–288.
- Huang, C.Y., Chen, W.H., Wang, M.H., Lin, C.T., Yang, S., Li, X., Yu, M., Zhao, X., Yang, K.M., Liu, C.S., Hsieh, Y.H., and Harris R., 2018. Juxtaposed sequence stratigraphy, temporal-spatial variations of sedimentation and development of modern-forming forearc Lichi Mélange in North Luzon Trough forearc basin onshore and offshore eastern Taiwan: an overview. *Earth-Science Reviews*, 182: 102–140.
- Huang, C.Y., Wang, P., Yu, M., You, C.F., Liu, C.S., Zhao, X., Shao, L., Zhong, G., and Yumul, Jr G.P., 2019. Potential role of strike-slip faults in opening up the South China Sea. *National Science Review*, 6(5): 891–901.
- Jian, Z., Jin, H., Kaminski, M.A., Ferreira, F., Li, B., and Yu, P.-S., 2019. Discovery of the marine Eocene in the northern South China Sea. *National Science Review*, 6(5): 881–885.
- Lee, Y.H., Chen, C.C., Liu, T.K., Ho, H.C., Lu, H.Y., and Lo, W., 2006. Mountain building mechanisms in the Southern Central Range of the Taiwan Orogenic Belt—From accretionary wedge deformation to arc-continental collision. *Earth and Planetary Science Letters*, 252: 413–422.
- Lei, C., Ren, J., Pang, X., Chao, P., and Han, X., 2018. Continental rifting and sediment infill in the distal part of the

- northern South China Sea in the Western Pacific region: Challenge on the present-day models for the passive margins. *Marine and Petroleum Geology*, 93: 166–181.
- Lei, C., Alves, T.M., Ren, J., and Tong, C., 2020. Rift structure and sediment infill of hyperextended continental crust: insights from 3D seismic and well data (Xisha Trough, South China Sea). *Journal of Geophysical Research: Solid Earth*, 125(5), doi: 10.1029/2019JB018610.
- Lepvrier, C., Maluski, H., Vu, V.T., Leyreloup, A., Phan, T.T., and Nguyen, V.V., 2004. The Early Triassic Indosinian orogeny in Vietnam (Truong Son Belt and Kontum Massif): implications for the geodynamic evolution of Indochina. *Tectonophysics*, 393: 87–118.
- Lester, R., McIntosh, K., Van Avendonk, H.J.A., Lavier, L., Liu, C.-S., and Wang, T.K., 2013. Crustal accretion in the Manila trench accretionary wedge at the transition from subduction to mountain-building in Taiwan. *Earth and Planetary Science Letters*, 375: 430–440.
- Li, C., Ma, M., Lv, C., Zhang, G., Chen, G., Yan, Y., and Bi, G., 2017. Sedimentary differences between different segments of the continental slope-parallel Central Canyon in the Qiongdongnan Basin on the northern margin of the South China Sea. *Marine and Petroleum Geology*, 101: 162–179.
- Li, C.F., Xu, X., Lin, J., Sun, Z., Zhu, J., Yao, Y., Zhao, X.X., Liu, Q.S., Kulhanek, D.K., Wang, J., Song, T.R., Zhao, J.F., Qiu, N., Guan, Y.X., Zhou, Z.Y., Williams, T., Bao, R., Briais, A., Brown, E.A., Chen, Y.F., Clift, P.D., Colwell, F.S., Dadd, K.A., Ding, W.W., Almeida, I.H., Huang, X.L., Hyun, S., Jiang, T., Koppers, A.A.P., Li, Q.Y., Liu, C.L., Liu, Z.F., Nagai, R.H., Pele-Alampay, A., Su, X., Tejada, M.L.G., Trinh, H.S., Yeh, Y.C., Zhang, C.L., Zhang, F., and Zhang, G.L., 2015. Ages and magnetic structures of the South China Sea constrained by deep tow magnetic surveys and IODP Expedition 349. *Geochemistry Geophysics Geosystem*, 15: 4958–4983.
- Li, F., Sun, Z., Hu, D., and Wang, Z., 2013. Crustal structure and deformation associated with seamount subduction at the north Manila Trench represented by analog and gravity modeling. *Marine Geophysical Research*, 34(3–4): 393–406.
- Lin, A.T., Yao, B.C., Hsu, S.K., Liu, C.S., and Huang, C.Y., 2009. Tectonic features of the incipient arc-continent collision zone of Taiwan: Implications for seismicity. *Tectonophysics*, 479: 28–42.
- Liu, B., Shao, L., Wang, W., Huang, X., Liu, W., Zhang, S., Zhang, H., Lu, J., 2020. Sedimentary characteristics and depositional model of deep-water deposits dominated by gravity flow: A case study from the Lower Triassic in the Gonghe Basin. *Acta Geologica Sinica*, 94(4): 1106–1127 (in Chinese with English Abstract).
- Liu, J., Sun, M., Gao, H., Li, X., 2019. Features and origin of turbidity current sediment waves in the Huatung Basin off the eastern Taiwan Island. *Acta Geologica Sinica (English Edition)*, 93(4): 1088–1096.
- Ma, M., Li, C., Lv, C., Chen, G., Yang, F., Yan, Y., Yin, N., and Zhang, G., 2017. Geochemistry and provenance of a multiple-stage fan in the Upper Miocene to the Pliocene in the Yinggehai and Qiongdongnan basins, offshore South China Sea. *Marine and Petroleum Geology*, 79: 64–80.
- Meng, X., Shao, L., Cui, Y., Zhu, W., Qiao, P., Sun, Z., and Hou, Y., 2020. Sedimentary records from Hengchun accretionary prism turbidites on Taiwan Island: Implication on late Neogene migration rate of the Luzon subduction system. *Marine and Petroleum Geology*, <https://doi.org/10.1016/j.marpetgeo.2020.104820>.
- Mi, L., Zhang, Z., Pang, X., Liu, J., Zhang, B., Zhao, Q., and Feng, X., 2018. Main controlling factors of hydrocarbon accumulation in Baiyun Sag at northern continental margin of South China Sea. *Petroleum Exploration and Development*, 45(5): 902–913 (in Chinese with English Abstract).
- Page, B.M., and Lan, C.Y., 1983. The Kenting mélange and its record of tectonic events. *Memoir of the Geological Society of China*, 5: 227–248.
- Pang, X., Chen, C.M., Wu, M.S., He, M., and Wu, X.J., 2006. The Pearl River deep-water fan systems and significant geological events. *Advances in Earth Science*, 21: 793–799.
- Pang, X., Ren, J., Zheng, J., Liu, J., Yu, P., and Liu, B., 2018. Petroleum geology controlled by extensive detachment thinning of continental margin crust: A case study of Baiyun sag in the deep-water area of northern South China Sea. *Petroleum Exploration and Development*, 45(1): 27–39 (in Chinese with English Abstract).
- Pelletier, B., and Stephan, J.F., 1986. Middle Miocene deduction and late Miocene beginning of collision registered in the Hengchun Peninsula: Geodynamic implications for the evolution of Taiwan. *Tectonophysics*, 125: 133–160.
- Shan, Y., Nie, G., Yan, Y., and Huang, C.Y., 2013. The transition from the passive to active continental margin: A case study of brittle fractures in the Miocene Loshui Sandstone on the Hengchun Peninsula, southern Taiwan. *Tectonics*, 32: 65–79.
- Shao, L., Li, X.H., Wei, G., Liu, Y., and Fang, D., 2001. Provenance of a prominent sediment drift on the northern slope of the South China Sea. *Science in China Series D: Earth Sciences*, 44(10): 919.
- Shao, L., Li, X.H., Geng, J., Pang, X., Lei, Y., Qiao, P., Wang, L., and Wang, H., 2007. Deep water bottom current deposition in the northern South China Sea. *Science in China Series D: Earth Sciences*, 50(7): 1060–1066.
- Shao, L., Qiao, P., Zhao, M., Li, Q., Wu, M., Pang, X., and Zhang, H., 2016. Depositional style of the northern South China Sea between Oligocene and Miocene in Response to the Evolution of the Pearl River. *Geological Society, London, Special Publications*, 429: 31–44.
- Shao, L., Meng, A., Li, Q., Qiao, P., Cui, Y., Cao, L., and Chen, S., 2017. Detrital zircon ages and elemental characteristics of the Eocene sequence in IODP Hole U1435A: Implications for rifting and environmental changes before the opening of the South China Sea. *Marine Geology*, 394: 39–51.
- Shao, L., Cui, Y., Statterger, K., Zhu, W., Qiao, P., and Zhao, Z., 2019a. Drainage control of Eocene to Miocene sedimentary records in the southeastern margin of Eurasian Plate. *Geological Society of America, Bulletin*, 131: 461–478.
- Shao, L., Cui, Y., Qiao, P., Zhu, W., Zhong, K., and Zhou, J., 2019b. Implications on the Early Cenozoic palaeogeographical reconstruction of SE Eurasian margin based on northern South China Sea palaeo-drainage system evolution. *Journal of Palaeogeography*, 21(2): 216–231 (in Chinese with English Abstract).
- Sibuet, J.C., and Hsu, S.K., 2004. How was Taiwan created? *Tectonophysics*, 379: 159–181.
- Stock, J.M., Sun, Z., Klaus, A., Larsen, H.C., Jian, Z., Alvarez Zarikian, C.A., and Boaga, J., 2018. South China Sea Rifted Margin. *Proceedings of the International Ocean Discovery Program*, 367/368: College Station, TX (International Ocean Discovery Program), <https://doi.org/10.14379/iodp.proc.367368.104.2018>.
- Sun, Z., Stock, J., Klaus, A., and the Expedition 367 Scientists, 2018. Expedition 367 Preliminary Report: South China Sea Rifted Margin. *International Ocean Discovery Program*, <https://doi.org/10.14379/iodp.pr.367.2018>.
- Tang, X., Hu, S., Zhang, G., Liang, J., Yang, S., Shen, H., Rao, S., and Li, W., 2014. Geothermal characteristics and hydrocarbon accumulation of the northern marginal basins, South China Sea. *Chinese Journal of Geophysics*, 57(2): 572–585 (in Chinese with English Abstract).
- Teng, L.S., 1996. Extensional collapse of the northern Taiwan mountain belt. *Geology*, 24: 949–952.
- Tian, Z.X., Yan, Y., Huang, C.Y., Zhang, X.C., Liu, H.Q., Yu, M.M., Yao, D., and Dilek, Y., 2019. Geochemistry and geochronology of the accreted mafic rocks from the Hengchun Peninsula, southern Taiwan: Origin and tectonic implications. *Journal of Geophysical Research: Solid Earth*, 124: 2469–2491.
- Tsai, C.H., Shyu, J.B.H., Chung, S.L., Ramos, N.T., and Lee, H.Y., 2019. Detrital zircon record from major rivers of Luzon Island: implications for Cenozoic continental growth in SE Asia. *Journal of the Geological Society*, 176(4): 727–735.
- Tu, K., Flower, M.F., Carlson, R.W., Xie, G., Chen, C.Y., and Zhang, M., 1992. Magmatism in the South China Basin: 1. Isotopic and trace-element evidence for an endogenous Dupal

- mantle component. *Chemical Geology*, 97(1–2): 47–63.
- Wang, C., Liang, X., Zhou, Y., Fu, J., Jiang, Y., Dong, C., Xie, Y., Tong, C., Pei, J., and Liu, P., 2015. Construction of age frequencies of provenances on the eastern side of the Yinggehai Basin: Studies of LA-ICP-MS U-Pb ages of detrital zircons from six modern rivers, western Hainan, China. *Earth Science Frontiers*, 22(4): 277–289 (in Chinese with English Abstract).
- Wang, C., Liang, X., Foster, D.A., Tong, C., Liu, P., Liang, X., and Zhang, L., 2019. Linking source and sink: Detrital zircon provenance record of drainage systems in Vietnam and the Yinggehai-Song Hong Basin, South China Sea. *Geological Society of America, Bulletin*, 131(1/2): 191–204.
- Xu, Y., Sun, Q., Cai, G., Yin, X., and Chen, J., 2014. The U-Pb ages and Hf isotopes of detrital zircons from Hainan Island, South China: Implications for sediment provenance and the crustal evolution. *Environmental Earth Sciences*, 71(4): 1619–1628.
- Yu, M., Yan, Y., Huang, C.Y., Liu, H., Zhang, X., Lan, Q., Chen, W., and Qian, K., 2015. Philippine ophiolites and their tectonic significance. *Marine Geology and Quaternary Geology*, 35(6): 53–71 (in Chinese with English Abstract).
- Yu, M., Yan, Y., Huang, C.Y., Zhang, X., Tian, Z., Chen, W.H., and Santosh, M., 2018. Opening of the South China Sea and upwelling of the Hainan plume. *Geophysical Research Letters*, 45(6): 2600–2609.
- Zhang, G., 2010. Tectonic evolution of deepwater area of northern continental margin in South China Sea. *Acta Petrologica Sinica*, 31(4): 528–533 (in Chinese with English Abstract).
- Zhang, G., Wang, P., Wu, J., Liu, S., and Xie, X., 2015a. Tectonic cycle of marginal oceanic sea: A new evolution model of the South China Sea. *Earth Science Frontiers*, 22(3): 27–37 (in Chinese with English Abstract).
- Zhang, G., Qu, H., Liu, S., Xie, X., Zhao, Z., and Shen, H., 2015b. Tectonic cycle of marginal sea controlled the hydrocarbon accumulation in deep-water areas of South China Sea. *Acta Petrologica Sinica*, 36(5): 533–545 (in Chinese with English Abstract).
- Zhang, G., Jia, Q., and Wang, W., 2018. On tectonic framework and evolution of the South China Sea. *Chinese Journal of Geophysics*, 61(10): 4194–4215 (in Chinese with English Abstract).
- Zhang, G.L., Luo, Q., Zhao, J., Jackson, M.G., Guo, L.S., and Zhong, L.F., 2018. Geochemical nature of sub-ridge mantle and opening dynamics of the South China Sea. *Earth and Planetary Science Letters*, 489: 145–155.
- Zhang, G., Shao, L., Qiao, P., Cao, L., Pang, X., Zhao, Z., Xiang, X., and Cui, Y., 2019. Cretaceous–Paleogene sedimentary evolution of the South China Sea region: A preliminary synthesis. *Geological Journal*, 55(4): 2662–2683.
- Zhang, H., Shao, L., Zhang, G., Cui, Y., Zhao, Z., and Hou, Y., 2020. The response of Cenozoic sedimentary evolution coupled with the formation of the South China Sea. *Geological Journal*, doi:10.1002/gj.3856.
- Zhang, X., Yan, Y., Huang, C.Y., Chen, D., Shan, Y., Lan, Q., Chen, W., and Yu, M., 2014. Provenance analysis of the Miocene accretionary prism of the Hengchun Peninsula, southern Taiwan, and regional geological significance. *Journal of Asian Earth Sciences*, 85: 26–39.
- Zhang, X., Cawood, P.A., Huang, C.Y., Wang, Y., Yan, Y., Santosh, M., Chen, W., and Yu, M., 2016. From convergent plate margin to arc-continent collision: Formation of the Kenting Mélange, Southern Taiwan. *Gondwana Research*, 38: 171–182.
- Zhang, X., Huang, C.Y., Wang, Y., Clift, P.D., Yan, Y., Fu, X., and Chen, D., 2017. Evolving Yangtze River reconstructed by detrital zircon U-Pb dating and petrographic analysis of Miocene marginal Sea sedimentary rocks of the Western Foothills and Hengchun Peninsula, Taiwan. *Tectonics*, 36: 634–651.
- Zhong, L., Li, G., Yan, W., Xia, B., Feng, Y., Miao, L., and Zhao, J., 2017. Using zircon U-Pb ages to constrain the provenance and transport of heavy minerals within the northwestern shelf of the South China Sea. *Journal of Asian Earth Science*, 134: 176–190.

About the first author



CUI Yuchi, female, born in 1991 in Baoding City, Hebei Province; a PhD graduate in both Tongji University and Curtin University. She is now interested in sedimentology and tectonics. Email: cuiyuchi@tongji.edu.cn; phone: 15301756572.

About the corresponding author



SHAO Lei, male, born in 1960 in Baoji City, Shaanxi Province; PhD; graduated from Kiel University; professor of Tongji University. He is now interested in marine geology, sedimentology, geochemistry and geochronology. Email: lshao@tongji.edu.cn; phone: 021-65984879, 13641897306.



Research paper

Sedimentary records from Hengchun accretionary prism turbidites on Taiwan Island: Implication on late Neogene migration rate of the Luzon subduction system

Xianbo Meng^a, Lei Shao^{a,*}, Yuchi Cui^{a,b,**}, Weilin Zhu^a, Peijun Qiao^a, Zhen Sun^c, Yuanli Hou^a

^a State Key Laboratory of Marine Geology, Tongji University, Shanghai, 200092, China

^b Earth Dynamics Research Group, The Institute for Geoscience Research (TIGeR), School of Earth and Planetary Sciences, Curtin University, GPO Box U1987, Perth, WA, 6845, Australia

^c Key Laboratory of Marginal Sea Geology, South China Sea Institute of Oceanology, Chinese Academy of Sciences, Guangzhou, China



ARTICLE INFO

Keywords:

Hengchun peninsula
Mafic pebbles
Turbidites
Zircon U–Pb dating
Philippine sea plate motion
International ocean drilling program

ABSTRACT

Although plate motion models for the Philippine Sea Plate (PSP) are relatively well established, they remain to be confirmed by reliable geological records. Oblique convergence between Eurasia and the PSP has resulted in the uplift of Taiwan Island along the plate boundary. As the latest exposed portion of Taiwan, the Hengchun Peninsula features well-preserved deep-sea turbidites with rounded mafic conglomerate clasts. We apply an integrated source-to-sink analysis and broad field investigations to generate a reliable kinematic reconstruction linking the Hengchun turbidite outcrops with South China Sea (SCS) borehole sediments. Deposited in the lowermost turbidite layer, the Hengchun rounded gabbro and basalt clasts resemble the SCS oceanic crust based on our U–Pb geochronological (~23.6–25.4 Ma) and elemental geochemical results (normal mid-ocean ridge basalts), along with previous magnetic anomaly constraints. The multimodal U–Pb spectra of the matrix-supported sandstones suggest a mixed provenance including central Vietnam, the Pearl River tributaries and potential intrabasinal uplifts, which have not received prior consideration. During the late Miocene, abundant terrigenous sediments from the eastward-flowing “Kontum-Ying-Qiong River” and Pearl River were transported into the submarine environment. The extensive turbidity currents scoured and eroded the SCS mid-ocean ridges, which feature numerous low-angle detachment faults. These materials of various sources were transported eastwards for thousands of kilometers prior to their incorporation into the accretionary prism adjacent to the Manila Trench. From the late Miocene to Pleistocene, the PSP moved northwestward at estimated velocities of ~61–65 mm/yr, facilitating the final uplift and exposure of the accretionary prism.

1. Introduction

An accretionary prism is generally formed by frontal accretion in a subduction zone by scraping marine sediments off the downgoing oceanic slab or forearc underplating at convergent margins (e.g. Abbott et al., 1994; Brown and Spadea, 1999; Moore et al., 2001; Clift and Vannucchi, 2004). As a typical accretionary wedge, Taiwan Island is well known for its geodynamic processes associated with subduction and oblique collision between the Eurasian continent and the Philippine Sea Plate (PSP). After cessation of seafloor spreading at ca. 16 Ma, the South China Sea (SCS) began to subduct eastward beneath the northwest-moving PSP along the Manila Trench, generating the

Hengchun accretionary prism and Luzon forearc basin (Briais et al., 1993; Huang et al., 1997; Sibuet and Hsu, 2004; Barckhausen et al., 2014; Richter and Ali, 2015) (Fig. 1A). The accretionary prism progressively increased in size, thickened and was then uplifted when the Luzon Arc of the PSP encroached upon the Eurasian continental margin (Huang et al., 2006; Lester et al., 2013). Since this collision takes place in an oblique direction to the convergent boundary, the orogenic belt has been propagating southward on Taiwan Island (Suppe, 1984). The Hengchun Peninsula is the most recently exposed part of Taiwan Island and preserves relatively intact upper Miocene deep-sea successions. Therefore, the Hengchun Peninsula represents a superb setting to address unresolved problems related to SCS sedimentology and plate

* Corresponding author.

** Corresponding author. State Key Laboratory of Marine Geology, Tongji University, Shanghai, 200092, China.

E-mail addresses: lshao@tongji.edu.cn (L. Shao), cuiyuchi@tongji.edu.cn (Y. Cui).

<https://doi.org/10.1016/j.marpetgeo.2020.104820>

Received 19 August 2020; Received in revised form 14 October 2020; Accepted 13 November 2020

Available online 16 November 2020

0264-8172/© 2020 Elsevier Ltd. All rights reserved.

motion histories.

Deep-marine turbidite sandstones have been documented on both sides of the Hengchun accretionary prism. However, many disputes remain regarding their provenances and transport routes. Based on paleocurrent measurements and geochemical analyses, the SE coastal South China Block was originally thought to have supplied sediments from the northwest but is currently hundreds of miles from the Hengchun Peninsula. In previous source-to-sink analyses, scholars attributed the Hengchun turbidites to the mainland of southern China via the paleo-Minjiang or Jiulongjiang River (e.g., Chen et al., 1990; Xu and Chen, 2010; Zhang et al., 2014, 2017). These interpretations are mostly supported by the speculation of seaward shifts in the SE China coastline and late Miocene monsoon intensification, which possibly facilitated sedimentary delivery from broad inland areas. Alternatively, these paleo-tributaries, such as paleo-Minjiang or Jiulongjiang River, were recently implied to be associated with short-distance runoff with confined drainage areas (Chen et al., 2018b). The sediments transported by these rivers and the Hengchun Peninsula turbidites actually show differences on their U–Pb spectra. In any case, regarding the mineral compositions and properties of the Hengchun turbidites, their depositional and hydrodynamic conditions seem less closely linked with the coastal SE South China Block as a dominant provenance. Contrasting paleocurrent directions (SE to NW) and tectonic rotation have further complicated the transport pathway of the Hengchun turbidites (Chang et al., 2003; Shan et al., 2013). The distinct transport routes were ascribed potentially to intense compression and rotation activities. Proto-Taiwan (or the Central Ridge), the Luzon Arc and the SCS or PSP oceanic lithosphere have also been suggested as minor sources (e.g., Page and Lan, 1983; Kirstein et al., 2010; Chen et al., 2019; Tian et al., 2019). However, previous interpretations do not provide convincing geological evidence for basal paleo-uplift or active forearc contributions.

In addition to the prevalence of deep-marine sandstone deposits, the

Hengchun Peninsula remarkably features abundant mafic rocks. These accreted mafic clasts exhibit different degrees of roundness and metamorphism. Most scholars consider that Hengchun Peninsula contains several ophiolite-bearing stratigraphic units, including the Kenting Mélanges, Shihmen Conglomerate, the Cingwashih slump deposits and Lilungshan Sandstone. Of these igneous materials, rounded basalt and gabbro conglomerates are valuable sedimentary deposits for revealing the crustal properties of the convergent plates and were deposited synchronously within thick-bedded turbidite sandstones. According to previous research (e.g. Page and Lan 1983; Pelletier and Stephan, 1986), fragments of the SCS oceanic crust were incorporated into the accretionary wedge along the Manila Trench since the middle Miocene. The ophiolitic materials were possibly originated from a slice of Oligocene-lower Miocene SCS crust obducted upon the Chinese passive margin (Zhang et al., 2014). In those studies, dating of the mafic rocks resulted in ambiguous ages which are mostly based on biostratigraphy, structural analysis and regional geophysics. A recent study suggested that the overriding PSP possibly provided one source region of both normal and enriched mid-ocean ridge basalts (N-MORBs and E-MORBs, respectively) accreted onto the Hengchun Peninsula (Chen et al., 2018a). However, this model appears to neglect the significant role of the Gagua Ridge, which blocks any potential constituents from the PSP slab (Fig. 1A). Instead, Tian et al. (2019) attributed the E-MORBs to fragments of the Luzon volcanic arc or the Huatung Basin. Additionally, Hengchun ocean island basalts (OIBs), with later recycling and rounding, might represent the product of SCS seamount subduction under a submarine eruption environment (Lin et al., 2009; Tian et al., 2019). In summary, the age and origin of these mafic clasts remain controversial, with numerous models proposed to explain their separate emplacement mechanism. Mafic materials (N-MORBs and E-MORBs) from both subducting and overlying slabs were mixed with the fine-grained sediments, and were widely distributed in the Hengchun accretionary wedge (Kirstein et al., 2010; Zhang et al., 2014; Tian et al., 2019). In particular,

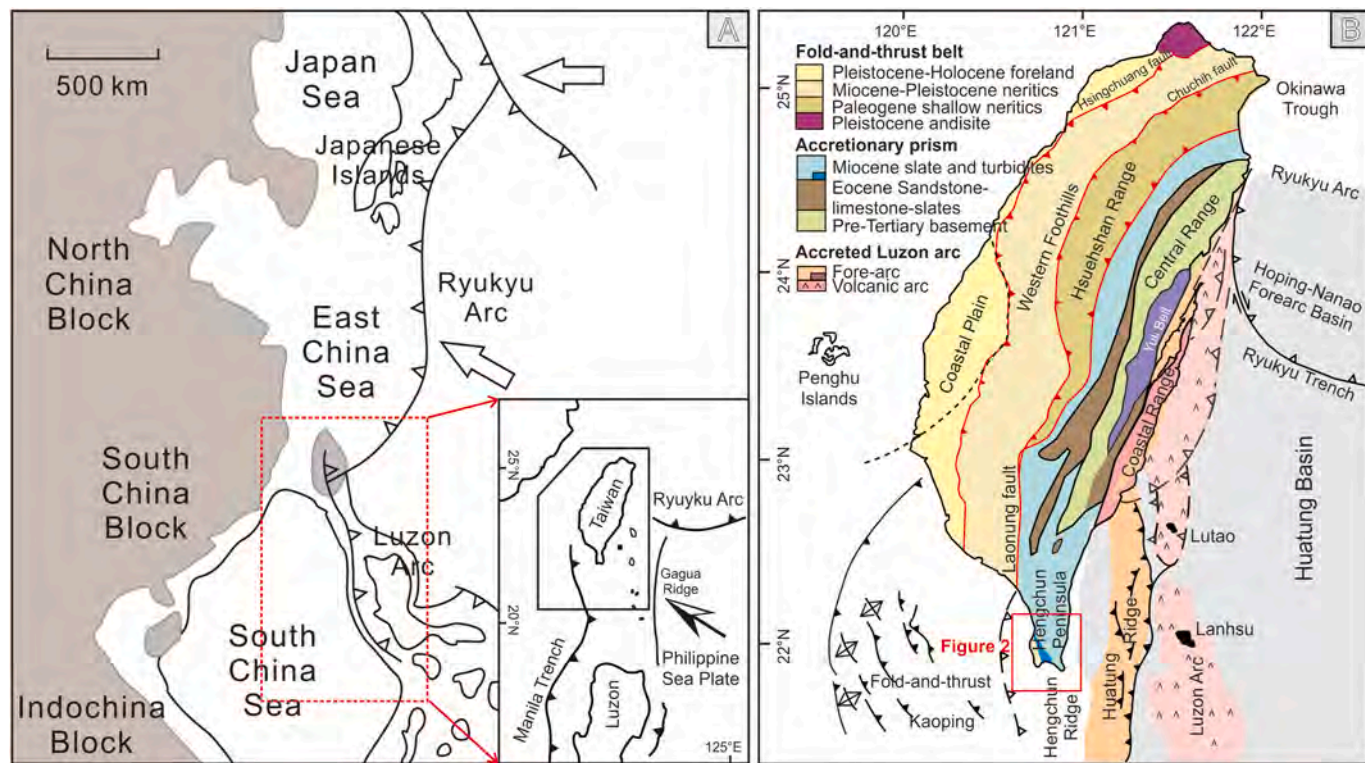


Fig. 1. (A) Simplified tectonic sketch of southeastern Eurasia. The bold arrow shows the motion direction of the Philippine Sea Plate. The tectonic sketch map in the bottom right corner shows a zoomed-in view of Taiwan Island and its surrounding areas. (B) Tectonic map of Taiwan Island. From west to east, the geological divisions include the Coastal Plain, Western Foothills, Hsuehshan Range, Central Range (with the Hengchun Peninsula at the southernmost point), Coastal Range (with the Yuli Belt as part of the Coastal Range) and Luzon Arc (modified from Huang et al. (2006)).

the OIB-type rounded Shihmen Conglomerates were attributed to the gravity-driven collapse of seamounts. Mafic rocks dispersed in the Kenting Mélanges and slump deposits in the Cingwashih area, on the other hand, might directly derive from the intensive tectonic shearing of the accretionary complex (Zhang et al., 2016). However, the presence of rounded mafic pebbles within the complete records of turbidite sequences is still problematic and thus remains a goal of further investigation. Namely, the mafic pebbles seem to have been uniquely and abundantly deposited as the bottom layers of the turbidites rather than subsequently mixing with exotic sedimentary clasts.

In this work, we combine field observations, petrography, geochemistry and U–Pb geochronology of Hengchun polygenetic blocks, and samples from International Ocean Discovery Program (IODP) 367/368 and commercial boreholes in the northern SCS to address the following questions:

- 1) What are the precise ages of the mafic pebbles in the Hengchun turbidites? Are they derived from typical oceanic crust or submarine seamounts?
- 2) What is the dominant provenance of the thick-bedded turbiditic sandstones on the Hengchun Peninsula?
- 3) What mechanisms are responsible for the deposition of mafic pebbles as the T_a conglomerate layer (basal layer) within turbidite sequences?
- 4) Finally, what regional tectonic and geodynamic implications for the interacting SCS and PSP plates can be inferred from our sedimentary constraints?

2. Geologic background and stratigraphic framework

Intense rifting led to continental edge breakup, which was followed by seafloor spreading in the SCS from the early Oligocene to middle Miocene (e.g., Sibuet et al., 2016; Larsen et al., 2018). The SCS is confirmed to have experienced a single episode of extension instead of multiple episodes within separate subbasins (Barckhausen et al., 2014; Sibuet et al., 2016). Generally, the onset of seafloor spreading occurred around chron C12n (ca. 33 Ma), with a ridge jump subsequently occurring between chron C7 (ca. 26.5 Ma) and chron C6cr (ca. 23 Ma) in the eastern basin. However, strong post-spreading volcanism has hidden the initial spreading fabric, causing highly variable extension rate estimates. Ages are also divergent for the latest magnetic lineation among different models (younger than chron C5c (15.5 Ma), C5b (15 Ma) or C6a1 (20.5 Ma)) (Briais et al., 1993; Barckhausen et al., 2014; Li et al., 2015). During the early-middle Miocene, the SCS started to subduct eastward under the moving PSP along the Manila Trench, resulting in the sequential consumption of oceanic crust (Li et al., 2011). The Luzon Arc of the PSP subsequently collided with and deformed the Eurasian Plate along a direction of $\sim 307^\circ$. Since 8 Ma, the PSP rotated clockwise about 9° with respect to Eurasia, with the PSP/Eurasia pole of rotation located northeast of Japan (Hall, 2002). In the Taiwan area, the PSP/Eurasia convergence rate was a mean 56 mm/yr during the last 9 Ma as suggested by Sibuet and Hsu (2004). This velocity is lower than the present-day PSP motion rate (~ 60 – 110 mm/yr) to the WNW relative to eastern Eurasia (DeMets et al., 2010; Wu et al., 2016). Continued research on the PSP motion history is motivated by its significance for deciphering the tectonic development of SE Asia. Unfortunately, isolation from the main ocean ridge spreading and a lack of clear hotspot tracks have resulted in many uncertainties in past PSP reconstructions. Despite abundant seismic reflection, paleomagnetic and seafloor topographic data, contrasting models have been proposed and debated between different authors.

Taiwan Island is situated on the convergent margin of the Eurasian continent and the PSP (Fig. 1A). Eastward subduction of the SCS oceanic lithosphere has resulted in the initiation of the North Luzon Arc and the growth of the accretionary prism since the middle Miocene. Subsequent arc-continent collision between the North Luzon Arc and the Eurasian

passive margin led to crustal shortening and rapid uplift at ca. 7–5 Ma (e.g. Huang et al., 2006; Lee et al., 2006). Oblique collision has induced southeastward propagation of the orogenic buildup across Taiwan Island. Meanwhile, the northwest-facing PSP was subducting beneath the Ryukyu Arc, causing the eventual collapse of the orogenic belt (Teng, 1996; Sibuet and Hsu, 2004). The Hengchun Peninsula is located at the southernmost tip of Taiwan Island, extending north towards the Central Range and its offshore equivalent, the submarine Hengchun Ridge (Fig. 1B). As the most recently emerged accretionary complex, this region provides a unique opportunity to sample accreted deep-marine sediments which were unaltered and recently exhumed (Pelletier and Stephan, 1986; Chang et al., 2003; Lester et al., 2013).

The Hengchun Peninsula is primarily composed of two sedimentary sequences that are folded and thrust upon a chaotic unit of Kenting mélanges (Fig. 1B). The Mutan Formation consisting of approx. 2000 m thick middle to upper Miocene turbidites (11.6–6.4 Ma according to planktonic foraminiferal zones) is generally considered a single tectonostratigraphic unit that composes the main body of the Hengchun Peninsula (Fig. 2; Chang, 1964; Cheng et al., 1984; Chang et al., 2003). It is characterized by alternating sandstones and siltstones intercalated with massive lentiform bodies of conglomerates, indicating a slope to deep-water depositional environment. The Shihmen Conglomerate, Loshui Sandstone and Lilungshan Sandstone are intercalated into sediments of Mutan Formation (Fig. 2). In particular, the Shihmen Conglomerate in the lower part of Mutan Formation exhibits many clast-supported magmatic blocks, including basalt, gabbro, diabase, etc., at various scales. These igneous components are generally well sorted and mostly rounded to subrounded, crop out widely within the Si-Chung Creek area and are also recognized as slump structures in the Cingwashih area (Fig. 2). The approx. 1000 m thick Loshui Sandstone (ca. 12 Ma according to planktonic foraminiferal zones; Chang, 1964) mainly consists of thick-bedded fine-to medium-grained sandstones. It mainly crops out in the eastern part of the Hengchun Peninsula. The lithofacies and ichnofacies of the Loshui Sandstone indicate a middle-to-lower delta slope environment (Pelletier and Stephan, 1986). The approx. 2000 m thick Lilungshan Sandstone (11.2–6.4 Ma; Chang, 1964) exposes along the western coast of Hengchun Peninsula and shows a coarsening- and thickening-upward sequence. It possibly represents the upper member of a submarine delta environment (Pelletier and Stephan, 1986).

The western Hengchun Platform has progressively accumulated Plio-Pleistocene foreland sediments (Maanshan Formation: 3.7–1 Ma) in a shallow marine environment, and these deposits crop out at sea level with a comparatively low average elevation (~ 200 – 300 m). The Maanshan Formation represents the onset of the arc-continent collision and unconformably overlies the Miocene deep marine turbidites (Fig. 2). The Pleistocene strata (<0.5 Ma) are dominated by a reef-lagoon complex and fluvial deposits, which imply the recent uplift and exposure of the slope basin. Interbedded with the upper Miocene turbidites, the Kenting Mélange is located between the Hengchun and Kenting Faults as a unique structure (Fig. 2). This unit is tectonically sheared without any discernible stratification and is characterized by fairly widespread badland topography. Polygenetic clasts, consisting mainly of mafic blocks and fragments of sedimentary sequences (Zhang et al., 2014), are embedded in a scaly argillaceous matrix in the Kenting Mélange.

3. Field observations

3.1. Sedimentary characteristics of the Hengchun conglomerates

The mafic rocks on the Hengchun Peninsula can be divided into three types: pillow lava, blocks in sheared scaly argillaceous matrix, and subrounded to rounded pebbles. Based on broad field observations, here, we highlight the sedimentary characteristics of the representative mafic gravels according to their size, roundness, sorting, combination patterns and sedimentary structures. The constituents of these conglomerates are mostly basalt, gabbro and metamorphic detritus in

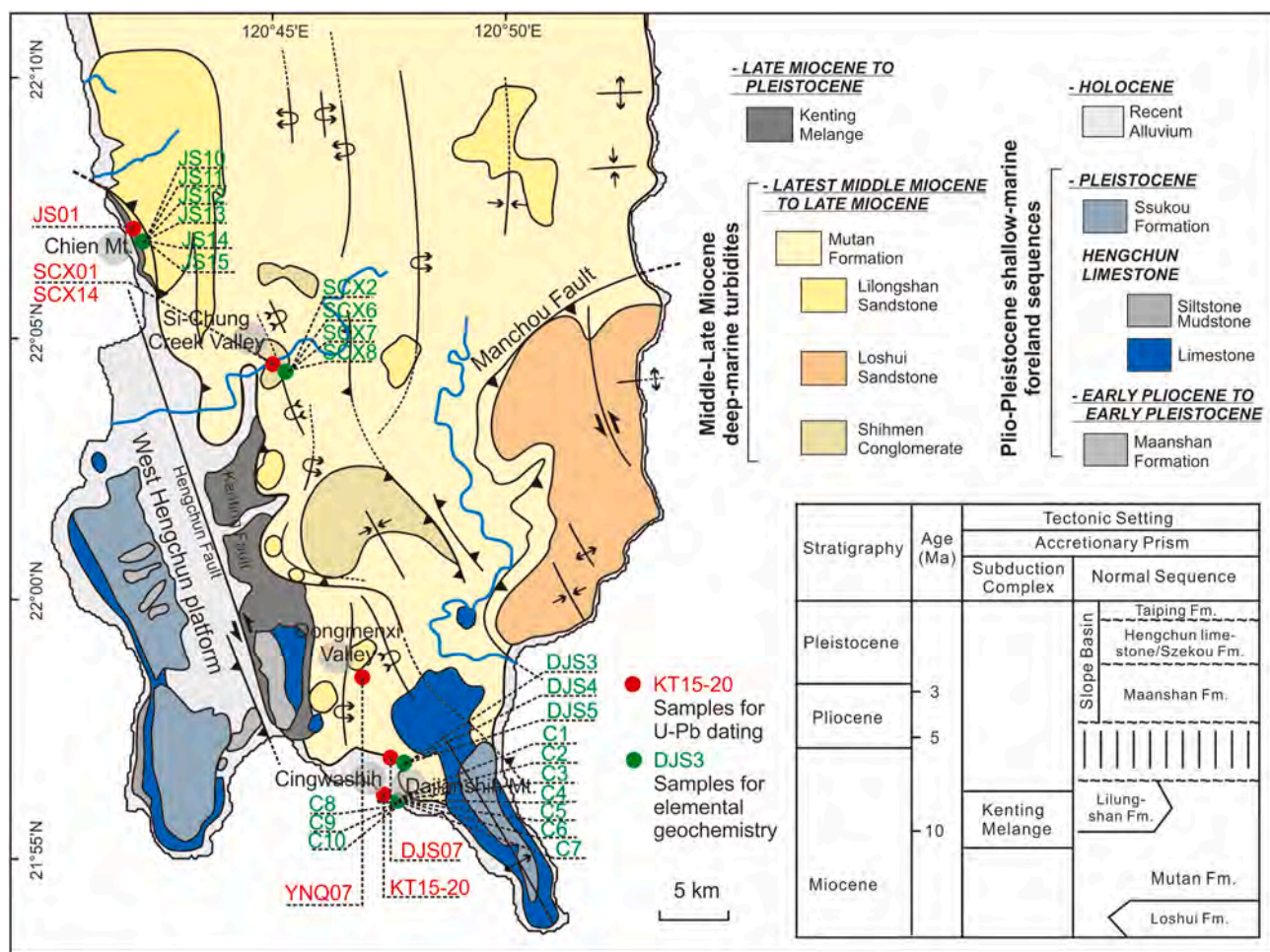


Fig. 2. Geological map of the Hengchun Peninsula showing the major stratigraphic units, sampling positions and distribution of the middle Miocene accretionary prism sediments. Mt. = Mountain.

various proportions (see Dataset S3 for conglomerate component calculation results). Overall, the conglomerate layers range in thickness from 0.5 m to several meters. Rounded clasts are widely distributed and are commonly embedded in the sand- or clast-supported matrix (Fig. 3A, B, C; See Dataset S4 for the roundness and size of mafic clasts; Wadell, 1932; Blott and Pye, 2008). As presented in Fig. 3A, poorly sorted clasts are synchronously deposited with the fine-grained mud matrix. These mafic components are mostly aligned parallel with the mass transport or flow directions, along with less common development of imbricate stacking structures (Fig. 3B and C). Parallel bedding structures were also identified within the layer (Fig. 3C). Normally graded units are well preserved, and the conglomerate layer exhibits a gradational contact with the overlying sand-rich layers (Fig. 3E and F). Therefore, we interpret these syndepositional mafic clasts and thick-bedded sandstones as representing the same depositional unit. In particular, a debris flow is also pictured in Fig. 3D and is marked by a bidirectional rhythmic pattern. Basal and top contacts are commonly marked by sharp erosional boundaries. Apparently, the transition from inverse to normal grading indicates that debris flows and other typical turbidity currents formed the conglomerate deposits.

3.2. Turbidite sequences

Conventionally, a Bouma sequence is interpreted as the product of a turbidity current composed of T_a, T_b, T_c, T_d and T_e divisions. In this study, most of the upper Miocene deep-water sandstone units are deposited as T_a (massive graded conglomerates) and T_b (thick-bedded

sandstones) with subordinate T_d (parallel-laminated sand or siltstones) and T_e (laminated to homogeneous mudstones) (Fig. 4). In Dongmenxi Valley, flute casts and coarse granules are observed at the base, indicating the T_a division in the lower section of a classic turbidite sequence (Fig. 4A, C). Fig. 4D shows the consistent presence of flakes and blocks of mud layers scoured off from a riverbed. Parallel to the interbedded sandstone or mudstone layers, *Nereites* fossils further indicate a pelagic to hemipelagic environment (Fig. 4B; Cheng et al., 1984). Subaqueous gravity flows also generated dish-shaped structures within the T_b or T_c divisions during the dewatering of rapidly deposited or under-consolidated beds. Interestingly, a debris flow, bounded by sharp erosional contacts, is identified in the Shihmen Formation near Syuhai village. The debris flow is also recognized with its apparent normal and inverse grading patterns (Fig. 4E). In the overlying turbidite successions, the T_a division with a fining-upward sequence is in gradational contact with the overlying T_b, in which plane-parallel bedding is present (Fig. 4F). Notably, deformed flysch deposits in Si-Chung Creek Valley are rhythmically interbedded with fine-grained sandstones or mudstones (Fig. 4G and H). Highly deformed by faulting and folding, these structures typically suggest a shearing and compressional environment (Fig. 4G). However, in the dislocated sandstone blocks, ripple or wavy bedding is observed above underlying parallel bedding (Fig. 4H).

4. Analytical methods

Aside from the broad field investigation (~20 km × 20 km) in the Hengchun Peninsula, 19 mafic pebbles were subjected to petrographic



Fig. 3. Field photographs of mafic clasts on the Hengchun Peninsula, refer to Fig. 2 for photo-taking locations. (A) Rubble conglomerates with a reddish tuffaceous matrix, Chien Mountain. (B) Imbricate bedding in a deposit of disk-shaped pebbles or cobbles, Cingwashih. (C) Stratified matrix-supported conglomerate layer, Cingwashih. (D) Conglomerates with inversely (bottom) and normally (top) graded bedding structures, Si-Chung Creek Valley. (E) Conglomerates with normally graded bedding structures, Si-Chung Creek Valley. (F) Stratified pebbly sand, Cingwashih.

analyses. Altogether, 26 igneous samples were collected for elemental geochemistry analyses at the State Key Laboratory of Marine Geology, Tongji University. Among them, 3 gabbro samples and turbidite sandstone samples were also selected for zircon U–Pb dating analysis. As a comparison, Borehole samples from IODP Expedition 367/368 and the commercial drilling program from the China National Offshore Oil Company (CNOOC) were also analyzed for comparison. The assigned stratigraphic ages refer to the IODP Expedition 367/368 Preliminary Report and unpublished seismic and paleontological data from the CNOOC (see Table 1 for detailed sample information).

4.1. Elemental geochemical analyses

The crushed bulk sediments were first immersed in deionized water to prevent external contamination. Approximately 50 mg of dry sample

was digested by a concentrated HF + HNO₃ mixture and then measured with an Agilent 7900 inductively coupled plasma mass spectrometer (ICP-MS) for trace element concentrations. Certified materials BCR-2 and BHVO-2 were repeatedly analyzed as unknown samples to assess precision and accuracy. The external precision (1 s) was usually better than 5%, and the concentrations obtained agreed with the recommended data for these reference materials. Three pebble samples were measured in duplicate during this study, and the relative differences in concentration between duplicates were usually less than 5%.

4.2. U–Pb dating

The zircon extraction and pretreatment processes in this study were based on Shao et al. (2019). Cathodoluminescence (CL) images were employed to locate analytical spots (20–30 μm) based on zircon

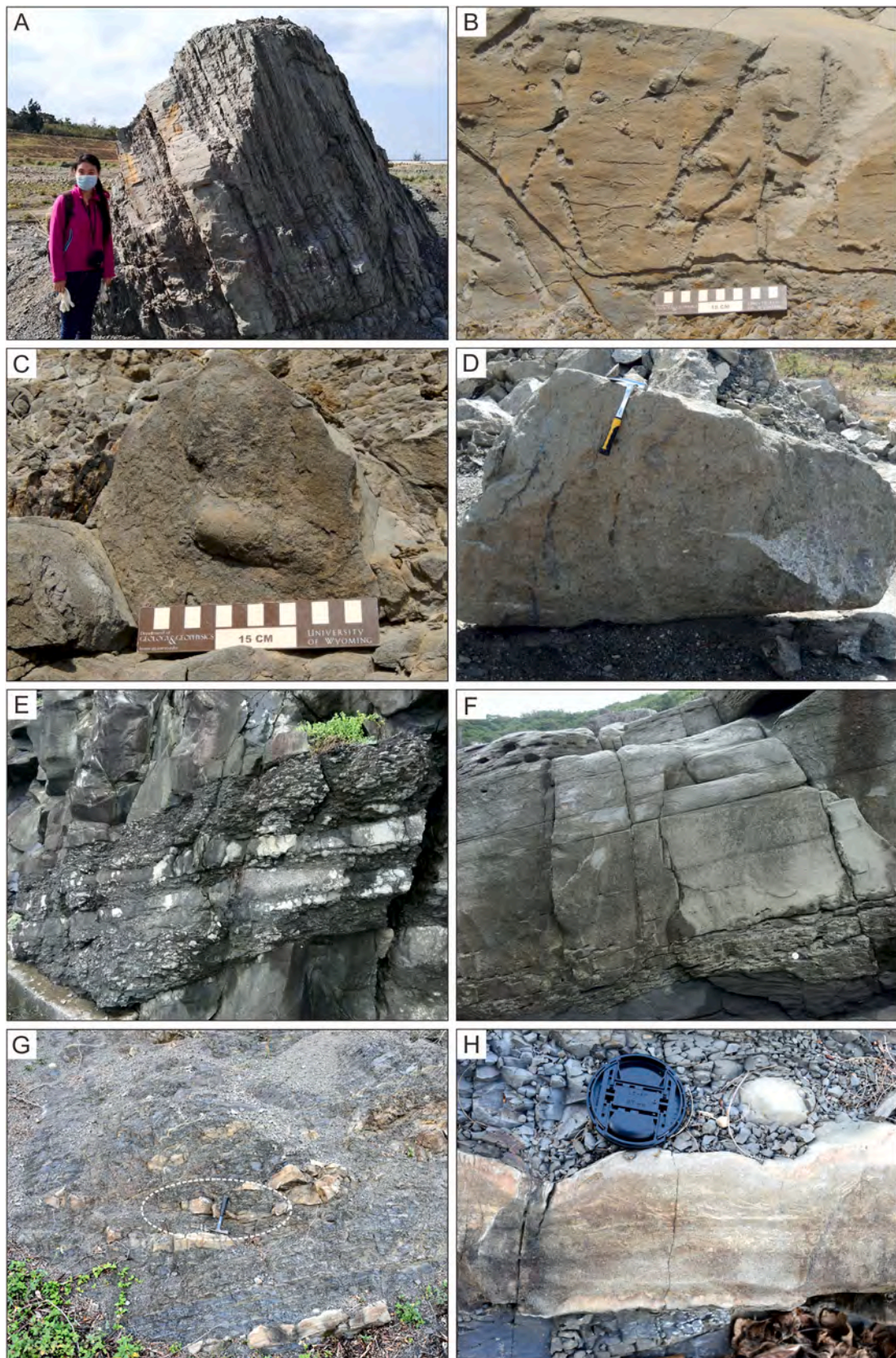


Fig. 4. Field photographs of Miocene turbidites on the Hengchun Peninsula, refer to Fig. 2 for photo-taking locations. (A) Alternating sandstone and mudstone, Dongmenxi Valley. (B) *Nereites* on Bottom B marked in A. (C) Flute cast on Bottom C marked in A. (D) Mud rip-up structures within the basal surface of the sandstone layer, Dongmenxi Valley. (E) Debris flow with normal and inverse grading patterns, Shihmen Formation, Syuhai village. (F) Sharp contacts between the underlying mudstone layer and overlying turbiditic sandstones, Shihmen Formation, Syuhai village. (G) Deformed flysch deposits consisting of interbedded sandstone and mudstone layers, Si-Chung Creek Valley. The highlighted white-bordered ellipse is enlarged in H. (H) Wavy and parallel bedding in turbiditic sandstone blocks.

Table 1

Sample data including sample names (outcrops and boreholes), locations, depths for boreholes, stratigraphic ages, methods (geochemistry or U–Pb), and lithological characteristics.

Sample/Borehole	Location	Depths (m)	Stratigraphic age	Method	Lithological characteristics
C1	Cingwashih	Outcrop	–	Geochemistry	Basalt
C2	Cingwashih	Outcrop	–	Geochemistry	Basalt
C3	Cingwashih	Outcrop	–	Geochemistry	Basalt
C4	Cingwashih	Outcrop	–	Geochemistry	Basalt
C5	Cingwashih	Outcrop	–	Geochemistry	Basalt
C6	Cingwashih	Outcrop	–	Geochemistry	Basalt
C7	Cingwashih	Outcrop	–	Geochemistry	Basalt
C8	Cingwashih	Outcrop	–	Geochemistry	Basalt
C9	Cingwashih	Outcrop	–	Geochemistry	Basalt
C10	Cingwashih	Outcrop	–	Geochemistry	Basalt
KT15-20	Cingwashih	Outcrop	–	Geochemistry/U–Pb	Gabbro
DJS3	Dajianshih Mount	Outcrop	–	Geochemistry	Basalt
DJS4	Dajianshih Mount	Outcrop	–	Geochemistry	Basalt
DJS5	Dajianshih Mount	Outcrop	–	Geochemistry	Basalt
DJS07	Dajianshih Mount	Outcrop	–	Geochemistry/U–Pb	Gabbro
JS01	Chien Mount	Outcrop	Upper Miocene	U–Pb	Sandstone
JS10	Chien Mount	Outcrop	–	Geochemistry	Basalt
JS11	Chien Mount	Outcrop	–	Geochemistry	Basalt
JS12	Chien Mount	Outcrop	–	Geochemistry	Basalt
JS13	Chien Mount	Outcrop	–	Geochemistry	Basalt
JS14	Chien Mount	Outcrop	–	Geochemistry	Basalt
JS15	Chien Mount	Outcrop	–	Geochemistry	Basalt
SCX01	Si-Chung Creek Valley	Outcrop	Upper Miocene	U–Pb	Sandstone
SCX2	Si-Chung Creek Valley	Outcrop	–	Geochemistry	Basalt
SCX6	Si-Chung Creek Valley	Outcrop	–	Geochemistry	Basalt
SCX7	Si-Chung Creek Valley	Outcrop	–	Geochemistry	Basalt
SCX8	Si-Chung Creek Valley	Outcrop	–	Geochemistry	Basalt
SCX14	Si-Chung Creek Valley	Outcrop	–	Geochemistry/U–Pb	Gabbro
YNQ07	Liangluan Creek	Outcrop	Upper Miocene	U–Pb	Sandstone
W-1	Qiongdongnan Basin	3500–3755	Lower Miocene	U–Pb	Sandstone
U1500B 22 R	18°18.2707'N, 116°13.195 1'E	1039.3–1049	Upper Miocene	U–Pb	Sandstone
U1500B 25 R	18°18.2707'N, 116°13.195 1'E	1068.4–1078.1	Upper Miocene	U–Pb	Sandstone
U1499B 33 R	18°24.5750'N, 115°51.5990'E	3758.1	Upper Oligocene	U–Pb	Sandstone

oscillatory zoning. Zircon U–Pb dating was performed using a Thermo Elemental X-Series ICP-MS coupled to a New Wave 213 nm laser ablation system. Zircon 91500 (1065.4 ± 0.3 Ma) was used as an external calibration standard and analyzed twice for every seven analyses. Plešovice zircon (337.1 ± 0.4 Ma) was simultaneously included for further accuracy calibration (Sláma et al., 2008). Isotopic ratios were calculated using ICPMSDataCal 10.2 (Liu et al., 2009) after the common Pb correction from Andersen (2002). We followed the convention of using $^{206}\text{Pb}/^{238}\text{U}$ ages for younger grains (<1000 Ma) and $^{207}\text{Pb}/^{206}\text{Pb}$ ages for older grains (>1000 Ma) (Compston et al., 1992). The age spectra measured in this study and other published data were plotted as kernel density estimates and histograms using DensityPlotter (Vermeesch, 2013). Concordia plots and weighted mean age calculations were conducted via Isoplot (Version 4.15).

5. Results

5.1. Elemental geochemistry of Hengchun mafic pebbles

The total rare earth element (ΣREE) concentrations of the Hengchun gabbros and basalts range from 8.47 to 97.12 ppm (Fig. 5A; Dataset S1). In particular, KT15-20 and SCX14 yield significantly low REE contents (8.47 and 18.13 ppm, respectively). Most of the samples display light REE (LREE)-depleted and heavy REE (HREE)-flat patterns parallel to the N-MORB model, with $(\text{LREE}/\text{HREE})_{\text{N}}$ values falling between 1.44 and 0.55. The left-dipping trend is exemplified by $(\text{La}/\text{Yb})_{\text{N}}$ and $(\text{La}/\text{Sm})_{\text{N}}$ values ranging from 0.48 to 2.00 (mostly centered in 0.48–0.91) and from 0.49 to 1.67 (mostly centered in 0.49–0.98), respectively. A few samples display relatively flat or right-dipping distribution patterns, such as C7, JS14 and JS15, which differ from the dominant LREE-

depleted patterns in other samples. Additionally, almost all of these samples have slightly positive Eu anomalies ($\delta\text{Eu} = 0.70\text{--}6.98$). Caution is required when interpreting the slight Eu depletions in JS11, C2, C7 and SCX7.

On the N-MORB-normalized incompatible elemental distribution patterns (Fig. 5B), samples consistently display enrichments in large ion lithophile elements (LILEs), such as Rb, Ba, Pb and Sr. In contrast, slight or clear depletions in high field strength elements (HFSEs) are represented by Nb and Zr, along with the positive Ta anomaly. Despite certain elemental fluctuations, elements from Nd to Lu commonly show a flat pattern without apparent anomalies. Overall, a dominant group of data largely resembles the N-MORB distribution pattern. Of these samples, KT15-20 is distinct in its uniquely low concentrations compared to standard N-MORBs. Typical geochemical signatures of La/Nb, Zr/Nb and Th/Ta are also calculated as 0.64–7.67, 9.48–93.83 and 0.05–17.72, respectively (Dataset S1).

5.2. Zircon U–Pb dating

5.2.1. Gabbro outcrops on the Hengchun Peninsula

Zircon grains were extracted from three holocrystalline gabbro samples for U–Pb dating analyses. Most of them exhibit angular shapes with typical oscillatory zoning in CL images (Fig. S1). Th/U ratios generally exceed 0.1 for both gabbro and sandstone zircon samples, indicating a common magmatic origin (Fig. 6; Hoskin and Schaltegger, 2003).

Concordia plots and weighted mean ages of the examined gabbro samples are shown in Fig. 7A. Twenty-three effective spots were obtained for KT15-20, which generated a concordia age of 23.60 ± 0.20 Ma with a mean square weighted deviation (MSWD) of 0.11. SCX14

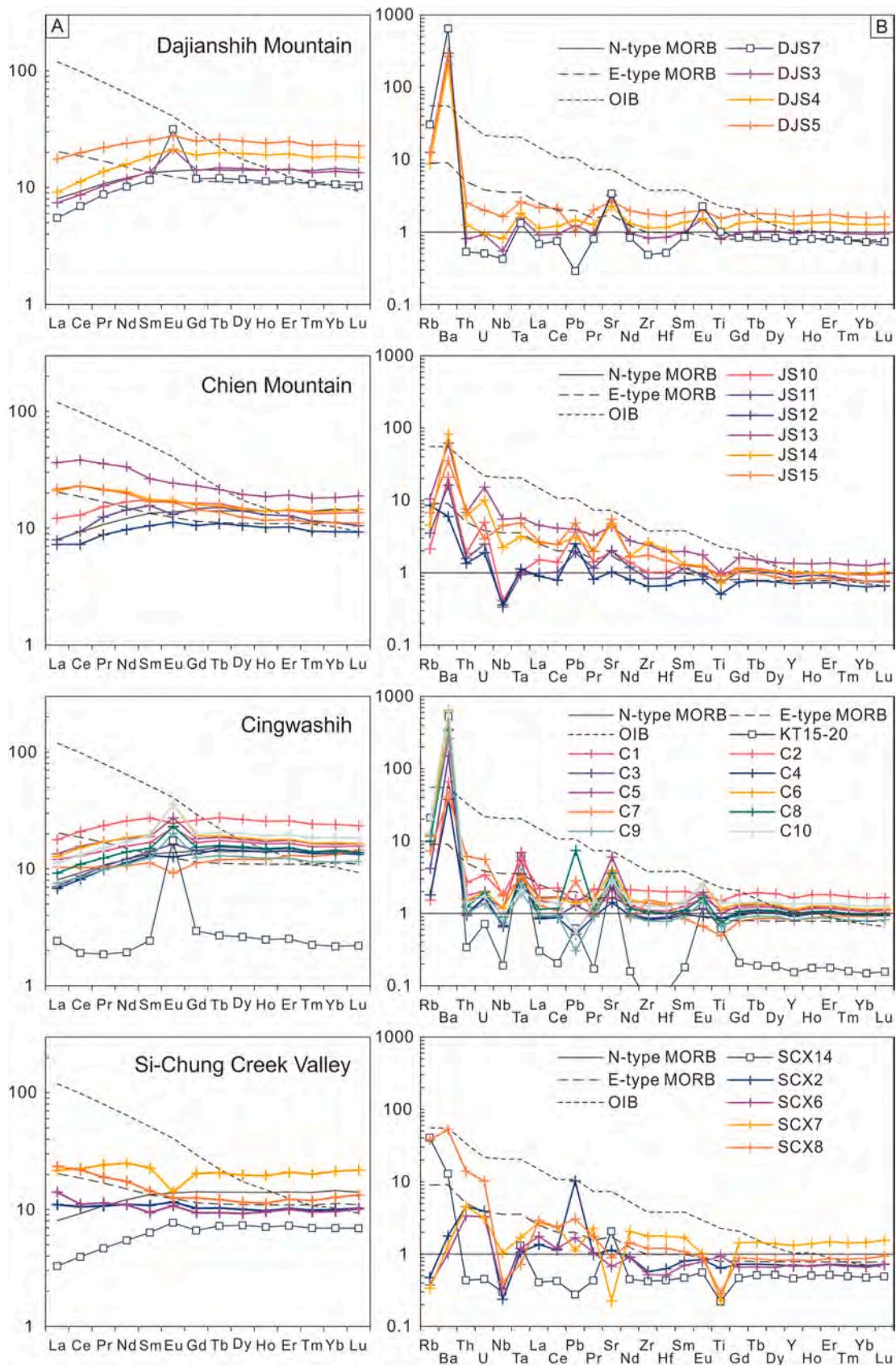


Fig. 5. (A) Chondrite-normalized rare earth element distribution patterns and (B) normal mid-ocean ridge basalt (N-MORB)-normalized incompatible element distribution patterns for the Dajianshih Mountain, Chien Mountain, Cingwashih and Si-Chung Creek Valley outcrops. The dated gabbro samples are represented by solid blue squares (DJS7, KT15-20 and SCX14). Chondrite, N-MORB, enriched MORB (E-MORB), and ocean island basalt (OIB) values are from [Sun and McDonough \(1989\)](#). (For interpretation of the references to colour in this figure legend, the reader is referred to the Web version of this article.)

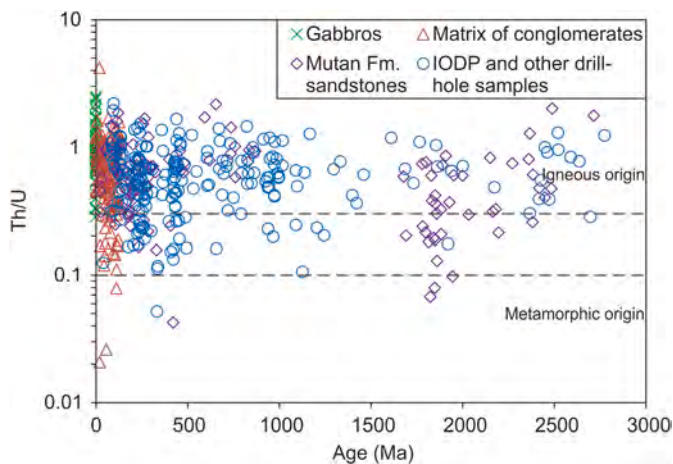


Fig. 6. Plots of Th/U ratios vs. U–Pb ages for all dated zircon grains.

shows an approximate concordia age of 23.78 ± 0.41 Ma (MSWD = 1.40) based on 10 valid spots. In comparison, DJS7 yields a relatively older age of 25.40 ± 0.24 Ma (MSWD = 0.99) according to 18 valid analyses. The concordia ages of these three samples are fairly consistent with their individual weighted mean ages (see Dataset S2 for the U–Pb isotope ratios).

5.2.2. Turbidite sandstones from both Hengchun outcrops and SCS boreholes (Fig. 8)

Detrital zircons from sandy matrix and upper sandstone divisions mostly range in size from ~50 to 180 μm in length for SCX01, JS01 and YNQ07 (Fig. S1). Almost all analyses are concordant within uncertainties for both Hengchun turbidite and SCS borehole sandstones (Fig. 7B). Briefly, the main clusters do not vary greatly between different Hengchun turbidite samples (Fig. 8B; see Dataset S2 for U–Pb isotope ratios). The measured ages form a broad age spectra ranging from the Archean to the Cenozoic and display several distinct Yanshanian (~150–65 Ma), Indosinian (~260–200 Ma) and Lvlngian (~2500–1800 Ma) peaks. Minor age intervals are also evident, including Caledonian (~550–350 Ma) and Jinningian (~1000–800 Ma) peaks. Interestingly, both SCX01 and JS01 feature centralized ~23 Ma populations, whereas

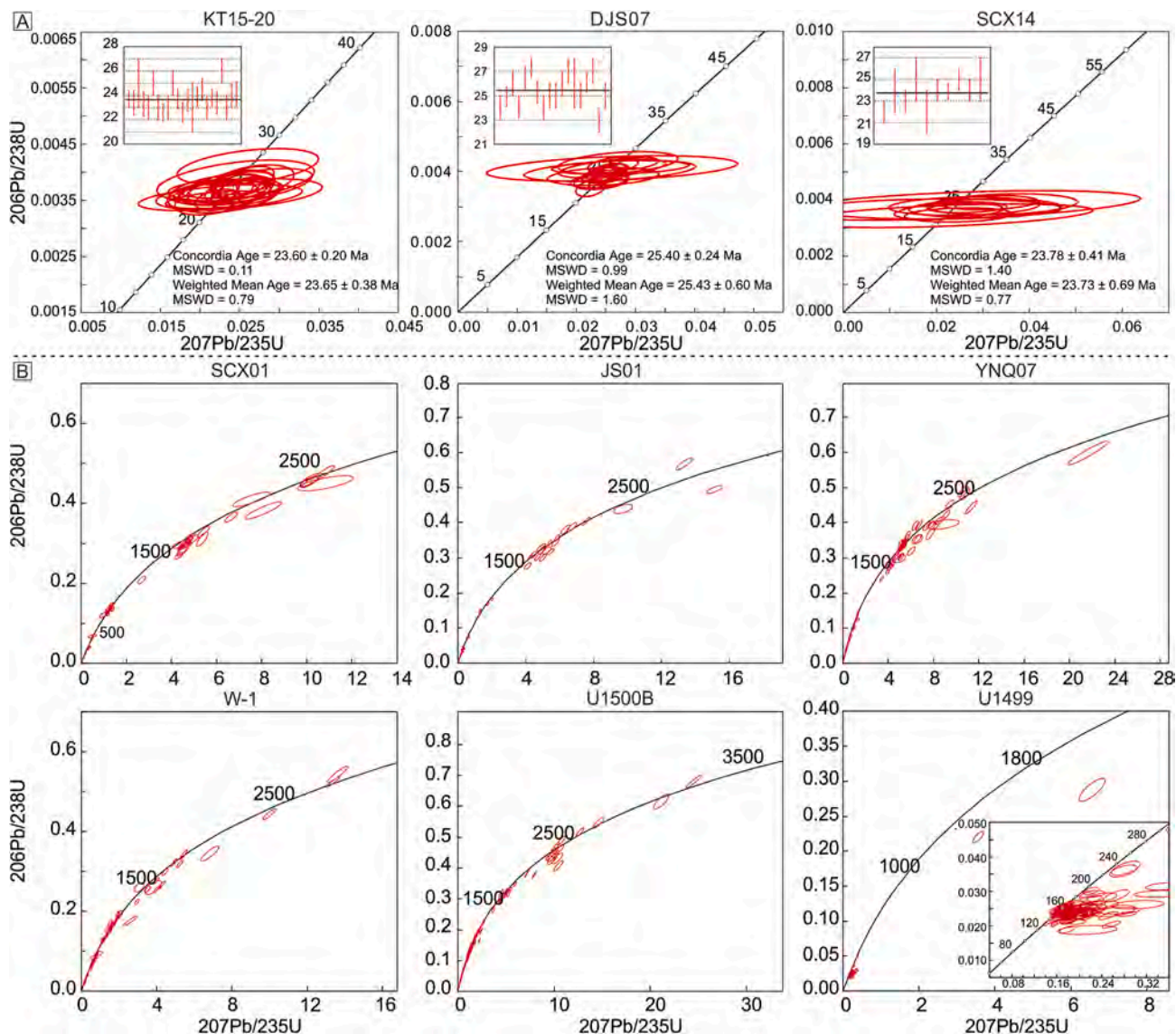


Fig. 7. (A) U–Pb concordia ages and weighted mean ages of the rounded gabbro gravels from Si-Chung Creek Valley, Cingwashih and Dajianshih Mountain. (B) U–Pb concordia plots of the sandy matrix and upper turbiditic sandstones on the Hengchun Peninsula and the borehole sandstones in the northern South China Sea.

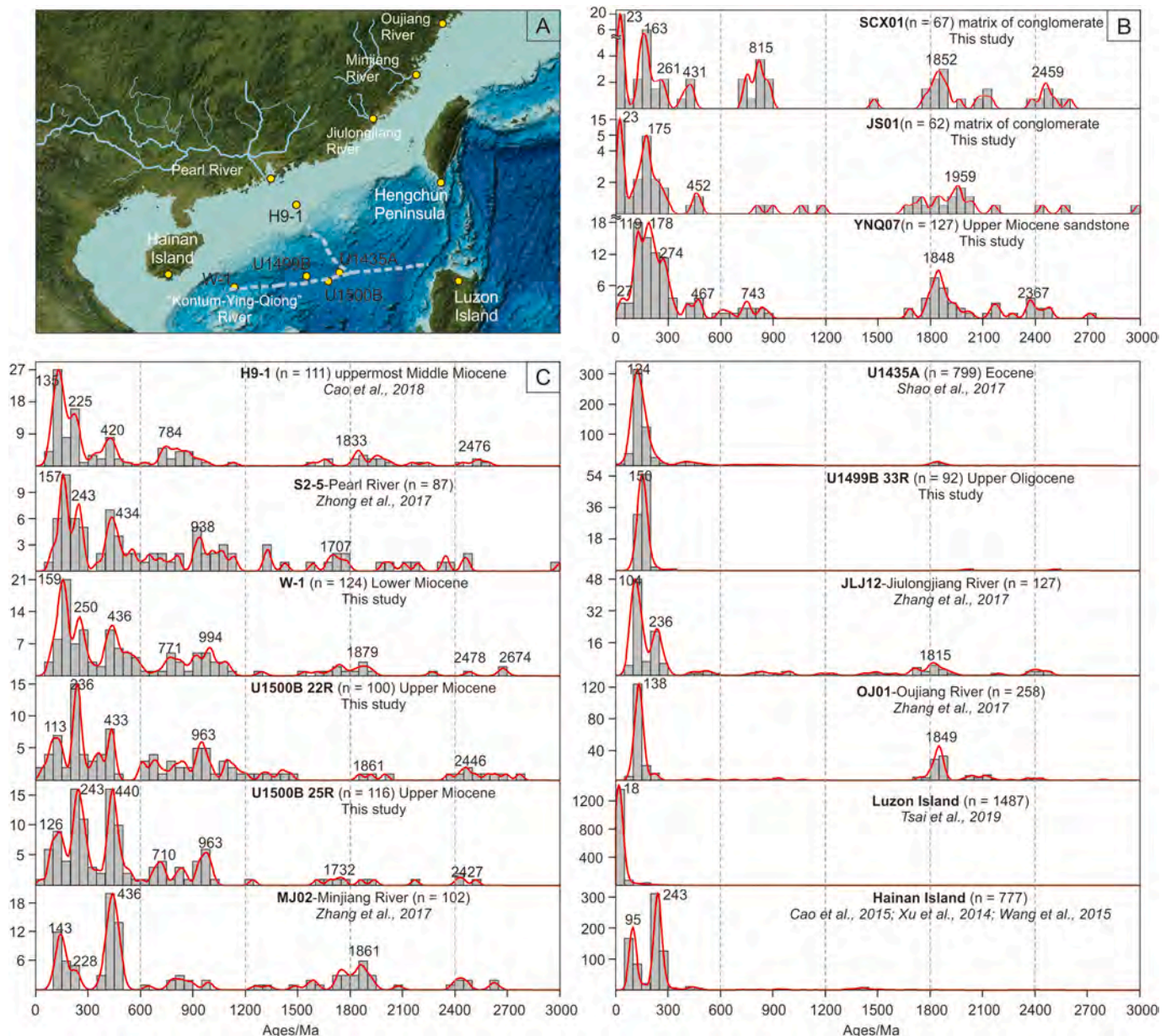


Fig. 8. (A) Topographic map showing the major rivers around the potential source areas. Sample locations are indicated by yellow dots for the onshore outcrops and basinal boreholes in this study or from previously published data. (B) Detrital zircon U–Pb age spectra of the upper Miocene strata, Hengchun Peninsula. The term “n” denotes the number of concordant analyses. (C) U–Pb age patterns of the potential source areas represented by the Pearl River fluvial network, the Pearl River Mouth Basin, Qiongdongnan Basin, modern Minjiang River, modern Jiulongjiang River, Oujiang River, Luzon Island and Hainan Island. See Table 1 for sample details. The published data of the Pearl River (H9-1, S2-5), Minjiang River (MJ02), Jiulongjiang River (JLJ12), Oujiang River (OJ01), U1435A, Luzon Island and Hainan Island are from Cao et al. (2018), Zhong et al. (2017), Zhang et al. (2017), Shao et al. (2017), Tsai et al. (2019), Cao et al. (2015), Xu et al. (2014) and Wang et al. (2015), respectively. (For interpretation of the references to colour in this figure legend, the reader is referred to the Web version of this article.)

YNQ07 features an indistinguishable Cenozoic peak.

Here, we have conducted a systematic investigation of the age distribution patterns in the potential terrestrial and intrabasinal source areas. Similarly broad spectra are observed in the SCS Miocene boreholes W-1, U1500B 22 R and U1500B 25 R in this study. These spectra are mainly characterized by Yanshanian, Indosinian and Caledonian peaks with minor Jinningian and Proterozoic groups (Fig. 8C). As a continental-scale fluvial network, the Pearl River also displays a complicated U–Pb spectrum since the middle Miocene. Alternatively, the upper Oligocene sample U1499 33 R is uniquely characterized by a single Yanshanian peak (~150 Ma), which resembles U1435A as a local provenance. In comparison, other potential source areas display relatively confined U–Pb spectra, represented by Hainan Island, the

Minjiang River, the Jiulongjiang River, and other areas (Fig. 8C).

6. Discussion

6.1. Origin and formation of mafic conglomerate clasts

Antecedent studies have highlighted the significant impact of rapid tectonic events on both Shihmen Conglomerates and Kenting mélanges in the Cingwashih area (Fig. 2). The intensely fractured and sheared fragments of Kenting mélanges were considered as products of gravity-driven collapse of seamount volcanic clasts during their incorporation into the accretionary prism (e.g. Lin et al., 2009; Zhang et al., 2016). The rounded mafic conglomerates were presumed to have been subjected to

intense recycling and rounding processes during the temporary and abrupt emergence of the accretionary prism (e.g. Tian et al., 2019). However, in our field observations, we have identified numerous outcrops of conglomerate deposits of rounded mafic clasts throughout the Hengchun Peninsula as part of the thick T_a turbidite division. In terms of the original depositional environment, these massive mafic conglomerates mainly consist of basalt and gabbro clasts and show pebble alignment structures based on our field description. This sedimentary feature clearly reflects the direction of turbulent flows. Petrographic identification also reveals intergranular to intersertal basalt textures. Olivine and pyroxene phenocrysts are embedded within the cryptocrystalline matrix of tiny acicular feldspar crystals. The holocrystalline gabbro, in particular, shows poikilitic textures, in which idiomorphic plagioclase is enclosed by pyroxene crystals and shows reaction rim textures (Fig. S2). Our U–Pb dating results (23.60–25.40 Ma) further confirm the close affinity between these rocks and the SCS spreading, similar to other related paleontological and geochronological analyses on both Hengchun outcrops and SCS extension interpretations (e.g., Pelletier and Stephan, 1986; Briais et al., 1993; Barckhausen et al., 2014; Li et al., 2015). Therefore, the Hengchun mafic pebbles do not appear to be closely linked with the Early Cretaceous Huatung Basin or the Paleogene West Philippine Basin (Chen et al., 2018a).

The geochemical plots of our studied mafic conglomerate clasts commonly demonstrate similar tectonic origins according to the highly consistent distribution patterns. Generally, the dominant left-dipping REE patterns of N-MORBs are fairly distinguishable from the minor group of typical E-MORBs or OIBs (Fig. 5A). The low Σ REE average (47.98 ppm) is approximately equal to those of IODP Site U1431 (36.35 ppm) or classic N-MORB (39.11 ppm) (Sun and McDonough, 1989; Zhang et al., 2018). While the Eu anomalies vary greatly (0.70–6.98), indicating various degrees of plagioclase fractionation, the majority of values are concentrated in the range of 0.92–1.73. Given the possible diagenesis resulting from hydrothermal alteration and accretion-related metamorphism at the convergent plate boundary, the contents of major elements and LILEs might be distorted or preferentially indicate diverse elemental mobilization. Nevertheless, HFSEs are recognized as relatively immobile and can be used as reliable indicators to constrain rock genesis and mantle sources. Similarly, low concentrations of HFSEs and flat patterns from Nd to Lu are also suggestive of average N-MORB basalt sourced from a depleted mantle substance (Fig. 5B). Despite displaying broad ranges, the values of La/Nb, Zr/Nb and Th/Ta are still largely constrained within the range of MORB types, as defined by Sun and McDonough (1989). Incompatible multielemental trends almost exclusively resemble those of typical MORBs instead of intraplate OIBs. For the Hengchun gabbro and basalt rounded clasts, the geochemical signatures found in this study preferentially reflect an origin from a depleted mantle source within a mid-ocean ridge tectonic setting.

6.2. Sedimentary provenance of the Hengchun turbidite sandstones

The numerical approach of nonmetric multidimensional scaling (MDS) has been adopted by numerous scholars to assess the similarities and dissimilarities between samples on a quantitative basis (Vermeesch, 2013; Vermeesch et al., 2016). This method is based on the Kolmogorov-Smirnov test, assuming that all the samples share identical analytical uncertainty. In the MDS plot, samples with similar U–Pb age spectra are grouped together, while those with distinct age spectra being form separate groups. The final stress value is normally used to evaluate the quality of the MDS fit. According to the rules of thumb (Vermeesch, 2013), the stress value lower than 0.1 qualifies as a “fair” fit for the nonmetric MDS result, the one lower than 0.05 qualifies as a “good” fit, and the one lower than 0.025 qualifies as an “excellent” fit. The MDS plot was introduced as a complementary method in this study, in order to eliminate the weakness of traditional visual examination of age frequency distributions. Similar to any other dimension-reducing methods, MDS plot makes an abstraction of the dataset and cannot always explain

the full richness of all age combinations. Despite the limitations, the MDS technique is still proved to capture the main features of detrital zircon U–Pb ages. Therefore, the interpretations of the provenance distribution patterns should be compatible with geological plausibility when using the MDS results.

The sandstones were formerly interpreted to have undergone rapid sedimentary transport and low to moderate metamorphism, with an inferred provenance of a magmatic arc and recycled orogen in the SE China continent (Xu and Chen, 2010; Zhang et al., 2017). Based on the U–Pb age spectra, there is indeed visual difference, to a certain extent, between the Hengchun turbidite sandstones and the sediments from rivers in coastal SE China (e.g., the Minjiang River and Jiulongjiang River, Fig. 8A). It seems that this difference can be interpreted by another reasonable source-to-sink sedimentary infilling model. In this study, the MDS plot indeed shows the linkage between the Pearl River, Minjiang River and other fluvial networks and the Hengchun turbiditic deposition (Fig. 9). However, the age similarities between the Minjiang River and other potential tributaries (Fig. 8C) could be attributed to the regional development of the SE coastal China fluvial system. During late-stage drainage evolution, headward erosion possibly started to occur in the upper reaches of the Minjiang River, extending into the broad interior of the South China. Therefore, an increasing number of old zircon grains is included in the Minjiang River U–Pb spectrum, in addition to its notable Caledonian (~436 Ma) and subordinate Yanshanian group (~143 Ma) peaks.

However, sand from the modern Minjiang River estuary has U–Pb spectrum almost as distinct from the Hengchun Miocene turbiditic sandstones as other potential river systems, particularly regarding the obvious absence of abundant Neo- and Mesoproterozoic zircon grains (Fig. 8B). Additionally, the spectra of the modern Jiulongjiang and Oujiang Rivers are even less likely to transport materials into Hengchun area, as expressed by the large distance between these groups in the MDS map, and display relatively simple U–Pb patterns (Figs. 8B and 9). Yanshanian or Indosinian clusters are dominant, and fairly minor Proterozoic groups are present. With confined drainage areas, most of the tributaries in coastal SE China are seemingly not that closely related to the Hengchun upper Miocene sandstones.

Alternatively, the Hengchun turbidite sandstones might have derived different provenance areas. Several outcrops, boreholes, and potential provenance areas are considered by jointly plotting the respective age spectra (Fig. 8B and C). W-1 is the westernmost core in this study. It is characterized by a wide range of U–Pb ages, including both apparent Indosinian and Caledonian populations and a subordinate Jinningian group beside its predominant Yanshanian peak, indicating an increasing supply from proximal Hainan Island (Fig. 8C; Cui et al., 2019). Farther east, IODP Expedition 367/368 cored turbidite sandstone sequences hundreds of meters thick at Sites U1499B and U1500B within the northern SCS. Interestingly, upper Miocene samples from both U1500B 22 R and U1500B 25 R display multimodal patterns that closely resemble those from the lower Miocene W-1 (Fig. 8C). Represented by Indosinian and Caledonian groups in similarly large proportions, U1500B strongly indicates sedimentary transport and deposition from the west. On the MDS plot, two U1500B samples are also close to W-1 and the turbiditic sandstones on the Hengchun Peninsula (Fig. 9).

Similarities between these borehole samples indicate a potential western source which has been casting an important impact on the northern SCS. The Central Canyon which formed during regional transgression-regression cycles since the late Miocene, was investigated in earlier studies (e.g. Li et al., 2017; Ma et al., 2017; Liu et al., 2019). Displaying signatures from both Hainan Island and central Vietnam of Indochina Block, large amounts of sediment have been transported through this canyon eastwards to the broad abyssal plain by long-distance turbidity flows. This submarine channel appears to be analogous to other traditional deep-water conduits around the world, e.g., Canyon San Fernando of Baja California, canyons in the northern Gulf of Mexico, etc. (Kane et al., 2007; Callow et al., 2014; Hansen et al.,

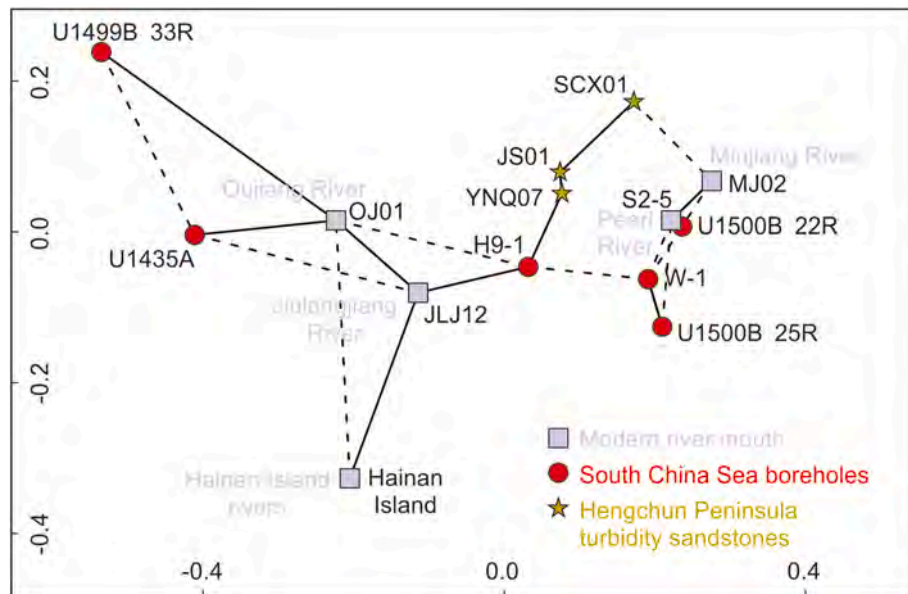


Fig. 9. Nonmetric multidimensional scaling map (MDS) of U–Pb ages for the studied samples from the Hengchun Peninsula outcrops and the northern South China Sea basin, in reference to the potential source areas exemplified by modern river mouths or ancient paleo-uplifts. Solid and dashed lines indicate the closest and second closest neighbors, respectively. The stress value is 0.056, implying high goodness-of-fit (Vermeesch, 2013).

2015). Commonly initiated at well-developed shelf breaks, these canyons are dominated by intense gravity-driven processes. However, recent research has proposed that the ancient eastward-flowing “Kontum-Ying-Qiong River” might have delivered massive amounts of sediments from central Vietnam to the further eastern SCS, starting in at least the late Oligocene (Shao et al., 2019). Geographically, the ancient “Kontum-Ying-Qiong River” seems to have then become a fairly long-distance submarine canyon spanning the overall northern SCS margin in Late Miocene (Ma et al., 2018; Cui et al., 2019). As a pronounced supplier of sediment, central Vietnam has been paid increasing attention (e.g. Jonell et al., 2016; Fyhn et al., 2019; Wang et al., 2019), in contrast to previous studies (e.g., Yan et al., 2011; Wang et al., 2011; Sun et al., 2015). Central Vietnam underwent polycyclic evolution since the early Paleozoic. The anatectic magmatism and high-degree metamorphism in this region are related to the Caledonian and Indosinian events, with age intervals of ~470–400 Ma and ~250–210 Ma, respectively (e.g., Carter et al., 2001; Lepvrier et al., 2004; Metcalfe, 2011). Notably, prominent Indosinian orogenic and metamorphic activities took place in this area during the late Triassic (e.g., Findlay and Trinh, 1997; Halpin et al., 2016; Wang et al., 2018).

In addition, the paleo-Pearl River might have already established its continental-scale drainage configuration by the early-middle Miocene (Cao et al., 2018; Shao et al., 2019). This large-scale river drained the wide South China Block, providing massive amounts of sediments to the southern parts of northern SCS basins. Seismic profiles accordingly reveal numerous parallel submarine deltas stretching into the deep-sea basins (Pang et al., 2006). Located near the Pearl River estuary, the uppermost middle Miocene borehole H9-1 exhibits a broad age spectrum with a centralized Yanshanian-Indosinian peak and a substantial amount of older zircons (Fig. 8C). This U–Pb signature apparently shows a certain similarity to that of U1500B, as linked by the dashed lines in Fig. 9, and points to a mixed provenance pattern. It requires to be clarified that nearby regions might alternatively have been influenced by local provenances from certain paleo-uplifts, as indicated by the existence of U1435A and U1499B. The occurrence of a single Yanshanian peak reasonably reveals a source other than the long-distance transport system for these two drilling areas (Fig. 8C).

Based on investigations of the surrounding source areas, we tentatively suggest a mixed provenance combination via long-distance mass

transport resulting in thick sedimentary successions. We also note that the SCS regional sea level rose significantly at ca. 10.5 Ma due to post-rifting subsidence in contrast with the ubiquitous fall of the global eustatic level (e.g., Zhao et al., 2016). Consequently, the “Kontum-Ying-Qiong River” was a submarine canyon that extended eastwards in a subaqueous environment for thousands of kilometers. Both the Pearl River fluvial system to the north and the “Kontum-Ying-Qiong River” to the west delivered large amounts of terrigenous sediments to the northern SCS oceanic basin. The upper Miocene turbidites on the Hengchun Peninsula appear to be closely correlated to the thick sandstone sequences drilled in IODP core U1500B. In addition to the close resemblance of the U–Pb age spectra between Miocene IODP core U1500B and Hengchun turbidites (Fig. 9), the incorporation of considerable Cenozoic zircons is evidently related to the incorporation of relatively young oceanic crust (Fig. 8B and C). Supported by the geochronological and geochemical analyses, the SCS MORBs and gabbros might have been partially eroded and entrained under turbulent hydrodynamic conditions. The brittle SCS upper crust also features abundant low-angle detachment faults (Lei et al., 2018, 2020; Sun et al., 2018), which coincidentally facilitate erosion and entrainment by underwater flows.

6.3. Formation of the Hengchun deep marine turbidites

Many scholars have investigated the formation of fragmented Kenting mélanges and the Miocene deep-sea alternating mudstone-sandstone strata. On the one hand, the Kenting mafic protoliths were inferred to be originally sourced from the nearby downgoing slab during the transition from early-stage intraoceanic subduction to the present arc-continent collision setting (e.g., Lin et al., 2009; Zhang et al., 2016). These mafic materials were considered to subsequently experience intense tectonic disruptions within the subduction channel to generate the scaly foliation observed in the Kenting mélanges. On the other hand, the Miocene deep-sea turbidites exhibit good preservation of typical sedimentary structures outcropped on the Hengchun Peninsula. Tectonic events near the subduction zone were also considered to explain the present-day setting of Hengchun turbidites (e.g. Zhang et al., 2014; Tian et al., 2019). According to those researchers, pelagic to terrigenous sandstone sediments, together with oceanic crust fragments, were likely to have

been heavily mixed and abraded by rapid tectonic events near the subduction zone.

Our investigations elucidate the relationships between mafic basal conglomerates and overlying sandstones. The rounded mafic clasts within the Hengchun turbidite sequences are composed of gabbros and basalts yielding U–Pb ages of 23.60–25.40 Ma (Fig. 6). Geochemical analyses further demonstrate a strong affinity with the SCS oceanic crust extension for the gabbros and basalts (Fig. 5). According to our field observations, the accumulated mafic clasts are more likely to be intensely scoured and entrained as clasts from a riverbed than to be exotic blocks that experienced friction and abrasion processes. In particular, considering the matrix-supported conglomerate and upper turbidity successions, the sedimentary origin is correlated to a submarine channel or underwater canyon system (Figs. 3 and 4). The sedimentary structures include flute casts, parallel bedding and fining-upward patterns within different stratigraphic units. Our source-to-sink analysis implies a western source from Central Vietnam and a northern source from the Pearl River. In the submarine turbidity currents, rounded clasts were first eroded from the SCS normal oceanic crust under drastic hydrodynamic condition and then deposited within the basal division of a turbidite when the turbidity current was traveling eastward. After being incorporated into the subduction zone near Manila Trench, turbidites were stacked in the accretionary prism, migrated and finally exposed on the Hengchun Peninsula.

6.4. Regional geodynamic reconstruction and plate interaction history

Sedimentary evidence extracted from the subduction zones is likely to present reliable interpretations of the plate interaction history. In this study, IODP drilling cores surprisingly feature thick successions of hemipelagic and turbidity deposits with high sedimentation rates during the late Miocene. The turbidite sequence from Site U1500 is organized into both massive and stratified beds, including a range of parallel, cross-bedded and convolute laminations along with fining-upward sequences. Planktonic foraminiferal and calcareous nannofossil biostratigraphic constraints indicate depositional ages of 8.12 Ma (Zone NN11) and 8.58 Ma (M13 b/M13a), respectively (Stock et al., 2018). Clearly flowing from west to east, the “Kontum-Ying-Qiong River” produced turbidity currents that extended farther into the ocean basin and simultaneously swept up abundant mafic-ultramafic fragments within its bottom layer. Additionally, the well-established Pearl River tributary network also carried high concentrations of materials reaching the ocean basin of the SCS (Fig. 10A). This rapidly moving flow encountered the ca. 23.60–25.43 Ma SCS oceanic crust around $\sim 17^\circ$ N. Our geochronological results coincide with previous magnetic anomaly lineations, which have been used to confine the directions and ranges of SCS seafloor spreading (Fig. 10B and C; Briaies et al., 1993; Li et al., 2015; Sibuet et al., 2016). Together with the mafic gravels and boulders, these turbidity components were ultimately deposited in the subduction channel and were incorporated into the initial accretionary prism (Fig. 10D). As the plates converged, the Manila Trench later migrated gradually in the direction of 307° during continual subduction of the SCS under the PSP (Seno et al., 1993; Yu et al., 1997). The PSP is speculated to have moved at an unsteady rate and have experienced clockwise rotation during the process (Wu et al., 2016).

Lines of sedimentary evidence correspondingly suggest that the original accretionary prism was eventually uplifted and exposed in the Hengchun area after moving potentially ~ 500 km from its origin (Fig. 10A). During the middle and late Pleistocene (<0.5 Ma), the Hengchun Peninsula was covered by reef-lagoonal complexes and fluvial deposits, which mark the onset of accretionary prism emergence (Chang, 1964; Chang et al., 2003). Therefore, the northwestward migration of the Manila accretionary prism progressed at average velocities of ~ 61 – 65 mm/yr from the late Miocene to the Pleistocene. A conceptual model generated by Sibuet and Hsu (2004) initially indicated that the PSP moved continuously through time in a westward direction,

at a mean velocity of 56 mm/yr since ca. 9 Ma (even earlier) with respect to the Eurasian Plate. Our sedimentary estimates appear to yield a comparatively higher rate. It is probably caused by a larger migration distance of the Hengchun accretionary complex, based on our new source-to-sink provenance analysis. This higher convergence rate is otherwise consistent with the speculation that the PSP attained movement speeds of 71–80 mm/yr (Seno et al., 1993; Yu et al., 1997). However, these authors preferred that the beginning of collision would have occurred more recently in this case, prior to at least 8 Ma. In addition, the fact should not be neglected that SE to NW oriented paleocurrent directions are interestingly consistent with minor amounts of clockwise rotation from 25 to 5 Ma (Hall, 1997). Although requiring further confirmation, the turbidity flows might have been kinematically shifted by the complicated motion and rotation of the PSP.

7. Conclusions

Our findings suggest a more integrated interpretation of the upper Miocene turbidite deposition containing conglomerates of massive well-rounded mafic clasts on the Hengchun Peninsula than previously considered. Qualitative and quantitative source-to-sink comparisons confirm significant contributions from the “Kontum-Ying-Qiong River” and Pearl River tributaries. Based on field observations and elemental geochemical and detrital zircon U–Pb geochronological results, we conclude:

1. Rounded mafic conglomerate clasts in the Hengchun turbidite deposits have affinities with SCS mid-ocean ridges (~ 23.6 – 25.4 Ma). Composed of gabbros and basalts, these mafic clasts might have been intensely scoured and eroded from oceanic crust that had been fractured by numerous low-angle detachment faults.
2. Stratigraphically, the rounded gabbro and basalt clasts are widely deposited on the Hengchun Peninsula and occur in the lowest unit of the turbidite sequences. The matrix-supported and upper turbiditic sandstone layers are mainly linked to the vast amounts of sediments delivered by both the Pearl River and Central Vietnam to the north and west of the SCS, respectively. During the late Miocene, voluminous terrigenous materials were transported eastward from the Kontum Massif, central Vietnam, via the “Kontum-Ying-Qiong River” on a considerably large scale. Subordinate contributions from the Pearl River fluvial network and certain intrabasinal local uplifts also provided modest amounts of sediments to the northern SCS basin. The large turbidity current of which the pathway is constrained by relative magnetic anomalies scoured and eroded the SCS mid-ocean ridge oceanic crust. As a typical submarine gravity flow, this turbidity current traveled east for hundreds of kilometers prior to incorporation into the accretionary prism of the Manila Trench. During these processes, the broken eroded SCS oceanic clasts were transported in high-energy flow conditions, which resulted in their good roundness observed in the turbidites.
3. As determined by magnetic anomaly distribution patterns and IODP geological samples, the accretionary prism was initially generated during SCS subduction along the Manila Trench at approximately 17° N. From the late Miocene to Pleistocene, the accretionary prism gradually migrated ~ 500 km northwestward from its origin. Middle Pleistocene (<0.5 Ma) development of reef-lagoonal complexes marks the onset of its exposure on the Hengchun Peninsula. Average velocities of ~ 61 – 65 mm/yr are suggested for the northwestward motion of the PSP.

CRedit authorship contribution statement

Xianbo Meng: Conceptualization. **Lei Shao:** Supervision, Visualization. **Yuchi Cui:** Conceptualization, Validation, Formal analysis, Writing - review & editing. **Weilin Zhu:** Project administration. **Peijun Qiao:** Methodology, Data curation. **Zhen Sun:** Resources. **Yuanli Hou:** Investigation.

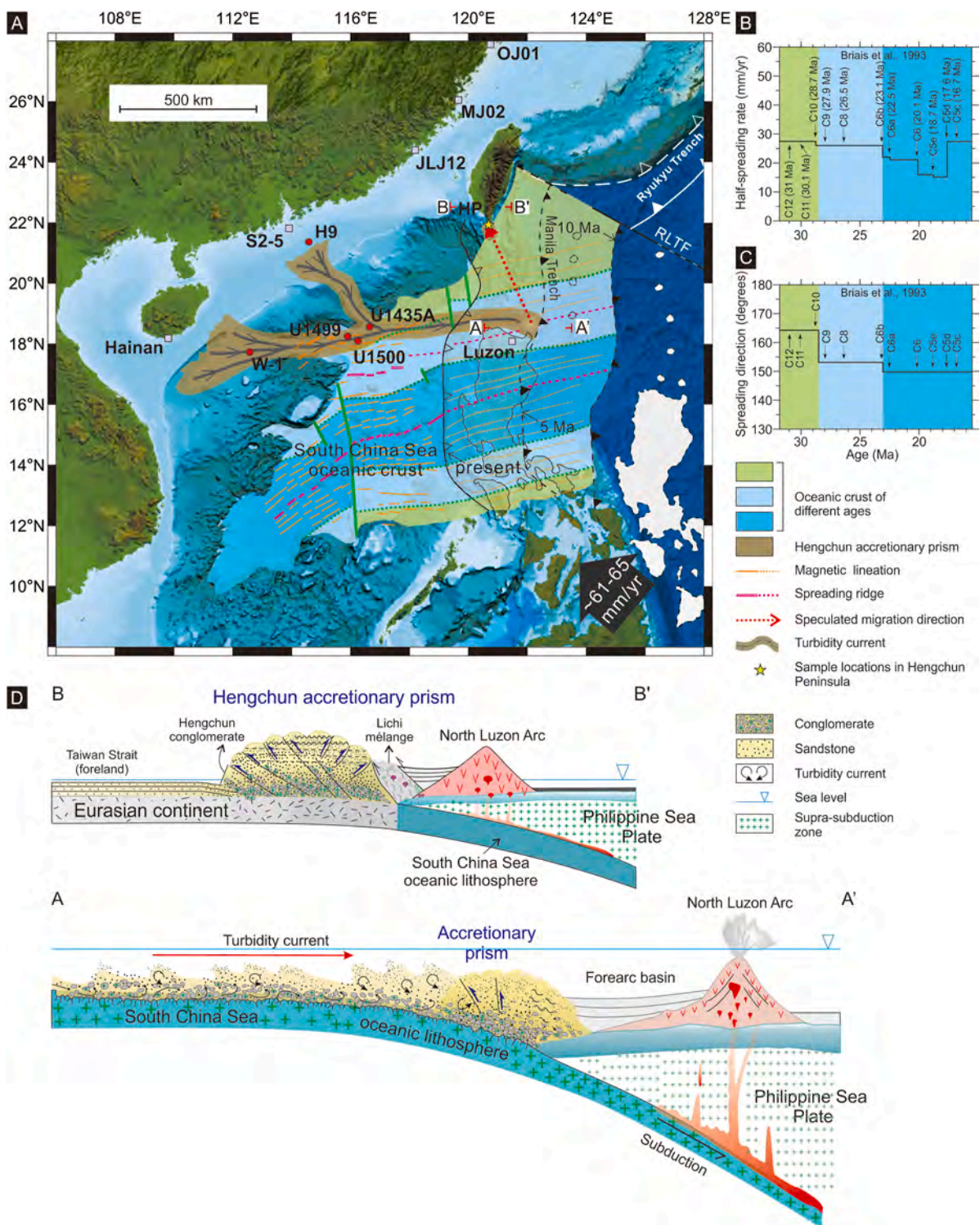


Fig. 10. (A) Schematic reconstruction map of the turbidity current across the northern SCS and the final deposition on the Hengchun Peninsula. Presumed paleogeographic locations of the Manila Trench and Luzon Arc are given in the figure (modified after Sibuet et al. (2016) and Wu et al. (2016)). Black dashed lines indicate the present Luzon Arc. Black solid lines indicate the Luzon Arc at approximately 10 and 5 Ma. Dark blue, light blue and green areas separated by green dashed lines mark oceanic domains formed during different kinematic phases, represented by changes in spreading rates, spreading directions or both parameters (Briais et al., 1993). Orange dashed lines show the magnetic anomalies during the SCS oceanic crust extension. Rose red dashed lines show the SCS mid-ocean spreading ridges. Red dots indicate the studied or published boreholes representing different source areas. The black bold arrow shows the estimated average speed of the PSP movement relative to the Eurasian Plate. Red dashed lines indicate migration pathway of the accretionary prism (B) Half-spreading rates are calculated from chrons C12 to C8c using magnetic models from Briais et al. (1993). (C) Spreading directions are calculated based on the assumption that they are perpendicular to the trends of magnetic lineations. (D) Two transects subduction zones in the geographic map (A) are illustrated by geological profiles AA' and BB'. (For interpretation of the references to colour in this figure legend, the reader is referred to the Web version of this article.)

Declaration of competing interest

The authors declare that they have no known competing financial interests or personal relationships that could have appeared to influence the work reported in this paper.

Acknowledgments

We thank the China National Offshore Oil Corporation (CNOOC) and the International Ocean Discovery Program (IODP) for providing geological data and borehole samples from the northern South China Sea. We thank Prof. Zheng-Xiang Li in Curtin University, Australia, for the insightful discussion on the tectonic background and tectonic implications, and for his help on language polishing. Ms. Hailin Ren kindly introduced us to the Hengchun geology during a field trip. Constructive and careful reviews by two anonymous referees and efficient handling by Editor Yingchang Cao are gratefully appreciated. This work was supported by the National Natural Science Foundation of China (grant numbers 42076066, 41576059 and 91528302), the National Science and Technology Major Project of China (grant number 2016ZX05026004-002) and the National Key Research and Development Program of China (grant number 2018YFE0202400). Supplementary data to this article can be found online at the general repository of Mendeley Data.

References

- Abbott, L.D., Silver, E.A., Galewsky, J., 1994. Structural evolution of a modern arc-continent collision in Papua New Guinea. *Tectonics* 13, 1007–1034.
- Andersen, T., 2002. Correction of common lead in U–Pb analyses that do not report 204 Pb. *Chem. Geol.* 192 (1), 59–79.
- Barckhausen, U., Engels, M., Franke, D., Ladage, S., Pubellier, M., 2014. Evolution of the South China Sea: revised ages for breakup and seafloor spreading. *Mar. Petrol. Geol.* 58, 599–611.
- Blott, S.J., Pye, K., 2008. Particle shape: a review and new methods of characterization and classification. *Sedimentology* 55 (1), 31–63.
- Briais, A., Patriat, P., Tapponnier, P., 1993. Updated interpretation of magnetic anomalies and seafloor spreading stages in the South China Sea: implications for the Tertiary tectonics of Southeast Asia. *J. Geophys. Res.* 98, 6299–6328.
- Brown, D., Spadea, P., 1999. Processes of forearc and accretionary complex formation during arc-continent collision in the southern Ural Mountains. *Geology* 27, 649–652.
- Callow, R.H.T., Kneller, B., Dykstra, M., McLroy, D., 2014. Physical, biological, geochemical and sedimentological controls on the ichnology of submarine canyon and slope channel systems. *Mar. Petrol. Geol.* 54, 144–166.
- Cao, L., Jiang, T., Wang, Z., Zhang, Y., Sun, H., 2015. Provenance of upper Miocene sediments in the Yinggehai and Qiongdongnan basins, northwestern South China sea: evidence from REE, heavy minerals and zircon U–Pb ages. *Mar. Geol.* 361, 136–146.
- Cao, L., Shao, L., Qiao, P., Zhao, Z., van Hinsbergen, D.J.J., 2018. Early Miocene birth of modern Pearl River recorded low-relief, high-elevation surface formation of SE Tibetan Plateau. *Earth Planet Sci. Lett.* 496, 120–131.
- Carter, A., Roques, D., Bristow, C.S., Kinny, P., 2001. Understanding mesozoic accretion in southeast Asia: significance of triassic thermotectonism (Indosinian orogeny) in Vietnam. *Geology* 29, 211–214.
- Chang, C.-P., Angelier, J., Lee, T.-Q., Huang, C.-Y., 2003. From continental margin extension to collision orogen: structural development and tectonic rotation of the Hengchun peninsula, southern Taiwan. *Tectonophysics* 361, 61–82.
- Chang, L.S., 1964. A biostratigraphic study of the Tertiary in the Hengchun peninsula, Taiwan, based on smaller Foraminifera (I. Northern Part). *Proc. Geol. Soc. China* 7, 48–62.
- Cheng, Y.M., Huang, C.Y., Yen, J.J., 1984. The Loshui formation: deeper-water sandstones on the Hengchun peninsula, southern Taiwan. *Acta Geol. Taiwan.* 22, 100–117.
- Chen, C.H., Jahn, B.M., Lee, T.P., Chen, C.H., Jean, C., 1990. Sm–Nd isotopic geochemistry of sediments from Taiwan and implications for the tectonic evolution of southeast China. *Chem. Geol.* 88, 317–332.
- Chen, C.-H., Lee, C.-Y., Lin, J.-W., Chu, M.-F., 2019. Provenance of sediments in western Foothills and Hsuehshan Range (Taiwan): a new view based on the EMP monazite versus LA-ICPMS zircon geochronology of detrital grains. *Earth Sci. Rev.* 190, 224–246.
- Chen, H.Y., Yang, H.J., Liu, Y.H., Huang, K.F., Takazawa, E., 2018a. Tectonic affinities of the accreted basalts in southern Taiwan. *J. Asian Earth Sci.* 158, 253–265.
- Chen, X.Y., Huang, C.-Y., Shao, L., 2018b. Characteristics of heavy minerals in modern sediments of Minjiang and Jiulongjiang Rivers, Fujian Province and their provenance implication. *J. Palaeogeogr.* 20, 637–650 (In Chinese with English Abstract).
- Clift, P.D., Vannucchi, P., 2004. Controls on tectonic accretion versus erosion in subduction zones: implications for the origin and recycling of the continental crust. *Rev. Geophys.* 42, RG2001. <https://doi.org/10.1029/2003RG000127>.
- Compston, W., Williams, I.S., Kirkschvink, J.L., Zhang, Z., Guogan, M.A., 1992. Zircon U–Pb ages for the early cambrian time-scale. *J. Geol. Soc.* 149, 171–184.
- Cui, Y., Shao, L., Qiao, P., Pei, J., Zhang, D., Tran, H., 2019. Upper miocene-pliocene provenance evolution of the central canyon in northwestern South China sea. *Mar. Geophys. Res.* 40, 223–235.
- Findlay, R.H., Trinh, P.T., 1997. The structural setting of the song Ma region, Vietnam and the indochina-south China plate boundary problem. *Gondwana Res.* 1, 11–33.
- Fyhn, M.B.W., Thomsen, T.B., Keulen, N., Knudsen, C., Rizzi, M., et al., 2019. Detrital zircon ages and heavy mineral composition along the Gulf of Tonkin – implication for sand provenance in the Yinggehai-Song Hong and Qiongdongnan basins. *Mar. Petrol. Geol.* 101, 162–179.
- Hall, R., 1997. Cenozoic plate tectonic reconstructions of SE Asia. In: Fraser, A.J., Matthews, S.J., Murphy, R.W. (Eds.), *Petroleum Geology of Southeast Asia*, vol. 126. *Geol. Soc. London Spec. Publ.*, pp. 11–23.
- Halpin, J.A., Tran, H.T., Lai, C.-K., Meffre, S., Crawford, A.J., Zaw, K., 2016. U–Pb zircon geochronology and geochemistry from NE Vietnam: a “tectonically disputed” territory between the Indochina and South China blocks. *Gondwana Res.* 34, 254–273.
- Hansen, L.A.S., Callow, R.H.T., Kane, I.A., Camberi, F., Rovere, M., Cronin, B.T., Kneller, B., 2015. Genesis and character of thin-bedded turbidites associated with submarine channels. *Mar. Petrol. Geol.* 67, 852–879.
- Hoskin, P.W.O., Schaltegger, U., 2003. The composition of zircon and igneous and metamorphic petrogenesis. *Rev. miner. Geochem.* 53, 27–62.
- Huang, C.-Y., Wu, W.-Y., Chang, C.-P., Tsao, S., Yuan, P.B., Lin, C.W., Xia, K.-Y., 1997. Tectonic evolution of accretionary prism in the arc-continent collision terrane of Taiwan. *Tectonophysics* 281 (1–2), 31–51.
- Huang, C.-Y., Yuan, P.B., Tsao, S.-J., 2006. Temporal and spatial records of active arc-continent collision in Taiwan: a synthesis. *Geol. Soc. Am. Bull.* 118, 274–288.
- Jonell, T.N., Clift, P.D., Hoang, L.V., Hoang, T., Carter, A., Wittmann, H., Böning, P., Pahnke, K., Rittenour, T., 2016. Controls on erosion patterns and sediment transport in a monsoonal tectonically quiescent drainage, Song Gianh, Central Vietnam. *Basin Res.* S9 (S1).
- Kane, I.A., Kneller, B.C., Dykstra, M., Kassem, A., McCaffrey, W.D., 2007. Anatomy of a submarine channel-levee: an example from upper cretaceous slope sediments, rosario formation, Baja California, Mexico. *Mar. Petrol. Geol.* 24, 540–563.
- Kirstein, L.A., Carter, A., Chen, Y.-G., 2010. Testing inferences from paleocurrents: application of zircon double-dating to Miocene sediments from the Hengchun Peninsula, Taiwan. *Terra. Nova* 22, 483–493.
- Larsen, H.C., Mohn, G., Nirrengarten, M., Sun, Z., Stock, J., Jian, Z., Klaus, A., Alvarez-Zarikian, C.A., Boaga, J., Bowden, S.A., Briais, A., Chen, Y., Cukur, D., Dadd, K., Ding, W., Dorais, M., Ferré, E.C., Ferreira, F., Furusawa, A., Gewecke, A., Hinojosa, J., Höflig, T.W., Hsiung, K.H., Huang, B., Huang, E., Huang, X.L., Jiang, S., Jin, H., Johnson, B.G., Kurzwski, R.M., Lei, C., Li, B., Li, L., Li, Y., Lin, J., Liu, C., Liu, Z., Luna, A.J., Lupi, C., McCarthy, A., Ningthoujam, L., Osono, N., Peate, D.W., Persaud, P., Qiu, N., Robinson, C., Satolli, S., Sauermilch, I., Schindlbeck, J.C., Skinner, S., Straub, S., Su, X., Su, C., Tian, L., van der Zwan, F.M., Wan, S., Wu, H., Xiang, R., Yadav, R., Yi, L., Yu, P.S., Zhang, C., Zhang, J., Zhang, Y., Zhao, N., Zhong, G., Zhong, L., 2018. Rapid transition from continental breakup to igneous oceanic crust in the South China Sea. *Nat. Geosci.* 11, 782–789.
- Lepvrier, C., Maluski, H., Vu, V.T., Leyreloup, A., Phan, T.T., Nguyen, V.V., 2004. The early triassic indosinian orogeny in Vietnam (truong son belt and Kontum Massif): implications for the geodynamic evolution of Indochina. *Tectonophysics* 393, 87–118.
- Lee, Y.-H., Chen, C.-C., Liu, T.-K., Ho, H.-C., Lu, H.-Y., Lo, W., 2006. Mountain building mechanisms in the Southern Central Range of the Taiwan Orogenic Belt—From accretionary wedge deformation to arc-continent collision. *Earth Planet Sci. Lett.* 252, 413–422.
- Lei, C., Ren, J., Pang, X., Chao, P., Han, X., 2018. Continental rifting and sediment infill in the distal part of the northern South China Sea in the Western Pacific region: challenge on the present-day models for the passive margins. *Mar. Petrol. Geol.* 93, 166–181.
- Lei, C., Alves, T.M., Ren, J., Tong, C., 2020. Rift structure and sediment infill of hyperextended continental crust: insights from 3D seismic and well data (Xisha trough, South China sea). *J. Geophys. Res. Solid Earth* 125 (5), e2019JB018610. <https://doi.org/10.1029/2019JB018610>.
- Lester, R., McIntosh, K., Van Avendonk, H.J.A., Lavier, L., Liu, C.-S., Wang, T.K., 2013. Crustal accretion in the Manila trench accretionary wedge at the transition from subduction to mountain-building in Taiwan. *Earth Planet Sci. Lett.* 375, 430–440.
- Li, C., Ma, M., Lv, C., Zhang, G., Chen, G., Yan, Y., Bi, G., 2017. Sedimentary differences between different segments of the continental slope-parallel Central Canyon in the Qiongdongnan Basin on the northern margin of the South China Sea. *Mar. Petrol. Geol.* 101, 162–179.
- Li, C.F., Xu, X., Lin, J., Sun, Z., Zhu, J., Yao, Y., Zhao, X.X., Liu, Q.S., Kulhanek, D.K., Wang, J., Song, T.R., Zhao, J.F., Qiu, N., Guan, Y.X., Zhou, Z.Y., Williams, T., Bao, R., Briais, A., Brown, E.A., Chen, Y.F., Clift, P.D., Colwell, F.S., Dadd, K.A., Ding, W.W., Almeida, I.H., Huang, X.-L., Hyun, S., Jiang, T., Koppers, A.A.P., Li, Q.Y., Liu, C.L., Liu, Z.F., Nagai, R.H., Pelelo-Alampay, A., Su, X., Tejada, M.L.G., Trinh, H.S., Yeh, Y.-C., Zhang, C.-L., Zhang, F., Zhang, G.-L., 2015. Ages and magnetic structures of the South China Sea constrained by deep tow magnetic surveys and IODP Expedition 349. *G-cubed* 15, 4958–4983.
- Li, S., Zhang, G., Zhou, L., Zhao, G., Liu, X., Suo, Y., Liu, B., Jin, C., Dai, L., 2011. The opposite Meso-Cenozoic intracontinental deformations under the super-convergence: rifting and extension in the North China Craton and shortening and thrusting in the South Chin Craton. *Earth Sci. Front.* 18 (3), 79–107 (in Chinese with English Abstract).

- Lin, A.T., Yao, B.C., Hsu, S.K., Liu, C.S., Huang, C.Y., 2009. Tectonic features of the incipient arc-continent collision zone of Taiwan: implications for seismicity. *Tectonophysics* 479, 28–42.
- Liu, C., Clift, P.D., Giosan, L., Miao, Y., Warny, S., Wan, S., 2019. Paleoclimatic evolution of the SW and NE South China Sea and its relationship with spectral reflectance data over various age scales. *Palaeogeogr. Palaeoclimatol. Palaeoecol.* 525, 25–43.
- Liu, Y.S., Gao, S., Hu, Z.C., Gao, C.G., Zong, K.Q., Wang, D.B., 2009. Continental and oceanic crust recycling-induced melt-peridotite interactions in the trans-north China orogen: U-Pb dating, Hf isotopes and trace elements in zircons from mantle xenoliths. *J. Petrol.* 51, 537–571.
- Ma, M., Li, C., Lv, C., Chen, G., Yang, F., Yan, Y., Yin, N., Zhang, G., 2017. Geochemistry and provenance of a multiple-stage fan in the upper Miocene to the pliocene in the yinggehai and qiongdongnan basins, offshore South China sea. *Mar. Petrol. Geol.* 79, 64–80.
- Metcalfe, I., 2011. Tectonic framework and phanerozoic evolution of Sundaland. *Gondwana Res.* 19, 3–21.
- Moore, G.F., Taira, A., Klaus, A., Becker, L., Boecker, B., Cragg, B.A., Dean, A., Fergusson, C.L., Henry, P., Hirano, S., Hisamitsu, T., Hunze, S., Kastner, M., Maltman, A.J., Morgan, J.K., Murakami, Y., Saffer, D.M., Sánchez-Gómez, M., Screaton, E.J., Smith, D.C., Spivack, A.J., Steurer, J., Tobin, H.J., Ujiie, K., Underwood, M.B., Wilson, M., 2001. New insights into deformation and fluid flow processes in the Nankai trough accretionary prism: results of ocean drilling program leg 190 geochem. *Geophys. Geosyst.* 2, 10.129/2001GC000166.
- Page, B.M., Lan, C.Y., 1983. The Kenting Mélange and its record of tectonic events. *Mem. Geol. Soc. China* 5, 227–248.
- Pang, X., Chen, C.M., Wu, M.S., He, M., Wu, X.J., 2006. The Pearl River deep-water fan systems and significant geological events. *Adv. Earth Sci.* 21, 793–799.
- Pelletier, B., Stephan, J.F., 1986. Middle Miocene deduction and late Miocene beginning of collision registered in the Hengchun Peninsula: geodynamic implications for the evolution of Taiwan. *Tectonophysics* 125, 133–160.
- Richter, C., Ali, J.R., 2015. Philippine Sea plate motion history: eocene-recent record from ODP site 1201, central West Philippine basin. *Earth Planet Sci. Lett.* 410, 165–173.
- Seno, T., Stein, S., Gripp, A.E., 1993. A model for the motion of the Philippine Sea Plate consistent with NUVEL-1 and geologic data. *J. Geophys. Res.* 98, 17941–17948.
- Shan, Y., Nie, G., Yan, Y., Huang, C.-Y., 2013. The transition from the passive to active continental margin: a case study of brittle fractures in the Miocene Loshui Sandstone on the Hengchun Peninsula, southern Taiwan. *Tectonics* 32, 65–79.
- Shao, L., Meng, A., Li, Q., Qiao, P., Cui, Y., Cao, L., Chen, S., 2017. Detrital zircon ages and elemental characteristics of the Eocene sequence in IODP Hole U1435A: implications for rifting and environmental changes before the opening of the South China Sea. *Mar. Geol.* 394, 39–51.
- Shao, L., Cui, Y., Statterger, K., Zhu, W., Qiao, P., Zhao, Z., 2019. Drainage control of Eocene to Miocene sedimentary records in the southeastern margin of Eurasian Plate. *Geol. Soc. Am. Bull.* 131, 461–478.
- Sibuet, J.-C., Hsu, S.-K., 2004. How was Taiwan created? *Tectonophysics* 379, 159–181.
- Sibuet, J.-C., Yeh, Y.-C., Lee, C.-S., 2016. Geodynamics of the south China sea. *Tectonophysics* 692, 98–119.
- Sláma, J., Košler, J., Condon, D.J., Crowley, J.L., Gerdes, A., Hanchar, J.M., Horstwood, M.S.A., Morris, G.A., Nasdala, L., Norberg, N., Schaltegger, U., Schoene, B., Tubrett, M., Whitehouse, M.J., 2008. Plešovice zircon—a new natural reference material for U-Pb and Hf isotopic microanalysis. *Chem. Geol.* 249 (1–2), 1–35.
- Stock, J.M., Sun, Z., Klaus, A., Larsen, H.C., Jian, Z., Alvarez Zarikian, C.A., Boaga, J., Bowden, S.A., Briais, A., Chen, Y., Cukur, D., Dadd, K.A., Ding, W., Dorais, M.J., Ferré, E.C., Ferreira, F., Furusawa, A., Gewecke, A.J., Hinojosa, J.L., Höfig, T.W., Hsiung, K.-H., Huang, B., Huang, E., Huang, X.-L., Jiang, S., Jin, H., Johnson, B.G., Kurzawski, R.M., Lei, C., Li, B., Li, L., Li, Y., Lin, J., Liu, C., Liu, Z., Luna, A., Lupi, C., McCarthy, A.J., Mohn, G., Ningthoujam, L.S., Nirrengarten, M., Osono, N., Peate, D.W., Persaud, P., Qui, N., Robinson, C.M., Satolli, S., Sauerlich, I., Schindlbeck, J.C., Skinner, S.M., Straub, S.M., Su, X., Tian, L., van der Zwan, F.M., Wan, S., Wu, H., Xiang, R., Yadav, R., Yi, L., Zhang, C., Zhang, J., Zhang, Y., Zhao, N., Zhong, G., Zhong, L., 2018. Site U1500. and the Expedition 367/368 Scientists, 2018. South China Sea Rifted Margin. In: Sun, Z., Jian, Z., Stock, J.M., Larsen, H.C., Klaus, A., Alvarez Zarikian, C.A. (Eds.), *Proceedings of the International Ocean Discovery Program*, 367/368. International Ocean Discovery Program, College Station, TX. <https://doi.org/10.14379/iodp.proc.367368.104.2018>.
- Sun, H., Wang, Z., Jiang, T., 2015. Provenance of upper Miocene sediments in the yinggehai and qiongdongnan basins, northwestern South China sea: evidence from REE, heavy minerals and zircon U-Pb ages. *Mar. Geol.* <https://doi.org/10.1016/j.margeo.2015.01.007>.
- Sun, S., McDonough, W., 1989. Chemical and isotopic systematics of ocean basalts: implications for mantle composition and processes. *Spec. Publ. Geol. Soc. Lond.* 42, 313–346.
- Suppe, J., 1984. Kinematics of arc-continent collision, flipping of subduction and back-arc spreading near Taiwan. *Mem. Geol. Soc. China* 6, 21–34.
- Teng, L.S., 1996. Extensional collapse of the northern Taiwan mountain belt. *Geology* 24, 949–952.
- Tian, Z.-X., Yan, Y., Huang, C.-Y., Zhang, X.-C., Liu, H.-Q., Yu, M.-M., Yao, D., Dilek, Y., 2019. Geochemistry and geochronology of the accreted mafic rocks from the Hengchun Peninsula, southern Taiwan: origin and tectonic implications. *J. Geophys. Res.: Solid Earth* 124, 2469–2491.
- Tsai, C.-H., Shyu, J.B.H., Chung, S.-L., Ramos, N.T., Lee, H.-Y., 2019. Detrital zircon record from major rivers of Luzon Island: implications for Cenozoic continental growth in SE Asia. *J. Geol. Soc.* 176 (4), 727–735.
- Vermeesch, P., 2013. Multi-sample comparison of detrital age distributions. *Chem. Geol.* 341, 140–146.
- Vermeesch, P., Resentini, A., Garzanti, E., 2016. An R package for statistical provenance analysis. *Sediment. Geol.* 336, 14–25.
- Wadell, H., 1932. Volume, shape, and roundness of rock particles. *J. Geol.* 40 (5), 443–451.
- Wang, C., Liang, X., Zhou, Y., Fu, J., Jiang, Y., Dong, C., Xie, Y., Tong, C., Pei, J., Liu, P., 2015. Construction of age frequencies of provenances on the eastern side of the Yinggehai Basin: studies of LA-ICP-MS U-Pb ages of detrital zircons from six modern rivers, western Hainan, China. *Earth Sci. Front.* 22 (4), 277–289 (in Chinese with English abstract).
- Wang, C., Liang, X., Foster, D.A., Tong, C., Liu, P., Liang, X., Zhang, L., 2019. Linking source and sink: detrital zircon provenance record of drainage systems in Vietnam and the yinggehai-song hong basin, South China sea. *Geol. Soc. Am. Bull.* 131 (1/2), 191–204.
- Wang, Y., Qian, X., Cawood, P.A., Liu, H., Feng, Q., Zhao, G., Zhang, Y., He, H., Zhang, P., 2018. Closure of the east paleotethyan ocean and amalgamation of the Eastern Cimmerian and southeast Asia continental fragments. *Earth Sci. Rev.* 186, 195–230.
- Wang, Y.M., Xu, Q., Li, D., Han, J.H., Lv, M., Wang, Y.F., Li, W.G., Wang, H.R., 2011. Late Miocene red river submarine fan, northwestern South China sea. *Chin. Sci. Bull.* 56 (11). DOI: CNKI:SUN:JXTW.0.2011-14-012.
- Wu, J., Suppe, J., Lu, R., Kanda, R., 2016. Philippine Sea and East Asian plate tectonics since 52 Ma constrained by new subducted slab reconstruction methods. *J. Geophys. Res.: Solid Earth* 121. <https://doi.org/10.1002/2016JB012923>.
- Xu, Y.H., Chen, J., 2010. Uranium-lead dating of detrital zircons from the Minjiang and Jiulong Estuaries in the western coast of the Taiwan Strait: implication for its provenance. *Acta Oceanol. Sin.* 32, 110–117 (in Chinese with English abstract).
- Xu, Y., Sun, Q., Cai, G., Yin, X., Chen, J., 2014. The U-Pb ages and Hf isotopes of detrital zircons from Hainan Island, South China: implications for sediment provenance and the crustal evolution. *Environ. Earth Sci* 71 (4), 1619–1628.
- Yan, Y., Carter, A., Palk, C., Bricchau, S., Hu, X., 2011. Understanding sedimentation in the song hong-yinggehai basin, South China sea. G-cubed 12, Q06014.
- Yu, S.B., Chen, H.Y., Kuo, L.C., 1997. Velocity field of GPS stations in the Taiwan area. *Tectonophysics* 247, 41–59.
- Zhang, G.L., Luo, Q., Zhao, J., Jackson, M.G., Guo, L.S., Zhong, L.F., 2018. Geochemical nature of sub-ridge mantle and opening dynamics of the South China Sea. *Earth Planet Sci. Lett.* 489, 145–155.
- Zhang, X., Yan, Y., Huang, C.-Y., Chen, D., Shan, Y., Lan, Q., Chen, W., Yu, M., 2014. Provenance analysis of the Miocene accretionary prism of the Hengchun Peninsula, southern Taiwan, and regional geological significance. *J. Asian Earth Sci.* 85, 26–39.
- Zhang, X., Cawood, P.A., Huang, C.-Y., Wang, Y., Yan, Y., Santosh, M., Chen, W., Yu, M., 2016. From convergent plate margin to arc-continent collision: formation of the Kenting Mélange, Southern Taiwan. *Gondwana Res.* 38, 171–182.
- Zhang, X., Huang, C., Wang, Y., Clift, P.D., Yan, Y., Fu, X., Chen, D., 2017. Evolving yangtze river reconstructed by detrital zircon U-Pb dating and petrographic analysis of Miocene marginal sea sedimentary rocks of the western Foothills and Hengchun peninsula, taiwan. *Tectonics* 36, 634–651.
- Zhao, Z., Sun, Z., Sun, L., Wang, Z., Sun, Z., 2016. Cenozoic tectonic subsidence in the Qiongdongnan Basin, northern South China sea. *Basin Res.* 1–20.
- Zhong, L., Li, G., Yan, W., Xia, B., Feng, Y., Miao, L., Zhao, J., 2017. Using zircon U-Pb ages to constrain the provenance and transport of heavy minerals within the northwestern shelf of the South China Sea. *J. Asian Earth Sci.* 134, 176–190.

Reinterpretation of the northern South China Sea pre-Cenozoic basement and geodynamic implications of the South China continent: constraints from combined geological and geophysical records

Weilin Zhu¹, Yuchi Cui^{1,2*}, Lei Shao^{1*}, Peijun Qiao¹, Peng Yu¹, Jianxiang Pei³, Xinyu Liu³, Hao Zhang¹

¹ State Key Laboratory of Marine Geology, Tongji University, Shanghai 200092, China

² The Institute for Geoscience Research (TIGeR), School of Earth and Planetary Sciences, Curtin University, Perth 6845, Australia

³ Hainan Energy Co., Ltd., CNOOC, Haikou 570145, China

Received 20 November 2019; accepted 3 June 2020

© Chinese Society for Oceanography and Springer-Verlag GmbH Germany, part of Springer Nature 2021

Abstract

The pre-Cenozoic northern South China Sea (SCS) Basin basement was supposed to exist as a complex of heterogeneous segments, divided by dozens of N–S faulting. Unfortunately, only the Hainan Island and the northeastern SCS region were modestly dated while the extensive basement remains roughly postulated by limited geophysical data. This study presents a systematic analysis including U–Pb geochronology, elemental geochemistry and petrographic identification on granite and meta-clastic borehole samples from several key areas. Constrained from gravity-magnetic joint inversion, this interpretation will be of great significance revealing the tectono-magmatic evolution along the southeastern margin of the Eurasian Plate. Beneath the thick Cenozoic sediments, the northern SCS is composed of a uniform Mesozoic basement while the Precambrian rocks are only constricted along the Red River Fault Zone. Further eastern part of the northern SCS below the Cenozoic succession was widely intruded by granites with Jurassic-to-early Cretaceous ages. Further western part, on the other hand, is represented by meta-sedimentary rocks with relatively sporadic granite complexes. To be noted, the western areas derived higher-degree and wider metamorphic zones, which is in contrast with the lower-degree and narrower metamorphic belt developed in the eastern region. Drastic collisions between the Indochina Block and South China continent took place since at least late Triassic, resulting in large-scale suturing and deformation zones. At the westernmost part of the northern SCS, the intracontinental amalgamation with closure of the Meso-Tethys has caused fairly stronger and broader metamorphism. One metamorphic biotite granite is located on the suturing belt and yields a Precambrian U–Pb age. It likely represents the relict from the ancient Gondwana supercontinent or its fringes. Arc-continental collision between the Paleo-Pacific and the southeast China Block, on the other hand, results in a relatively narrow NE–SW trending metamorphic belt during the late Mesozoic. Within the overall geological setting, the Cenozoic SCS oceanic basin was subsequently generated from a series of rifting and faulting processes along the collisional-accretionary continental margin.

Key words: South China Sea, pre-Cenozoic basement, U–Pb geochronology, Paleo-Pacific subduction, intracontinental collision, metamorphic belt

Citation: Zhu Weilin, Cui Yuchi, Shao Lei, Qiao Peijun, Yu Peng, Pei Jianxiang, Liu Xinyu, Zhang Hao. 2021. Reinterpretation of the northern South China Sea pre-Cenozoic basement and geodynamic implications of the South China continent: constraints from combined geological and geophysical records. *Acta Oceanologica Sinica*, 40(2): 13–28, doi: 10.1007/s13131-021-1757-7

1 Introduction

The South China Sea (SCS) is the largest marginal sea within the western Pacific. Extensive investigations have been conducted on the SCS, including scientific and industrial drilling, dredging, and multiple-channel seismic profiles. These surveys have significantly refined the understandings on the origin and subsequent opening of the SCS (Briaies et al., 1993; Hsu et al., 2004; Franke et al., 2011; Barckhausen et al., 2014). In particular, recent International Ocean Drilling Program expeditions revealed that the northern SCS margin was neither completely “magma-rich” nor “magma-poor” identified in the other North

Atlantic magmatism models (Larsen et al., 2018). Instead, the northern SCS is a representative of hyperextended margin, which is now considered as a missing link between “magma-rich” and “magma-poor” margins (Lei and Ren, 2016; Lei et al., 2019a). In order to precisely evaluate the Cenozoic tectonic evolution of the SCS, researchers are also urged to be underpinned from the pre-Cenozoic framework and the geological processes which have greatly controlled the following Cenozoic evolutionary events. Beneath the Cenozoic sedimentary layer, the SCS Basin basement study is of crucial significance in structural geology and regional geodynamic reconstruction (Nissen et al., 1995a, 1995b;

Foundation item: The National Natural Science Foundation of China under contract Nos 42076066, 92055203 and 41874076; the National Science and Technology Major Project under contract Nos 2016ZX05026004-002 and 2017ZX05026005-005; the Fund of China Association for Science and Technology under contract No. 2018CASRQNJL18.

*Corresponding author, E-mail: cuiyuchi@tongji.edu.cn; lshao@tongji.edu.cn

Braitenberg et al., 2006). However, ages and properties of the pre-Cenozoic basement still require accurate geological evidence to improve interpretation and integrated reviews of previous studies (Fig. 1a).

Antecedent attempted to illustrate the formation and composition of the SCS Basin basement were based on sketchy petrographic description as well as insufficient geochronological data. Particularly, the wide underlying components of Yinggehai Basin and Qiongdongnan Basin still were proved to be fairly problematic and poorly explored (Pigott and Ru, 1994; Braitenberg et al., 2006; Franke et al., 2011; Pichot et al., 2014). Their onshore continental margins were identified with Proterozoic schists and gneiss, Paleozoic and Mesozoic metaclastic rocks, carbonates and volcanic rocks (Sun et al., 2014). For the seaward extension, this offshore part is even harder to trace due to scarce borehole penetration and lacking of precise dating analyses. It was extrapolated that the Yinggehai and Qiongdongnan Basin basements might have generated similar lithological and tectonic features to the northern Indochina Block margin (Nielsen et al., 1999). This assumption is in the light of basement consolidation during the collision and convergence between major continental blocks and scattered micro-terranes (Carter et al., 2001; Lepvrier et al., 2004; Li et al., 2006). According to previous studies, the onshore pre-Cenozoic meta-sedimentary strata and magmatic arc were likely to extend from land to sea. In some areas of Qiongdongnan Basin, the well-stratified formations are Mesozoic low-grade metamorphic sedimentary rocks (Nielsen et al., 1999). In the other sections, Precambrian metamorphic complexes were only restricted within continental shelf basement proximal to Vietnam (Hutchison, 1989; Dien, 1998). However, the low-resolution seismic profiles caused these considerations to remain uncertain. Upper Paleozoic carbonate platform deposits were also sporadically developed from the coastal region, such as the Beibu Gulf Basin and areas through the continental interior (Fyhn et al., 2018) (Fig. 1a). Tectonically, this heterogeneous Paleozoic-Mesozoic basement surrounding the Hainan Island seems to be mainly controlled from a NW–SE fault system (Sun et al., 2014). These early discoveries have led to a series of questions on the overall assessment of the pre-Cenozoic SCS Basin basement regarding its physical properties and distribution patterns. Under

which type of geodynamic background was the basement generalized? How did the basement control or influence the subsequent rifting of the Cenozoic SCS basins?

Along the South China Block southeastern margin, the broad distribution of granitic and granodioritic magmatic records show that an Andean-type active continental margin has already existed from late Triassic or early Jurassic, to Cretaceous (Zhou and Li, 2000; Li and Li, 2007; Yui et al., 2012; Faure et al., 2016; Xu et al., 2017). A drastic transformation from active to passive margin followed during the late Mesozoic (Li et al., 2012). The northern SCS Basin basement was considered as the southward extension of the South China Block, where thinned continental crust displays variable thicknesses (Hayes and Nissen, 2005; Lei and Ren, 2016; Lei et al., 2019a). According to Sun et al. (2014), lower-to-upper Paleozoic strata are supposed to be unevenly preserved in the Beibu Gulf Basin, western Zhujiang River Mouth Basin and Taixinan Basin (Fig. 1a). In early studies, sedimentary facies and seismic lines indicated that the pre-Cenozoic basement was divided into several separate sections and displayed an eastward trending of younger ages (Wang et al., 2002; Sun et al., 2014). The case lacking geochronological evidence has been changed until recent detrital zircon U-Pb dating results were obtained. Therein, two granite dredge samples were dated with magmatic ages varying from 159 Ma to 127 Ma in Nansha area (Yan et al., 2010) (Fig. 1b). Additionally, Xisha area, to the southeast of Hainan Island, was previously postulated to be part of the Precambrian crystalline basement dated by Rb-Sr isochrones (Qin, 1987). Instead, the updated U-Pb age has confirmed its late Jurassic amphibole plagiogneisses which was later intruded by Cretaceous magmatic bodies (Zhu et al., 2017). Therefore, it is questionable whether the Paleozoic or even Precambrian strata have ever been widely distributed beneath the Cenozoic northern SCS sediments? In addition, located in the conjunction of Yinggehai Basin, Qiongdongnan Basin and Zhujiang River Mouth Basin, the Hainan Island together with other dispersed micro-blocks were rifted from Gondwana supercontinent during the opening of the Palaeo-Tethys in the Devonian (Metcalfe, 1996, 2011, 2013; Xu et al., 2008). Numerous researches show that the Hainan Island has recorded multiple thermal events and tectonic regime transitions since the late Paleozoic (Li et al., 2006; Jiang et al., 2015; Yao et

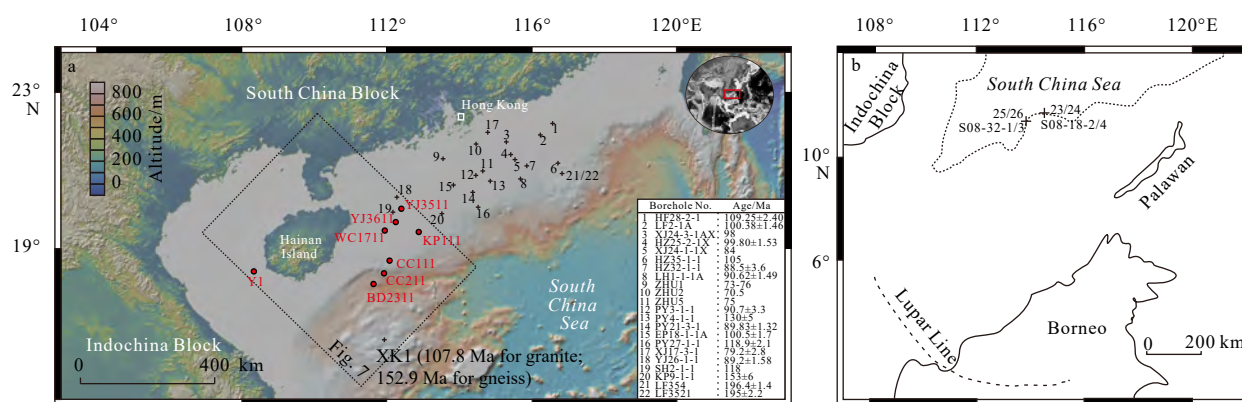


Fig. 1. Map of Beibu Gulf Basin, Yinggehai Basin, Qiongdongnan Basin and Zhujiang River Mouth Basin in the South China Sea with studied borehole samples and published data (a). Plot zoomed out in the upper right corner shows the study area under the global background. Red filled circles represent the analyzed boreholes of detrital zircon U-Pb dating or elemental geochemistry in this study. Black numbered crosses mainly centralized in the northeastern Zhujiang River Mouth Basin show some important samples analyzed by U-Pb, K-Ar or Rb-Sr dating in other studies. XK1 is from Zhu et al. (2017). Ages of these previous researches are shown in the lower right corner (Qiu et al., 1996; Li et al., 1999; Xu et al., 2017). For detailed sample information, refer to Tables 1 and 2. Sketch map of the Nansha area (b), its surrounding terranes and two dredge sampling locations (black cross) (Yan et al., 2010).

al., 2017). As a key component of the SCS region, the Hainan Island as well as its surrounding areas still require further basement evaluation.

Principle of isostatic balance and gravity-field modeling are helpful in estimating the lateral density or thickness variations of the interior structure of the lithosphere (Braitenberg et al., 2006; Ebbing et al., 2006; Franke et al., 2011). These are essential methods and techniques in revealing lithospheric velocity anomalies. Another technique involves magnetic anomaly interpretations, which could reflect directions and speeds of the ridge spreading processes (Briaies et al., 1993; Hsu et al., 2004; Braitenberg et al., 2006; Li et al., 2008a, 2008b; Barckhausen et al., 2014). However, amplitudes of the basement features may be reduced in special cases where anomalies bend or two distinct directionalities meet. Moreover, due to the thick Cenozoic sedimentary blanket, the underlying flat-appearance structure might conceal different tectonic lineaments, tilted crustal highs, complicate-oriented ridges or faults. Therefore, ocean bottom topography not well charted could be very misleading in the crustal structure evaluation. Except for the weaknesses of the typical geophysical techniques, the subsequent rifting processes might also produce certain alteration onto the original pre-Cenozoic crustal structure (Nissen et al., 1995a, 1995b). In this case, the amount of crustal extension might be manifested in complicated manners in response to effective strengths, thicknesses, thermal structures and other rheological features according to disparate formation ages (Ebinger and Hayward, 1996; Clift and Lin, 2001; Qiu et al., 2001). For instance, the eastern SCS Basin basement generated widespread granite and sedimentary rocks during the late Mesozoic, where much extension is concentrated within younger, weaker and more ductile zones. Within the basement near eastern Hainan Island, on the other hand, the Paleozoic crust tends to be stretched in a similar degree to the more ancient Proterozoic crust (Hayes and Nissen, 2005). Hence, without constraints from any other supportive dating analyses, these geophysical parameters are likely to allow possible uncertainties.

Due to the limitation of the basinal geological evidence and ongoing controversy over the formation of the pre-Cenozoic basement, this study aims to present a comprehensive interpretation by deriving a dense set of data, including petrographic identification, elemental geochemistry analysis, gravity-magnetic joint inversion and zircon U-Pb dating. Specifically, zircons are considered as a kind of widely formed and extremely stable minerals, which are resistant to chemical alteration by long-distance sedimentation and low- or medium-degree metamorphism. Since U-Pb isotopic system possesses the highest closure temperature, it is optimal to use U-Pb dating for the age determination of igneous or high-grade metamorphic rocks. Lithological combination characteristics and gravity-magnetic constraints are also instrumental in examining whether the results are internally consistent in this study. Questions remaining to be answered include: (1) what is the precise aging framework for the pre-Cenozoic SCS Basin basement? (2) what types of rock assemblages have been generalized with respect to different sections of the SCS Basin basement? (3) what tectonic events and geodynamic processes might have caused such distribution patterns of the answers to questions 1 and 2?

2 Geological history

The southeastern Asia was principally under control from two of the most critical geodynamic domains: the Paleo-Pacific subduction zone to the east and the Tethys subduction zone to the west (Carter et al., 2001; Li and Powell, 2001; Hall, 2002, 2012;

Lepvrier et al., 2004; Zhou et al., 2008; Wallace et al., 2009; Li et al., 2011). A general consensus is reached that a well-developed Andean-type of volcanic arc existed along the southeastern Asian margin (e.g. South China southeastern margin) lasting from Triassic-Jurassic to Cretaceous (Maruyama, 1997; Zhou and Li, 2000; Li and Li, 2007; Li et al., 2012). The Paleo-Pacific subduction beneath the eastern Asian margin led to extremely drastic and complex tectonic activities across the South China Block. Multi-stage structural deformation, magmatism as well as local stress field changes took place in this region (Jahn et al., 1990; Zhou et al., 2006; Li et al., 2014). Further west, the Indochina Block collided obliquely with the South China along the Song-Ma Suture and Red River Fault Zone (Leloup et al., 2001; Lepvrier et al., 2004; Metcalfe, 2011, 2013). Therein, narrowing and closure of the Meso-Tethys was likely responsible for the late Triassic regional folding, uplifting and orogeny over the Indochina Continent (Metcalfe, 1996; Roger et al., 2000; Lepvrier et al., 2008; Sone and Metcalfe, 2008). Subsequently, the convergent Andean-type continental margin was transferred into the divergent western Pacific margin prior to the opening of the SCS (Zhou et al., 2006; Schellart et al., 2006; Li et al., 2012, 2014; Shi and Li, 2012). This sudden “transpression-transension” switching process might be largely triggered by oceanward retreat of the Paleo-Pacific subduction zone in the late Mesozoic (Jahn et al., 1990; Lapierre et al., 1997; Li et al., 2014). The plate driving forces experienced fundamental changes during this time. Large-scale rifting started around the coastal South China, which resulted in the thinning of continental margin (Lei et al., 2019a). During the Eocene–early Miocene, southward slab pull of the oceanic crust led to elimination of the Proto-SCS (Hall, 2002, 2012; Morley, 2002; Hayes and Nissen, 2005). The present SCS was eventually generated, displaying a sequential pattern of continental margin–transitional crust–oceanic crust. During the long-term extensional and thermal-subsidence stages, thick sedimentary strata were formed over the SCS Basin basement during Cenozoic, and were influenced from different source-to-sink systems (Shao et al., 2015, 2017, 2019; Cao et al., 2018; Lei et al., 2018, 2019b). These sedimentary basins mainly include the Beibu Gulf, Yinggehai, Qiongdongnan and the Zhujiang River Mouth Basin (Briaies et al., 1993; Rangin et al., 1995; Yao, 1996; Morley, 2002, 2016) (Fig. 1a).

Previous studies show that a number of East Asian and Southeast Asian continental terranes, e.g. the North China Block and the South China Block, the Indochina Block, have the origin of the northern Gondwana supercontinental margin (Veevers, 2004; Metcalfe, 2011; Cocks and Torsvik, 2013; Metcalfe, 2013). Separation, drifting and amalgamation of the Gondwana-related continental blocks as well as the accompanying oceans might have largely shaped the southeastern Eurasian margin before Cenozoic (Metcalfe, 1996). As a key region of the southeast Asia, the SCS Basin basement has been the focus of numerous plate geodynamic reconstructions (Zhou et al., 2008; Metcalfe, 2011; Morley, 2012; Zhu et al., 2017). However, there are still hot debates on its tectonic affiliation. Some researchers propose that the pre-Cenozoic lithospheric layer was partly derived from the South China terrain, i.e., discrete micro-fragments of the Beibu Gulf Basin together with the Hainan Island. These micro-terranes were inferred to commonly develop on a Proterozoic folded continental massif (Liu et al., 2006, 2011; Li et al., 2008c; Sun et al., 2014). Other scholars suggest that the SCS Basin basement is likely to be a missing linkage (or an individual tectonic domain) between the Cathaysia Block and Indochina Block, which was dated by scattered Precambrian ages (Lan et al., 2003; Wan et al., 2006; Lu et al., 2011; Yu et al., 2012). To be noted, the early Paleozoic

metamorphism and magmatism have been confirmed within the Cathaysia Block and Indochina Block by massive geochronological and thermochronological studies (Lepvrier et al., 2008; Charvet et al., 2010; Wang et al., 2011; Vưong et al., 2013; Faure et al., 2014). Therefore, it also suggested that the SCS Basin basement dominated by Paleozoic strata, i.e., Yinggehai Basin, the east of Hainan Island, etc. was mainly sourced from the Paleozoic outer extension of the Cathaysia Block or Indochina Block. Previous studies mainly concentrated on the Zhujiang River Mouth Basin of the northeastern SCS were also reanalyzed (Qiu et al., 1996; Li et al., 1999; Xu et al., 2017). As complementary information, the data synthesis will largely enable us to obtain a more comprehensive interpretation across the whole basement (refer to Fig. 1 and Table 1 for geographical locations and more details of the published data).

3 Analytical procedures

In order to verify the complicated nature of the basement structure and its regional tectonic significance, this study collected one biotite granite and eight metamorphic clastic rock samples for geochemistry and geochronology analysis together with petrography identification (refer to Table 2 for detailed sample information on detrital zircon U-Pb geochronology study). These samples were straight drilled through the pre-Cenozoic basement by the China National Offshore Oil Corporation.

3.1 Elemental geochemistry analysis

Geochemical analyses for the SCS Basin basement metamorphic clastic rock samples were carried out at the State Key

Laboratory of Marine Geology of Tongji University, China. After being washed by deionized distilled water, bulk sediments were then dried at 50°C for 48 h to prevent external contamination. Meta-sedimentary rocks were heated to 600°C for 2 h to remove the organic matter and interlayer water. Dissolved in a 1:1 HF-HNO₃ mixture, samples were finally measured for their major and trace elemental concentration. The instrumentation was constituted by an inductively coupled plasma optical emission spectrometry (ICP-OES, Thermo Fisher Scientific, USA) and Thermo Elemental X-Series inductively coupled plasma mass spectrometry (ICP-MS, Thermo Fisher Scientific, USA), respectively. Three certified materials (GSR-5, GSR-6, and GSD-9 from the Institute of Geophysical and Geochemical Exploration, China) were repeatedly used as unknown samples for the precision and accuracy assessment. The external precision (1 σ) was generally better than 5% for trace elements (Fig. 2). And results were usually in agreement with the reference materials (modified from Li et al. (2003) and Wei et al. (2006)).

3.2 Detrital zircon U-Pb dating

In this study, zircon grains were separated from meta-sedimentary rocks using standard density and magnetic separation techniques at the laboratory of the Institute of Regional Geology and Mineral Resources, Hebei, China. Over 200 chosen zircons were randomly pasted on adhesive tape and then cast in an epoxy mount prior to the polishing process. Zircons were examined with cathodoluminescence images (CL) to determine their internal structures and microzonation positions (20–30 μm) (refer to Fig. 3 for CL images of representative samples). Meas-

Table 1. Summary of published data of SCS pre-Cenozoic basement (refer to Fig. 1 for detailed sample locations)

Number in Fig. 1a	Sample No.	Depth/m	Isotopic ages/Ma	Analytical method	Lithology	References
1	HF28-2-1	3 942.0–3 943.6	109.25±2.40	K-Ar	cataclastic granodiorite	Li et al. (1999)
2	LF2-1A	2 480.0–2 483.5	100.38±1.46	K-Ar	cataclastic dimicaceous granite	Li et al. (1999)
2	LF2-1A	2 480.0–2 483.5	94.83±1.89	Rb-Sr	cataclastic dimicaceous granite	Li et al. (1999)
3	XJ24-3-1AX	4 318–4 319	98	K-Ar	cataclastic granite	Li et al. (1999)
4	HZ25-2-1X	3 196.4	99.80±1.53	K-Ar	cataclastic granite	Qiu et al. (1996)
5	XJ24-1-1X	3 851.0–3 851.5	84	K-Ar	granite	Li et al. (1999)
6	HZ35-1-1	2 218.9	105	K-Ar	cataclastic quartz diorite	Li et al. (1999)
7	HZ32-1-1	2 791	88.5±3.6	K-Ar	cataclastic granite	Li et al. (1999)
8	LH1-1-1A	1 836.5	90.62±1.49	K-Ar	cataclastic granodiorite	Li et al. (1999)
8	LH1-1-1A	1 822.0–1 837.5	72.78±1.37	Rb-Sr	cataclastic granodiorite	Li et al. (1999)
9	ZHU1	1 846–1 847	73–76	K-Ar	granite	Li et al. (1999)
10	ZHU2	2 379–2 380	70.5	K-Ar	biotite granite	Li et al. (1999)
11	ZHU5	3 261.8–3 262.3	75	K-Ar	granite porphyry	Li et al. (1999)
12	PY3-1-1	3 192	90.7±3.3	K-Ar	granite	Li et al. (1999)
13	PY4-1-1	3 160	130±5	K-Ar	granite	Qiu et al. (1996)
14	PY21-3-1	4 068.0–4 019.5	89.83±1.32	K-Ar	cataclastic biotite granite	Li et al. (1999)
15	EP18-1-1A	3 448.25	100.5±1.7	K-Ar	granite	Qiu et al. (1996)
16	PY27-1-1	3 607–3 609	118.9±2.1	K-Ar	quartz monzonite	Li et al. (1999)
17	XJ17-3-1	2 122–2 124	79.2±2.8	K-Ar	cataclastic granite	Li et al. (1999)
18	YJ26-1-1	1 700–1 702	89.20±1.58	K-Ar	rhyolite porphyry	Li et al. (1999)
19	SH2-1-1	3 641.2	118	K-Ar	biotite hornblende diorite	Li et al. (1999)
20	KP9-1-1	1 662–1 774	153±6	K-Ar	cataclastic granite	Li et al. (1999)
21	LF354	2 472.3	196.4±1.4	U-Pb	granite	Xu et al. (2017)
22	LF3521	2 443.5	195.0±2.2	U-Pb	diorite	Xu et al. (2017)
23	S08-18-2	2 700	159.1±1.6	U-Pb	tonalite	Yan et al. (2010)
24	S08-18-4	2 700	157.8±1.0	U-Pb	tonalite	Yan et al. (2010)
25	S08-32-1	3 100	153.6±0.3	U-Pb	monzogranite	Yan et al. (2010)
26	S08-32-3	3 100	127.2±0.2	U-Pb	monzogranite	Yan et al. (2010)

Table 2. List of samples analyzed for Laser-ICP-MS detrital zircon U-Pb dating (refer to Fig. 1a for detailed sample locations)

Borehole No.	Geographical location	Sampling depth/m	Depth of basement/m	Previous geological times	Youngest age/Ma	Oldest depositional ages	Lithology
Y1	Yinggehai Basin	3 021–3 023	3 021	?	1 264±83	Precambrian	metamorphic biotite granite
WC1711	Qiongdongnan Basin	2 216	2 216	Paleozoic	114±4	early Cretaceous	meta-tuff
CC211	Qiongdongnan Basin	1 116	1 076	Paleozoic	129±7	early Cretaceous	meta-tuff
KP111	Zhujiang River Mouth Basin	1 893–1 897	1 884	Paleozoic	124±3	early Cretaceous	volcaniclastic rock
BD2311	Qiongdongnan Basin	2 166	2 166	Paleozoic	85±3	late Cretaceous	metamorphic quartzose sandstone
CC111	Qiongdongnan Basin	1 172	1 117	Paleozoic	125±4	late Cretaceous	metamorphic sandstone
YJ3511	Zhujiang River Mouth Basin	4 321–4 339	4 321	Paleozoic	88±2	late Cretaceous	metamorphic siltstone
YJ3611	Zhujiang River Mouth Basin	3 565–3 580	3 484	Paleozoic	88±2	late Cretaceous	metamorphic mudstone and siltstone

Note: ? represents not have been dated before.

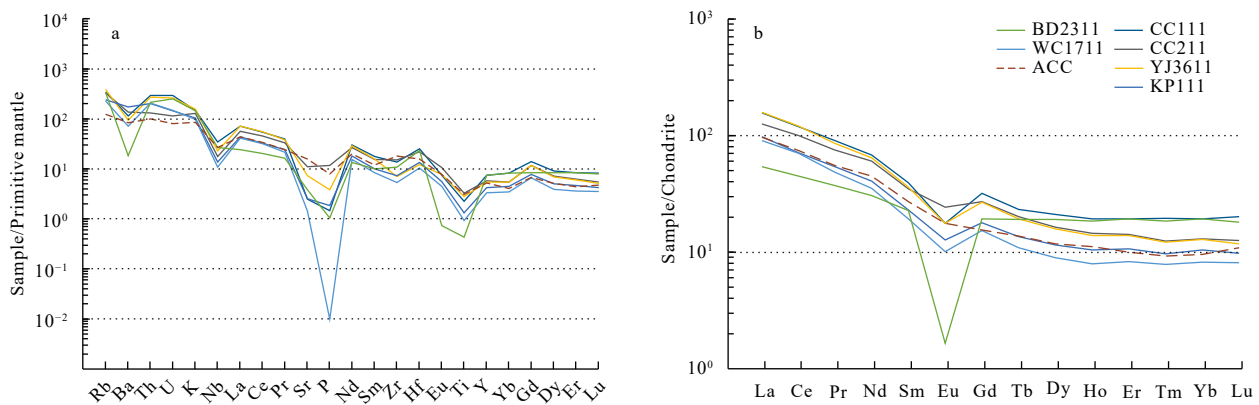


Fig. 2. Primitive mantle-normalized trace element spider diagrams (a) and chondrite-normalized rare earth elements (REE) distribution patterns (b) for the SCS Basin basement samples. Trace elements of the primitive mantle and chondrite REE are from Sun and McDonough (1989) and Taylor and McLennan (1985), respectively. Average continental crust (ACC) are from Rudnick and Gao (2003).

measurements of U, Th and Pb were later conducted at the State Key Laboratory of Marine Geology of Tongji University, China. The instrumentation is composed of a Thermo Elemental X-Series ICP-MS coupled to a New Wave 213 nm laser ablation system (Shao et al., 2016). Typically, 5-scan cycles were conducted for each analysis with a spot diameter of 30 μm . The 91 500 external standards ((1 065.4±0.3) Ma) were interspersed with tested samples to calculate isotopic ratios by ICPMSDataCal (Wiedenbeck et al., 1995; Liu et al., 2010). The glass NIST 610 was used to optimize the machine as an internal standard. Accuracy of our analytical results was validated by reference material Plešovice with an age of (337.1±0.4) Ma (Sláma et al., 2008). Measured compositions have been corrected for common Pb using the method of Andersen (2002). The $^{206}\text{Pb}/^{238}\text{U}$ and $^{207}\text{Pb}/^{206}\text{Pb}$ ages were finally adopted for younger or older zircons of 1 000 Ma, respectively. Wherein, uncertainties on individual U-Pb analyses are quoted at the 1 σ level. Age distributions in this study and other published documents are visualized as histograms and kernel density estimation plots (Vermeesch, 2012).

3.3 Gravity-magnetic-seismic joint inversion

Both gravimetric and magnetic measurements have been conducted in the study area. Free-air gravity anomalies were originally extracted from satellite-derived data of 2-min grid (Sandwell and Smith, 1997). Since there is an obvious density

contrast around the Cenozoic-Mesozoic regional unconformity, free-air gravity anomalies are sensitive to undulations caused by rifting and faulting structures in the pre-Cenozoic basement. The total field magnetic anomalies also contain rich geological implications. However, they could possibly be biased at middle-to-low latitudes because of the oblique inclinations of induced magnetizations. To facilitate the precision of our data interpretation, this study processed the magnetic anomalies calculation (source from compilation by Geological Survey of Japan and Coordinating Committee for Coastal and Offshore Geoscience Programmes in East and Southeast Asia (CCOP), 1996) by reducing to the pole (RTP magnetic anomalies), which are sharper to the existence of magmatic bodies. Here this study has also compiled seismic profiles and reconstructed the major stratigraphic framework to generalize a set of models between travel time and depth. In addition, this study obtained the relationship between travel time and rock density by conducting an integrated investigation on different types of rocks over the northern SCS Basin basement. This gravity-magnetic-seismic joint inversion shows less uncertainties and artificialities, which is largely discriminative from both traditional stripping method and interactive interpretation model. By recognizing the existence of geological anomaly bodies, this study is able to better describe the pre-Cenozoic SCS Basin basement.

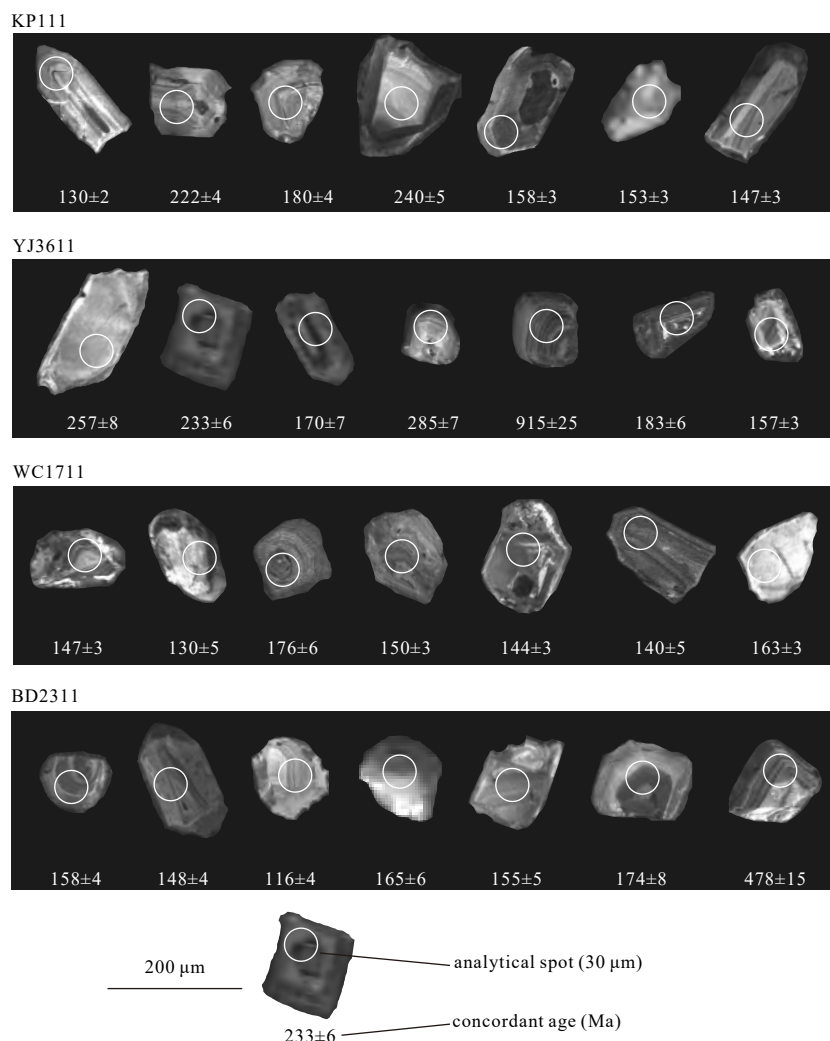


Fig. 3. Representative cathodoluminescence images showing the internal structures of the zircon grains and associated U-Pb ages.

4 Results

4.1 Geochemical variations

Primitive mantle-normalized trace element and chondrite-normalized rare earth element (REE) spider diagrams for the basement samples are exhibited in Fig. 2. Overall, the trace element distribution patterns are reported to be modestly different from the average continental crust (Rudnick and Gao, 2003). In the primitive mantle-normalized trace element diagram (Fig. 2a), our samples show obvious negative anomalies in element Ba, Nb, P and Ti while weak enrichment in element Rb, Th, U and K (regarded as heat-producing or radioactive elements). Chondrite-normalized REE patterns, on the hand, commonly display steep slopes with distinct negative Eu anomalies. Enrichment of light REE (LREE) ($(La/Yb)_N = 0.65-59.46$) can be seen with an assemblage of pronounced Eu depletions ($Eu/Eu^* = 0.03-0.98$, with a few exceptional analyses of 1.08, 1.44 and 1.92) (Fig. 2b). One single analysis of $(La/Yb)_N$ is lower than 1 (0.65) for borehole BD2311. Slightly distinct from the other boreholes, BD2311 is characterized by a relatively flat pattern with an extremely negative Eu anomaly averaging at 0.09.

4.2 U-Pb geochronology

As observed in CL images of representative samples (Fig. 3),

the clear oscillatory zones obviously indicate their magmatic origin for the analyzed zircon grains (Hoskin and Schaltegger, 2003). In addition, most Th/U ratios from the SCS Basin basement samples range between 0.1 and 1 (Fig. 4). U-Pb Concordia diagrams are shown in Fig. 5. Figure 6 shows the histograms and probability density distribution patterns, which are grouped respectively according to their peak combinations. Results of the detrital zircon U-Pb dating are outlined as follows according to lithological descriptions and their individual spectra features.

To the east of Hainan Island, the meta-tuff sample WC1711 is featured by rounded, sub-rounded to euhedral zircon grains with oscillatory zonings (Fig. 1a). WC1711 has a modestly wide variation of Th ($110.26 \times 10^{-6}-3 501.78 \times 10^{-6}$) and U ($152.23 \times 10^{-6}-3 729.32 \times 10^{-6}$) content, producing Th/U ratios larger than 0.1 (Fig. 4). Of all the sixty-five effective analyses, the youngest U-Pb age is (114 ± 4) Ma. Apart from one inherited $^{207}Pb/^{206}Pb$ age of $(2 503 \pm 42)$ Ma, WC1711 gives a major population of $^{206}Pb/^{238}U$ ratios between (114 ± 4) Ma and (252 ± 6) Ma, forming an upper Jurassic cluster centralized at ca. 150 Ma (Fig. 6a). Another meta-tuff sample CC211 is located further south to sample WC1711. Th and U contents are $86.29 \times 10^{-6}-1 756.57 \times 10^{-6}$ and $150.73 \times 10^{-6}-3 482.09 \times 10^{-6}$, respectively. Th/U ratios range between 0.34 and 1.14. Of all the sixty-four analyses, the youngest U-Pb age is (129 ± 7) Ma. Aside from one single Paleozoic analysis (342 ± 10) Ma, the re-

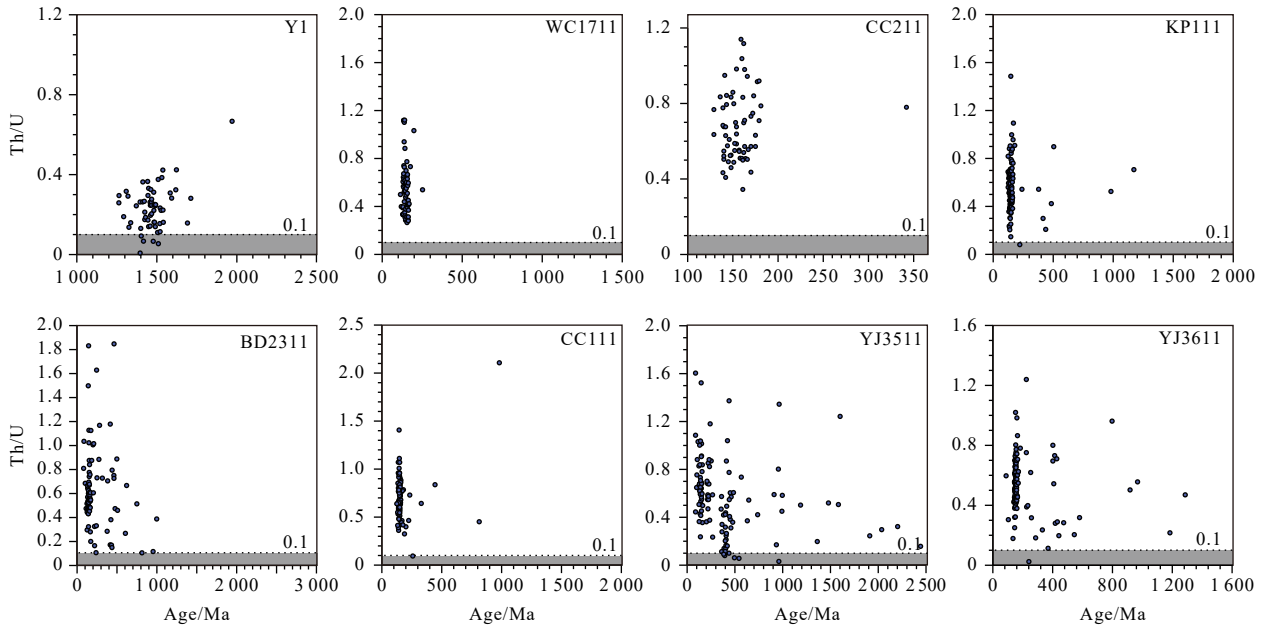


Fig. 4. Summary of the Th/U ratios versus U-Pb ages of the studied zircon grains from the SCS Basin basement. Grey shades indicate the Th/U variations are lower than 0.1.

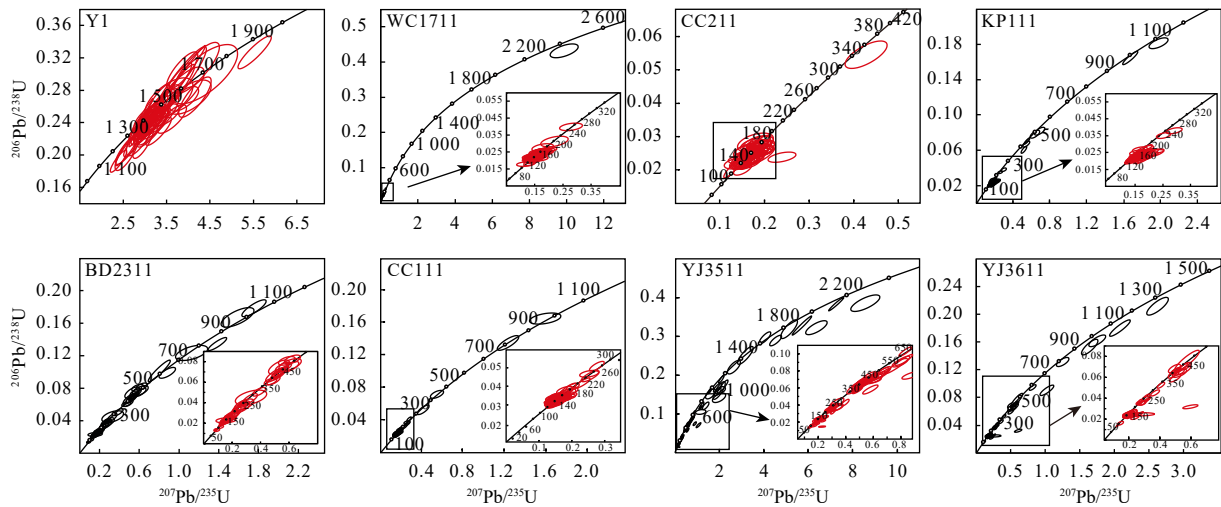


Fig. 5. Detrital zircon U-Pb Concordia diagrams for the SCS Basin basement samples. The lower right corner plots in some diagrams show magnified Concordia ages for samples WC1711, CC211, KP111, BD2311, CC111, YJ3511 and YJ3611. The numbers on the curve represent concordia U-Pb ages of a standard zircon grain.

maining are centralized at ca. 150 Ma.

Metamorphic sandstone CC111 is mostly characterized by sub-euhedral and euhedral zircon grains (Fig. 1a). Of all the ninety analyzed spots, Th (111.24×10^{-6} – $1\ 897.93 \times 10^{-6}$) and U (202.82×10^{-6} – $4\ 722.91 \times 10^{-6}$) concentrations are modestly high and variable. Almost all the analyses have Th/U ratios exceeding 0.1. About 94% of total spots are Mesozoic ages, based on $^{206}\text{Pb}/^{238}\text{U}$ ratios from (125±4) Ma to (233±5) Ma (Fig. 6a). The other five analyses include three Paleozoic ages (258±6) Ma, (329±14) Ma, (444±12) Ma, and two Proterozoic ages ((813±21) Ma, (981±15) Ma).

Volcaniclastic rock KP111 is dominated by euhedral to sub-euhedral grains with clear internal core-rim structures (Fig. 1a). Of the 117 analyzed spots, Th and U concentration is characterized by a broad variation from 32.24×10^{-6} to $2\ 730.38 \times 10^{-6}$, and

from 95.13×10^{-6} to $4\ 055.87 \times 10^{-6}$, respectively. KP111 has only one single Th/U analysis of 0.08 (Fig. 4). Two Proterozoic spots with ages of (982±17) Ma and (1 173±31) Ma probably indicate inherited cores. There are 108 concordant ages mostly fall within the group of Mesozoic 240–124 Ma (centralized around 145 Ma). Scattered spots are of Paleozoic 505–379 Ma ages. The youngest age of sample KP111 is (124±3) Ma (Fig. 6a).

Sample YJ3511 is extracted from a metamorphic siltstone. A total of 126 analyses were conducted on this sample. Th and U contents highly varied between 136.84×10^{-6} and $7\ 900.79 \times 10^{-6}$, between 110.07×10^{-6} and $10\ 989.99 \times 10^{-6}$, respectively. Six analyses display Th/U ratios falling between 0.03 and 0.10 (Fig. 4). The other analyses range between 0.11 and 1.60. YJ3511 shows an apparent peak at ca. 135 Ma and a subordinate peak at ca. 405 Ma (Fig. 6b). In detail, thirty-eight Paleozoic ages range between

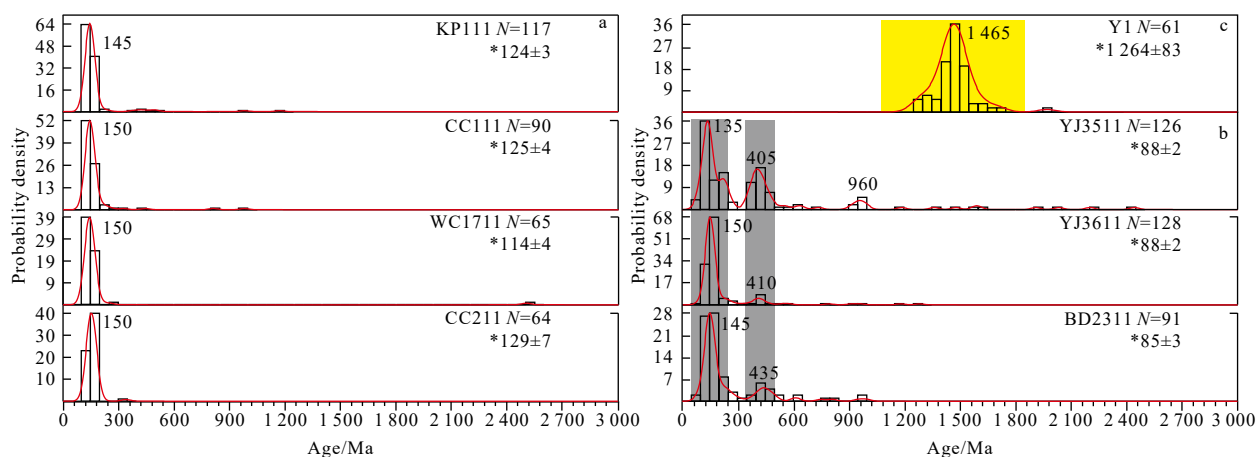


Fig. 6. Histograms and probability density distribution plots for detrital zircon U-Pb ages of the SCS Basin basement samples with characteristic age peaks numbered. Age spectra are grouped according to their specific distribution patterns into (a)–(c) sub-plots. *N* represents the number of concordant analyses for each sample. The youngest zircon U-Pb age in red is marked with * in the upper right corner. Dominant age peaks of sample Y1 are highlighted in light yellow shades; major peaks of YJ3511, YJ3611 and BD2311 are in gray shades.

(252±5) Ma and (495±10) Ma, while twenty-one Proterozoic ages range between (543±27) Ma and (2 443±36) Ma. The metamorphic mudstone-siltstone sample YJ3611 is located close to YJ3511 (Fig. 1a). Of all the adopted ninety-one analyses, significantly high values are identified within Th (122.90×10^{-6} – $8 349.25 \times 10^{-6}$) and U (373.64×10^{-6} – $33 224.03 \times 10^{-6}$) concentrations. In addition to one analysis at 0.02, the other spots have Th/U ratios falling between 0.11 and 1.24 (Fig. 4). About 90% of the total concordant $^{206}\text{Pb}/^{238}\text{U}$ values yield a large Mesozoic cluster at ca. 150 Ma. The rest, on the other hand, range between (252±5) Ma and (1 283±47) Ma (twenty-one analyses in total). Comparatively, the Caledonian peak at ca. 410 Ma is not as obvious as YJ3511. Both samples YJ3511 and YJ3611 have the youngest age of (88±2) Ma (Fig. 6b).

Sample BD2311 is from a metamorphic quartzose sandstone rock, located to the southeast of Hainan Island (Fig. 1a). It has modestly variable Th (37.62×10^{-6} – $6 348.54 \times 10^{-6}$) and U (72.99×10^{-6} – $4 127.31 \times 10^{-6}$) concentrations. All Th/U ratios fall between 0.10 and 1.85 (Fig. 4). More than 80% of the total calculations are centralized as a dominant Mesozoic age at ca. 145 Ma. Similar to sample YJ3611, the Caledonian cluster at ca. 435 Ma is not apparent on the U-Pb spectra of BD2311. The remaining twenty-six analyses in BD2311 include eighteen Paleozoic (509–252 Ma) and six Proterozoic zircons (998–607 Ma). Of all the 91 effective analyses, the youngest age of sample BD2311 is (85±3) Ma (Fig. 6b).

Sample Y1 is a metamorphic biotite granite to the west of Hainan Island (Fig. 1a). Its rounded to sub-rounded zircon crystals retain magmatic growth zonation, which commonly have light-color melting rims, range from 50 μm to 100 μm in length, and are featured by length to width ratios of ca. 1:1 to 2:1. Th concentration is modestly lower (25.09×10^{-6} – 371.50×10^{-6}) while U concentration is higher and more variable (191.30×10^{-6} – $3 362.47 \times 10^{-6}$), producing Th/U ratios with relatively lower values ranging between 0.01 and 0.40 (only a single Th/U analysis of 0.67).

Five analyses display Th/U ratios falling between 0.01 and 0.10. Much distinctive from other samples of younger depositional ages, Y1 shows an apparent Proterozoic cluster of concordant $^{207}\text{Pb}/^{206}\text{Pb}$ ratios from (1 264±83) Ma to (1 714±52) Ma in addition to an age of (1 972±23) Ma. These data commonly form a predominant Meso-Proterozoic population clustering at ca. 1 465 Ma (Fig. 6c).

4.3 Lithological and petrographical identification

Mineral composition, content, structure and texture were identified and classified for each sample under both crossed and polarized light microscope. Figure 7 shows the representative rock samples of KP111, YJ3511, YJ3611 and Y1. The volcanoclastic rock sample KP111 is comprised of metamorphic pyroclastic and quartzite (Figs 7a and b). Obvious porphyritic structures were generated in sample KP111, of which phenocrysts are mainly quartz grains. The corrosion structures and micro-surface cracking of the minerals imply the drastic temperature changes during eruptions. The matrix minerals are mainly comprised of microcrystalline feldspar and quartz which were formed during vitric recrystallization. KP111 also displays obvious high sericite contents and slight-to-moderate directional alignments. Similarly, the mosaic structures and directional arrangements are also identified within the quartzite composition. Sample YJ3511 is comprised of low-degree slates and metamorphic siltstones (Figs 7c and d). The slates are mainly composed of cryptocrystalline or microcrystalline clay minerals. The metamorphic siltstones, on the other hand, are mostly microcrystalline quartz and feldspar minerals with some directionally arranged schistose minerals, e.g. metamorphosed sericite. Sample YJ3611 mainly consists of low-degree metamorphic mudstones and siltstones (Figs 7e and f). The metamorphic mudstones contain cryptocrystalline clay minerals, in addition to low contents of quartz and microcrystalline feldspar. The metamorphic siltstones, on the other hand, contain microcrystalline quartz and feldspar, which commonly display mosaic textures and directional alignments. The westernmost sample Y1 is featured by an obvious granitic texture, including orthoclase, quartz and low contents of plagioclase and biotite (Figs 7g and h). Kaolinization, carbonatization and sodium zoisitization are identified within feldspar, while chloritization is observed within biotite.

5 Discussion

5.1 Petrogenesis based on elemental geochemistry and petrography studies

Samples KP111, YJ3511 and YJ3611 are typically low-degree metamorphic rocks. They commonly display high content of metamorphosed sericite, mosaic structures and slight-to-moder-

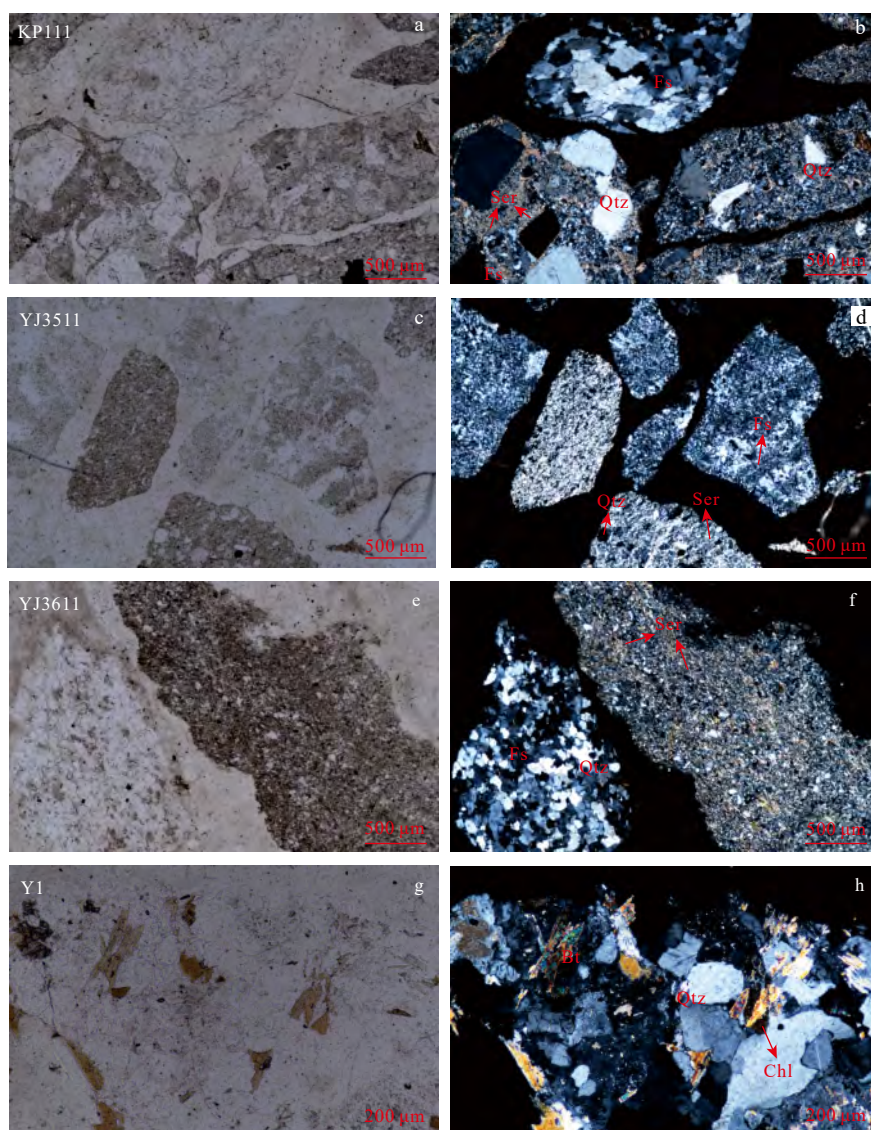


Fig. 7. Lithological and petrographic characteristics of SCS Basin basement samples under both plane-polarized light and cross-polarized light microscope. a. KP111, metamorphic volcanoclastic rock; c. YJ3511, metamorphic siltstone; e. YJ3611, metamorphic mudstone and siltstone; g. Y1, metamorphic biotite granite slices under plane-polarized light; b. KP111, d. YJ3511, f. YJ3611 and h. Y1 slices under cross-polarized light. Fs: feldspar, Qtz: quartz, Ser: sericite, Bt: biotite, Chl: chlorite. Refer to Fig. 1 for detailed sample location.

ate directional alignments (Figs 7a–f). KP111 is also marked by clear melting-corrosion textures and fission cracks on its quartz phenocrysts. The other meta-sedimentary samples, YJ3511 and YJ3611, are observed with palimpsest structures (or relict structures) within their meta-mudstone or siltstone components, which indicate incomplete recrystallization processes and preservation of the original mineral textures. To the west of Hainan Island, sample Y1 is uniquely featured by muscovite alteration and might have experienced metamorphism by displaying more evident directional arrangements of chlorite, muscovite and quartz minerals (Figs 7g and h). However, zircon grains of metamorphic origin were actually not generalized in this study since the samples are mostly featured by Th/U values exceeding 0.1 (Fig. 4).

High field strength elements (HFSE) are typically regarded as relatively immobile elements which are least susceptible to metamorphism and alteration, such as Nb, Ta, Zr, Hf, Th, etc. The

studied samples exhibit Ba, Nb, Ti and P negative anomalies, weak-to-strong positive anomalies in Rb, K, Hf and several heat-producing or radioactive elements Th and U (Fig. 2a). To be noted, concurrent existences of Nb-Ti depletion and Rb enrichment could not be simply attributed to fractional crystallization. According to Pearce (1983), the large ion lithophile elements (LILE) abundances and HFSE depletion are indicative of the arc affinity and source characteristics. As implied by previous researches, Hf enrichment or Nb-Ti depletion in arc-related rocks can be explained by slab-derived melts or subducted sediments (Pearce and Peate, 1995). In this study, positive anomalies of fluid-mobile element Rb together with melt-mobile elements Th and LREE commonly indicate fluid and melting in the SCS Basin basement rocks. Consistently, REE patterns in the samples are almost entirely featured by considerably negative Eu anomalies (Eu/Eu^* values vary from 0.03 to 0.98), and LREE enrichment with broadly variable $(\text{La}/\text{Yb})_N$ ratios from 0.65 to 59.46 (Fig. 2b).

As a preliminary conclusion, geochemical results and petrographic thin sections commonly indicate that source magma rocks might have been metasomatized by subduction-released fluids and hydrous melting materials.

5.2 Geochronology and texture reinterpretation of the northern SCS Basin basement

It was previously postulated that the pre-Cenozoic SCS Basin residual basement was divided into several parts by near N-S or NW-SE directional faulting and rifting (Wang et al., 2002; Liu et al., 2006, 2011; Lu et al., 2011; Sun et al., 2014). Unfortunately, most of these basinal areas were roughly constrained by petrographic observation and deep seismic reflections, which lacked high-precision dating analyses (Dien et al., 1998; Nielsen et al., 1999; Wan et al., 2006; Hao et al., 2011; Sun et al., 2014). The poor geochronological investigation has long been a hindrance for the SCS Basin basement interpretation. However, Zhu et al. (2017) recently revealed the Xisha late Jurassic (152.9 ± 1.7 Ma) to early Cretaceous (137 Ma) metamorphism as well as the Cretaceous (107.8 ± 3.6 Ma) granite intrusive ages. These updated dating studies are contrast with the antecedent Rb-Sr isochron age of 627 Ma (Qin, 1987). The fairly young U-Pb ages cast further doubts on the traditional understanding of the wide distribution of ancient Precambrian or Paleozoic basement.

According to our kernel density estimate plotting, most of the basement samples commonly display a prominent late Mesozoic cluster (Fig. 6a). The southernmost granite intrusion, represented by borehole XK1, is practically dated by a Cretaceous age of (107.8 ± 3.6) Ma (Zhu et al., 2017). This sample provides reliable basinal evidence for the late Yanshanian magmatic activity surrounding the South China continental margin. To the east of Hainan Island, meta-clastic rocks have been first examined for U-Pb geochronology studies. The youngest U-Pb ages are generally considered as the largest deposition age. In view of the thick

overlying Cenozoic successions, the studied zircon U-Pb ratios imply the formation of the extensive late Mesozoic strata (Fig. 8). Meta-tuffs and other meta-clastic samples, including KP111, CC111, WC1711 and CC211, commonly feature early Yanshanian ages (ca. 150–140 Ma) as their centralized age populations.

The remaining meta-sedimentary rock samples BD2311, YJ3511 and YJ3611 exhibit appearance of Caledonian peaks in addition to the dominant Yanshanian peaks (Fig. 6b). Briefly, the significantly high Yanshanian (ca. 150–135 Ma) and minor Caledonian (ca. 435–405 Ma) peaks could have been caused by provenance containing both Paleozoic and Mesozoic zircons. These sediments along with a small number of recycling Proterozoic grains were delivered into the areas to the east of Hainan Island. Based on petrographic identification and Th/U measurements, the studied meta-clastic samples mostly indicate low degree metamorphism. It is traditionally far below the thermal condition where zircon grains of metamorphic origin can be formed. Therefore, possibility could be excluded of certain that the younger peaks were caused by post-metamorphism in these bimodal-pattern U-Pb spectra. In other words, a population of metamorphosed zircon grains was unlikely to be subsequently generated from Mesozoic metamorphism, aside from their initial magmatic origin within source areas. These boreholes are also altogether characterized by youngest zircon ages of the late Cretaceous (Figs 6b and 8). Given the superimposed angular discordance as a boundary between Cenozoic and pre-Cenozoic records, erosion and uplifting gradually ceased which were followed by a suite of sedimentary depositions in the western SCS region.

Additionally, the studied gravity-magnetic-seismic anomaly interpretations provide supporting evidence for a uniform Mesozoic SCS Basin basement (Fig. 9). The overall basement is more likely to generate relatively small-scale N-S directional faulting or rifting than previously being suggested (Fig. 9f, modified from

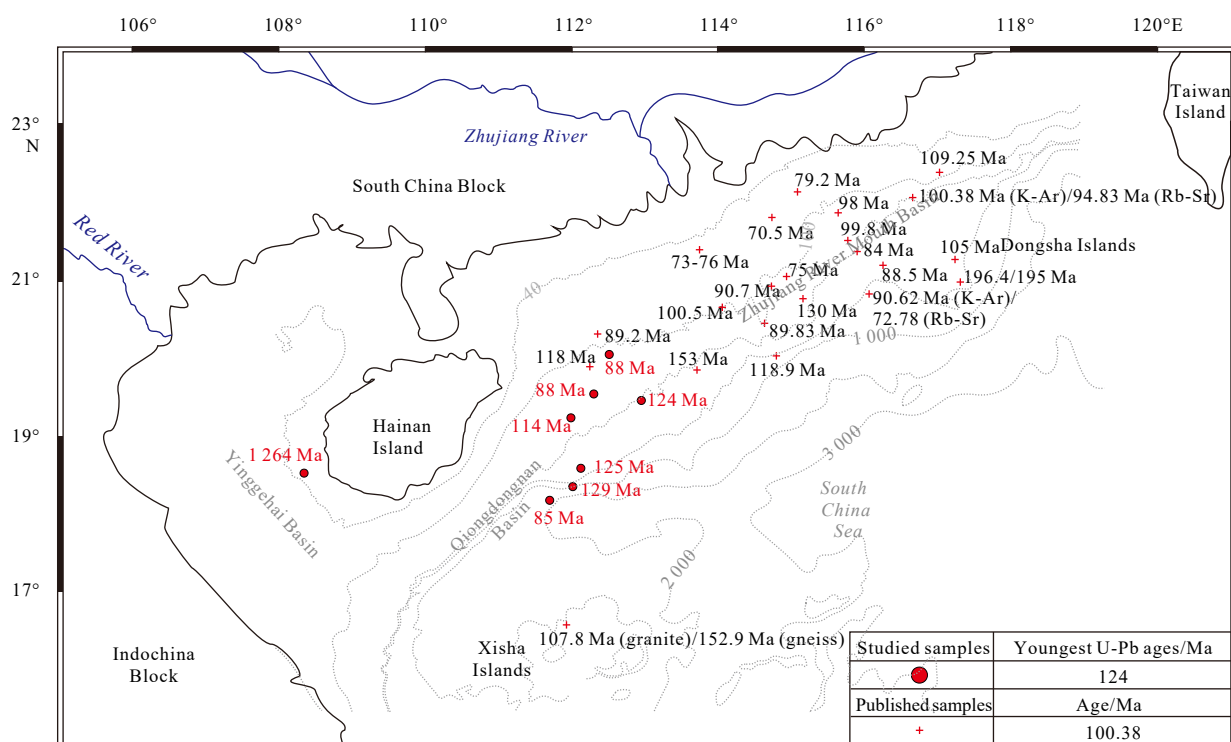


Fig. 8. Distribution map of the youngest ages dated by detrital zircon U-Pb ages for the studied meta-clastic rock samples, and K-Ar or Rb-Sr ages of previous researches for the northern SCS Basin basement.

Pubellier et al. (2008)). To be more detailed, RTP magnetic anomalies can effectively pinpoint the Mesozoic sedimentary deposition, which has extremely low-magnetic susceptibility. This parameter is also suited for late-stage magmatism detection. A high-value anomaly belt with NE trending is developed on Fig. 9a, which roughly corresponds to the Dongsha basement high and the strong Mesozoic magmatic activities (Li et al., 2008a, 2008b). Patches of obvious magnetic quiescence, on the other hand, are also recognized within the eastern SCS. They are possibly related to the residual distributions of thick Mesozoic sedimentary strata. Comparatively, the free-air gravity map shows that a relatively high-anomaly zone develops around the Dongsha Islands of the

eastern SCS. The free-air gravity pattern is in line with the RTP magnetic anomalies. Briefly, both of these data highs are likely to be caused by Mesozoic magmatic events. However, low-gravity anomalies are also sparsely displayed along the high-anomaly magmatic belt mentioned above (Fig. 9b). This could be interpreted as the existence of a fault and sag zone, which was formed adjacent to the Dongsha igneous bodies. Partly within the eastern SCS region, it might be a little contradictory to find that, higher gravity-anomaly values (between -5 mGal and 10 mGal) are linked to relatively lower RTP magnetic anomalies. In this regard, this observation suggests that these areas are possibly basement uplifts mainly comprised of Mesozoic sedimentary bodies. Con-

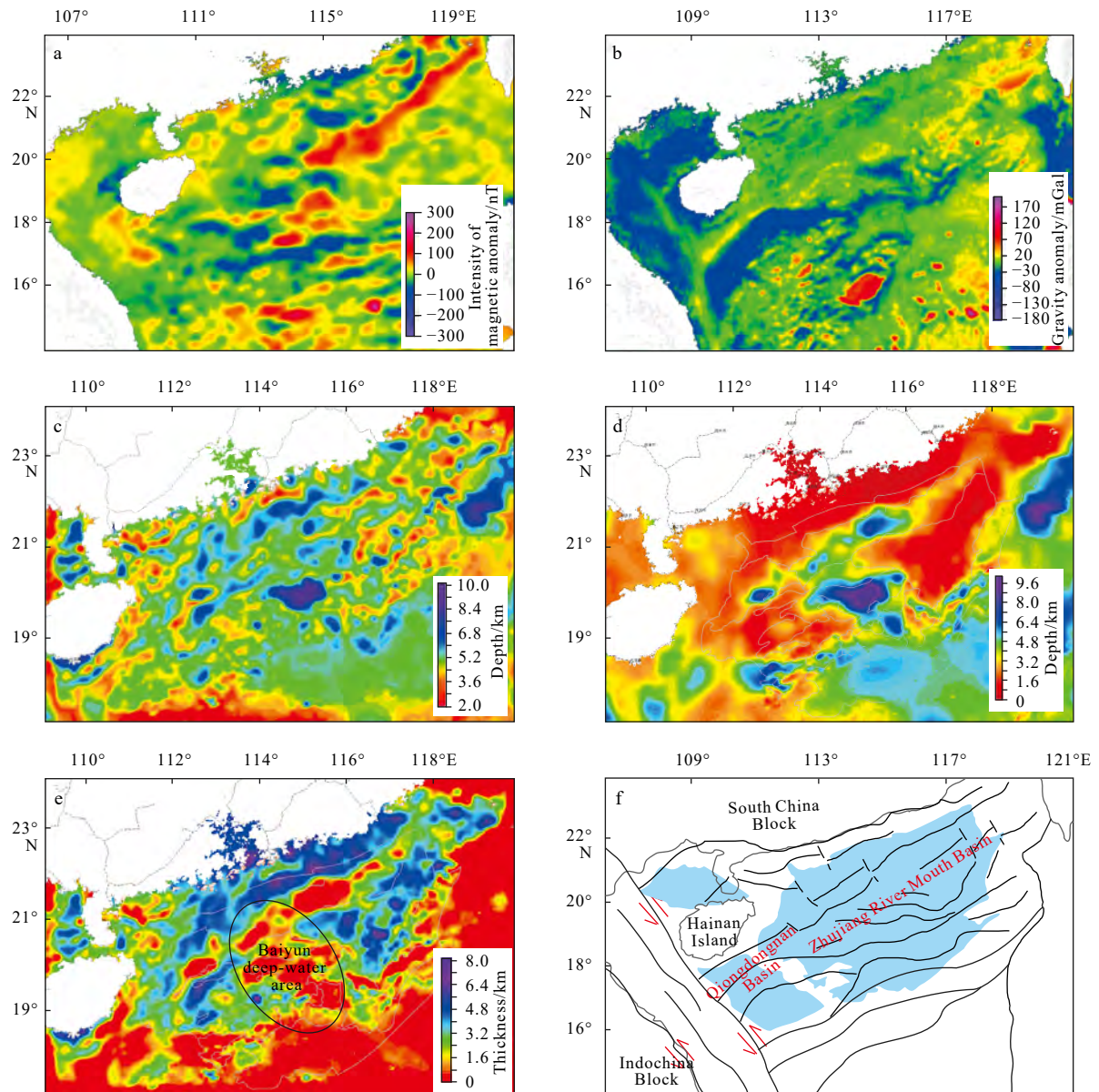


Fig. 9. Map of magnetic anomalies after reduction to the pole to precisely relocate magnetic boundaries and facilitates data interpretation (a); regional free-air gravity anomaly map based on high-resolution shipborne surveying and satellite measurements offshore (b) (Sandwell and Smith, 1997); regional bathymetrical map showing the bottom layer of the pre-Cenozoic basement based on gravity-magnetic-seismic joint inversion, assuming an average of 2.67 g/cm³ for shallow crustal materials (c); regional bathymetrical map showing the bottom layer of the Cenozoic sedimentary sequences (d); thickness reconstruction map of the northern South China Sea pre-Cenozoic sedimentary basin basement (e); sketch map showing the SCS Basin basement tectonic units and major faults (f). Dash lines are faults which are drawn based on both gravity-magnetic-seismic anomaly interpretations in this study and published geological data (modified from Pubellier et al. (2008)).

strained by the precise dating of our penetrations and previous studies, the SCS basement is more reasonable to be described as an overall Mesozoic stratigraphic framework instead of a faulting-division system.

It should also be dealt with much precaution for the westernmost metamorphic granite sample Y1 on the eastern margin of Yinggehai Basin (Fig. 1a). The prominent single peak of significantly old Precambrian age makes it distinct from other results (Fig. 6c). The typical directional-alignment textures indicate a relatively stronger metamorphism under crossed polarized microscope (Figs 7g and h). However, zircon grains of metamorphic origin were unlikely to be practically produced in light of their Th/U ratios (> 0.1) as well as oscillatory-zoning crystal structures. Based on a review of related literature, the Mesozoic SCS region was well-known to be controlled under a drastically changing tectonic background (Hall, 2002, 2012; Zhou et al., 2008; Li et al., 2012). This area is supposed to have experienced an episode of Meso-Tethys and Paleo-Pacific interactions where drastic subduction, collision as well as suturing continually took place (Fig. 10). Under the active Paleo-Pacific subduction geological setting, abundant Cretaceous ages for granite intrusive bodies gathering around the eastern SCS region indeed provide direct lines of evidence for the Mesozoic magmatic arc along the continental margin (Table 1, Fig. 8). Comparatively, meta-clastic rocks with Mesozoic ages (mainly early Cretaceous) are dominant of presence in the eastern Hainan Basin, the western SCS (Fig. 8). Further west, the Indochina Block has been continually colliding with the Cathaysian Landmass during the late Triassic (Roger et

al., 2000; Lepvrier et al., 2004, 2008). The fact that Y1 lies coincidentally along the Red River Fault Zone strongly indicates large-scale preservation of the old continental relicts during this suite of continental collisions and Tethyan suffocation processes. These ancient records might be largely related to the Gondwanaland-derived Indochina Block, as suggested from metamorphic granite Y1 and the old basement of Hainan Island. To a certain degree, it further confirms potential provenances of Proterozoic or Paleozoic materials for the minor age populations in the studied metamorphic sedimentary samples (Fig. 6b).

Fairly homogeneous properties are recognized across the western Zhujiang River Mouth Basin as well as Qiongdongnan Basin based on the magnetic and gravity anomalies (Figs 9a and b). On the RTP map, a near-uniform distribution pattern is observed with moderately negative to slightly positive magnetic anomalies. Clear dividing boundaries are not identified for the extensive quiet magnetic zones of Mesozoic sediments. To be noted, Yinggehai Basin displays conspicuously negative gravity anomalies, which is in contrast with the wide distribution of medium-value positive anomalies to the east of Hainan Island (Fig. 9b). It is postulated to be physical property distinction as confirmed by petrographic and geochronological evidences. Furthermore, the 2D thickness reconstruction map of the pre-Cenozoic strata has been obtained as shown in Fig. 9e. It was achieved by subtracting the Cenozoic sedimentary cover from the total Mesozoic-upward sequences (Figs 9c and d). It reveals that the Mesozoic strata are generally distributed in the western SCS region, east of Hainan Island. With regard to the Baiyun deep-water area, the

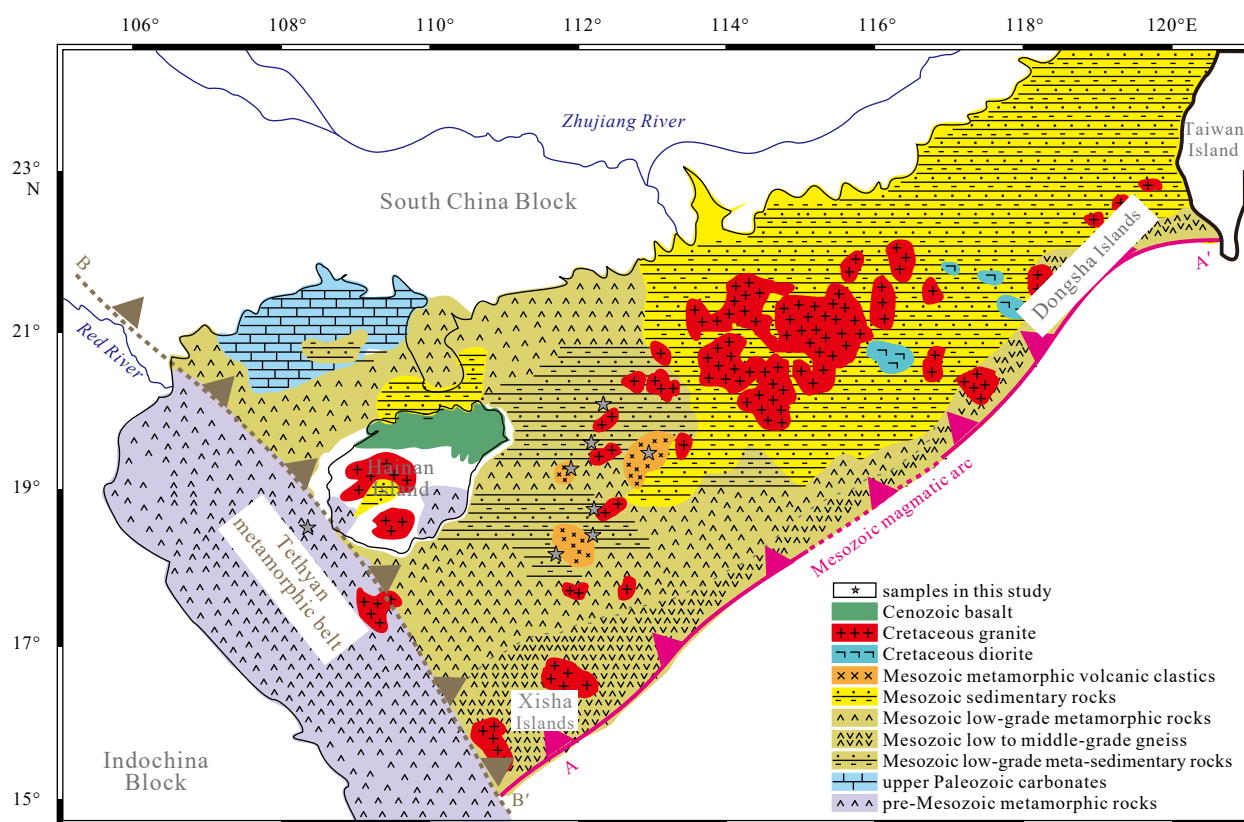


Fig. 10. Systematic northern SCS pre-Cenozoic basement lithological map with an interpreted Mesozoic magmatic arc A-A' shown along the continental margin. This lithological pattern is constrained by the new ages, geochemical analysis, petrographic slice observation and gravity-magnetic-seismic joint inversion results reported in this study as well as other published data (Qiu et al., 1996; Li et al., 1999; Xu et al., 2017). A postulated Tethyan subduction direction is also shown to the west of Hainan Island. Section B-B' shows the possible active boundary of the pre-Cenozoic metamorphic belt along the present extension of the Red River Fault Zone (modified from Wang et al. (2002) and Sun et al. (2014)).

obviously thinning basement could possibly be explained by the relationship between crustal stretching and basin structure (Fig. 9e). During the early stage of the syn-rifting period, the Baiyun deep-water area was mainly influenced from the brittle extension of the upper crust. When it came to the late stage of the syn-rifting period, the strongly crustal ductile deformation caused a saucer-shaped rheology change. After eliminating the influence from the overlying sedimentary sequences, it seems that the depths of Moho and SCS sedimentary basin basement are displayed as mirrorimage relationship (Pang et al., 2018; Lei et al., 2019a). In any case, the sketched tectonic-unit reconstruction firstly attempts to show that the northern SCS Basin basement was formed under the mechanism of spatially uniform stress-field (Fig. 9f).

5.3 SCS Basin basement evolution and regional geodynamic implications

From at least late Triassic to early Cretaceous, the SCS area has been influenced from both Meso-Tethys and Paleo-Pacific domains (Metcalf, 1996; Carter et al., 2001; Hall, 2002, 2012; Zhou et al., 2008). The southeastern Eurasian margin has been experiencing a very complicated evolutionary history (Lei et al., 2019a) (Fig. 11a). The lack of basinal evidence has led to misleading interpretations on the pre-Cenozoic SCS basement prior to the subsequent generation of Tertiary oceanic basins. The newly obtained zircon U-Pb ages, elemental geochemistry and petrographic identification commonly provide significant constraints on the pre-Cenozoic SCS basement as well as geodynamic evolution of the Southeast Asia. From late Triassic to early Jurassic, a Meso-Tethyan subduction environment was likely to exist between the Indochina Block and Cathaysian Block extending from the northwest to southeast (Roger et al., 2000; Lepvrier et al., 2004, 2008; Sone and Metcalfe, 2008) (Fig. 11b). As a separate micro-continental terrane, the original structure of the Hainan Island (or considered as “proto-Hainan Island”) was likely to have occurred within the front of Meso-Tethyan subduction under this overall compressional tectonic setting. Although the final amalgamation remains unclear on its precise timing, formation of Hainan Island can be considered as a part of accretionary prism during the drastic intercontinental collision. With respect to the NE–SW trending of stronger metamorphism over the broad SCS

Basin basement, the Indochina Block might have been driven for continual collision and deformation with the Cathaysia during the whole Mesozoic. These long-lasting subduction processes undoubtedly led to stronger contact metamorphism between rigid continental terranes. From late Jurassic to early Cretaceous (Fig. 11c), the Paleo-Pacific subduction system kept affecting the SCS area to the east, which led to the development of the Andean-type continental margin. With the Paleo-Pacific Plate subducting under the South China Block, a series of large-scale magmatic and orogenic movements took place within the South China during the late Mesozoic (Zhou and Li, 2000; Zhou et al., 2006). The acceleration of subduction also resulted in broader arc magmatism and accompanied back-arc extensional basins when it turned to late Jurassic–early Cretaceous. The oceanic-continental collision has caused relatively weaker metamorphism in the eastern area of the northern SCS Basin basement. Compared to the more complicated and intense metamorphism to the west of Hainan Island, influence from the Paleo-Pacific subduction system seems limited by resulting in narrower and weaker metamorphic belt (Fig. 10). Away from the subduction zone, metamorphism tends to be sharply weakened from south to further north. It should also be noted that Xisha area might be sequentially influenced from multi-stage collisions of both the Indochina Block and Paleo-Pacific. As the significant intersection of the northern SCS Basin basement, a more intense and extensive metamorphic belt has been possibly generated under these different geotectonic domains.

6 Conclusions

Geochemical analyses, petrographic identification, detrital zircon U-Pb geochronology as well as geophysical constraints from gravity-magnetic joint inversion have been conducted on the northern SCS pre-Cenozoic basement samples. In this study, it is reinterpreted that the pre-Cenozoic crustal structure is actually dominated by the widespread distribution of Mesozoic strata, rather than a matching basement of heterogeneous segments. Corroborated from the previous U-Pb, K-Ar and Rb-Sr Cretaceous isochron ages on granite intrusives within the north-eastern SCS region, it is proposed that the regional magmatic arc surrounding the South China continental margin was under con-

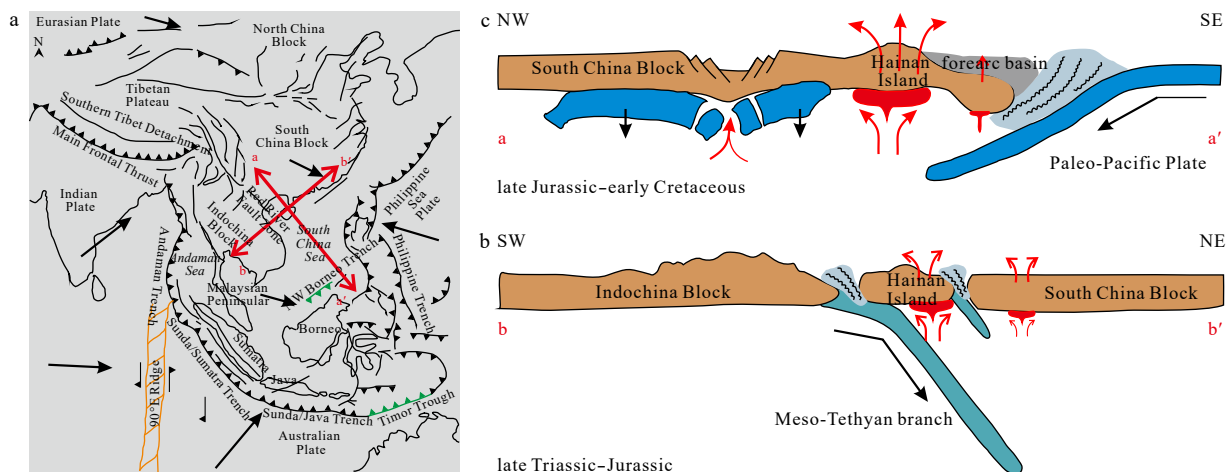


Fig. 11. Sketch map showing the present topographic and active faults of the east Asia at the convergence zone of the Eurasian Plate, Philippine Sea Plate and Australian-Indian Plate (a) (modified from Metcalfe (1996, 2011)). A cartoon illustrating the switch-on and switch-off evolution of the Meso-Tethyan tectonic regime in the late Triassic–Jurassic (b) and the Paleo-Pacific regime in the late Jurassic–early Cretaceous (c).

trol from the drastic Paleo-Pacific subduction. Displaying depositional ages of late Jurassic to Cretaceous, the studied tuff and volcanoclastic rock samples suggest a western extension of this active magmatic belt. A suite of meta-clastic rock samples to the east of Hainan Island, the western SCS, have also been examined indicating the existence of a low-grade metamorphosed Mesozoic basement. Bimodal patterns of Yanshanian and Caledonian peaks in part of the studied samples suggest provenances consisting of Mesozoic and Paleozoic zircon grains. Finally, located on the Red River Fault Zone, the metamorphic granites with Precambrian zircon ages imply extensive preservation of ancient continental landmasses during the subduction, collision and uplifting activities between the Indochina Block and Cathaysian Block. In fact, the Red River Fault Zone could be considered as the reactivation of the suturing belt along these contiguous plate margins during the Cenozoic. Tectonically, the Hainan Island is actually regarded to be part of the accretionary complex on the continental boundaries. Apparently, the northern SCS Basin basement was practically generated from both intracontinental amalgamation and oceanic-continental collision processes. The Tertiary SCS oceanic basin was finally developed from a series of rifting and faulting along the collisional-accretionary continental margin.

Acknowledgements

We thank China National Offshore Oil Corporation (CNOOC) for providing geological data and borehole samples from the northern South China Sea basement. Reviewers and guest editors offered critical comments and suggestions, which greatly improved this presentation. Yuchi Cui acknowledges the China Scholarship Council and Curtin CIPRS for providing research scholarship for her Joint PhD study at Curtin University.

References

- Andersen T. 2002. Correction of common lead in U-Pb analyses that do not report ²⁰⁴Pb. *Chemical Geology*, 192(1–2): 59–79
- Barckhausen U, Engels M, Franke D, et al. 2014. Evolution of the South China Sea: Revised ages for breakup and seafloor spreading. *Marine and Petroleum Geology*, 58: 599–611, doi: 10.1016/j.marpetgeo.2014.02.022
- Braitenberg C, Wienecke S, Wang Yong. 2006. Basement structures from satellite-derived gravity field: South China Sea ridge. *Journal of Geophysical Research*, 111(B5): B05407
- Briaux A, Patriat P, Tapponnier P. 1993. Updated interpretation of magnetic anomalies and seafloor spreading stages in the South China Sea: implications for the Tertiary Tectonics of Southeast Asia. *Journal of Geophysical Research*, 98(B4): 6299–6328, doi: 10.1029/92JB02280
- Cao Licheng, Shao Lei, Qiao Peijun, et al. 2018. Early Miocene birth of modern Pearl River recorded low-relief, high-elevation surface formation of SE Tibetan Plateau. *Earth and Planetary Science Letters*, 496: 120–131, doi: 10.1016/j.epsl.2018.05.039
- Carter A, Roques D, Bristow C, et al. 2001. Understanding Mesozoic accretion in Southeast Asia: Significance of Triassic thermotectonism (Indosinian orogeny) in Vietnam. *Geology*, 29(3): 211–214, doi: 10.1130/0091-7613(2001)029<0211:UMAI>2.0.CO;2
- Charvet J, Shu Liangshu, Faure M, et al. 2010. Structural development of the Lower Paleozoic belt of South China: genesis of an intracontinental orogen. *Journal of Asian Earth Sciences*, 39(4): 309–330, doi: 10.1016/j.jseas.2010.03.006
- Clift P, Lin Jian. 2001. Preferential mantle lithospheric extension under the South China margin. *Marine and Petroleum Geology*, 18(8): 929–945, doi: 10.1016/S0264-8172(01)00037-X
- Cocks L R M, Torsvik T H. 2013. The dynamic evolution of the Palaeozoic geography of eastern Asia. *Earth-Science Reviews*, 117: 40–79, doi: 10.1016/j.earscirev.2012.12.001
- Dien P T, Nielsen L H, Andersen C, et al. 1998. Late-Mesozoic and Cenozoic basin development along the northwest margin of Vietnam. In: American Association of Petroleum Geologists Annual Convention. Salt Lake City, UT, USA: American Association of Petroleum Geologists, 1–6, doi: 10.1306/00AA84F4-1730-11D7-8645000102C1865D.
- Ebbing J, Braitenberg C, Götze H J. 2006. The lithospheric density structure of the Eastern Alps. *Tectonophysics*, 414(1–4): 145–155
- Ebinger C J, Hayward N J. 1996. Soft plates and hot spots: Views from afar. *Journal of Geophysical Research*, 101(B10): 21859–21876, doi: 10.1029/96JB02118
- Faure M, Lepvrier C, Van Nguyen V, et al. 2014. The South China block-Indochina collision: Where, when, and how?. *Journal of Asian Earth Sciences*, 79: 260–274, doi: 10.1016/j.jseas.2013.09.022
- Faure M, Lin Wei, Chu Yang, et al. 2016. Triassic tectonics of the southern margin of the South China Block. *Comptes Rendus Geoscience*, 348(1): 5–14, doi: 10.1016/j.crte.2015.06.012
- Franke D, Barckhausen U, Baristean N, et al. 2011. The continent-ocean transition at the southeastern margin of the South China Sea. *Marine and Petroleum Geology*, 28(6): 1187–1204, doi: 10.1016/j.marpetgeo.2011.01.004
- Fyhn M B W, Cuong T D, Hoang B H, et al. 2018. Linking Paleogene rifting and inversion in the northern Song Hong and Beibuwan Basins, Vietnam, with left-lateral motion on the Ailao Shan-Red River Shear Zone. *Tectonics*, 37(8): 2559–2585, doi: 10.1029/2018TC005090
- Geological Survey of Japan and Coordinating Committee for Coastal and Offshore Geoscience Programmes in East and Southeast Asia (CCOP). 1996. Magnetic Anomaly Map of East Asia 1: 4,000,000. Tsukuba-shi, Ibaraki-ken: The Survey
- Hall R. 2002. Cenozoic geological and plate tectonic evolution of SE Asia and the SW Pacific: computer-based reconstructions, model and animations. *Journal of Asian Earth Sciences*, 20(4): 353–431, doi: 10.1016/S1367-9120(01)00069-4
- Hall R. 2012. Late Jurassic-Cenozoic reconstructions of the Indonesian region and the Indian Ocean. *Tectonophysics*, 570–571: 1–41
- Hao Tianyao, Xu Ya, Sun Fuli, et al. 2011. Integrated geophysical research on the tectonic attribute of conjugate continental margin of South China Sea. *Chinese Journal of Geophysics (in Chinese)*, 54(12): 3098–3116
- Hayes D E, Nissen S S. 2005. The South China sea margins: Implications for rifting contrasts. *Earth and Planetary Science Letters*, 237(3–4): 601–616
- Hoskin P W O, Schaltegger U. 2003. The composition of zircon and igneous and metamorphic petrogenesis. *Reviews in Mineralogy and Geochemistry*, 53(1): 27–62, doi: 10.2113/0530027
- Hsu S K, Yeh Y C, Doo W B, et al. 2004. New bathymetry and magnetic lineations identifications in the northernmost South China Sea and their tectonic implications. *Marine Geophysical Researches*, 25(1–2): 29–44
- Hutchison C S. 1989. Geological evolution of South-east Asia. In: Oxford Monographs on Geology and Geophysics. Oxford, England: Clarendon Press, 368
- Jahn B M, Zhou Xinhua, Li Jiliang. 1990. Formation and tectonic evolution of Southeastern China and Taiwan: Isotopic and geochemical constraints. *Tectonophysics*, 183(1–4): 145–160
- Jiang Xiaoyan, Li Xianhua, Collins W J, et al. 2015. U-Pb age and Hf-O isotopes of detrital zircons from Hainan Island: Implications for Mesozoic subduction models. *Lithos*, 239: 60–70, doi: 10.1016/j.lithos.2015.10.006
- Lan C Y, Chung S L, Van Long T, et al. 2003. Geochemical and Sr-Nd isotopic constraints from the Kontum massif, central Vietnam on the crustal evolution of the Indochina block. *Precambrian Research*, 122(1–4): 7–27
- Lapierre H, Jahn B M, Charvet J, et al. 1997. Mesozoic felsic arc magmatism and continental olivine tholeiites in Zhejiang Province and their relationship with the tectonic activity in southeastern China. *Tectonophysics*, 274(4): 321–338, doi: 10.1016/S0040-1951(97)00009-7
- Larsen H C, Mohn G, Nirrengarten M, et al. 2018. Rapid transition from continental breakup to igneous oceanic crust in the South China Sea. *Nature Geoscience*, 11(10): 782–789, doi: 10.1038/

- s41561-018-0198-1
- Lei Chao, Alves T M, Ren Jianye, et al. 2019a. Depositional architecture and structural evolution of a region immediately inboard of the locus of continental breakup (Liwan Sub-basin, South China Sea). *GSA Bulletin*, 131(7–8): 1059–1074, doi: 10.1130/B35001.1
- Lei Chao, Clift P D, Ren Jianye, et al. 2019b. A rapid shift in the sediment routing system of Lower-Upper Oligocene strata in the Qiongdongnan Basin (Xisha Trough), Northwest South China Sea. *Marine and Petroleum Geology*, 104: 249–258, doi: 10.1016/j.marpetgeo.2019.03.012
- Lei Chao, Ren Jianye. 2016. Hyper-extended rift systems in the Xisha Trough, northwestern South China Sea: Implications for extreme crustal thinning ahead of a propagating ocean. *Marine and Petroleum Geology*, 77: 846–864, doi: 10.1016/j.marpetgeo.2016.07.022
- Lei Chao, Ren Jianye, Pang Xiong, et al. 2018. Continental rifting and sediment infill in the distal part of the northern South China Sea in the Western Pacific region: Challenge on the present-day models for the passive margins. *Marine and Petroleum Geology*, 93: 166–181, doi: 10.1016/j.marpetgeo.2018.02.020
- Leloup P H, Arnaud N, Lacassin R, et al. 2001. New constraints on the structure, thermochronology, and timing of the Ailao Shan-Red River shear zone, SE Asia. *Journal of Geophysical Research*, 106(B4): 6683–6732, doi: 10.1029/2000JB900322
- Lepvrier C, Maluski H, Van Tich V, et al. 2004. The Early Triassic Indosinian orogeny in Vietnam (Truong Son Belt and Kontum Massif); implications for the geodynamic evolution of Indochina. *Tectonophysics*, 393(1–4): 87–118
- Lepvrier C, Van Vuong N, Maluski H, et al. 2008. Indosinian tectonics in Vietnam. *Comptes Rendus Geoscience*, 340(2–3): 94–111
- Li Chunfeng, Zhou Zuyi, Hao Hujun, et al. 2008a. Late Mesozoic tectonic structure and evolution along the present-day northeastern South China Sea continental margin. *Journal of Asian Earth Sciences*, 31(4–6): 546–561
- Li Chunfeng, Zhou Zuyi, Li Jiabiao, et al. 2008b. Magnetic zoning and seismic structure of the South China Sea ocean basin. *Marine Geophysical Researches*, 29(4): 223–238, doi: 10.1007/s11001-008-9059-4
- Li Jianhua, Zhang Yueqiao, Dong Shuwen, et al. 2014. Cretaceous tectonic evolution of South China: A preliminary synthesis. *Earth-Science Reviews*, 134: 98–136, doi: 10.1016/j.earscirev.2014.03.008
- Li Pinglu, Liang Huixian, Dai Yiding, et al. 1999. Origin and tectonic setting of the Yanshanian igneous rocks in the Pearl River Mouth Basin. *Guangdong Geology (in Chinese)*, 14(1): 1–8
- Li Sanzhong, Zhang Guowei, Zhou Lihong, et al. 2011. The opposite Meso-Cenozoic intracontinental deformations under the super-convergence: Rifting and extension in the North China Craton and shortening and thrusting in the South China Craton. *Earth Science Frontiers (in Chinese)*, 18(3): 79–107
- Li Xianhua, Li Zhengxiang, Li Wuxian, et al. 2006. Initiation of the Indosinian orogeny in South China: Evidence for a Permian magmatic arc on Hainan Island. *The Journal of Geology*, 114(3): 341–353, doi: 10.1086/501222
- Li Xianhua, Wei Gangjian, Shao Lei, et al. 2003. Geochemical and Nd isotopic variations in sediments of the South China Sea: a response to Cenozoic tectonism in SE Asia. *Earth and Planetary Science Letters*, 211(3–4): 207–220
- Li Zhengxiang, Li Xianhua. 2007. Formation of the 1300-km-wide intracontinental orogen and postorogenic magmatic province in Mesozoic South China: A flat-slab subduction model. *Geology*, 35(2): 179–182, doi: 10.1130/G23193A.1
- Li Zhengxiang, Li Xianhua, Chung S L, et al. 2012. Magmatic switch-on and switch-off along the South China continental margin since the Permian: Transition from an Andean-type to a Western Pacific-type plate boundary. *Tectonophysics*, 532–535: 271–290
- Li Zhengxiang, Li Xianhua, Li Wuxian, et al. 2008c. Was Cathaysia part of Proterozoic Laurentia?—New data from Hainan Island, South China. *Terra Nova*, 20(2): 154–164, doi: 10.1111/j.1365-3121.2008.00802.x
- Li Zhengxiang, Powell C M. 2001. An outline of the palaeogeographic evolution of the Australasian region since the beginning of the Neoproterozoic. *Earth-Science Reviews*, 53(3–4): 237–277
- Liu Hailing, Yan Pin, Liu Yingchun, et al. 2006. Existence of Qiongan suture zone on the north margin of South China Sea. *Chinese Science Bulletin*, 51(S2): 107–120, doi: 10.1007/s11434-006-9107-x
- Liu Hailing, Zheng Hongbo, Wang Yanlin, et al. 2011. Basement of the South China Sea area: Tracing the Tethyan realm. *Acta Geologica Sinica*, 85(3): 637–655, doi: 10.1111/j.1755-6724.2011.00457.x
- Liu Yongsheng, Gao Shan, Hu Zhaochu, et al. 2010. Continental and oceanic crust recycling-induced melt-peridotite interactions in the trans-north China orogen: U-Pb dating, Hf isotopes and trace elements in zircons from mantle xenoliths. *Journal of Petrology*, 51(1–2): 537–571
- Lu Baoliang, Sun Xiaomeng, Zhang Gongcheng, et al. 2011. Seismic-potential field response characteristics and identification of basement lithology of the northern South China Sea basin. *Chinese Journal of Geophysics (in Chinese)*, 54(2): 563–572
- Maruyama S. 1997. Pacific-type orogeny revisited: Miyashiro-type orogeny proposed. *Island Arc*, 6(1): 91–120, doi: 10.1111/j.1440-1738.1997.tb00042.x
- Metcalfe I. 1996. Gondwanaland dispersion, Asian accretion and evolution of eastern Tethys. *Australian Journal of Earth Sciences*, 43(6): 605–623, doi: 10.1080/08120099608728282
- Metcalfe I. 2011. Palaeozoic-Mesozoic history of SE Asia. In: *Geological Society London Special Publications*. London: The Geological Society of London, 355(1): 7–35, doi: 10.1144/SP355.2
- Metcalfe I. 2013. Gondwana dispersion and Asian accretion: Tectonic and palaeogeographic evolution of eastern Tethys. *Journal of Asian Earth Sciences*, 66: 1–33, doi: 10.1016/j.jseas.2012.12.020
- Morley C K. 2002. A tectonic model for the Tertiary evolution of strike-slip faults and rift basins in SE Asia. *Tectonophysics*, 347(4): 189–215, doi: 10.1016/S0040-1951(02)00061-6
- Morley C K. 2012. Late cretaceous-Early Palaeogene tectonic development of SE Asia. *Earth-Science Reviews*, 115(1–2): 37–75
- Morley C K. 2016. Major unconformities/termination of extension events and associated surfaces in the South China seas: Review and implications for tectonic development. *Journal of Asian Earth Sciences*, 120: 62–86, doi: 10.1016/j.jseas.2016.01.013
- Nielsen L H, Mathiesen A, Bidstrup T, et al. 1999. Modelling of hydrocarbon generation in the Cenozoic Song Hong Basin, Vietnam: a highly prospective basin. *Journal of Asian Earth Sciences*, 17(1–2): 269–294
- Nissen S S, Hayes D E, Buhl P, et al. 1995a. Deep penetration seismic soundings across the northern margin of the South China Sea. *Journal of Geophysical Research*, 100(B11): 22407–22433, doi: 10.1029/95JB01866
- Nissen S S, Hayes D E, Yao Bochu, et al. 1995b. Gravity, heat flow, and seismic constraints on the processes of crustal extension: Northern margin of the South China Sea. *Journal of Geophysical Research*, 100(B11): 22447–22483, doi: 10.1029/95JB01868
- Pang Xiong, Ren Jianye, Zheng Jinyun, et al. 2018. Petroleum geology controlled by extensive detachment thinning of continental margin crust: A case study of Baiyun sag in the deep-water area of northern South China Sea. *Petroleum Exploration and Development (in Chinese)*, 45(1): 27–39
- Pearce J A. 1983. Role of the sub-continental lithosphere in magma genesis at active continental margins. In: Hawkesworth C J, Norry M J, eds. *Continental Basalts and Mantle Xenoliths*. Nantwich: Shiva Publishing, 230–249
- Pearce J A, Peate D W. 1995. Tectonic implications of the composition of volcanic arc magmas. *Annual Review of Earth and Planetary Sciences*, 23: 251–285, doi: 10.1146/annurev.earth.23.050195.001343
- Pichot T, Delescluse M, Chamot-Rooke N, et al. 2014. Deep crustal structure of the conjugate margins of the SW South China Sea from wide-angle refraction seismic data. *Marine and Petroleum Geology*, 58: 627–643, doi: 10.1016/j.marpetgeo.2013.10.008
- Pigott J D, Ru Ke. 1994. Basin superposition on the northern margin of the South China Sea. *Tectonophysics*, 235(1–2): 27–50
- Pubellier M, Chamot-Rooke N, Ego F, et al. 2008. Structural map of eastern Eurasia, scale 1/12 500 000. Paris: Commission for the Geological Map of the World

- Qin Guoquan. 1987. A preliminary study on foraminiferal assemblages of well 1 Xiyong, Xisha Islands and their coral reef formation. *Tropic Oceanology* (in Chinese), 6(3): 10–20
- Qiu Xuelin, Ye Sanyu, Wu Shimin, et al. 2001. Crustal structure across the Xisha Trough, northwestern South China Sea. *Tectonophysics*, 341(1–4): 179–193
- Qiu Yuanxi, Li Pinglu, Liang Huixian. 1996. Late Cretaceous–Cenozoic tectonic evolution and nature of continental margin in the northern South China Sea and Taiwan Strait. *Guangdong Geology* (in Chinese), 11(3): 10–16
- Rangin C, Klein M, Roques D, et al. 1995. The Red River fault system in the Tonkin Gulf, Vietnam. *Tectonophysics*, 243(3–4): 209–222
- Roger F, Leloup P H, Jolivet M, et al. 2000. Long and complex thermal history of the Song Chay metamorphic dome (Northern Vietnam) by multi-system geochronology. *Tectonophysics*, 321(4): 449–466, doi: 10.1016/S0040-1951(00)00085-8
- Rudnick R L, Gao Shan. 2003. The composition of the continental crust. In: Holland HD, Turekian KK, eds. *Treatise on Geochemistry*. Oxford: Elsevier-Pergamon, 1–64
- Sandwell D T, Smith W H F. 1997. Marine gravity anomaly from Geosat and ERS 1 satellite altimetry. *Journal of Geophysical Research*, 102(B5): 10039–10054, doi: 10.1029/96JB03223
- Schellart W P, Lister G S, Toy V G. 2006. A Late Cretaceous and Cenozoic reconstruction of the southwest Pacific region: Tectonics controlled by subduction and slab rollback processes. *Earth-Science Reviews*, 76(3–4): 191–233
- Shao Lei, Cao Licheng, Pang Xiong, et al. 2016. Detrital zircon provenance of the Paleogene syn-rift sediments in the northern South China Sea. *Geochemistry, Geophysics, Geosystems*, 17(2): 255–269, doi: 10.1002/2015GC006113
- Shao Lei, Cao Licheng, Qiao Peijun, et al. 2017. Cretaceous–Eocene provenance connections between the Palawan Continental Terrane and the northern South China Sea margin. *Earth and Planetary Science Letters*, 477: 97–107, doi: 10.1016/j.epsl.2017.08.019
- Shao Lei, Cui Yuchi, Statterger K, et al. 2019. Drainage control of Eocene to Miocene sedimentary records in the southeastern margin of Eurasian Plate. *GSA Bulletin*, 131(3–4): 461–478
- Shao Lei, Qiao Peijun, Zhao Meng, et al. 2015. Depositional style of the northern South China Sea between Oligocene and Miocene in response to the evolution of the Pearl River. In: Clift P D, Harff J, Wu J, et al, eds. *River-Dominated Shelf Sediments of East Asian Seas*. London: The Geological Society of London
- Shi Hesheng, Li Chunfeng. 2012. Mesozoic and early Cenozoic tectonic convergence-to-rifting transition prior to opening of the South China Sea. *International Geology Review*, 54(15): 1801–1828, doi: 10.1080/00206814.2012.677136
- Sláma J, Košler J, Condon D J, et al. 2008. Plešovice zircon—A new natural reference material for U–Pb and Hf isotopic microanalysis. *Chemical Geology*, 249(1–2): 1–35
- Sone M, Metcalfe I. 2008. Parallel Tethyan sutures in mainland Southeast Asia: New insights for Palaeo-Tethys closure and implications for the Indosinian orogeny. *Comptes Rendus Geoscience*, 340(2–3): 166–179, doi: 10.1016/j.crte.2007.09.008
- Sun S S, McDonough W F. 1989. Chemical and isotopic systematics of oceanic basalts: Implications for mantle composition and processes. London: The Geological Society of London, 42(1): 313–345, doi: 10.1144/GSL.SP.1989.042.01.19
- Sun Xiaomeng, Zhang Xuqing, Zhang Gongcheng, et al. 2014. Texture and tectonic attribute of Cenozoic basin basement in the northern South China Sea. *Science China: Earth Sciences*, 57(6): 1199–1211, doi: 10.1007/s11430-014-4835-2
- Taylor S R, McLennan S M. 1985. *The Continental Crust: Its Composition and Evolution*. Oxford: Blackwell Scientific Publications, 1–312
- Veevers J J. 2004. Gondwanaland from 650–500 Ma assembly through 320 Ma merger in Pangea to 185–100 Ma breakup: supercontinental tectonics via stratigraphy and radiometric dating. *Earth-Science Reviews*, 68(1–2): 1–132
- Vermeesch P. 2012. On the visualisation of detrital age distributions. *Chemical Geology*, 312–313: 190–194
- Vương N V, Hansen B T, Wemmer K, et al. 2013. U/Pb and Sm/Nd dating on ophiolitic rocks of the Song Ma suture zone (northern Vietnam): Evidence for Upper Paleozoic Paleotethyan lithospheric remnants. *Journal of Geodynamics*, 69: 140–147, doi: 10.1016/j.jog.2012.04.003
- Wallace L M, Ellis S, Miyao K, et al. 2009. Enigmatic, highly active left-lateral shear zone in southwest Japan explained by aseismic ridge collision. *Geology*, 37(2): 143–146, doi: 10.1130/G25221A.1
- Wan Ling, Yao Bochu, Zeng Weijun, et al. 2006. Lithospheric structure and petroleum distribution in the South China Sea. *Geology in China* (in Chinese), 33(4): 874–884
- Wang Jialin, Zhang Xinbing, Wu Jiansheng, et al. 2002. Integrated geophysical researches on base texture of Zhujiang River Mouth basin. *Journal of Tropical Oceanography* (in Chinese), 21(2): 13–22
- Wang Yuejun, Zhang Aimei, Fan Weiming, et al. 2011. Kwangian crustal anatexis within the eastern South China Block: Geochemical, zircon U–Pb geochronological and Hf isotopic fingerprints from the gneissoid granites of Wugong and Wuyi-Yunkai Domains. *Lithos*, 127(1–2): 239–260
- Wei Gangjian, Li Xianhua, Liu Ying, et al. 2006. Geochemical record of chemical weathering and monsoon climate change since the early Miocene in the South China Sea. *Paleoceanography*, 21(4): PA4214, doi: 10.1029/2006PA001300
- Wiedenbeck M, Allé P, Corfu F, et al. 1995. Three natural zircon standards for U–Th–Pb, Lu–Hf, trace element and REE analyses. *Geostandards and Geoanalytical Research*, 19(1): 1–23, doi: 10.1111/j.1751-908X.1995.tb00147.x
- Xu Changhai, Zhang Lu, Shi Hesheng, et al. 2017. Tracing an early Jurassic magmatic arc from South to East China Seas. *Tectonics*, 36(3): 466–492, doi: 10.1002/2016TC004446
- Xu Deru, Xia Bin, Bakun-Czubarow N, et al. 2008. Geochemistry and Sr–Nd isotope systematics of metabasites in the Tunchang area, Hainan Island, South China: implications for petrogenesis and tectonic setting. *Mineralogy and Petrology*, 92(3): 361–391
- Yan Quanshu, Shi Xuefa, Liu Jihua, et al. 2010. Petrology and geochemistry of Mesozoic granitic rocks from the Nansha microblock, the South China Sea: Constraints on the basement nature. *Journal of Asian Earth Sciences*, 37(2): 130–139, doi: 10.1016/j.jseas.2009.08.001
- Yao Bochu. 1996. Tectonic evolution of the South China Sea in Cenozoic. *Marine Geology & Quaternary Geology* (in Chinese), 16(2): 1–13
- Yao Weihua, Li Zhengxiang, Li Wuxian, et al. 2017. Proterozoic tectonics of Hainan Island in supercontinent cycles: New insights from geochronological and isotopic results. *Precambrian Research*, 290: 86–100, doi: 10.1016/j.precamres.2017.01.001
- Yu Jinhai, O'Reilly S Y, Zhou Meifu, et al. 2012. U–Pb geochronology and Hf–Nd isotopic geochemistry of the Badu Complex, Southeastern China: Implications for the Precambrian crustal evolution and paleogeography of the Cathaysia Block. *Precambrian Research*, 222–223: 424–449
- Yui T F, Maki K, Lan C Y, et al. 2012. Detrital zircons from the Tananao metamorphic complex of Taiwan: Implications for sediment provenance and Mesozoic tectonics. *Tectonophysics*, 541–543: 31–42
- Zhou Di, Sun Zhen, Chen Hanzong, et al. 2008. Mesozoic paleogeography and tectonic evolution of South China Sea and adjacent areas in the context of Tethyan and Paleo-Pacific interconnections. *Island Arc*, 17(2): 186–207, doi: 10.1111/j.1440-1738.2008.00611.x
- Zhou Xinmin, Li Wuxian. 2000. Origin of Late Mesozoic igneous rocks in southeastern China: implications for lithosphere subduction and underplating of mafic magmas. *Tectonophysics*, 326(3–4): 269–287
- Zhou Xinmin, Sun Tao, Shen Weizhou, et al. 2006. Petrogenesis of Mesozoic granitoids and volcanic rocks in South China: A response to tectonic evolution. *Episodes*, 29(1): 26–33, doi: 10.18814/epiugs/2006/v29i1/004
- Zhu Weilin, Xie Xinong, Wang Zhenfeng, et al. 2017. New insights on the origin of the basement of the Xisha Uplift, South China Sea. *Science China: Earth Sciences*, 60(12): 2214–2222, doi: 10.1007/s11430-017-9089-9



Evolution of the Pearl River and its Implication for East Asian Continental Landscape Reversion

ZHANG Hao¹, CUI Yuchi^{1,2,*}, QIAO Peijun¹, ZHAO Meng³ and XIANG Xuhong⁴

¹ State Key Laboratory of Marine Geology, Tongji University, Shanghai 200092, China

² Earth Dynamics Research Group, the Institute for Geoscience Research (TIGeR), School of Earth and Planetary Sciences, Curtin University, GPO Box U1987, Australia

³ Tianjin Branch of China National Offshore Oil Corporation, Tianjin 300459, China

⁴ Shenzhen Branch of China National Offshore Oil Corporation Ltd., Shenzhen 518054, China

Abstract: As the link connecting the South China Continent and the northern South China Sea (SCS), the Pearl River is the focus of sedimentology and petroleum geology research. Its evolutionary process and controlling factors are of great significance in revealing the East Asian continental landscape reorganization during the Late Cenozoic. Based on published data, ‘source-to-sink’ provenance analyses allow systematic deliberation on the birth and evolutionary history of the Pearl River. Close to the Oligocene/Miocene boundary, an abrupt shift in the sedimentary composition indicates significant westward and northward expansion of the river’s watershed area, followed by the establishment of a near-modern fluvial network. This sedimentary change generally concurred with a series of regional geological events, including the onset of the Yangtze throughflow, large-scale development of the loess plateau, and formation of the northwestern arid zone and Asian Monsoon system. These major changes in the geology-climate-ecoenvironment system are in close response to the process of the Cenozoic Xizang (Tibetan) Plateau uplift. Consequently, the East Asian continental landscape and most of mid-Cenozoic drainage systems underwent critical reversion into east-tilting, or east-flowing networks.

Key words: Oligocene–Miocene, landscape reversion, source to sink provenance analyses, East Asian continental landforms, Pearl River, South China

Citation: Zhang et al., 2021. Evolution of the Pearl River and its Implication for East Asian Continental Landscape Reversion. *Acta Geologica Sinica (English Edition)*, 95(1): 66–76. DOI: 10.1111/1755-6724.14641

1 Introduction

The Pearl River is one of the most important rivers along the South China continental margin. It has been transporting a large amount of sediments to the northern South China Sea (SCS) since at least the mid-Cenozoic. As a result, large-scale deltas and submarine fans were formed throughout the Oligocene–Miocene in the Pearl River Mouth Basin (Peng et al., 2004; Pang et al., 2007; Wang et al., 2012); here many oil and gas reservoirs have been explored. Research on the evolution of the Pearl River is significant not only for systematically understanding ‘source-to-sink’ sedimentary processes in the SCS, but also for petroleum exploration in this region.

East Asia is known as the third pole on the planet, where the world’s highest plateau and numerous fluvial systems all develop. During the Cenozoic, plate collision led to the uplift of the Xizang (Tibetan) Plateau, and East Asia experienced drastic topographic reversion from east-high–west-low to west-high–east-low. Accordingly, the development and reorganization of the river systems can directly reflect the general geomorphic evolution (e.g., Zheng et al., 2017). The Pearl River originates from the southeastern margin of the Xizang (Tibetan) Plateau, and

its evolutionary process has been under direct control from the East Asian topography. Earlier research demonstrated that the Pearl River experienced stepwise evolution into its modern continental scale, in close relation to the multi-phase topographic inversion caused by the Xizang (Tibetan) uplift and SCS expansion (Wang, 2005). ODP site 1148 revealed that the northern SCS was influenced from different provenances across the Oligocene/Miocene boundary with unconformities possibly formed by regional tectonic events (Clift et al., 2002; Li et al., 2003). Increasing lines of evidence confirm that the evolution of the northern SCS provenance has been closely linked with the continental-scale fluvial networks, such as the Pearl River (Shao et al., 2015, 2017, 2019a, b; Cao et al., 2018; Zhang et al., 2020). Apparently, the coupling relationship between the Pearl River evolution and the Xizang (Tibetan) uplift is significant for restoring the East Asian topography–geomorphology evolution.

In this paper, we use published data to make ‘source-to-sink’ provenance analyses with the aim of systematically deliberating the birth and evolutionary history of the Pearl River.

2 Geological Background

The northern SCS source-to-sink system is mainly

* Corresponding author. E-mail: cuiyuchi@tongji.edu.cn

composed of the South China continent (the source) and the Pearl River Mouth Basin (the sink). The Pearl River fluvial system initiates from the southeastern margin of the Xizang (Tibetan) Plateau (XTP) and flows across the extensive South China Block (Fig. 1). In addition to shaping regional topography, Asian monsoon and river systems, the XTP has also played an important role in controlling the sedimentary transport to the northern SCS (Clark et al., 2004; Zhang et al., 2012).

2.1 The Pearl River fluvial network

The Pearl River fluvial network stretches across a wide complex area, and its tributaries erode significantly different types of basement parent rocks (Fig. 1). Middle and lower reaches of the Xi River drainage basin are dominated by limestones, together with Paleozoic strata of quartz sandstones and shales and sporadic granite intrusions. The Liu and Gui rivers are tributaries from the middle reaches of the Xi River, which expose mainly Paleozoic strata, but rarely erode Mesozoic strata. The upper reaches of the Xi River, with the Nanpan and Beipan river tributaries, mainly expose Proterozoic parent rocks. The lower reaches of the Pearl River, represented by the Dong and Bei rivers, run mainly across the Mesozoic orogenic uplift of widespread granite and other volcanic rocks. Sediments from different parent rocks have been transported by the Pearl River tributaries and finally deposited in the offshore Pearl River Mouth Basin. Altogether these sedimentary records contribute greatly to

understanding the evolution of the Pearl River based on the use of integrated source-to-sink provenance analyses.

2.2 Xizang (Tibetan) Uplift

Continuous uplift of the XTP has directly affected the formation and evolution of the Pearl River since the Middle Cenozoic. Numerous studies indicate that the XTP has experienced multiple-stage uplifting processes (Clark and Royden, 2000; Tapponnier et al., 2001; Rowley and Garzione, 2007; Wang et al., 2011; Li et al., 2020). Its central and southern parts were possibly uplifted first, followed by the Himalayan area, and finally the northern (northeastern) part (Tapponnier et al., 2001; Lu and Guo, 2013).

Although there are several classification schemes (three or more stages) for the Cenozoic XTP Uplift, a systematic reconstruction of the uplifting history is still required. By using lithofacies paleogeography analysis, apatite fission track thermochronology analysis and other compiled data, Zhang et al. (2013) recognized five uplifting intervals for the XTP, including ca. 58–53 Ma, ca. 45–30 Ma, ca. 25–20 Ma, ca. 13–7 Ma and ca. 5 Ma to present. Notably, these large-scale structural uplift and denudation stages with some geological synchronicity can be observed in certain regions of the XTP (Clift et al., 2008; Zhang et al., 2010). In general, the XTP was dominated by an east-high–west-low pattern geomorphology prior to the Oligocene. This topography was replaced during the Oligocene–Miocene by an uneven distribution of uplifting and

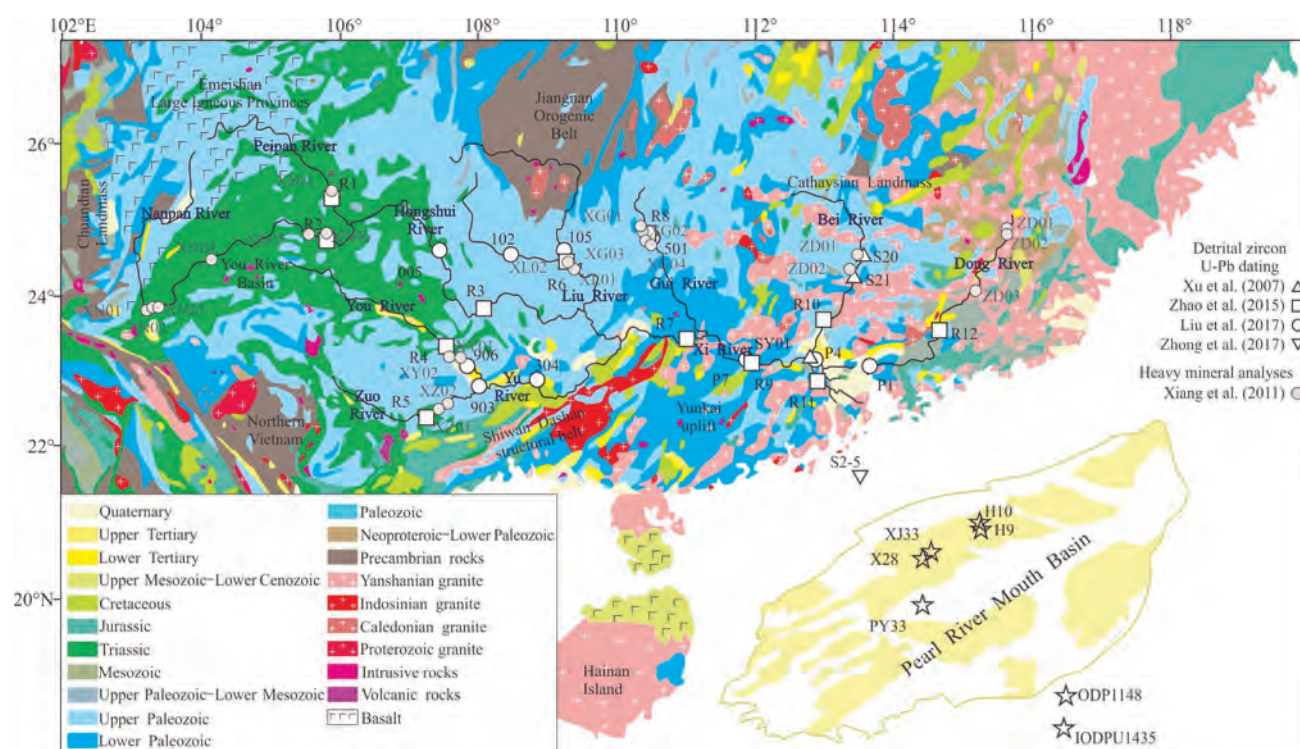


Fig. 1. Geological map of the Pearl River drainage areas and sampling locations from previous researches (modified from Cao et al., 2018).

U-Pb dating sample information: sample R1 to R12 according to Zhao et al., 2015, sample P1, P4, P7, 005, 102, 105, 304, 501, 903 and 906 according to Liu et al., 2017, sample S20, S21 and SY01 according to Xu et al., 2007, sample S2-5 according to Zhong et al., 2017, sample X28-4 to X28-9, H9-1 and H9-2 according to Cao et al., 2018, sample X28-1 and X28-2 according to Shao et al., 2016; Heavy minerals sample information: sample ZD01, ZD02, XG01 to XG04, XL01, XL02, XY01, XY02, XZ01, XZ02, XB01, and XN01 to XN06 according to Xiang et al., 2011; Elemental geochemistry sample information: sample ODP1148, XJ33 according to Shao et al., 2008, sample PY33, H9 according to Shao et al., 2013.

depression structures. Since the Late Miocene, the XTP eventually evolved into a west-high–east-low landform, which ended the drastic topographical and geomorphological reversion in this region (Zhang et al., 2010).

2.3 The Pearl River Mouth Basin

Since the Early Cenozoic, the South China continental margin has undergone long-term extension processes, leading to the formation of a series of grabens and faults along the border of SE South China and the northern SCS areas (Li and Li, 2007). As a representative faulted basin, the Pearl River Mouth Basin (PRMB) accumulated a thick Cenozoic sedimentary succession (Pang et al., 2009; Zhou et al., 2009; Zhang et al., 2019) overlying a Mesozoic basement of granites and sedimentary rocks (Li et al., 2012; Zhu et al., 2021). The oldest Cenozoic sediment sequences in the PRMB are of Early–Middle Eocene age (Fig. 2; Zhang et al., 2007, Zhang, 2010; Mi et al., 2018), interbedded with volcanoclastic strata (Wang et al., 2017). With the onset of the SCS spreading at ca. 34 Ma (Li et al., 2014; Huang et al., 2019), the PRMB was dominated by transitional sandstones during the Late Oligocene, and truncated by a sedimentary discontinuity of 2.5–3 Ma (Zhao, 2005; Jian et al., 2019). This marks the transition from rifting into depression. Since the Miocene, the PRMB has developed large-scale deltas and deep-water submarine fans, while patches of carbonate platforms were initiated in the submerging highlands (Wu, 2014).

3 Source-to-sink Analyses of the Pearl River System

Detrital zircon U-Pb dating has played an increasingly important part in provenance evolutionary analyses in recent years (Gehrels and Dickinson, 1995; Cao et al., 2015). However, due to the complexity of the actual ‘source-to-sink’ system, this method can be better utilized combined with elemental geochemistry, isotopic geochemistry, heavy mineral analysis, clay mineral analysis and other techniques (Fedo et al., 2003; Cao et al., 2018; Cui et al., 2019). This study aims to provide a comprehensive insight into the formation and evolution of the Pearl River based on detrital zircon U-Pb ages, heavy mineral assemblages and elemental geochemical variations.

3.1 Detrital zircon U-Pb age distribution patterns

In order to achieve a better coverage and representability for the complexity of the geological structure and bedrock types in the South China continent, our studied samples were mainly collected from different branches of the Pearl River in order to reflect lithological characteristics of the parent rocks and to minimize possible misinterpretations caused by the downstream mixing effect. The Pearl River Delta in the Zhu-I Depression, on the other hand, was sampled to conduct a source-to-sink comparative analysis.

3.1.1 U-Pb age spectra of Pearl River tributaries

Detrital zircon U-Pb age histogram and Kernel Density

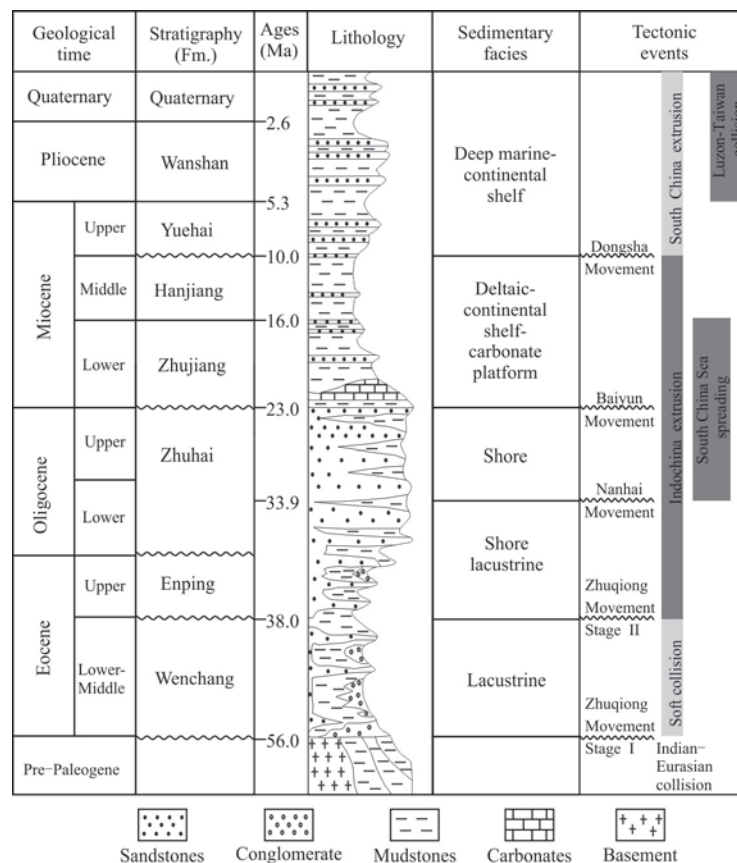


Fig. 2. Schematic stratigraphic column of the northern Pearl River Mouth Basin (modified from Shi et al., 2014; Mi et al., 2019).

Estimation (KDE) plots (Fig. 3) show clear distinctions between the different Pearl River tributaries. For example, in the upper reaches, represented by the Beipan River (sample R1) and the Nanpan River (sample R2), the results feature prominent Indosinian peaks (ca. 380–200 Ma) clustering at ca. 275 Ma and ca. 270 Ma, respectively, plus also discernible Caledonian (ca. 600–400 Ma) and Jinningian (ca. 1200–700 Ma) peaks. At the confluence flow of the Beipan and Nanpan rivers, in the Hongshui River samples (005 and R3) the U-Pb date exhibits a typical combination pattern of these two rivers. The Liu River samples (R6, 102 and 105) show a dominant Jinningian cluster (ca. 1200–700 Ma), with scattered zircons of other ages. The You River samples (R4 and 906) mainly comprise Indosinian (ca. 380–200 Ma) and Caledonian (ca. 600–400 Ma) populations, clustering around 270 Ma and 465 Ma, respectively. The Zuo River samples (R5 and 903) are also dominated by clear Indosinian (ca. 380–200 Ma) peaks centralized at ca. 250 Ma, accompanied by some Lvliangian zircons (ca. 2000–1800 Ma). Noteworthy is that the Caledonian peak in the Zuo River is less significant compared to that of the You River. Not surprisingly, the U-Pb age spectrum of the Yu River (sample 304) and its upstream Zuo and You rivers are similar. The Gui River samples (R8 and 501) are dominated by Caledonian (600–400 Ma) and Jinningian (1200–700 Ma) clusters, centralized at ca. 555 Ma and ca. 970 Ma, respectively, in addition to a small group of

Archean zircons, which reflect the South China basement. On the other hand, the Bei River samples (S20, S21 and R10) display an apparent Yanshanian (ca. 200–80 Ma) peak and a secondary Caledonian (ca. 500–300 Ma) peak. Similarly, the Dong River samples (R12 and P1) also display Yanshanian (ca. 200–80 Ma) and Caledonian (500–300 Ma) clusters, with age peaks centralized around 100 Ma, 160 Ma, 240 Ma, and 450 Ma (Figs. 3, 4).

As the main western branch of the Pearl River, the Xi River lower reaches can be grouped into the upper, middle and lower sampling sections. The upper section (sample R7), including the Hongshui River upper reaches of the Nanpan and Beipan rivers, the Yu River upper reaches of the You and Zuo rivers, as well as the Liu River, is characterized by a mixed U-Pb age pattern of these tributaries. The middle section (samples P7 and R9) also represents the features of the aforementioned tributaries plus the Gui River. The lower section (samples P4 and R11) also includes all sediments from the upstream as well as from the Bei River, and reflects further mixing of different provenances. Finally, the modern Pearl River estuary sample (S2-5) shows a mixed provenance pattern of all tributaries, including the Dong River.

3.1.2 Source area division and basinal sedimentary responses

Potential source areas are determined by grouping samples with similar age combination and by linking them

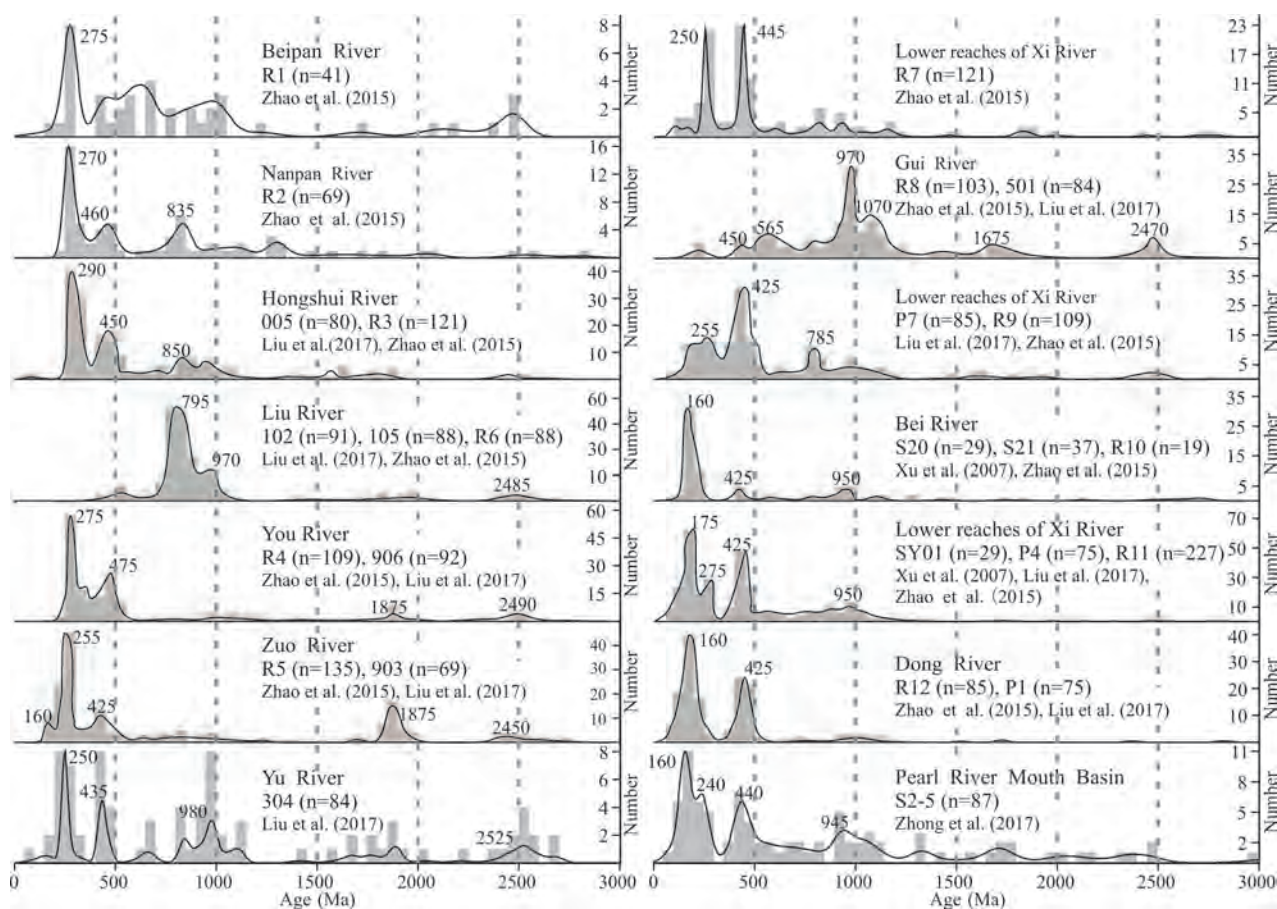


Fig. 3. Detrital zircon U-Pb age histograms and Kernel Density Estimation (KDE) of modern sediments in the Pearl River tributaries and estuary.

with regional lithological distribution and corresponding magmatic events. Therefore, the Pearl River fluvial system can be divided into seven provenances (Fig. 4), including the Hongshui River upstream (UHRP), Liu River (LRP), You River (YRP), Zuo River (ZRP), Gui River (GRP), Bei River (BRP) and Dong River (DRP) provenances.

UHRP is (samples R1 and R2) characterized by an Indosinian (ca. 380–200 Ma) cluster in addition to a small group of Proterozoic ages (Fig. 4). The middle reaches of the Pearl River are mainly the Liu and Gui rivers, which flow through the western Jiangnan Orogenic Belt and Paleozoic strata (Fig. 1). LRP (samples R6, 102 and 105) is characterized basically by a single peak of ca. 790 Ma (Fig. 4), whereas GRP (samples R8 and 501) features a dominant ca. 970 Ma age group and several small clusters of Mesozoic and Late Neoproterozoic–Early Paleozoic zircons. The upper reaches of the Yu River are mainly composed of the You and Zuo rivers, which flow southeast through the Youjiang Basin with intensive Upper Paleozoic carbonate rocks and Triassic deep-sea turbidites (Fig. 1). Accordingly, YRP (samples R4 and 906) mainly displays Caledonian and Hercynian ages, which are centralized at ca. 465 Ma and 270 Ma, respectively (Fig. 4). By contrast, the adjacent ZRP (samples R5 and 903) shows less significant Caledonian ages but more significant Paleoproterozoic, Indosinian (250–200 Ma) and early Yanshanian ages (Fig. 4). Presence of these Mesozoic age groups are closely related to the Jurassic–Cretaceous strata and Indosinian granites outcropping along the Shiwandashan orogenic belt (Fig. 1). The distribution patterns of lithology in the mainstream of the Xi River lower reaches and East China (Fig. 1) determine the contribution of different provenances. As indicated by sample R11 located near the Xi River estuary mouth, the provenance of the Xi River lower reaches highlights the combination of both BRP and DRP, with U-Pb age spectra markedly different from those of others from the Xi River lower reaches (samples P7, R9, SY01 and P4), but comparable to those of the Dong River samples (Figs. 3, 4). Both the Bei River and the Dong River flowed through the eastern Cathaysia landmass and erode bedrocks of Yanshanian (ca. 190–70 Ma) granites (Fig. 1). Thus, DRP (samples P1 and R12) shows two dominant peaks of ca. 160 Ma and ca. 450 Ma (Fig. 4), which are distinct from the overall U-Pb pattern of BRP. The Bei River upper reaches (sample S20) and lower reaches (samples S21 and R10) are slightly different, but they both lack Caledonian (ca. 500–400 Ma) and late Yanshanian age groups (Fig. 4).

The detrital zircon U-Pb age combination patterns (Shao et al., 2016; Cao et al., 2018) in different stratigraphic units of boreholes X28 and H9 from the Pearl River Mouth Basin (the ‘sink’ area) are largely comparable between the upper and lower samples of the same strata, with minor variations only in the proportion of their individual age peaks. Therefore, we combined samples of the same stratigraphic strata into a single analysis in our study (Fig. 4). Sample S2-5 from the surface sediment near the Pearl River estuary, on the other hand, was used as a modern representative in the source-to-sink analysis (Zhong et al., 2017).

Detrital zircon U-Pb age spectra show that the Lower and Upper Oligocene basal samples are comparable in their age combination with a dominant Yanshanian peak and secondary Indosinian and Caledonian peaks (Fig. 4). However, differing from the Lower Oligocene samples, the Upper Oligocene samples feature more concentrated age clusters in their width and steepness, possibly indicating increasing sedimentary input as a result of the westward expansion of the drainage basin. In addition to the aforementioned age peaks, the Lower Miocene basal samples begin to show apparent Jinningian (ca. 945 Ma) and other older age zircon populations. Moreover, the Yanshanian, Indosinian, and Caledonian peaks all changed significantly in their relative percentages and centralized ages (Fig. 4). In particular, the Caledonian and older age zircons (ca. 3000–500 Ma) increased abruptly from the Oligocene to Miocene, and continue to gain higher contents in the modern Pearl River estuary sediments.

Therefore, all the zircon age evidence indicates that the Pearl River fluvial system experienced drastic changes across the Oligocene/Miocene boundary, marking the most significant watershed change in its evolutionary history. After the Miocene, the Pearl River fluvial network developed into nearly its modern scale, as indicated by relatively stable U-Pb age spectra through to the present.

3.2 Heavy minerals

A heavy mineral assemblage combination is one of the robust proxies for reflecting potential provenances (Morton and Hallsworth, 1999). As shown in Figure 5a, the Apatite-Tourmaline index (ATi) and Gamet-Zircon index (GZi) ratios in the Pearl River tributaries differ significantly. Both the Dong River and the Bei River have extremely low ATi ratios whereas their GZi values vary greatly between 10 and 80, implying that the eroded parent rocks were predominantly acidic magmatic rocks and a small amount of low-degree contact metamorphic rocks. The Xi River upper reaches, including the Nanpan River, the Beipan River, the Hongshui River, and the middle reaches of the You River, have ATi values ranging broadly from 20 to 100, and extremely low GZi ratios, indicating that the parent bedrocks were rich with low-degree contact metamorphic rocks and basic magmatic bodies. The Xi River middle reaches, including the Zuo River, the Gui River, and the Liu River, commonly display negligible ATi and GZi values, indicating mainly clastic and carbonate parent rocks, which had undergone strong weathering processes and lacked stable heavy mineral assemblages (Xiang et al., 2011).

From the Oligocene to the Miocene, heavy minerals of the northern SCS sediments changed greatly, with an overall increase in compositional maturity likely because of a larger sedimentary input from further source areas (Fig. 5b). In the Lower Oligocene samples, for example, unstable minerals including apatites, epidotes, and garnets are relatively high in content (Fig. 5b), implying relatively short-distance transport of granite and metamorphic parental rocks. Upper Oligocene samples, on the other hand, contain more stable minerals like zircons, garnets and tourmalines, while their apatite and epidote contents decrease significantly (Fig. 5b). These heavy mineral

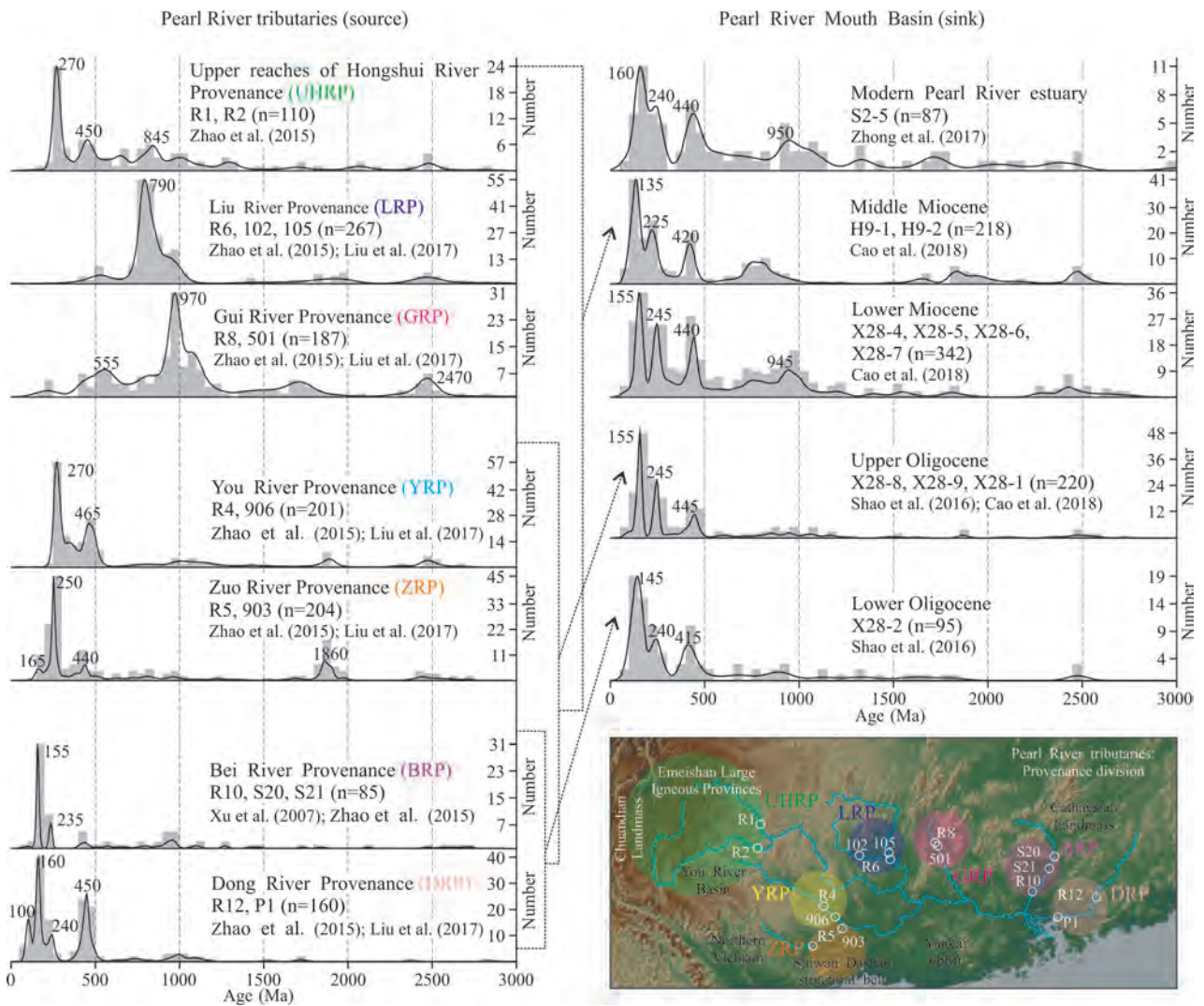


Fig. 4. Comparative analysis of the Pearl River drainages ('source') and the Pearl River Mouth Basin ('sink') areas (n indicates the number of zircons analyzed).

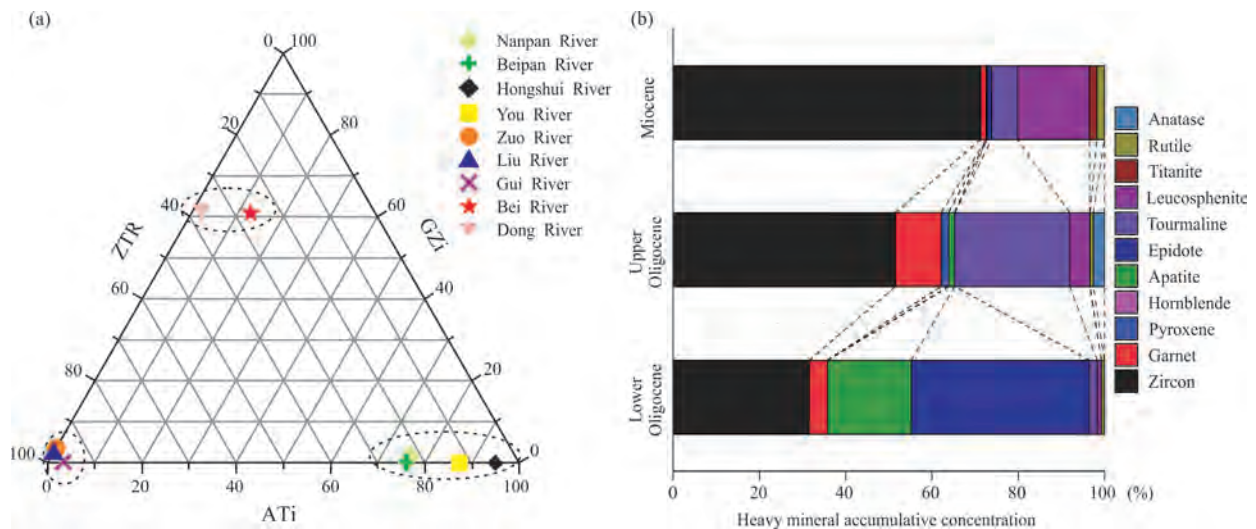


Fig. 5. Heavy mineral assemblage plots.

(a) ATi and GZi indexes for Pearl River heavy mineral components; (b) heavy mineral variations of H10, northern South China Sea.

changes strongly indicate the accumulation of Mesozoic granite, skarn metamorphic rocks and recycled sedimentary rocks during the Late Oligocene when the Pearl River drainage basin expanded further into the South China inland areas. The Miocene samples contain comparatively fewer types of heavy minerals, mainly such stable minerals as zircons (about 70%) and leucosphenites (about 15%), as well as <10% other heavy minerals (Fig. 5b). This evidence suggests that the Pearl River then most likely reached much further inland, resulting in a heavy mineral assemblage dominated by stable components like the zircon and leucosphenite due to long-distance transport.

3.3 Elemental geochemistry

Elemental geochemistry is of great significance in revealing the sedimentary composition variations in the northern SCS under the control from the Pearl River evolution. In general, CaO increase and Al₂O₃ decrease suggest more input of carbonate rocks and less input of silicates from parental source areas. The Chemical Index of Alteration (CIA) is a useful parameter widely used to measure the intensity of the chemical weathering processes, as higher CIA is often linked to greater intensity of chemical weathering. However, this parameter is also affected by the parent rock types, for example, a low CIA might be due to a high proportion of carbonate parent rocks.

Samples of ODP Site 1148 and boreholes PY33, XJ33 and H9 all show large elemental geochemistry variations across the Oligocene/Miocene boundary (ca. 23.8 Ma) (Fig. 6), as marked by CaO significantly increasing and Al₂O₃ decreasing during this time. The CIA index also displays an abrupt change around the stratigraphic boundary followed by a gradual decreasing trend upward. Apparently, the northern SCS was dominated by silicate sediments during the Oligocene, before being replaced by carbonate sediments during the Miocene. Combined with the eroded bedrocks discussed above, these elemental changes imply that the main sediment load transported by the Pearl River underwent a transition from the silicate rocks of coastal South China before the Miocene to the carbonate rocks of the Yunnan–Guizhou Plateau since the Miocene (Shao et al., 2013).

4 Coupling Relationship between the Pearl River and East Asian Topographic Evolution

During the Early Oligocene, the XTP might have partly

experienced an uplifting process within the proto-Mount Gangdise area (Fig. 7a). This uplift, however, was likely a regional tectonic event that was too weak to greatly influence the evolution of the eastern fluvial network and Asian Monsoon system. At the same time, the northern SCS started to form deltas containing dominant Yanshanian zircons and secondary Indosinian and Caledonian zircon populations. The U-Pb age spectra of the northern SCS show consistency with those of the Bei River and the Dong River (Fig. 4). In addition, the Pearl River tributaries were composed of abundant unstable heavy mineral assemblages (Fig. 5b), which was likely influenced from the silicate source areas as implied by element geochemical indicators. Therefore, we infer that the Pearl River was fairly constrained during the Early Oligocene and mainly eroded the Mesozoic granites along the coastal South China area (Fig. 7b).

During the Late Oligocene, the central, northern and southern parts of the XTP all experienced accelerated uplift (Fig. 7a), which not only resulted in more significant changes in regional topography and geomorphology compared to the Early Oligocene (Bluisik et al., 2001; Specier et al., 2003; Rowley and Currie 2006; Wang et al., 2008; Deng et al., 2011), but also had greater impact in shaping the eastern river systems. Although the U–Pb age spectra between the Lower and Upper Oligocene sediments in the Pearl River Mouth Basin are similar, their distinctions in heavy mineral assemblages imply longer-distance sedimentary transport. Sedimentary composition changes and depositional input increase were likely caused by the formation and/or expansion of the Zuo River, the You River and a part of the Hongshui River drainages in the Pearl River system. During the Late Oligocene, the Pearl River network developed more tributaries and its catchment expanded to the wider inland area of South China (Fig. 7c).

Many scholars considered that the XTP Uplift occurred mainly in the Early–Middle Miocene (Yin, 2006; Royden et al., 2008; Molnar and Stock, 2009; Xu et al., 2013), thus the overall geomorphic pattern of the XTP was most likely formed at least during this time. The general geomorphology may have remained stable throughout this interval although local uplifting might have occasionally taken place since the Late Miocene (Lu and Guo, 2013). During the Early Miocene, the Pearl River Mouth Basin was characterized by major shelf delta deposits (Fig. 2) with a large number of Proterozoic and Archean zircons

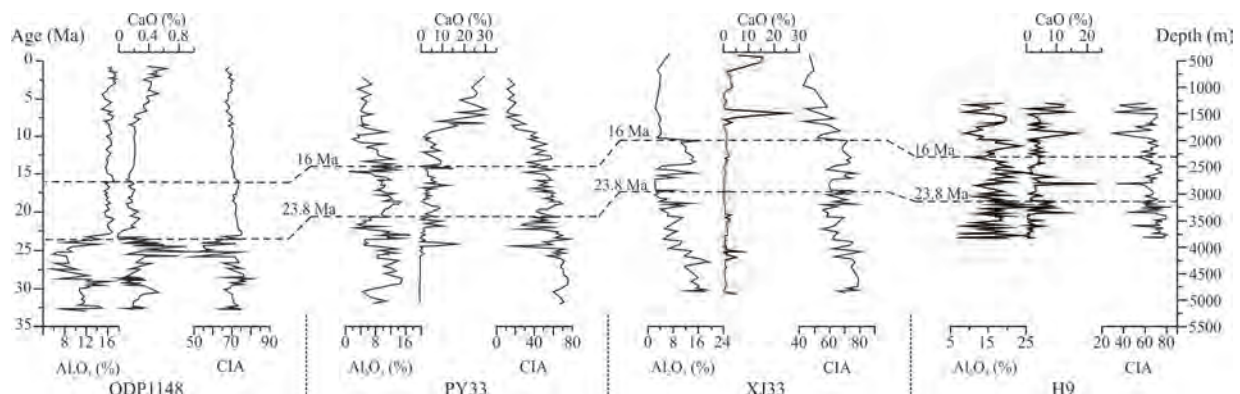


Fig. 6. Elemental geochemistry variations of the northern South China Sea borehole samples (modified from Shao et al., 2008, 2013).

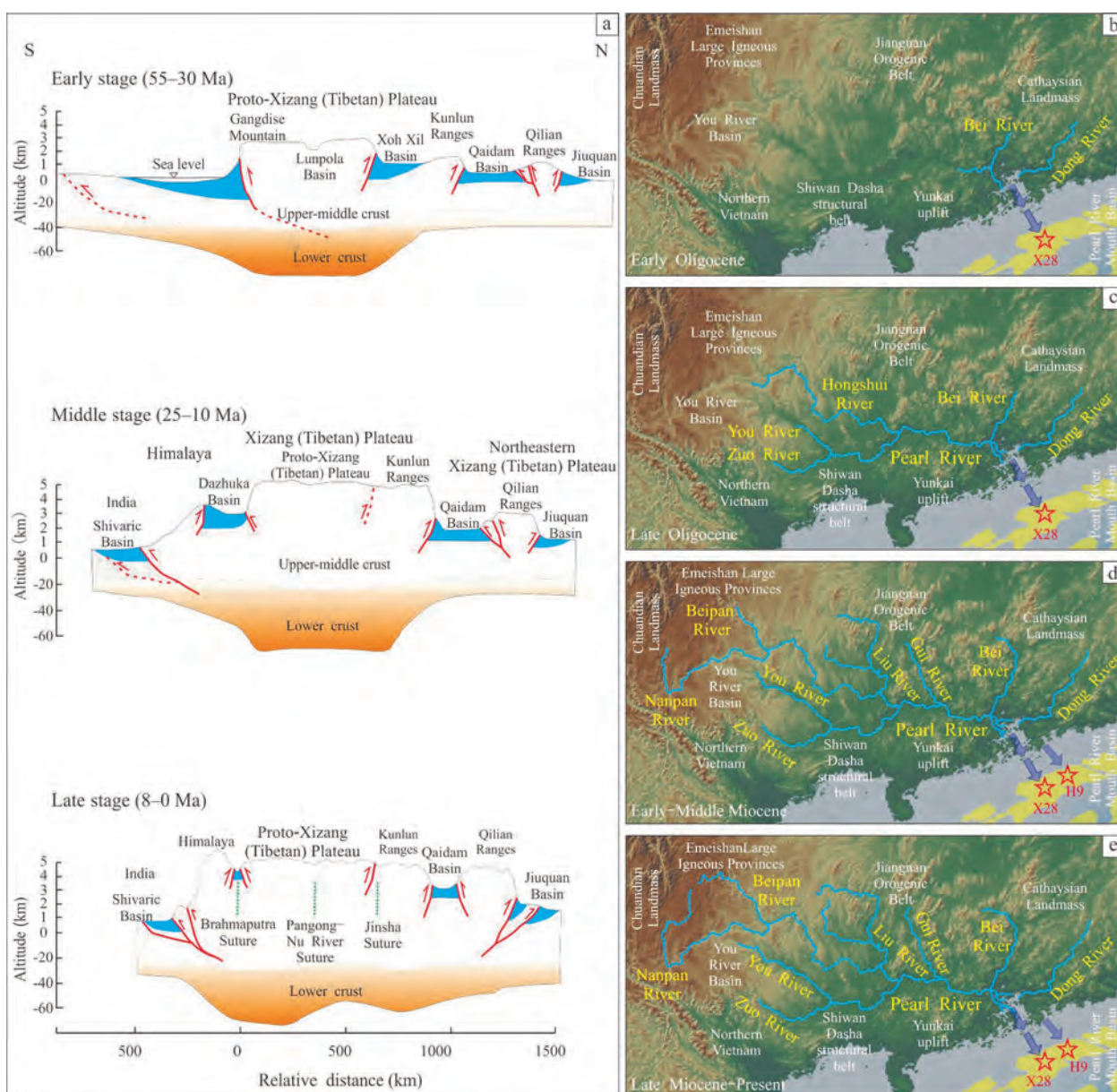


Fig. 7. Multi-stage evolution of the Xizang (Tibetan) Plateau (modified from Wang et al. 2008; Fang, 2017). (a) Sketch map of the Cenozoic Xizang (Tibetan) Uplift; (b-e) schematic reconstructions for the Pearl River stepwise evolution.

present, indicating an abrupt expansion of the Pearl River into the Cathaysia hinterland and the Lower Yangtze region. During this period, the Gui River, the Liu River and the You River were included in the Pearl River system, in addition to the Nanpan and Beipan rivers of the Hongshui River upper reaches. Changes in the Pearl River tributary organization were completely coupled with the XTP Uplift (Fig. 7d). Similarly, as confirmed by elemental geochemistry indicators, the Pearl River started to erode carbonate rock source areas during the Early Miocene, while headwater erosion within the Pearl River upstream tributaries still occurred into the Late Miocene and since then subsequently developed into the present continental-scale river system (Fig. 7e).

5 Paleoenvironmental Responses to the East Asian Topographic Reversion

The multi-stage uplift of the XTP led to the complete reversion of the East Asian topography during the Cenozoic. In turn, it not only reshaped the paleogeography and paleogeomorphology, but also drastically affected the atmosphere, hydrosphere, and biosphere in the region. In particular, the East Asian topographic reversion has played a consistent influence on the formation of large river systems, development and strengthening of the monsoon climate, the generation of loess sediments, and changes in the marginal basin sedimentary composition. For a unique earth system perspective, a comprehensive understanding of their interactions over time necessarily requires

integrated analyses on their roles.

The origination of many large rivers in Asia from the XTP itself strongly indicates the close relationship between the evolution of the large fluvial systems and the XTP Uplift. Under the control of this geomorphological change, for example, the birth and development of the Yangtze River marked by the connection of the Three Gorges, can be viewed as an optimal indicator for the initial establishment of the East Asian west-high–east-low landform close to the Oligocene/Miocene boundary (Zheng et al., 2013). In addition, the capture event of the Jinsha River upper reaches by the Yangtze might also have occurred during this period (Zheng et al., 2017). These discoveries show complete consistence with the contemporaneous abrupt provenance changes in the Pearl River network. Therefore, all these factors point to the strong impact of the East Asian topographic evolution on regional fluvial transporting systems.

Previous studies found the controlling role played by the XTP Uplift on the formation of the East Asian monsoon climate and arid zones within Central Asia. Cenozoic vegetation changes imply that arid zones of the Asian hinterland were possibly formed around the Late Oligocene/Early Miocene boundary (Sun and Wang, 2005). This timing coincided with the transition from a planetary to a monsoonal climate system in East Asia (Wang, 1990; Liu et al., 1998; Guo et al., 2008). Similar paleoenvironmental changes were also revealed in the records of the long-term loess sediments (Rea et al., 1998; Guo et al., 2002).

To sum up, East Asian geomorphology started to develop a west-high–east-low pattern during the Late Oligocene–Early Miocene due to the major uplift of the XTP. Prominent river systems, including the Pearl River and the Yangtze River, all started to flow eastward. Concomitantly, the East Asian topographic reversion also played the most important controlling role in the changes of the Asian monsoon system and the inland arid zones.

6 Conclusions

Prior to the Eocene, the Pearl River Mouth Basin mainly accumulated sediments from local paleo-uplifts under the influence of the general west-low–east-high topography without a meaningful Pearl River waterway. It was not until the close to the Eocene/Oligocene boundary that the Pearl River first developed, coinciding with the onset of the SCS spreading at ca. 34 Ma. During the Early Oligocene, the Pearl River remained as a relatively limited catchment, mainly eroding granite and other magmatic rocks from coastal South China. During the Late Oligocene, the Pearl River initially expanded westward into the frontal margin of the Yunnan–Guizhou Plateau. Since the Early Miocene, the Pearl River has reached further into the Yangtze Block and Cathaysian hinterland. The stepwise expansion of the Pearl River network was closely linked to the Xizang (Tibetan) Uplift (ca. 25–20 Ma), which marked the end of East Asian landform reversion into a west-high–east-low pattern. Since the Late Miocene, the Pearl River remained relatively stable in approaching the modern continental scale. In addition to

its influence on river development and the ‘source to sink’ sedimentary process, this prominent landform reorganization is also of great significance in understanding the coupled relationship between the Indian–Eurasian plate collision, the Xizang (Tibetan) Uplift and the expansion of marginal oceans in the Asia-Pacific region.

We conclude that the East Asian continental landscape and most of drainage underwent critical reversion into east-tilting, or east-flowing networks across the Oligocene/Miocene boundary.

Acknowledgements

We thank the China National Offshore Oil Corporation (CNOOC) for providing geological data and borehole samples from the northern SCS. Constructive and careful reviews by two referees are gratefully appreciated. This work was supported by the National Natural Science Foundation of China (grant Nos. 42076066, 92055203 and 41874076), the National Science and Technology Major Project of China (grant No. 2016ZX05026004-002), the National Key Research and Development Program of China (grant No. 2018YFE0202400).

Manuscript received May 22, 2020

accepted Nov. 7, 2020

associate EIC: ZHANG Gongcheng

edited by Susan TURNER and FANG Xiang

References

- Blisniuk, P.M., Hacker, B.R., Glodny, J., Ratschbacher, L., Bi, S.W., Wu, Z.H., McWilliams, M.O., and Calvert, A., 2001. Normal faulting in central Tibet since at least 13.5 Myr ago. *Nature*, 412(6847): 628–632.
- Cao, L.C., Jiang, T., Wang, Z.F., Zhang, Y.Z., and Sun, H., 2015. Provenance of Upper Miocene sediments in the Yinggehai and Qiongdongnan basins, northwestern South China Sea: Evidence from REE, heavy minerals and zircon U–Pb ages. *Marine Geology*, 361: 136–146.
- Cao, L.C., Shao, L., Qiao, P.J., Zhao, Z.G., and van Hinsbergen, D.J.J., 2018. Early Miocene birth of modern Pearl River recorded low-relief, high-elevation surface formation of SE Tibetan Plateau. *Earth and Planetary Science Letters*, 496: 120–131.
- Clark, M.K., and Royden, L.H., 2000. Topographic ooze: Building the eastern margin of Tibet by lower crustal flow. *Geology*, 28(8): 703–706.
- Clark, M.K., Schoenbohm, L.M., Royden, L.H., Whipple, K.X., Burchfiel, B.C., Zhang, X., Tang, W., Wang, E., and Chen, L., 2004. Surface uplift, tectonics, and erosion of eastern Tibet from large-scale drainage patterns. *Tectonics*, 23: TC1006.
- Clift, P.D., Hodges, K.V., Heslop, D., Hannigan, R., Van Long, H., and Calves, G., 2008. Correlation of Himalayan exhumation rates and Asian monsoon intensity. *Nature Geoscience*, 1: 875–880.
- Clift, P., Lee, J.I., Clark, M.K., and Blusztajn, J., 2002. Erosional response of South China to arc rifting and monsoonal strengthening; a record from the South China Sea. *Marine Geology*, 184(3–4): 207–226.
- Cui, Y.C., Shao, L., Qiao, P.J., Pei, J.X., Zhang, D.J., and Tran, H., 2019. Upper Miocene–Pliocene provenance evolution of the Central Canyon in northwestern South China Sea. *Marine Geophysical Research*, 40: 223–235.
- Deng, T., Wang, S.Q., Xie, G.P., Li, Q., Hou, S.K., and Sun, B.Y., 2011. A mammalian fossil from the Dingqing Formation in the Lunpola Basin, northern Tibet, and its relevance to age and paleo-altimetry. *Chinese Science Bulletin*, 56(34): 2873–

- 2880 (in Chinese with English Abstract).
- Fang, X.M., 2017. Phased uplift of the Tibetan Plateau. *Science and Technology Review*, 35(06): 42–50 (in Chinese with English Abstract).
- Fedo, C.M., Sircombe, K.N., and Rainbird, R.H., 2003. Detrital zircon analysis of the sedimentary record. *Reviews in Mineralogy and Geochemistry*, 53(1): 277–303.
- Gehrels, G.E., and Dickinson, W.R., 1995. Detrital zircon provenance of Cambrian to Triassic miogeoclinal and eugeoclinal strata in Nevada. *American Journal of Science*, 295(1): 18–48.
- Guo, Z.T., Ruddiman, W.F., Hao, Q.Z., Wu, H.B., Qiao, Y.S., Zhu, R.X., Peng, S.Z., Wei, J.J., Yuan, B.Y., and Liu, T.S., 2002. Onset of Asian desertification by 22 Myr ago inferred from loess deposits in China. *Nature*, 416: 159–163.
- Guo, Z.T., Sun, B., Zhang, Z.S., Peng, S.Z., and Wei, J.J., 2008. A major reorganization of Asian climate regime by the early Miocene. *Climate of the Past*, 4: 153–174.
- Huang, C.Y., Wang, P.X., Yu, M.M., You, C.F., Liu, C.S., Zhao, X.X., Shao, L., Zhong, G.F., and Graciano, P.Y.Jr., 2019. Potential role of strike-slip faults in opening up the South China Sea. *National Science Review*, 5(6): 891–901.
- Jian, Z.M., Jin, H.Y., Kaminski, M.A., Ferreira, F., Li, B.H., and Yu, P.S., 2019. Discovery of the marine Eocene in the northern South China Sea. *National Science Review*, 6(5): 881–885.
- Li, C.F., Xu, X., Lin, J., Sun, Z., Zhu, J., Yao, Y., Zhao, X.X., Liu, Q.S., Kulhanek, D.K., Wang, J., Song, T.R., Zhao, J.F., Qiu, N., Guan, Y.X., Zhou, Z.Y., Williams, T., Bao, R., Briaies, A., Brown, E.A., Chen, Y.F., Clift, P.D., Colwell, F.S., Dadd, K.A., Ding, W.W., Almeida, I.H., Huang, X.-L., Hyun, S., Jiang, T., Koppers, A.A.P., Li, Q.Y., Liu, C.L., Liu, Z.F., Nagai, R.H., Peleo-Alampay, A., Su, X., Tejada, M.L.G., Trinh, H.S., Yeh, Y.-C., Zhang, C.-L., Zhang, F., and Zhang, G.-L., 2014. Ages and magnetic structures of the South China Sea constrained by deep tow magnetic surveys and IODP Expedition 349. *Geochemistry, Geophysics, Geosystems*, 15 (12): 4958–4983.
- Li, L.Y., Chang H., Guan C., Liu, W.G., and Cao, Y.N., 2020. Early Miocene Paleoelevation of the Tuotuohe Basin, Central-Northern Tibetan Plateau and its Tectonic Implications. *Acta Geologica Sinica (English Edition)*, 94(5): 1364–1372.
- Li, X.H., Wei, G.J., Shao, L., Liu, Y., Liang, X.R., Jian, Z.M., Sun, M., and Wang, P.X., 2003. Geochemical and Nd isotopic variations in sediments of the South China Sea: a response to Cenozoic tectonism in SE Asia. *Earth and Planetary Science Letters*, 211(3–4): 207–220.
- Li, X.H., and Li, X.H., 2007. Formation of the 1300-km-wide intracontinental orogen and postorogenic magmatic province in Mesozoic South China: A flat-slab subduction model. *Geology*, 35(2): 179–182.
- Li, X.X., Li, X.H., Chuang, S.L., Lo, C.H., Xu, X.S., and Li, W.X., 2012. Magmatic switch-on and switch-off along the South China continental margin since the Permian: Transition from an Andean-type to a Western Pacific-type plate boundary. *Tectonophysics*, 532–535: 271–290.
- Liu, C., Clift, P.D., Carter, A., Böning, P., Hu, Z.C., Sun, Z., and Pahnke, K., 2017. Controls on modern erosion and the development of the Pearl River drainage in the late Paleogene. *Marine Geology*, 394: 52–68.
- Liu, D.S., Zheng, M.P., and Guo, Z.T., 1998. Initiation and evolution of the Asian monsoon system timely coupled with the ice-sheet growth and the tectonic movements in Asia. *Quaternary Sciences*, 3:194–204 (in Chinese with English Abstract).
- Lu, H.Y., and Guo, Z.T., 2013. Evolution of the Monsoon and dry climate in East Asia during Late Cenozoic: A review. *Science China: Earth Sciences*, 43(12): 1907–1918 (in Chinese with English Abstract).
- Molnar, P., and Stock, J.M., 2009. Slowing of India's convergence with Eurasia since 20 Ma and its implications for Tibetan mantle dynamics. *Tectonics*, 28: TC3001.
- Morton, A.C., and Hallsworth, C.R., 1999. Processes controlling the composition of heavy mineral assemblages in sandstones. *Sedimentary geology*, 124(1–4): 3–29.
- Mi, L.J., Zhang, Z.T., Pang, X., Liu, J., Zhang, B., Zhao, Q., and Feng, X., 2018. Main controlling factors of hydrocarbon accumulation in Baiyun Sag at northern continental margin of South China Sea. *Petroleum Exploration and Development*, 45 (5): 902–913 (in Chinese with English Abstract).
- Mi, L.J., Zhang, X.T., Pang, X., Zheng, J.Y., and Zhang, L.L., 2019. Formation mechanism and petroleum geology of Pearl River Mouth Basin. *Acta Petrolei Sinica*, 40(s1): 1–10 (in Chinese with English Abstract).
- Pang, X., Chen, C.M., Peng, D.J., Zhu, M., Shu, Y., He, M., Shen, J., and Liu, B.J., 2007. Sequence stratigraphy of deep-water fan system of Pearl River, South China Sea. *Earth Science Frontiers*, 14: 220–229.
- Pang, X., Chen, C.M., Zhu, M., He, M., Shen, J., Lian, S.Y., Wu, X.J., and Shao, L., 2009. Baiyun movement: a significant tectonic event on Oligocene/Miocene boundary in the northern South China Sea and its regional implications. *Journal of Earth Science*, 20(1): 49–56.
- Peng, D.J., Chen, C.M., Pang, X., Zhu, M., and Yang, F., 2004. Discovery of deep-water fan system in South China Sea. *Acta Petrolei Sinica*, 25(05): 17–23 (in Chinese with English Abstract).
- Rea, D.K., Snoeckx, H., and Joseph, L.H., 1998. Late Cenozoic eolian deposition in the North Pacific: Asian drying, Tibetan up lift and cooling of the Northern Hemisphere. *Paleoceanography*, 13: 215–224.
- Rowley, D.B., and Currie, B.S., 2006. Palaeo-altimetry of the late Eocene to Miocene Lunpola Basin, central Tibet. *Nature*, 439: 677–681.
- Rowley, D.B., and Garzione, C.N., 2007. Stable isotope-based paleoaltimetry. *Annual Review of Earth and Planetary Sciences*, 35: 463–508.
- Royden, L.H., Burchfiel, B.C., and van der Hilst, R.D., 2008. The geological evolution of the Tibetan Plateau. *Science*, 321: 1054–1058.
- Shao, L., Pang, X., Qiao, P.J., Chen, C.M., Li, Q.Y., and Miao, W.L., 2008. Sedimentary filling of the Pearl River Mouth Basin and its response to the evolution of the Pearl River. *Acta Sedimentologica Sinica*, 26(2): 179–185 (in Chinese with English Abstract).
- Shao, L., Zhao, M., Qiao, P.J., Pang, X., Wu, M.S., 2013. The characteristics of the sediment in northern South China Sea and its response to the evolution of the Pearl River. *Quaternary Sciences*, 33(4): 760–770 (in Chinese with English Abstract).
- Shao, L., Qiao, P.J., Zhao, M., Li, Q.Y., Wu, M.S., Pang, X., and Zhang, H., 2015. Depositional characteristics of the northern South China Sea in response to the evolution of the Pearl River. *Geological Society, London, Special Publications*, 429: 31–44.
- Shao, L., Cao, L.C., Pang, X., Jiang, T., Qiao, P.J., and Zhao, M., 2016. Detrital zircon provenance of the Paleogene syn-rift sediments in the northern South China Sea. *Geochemistry Geophysics Geosystems*, 17: 255–269.
- Shao, L., Meng, A.H., Li, Q.Y., Qiao, P.J., Cui, Y.C., Cao, L.C., and Chen, S.H., 2017. Detrital zircon ages and elemental characteristics of the Eocene sequence in IODP Hole U1435A: implications for rifting and environmental changes before the opening of the South China Sea. *Marine Geology*, 394: 39–51.
- Shao, L., Cui, Y.C., Statterger, K., Zhu, W.L., Qiao, P.J., and Zhao, Z.G., 2019a. Drainage control of Eocene to Miocene sedimentary records in the southeastern margin of Eurasian Plate. *Geological Society of America, Bulletin*, 131(3–4): 461–478.
- Shao, L., Cui, Y.C., Qiao, P.J., Zhu, W.L., Zhong, K., and Zhou, J.S., 2019b. Implications on the Early Cenozoic palaeogeographical reconstruction of SE Eurasian margin based on northern South China Sea palaeo-drainage system evolution. *Journal of Palaeogeography*, 21(2): 216–231 (in Chinese with English Abstract).
- Shi, H.S., He, M., Zhang, L.L., Yu, Q.H., Pang, X., Zhong, Z.H., and Liu, L.H., 2014. Hydrocarbon geology, accumulation pattern and the next exploration strategy in the eastern Pearl River Mouth basin. *China Offshore Oil and Gas*, 26(3): 11–22

- (in Chinese with English Abstract).
- Specier, R.A., Harris, N.B.W., Widdowson, M., Herman, A.B., Guo, S.X., Valdes, P.J., Wolfe, J.A., and Kelley, S.P., 2003. Constant elevation of southern Tibet over the past 15 million years. *Nature*, 421: 622–624
- Sun, X.J., and Wang, P.X., 2005. How old is the Asian monsoon system?—Palaeobotanical records from China. *Palaeogeography, Palaeoclimatology, Palaeoecology*, 222: 181–222.
- Taponnier, P., Xu, Z.Q., Roger, F., Meyer, B., Arnaud, N., Wittlinger, G., and Yang, J., 2001. Oblique stepwise rise and growth of the Tibet Plateau. *Science*, 294(5547): 1671–1677.
- Wang, C.S., Zhao, X.X., Liu, Z.F., Lippert, P.C., Graham, S.A., Coe, R.S., Yi, H., Zhu, L., Liu, S., and Li, Y., 2008. Constraints on the early uplift history of the Tibetan Plateau. *Proceedings of the National Academy of Sciences, USA*, 105: 4987–4992.
- Wang, G.C., Cao, K., Zhang, K.X., Wang, A., Liu, C., Meng, Y.N., and Xu, Y.D., 2011. Spatio-temporal framework of tectonic uplift stages of the Tibetan Plateau in Cenozoic. *Science China Earth Science*, 54: 29–44 (in Chinese with English Abstract).
- Wang, P.X., 1990. Neogene stratigraphy and paleoenvironments of China. *Palaeogeography, Palaeoclimatology Palaeoecology*, 77: 315–334.
- Wang, P.X., 2005. Cenozoic Deformation and history of sea-land interactions in Asia. *Earth Science-Journal of China University of Geosciences*, 30(1): 1–18 (in Chinese with English Abstract).
- Wang, W., Ye, J.R., Bidgoli, T., Yang, X.H., Shi, H.S., and Shu, Y., 2017. Using detrital zircon geochronology to constrain Paleogene provenance and its relationship to rifting in the Zhu 1 Depression, Pearl River Mouth Basin, South China Sea. *Geochemistry, Geophysics, Geosystems*, 18(11): 3976–3999.
- Wang, Y.F., Wang, Y.M., Xu, Q., Li, D., Zhuo, H.T., and Zhou, W., 2012. The Early-Middle Miocene submarine fan system in the Pearl River mouth Basin, South China Sea. *Petroleum Science*, 9(1): 1–9.
- Wu, S.G., Yang, Z., Wang, D.W., Lv, F.L., Ludmann, T., Fulthorpe, C., and Wang, B., 2014. Architecture, development and geological control of the Xisha carbonate platforms, northwestern South China Sea. *Marine Geology*, 350: 71–83.
- Xiang, X.H., Shao, L., Qiao, P.J., and Zhao, M., 2011. Characteristics of heavy minerals in Pearl River sediments and their implications for provenance. *Marine Geology and Quaternary Geology*, 31(06): 27–35 (in Chinese with English Abstract).
- Xu, X.S., O'Reilly, S.Y., Griffin, W.L., Wang, X.L., Pearson, N.J., and He, Z.Y., 2007. The crust of Cathaysia: Age, assembly and reworking of two terranes. *Precambrian Research*, 158: 51–78.
- Xu, Z.Q., Wang, Q., Arnaud, P., Liang, F., Qi, X., Cai, Z., Li, H., Zeng, L., and Cao, H., 2013. Orogen-parallel ductile extension and extrusion of the Greater Himalaya in the late Oligocene and Miocene. *Tectonics*, 32: 191–215.
- Yin, A., 2006. Cenozoic tectonic evolution of the Himalayan orogen as constrained by along-strike variation of structural geometry, exhumation history, and foreland sedimentation. *Earth-Science Reviews*, 76: 1–131.
- Zhang, G.C., Mi, L.J., Wu, S.G., Tao, W.X., He, S.B., and Lv, J.J., 2007. Deepwater area—the new prospecting targets of northern continental margin of South China Sea. *Acta Petrologica Sinica*, 28(2): 15–21 (in Chinese with English Abstract).
- Zhang, G.C., 2010. Tectonic evolution of deepwater area of northern continental margin in South China Sea. *Acta Petrologica Sinica*, 31(4): 528–533 (in Chinese with English Abstract).
- Zhang, G.C., Jia, Q.J., Wang, W.Y., Wang, P.J., Zhao, Q.L., Sun, M.X., Xie, X.J., Zhao, Z., and Tang, W., 2018. On tectonic framework and evolution of the South China Sea. *Chinese Journal of Geophysics*, 61(10): 4194–4215 (in Chinese with English Abstract).
- Zhang, G.C., Shao, L., Qiao, P.J., Cao, L.C., Pang, X., Zhao, Z.G., Xiang, X.H., and Cui, Y.C., 2019. Cretaceous–Paleogene sedimentary evolution of the South China Sea region: a preliminary synthesis. *Geological Journal*, 55(4): 2662–2683.
- Zhang, H., Shao, L., Zhang, G.C., Cui, Y.C., Zhao, Z.G., and Hou, Y.L., 2020. The response of Cenozoic sedimentary evolution coupled with the formation of the South China Sea. *Geological Journal*: 1–22, doi: 10.1002/gj.3856.
- Zhang, K.X., Wang, G.C., Ji, J.L., Luo, M.S., Kou, X.H., Wang, Y.M., Xu, Y.D., Chen, F.N., Chen, R.M., Song, B.W., Zhang, J.Y., and Liang, Y.P., 2010. Paleogene-Neogene stratigraphic realm and sedimentary sequence of the Qinghai-Tibet Plateau and their response to uplift of the plateau. *Science China Earth Sciences*, 53(9): 1271–1294.
- Zhang, K.X., Wang, G.C., Hong, H.L., Xu, Y.D., Wang, A., Cao, K., Luo, M.S., Ji, J.L., Xiao, G.Q., and Lin, X., 2013. The study of the Cenozoic uplift in the Tibetan Plateau: A review. *Geological Bulletin of China*, 32(01): 1–18 (in Chinese with English Abstract).
- Zhang, Q.Q., Ferguson, D.K., Mosbrugger, V., Wang, Y-F., and Li, C-S., 2012. Vegetation and climatic changes of SW China in response to the uplift of Tibetan Plateau. *Palaeogeography, Palaeoclimatology, Palaeoecology*, 363: 23–36.
- Zhao, Q.H., 2005. Late Cainozoic ostracod faunas and paleoenvironmental changes at ODP site 1148, South China Sea. *Marine Micropaleontology*, 54: 27–47.
- Zhao, M., Shao, L., and Qiao, P.J., 2015. Characteristics of detrital zircon U-Pb geochronology of the Pearl River sands and its implication on provenances. *Journal of Tongji University (Natural Science)*, 43(06): 915–923 (in Chinese with English Abstract).
- Zheng, H.B., Clift, P.D., Wang, P., Tada, R., Jia, J.T., He, M.Y., and Jourdan, F., 2013. Pre-Miocene birth of the Yangtze River. *Proceedings of National Academy of Sciences, USA*, 110(19): 7556–7561.
- Zheng, H.B., Wei, X.C., Wang, P., He, M.Y., Luo, C., and Yang, Q., 2017. Geological evolution of the Yangtze River. *Scientia Sinica Terrae*, 47: 385–393 (in Chinese with English Abstract).
- Zhong, L.F., Li, G., Yan, W., Xia, B., Feng, Y.X., Miao, L., and Zhao, J.X., 2017. Using zircon U-Pb ages to constrain the provenance and transport of heavy minerals within the northwestern shelf of the South China Sea. *Journal of Asian Earth Sciences*, 134: 176–190.
- Zhou, D., Sun, Z., Liao, J., Zhao, Z.X., He, M., Wu, X.J., and Pang, X., 2009. Filling history and post-breakup acceleration of sedimentation in Baiyun Sag, deepwater northern South China Sea. *Journal of Earth Science*, 20(1): 160–171.
- Zhu, W.L., Cui, Y.C., Shao, L., Qiao, P.J., Yu, P., Pei, J.X., Zhang, D.J., and Zhang, H., 2021. Reinterpretation of the South China Sea pre-Cenozoic basement and geodynamic implications of the SE Asia: constraints from combined geological and geophysical records. *Acta Oceanologica Sinica* (in press).

About the first author



ZHANG Hao, male, born in 1990 in Aksu City, Xinjiang Province; a PhD graduate in Tongji University. He is now interested in sedimentology and geochemistry. Email: zhanghao330@tongji.edu.cn; phone: 15801756280.

About the corresponding author



CUI Yuchi, female, born in 1991 in Baoding City, Hebei Province; a PhD graduate in both Tongji University and Curtin University. She is now interested in sedimentology and tectonics. Email: cuiyuchi@tongji.edu.cn; phone: 15301756572.

摘要

本论文着眼于南海北部地区晚中生代至新生代地层，在系统搜集和整理前人已发表研究成果和资料的基础上，结合盆地关键区域内的地震剖面和最新重-磁-震联合反演成果，对华南大陆边缘（特别是南海北部）钻井及野外露头样品开展岩石学、矿物学、地球化学、锆石 U-Pb 年代学及 Lu-Hf 同位素分析。通过“源—汇”对比综合示踪技术、构造环境判别和沉积环境沉积相的恢复，系统揭示了南海北部中生代基底特征，探讨了中生代安第斯型主动大陆边缘的时空演化规律，明确了华南大陆由主动向被动陆缘转换的时间；重点探讨了伴随新生代南海形成与沉积物搬运充填演变过程，聚焦南海西侧物源与“崑-莺-琼”大型轴向运输系统之间的关系、珠江流域的形成与发展、晚中新世中央峡谷物源演变及台湾恒春半岛增生楔浊积体形成等几个关键科学问题，发现这些沉积充填过程均受南海构造-古地理演化的控制。依据具体的“源—汇”系统重建模式，在综合考虑区域构造、古地形地貌等控制因素的基础上，本论文完成对南海地区中生代末期至新生代古水系和盆地沉积充填过程的重建工作。本研究取得的主要成果如下。

1. 南海北部基底特征新认识

南海北部基底主要由中生代岩浆岩、变质岩和沉积岩组成，并非前人猜想的那样，“南海北部基底呈现分区、分块、分带的特点，大量分布前寒武和古生代地层”：东侧以大量白垩系岩浆岩和沉积岩为主，受古太平洋和华南大陆洋—陆碰撞的影响；西侧以上侏罗统至白垩系沉积岩和变质碎屑岩为主，也是东侧大陆岩浆弧的延伸，部分基底样品呈现燕山期和加里东期的双峰年龄模式，指示附近存在包含中生代和古生代锆石年龄的潜在物源；海南岛西侧变质花岗岩具有 1.4 Ga 中元古代年龄，可能为印支和华夏地块俯冲拼合过程中，混入的古老陆块基底残余。整体而言，南海北部盆地基底实际受印支与华南陆—陆碰撞、古太平洋与华南洋—陆碰撞的共同作用。

2. 华南大陆中生代安第斯型大陆边缘发育演化过程

南海北部和东海陆架盆地基底钻井岩浆岩样品锆石 U-Pb 年代学、锆石元素地球化学和 Lu-Hf 同位素化学，以及凝灰岩、火山碎屑岩和变质沉积岩物源分析结果共同显示，大多数样品以 190–90 Ma（集中在 180–120 Ma）锆石为主，具体可见多个中生代年龄组分，峰值年龄包括 175 Ma、155 Ma、150 Ma、145 Ma、120 Ma 等。锆石晶型相对完整且地球化学属性不成熟，未经历远距离搬运，表明沿华南大陆海岸区域存在原地或相邻的岩浆岩源区；少数样品含有元古代和古生代碎屑锆石，可能来自华南大陆结晶基底；最年轻锆石年龄组分表明，华南陆缘广泛沉积白垩系（145/140–85 Ma）。

变质沉积地层还受到花岗岩岩体的侵入, 锆石 U-Pb 年龄分别为 98.4 ± 1.7 Ma、 98.6 ± 2.1 Ma、 103.3 ± 1.1 Ma、 111.8 ± 3.3 Ma、 115.4 ± 0.7 Ma、 115.1 ± 0.9 Ma 和 163.5 ± 2.1 Ma, 均为大陆弧岩浆岩, 南海样品锆石 $\epsilon\text{Hf}(t)$ 值介于 -14 到 +5.9 之间, 东海样品 $\epsilon\text{Hf}(t)$ 值变化范围较大, 介于 -24.5 到 +13.9 之间。综合华南大陆东南沿海、海南岛和台湾岛发现的大量 I 型花岗岩, 本论文明确了 190 Ma 至 90 Ma 沿华南大陆边缘发育的大型安第斯大陆岩浆弧的具体空间展布范围。

综合盆地基底与陆上岩浆记录及物源分析, 本研究认为大约 280 Ma 开始发育大陆弧, 大约 250–200 Ma 进入平板俯冲过程; 190 Ma 重新发育正常安第斯弧并持续至 90 Ma 前后, 随后岩浆活动迅速减弱并逐渐停止, 仅在南海东北部地区和东海局部地区发现年龄为 85–80 Ma 的岩浆岩和相应的碎屑锆石组分。本研究解释为俯冲带向洋壳方向跳跃, 向现今西太平洋型板块边缘转变迁移。在南海北部经历大规模裂谷作用之前, 只存在零星分散的岩浆活动 (70–60 Ma)。

3. 南海北部早新生代岩浆活动时空分布特征

南海北部早新生代地层年龄小于古新统, 并非前人认为的“存在神狐组古新统”。本研究根据碎屑锆石 U-Pb 年龄谱系, 发现大部分碎屑锆石新生代年龄集中于 63–50 Ma 以及 45–35 Ma 两个阶段, 代表了南海北部早新生代岩浆活动发育的两个主要时期。锆石微量元素构造判别图解显示, 大部分新生代锆石形成于板内环境, $\epsilon\text{Hf}(t)$ 正值可能反映来自于幔源岩浆, 与之前中生代时期的大陆弧活动陆缘环境明显不同。可以认为南海在经历拉伸和薄化作用之前, 早新生代岩浆作用活跃度不高, 整体表现为贫岩浆型大陆边缘。

4. 南海西侧物源、“崑-莺-琼”古河的发现、南海北部早新生代物源演变过程

印支半岛与华南大陆在早中生代发生剧烈的板块俯冲拼合与抬升作用, 形成了越中地区广阔的造山带, 发育了包括大量基性-超基性物质在内的古特提斯洋的残留记录, 具有独特的 Eu 元素正异常特征, 成为南海西侧沉积物源区的标志特征。

由于中生代末太平洋板块俯冲拼合与安第斯型大陆弧的发育, 华南大陆东南缘形成了近东西向展布、隆坳相间的地貌特征。南海北部地区早新生代开始经历大规模裂谷阶段, 西侧靠近印支半岛的地区以隆升剥蚀区为主, 东侧以河流相、湖泊-沼泽相为主。再此构造古地理整体格局下, 本论文发现南海西部自始新世发育一条东西向古河——“崑—莺—琼”古河, 向南海东侧珠二凹陷输送了大量基性物质; 珠一凹陷在靠近华南沿海地区接受了来自流经华南东南火成岩源区的河流搬运的碎屑物质。晚渐新世这条东西向古河的规模达到顶峰, 北侧的珠江水系也已接近现在的规模, 其搬运的物质越过番禺低隆起延伸至珠江口盆地南侧, 两大水系共同影响了南海北部的沉积格局。早中新世, 珠江流域进一步扩大, “崑—莺—琼”古河逐步萎缩, 而晚中新世以来在琼东南深水区发育的中央峡谷便是该古河的残余; 现代珠江基本形成, 全面控制珠一与珠二凹陷。

5. 琼东南盆地中央峡谷晚中新世至上新世物源演变

本论文研究采用稀土元素及碎屑锆石 U-Pb 定年等方法,对中央峡谷上中新统一上新统以及盆地基底、周围潜在源区开展“源—汇”对比分析。中央峡谷西侧样品大都呈 Eu 元素正异常,东侧样品以 Eu 元素负异常为主。同时,随着地层变年轻,呈现 Eu 元素亏损的样品数量增多。碎屑锆石年龄谱系表现出一定的时空演变规律,西侧沉积物包含较多的古生代及元古代等古老锆石,东侧以燕山期和印支期峰值为主。可以认为,中南半岛印支期的板块俯冲拼合带是琼东南盆地中央峡谷的主要源区;海南岛是另一重要源区,其在中央峡谷西侧沉积物中为次要物源,但对于中央峡谷东侧沉积物则变为主要物源。

6. 台湾恒春半岛晚中新世增生楔浊积体发育演化过程及对南海北部沉积格局重建的启示

恒春浊积体以含有大量具有一定磨圆度的正常洋壳基性砾石为特征,这些砾石的 U-Pb 年龄范围在 23.6-25.4 Ma 之间。本研究结果显示,晚中新世,源自中南半岛的“崑—莺—琼”古河和华夏地块的珠江均向南海北部深水区提供了大量陆源物质,形成数百米厚的深海砂质沉积。这些砂质沉积物以浊流形式继续自西向东搬运,并下切侵蚀沿途洋壳基性物质,最终进入马尼拉海沟堆积下来,形成包含洋壳基性砾石在内的浊积体。伴随菲律宾海板块向西北方向顺时针旋转漂移,这些浊积体被推挤、迁移并最终增生楔的形式在中更新世出露于恒春半岛地区。

关键词: 南海,“源—汇”对比,岩浆活动,中生代,新生代,古水系演变,古地理重建

目录

第 1 章 引言.....	1
1.1 研究背景和意义.....	1
1.2 选题来源.....	6
1.3 “源—汇”系统.....	7
1.4 盆山耦合.....	11
1.5 古地理恢复与板块重建.....	12
1.6 研究思路与技术路线.....	13
1.7 论文工作量.....	15
第 2 章 争议热点及关键科学问题.....	19
2.1 南海北部基底年龄组成与结构特征有待证实.....	19
2.2 华南陆缘晚中生代构造转换及其控制因素尚存争议.....	21
2.3 南海北部早新生代岩浆记录与断陷活动缺少研究.....	24
2.4 南海北部源汇体系及古地理发育演化中的争议问题.....	25
2.4.1 南海北部新生代沉积受单物源还是混合物源模式控制?	25
2.4.2 晚新生代中央峡谷源—汇系统如何演变?	27
2.4.3 恒春半岛增生楔浊积岩物质来源是什么?	29
第 3 章 材料与方法.....	32
3.1 资料收集与样品来源.....	32
3.2 元素地球化学分析.....	32
3.3 锆石 U-Pb 年代学及微量元素分析.....	32
3.4 锆石 Lu-Hf 同位素体系分析.....	34
第 4 章 南海北部基底属性及其构造指示意义.....	37
4.1 南海北部基底特征新认识.....	37
4.1.1 镜下薄片观察.....	39
4.1.2 全岩元素地球化学结果.....	41
4.1.3 锆石 U-Pb 定年结果.....	42
4.1.4 重磁震联合反演结果.....	45
4.1.5 讨论.....	46
4.1.6 初步结论.....	50
4.2 华南陆缘中生代安第斯型岩浆弧发育演化过程.....	51
4.2.1 薄片镜下观察与锆石 U-Pb 定年结果.....	57
4.2.2 锆石微量元素结果.....	72
4.2.3 Lu-Hf 同位素分析结果.....	75
4.2.4 讨论.....	78

4.2.5 初步结论	89
4.3 海南岛前寒武基底组成及对超大陆循环的指示意义：来自南海西部基底 钻井 Y1 的新启示	90
4.3.1 镜下薄片观察及锆石 U-Pb 定年结果	90
4.3.2 锆石微量元素结果	92
4.3.3 Lu-Hf 同位素结果	94
4.3.4 讨论	94
4.3.5 初步结论	97
第 5 章 南海北部早新生代岩浆活动	99
5.1 资料收集与样品来源	99
5.2 锆石 U-Pb 年代学结果	100
5.3 锆石元素地球化学结果	105
5.4 锆石 Lu-Hf 同位素体系分析结果	106
5.5 南海北部早新生代岩浆活动时空分布特征	107
第 6 章 南海物源演化特征及其指示意义	109
6.1 南海北部西侧物源与“崑-莺-琼”大型古河的发现	109
6.1.1 南海北部潜在源区特征	112
6.1.2 南海北部盆地碎屑锆石 U-Pb 年龄结果	115
6.1.3 南海北部盆地稀土元素含量及配分模式	118
6.1.4 南海北部“源—汇”系统重建	121
6.1.5 珠江流域与“崑—莺—琼”古河对南海北部沉积格局的影响	127
6.2 中央峡谷晚中新世-上新世物源演变特征	129
6.2.1 上中新统-上新统样品碎屑锆石 U-Pb 年龄	130
6.2.2 上中新统-上新统样品稀土元素含量及配分模式	130
6.2.3 中央峡谷物源演变特征	131
6.3 恒春半岛增生楔浊积岩晚中新世形成发育演化过程及对南海北部深水搬 运过程的启示	133
6.3.1 恒春半岛地层格架	134
6.3.2 野外观察结果	134
6.3.3 锆石 U-Pb 定年及元素地球化学结果	135
6.3.4 恒春半岛浊积岩基性砾石形成机制	137
6.3.5 恒春半岛浊积砂岩物源及砂体形成演化过程	138
第 7 章 南海新生代古水系古地理重建	142
7.1 晚中生代 - 古新世	142
7.2 早 - 中始新世	143
7.3 晚始新世	144
7.4 早渐新世	145
7.5 晚渐新世	145

目录

7.6 早中新世	146
第8章 结论与展望	147
8.1 结论	147
8.2 进一步工作的方向	148
参考文献	150
致谢	168
个人简历、在读期间发表的学术成果	170

第1章 引言

1.1 研究背景和意义

边缘海（marginal sea basin）又称陆缘海，位于大陆和大洋边缘，通过半岛、岛屿或岛弧与大洋分隔开来，仅以海峡或水道和正常大洋相连^[1-6]。西太平洋地区集中了全球 3/4 以上的边缘海海盆（仅有少数盆地发育在大西洋西侧），绝大多数分布于陆缘东侧，从南向北依次发育塔斯曼海、新喀里多尼亚海、南斐济海、珊瑚海、劳哈尔夫海、伍德拉克海、所罗门海、马努斯海、帕勒斯维拉海、班达海、苏拉威西海、西里伯斯海、苏禄海、西菲律宾海、南海、东海、黄海、渤海、日本海、鄂霍次克海等（图 1.1），是地质构造和海—陆相互作用最活跃的区域。边缘海盆地的发育演化通常会经历初始形成期，岛弧或陆壳拉张减薄，盆地此时尚未扩张；随后进入活跃扩张的青年发育期，新洋壳形成；之后进入壮年鼎盛期，洋壳停止扩张；最后是老年消亡期，盆地趋于俯冲消亡，例如南海和菲律宾海目前正沿 Naikai-Ryukyu-Philippine Trench 俯冲关闭^[5]。大多数边缘海盆地都很短命，其生存时限一般不超过 25 Ma（只有位于 Caribbean Sea 的 Cayman Trough 自 42 Ma 以来活跃至今），且较易受周缘构造单元的影响，其扩张轴方向可能因此发生改变。另外，边缘海盆地与正常开放大洋相比，其深水沉积速率、陆源碎屑物质供给、生产力以及生物多样性均高出一至两个数量级^[1]。

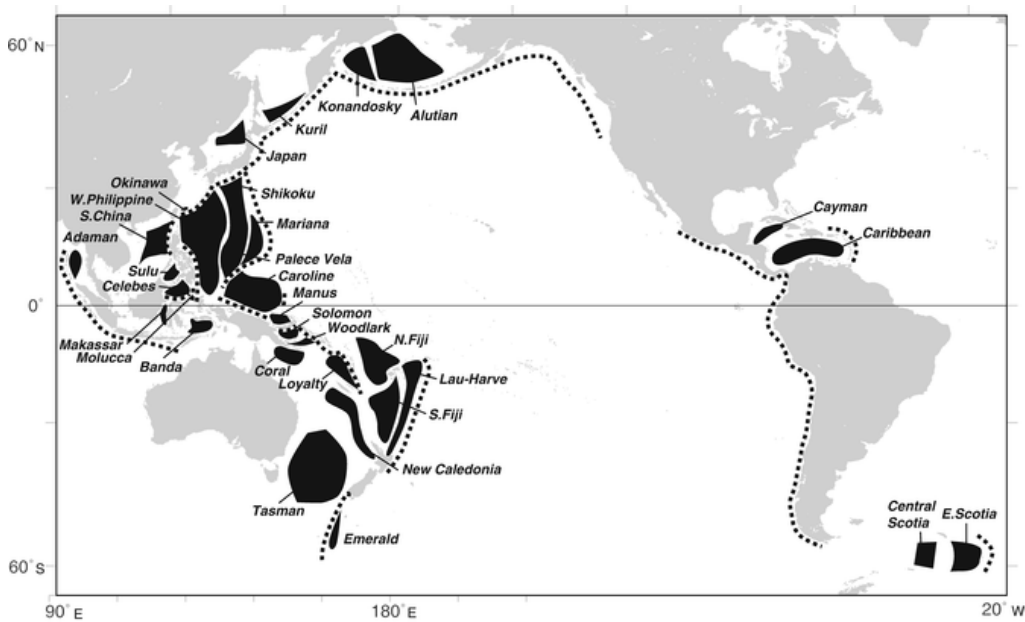


图 1.1 边缘海洋盆分布图（据 Honza, 1995^[4]）

Fig. 1.1 Geographical locations of marginal sea basins (modified from Honza (1995)^[4]).

前人根据边缘海盆地与沟—弧—盆俯冲体系的关系，将其划分成与俯冲作用有关和无关两大类^[4]。与俯冲带有关的包括弧后及捕获洋壳型盆地，前者形成于 Island arc 或 Continental arc 的弧后一侧，分布非常广泛，例如 Mariana Basin、Lau Basin（大洋型弧后盆地）和 Japan Sea Basin（大陆型弧后盆地）；后者一般通过捕获洋壳形成，例如 Tasman Basin 和 Aleutian Basin。研究表明，边缘海盆地大约形成于白垩纪晚期（80 Ma 以来），而西太平洋大规模俯冲体系至少在 180 Ma 以前便开始发育并活跃至今，其俯冲方向曾经历多次转变^[1]。虽然各个边缘海洋盆在大小、形态、年龄和深度等方面均不相同，打开机制也存在一定差异，但它们的形成都直接或间接地与西太平洋俯冲带有关。

研究者针对弧后盆地的形成机制曾提出多个扩张模式，这里可简要概括为主动和被动扩张两个基本类型^[5]（图 1.2）。其中，Slab-induced upwelling model

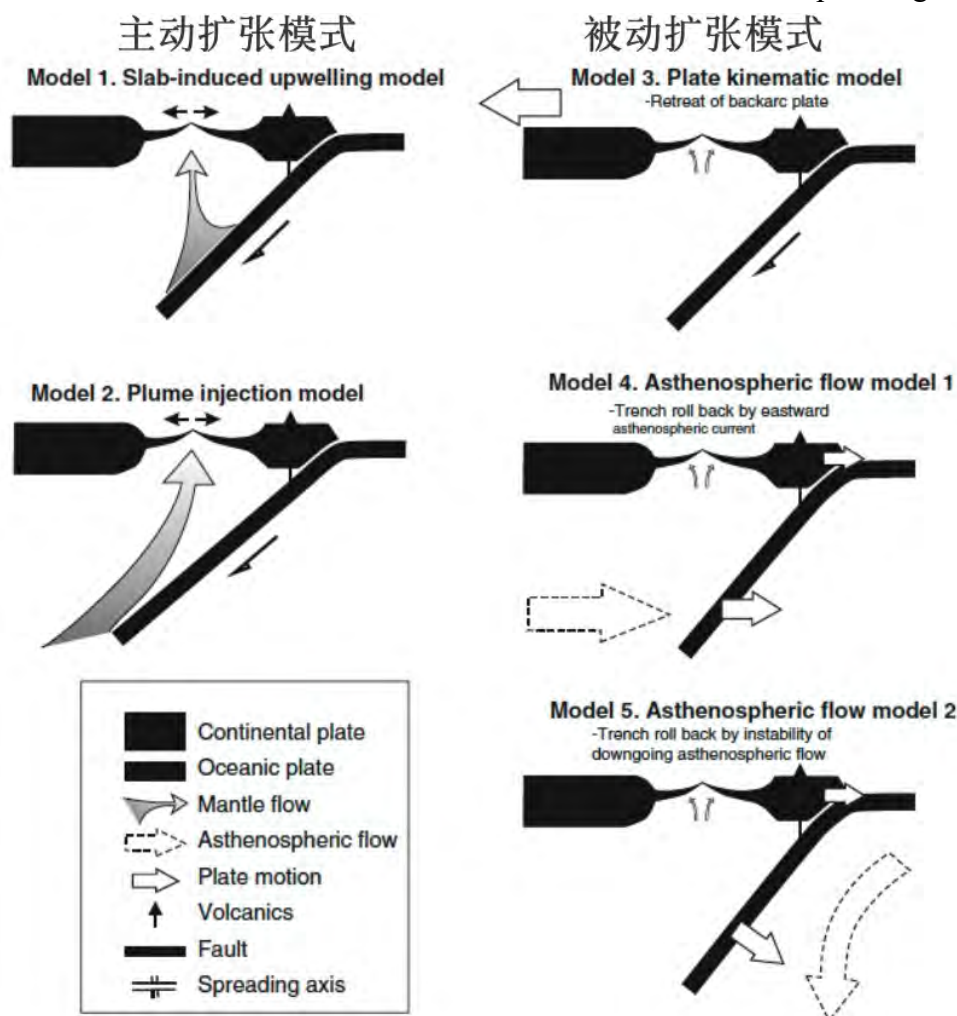
图 1.2 弧后盆地扩张机制示意图（据 Tamaki and Honza, 1991^[1]）

Fig. 1.2 Sketch-up cartoons of back-arc basin formation dynamics (modified from Tamaki and

代表由于地幔上涌导致的扩张模式，地幔上涌可由俯冲板片与上覆板片摩擦生热熔融诱发^[6]，也可由与俯冲板片有关的次生地幔对流造成^[3]。Plume injection model代表地幔热柱注入引发的打开方式，即东亚下方的地幔向东流动时，受到了向西俯冲板片的阻挡，部分地幔物质在弧后位置向上注入，从而导致盆地扩张，例如 Japan Sea Basin 在 21 至 14 Ma 之间发生的弧后扩张^[2]。与主动扩张模式不同，Plate kinematic model 不涉及地幔对流活动，位于大陆一侧的上覆板片发生后撤最终导致弧后扩张^[7]。与上覆板片后撤模式相反，Asthenospheric flow model 1 中俯冲带下部软流圈水平移动并造成岩石圈不稳定，最终引发破裂，也是海沟向洋壳方向后退的主要原因，从而被动地造成盆地打开^[8]。Asthenospheric flow model 2 中软流圈垂流流动，造成俯冲板片角度增大，也可导致盆地被动拉张。然而，对于部分正在发生俯冲的岛弧后侧，并未发育相应的弧后盆地；另外，有些盆地拉开的时间短于相应岛弧俯冲的时间。不同边缘海盆地具有特殊的时空分布特征，即使都属于弧后拉张类型，也很难用一个普遍适用的机制一概而论。

与俯冲无关的边缘海洋盆数量较少，例如，Cayman Trough 位于 North American 和 Caribbean Plate 之间（图 1.1），属于拉分盆地；按照 South China Sea、Sulu Sea、Celebes Sea 以及 Coral Sea 现在所处的地理位置，这些洋盆均远离海沟，其形成机制似乎也与俯冲带无关，但根据构造演化及板块重建等区域地质研究，这些地区在边缘海形成之前可能曾受西太俯冲体系的强烈影响或改造，后因俯冲带后撤而成为残余盆地^[5]。对于某些在陆壳基础上形成的边缘海，例如 Japan Sea Basin，也可能受到与板块相互作用有关的陆内应力传递、挤压变形以及伴生的走滑拉分等因素的影响^[9]（图 1.3）。



图 1.3 弧后盆地扩张机制（据 Zhou, 2016^[10,11]）

Fig. 1.3 Sketch-up cartoons of back-arc basin formation dynamics (modified from Zhou (2016)^[10,11]).

另外，某些边缘海盆地的发育可能同时受多个区域构造事件的综合控制，例如南海形成演化的动力学机制，部分学者指出新生代印度与青藏发生碰撞，印支

地块顺时针旋转的同时沿 Red River Fault Zone 向东南方向大规模挤出逃逸（断裂带累计总滑移量达 500–1200 km），左行走滑拉分作用最终导致南海打开^[12,13]；部分学者强调南海的打开主要受古南海（proto-South China Sea）消亡关闭过程中板片俯冲拖曳作用的控制^[14]；另外，越来越多的学者指出，海底扩张与先前存在的转换断层（沿岩石圈薄弱面发育）可能有关，而东亚大陆边缘在晚侏罗世至白垩纪期间曾发育大规模安第斯型大陆弧（Andean-type Continental Arc），以及一系列 NE 向、NNE 向活跃的走滑断裂系统，华南大陆自晚白垩世以来广泛分布的右行走滑断裂在南海东侧地区继续延伸，最终诱发大陆边缘裂解及南海扩张，在几何学和运动学角度上表现出“东强西弱”、“东早西晚”的特点，且不同地区剪切程度存在差异^[11,15,16]。因此，研究边缘海成因不仅需要考虑与俯冲有关的深部过程，还需全面探讨上覆大陆板块的移动方向以及应力平衡关系等因素。

南海是西太平洋面积最大的边缘海，位于欧亚大陆东南缘、太平洋及印度—澳大利亚板块的交界处，四周包含主动型、被动型及转换型三大类大陆边缘，不仅自身具有特殊的发育演化模式，其岩浆记录和沉积地层还反映了周边地区构造与古地理变迁的诸多科学信息（图 1.4）。具体而言，南海地区在中生代末

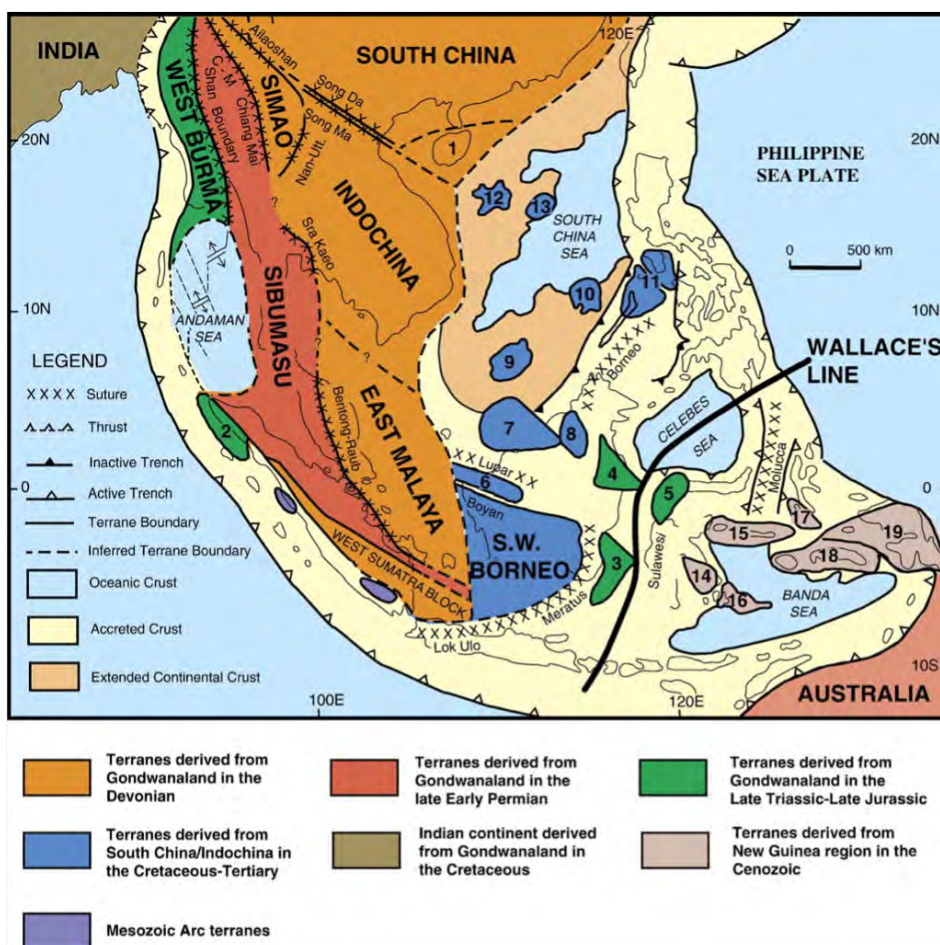


图 1.4 东南亚主要构造单元，其中数字 1-海南岛; 2-Sikuleh of Woyla Terrane (西苏门答腊); 3-Paternoster Islands (即 Balabalagan Islands); 4-Mangkalihat (东加里曼丹); 5-西苏拉威西; 6-Semitau Block (西加里曼丹); 7-Luconia Block; 8-Kelabit-Longbowan (沙捞越/北加里曼丹); 9-Dangerous Ground; 10-Reed Bank; 11-北巴拉望岛; 12-西沙群岛; 13-中沙群岛; 14-东苏拉威西; 15-Bangai-Sula; 16-Buton; 17-Obi-Bacan; 18-Buru-Seram; 19-West Irian Jaya (据 Metcalfe, 1996, 2006^[17,18])

Fig. 1.4 Major tectonic units of SE Asia, where 1-Hainan Island; 2- Sikuleh of Woyla Terrane; 3- Paternoster Islands; 4-Mangkalihat; 5-west Sulawesi; 6-Semitau Block; 7-Luconia Block; 8- Kelabit-Longbowan; 9-Dangerous Ground; 10-Reed Bank; 11-North Palawan; 12-Xisha Islands; 13-Zhongsha Islands; 14-East Sulawesi; 15-Bangai-Sula; 16-Buton; 17-Obi-Bacan; 18-Buru-Seram; 19-West Irian Jaya (modified from Metcalfe (1996, 2006)^[17,18]).

期经历了主动向被动陆缘的构造转换和新生代晚期从海底扩张到俯冲关闭的转换，因此得以保留与华南大陆、印支地块等周缘板块有关的构造运动学和岩石圈深部活动的动力学信息；另外由于地理位置特殊，南海地区不仅是研究太平洋和特提斯两大构造域相互叠合的重要窗口，且是深入了解海洋—大陆岩石圈交互影响的关键区块^[19-23]。但是，作为西太地区边缘海盆地的典型代表，尽管国内外学者已经对南海开展了大量地质地球物理学研究，但对其形成过程中究竟主要受太平洋俯冲板片的影响，或是来自印度—欧亚板块的碰撞—挤出一逃逸作用，还是地球深部过程起主导作用，至今仍存在很大争议^[12, 14, 21, 24, 25]。另外，把南海置于更大区域，甚至将其放在全球板块构造范围以及深部构造格架内部进行综合分析探讨，全面认识西太地区边缘海的扩张与闭合机制，也是当前地学界关注的热点问题。

学术界针对南海地区晚中生代—早新生代的沉积物源及构造演化历史主要存在以下争议：在古太平洋板片向欧亚大陆俯冲背景下，南海地区在中生代末期经历了从主动向被动大陆边缘的构造转换，由于前人研究大都建立在华南大陆、印支地块或其他东南亚陆块出露的岩浆记录与沉积地层的基础上，因此该过程发生的准确时间及空间展布尚不清楚^[26-32]；大陆周缘基底的年龄组成和构造属性目前仍主要基于地球物理解释，且深部地层的地震剖面分辨率相对较低，更缺乏可靠的新生代盆地基底钻井资料的证实^[31]；早新生代南海地区发生断陷扩张后，在中生代时期位于华南陆缘的南沙地块、礼乐盆地和巴拉望陆块脱离南海北侧并逐步漂移至当前位置，同时伴随古洋壳在南海南侧的俯冲消亡过程^[33]，然而由于南海早新生代盆地资料匮乏，大多数已有研究仅能刻画该时期构造沉积演化的大致轮廓，且与南海北部具有共轭关系的南海南部发育演化的地质资料与分析研究都还非常有限；需要特别指出的是，2014 和 2017 年完成的大洋钻探 IODP349、367/368 三个航次揭示了南海是一次扩张形成^[34-38]，其东部次海盆初始拉张时间大约为 34 Ma，西南次海盆为 23 Ma，南海实际最先发生断陷并接

受沉积的时间却远远早于上述洋壳出现的时间，而准确厘定南海地区初始断陷的时间与构造沉积环境，对全面认识南海的前身-发育-演化过程非常重要；伴随多阶段的、穿时性断陷张裂过程，南海北部与南部地区经历的复杂源-汇、陆上水系发育/重组事件、盆地内物源转变及相应古地理-古环境演化历史仍有待开展全面系统的研究及对比工作。相关热点争议及关键科学问题将在本论文第二章进行详细阐述。

本研究对南海及周缘地区晚中生代-新生代岩浆记录和沉积地层开展综合调查，研究区空间范围既包含区域构造运动更加活跃、与板块应力场变化及板块边界类型转变紧密相关的南海东部地区，也包含与印支地块挤出、逃逸和走滑作用有关但盆地资料相对匮乏的南海西部地区，还包括与古南海向南俯冲消亡至婆罗洲之下，持续发生弧陆碰撞造山运动的南海南部地区；研究时间尺度涵盖前新生代至新生代晚期，可系统揭示华南陆缘由挤压向伸展环境转换的动力学机制、沉积响应过程以及构造古地理格局；研究材料和数据来自南海南北两侧及周围潜在源区的野外露头、河流沉积物和大洋钻探/商业钻井样品，以及对前人已发表资料开展大数据分析工作。

1.2 选题来源

本论文主要依托于国家自然科学基金项目《印支半岛源区地质特征及对南海北部的沉积充填作用》、《南海东部白垩-古近纪构造演变及沉积响应，国家自然科学基金项目》、科技部十三五国家重大专项《曾母-北康盆地群及邻区区域沉积演化》以及《礼乐-万安-南薇西盆地发育背景及古海洋学条件对油气成藏的控制》，对南海北部及周缘地区新生代岩浆-沉积记录及其前新生代盆地基底、南海南部婆罗洲和周边潜在源区开展系统的构造判别、源-汇对比以及古地理重建工作（图 1.5）。另外，本论文还涉及南海北部大量地质地球物理资料和相关野外露头/钻井样品分析化验数据，均得益于项目组曾经承担的多个国家自然科学基金、科技部重大专项和中海油科技攻关项目等。

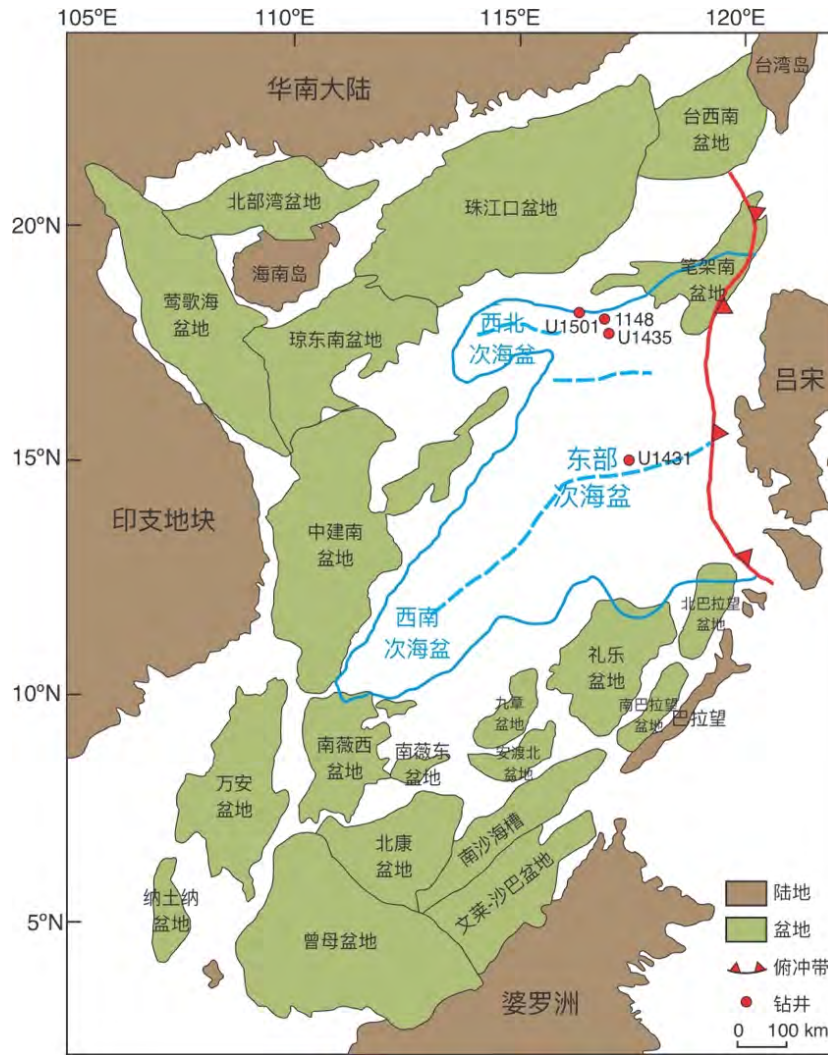


图 1.5 南海沉积盆地及周缘主要构造单元分布图（据孙珍等，2011; Pubellier and Morley, 2014^[39, 40]）

Fig. 1.5 Locations of major sedimentary basins and surrounding tectonic units of the South China Sea (modified from Sun et al. (2011); Pubellier and Morley (2014)^[39, 40]).

1.3 “源—汇”系统

进入二十一世纪以来，地学研究重点已经从早期独立研究各个子系统，逐渐转变为关注地球岩石圈、大气圈、水圈和生物圈多个圈层之间的相互作用。沉积盆地作为地球系统重要的组成部分之一，是深刻理解表层动力学过程的关键环节，对揭示地球整体动力学过程具有重要作用。为了将沉积学研究提升至地球系统层面，“源—汇”系统（Source-to-Sink system）应运而生，也叫沉积路径系统（Sediment routing system）。简言之，来自剥蚀地貌的碎屑物质，经地表输送体系搬运至海相或陆相沉积盆地的这一过程统称为“源—汇”系统。

“Source-to-Sink system”本质上是物质守恒定律的延伸，最早起源于美国国家自然科学基金会（National Science Foundation, NSF）和联合海洋学协会（Joint Oceanographic Institution, JOI）在1998年组织的“大陆边缘计划”（Margins Program Science Plans），即对造山带-冲击平原-浅海陆架-深海盆地的复合体系开展从源到汇的研究计划，并将其列为十年计划的重要科学领域之一。其他国家学者及研究机构也相继开展多个“源—汇”系统研究项目，包括“Inter Margins”、“Eurostrataform”、“亚洲三角洲：演化与近代变化”等。我国也于2000年启动了“中国边缘海的形成演化及重要资源的关键问题”，针对“源—汇”系统进行具体研究^[41-43]，其中对洋陆边缘“源—汇”系统开展的构造—气候驱动机制、物源搬运及示踪分析、汇水区沉积体系精细刻画与预测方法等工作已取得突破性进展，对经济矿物特别是油气勘探的指导意义非常深远^[44]。“源—汇”系统将研究范围扩展至剥蚀区和输送过程，并非仅局限于沉积学和层序地层学的沉积区，且更注重利用定量与定性相结合的手段，通过重塑沉积物从源到汇的动态演化历史，深刻揭示影响沉积盆地形成的机制。然而，对于不同类型的沉积盆地和不同时空尺度，“源—汇”系统研究进展存在明显差异，其理论和方法体系尚有待完善。

根据地貌空间结构特征，地表上的“源—汇”系统可大致分为近源—陡坡—深水、远源—缓坡—深水和远源—缓坡—浅水三大类，第一类地势陡峭，搬运体系长度较短，多发育在活动板块边界，物源供给相对充分，大量碎屑物质沿陡坡带迅速运移至深水区；第二类地势平缓，高地剥蚀区与沉积盆地由大型运输体系连通，通常表现为横跨大陆的河流水系和广阔的滨岸平原，多发育在构造环境相对稳定的被动大陆边缘；第三类同样表现为整体平缓的地势特征，但沉积盆地水体相对较浅^[45,46]。

物源是“源—汇”系统中的基本要素，主要受1)原始沉积物组分特征和2)源区物质供给速率两方面的约束，二者本质上是风化作用时间和强度的产物。大多数情况下，源区物质组分特征与母岩类型和源区化学风化作用（能够从源区被剥离搬运的最终产物）密切相关，而化学风化作用受构造、气候和植被等多个因素控制。源区物质供给速率主要受源区规模大小（宏观）和化学与物理风化速率（微观）共同控制。其中化学风化速率与风化强度、沉积物剥蚀速率几乎线性相关，当二者同时增长时化学风化速率显著提高；另外当源区存在年轻地层和大量地表径流时，剥蚀速率也会显著提高，进而提升化学风化速率^[47]；对于物理风化速率，主要是山体崩塌和河道侵蚀动态平衡的结果，河道下切作用造成山体坡度角增加，从而引发山崩现象，大量山崩物质进入河道并一定程度抑制下切作用，地貌逐渐趋于稳定，当山崩物质输送完毕，下切作用再次恢

复，又引发新一轮山崩过程^[47-49]。在区域运动相对活跃的地区，地震多发，河道侵蚀下切作用强烈，山崩作用频繁剧烈，大量物质进入河流输送体系，物理风化速率极高^[42,50]。

在长距离搬运过程中，沉积物往往会经历某种程度的物理破碎（abrasion）、分选（sorting）、混合（mixing）以及再旋回（recycling）作用，然而这些改造过程对沉积物矿物成分、粒度、分选和形态上的影响并非呈简单的线性关系。首先，研究表明砂岩在经历远距离搬运后仍包含较多长石、岩屑、角闪石这些“不稳定”矿物，并非单纯保留“稳定”矿物，如密西西比河、尼罗河等，说明物理破碎作用仅对耐磨性差、结构疏松的沉积岩和变质沉积岩岩屑组分有一定影响。物理破碎虽然可以快速提高砾石磨圆度，然而对砂粒的改造程度却极为有限，且流水搬运体系中的砂粒粒径也大多由母岩决定。研究者通常认为再旋回作用可以提高成分成熟度，因为沉积物稳定组分富集，不稳定组分比例降低。然而某些研究发现在化学风化作用起主导地位的地貌剥蚀区，再旋回作用只是复制母岩矿物信息，成分成熟度保持不变，甚至由于岩屑比例提高，成分成熟度不升反降。混合作用对“源—汇”系统的影响更为复杂，表现在次要源区携带不同物源信号进入主要源区沉积物时，会稀释甚至完全改变先前源区和搬运过程中的原有特征^[42,51]。

“源—汇”系统的汇水区特征其实是源区格局及演化历史控制下的物质供给、剥蚀输送和沉积物分配的综合响应^[42,52,53]，它继承了源区地质学和流水搬运过程中的复杂性，同时还叠加了沉积盆地物质空间分布的多变性与不均一性。数值模拟结果指示稳定型和突变型两种沉积响应演化模式：稳定模式中物质供给速率持续增长，降水和区域构造活动相对稳定，沉降区堆积体持续进积，物质供给速率大于活动构造速率，二者由于呈动态不平衡造成河道侵蚀，沉积体缓慢向前推进增长^[48]。突变模式中气候条件可能发生剧烈变化，降水量激增，物质供给量突然增大后逐渐趋于稳定，堆积体大规模进积后趋于平缓增长；降水量突然减小，源—汇体系则演化为与上述情况相反的反应过程。另一种情况下，当构造活跃导致断层移动速率骤然增大时，物质供给量同样先大幅提高，在沉积体最终进入缓慢进积，坡度也趋于平缓之前，沉积体反而先突然退积，伴随坡度骤然增加；断层移动速率突然减小时，物质供给量先减小后趋于稳定，沉积体快速进积后逐渐保持稳定，但沉积体坡度不会出现明显波动，而是表现为持续稳定降低的态势。

汇水区沉积响应特征不完全只受控于源区物质供给规模，还受其他多种因素，即汇水区物质分配的影响^[54]。物质分配由剥蚀区物质供给量和沉降区可容空间协同决定，当气候条件发生变化时，可容空间基本不变，此时沉积响应几

乎只与物源供给有关；当区域构造运动开始活跃时，才会造成可容空间的增长或缩小，而物质供给速率相对可容空间的变化则相对滞后。具体表现为区域断层滑动速度增加而提供的可容空间突然远远大于源区提供的碎屑物质，此时堆积体迅速退积，随后源区物质供给量逐渐追上并超过可容空间增加的速度，沉积体转为进积；相反，区域断层滑动速度降低时，汇水区形成的可容空间远不足以追上物质供给速度（虽然同样呈降低趋势），堆积体则为进积状态，之后源汇系统达到动态平衡，沉积体也随之趋于稳定^[42, 48, 49]。需要注意的是，坡折带及其以下深度的区域较易发育大规模且相对稳定的沉积空间，使得碎屑物质在此处优先卸载堆积，并且坡折带不同部位的容纳空间与水动力环境也存在较大差异，可能造成沉积物类型在空间分布格局上表现不同，总体而言这一特殊地表地貌结构在沉积响应上表现复杂。

通过对基本组成要素及相互作用关系的分析，研究者发现陆相与海相盆地“源—汇”系统存在一系列差异，地处洋陆边界的源汇系统通常发育开阔盆地，组成也相对简单，从造山带到冲击平原，再到大陆架，最终至深海盆地；而陆相源汇系统则一般为封闭局限盆地，可包括断陷、断坳、前陆等多种类型。陆相盆地源汇系统除了受构造与气候两大因素控制以外，还具有多隆起、多洼陷、隆坳相间的复杂古地理地貌格局。某些洋陆边界源汇体系受单一物源影响，某些陆相盆地则表现为多物源特点，既有盆内也有盆外源区影响，近源与远源搬运过程并存。不同源汇体系发育复杂的搬运体系，包括下切河谷、河道、转换带通道等多种形式^[44]。针对不同源汇系统复杂的组成要素及耦合关系，我们需定量化描述各组成要素的特征，谨慎对其控制因素进行多变量分析，在利用统计学和数值模拟方法相结合的手段下，以期合理恢复剥蚀-输送-堆积整个沉积过程。

早期物源体系分析以沉积物成分特征分析为主，如 Q-F-L (Quartz-Feldspars-Lithic fragments) 砂岩组判别^[55]、全岩地球化学元素分析法^[56-59]和重矿物组合及指数分析法^[60]。其中，重矿物在岩石中含量普遍偏低（小于 1%），密度大于 2.89 g/cm³，矿物粒径在 0.05 mm 与 0.25 mm 之间，除了源区母岩类型与重矿物组分上存在定性关系，部分重矿物组合的百分含量也具有一定物源指示意义，例如 ZTR 指数（锆石、电气石和金红石占有所有透明重矿物的百分含量总和）可以反映源区构造活动强度和母岩成分成熟度。随着现代分析测试技术的发展，如 X-ray fluorescence (XRF)、Inductively Coupled Plasma Atomic/Optical Emission Spectrometry (ICP-AES/OES) 等，地学研究者使用极少量样品便可获得高精度地球化学元素含量，为物源信息提供了更为完整的视角，具体表现为砂岩和泥岩各类物源和气候判别指标。近年来，由于同位素地

球化学的进一步发展,特别是 electron microprobe (EMP)、Laser Ablation-ICP-Mass Spectrometry (LA-ICP-MS)、Thermal Ionization Mass Spectrometry (TIMS)、Secondary Ionization Mass Spectrometry (SIMS)、Sensitive High-Resolution Ion Microprobe (SHRIMP) 以及 Multiple Collector-LA-ICP-MS (MC-LA-ICP-MS) 等分析仪器可对单矿物进行形态、成分、年龄进行精细刻画,例如锆石微量元素含量、U-Pb 高温年代学、裂变径迹和 U-Th/He 低温年代学、Lu-Hf 同位素、O 同位素、Sm-Nd 同位素、单矿物颗粒形态学等。此外,单颗粒多法定年与单方法多颗粒定年技术也在物源研究领域受到持续关注。需要注意的是,单矿物颗粒物源分析都面临同位素年龄和组分含量的统计学处理问题,包括单个样品中矿物颗粒统计数量、如何随机挑选矿物颗粒以全面代表样品信息、微区位置的有效选择、针对性使用数据、数据展现与表达方式、不同样品之间的横向对比,是否合理解决这些问题密切关系到物源的准确判别,同时也有望推动地学数据的可验证性与可重复性。除此之外,以野外露头 and 钻井资料为基础的物源研究方法,不具备地震资料的系统性、连续性与全面性,不能对物源通道、搬运模式和沉积砂体空间展布特征进行综合恢复^[44]。因此对于无井及少井盆地区,沉积搬运过程我们通常利用地震相和地震资料得到的地层对比与追踪、地层厚度、属性图、沉积相图与古地貌图进行源汇系统重建。

伴随源汇系统研究在不同时空尺度上的深入,地学研究者需要面临越来越大的样本容量与数据,数理统计方法如 Multidimensional Scaling Analysis (MDS)、General Procrustes Analysis (GPA)、Individual Difference Scaling Analysis (INDSCAL)、Non-negative Matrix Factorization (NMF)、Monte Carlo Mixture Modeling (MCMC) 在源汇系统大数据分析中起到了重要的贡献^[61-64]。此外,Machine Learning 目前已被广泛应用于地球科学各个领域,前人研究表明锆石微量元素和岩浆成矿能力有关,但由于成矿过程、构造环境通常很复杂,而传统地球化学研究大都针对具体研究区,其数据往往缺乏可重复性,因此很容易忽略与经济矿物形成有内在联系的元素,而 Machine Learning 有潜力挖掘一些能反映岩浆成矿的新指标,从而提高成矿预测准确性和找矿效率^[65,66]。

1.4 盆山耦合

沉积盆地往往在时间和空间上与造山带相互依存,在几何学与运动学特征上造山带互相协调改造,这种明显的耦合关系可以作为探索地球表层动力学过程的重要切入点。造山带的活动不仅为盆地提供了大量物质来源,盆地基底特征反过来也可以影响甚至决定造山带的发育演化,二者之间的高程差则为沉积

物输送提供了动力条件和搬运通道^[67,68]。耦合关系不仅仅局限在纵向上,同样也表现在平面上受区域应力场控制之下,盆地与山脉之间发育的多种断裂、地貌、岩石变形等构造组合。

对于拉张应力条件下形成的大陆裂谷,初始阶段以横向物质供给为主,表现为单个或多个联合的冲积扇粗粒碎屑堆积物;河道沟谷形成后诱发了纵向物质供给,开始发育河流相沉积;在断陷中心形成湖泊后,横向与纵向物源供给均对沉积中心产生贡献。值得注意的是,随着剥蚀搬运作用持续进行,盆地与山脉高程差逐渐减小,高地侵蚀作用不再如先前剧烈,盆地也可能形成碳酸盐岩和蒸发岩沉积。对于慢速扩张的大洋中脊,早期阶段中央裂谷主要聚集垮塌而来的角砾物质,主要成分是蛇绿岩套;角砾之上覆盖层状的深海硅质岩、灰岩或深海红层。对于挤压应力条件下形成的前陆盆地,早期沉积前渊环境下的深海浊积岩,后面主要发育磨拉石建造;山脉隆升之后在靠近山地区域沉积砾岩、粗砂岩和部分粉砂岩,远离山地的区域堆积粉砂岩和泥岩,而更远处则开始沉积碳酸盐岩和蒸发岩,这些盆地内沉积变化与造山带构造活动之间存在密切联系。对于走滑/剪切应力条件下形成的盆地与之前提到的大陆裂谷有一定相似之处,也经历了起初横向物源供给转变为河流搬运体系的阶段,之后变为多个物源控制。但走滑拉张盆地在发育演化期间,多个活跃断层带诱发深盆形成,陡峭的断崖地貌导致了深水浊积岩大量堆积;另外水平方向的走滑造成了沉降中心不断迁移,形成复杂的隆起-凹陷分布格局^[67]。由于盆山耦合研究需建立在构造学与沉积学密切配合的基础之上,即对造山带和盆地的构造演化、沉积演化、源-汇系统以及岩石圈有效弹性厚度等方面均要有系统了解,且依赖多种手段互相证实,因此该领域目前在地学界尚有待深化。

1.5 古地理恢复与板块重建

“源-汇”系统相关数据有助于解决各类具体地质问题,例如古水系演化、区域地层格架重建、揭示局部隆升过程、记录岩浆活动及其演化特征、构造背景端元重建、反映地壳演化和沉积循环过程、解析地球重大气候事件等^[69-71]。而古地理恢复与重建便建立在这些具体地质问题的基础之上,其本质是研究板块相互作用背景下地理、地形和地貌随时间的演化史,除依靠源-汇系统分析之外,还涉及海底磁异常条带、断裂带几何及运动学、洋陆转换边界分析、hotspot 活动轨迹、古地磁数据、生物化石年龄与空间分布等一系列地质地球物理手段^[72-78]。

板块重建是全球构造研究领域的前沿,以多学科集成综合为主要特征。随

着大数据时代的到来,多学科多方向交叉协同的特点更加明显。其中以 Hall 为代表的许多研究者以东南亚地区和西太平洋边缘海为研究对象,基于大量野外露头,从古生物角度出发,建立了源区、生物多样性、气候事件和区域构造之间的关联,探讨了沟弧盆体系演化、沉积过程、地幔活动等一系列问题,对全球中-新生代板块进行构造重建^[14,79-81]。然而由于缺乏古地磁旋转极资料,很多重建结果不便于其他学者进行计算机重建检验,仍有待于进一步定量分析^[82]。而 EarthByte 团队基于海底磁异常条带、古水深、古气候、古地形等数据,开发出洋盆年龄、扩张速率和不对称性等数字模型,还进一步探讨了板缘和板内的构造变形带与沉积盆地的发育演化,主要集中在地质资料约束较完善的 100–50 Ma 期间的全球事件^[73]。其开发的 GPlates 板块重建平台不仅可用于区域构造研究,还允许我们在盆地尺度将板块相互作用、沉积演化、岩石圈伸展、地幔对流等地球不同圈层链接起来。当然,板块重建一个突出成就即发现了地球地质历史时期曾经存在以及将来出现的多个超大陆 (Supercontinent cycles),如 Zheng-Xiang Li 团体以古地磁和地质综合对比为基础,通过全球和区域构造-地层综合、盆地分析、造山带重构、低温和高温热年代学、地球化学、地球动力学模拟及大数据汇编等方法,开展 Nuna、Rodinia、Gondwana、Pangea 和 Amasia 超大陆的重建工作^[83, 84];再如 Peter Cawood 团体以碎屑锆石 U-Pb 年龄为主要手段,详细划分不同块体在各时期的亲缘性,重建洋陆转化格局,并发现 Boring Billion 等重要地球演化阶段^[85,86];除此之外,还有很多活跃在区域板块重建领域的学者,其精细化重构工作进一步丰富了全球板块重建模型^[18,87-89]。

1.6 研究思路与技术路线

研究思路,本论文以“源—汇”系统分析、盆山耦合以及古地理重建为宏观指导思想,针对南海地区晚中生代—早新生代的沉积物源及构造演化相关热点问题,在充分收集和整理前人实验数据、钻井资料及其他相关研究成果的基础上,采集南海北部莺歌海、琼东南、珠江口盆地以及华南陆缘东海陆架盆地大洋钻探和商业钻井的前新生代与新生代沉积-岩浆岩样品,结合野外露头描述、沉积环境与沉积相观察、岩石学与岩相学特征,开展系统的沉积地球化学、全岩主-微量元素地球化学、重矿物成分与组合分析、岩石矿物学、锆石 U-Pb 年代学和锆石 Lu-Hf 同位素地球化学室内分析,结合南海与周边地区已发表的大量物源和区域构造数据结果,以定性描述-定量计算为主线,系统揭示华南大陆边缘由挤压向伸展环境转换的动力学机制、源—汇系统突变界面、大型水系的发育/重组、沉积盆地响应过程以及南海南北两侧构造古地理格局差异这一系列

科学问题。具体技术路线如图 1.6 所示。

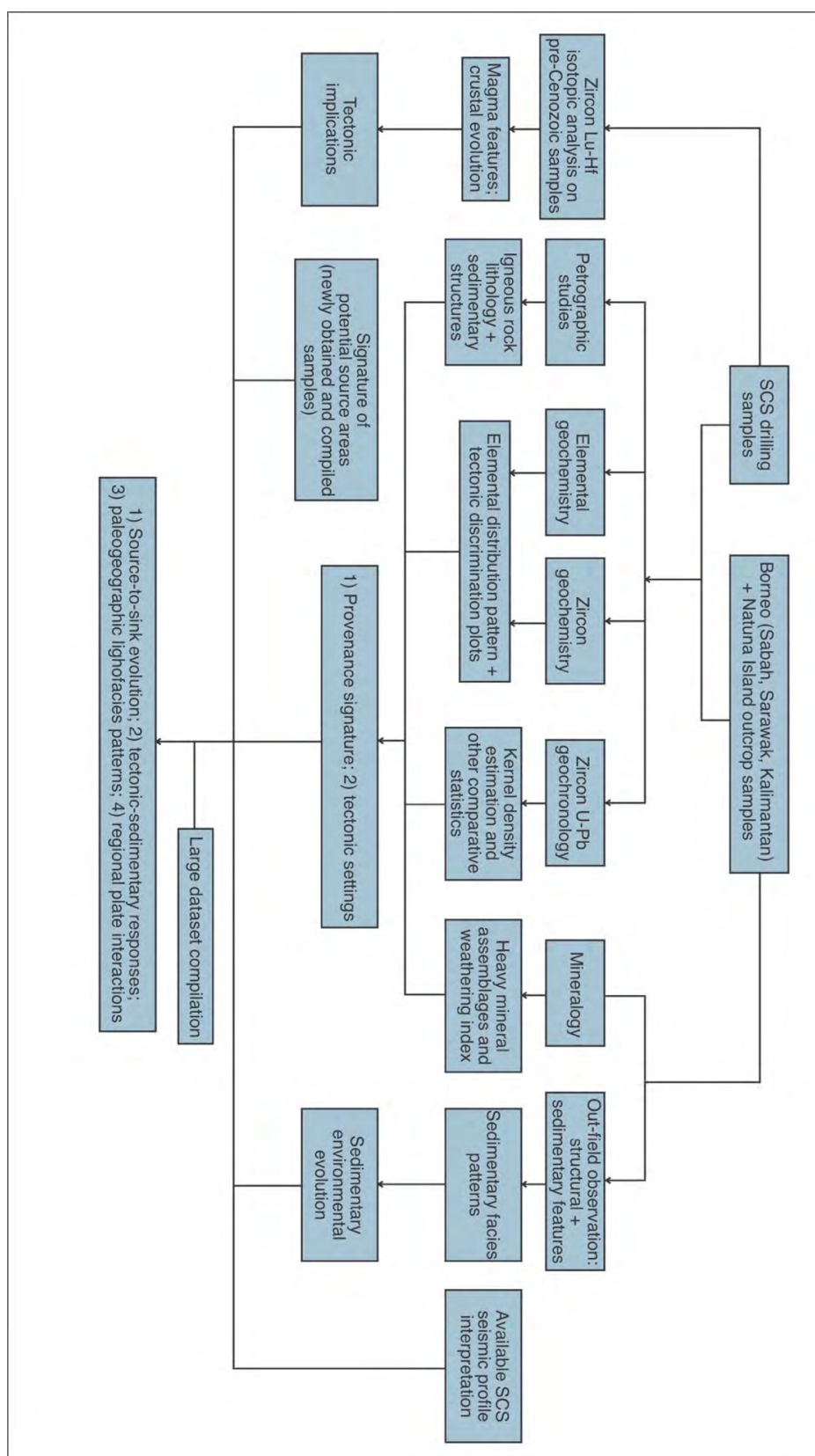


图 1.6 本论文技术路线图

Fig. 1.6 Sampling and methodology of this thesis

1.7 论文工作量

本论文涉及的具体工作内容和工作量如表 1.1 所示。

表 1.1 论文工作内容和工作量

工作内容		工作详情	完成数量
资料调研与整理	前人已发表成果, 数据收集与整合	中、外文参考文献, 相关科研报告	文献>500篇, 报告 10 份
		南海盆内、外潜在源区锆石年龄数据收集与再处理	样品>250 件 (锆石颗粒>35000 个)
		南海盆地样品锆石年龄、元素地球化学等地质资料收集与再处理	样品>150 件
野外地质调查与样品采集	地球物理资料收集与处理	地震剖面解析, 重磁震联合反演	重力、磁力异常分布及相关地震剖面图件 5 幅,
	野外地质调研	南海周缘野外露头观察, 岩石学、岩相学、构造-沉积特征分析, 沉积环境与沉积相恢复	越南北部及中北部、台湾岛野外考察
	露头样品采集	台湾恒春半岛野外露头	样品 29 件
	南海及周缘盆地钻井	盆地样品	钻井 73 口, 岩屑与岩芯样品>180 件
室内分析化验与数据处理、分析与解释	岩石矿物学	矿物组合与岩石成分分析	岩石薄片 50 件, 图件 10 幅
	元素地球化学	全岩地球化学元素样品分析	样品 30 件
		元素含量分布特征	图件 10 件
		构造判别与物源识别等图解	图件 7 件
	锆石 U-Pb 年代学、Lu-Hf 同位地球化学、微量元素含量分析	锆石 U-Pb 定年分析	样品 80 件
		岩浆岩锆石 U-Pb 结晶年龄	协和年龄、平均年龄、阴极发光等相关图件 20 件
		碎屑锆石 U-Pb 年龄	KDE 年龄谱系、阴极发光、协和图、MDS 相关性分析等图件 30 件

第 1 章 引言

		锆石微量元素成分及分布特征	样品 60 个，图件 10 件
		锆石 Lu-Hf 同位素体系	样品 7 个，图件 10 件
综合图解	源一汇系统重建	源一汇系统示意图	图件 7 幅
	构造演化	区域构造演化及主要板块相互作用示意图	图件 7 幅
	古地理演化	南海及周缘地区古水系、古地理重建	图件 8 幅
学术成果与交流	国内学术会议与专题讨论	地球系统科学大会、全国沉积学大会	口头 5 次
	国际学术会议与专题讨论	美国地球物理年会 AGU、澳大利亚地球科学年会、IGCP648、BasinWorkshop、ICAMG 等	口头 5 次，展板 1 次
	发表文章	正式发表于 GSA, Bulletin、Gondwana Research、MPG 等中英文地学期刊	第一或通讯作者 13 篇、合作作者 20 篇
	博士学位论文	正文	约 9 万字

Table 1.1 Statistical summary of this thesis

Items		Detailed description	Statistics
Literature review and data compilation		Literature in native language and English, scientific reports	Number of literature reviews: > 500, scientific reports: 10
		Zircon U-Pb age data collection and compilation of the South China Sea intra- and extrabasinal provenances	Number of reviewed samples: >250 (number of zircon grains: >35000)
		Zircon U-Pb geochronological and elemental geochemical data collection and compilation of the South China Sea drilling samples	Number of reviewed offshore drilling samples: >150
Field observation, sampling and data source	Geophysical data collection and interpretation	Seismic profile interpretation, gravity-magnetic-seismic three dimensional inversion	Interpretation and reconstruction figures based on seismic profiles and inversion: 5

第 1 章 引言

	Field observation	Petrological and petrographic analyses, tectonic setting discrimination, sedimentary facies reconstruction of the South China Sea surrounding regions	Completion of the northern-central Vietnam and Taiwan Island field trips
	Outcrop sampling	Hengchun Peninsula, Taiwan Island outcrops	Number of outcrop samples: 29
	Drill-hole sampling of sedimentary basins within the South China Sea and its surrounding areas	Offshore samples	Number of analytical drill-holes: 73; number of lithic and core samples: >180
Lab work and data analyses/interpretation	Petrography and mineralogy	Petrographic and mineralogical analyses of samples in this thesis	Number of thin sections: 50
	Elemental geochemistry	Whole-rock elemental geochemistry	Number of geochemical analyses: 30
		Geochemical concentration and variation analyses	Figures completed: 10
		Tectonic setting discrimination and provenance analyses	Figures completed: 7
	Zircon U-Pb geochronology, Lu-Hf isotopic geochemistry, zircon trace elemental geochemistry	Zircon U-Pb dating analyses	Number of samples analysed by zircon U-Pb geochronological analyses: 80
		Igneous zircon U-Pb dating analyses and crystallization ages	Concordia age plots, weighted mean age plots and CL images completed: 20
		Detrital zircon U-Pb dating analyses	KDE zircon U-Pb age pattern diagrams, CL images, concordia age plots and MDS plots completed: 30
		Zircon trace elemental concentration and variation analyses	Number of samples: 60; number of figures completed: 10
		Zircon Lu-Hf isotopic geochemistry	Number of samples: 7; number of figures: 10
Schematic plots	Source-to-sink reconstruction	Source-to-sink reconstruction maps	Number of figures completed: 7
	Geotectonic reconstruction	Regional tectonic evolution and plate reconstruction maps	Number of figures completed: 7
	Paleogeographical reconstruction	Paleo-drainage and paleogeographical reconstruction of the South China Sea and its surrounding areas	Number of figures completed: 8

第 1 章 引言

Academic outcomes	Domestic conferences and workshops	Earth System Conference, Shanghai; Sedimentology Conference	Oral presentations: 5
	International conferences and workshops	American Geophysical Union (AGU), Australian Earth Science Conference (AESC), IGCP648, BasinWorkshop, ICAMG, etc.	Oral presentations: 5; poster: 1
	Publication	Publication on journals including GSA Bulletin, Gondwana Research, MPG, etc.	First and corresponding author papers: 13, co-author papers: 20
	PhD thesis	Main context	Total words: approx. 100, 000

第2章 争议热点及关键科学问题

经过近四十年的研究积累，从早期野外露头观察描述和海底拖网研究，到后来1999年至2018年在南海地区实施的五个IODP航次与“南海深部过程演变重大科学计划”，研究者取得了大量珍贵第一手资料，实现了一系列创新成果和重大突破，但是有关南海物源演化及构造发育等问题仍存在若干争议，始终是学术界和工业界讨论的热点话题。本章节针对论文研究的时空尺度、地质资料和分析方法，系统介绍南海地区中生代末-新生代构造转换、物源演变和古水系古地理重建等争议焦点与需解决的关键科学问题。

2.1 南海北部基底年龄组成与结构特征有待证实

盆地基底研究对区域地质动力学非常重要，要全面了解南海新生代构造演化，就不能忽视对其前新生代地层框架，以及基底对上覆新生代沉积地层的控制等方面的探讨。前人通过地球物理资料对南海基底已取得初步了解，但基底岩石年龄组成和构造属性仍大都基于简略的岩石学描述和早期低温年代学数据。具体而言，位于南海西部的莺歌海与琼东南盆地基底，大多数地区地质资料匮乏，研究程度严重不足，早期观点认为^[26-30,90]：靠近陆上的部分由元古代片麻岩和片岩、古生代-中生代变质碎屑岩、碳酸盐岩和火山岩组成^[31]；向盆地内延伸的部分由于基底钻孔极少，缺乏年代学分析，其组成特征更是难以判定。早期学者依据板块演化模型推测，莺歌海与琼东南盆地基底可能与印支半岛北侧与东侧陆缘构造亲缘属性相似^[32]，这一假设基于华南大陆、印支地块这些主要陆块，和其他微陆块之间经历了一系列碰撞、拼合与增生过程^[91-93]，而陆上发育的前新生代变质沉积岩和火山弧等记录可能以一定地质演化规律向盆地内延伸。根据早期假说，琼东南盆地部分地区，其基底发育良好层理的中生代低级变质沉积岩^[32]；而靠近越南的区域，其基底则以前寒武变质复合体为主^[94,95]。另外，晚古生代碳酸盐岩台地也零星出露于华南大陆沿海地区，例如北部湾盆地边缘和更靠近陆内的地区^[96]。从整体构造角度来说，环绕海南岛发育的古-中生代基底似乎主要由NW-SE向的断裂系统控制^[31]。

华南大陆东南缘广泛分布花岗岩/二长花岗岩岩体，表明晚三叠世（或早侏罗世）至白垩纪该地区可能属于安第斯型活动大陆边缘^[97-101]；该地区很大程度上于晚中生代经历了从活动向被动陆缘的剧烈转变^[102]。研究者自然而然认为，南海北部新生代盆地基底便是华南大陆向东南方向的自然延伸，陆壳遭到不同程度的拉伸减薄，其厚度在空间分布上呈现出不均一的特点^[103-105]，沉积相与地震相结果显示具有“分区、分块、分带”的特性，以琼海断裂和阳江—统暗

沙断裂为边界，其结晶年龄从西向东逐渐变年轻（图 2.1）^[31, 106]。具体而言，Sun et al. (2014) 认为北部湾盆地、珠江口盆地西侧、广大琼东南—莺歌海盆地和台西南盆地沉积了部分早—晚古生代地层^[31]。前人根据 Rb-Sr 等时线定年结果，认为西沙基底由前寒武片麻岩（约 627 Ma）组成^[107]。

然而，最新取得的西沙基底钻井样品锆石 U-Pb 年代学显示，该地区晚侏罗世发育角闪斜长片麻岩，之后于白垩纪时期被花岗岩岩体侵入^[108]。南沙（目前位于南海南部地区）花岗岩拖网样品锆石 U-Pb 年代学结果表明，其岩浆活动范围也集中于晚侏罗世—白垩纪，大约从 159 Ma 持续至 127 Ma^[33]；南海南部中生代地层最大残余厚度位于礼乐盆地，其中部隆起区钻遇下白垩统沉积岩，为礼乐盆地最老地层。

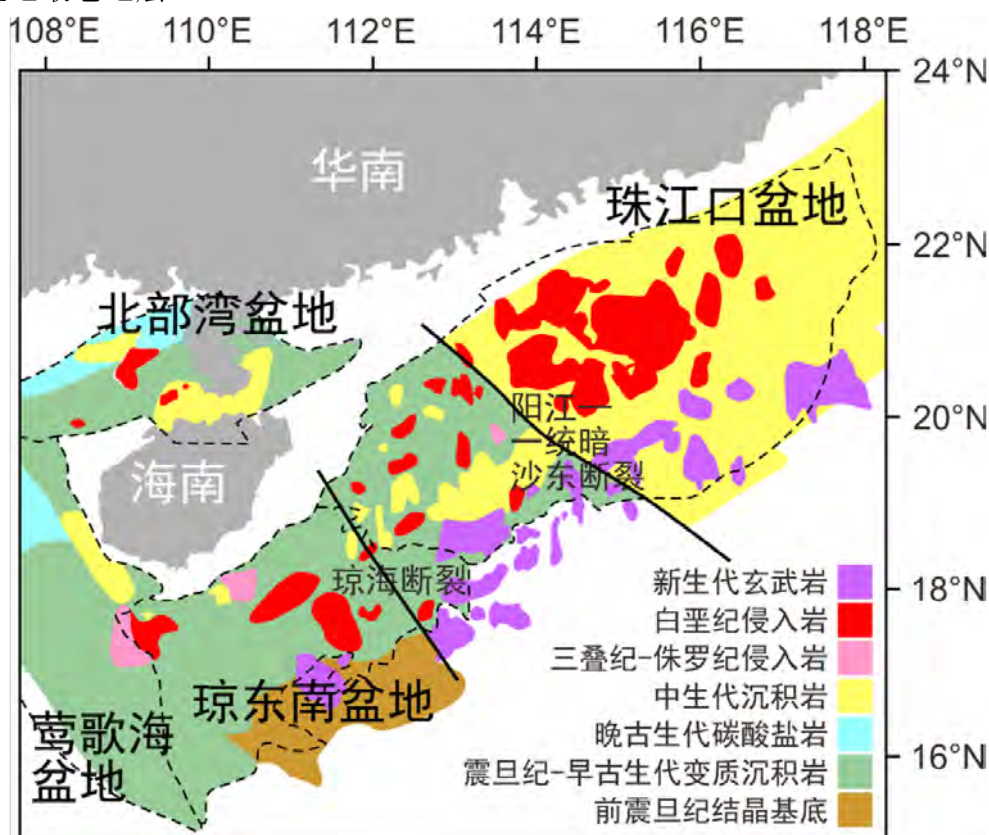


图 2.1 南海北部基底岩性分布图（据 Sun et al., 2014^[31]）

Fig. 2.1 Previous pre-Cenozoic basement lithological map of the northern South China Sea (modified from Sun et al. (2014)^[31])

技术角度上，地壳均衡原理和重力场模型是揭示岩石圈速度异常的基本方法之一，对计算地壳横向密度和厚度变化具有重要意义^[29, 90, 109]。除此之外，磁异常反演可以反映洋中脊扩张过程中的方向与速度，也是一种揭示地壳属性的有效方法^[21, 29, 34, 110-112]。然而，在磁异常条带异常弯曲或来自不同方向相遇的特殊情况下，基底磁异常特征信号可能会受到一定影响；另外，由于上覆巨厚的新生代沉积盖层，也增加了准确识别基底各类构造线、构造脊、倾斜高地和复杂

断裂体系的难度。除地球物理技术手段自身具有的局限性以外,南海地区早新生代断陷过程还可能极大程度地影响甚至改造前新生代基底性质^[27,28],地壳有效强度、厚度、热结构和其他流变属性会因其年龄不同而呈现出相应的响应特征^[113-115]:例如对于南海东部基底,在晚中生代发育大量花岗岩岩体和沉积地层,地球物理资料显示地壳伸展强度更弱时,可能代表年龄更年轻地壳;而对于南海西部靠近海南岛的盆地基底,拉伸程度趋于相近,却可能反映古生代地层或沉积年龄更老的地层^[103]。因此,仅仅依赖这些地球物理参数很大程度上将会导致年龄的多解性,南海盆地基底早期研究也正是局限于此。

近年来技术方法提升与部分研究进展引发了学术界对南海基底的重新思考,主要包括:南海北部基底究竟是否广泛发育并保留古生代甚至前寒武系地层?基底整体的年龄框架是怎样的?其岩石组合类型是什么?此外,海南岛位于莺歌海盆地、琼东南盆地和珠江口盆地地理交汇处,自晚古生代以来记录了多期热事件和构造环境转变,也是古太平洋域向特提斯域转变的潜在区域。而作为南海北部基底的重要组成部分,海南岛及其周缘盆地基底组成及亲缘属性究竟如何?该问题也迫切需要深入调查^[93,116,117]。

2.2 华南陆缘晚中生代构造转换及其控制因素尚存争议

典型大陆边缘包括安第斯型活动陆缘 (Andean-type plate margin) 和西太平洋型被动陆缘 (Western Pacific-type plate margin): 安第斯型大陆边缘以发育活跃的大陆弧为特征,具体表现为岩浆活动具有大陆弧属性、板内与板缘地震活动频发、大型褶皱与推覆带、前陆盆地发育等^[97,118-121]。该种板块边界较易形成平板俯冲类型 (flat-slab subduction),与典型的斜向俯冲不同,俯冲板片以较平坦角度进入地幔下层,下沉速度较慢,因此地壳不易诱发岩浆或地震活动,通常发生在碰撞带或特定构造环境下,如板块碰撞边界或海洋板片碰撞挤压的区域。另外,平板俯冲也可能形成特殊地质现象,例如在正常的岩浆弧形成区域出现岩浆空洞 (magmatic gap)^[121,122]。相反,西太平洋型大陆边缘主要发育一系列边缘海盆地,通常以张裂构造环境为特征,发育弧后盆地或边缘海洋盆,将大陆边缘与正常洋脊分隔开来。

东亚大陆由西伯利亚、蒙古、华北克拉通、华南大陆、中南半岛等一系列陆块组成,与古太平洋板块交界处曾长期处于活动大陆边缘的影响之下^[17]。大量陆上地质资料证实,华南大陆东南缘三叠纪至白垩纪期间为汇聚型板块边界,形成大规模大陆型火山弧构造^[97,99,102,119,123,124]。而最新研究结果表明,华南大陆东南地区的大陆岩浆弧可能在早二叠 (290–280 Ma) 就开始活跃^[125,126],位于西侧的海南岛也相应发现了中二叠统 (约 265 Ma) 岩浆岩^[93]。日本群岛地质记录指示古太平洋俯冲可能更早,在晚石炭世 (或早二叠世) 便已启动^[127]。

华南大陆陆内发育了长达 1300 公里的巨型褶皱带,呈东北-西南向展布,针

对这一引人注目的陆上构造现象,研究者曾提出多个模型以解释其形成机制(图 2.2)。早期学者认为该现象是由太平洋 250 Ma 至 200 Ma 与欧亚板块持续相互作用引发的大规模陆内变形运动,且不断向陆内方向迁移^[128](图 2.2B)。Hsu et al. (1990)提出陆-陆碰撞模型,并引发了华南大陆大规模造山带的形成^[129](图 2.2C)。还有学者认为该造山带受到了来自华南陆块北侧远端应力(far-field stress)的影响^[130](图 2.2D)。Zhou and Li (2000)则强调华南大陆东南地区侏罗纪至白垩纪期间火成岩爆发增长,其年龄由陆内向沿海呈逐渐年轻的规律,可能是由于俯冲板片倾斜角度逐渐加深、岩浆作用由此向海迁移的原因^[97](图 2.2E)。Li and Li (2007)和 Li et al. (2012)提出,华南沿海至内陆的广大地区在三叠纪(约 250 Ma 至 200 Ma)期间可能持续经历平板俯冲作用,也属于安第斯型大陆边缘的一种,该过程终止于大约 200 Ma 以前,沿海地带再次发育岩浆岩和火山碎屑岩,标志着正常斜向俯冲的再活化^[99,102](图 2.2F)。Xu et al. (2017)通过对南海东北部花岗岩和闪长岩钻井样品开展锆石 U-Pb 年代学和元素地球化学等研究^[101],发现早侏罗世该地区确实已开始出现大陆弧特征的岩浆活动。此外,南海东北部盆地基底以钻遇大量上白垩统花岗岩、花岗闪长岩、闪长岩和二长岩为主^[131,132](表 2.1)。

地学研究者除南海北部在越南东南部、北婆罗洲、巴拉望陆块以及巽他陆缘等东南亚地区均发现了相似大陆弧属性的花岗岩和变质火山岩^[133-136]: Nguyen et al. (2004)根据晚白垩世(112–88 Ma)发育的 I 型钙碱性花岗岩岩体,证实了越南南部该时期存在大陆弧岩浆活动; Hennig et al. (2017)发现婆罗洲西南部出露 130–80 Ma 的变质火成岩,认为是古太平洋板块俯冲至中南半岛-东马来地块之下形成的产物; Suggate et al. (2014)提出目前已漂移至南海南侧的巴拉望上白垩统变质沉积岩实际来自华南大陆陆缘,伴随新生代南海的打开,从南海北部裂离并移动至如今的地理位置^[137]。

近年来,一些研究者提出中生代华南陆缘可能发育非安第斯型(non-Andean-type active margin),即华夏型活动陆缘(Cathaysian-type active margin),强调南海及东海陆架盆地基底存在板块停滞现象^[138,139]。部分学者认为大约 200 Ma 以前非安第斯型活动陆缘开始启动,受古太平洋或伊邪那岐(Izanagi Plate)板块俯冲作用控制,表现为岩浆弧周期性发育、增厚、消减、岩浆弧根部移除以及岩浆弧迁移的特征。此外,华南大陆内部存在大量板内岩浆岩,可能与板片脱水、岩石圈剥离、地壳深融以及地壳—地幔熔体混合等一系列过程相互关联^[139]。这种地球动力学演化模式显然与 Suo et al. (2019)提出的经典安第斯型大陆边缘构造演化模式存在很大差异^[140],他们明确指出侏罗纪至白垩纪东海地区的大陆型岩浆弧沿东海向南海地区延伸,由 NNE 向分布转变为 ENE 向分布,在火山弧两侧发育了叠瓦状推覆构造,且与华南陆缘陆上保留的古地形地貌互相吻合^[141]。然而这些模型绝大多数基于野外露头资料,而缺乏相关华南陆缘盆地基底资料的证实。前人研究在年代学、同位素地球化学、元素地球化学等分

析精度上受当时技术和采样的限制，导致华南陆缘中生代构造亲缘关系和地球动力学演化机制一直饱受争议。

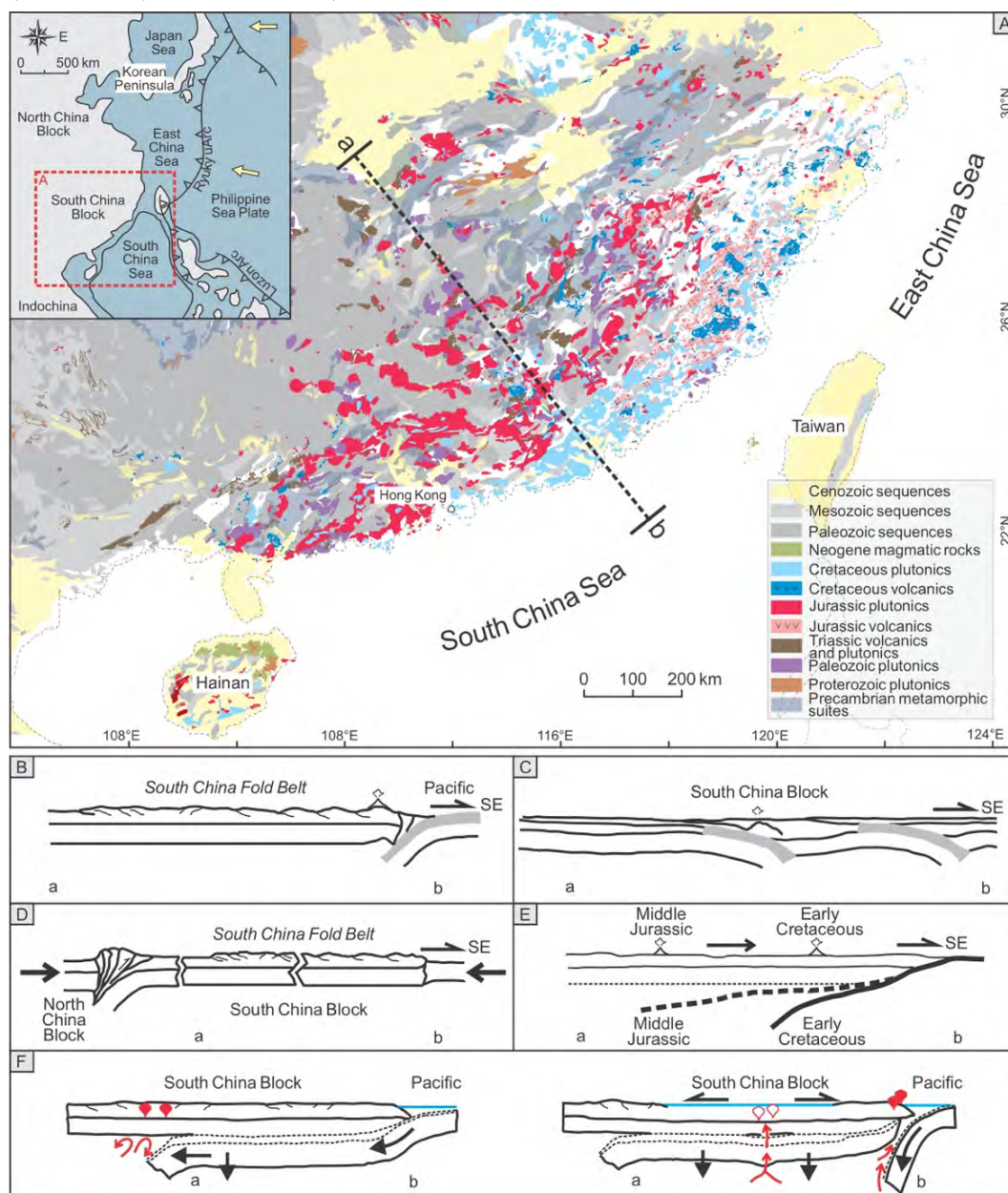


图 2.2 A) 华南大陆岩性分布图 (据 Cui et al. (2021)^[228]); B-F) 华南褶皱带形成机制示意图 (据 Li and Li (2007)^[99])

Fig. 2.2 (A) Simplified geological map of South China showing distribution of Palaeozoic–Cenozoic strata and Precambrian–Neogene magmatic/metamorphic rock units. Inset figure is the present-day geographic sketch of southeast Asia showing major continental blocks/terranes; the position of study area is also highlighted by a red dash-line rectangle (Cui et al. (2021)^[228]). (B–F) Cartoons showing some representative tectonic models for the current onshore region of South China and its extension to the southeast (modified after Li and Li (2007)^[99]).

基于上述研究背景，在系统研究南海北部盆地基底的前提下，仍有若干科学问题亟待解决，包括西太平洋沿岸地区是否曾经存在安第斯型大陆边缘？其

空间展布范围到底如何？南海与东海地区中生代十分均受控于安第斯型大陆边缘？何时开始发育西太平洋型大陆边缘？到底是何种构造过程及相关动力学机制引发了大陆边缘类型的转换？

2.3 南海北部早新生代岩浆记录与断陷活动缺少研究

被动大陆边缘可分为“富岩浆”的火山型陆缘（magma-rich margin），例如南大西洋和挪威陆缘地带^[142-145]，以及“贫岩浆”的非火山型裂谷陆缘（magma-poor margin），例如阿尔卑斯—特提斯和伊比利亚—纽芬兰裂谷陆缘地带^[142, 145-148]。对被动陆缘的岩浆活动性质及演化过程开展相应研究，有助于我们更准确理解大陆裂谷、海底扩张以及相应深水盆地的形成演化等地质现象^[142, 149, 150]。

前人针对南海地区新生代，特别是早新生代火成岩和沉积岩的形成时代、空间分布与岩石成因主要建立在地磁学、地震反射以及陆上邻近地区地质学的基础上^[151-153]，很大程度上阻碍了人们对南海扩张的理解。随着大量科学及工业钻井、深海拖网和多道地震剖面解析等研究的进行，人们对新生代南海海洋壳发育和后续拉张过程取得了进一步理解和认识^[21, 34, 90, 110]。南海及周缘地区新生代发育的花岗岩和玄武岩年龄主要包括三个阶段，即南海扩张前（约 33 Ma 以前），扩张期（约 33–16 Ma），扩张停止后（约 16 Ma 之后）^[151]。其中新近系至第四系火山岩在南海广泛分布，包括珠江口盆地白云凹陷、东沙和洋陆转换带，南海东北向、东西向和北北东向扩张脊，越南南部地区，台湾—吕宋岛弧以及南海南部 Dangerous Grounds 地区^[151]。扩张前与扩张同期的岩浆记录却相对较少，古新世和早—中始新世火山活动仅集中在南海北部珠江口盆地^[151]，因此研究程度相对较浅。

由于自晚白垩时期太平洋板块向华南大陆东缘和东南缘俯冲速度发生骤降，造成俯冲后撤和俯冲角度增大，中国东部大陆边缘由挤压转变为拉张环境，开始发育一系列断陷盆地，从西向东包括北部湾盆地、莺歌海—琼东南盆地、珠江口盆地和台西南盆地。早期研究显示，南海北部陆缘前新生代褶皱基底在古新世，大约距今 65 Ma 至 54 Ma 之间（也有学者认为白垩纪末期）发生大陆裂谷作用^[154]，形成一系列 NNE 向和 NE 向的断陷构造，相应发育珠江口盆地北部断陷带和北部湾盆地，也有学者称之为“神狐运动”。受早期技术手段限制，该时期形成的安山岩、流纹质岩屑晶屑熔岩和凝灰岩以 K-Ar 法或 Ar-Ar 法定年为主，测试年龄分别为 57 Ma、52 Ma 和 49 Ma。有人认为陆丰凹陷和韩江凹陷沉积了神狐组地层，表现为冲击相碎屑物质和火山碎屑岩、火山熔岩等，是南海北部断陷阶段最早发育的沉积地层和岩浆作用的产物。但该时期地层分布和属性受盆地资料限制，神狐组地层是否真正存在，一直存在较大争议。

早—中始新世之间，即大约距今 49 Ma 珠江口盆地发生一定程度的抬升与剥蚀作用，并伴随有断陷和岩浆活动，这次区域构造运动形成了多个 NE 向和 NEE

向断陷, 将盆地分隔成南、北两个主要凹陷, 发育众多深水湖盆, 也有学者称之为“珠琼运动一幕”。地震剖面显示, 早期火山岩通常沿断层带发育并受其控制。该阶段主要形成中酸性和基性岩浆岩, 早期同位素年代学揭示玄武岩、安山质角砾岩、英安斑岩年龄集中在 45–41 Ma 之间。随后在中–晚始新世与早渐新世之间珠江口盆地再次发生抬升和剥蚀作用, 即“珠琼运动二幕”, 大约距今 39 Ma 至 36 Ma, 盆地发生强烈的张裂作用。随后南海开始扩张, 由断陷向坳陷转变, 最终进入裂后沉降时期。珠琼运动二幕时期以发育中性岩浆岩为主, 蚀变安山岩和英安质凝灰岩同位素年龄集中于 35.5 Ma 至 33.6 Ma 之间。这些早期资料大致显示, 南海北部断陷期岩浆活动整体呈现出零星分布且规模较小的特点。

陆上资料显示, 位于华南大陆和印支半岛之间, 呈 NW-SE 走向的哀牢山-红河走滑断裂带也存在两个新生代岩浆活动时期^[149]。其中早新生代岩浆作用发生在断裂带的东南部地区, 主要由喷发性正长岩、流纹岩、碱长角闪岩和玄武质安山岩组成, 花岗岩岩体定年结果为 35–27 Ma^[13], 不过这些岩浆活动可能更与板块间走滑剪切导致的深熔作用有关。华南沿海地区也发育了若干新生代裂谷作用形成的陆上盆地, 例如三水盆地、河源盆地和连平盆地, 盆地规模都较小。三水盆地发育由流纹岩、英安岩和玄武岩组成的喷出岩层, 其 K-Ar 同位素年代学揭示其形成年龄在 64 Ma 和 43 Ma 之间^[149, 155]; 而河源盆地和连平盆地缺少同位素定年数据, 其上白垩统–始新统玄武岩和安山质熔岩与沉积岩呈层状产出。整体来看, 海盆与陆区早新生代火山活动研究整体上仍缺乏准确年代学、同位素特征、活动喷发时空演变规律以及岩浆来源等方面的地质资料 and 对比分析, 另外从构造演化角度来看, 伴随中生代末期安第斯型大陆弧的终止, 南海地区新生代岩浆活动又是如何反映该时期复杂的大陆张裂过程与断陷盆地形成的, 也亟待进一步探讨总结。

2.4 南海北部源汇体系及古地理发育演化中的争议问题

2.4.1 南海北部新生代沉积受单物源还是混合物源模式控制?

作为特提斯洋和古太平洋交汇和碰撞的关键区域, 学术界从未停止对欧亚大陆东南缘构造背景和古水系古地理演化之间关系的探讨^[88, 156, 157]。新生代南海扩张以前, 该地区在中生代持续经历剧烈的俯冲、碰撞、挤压、增生过程^[14, 21]。伴随从活动到被动陆缘的构造转换, 东南亚古水系的演化具有很大复杂性和不确定性的特点^[158, 159], 南海北部早新生代物源模式重建也一直受到钻井样品和年代学结果的限制, 存在诸多争议。例如, 南海西北部盆地新生代发育了巨厚沉积层(图 2.3A), 早期学者认为主要受红河流域影响, 堆积了大量来自青藏高原的碎屑物质, 然而该观点缺少盆地相应钻井资料的证实^[160, 161]; 后来元素地球化

学结果显示，莺歌海-琼东南晚渐新世至中新世形成的巨量沉积可能来自南海西侧的越中地区^[162, 163]。NW-SE 向穿过琼东南盆地的地震剖面显示，该地区自早中新世以来发育下切河道和三角洲前积体，表明确实可能接受了来自越南陆缘方向输送而来的沉积物^[164, 165]。本论文最新取得的地震资料甚至揭示了沿该空间方向展布的古河道可能于早渐新世便已发育（将于第六章展开详细论述）（图 2.3B）。近年来，越来越多的研究者开始关注盆地内局部物源的影响。另外，对于渐新世以后形成的沉积物，由于相对早新生代，钻井资料更充足，研究者发现在某些局部凹陷在较短时间尺度上，可能曾经历双物源甚至多物源影响的阶段^[166]。例如 Cui et al. (2018)指出，发育在琼东南盆地的晚中新世中央峡谷沉积了来自越南中部和海南岛两个源区的陆源碎屑物质^[167]。但对于较长演化尺度的源-汇系统演变，目前仍缺乏可靠的盆内样品，特别是广大的南海北部西侧地区，新生代早期地质资料更是匮乏，也很大程度上制约了整个南海北部盆地尺度的物源演变研究及古水系古地理重建。

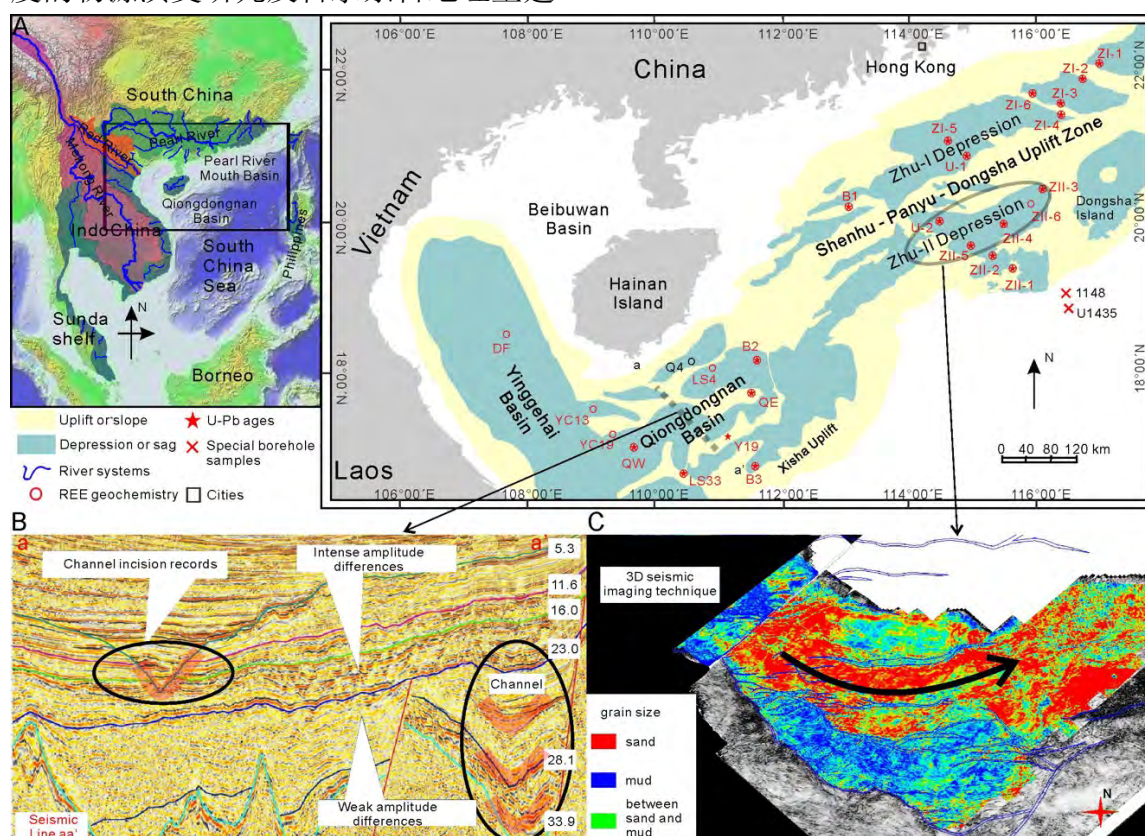


图 2.3A) 莺歌海、琼东南、珠江口盆地位置分布图及其构造单元；B) 琼东南盆地典型地震剖面；C) 琼东南盆地珠二凹陷三维地震成像（据 Shao et al., 2019^[135]）

Fig. 2.3 (A) Map of the Qiongdongnan and Pearl River Mouth Basins in the northern South China Sea (SCS) with tectonic units, studied borehole samples, and published data. Small circles and stars represent the analyzed samples of rare earth element (REE) and detrital zircon U-Pb dating, respectively. Crosses are other important borehole locations. (B) Seismic line a-a' transecting Qiongdongnan Basin are plotted for possible paleo-channel structure. Numbers on the seismic line represent identified strata ages. (C) Ellipse region shows the 3-D seismic image of Zhu-II

Depression indicating eastward sediment transport (modified from Shao et al. (2019) [135]).

位于东侧的珠江口盆地，随着始新-渐新统地层地质资料的增加和深入研究，人们对盆地沉积与陆上水系的发育演化和相互作用过程有了更为深刻的理解。例如，研究认为珠江流域逐步向西拓展，自渐新世以来逐渐加深对南海北部沉积格局的影响^[168, 169]。晚渐新世以来，南海进入热沉降时期，珠江口盆地珠二凹陷发育大规模沉积^[170]。该地区早期的物源研究主要为短时间尺度，集中在分散的局部洼陷或隆起带。除了华南大陆沿海地区广泛存在的中生代火成岩源区以及盆内局部隆起源区之外，珠江水系究竟何时、以何种方式进入南海北部，并以远距离搬运方式主导盆地整体的物源格局尚不清楚^[171]。此外，位于珠江口盆地南部的珠二凹陷可能曾经受到来自西侧物源的重要影响，地震资料揭示地质历史时期发育自西向东，或自西南向东北的沉积物搬运体系，该输送通道后来逐渐萎缩直至最终消亡。然而同样受早期钻孔数量限制，这一潜在物源尚有待进一步证实。

本论文将基于钻井样品、前人研究资料再整合以及源汇示踪综合技术，以期解决有关南海北部新生代沉积物源演变的具体问题，包括不同盆地究竟受单物源还是多物源控制，珠江流域是怎样影响南海北部整体沉积格局，是否存在南海西侧物源（如越中地区等）及其对周缘盆地的影响等热点问题。

2.4.2 晚新生代中央峡谷源—汇系统如何演变？

中央峡谷位于南海西北部地区，长约 570 公里，宽约 9 至 30 公里，呈 S 形沿陆架坡折带平行延伸，沿 NE-NEE 向展布，是一个大型轴向深海沉积构造（图 2.4B）。由于其独特的内部结构和剥蚀-搬运-堆积过程，中央峡谷的形成机制与沉积物源演化一直存在诸多不同观点^[172]：有人认为青藏高原在 5.5 Ma 以前经历了快速隆升，为中央峡谷的早期发育提供了大量沉积物^[173]；另外，此时红河走滑断裂也在经历活跃的右旋走滑作用，也引发了莺歌海-琼东南盆地重力流的形成，为中央峡谷输送了大量物质^[174]；相反，有些研究者认为自 10.5 Ma 以来中央峡谷便逐渐开始发育大规模海底扇，接受了大量来自越南东部剥蚀而来的沉积物^[175]。后来基于二维和三维地震解释与测井数据，研究者对中央峡谷不同区段进行了物源分析与重建^[176, 177]。在系统描述其形态特征与内部结构之后，Su et al. (2013)提出了中央峡谷初始发育、侵蚀填充、壮大发展以及再活化等多个演化阶段，以便恢复其物源演化过程^[177]：一方面，红河流域、越南东部以及海南岛可能是南海西北部地区的主要源区，另一方面，琼东南盆地的构造转变在 11.6 Ma 左右也可能一定程度影响中央峡谷东段的物源演化。

由于缺乏源—汇系统分析所需的可靠地质资料，自晚中新世以来中央峡谷的沉积物源时空演化过程仍然存在许多问题。同时，莺歌海-琼东南盆地曾受盆地内及周边多个潜在源区的影响，更增加了恢复其物质来源和充填机制的难度，例如：尽管红河流域自身发育演化过程仍存在诸如“红河袭夺”等争议，但研

究显示，现代红河新近纪时期的确向南海西北部地区输送了大量沉积物，而“古红河”（Paleo-Red River，并非现代红河河道）可能也曾是重要的源区之一^[158, 162, 178]；地震剖面显示海南岛在晚新生代开始发育前积体和斜坡断层^[179, 180]，锆石 U-Pb 年代学指示海南岛在渐新世至中新世已经对相邻盆地输送碎屑物质^[163, 181]；越南东缘发育向琼东南西部盆地延伸的前积体，另外地球化学结果显示自中新世以来，越南中部可能一直作为重要源区之一影响南海西部盆地沉积^[182]。值得注意的是，琼东南、莺歌海盆地晚新生代沉积还发现一系列 Eu 元素正异常现象^[162, 183]，然而这些发现究竟与中央峡谷的沉积演化过程有何关系，目前仍无具体定论。

总体来看，中央峡谷受哪些源区影响，其整个晚中新世至上新世的沉积填充历史如何，这些问题均需可靠的资料验证与深入探讨。

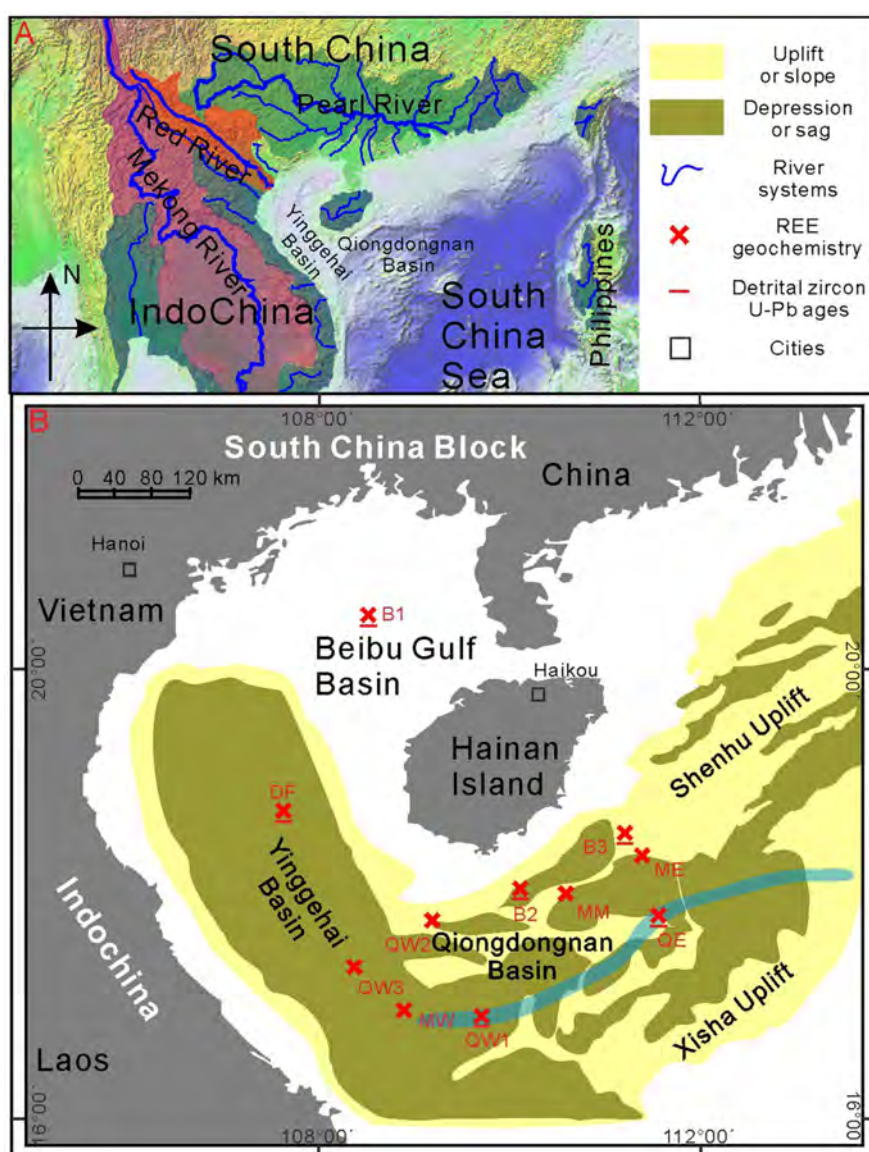


图 2.4A) 南海北部盆地位置分布图及周围潜在源区；B) 中央峡谷空间展布示意图（据 Cui et al., 2019^[167]）

Fig. 2.4 (A) Topographic map of the Yinggehai and Qiongdongnan Basins relative to Southeast Asia and the South China Sea (SCS) and the bottom zoomed plot. (B) The special tectonic units, studied borehole samples and published data. Crosses and lines represent the analysed samples of rare earth element (REE) and detrital zircon U–Pb dating, respectively (modified from Cui et al. (2019) [167]).

2. 4. 3 恒春半岛增生楔浊积岩物质来源是什么？

台湾岛位于欧亚与菲律宾海板块的交界处，是至今仍在活跃的弧-陆碰撞造山带。中中新世以来，南海洋壳沿马尼拉海沟向东俯冲至菲律宾海板块之下，形成了吕宋火山岛弧及西侧的增生楔体系。随着菲律宾海板块持续向西北方向漂移，吕宋岛弧与欧亚大陆于 6.5 Ma 发生斜向碰撞，造成华南陆缘沉积与马尼拉海沟增生楔发生强烈的挤压、变形、隆升，最终出露为如今的台湾岛。由于斜向碰撞作用持续进行，台湾地区由北向南不断进行造山运动，造成地层时代由北向南逐步变新的地质景观^[184]（图 2.5a）。

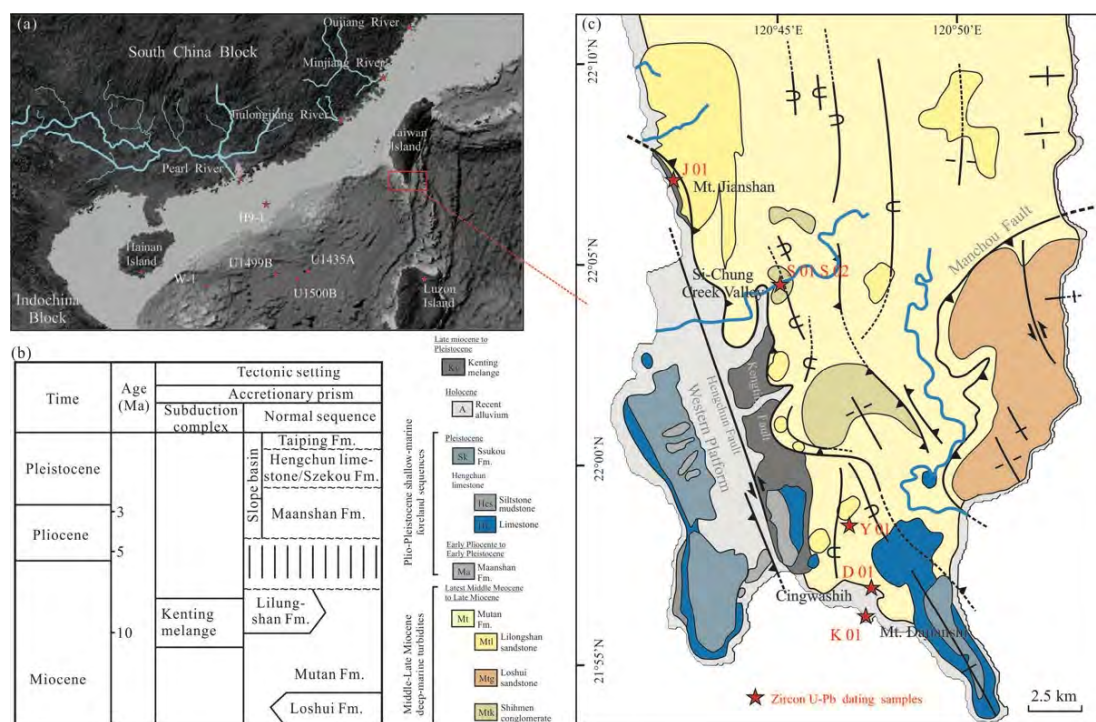


图 2.5a) 台湾岛位置及南海北部构造单元； b) 恒春半岛地层框架； c) 恒春半岛岩性分布图（据 Cui et al., 2021^[185]）

Fig. 2.5 (a) Topographic map of Taiwan Island and its surrounds – studied samples and published data marked with red stars; (b) stratigraphic framework of the Hengchun Peninsula; (c) geological map of the Hengchun Peninsula (modified from Cui et al. (2021) [185]).

根据地质构造单元（图 2.5a），台湾自西向东依次为海岸平原、西部麓山带、雪山山脉、中央山脉-恒春半岛以及岩浆岛弧海岸山脉，整体属增生楔的构造属

性^[186, 187]。对增生楔沉积物进行“源—汇”对比分析，不仅可以查明源区特征，重建增生楔的形成过程及板块俯冲拼合演化历史，还可为揭示南海形成初期东北边缘沉积充填过程提供有效的地质资料，一直是构造—沉积学关注的热点^[184, 188, 189]。

发育在台湾最南部的恒春半岛晚中新世增生楔，以厚层深海相浊积岩为主，厚度约 2000 米，上覆上新统及更新统浅海相砂岩与生物礁灰岩。恒春半岛是中央山脉最晚出露海平面的部分，向南延伸至海底的恒春海脊，没有受到后期变质作用的影响，较好地保留了初期弧—陆碰撞的信息，成为世界上研究增生楔地质的最佳地区之一^[186, 190]。然而，到目前为止，对恒春半岛增生楔的形成过程，特别是物质来源、输送路径及具体的沉积充填过程仍存在较大争议。该问题的解决不仅对准确构建南海北部沉积物的“源—渠—汇”系统极为关键，还对重建中新世以来南海东部俯冲带增生楔的形成模式具有重要意义。

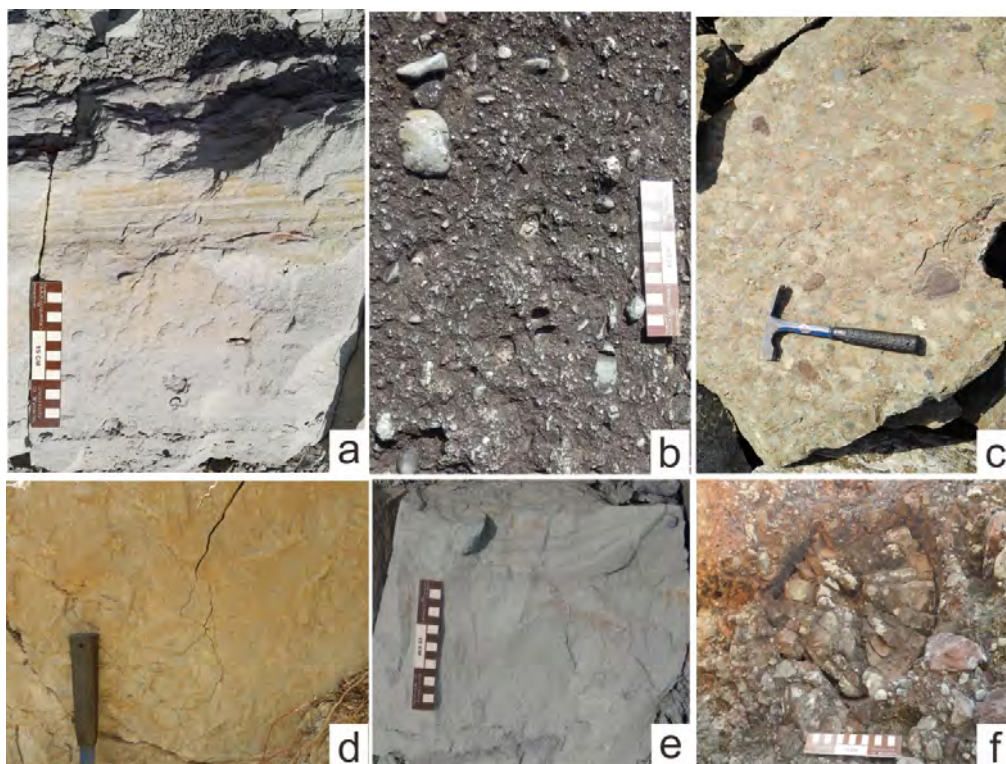


图 2.6 恒春半岛增生楔野外露头：a) 具有鲍玛序列的浊积岩，依次发育砾石层、平行层理、交错层理砂层及水平纹层泥岩；b) 玄武岩、辉长岩砾石；c) 基性砾岩，具有颗粒支撑结构；d) 深水遗迹化石；e) 包卷层理（分布于浊积岩鲍玛序列 C 段）；f) 枕状熔岩岩块（据 Cui et al., 2021^[185]）

Fig. 2.6. Turbidite outcrops of Hengchun Peninsula, Taiwan: (a) Turbidites showing typical Bouma sequences; (b) basic rock gravels; (c) basic rock conglomerate layer forming grain-supported sedimentary structure; (d) trace fossils parallel to the sedimentary strata; (e) convolute beddings; (f) pillow basalt gravel (modified from Cui et al. (2021)^[185]).

恒春半岛增生楔浊积体以发育典型的鲍玛序列为特征，常见磨圆较好、分

选差的基性岩砾石，集中分布在浊积层序的 A 段，底部具有明显的冲刷槽模；向上发育平行层理及交错层理，常见叠瓦状构造和平行层面的深水遗迹化石；顶部为具有水平层理的泥岩。除浊积砂体外，增生楔中还发育碎屑流、泥石流等重力流沉积，夹有枕状熔岩块体，共同构成混杂堆积（图 2.6）。恒春半岛增生楔中除了浊积体中包含大量磨圆度较好的玄武岩和辉长岩砾石外^[191]，还包括其他类型的基性岩砾石单元，如垦丁混杂岩、石门一里龙山砾岩和青蛙石垮塌沉积，主要为重力搬运的产物^[192]。这些基性岩砾石形成年龄介于 27.5–23.6 Ma^[193, 194]，在地球化学特征上类似于 N-MORB、E-MORB 或 OIB。关于基性岩砾石是如何进入恒春半岛浊积体，学术界一直存有争议。部分学者认为可能来自马尼拉海沟上覆的西菲律宾海板块，即花东海盆和吕宋岛弧^[195, 196]；部分学者认为来自南海俯冲板块上的碎片物质，经刮擦后进入增生楔^[192, 193]；南海海山发生剥蚀、搬运，与浊积砂体一起沉积，形成浊积体中的砾石层^[195]；还有学者认为，这些砾石来自于南海洋壳向北超覆至华南被动大陆边缘的超基性物质，最终进入恒春半岛的浊积岩层序中^[194]；除此之外，浊积体中的砾石层可能是南海北部深水搬运过程中，浊流向东侵蚀南海洋壳基底的产物^[197]。

微体古生物研究显示，恒春半岛浊积岩及混杂岩时代为晚中新世，整体处于半深海至深海环境。但是，对于浊积砂体的物质来源和沉积过程，不同学者观点迥异，认为来自华南大陆、北部中央山脉“古台湾”、菲律宾及吕宋岛弧等各种观点。由于复杂的俯冲增生过程造成沉积体的破碎、旋转，使不同剖面浊积体中存在古水流指示方向完全相反的现象。依据西北—东南向古水流指示构造及元素地球化学特征，有学者认为，可能是闽江、九龙江搬运了来自华南大陆东南沿海地区的陆源物质，与基性外来岩块共同构成增生楔浊积体^[188, 189]；依据东南—西北向或东西向古水流方向，有观点认为，浊积砂体可能来自南海南部微陆块^[198-200]；然而，这两种观点均较难解释浊积砂体中明显存在的新生代年龄峰值（约 25 Ma）以及基性岩块的来源。由于强烈的构造改造作用，利用增生楔中的古流向标志判断物质来源的方法有待商榷。也有观点认为，恒春半岛浊积砂体可能受到菲律宾海板块西部边界的影响^[196]，即花东海盆和吕宋岛弧在海沟前缘断离过程中，为增生楔提供物源；但其无法解释浊积砂体中大量出现的前寒武年龄的锆石。此外，南海西侧古河流、北侧珠江以及盆地古隆起带来的碎屑物质汇聚于南海北部深水区，可能与其他俯冲海沟内的混杂堆积共同迁移并最终出露于恒春半岛^[197]；然而这种远距离搬运过程涉及多个源区的混合作用，对增生楔的物源贡献究竟如何，仍需更全面的“源—汇”对比分析。

第3章 材料与方法

3.1 资料收集与样品来源

中国海洋石油集团有限公司在南海北部地区开展了大量钻井作业，取得了许多地质资料和岩芯岩屑样品。本人所在的项目组与中海油集团开展了长期科研合作，地层框架、沉积环境沉积相图、单井资料均是本论文的基础。在整理这些研究资料的同时，配合前人已发表的数据成果，本论文进一步采集了分布于南海北部多口钻井样品，井位展布图分别如第4章、第5章、第6章各节所示，涉及北部湾盆地2口井、莺歌海盆地6口井、琼东南盆地33口井、珠江口盆地32口井。针对第二章提及的热点问题之一，即华南陆缘中生代安第斯弧的时空分布规律，和晚中生代经历的构造转换及其控制因素这些科学问题，本论文还额外选取了东海陆架盆地4口钻井基底样品开展分析（详细见图4.13）。沉积地层和年龄框架划分主要根据中海油提供的地震层序界面、有孔虫、钙质超微化石和藻类等古生物地层信息。本论文涉及的沉积岩和岩浆岩样品包括前新生代、早新生代古近系和晚新生代新近系，具体采样深度、岩性及地层信息详见表4.2、4.3、4.4、6.1、6.2、6.3及6.4。

3.2 元素地球化学分析

元素地球化学分析预处理及室内分析化验工作均在同济大学海洋地质国家重点实验室完成。首先将砂岩和泥岩样品研磨成200目左右的粉末，在600摄氏度下灼烧两小时后称重，计算因去除有机质层间水而产生的烧失量，随后用0.1 M 盐酸去除碳酸钙组分。用HF+HNO₃进行溶样后，利用ICP-AES和ICP-MS分别测试样品中常量与微量元素含量。以1 ppb的Rb元素为内标，每件样品测试6次，使用国际标样、重复样和空白样监测数据结果。本论文涉及的元素地化分析外部精度（external precision, 1 sigma）基本优于5%，标样落在推荐值有效误差范围内，重复样相对偏差基本小于5%（详细处理分析过程参考Shao et al. (2019)^[135]）。

3.3 锆石 U-Pb 年代学及微量元素分析

首先砂岩样品经研磨、粉碎、淘洗、分选后挑出若干颗锆石，并在双目镜下随机选出200颗锆石粘在双面胶上，用环氧树脂固定后将锆石抛光，使锆石

内部结构充分暴露。锆石分选工作均在河北省廊坊市宇能岩石矿物分选技术服务有限公司进行。对锆石靶进行阴极发光 (CL) 图像采集, 根据得到的锆石内部结构选择合适的激光剥蚀位置。一般情况下, 具有环带结构的锆石颗粒代表岩浆成因。代表性锆石 CL 图像详见图 4.14、4.17、4.18 等。

锆石 U-Pb 年代学分析及数据处理工作均在同济大学海洋地质国家重点实验室完成, 测试仪器为 LA-ICP-MS, 其中 laser ablation 型号为 New Wave 213 nm, ICP-MS 型号为 Thermo Elemental X-Series。激光剥蚀中采用 He 为载气, Ar 为补偿气, 用来调节仪器灵敏度, 激光斑直径大小为 20 至 30 微米, 剥蚀频率为 10 Hz。每次分析包括大约 25 秒空白信号和 50 秒样品信号。本论文测年外标采用标准锆石 91500 (U-Pb 年龄 $1065.4 \pm 0.3 \text{ Ma}^{[201]}$) 进行同位素分馏校正, 每 5 个锆石激光点分析两次外标样品。另外采用标准锆石 plešovice ($337.1 \pm 0.4 \text{ Ma}^{[202]}$) 用以检验未知样品分析的准确度。

进行 U-Pb 同位素年代学测量的同时, 锆石微量元素含量的测定以 USGS reference glass 610 作为多外标, Si 单元素为内标。本论文使用 ICPMSDataCal 软件完成样品与空白信号积分区间选择、仪器灵敏度漂移校正、U-Th-Pb 同位素比值、 $^{206}\text{Pb}/^{238}\text{U}$ 和 $^{207}\text{Pb}/^{206}\text{Pb}$ 年龄计算和锆石微量元素计算^[135, 203]。

本论文采用 Andersen (2002) 的方法进行普通 Pb 校正, 选取锆石最佳计算年龄时, 对于小于 1000 Ma 的锆石颗粒选择 $^{206}\text{Pb}/^{238}\text{U}$ 年龄, 大于 1000 Ma 的锆石选择 $^{207}\text{Pb}/^{206}\text{Pb}$ 年龄^[204]。本论文年龄不确定度 (uncertainty; 1 sigma) 不超过 10%, 对于年轻锆石由于其 Pb 信号强度可能较低, 因此不确定度的筛查相对严格。另外, 应该谨慎确定锆石 U-Pb 年龄不谐合度 (discordance) 的阈值: 如果使用取得的全部 U-Pb 年龄数据集一般会造成整体质量较差; 而使用较低阈值进行筛查, 又很大程度上丢失锆石年龄分布的部分特征, 因为古老锆石常由于化学活动性流体、晶格损伤等原因发生 Pb 丢失, 造成不谐合度增加。

若要使得岩浆锆石具有统计意义, 所必需的锆石颗粒数目一般为 30 颗以上; 然而, 对于碎屑锆石所必需的统计数目尚存争议: Vermeesch (2004)^[64] 认为在 95% 置信度内, 至少需要 117 粒; 也有学者认为 35–70 粒即可达到要求。需要说明的是, 虽然增加锆石分析数目有助于识别比重较低的年龄组合, 且有利于比重较高的年龄组合之间相互对比, 但考虑到耗费时间长、花费较大等因素, 因此一味提升锆石测试数目在操作中并不实际。本论文针对具体情况, 最终岩浆岩锆石有效统计数目每件样品大于 30 粒, 沉积岩碎屑锆石有效统计数目每件样品在 50 至 150 之间, 综合下来符合统计要求。该统计方法和规则同样适用于已发表数据的再处理和分析工作。

本论文采用 DensityPlotter 以直方图和概率分布曲线的形式展示锆石 U-Pb 年龄分布特征, 概率分布曲线采用核密度估计方法 (KDE, Kernel density estimation)^[205]。KDE 方法相对于传统概率密度曲线 PDP (Probability density plot) 最大区别在于不考虑每个年龄的分析精度。一方面在处理大样本年龄数据

时产生的曲线过度平滑，另一方面处理高精度数据时避免产生噪声信号^[63]。无论 KDE 还是 PDP，在选择频宽 bandwidth 时，或多或少可能受到主观判断的影响，但还是能有效识别不同年龄集合之间的相对差异，从而有助于源—汇对比分析。

3.4 锆石 Lu-Hf 同位素体系分析

对已经在同济大学海洋地质国家重点实验室完成锆石 U-Pb 定年的，来自南海北部前新生代基底和早新生代钻井样品、东海陆架盆地基底钻井样品（其中样品 TB8 锆石 U-Pb 年代学和 Lu-Hf 同位素测试均在科廷大学完成）开展锆石原位 Lu-Hf 同位素含量测试，分析化验工作均在澳大利亚科廷大学 John De Laeter Centre 完成，采用 Resonetics RESolution SE 193 nm ArF 激光剥蚀系统作为进样采集系统，测试仪器为 Nu Plasma II 型 MC-ICP-MS。仪器条件和数据采集参考 Olierook et al. (2020)^[206]，能量密度为 3.8–5.2 J/cm²，重复频率为 8 Hz，激光斑束直径为 38 μm，每次测试包括 45 秒背景信号采集和 30–35 秒样品信号分析。所有分析均包括剥蚀之前的两次清洗脉冲，并在剥蚀完成后额外收集 15–18 秒的基线。样品室由高纯度 He 气（0.68 L/min）和 N₂ 气（2.8 mL/min）冲洗，高纯度 Ar 气被用于载气气体，分流至各个气室。同位素信号用法拉第杯接收，实现所有目标信号同时被接收，并且不同质量数的峰值基本平坦，从而保证数据的精确度。

Lu-Hf 同位素数据处理在 Iolite 软件平台上进行^[207]。为了校正 ¹⁷⁶Lu 和 ¹⁷⁶Yb 对 ¹⁷⁶Hf 的干扰，选取 ¹⁷⁶Lu/¹⁷⁵Lu = 0.02655 和 ¹⁷⁶Yb/¹⁷³Yb = 0.7962 作为定值，采用 ¹⁷²Yb/¹⁷³Yb = 1.35274 对 Yb 同位素比值进行指数归一化质量歧视校正，采用 ¹⁷⁹Hf/¹⁷⁷Hf = 0.7325 对 Hf 同位素比值进行指数归一化质量歧视校正。通过反复调整 ¹⁷⁶Yb/¹⁷³Yb 比率，直到监控标样的标准锆石校正比率落在合理范围内，以此确定有效的 ¹⁷⁶Yb/¹⁷³Yb 校正因子。本论文涉及的干扰同位素 Yb 或 Lu 丰度与校正后的 ¹⁷⁶Hf/¹⁷⁷Hf 比值之间不存在明显的相关性，如图 3.1 所示，说明 Yb 或 Lu 同位素存在并未对 ¹⁷⁶Hf/¹⁷⁷Hf 比值的准确性产生影响。

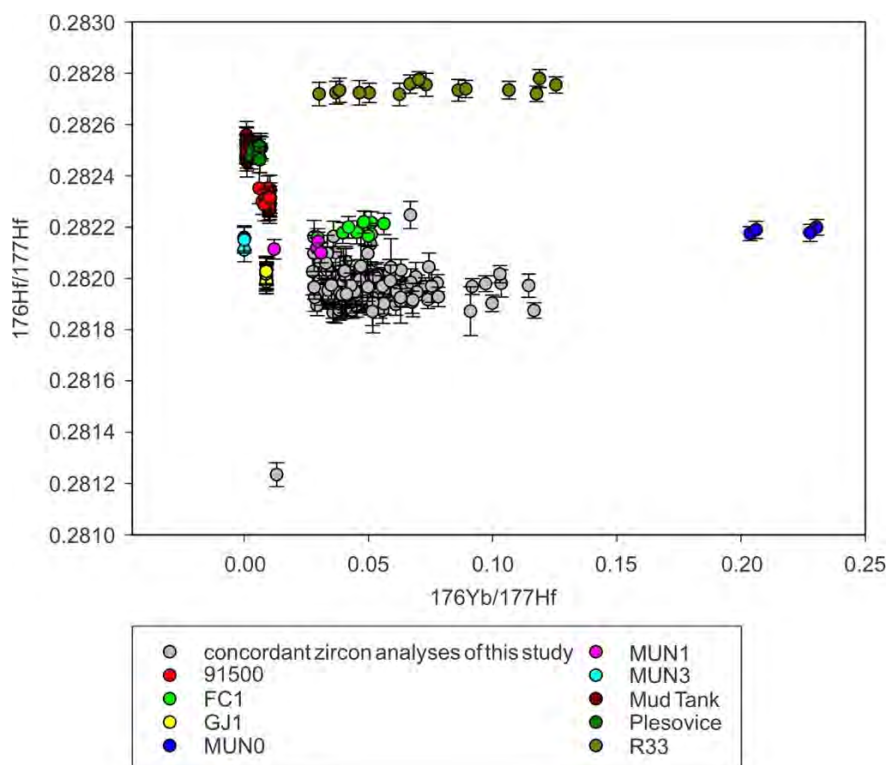


图 3.1 本论文第 4.3 节中岩浆岩样品的锆石 $^{176}\text{Hf}/^{177}\text{Hf}$ vs $^{176}\text{Yb}/^{177}\text{Hf}$

Fig. 3.1 The igneous zircon $^{176}\text{Hf}/^{177}\text{Hf}$ vs $^{176}\text{Yb}/^{177}\text{Hf}$ variations of section 4.3

本论文采用标准锆石 MudTank 为主标（标准值 $^{176}\text{Hf}/^{177}\text{Hf} = 0.282505 \pm 0.000044$ ），监控标样包括 R33（标准值 $^{176}\text{Lu}/^{177}\text{Hf} = 0.001989 \pm 0.000869$ ）、91500（标准值 $^{176}\text{Hf}/^{177}\text{Hf} = 0.282306 \pm 0.000008$ ）、FC-1（标准值 $^{176}\text{Hf}/^{177}\text{Hf} = 0.282172 \pm 0.000042$ ）、GJ-1（标准值 $^{176}\text{Hf}/^{177}\text{Hf} = 0.282000 \pm 0.000005$ ）。对主标 MudTank 进行校正后的 $^{178}\text{Hf}/^{177}\text{Hf}$ 与 $^{180}\text{Hf}/^{177}\text{Hf}$ 同位素比值计算，旨在监测质量偏差校正的准确性，结果分别为 1.4670851 ± 0.0000229 和 1.8866333 ± 0.0000490 ，落在标准值的合理误差范围内。

在计算 $(^{176}\text{Hf}/^{177}\text{Hf})_i$ 和 $\varepsilon\text{Hf}(t)$ 值时， ^{176}Lu 衰变常数采用 $1.867 \pm 0.015 \times 10^{-11} \text{ yr}^{-1}$ ，采用 Bouvier et al. (2008) 推荐的球粒陨石 Hf 同位素值 $^{176}\text{Lu}/^{177}\text{Hf}_{\text{CHUR}} = 0.0336$ 以及 $^{176}\text{Hf}/^{177}\text{Hf}_{\text{CHUR}} = 0.282785$ 。本论文计算 $\varepsilon\text{Hf}(t)$ 值的 2 sigma 误差是通过采用 Ickert et al. (2013)^[208] 模型 1 计算得到的，该方法综合考虑了锆石 U-Pb 年龄、 ^{176}Lu 衰变速率和 CHUR (Chondritic uniform reservoir) 不确定度。在 Hf 模式年龄计算过程中，亏损地幔值 (DM, depleted mantle) 采用 $^{176}\text{Lu}/^{177}\text{Hf} = 0.0384$ ， $(^{176}\text{Hf}/^{177}\text{Hf})_{\text{DM}} = 0.28325$ ，两阶段模式年龄采用上地壳 (UCC, upper continental crust) 的 $(^{176}\text{Hf}/^{177}\text{Hf})_{\text{UCC}} = 0.0093$ 进行计算。

本论文还引入了基于 MATLAB 平台而开发的 HafniumPlotter 程序，利用二元核密度估计 (bivariate kernel density estimates) 的方法，旨在更好地将锆石 U-Pb 年龄与对应的 Lu-Hf 同位素数据可视化展示^[209]。该程序在构建二元核密度估

计时基本遵循一元核密度估计的思路，但是会在原有的二维网格上增加一个密度的变量。利用二元核密度估计可以更方便地可视化大型二维数据集，以密度图的形式呈现出来，有助于研究者识别特征峰值，避免因主观因素造成的误判。

第4章 南海北部基底属性及其构造指示意义

4.1 南海北部基底特征新认识

前人针对南海北部基底开展的早期研究主要集中在东部的珠江口盆地，这些资料作为补充信息，一定程度上也有助于我们对南海基底产生更全面系统的理解^[101, 131, 154]。相关钻井的地理位置如图 4.1 所示，前人资料表 4.1 所示；本研究涉及的样品具体信息如表 4.2 所示。

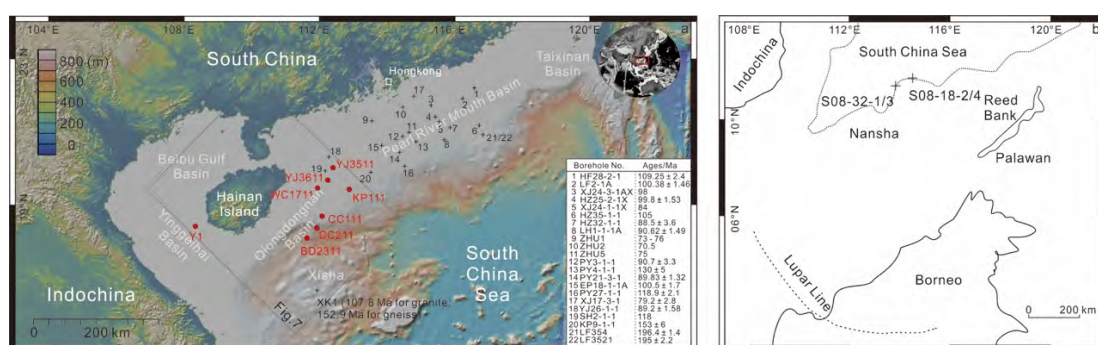


图 4.1a) 南海北部基底钻井位置图（红色字体代表本研究样品；黑色字体代表前人发表 K-Ar 或 Ar-Ar 同位素年龄）；b) 南沙地区花岗岩拖网样品位置图^[33]（据 Zhu et al., 2021^[210]）

Fig. 4.1 Map of Beibu Gulf Basin, Yinggehai Basin, Qiongdongnan Basin and Zhujiang River Mouth Basin in the South China Sea with studied borehole samples and published data (a). Plot zoomed in the upper right corner shows the study area under the global background. Red filled circles represent the analyzed boreholes of detrital zircon U-Pb dating or elemental geochemistry in this study. Black numbered crosses mainly centralized in the northeastern Zhujiang River Mouth Basin show some important samples analyzed by U-Pb, K-Ar or Rb-Sr dating in other studies. XK1 is from Zhu et al. (2017). Ages of these previous researches are shown in the lower right corner (Qiu et al., 1996; Li et al., 1999; Xu et al., 2017). For detailed sample information, refer to Tables 4.1 and 4.2. Sketch map of the Nansha area (b), its surrounding terranes and two dredge sampling locations (black cross) (Yan et al., 2010) (modified from Zhu et al. (2021)^[210]).

表 4.1 南海北部基底前人已发表中生代岩浆岩样品信息

Table 4.1. Summary of published data of South China Sea pre-Cenozoic basement (refer to Fig. 4.1 for detailed sample locations)

图 4.1 中标号	钻井名称	深度/m	年龄/Ma	方法	岩性	资料来源
1	HF28-2-1	3942.0–3943.6	109.25±2.4 0	K-Ar	catclastic granodiorite	Li et al. (1999)
2	LF2-1A	2480.0–2483.5	100.38±1.4 6	K-Ar	catclastic dimicaceous	Li et al. (1999)

第 4 章 南海北部基底属性及其构造指示意义

					granite	
3	XJ24-3-1AX	4318-4319	98	K-Ar	cataclastic granite	Li et al. (1999)
4	HZ25-2-1X	3196.4	99.80±1.53	K-Ar	cataclastic granite	Qiu et al. (1996)
5	XJ24-1-1X	3851.0-3851.5	84	K-Ar	granite	Li et al. (1999)
6	HZ35-1-1	2218.9	105	K-Ar	cataclastic quartz diorite	Li et al. (1999)
7	HZ32-1-1	2791	88.5±3.6	K-Ar	cataclastic granite	Li et al. (1999)
8	LH1-1-1A	1836.5	90.62±1.49	K-Ar	cataclastic granodiorite	Li et al. (1999)
8	LH1-1-1A	1822.0-1837.5	72.78±1.37	Rb-Sr	cataclastic granodiorite	Li et al. (1999)
9	ZHU1	1846-1847	73-76	K-Ar	granite	Li et al. (1999)
10	ZHU2	2379-2380	70.5	K-Ar	biotite granite	Li et al. (1999)
11	ZHU5	3261.8-3262.3	75	K-Ar	granite porphyry	Li et al. (1999)
12	PY3-1-1	3192	90.7±3.3	K-Ar	granite	Li et al. (1999)
13	PY4-1-1	3160	130±5	K-Ar	granite	Qiu et al. (1996)
14	PY21-3-1	4068.0-4019.5	89.83±1.32	K-Ar	cataclastic biotite granite	Li et al. (1999)
15	EP18-1-1A	3448.25	100.5±1.7	K-Ar	granite	Qiu et al. (1996)
16	PY27-1-1	3607-3609	118.9±2.1	K-Ar	quartz monzonite	Li et al. (1999)
17	XJ17-3-1	2122-2124	79.2±2.8	K-Ar	cataclastic granite	Li et al. (1999)
18	YJ26-1-1	1700-1702	89.20±1.58	K-Ar	rhyolite porphyry	Li et al. (1999)
19	SH2-1-1	3641.2	118	K-Ar	biotite hornblende diorite	Li et al. (1999)
20	KP9-1-1	1662-1774	153±6	K-Ar	cataclastic granite	Li et al. (1999)
21	LF354	2472.3	196.4±1.4	U-Pb	granite	Xu et al. (2017)
#	LF3521	2443.5	195.0±2.2	U-Pb	diorite	Xu et al. (2017)
#	S08-18-2	2700	159.1±1.6	U-Pb	tonalite	Yan et al. (2010)
#	S08-18-4	2700	157.8±1.0	U-Pb	tonalite	Yan et al. (2010)
#	S08-32-1	3100	153.6±0.3	U-Pb	monzogranite	Yan et al. (2010)
#	S08-32-3	3100	127.2±0.2	U-Pb	monzogranite	Yan et al. (2010)

表 4.2 本研究南海北部基底样品信息

Table. 4.2. List of samples analyzed for Laser-ICP-MS detrital zircon U-Pb dating (refer to Fig.

4.1a for detailed sample locations)

钻井名称	地理位置	取样深度/m	基底深度/m	前人时代定名	最年轻锆石年龄/Ma	最大沉积年龄	岩性
Y1	莺歌海盆地	3021–3023	3021	?	1264±83	前寒武	变质黑云母花岗岩
WC1711	琼东南盆地	2216	2216	古生代	114±4	早白垩	变质凝灰岩
CC211	琼东南盆地	1116	1076	古生代	129±7	早白垩	变质凝灰岩
KP111	珠江口盆地	1893–1897	1884	古生代	124±3	早白垩	火山碎屑岩
BD2311	琼东南盆地	2166	2166	古生代	85±3	晚白垩	变质石英砂岩
CC111	琼东南盆地	1172	1117	古生代	125±4	晚白垩	变质砂岩
YJ3511	珠江口盆地	4321–4339	4321	古生代	88±2	晚白垩	变质粉砂岩
YJ3611	珠江口盆地	3565–3580	3484	古生代	88±2	晚白垩	变质泥岩和粉砂岩

4.1.1 镜下薄片观察

南海北部前新生代基底钻井样品 KP111、YJ3511、YJ3611 和 Y1 岩石薄片单偏光镜和正交镜下观察结果如图 4.2 所示，本论文对其矿物组成、含量、结构和构造均进行了鉴定和分析。样品 KP111 主要由变质火山碎屑岩和石英岩组成（图 4.2a–b）：火山碎屑岩具有明显的斑状结构，主要斑晶为石英颗粒，矿物表面干净，呈自形及半自形晶体，发育熔蚀结构和炸裂纹，指示喷发结晶过程中

经历了剧烈的温度变化；基质主要由微晶长石和石英组成，由玻璃质重结晶而成。另外，样品 KP111 次生绢云母含量较高，略有定向排列现象，显示岩石经历了轻微变质作用。石英岩中石英也表现出一定的镶嵌结构和定向排列特征，同样显示低级变质作用的存在。

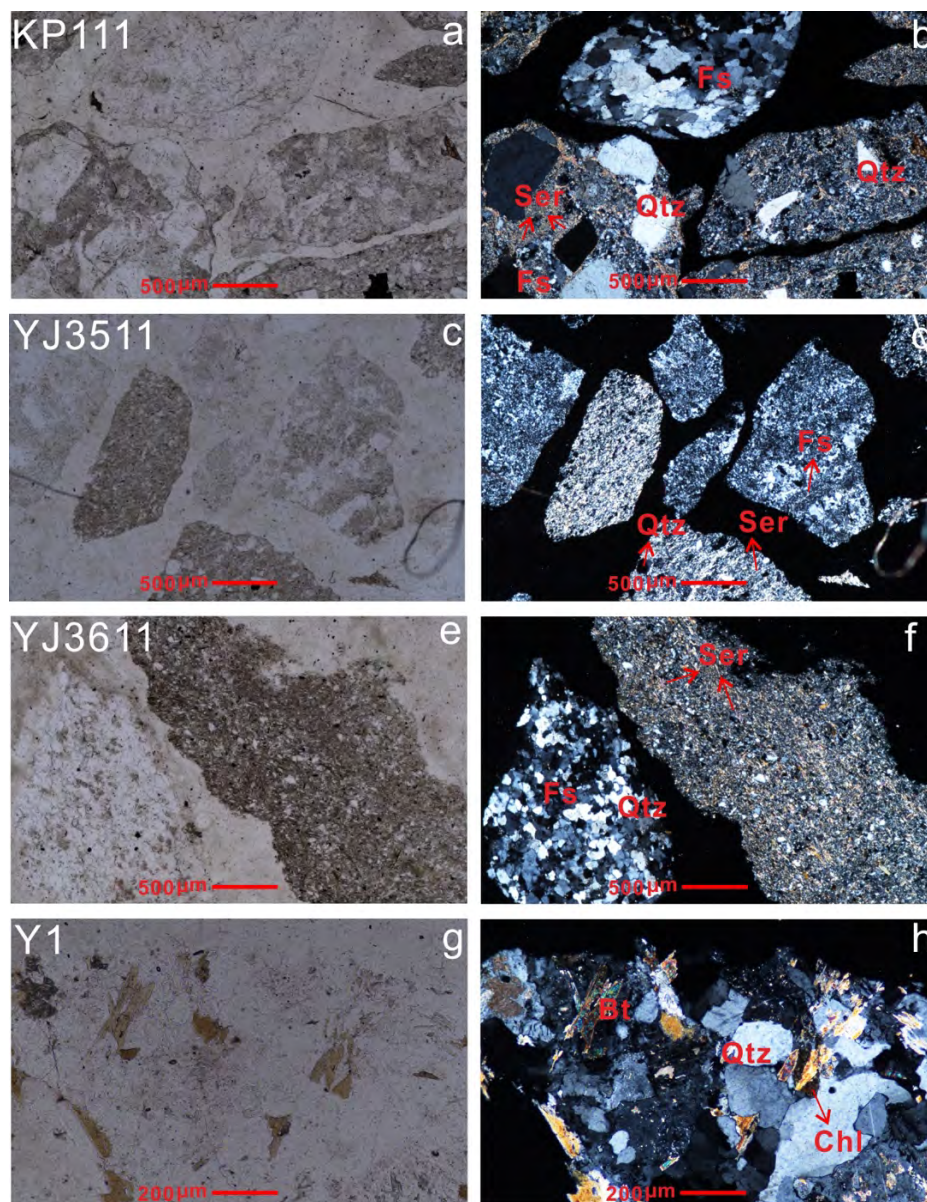


图 4.2 南海北部基底钻井样品单偏光及正交偏光镜下薄片 a-b) KP111; c-d) YJ3511; e-f) YJ3611; g-h) Y1

Fig. 4.2 Lithological and petrographic characteristics of SCS Basin basement samples under both plane-polarized light and cross-polarized light microscope. a. KP111, metamorphic volcaniclastic rock; c. YJ3511, metamorphic siltstone; e. YJ3611, metamorphic mudstone and siltstone; g. Y1, metamorphic biotite granite slices under plane-polarized light; b. KP111, d. YJ3511, f. YJ3611 and h. Y1 slices under cross-polarized light. Fs: feldspar, Qtz: quartz, Ser: sericite, Bt: biotite, Chl: chlorite.

样品 YJ3511 由低级变质的板岩及变质粉砂岩组成，其单偏光和正交镜下观察结果如图 4.2c-d 所示。板岩中粘土矿物呈隐晶状及微晶状，由长石及石英组成，可见定向排列的绢云母，具有变余泥质结构；变质粉砂质泥岩中可见微晶状石英及长石分布在粘土矿物中，新形成的绢云母等片状矿物定向排列，具变余粉砂泥质结构。

样品 YJ3611 由变质泥岩及变质粉砂岩组成，其单偏光和正交镜下观察结果如图 4.2e-f 所示。变质泥岩可以看到粘土矿物呈隐晶质，见少量石英及长石微晶，具有变余泥质结构，新形成的绢云母定向排列；变质粉砂岩中微晶石英及长石呈镶嵌状，定向排列。整体岩石遭受低级变质作用的影响。

样品 Y1 是变质花岗岩，其单偏光和正交镜下观察结果如图 4.2g-h 所示。岩石由正长石、石英及少量斜长石及黑云母组成，具花岗结构。长石发生高岭土化及碳酸盐化及钠黝帘石化，黑云母发生绿泥石化，可见绿泥石、白云母及石英定向排列，显示岩石遭受一定程度的变质作用。

4.1.2 全岩元素地球化学结果

南海北部前新生代基底钻井样品 (BD2311、WC1711、CC111、CC211、YJ3611 和 KP111) 微量元素原始地幔 (PM, primitive mantle) 标准化以及稀土元素球粒陨石 (chondrite) 标准化配分曲线如图 4.3 所示，总体而言，样品微量元素与稀土元素配分方式与平均陆壳 (ACC, average continental crust) 含量存在一定差异^[211]。一方面，微量元素配分特征表现为明显的 Ba、Nb、P 和 Ti 元素负异常，而 Rb、Th、U 和 K 元素表现为轻微的正异常，这些元素通常被认为是放射性产热元素 (图 4.3a)；另一方面，微量元素配分特征表现为明显的 Eu 元素负异常 ($Eu/Eu^* = 0.03-0.98$ ，少数样品为 1.08、1.44 和 1.92)，明显富集轻稀土元素 ($(La/Yb)_N = 0.65-59.46$) (图 4.3b)。只有井 BD2311 的 $(La/Yb)_N$ 比值小于 1，为 0.65，且稀土元素配分特征为平坦型，轻重稀土含量相近，Eu 元素表现为明显的负异常 ($Eu/Eu^* = 0.09$)。

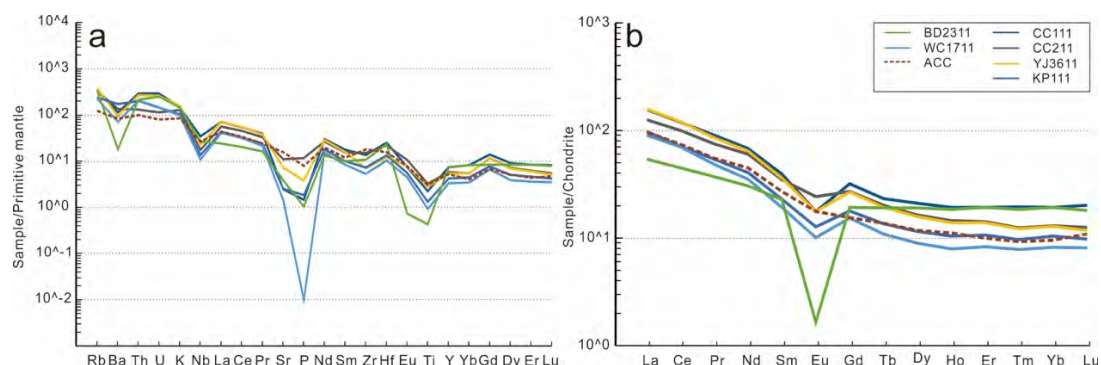


图 4.3 南海北部基底钻井样品 BD2311, WC1711, CC111, CC211, YJ3611 以及 KP111 (具体位置见图 4.1a) a) 微量元素原始地幔标准化及 b) 稀土元素球粒陨石标准化配分曲线

Fig. 4.3 Primitive mantle-normalized trace element spider diagrams (a) and chondrite-normalized

rare earth elements (REE) distribution patterns (b) for the SCS Basin basement samples BD2311, WC1711, CC111, CC211, YJ3611 and KP111.

4.1.3 锆石 U-Pb 定年结果

基底样品阴极发光图像显示，绝大多数锆石具有清晰的振荡环带，属于岩浆锆石，且大多数激光分析点 Th/U 比值在 0.1–1 之间^[212]（图 4.4）。锆石 U-Pb 年龄谐和图如图 4.5 所示，其年龄直方图和概率密度分布曲线如图 4.6a–c 所示，并根据样品岩性特征和年龄谱系分成三组。各样品锆石 U-Pb 定年结果具体描述如下。

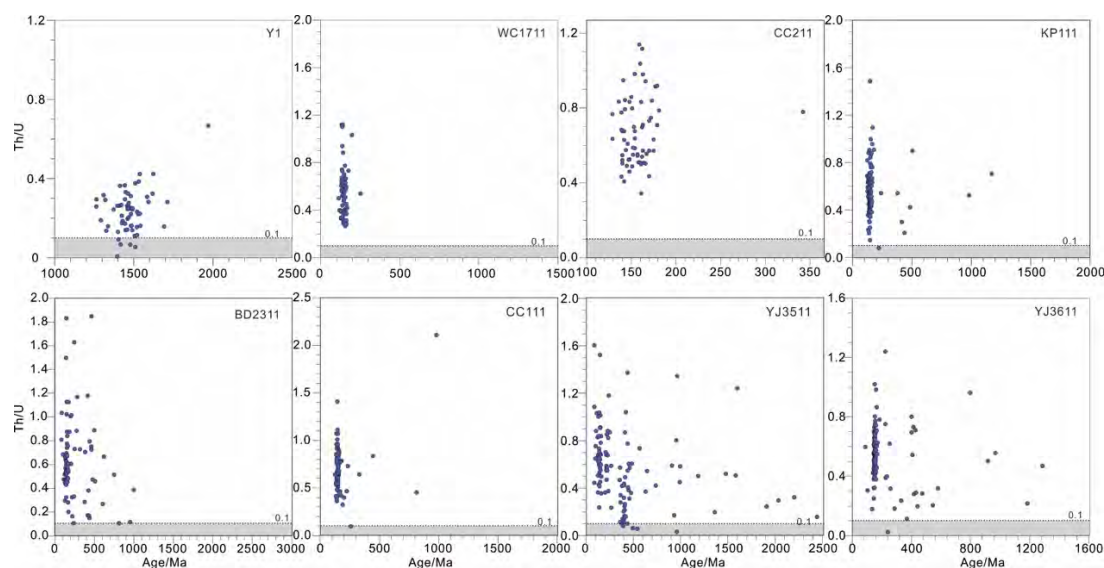


图 4.4 南海北部基底钻井样品 Y1, WC1711, CC211, KP111, BD2311, CC111, YJ3511 以及 YJ3611（具体位置见图 4.1a）Th/U vs. 锆石 U-Pb 年龄

Fig. 4.4 Summary of the Th/U ratios versus U-Pb ages of the studied zircon grains from the SCS Basin basement. Grey shades indicate the Th/U variations are lower than 0.1.

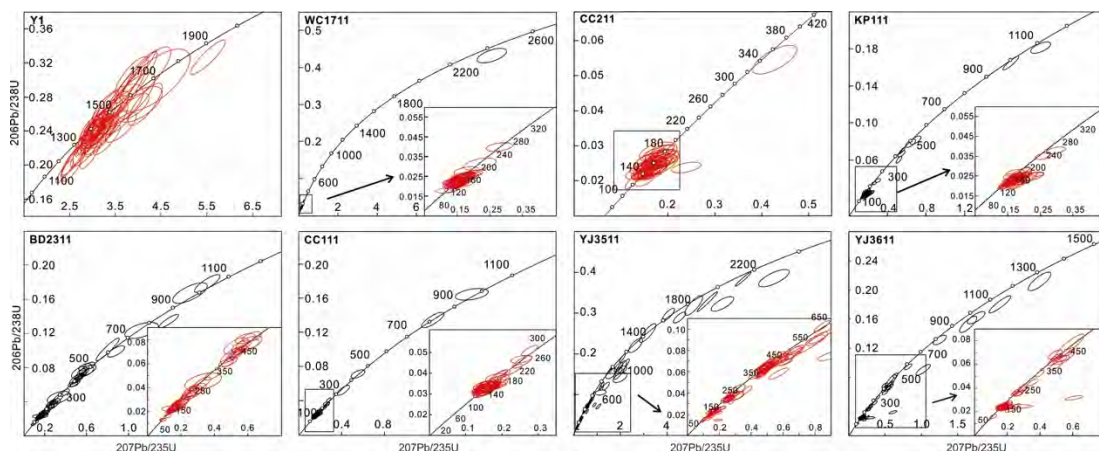


图 4.5 南海北部基底钻井样品 Y1, WC1711, CC211, KP111, BD2311, CC111, YJ3511 以及 YJ3611（具体位置见图 4.1a）锆石 U-Pb 年龄谐和图

Fig. 4.5 Detrital zircon U-Pb Concordia diagrams for the SCS Basin basement samples. The lower right corner plots in some diagrams show magnified Concordia ages for samples WC1711, CC211, KP111, BD2311, CC111, YJ3511 and YJ3611.

井 WC1711 位于海南岛东部，基底钻遇变质凝灰岩，锆石颗粒呈磨圆状、次圆状至自形形状，具有振荡环带（图 4.6a）。该样品 Th 元素（110.26–3 501.78 ppm）和 U 元素（152.23–3 729.32 ppm）含量变化较大，相应的 Th/U 比值大于 0.1（图 4.4）。本研究共取得 65 个有效年龄，最年轻锆石年龄为 114 ± 4 Ma。除了仅有一颗继承性锆石（ $^{207}\text{Pb}/^{206}\text{Pb}$ 年龄为 2503 ± 42 Ma）以外，WC1711 以中生代年龄为主，范围在 114 ± 4 Ma 至 252 ± 6 Ma 之间，年龄峰值集中在大约 150 Ma（图 4.6a）。另一个变质凝灰岩样品 CC211 位于 WC1711 南侧，其 Th 元素和 U 元素含量分别为 86.29–1756.57 ppm 和 150.73–3482.09 ppm，相应的 Th/U 比值在 0.34 至 1.14 之间。样品 CC211 共取得 64 个有效年龄，最年轻锆石年龄为 129 ± 7 Ma，除了一颗古生代锆石（ 342 ± 10 Ma）之外，其余年龄均为中生代年龄，峰值集中在 150 Ma 左右（图 4.6a）。

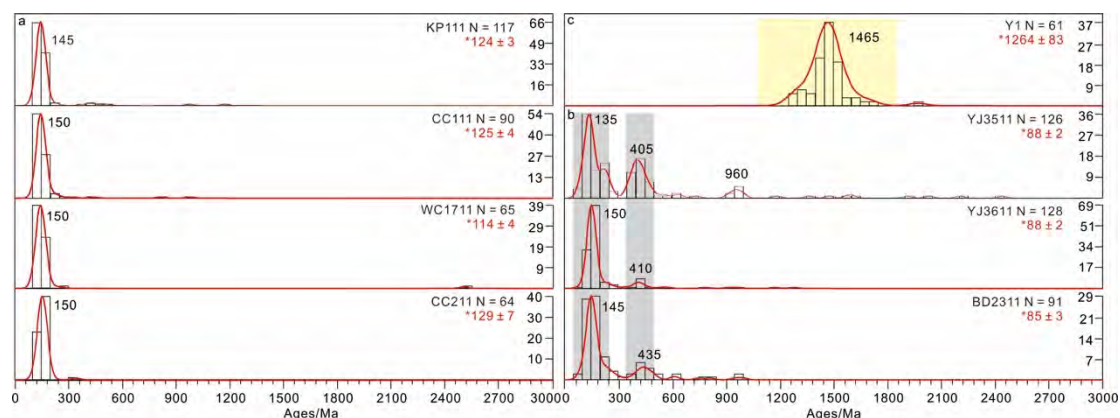


图 4.6 南海北部基底钻井样品 a) KP111, CC111, WC1711 和 CC211（年龄峰值集中于 150 Ma）；b) YJ3511, YJ3611 和 BD2311（双峰年龄模式，主峰为燕山期峰值，次峰为加里东期峰值）；c) Y1（中元古代单峰）锆石 U-Pb 年龄直方图和概率密度分布曲线

Fig. 4.6 Histograms and probability density distribution plots for detrital zircon U-Pb ages of the SCS Basin basement samples with characteristic age peaks numbered. Age spectra are grouped according to their specific distribution patterns into (a)–(c) sub-plots. N represents the number of concordant analyses for each sample. The youngest zircon U-Pb age in red is marked with * in the upper right corner. Dominant age peaks of sample Y1 are highlighted in light yellow shades; major peaks of YJ3511, YJ3611 and BD2311 are in gray shades.

变质砂岩样品 CC111 主要以次自形和自形状锆石颗粒为特征。该样品共取得 90 个有效年龄，Th 元素和 U 元素含量变化相对较小，分别为 111.24–1897.93 ppm 和 202.82–4722.91 ppm，几乎所有的 Th/U 比值大于 0.1。大约 94% 以上的锆石年龄均是中生代年龄，范围在 125 ± 4 Ma 至 233 ± 5 Ma 之间（图 4.6a）；剩余 5 个分析样点包括三个古生代年龄（ 258 ± 6 Ma， 329 ± 14 Ma 和 444 ± 12 Ma）和两个

元古代年龄 (813 ± 21 Ma 和 981 ± 15 Ma)。

井 KP111 基底钻遇火山碎屑岩, 锆石颗粒呈自形状至次自形状, 具有清晰的核-边结构。共取得 117 个有效年龄, Th 元素和 U 元素含量范围变化较大, 分别为 32.24–2730.38 ppm 和 95.13–4055.87 ppm, 相应得到的 Th/U 比值中只有一个分析点较小, 为 0.08 (图 4.4)。该样品得到两个元古代年龄, 分别为 982 ± 17 Ma 和 1173 ± 31 Ma, 表示可能存在继承核 (图 4.6a); 可见几个零散分布的古生代年龄, 范围在 505–379 Ma 之间; 共有 108 个中生代年龄, 范围在 240–124 Ma 之间, 年龄峰值集中在大约 145 Ma 附近。样品 KP111 最年轻年龄为 124 ± 3 Ma (图 4.6a)。

井 YJ3511 钻遇变质粉砂岩, 共取得 126 个有效年龄。Th 元素和 U 元素含量变化较大, 分别为 136.84–7900.79 ppm 和 110.07–10989.99 ppm, 其中有六个 Th/U 比值在 0.03 至 0.1 之间 (图 4.4), 剩余其他 Th/U 在 0.11 至 1.6 之间。样品 YJ3511 表现为两个峰值, 主要峰值集中于 135 Ma 左右, 次要峰值集中于 405 Ma 附近 (图 4.6b); 其中有 38 个古生代年龄, 范围在 252 ± 5 Ma 和 495 ± 10 Ma 之间; 21 个元古代年龄, 范围在 543 ± 27 Ma 至 2443 ± 36 Ma 之间。井 YJ3611 位于 YJ3511 附近, 基底钻遇变质泥岩和粉砂岩, 共取得 91 个有效年龄。Th 元素和 U 元素含量较高, 同样变化较大, 分别为 122.9–8349.25 ppm 和 373.64–33224.03 ppm, 除了一个分析点为 0.02 之外, 其余年龄 Th/U 比值在 0.11 至 1.24 之间 (图 4.x)。约 90% 的锆石年龄集中于大约 150 Ma 处, 21 个年龄组成次要峰值, 范围在 252 ± 5 Ma 和 1283 ± 47 Ma 之间。与样品 YJ3511 相比, YJ3611 的集中于 410 Ma 次要峰值较不明显 (图 4.6b)。两个样品的最年轻年龄均为 88 ± 2 Ma。

井 BD2311 位于海南岛东南方向, 基底钻遇变质石英砂岩。其 Th 元素和 U 元素含量变化适中, 分别为 37.62–6348.54 ppm 和 72.99–4127.31 ppm, 所有分析样点 Th/U 在 0.1 至 1.85 之间 (图 4.4)。超过 80% 以上的锆石颗粒为中生代年龄, 集中与大约 145 Ma 左右。与样品 YJ3611 类似, BD2311 锆石 U-Pb 年龄谱系表现为集中于 435 Ma 的次要峰值, 但较不明显, 26 个年龄包括 18 个古生代锆石 (509–252 Ma) 和 6 个元古代锆石 (998–607 Ma)。该样品共取得 91 个有效分析点, 其中最年轻年龄为 85 ± 3 Ma (图 4.6b)。

井 Y1 位于海南岛西南部, 基底钻遇变质黑云母花岗岩, 锆石颗粒呈圆形至次圆状, 一定程度上保留岩浆锆石的生长环带, 但通常具有浅色的熔融边构造, 长 50 μm 至 100 μm , 长宽比通常为 1:1 或 2:1。Th 元素含量较低, 为 25.09–371.5 ppm, 而 U 元素含量较高, 变化范围也较大, 为 191.30–3362.47 ppm, 相应的 Th/U 比值较低, 范围在 0.01 至 0.4 之间, 仅有一个值为 0.67, 五个分析点在 0.01 至 0.1 之间。Y1 与其他中生代基底样品存在较大差异, 以明显的元古代峰值为主, 年龄范围在 1264 ± 83 Ma 至 1714 ± 52 Ma 之间, 另外还有一个更老的 1972 ± 23 Ma 年龄。该中元古代年龄峰值主要集中在 1465 Ma 左右 (图 4.6c)。

4.1.4 重磁震联合反演结果

本研究开展的重-磁-震联合反演也一定程度反映南海北部基底的均一性和整体性(图 4.7a-f)。不同于前人“南海北部基底具有明显分区分块”的观点,图 4.x 显示其南北向断裂构造系统并不发育,规模较小(图 4.7f)。RTP 磁异常分布可有效指示中生代沉积地层,表现为极低的磁化率(图 4.7a)。此参数也可以检测岩浆活动,具体而言图 4.7a 可见东北向磁异常高值条带,大致对应东沙地势隆起区和中生代强烈岩浆活动^[111,112]。另一方面,南海东部同时可见明显的磁异常极低值,可能与厚层中生代残留沉积分布有关。自由空气重力图表明,东沙地区附近相应表现为较高的重力异常值(图 4.7b),很可能由中生代岩浆活动造成。值得注意的是,低重力异常也沿上述高重力异常岩浆区零星分布,推测为东沙地区岩浆体附近发育的小型断裂和凹陷造成的。另外,南海东部局部区域可见较高重力异常值(大约在-5 mGal 至 10 mGal 之间)却具有相对较低的 RTP 磁异常值,这种现象可能是基底物质由中生代沉积层组成,然而受后来区域构造运动影响发生隆升。

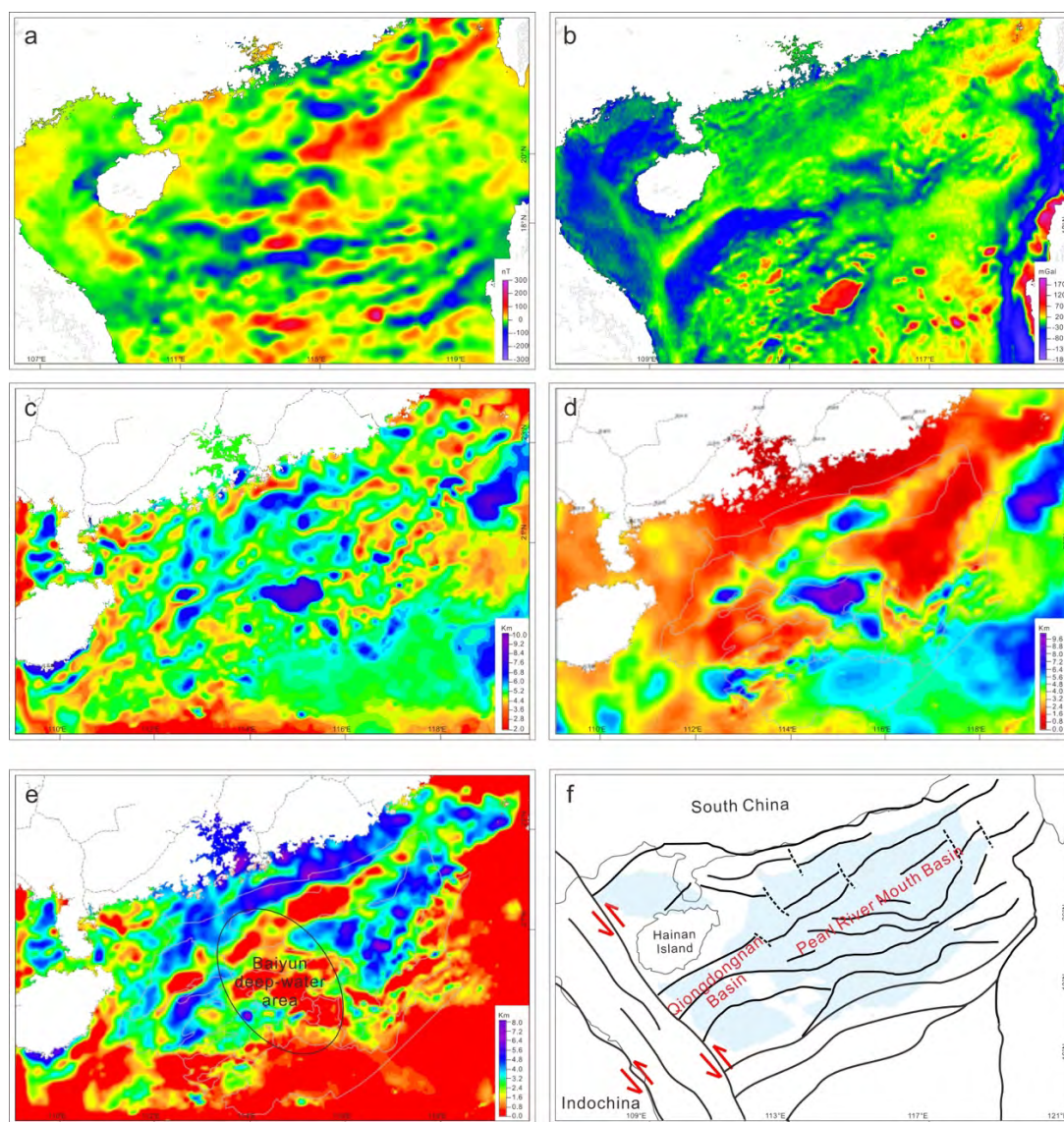


图 4.7 南海北部基底 a) 磁异常分布图; b) 自由重力异常分布图; c) 重磁震联合反演地层总厚度图 (新生代+前新生代); d) 新生代地层厚度图; e) 前新生代地层厚度图; f) 南海北部盆地区域构造单元及断裂体系示意图 (据 Zhu et al. (2021)^[210])

Fig. 4.7 Map of magnetic anomalies after reduction to the pole to precisely relocate magnetic boundaries and facilitates data interpretation (a); regional free-air gravity anomaly map based on high-resolution shipborne surveying and satellite measurements offshore (b); regional bathymetrical map showing the bottom layer of the pre-Cenozoic basement based on gravity-magnetic-seismic joint inversion, assuming an average of 2.67 g/cm³ for shallow crustal materials (c); regional bathymetrical map showing the bottom layer of the Cenozoic sedimentary sequences (d); thickness reconstruction map of the northern South China Sea pre-Cenozoic sedimentary basin basement (e); sketch map showing the SCS Basin basement tectonic units and major faults (f). Dash lines are faults which are drawn based on both gravity-magnetic-seismic anomaly interpretations in this study and published geological data (modified from Zhu et al. (2021)^[210]).

4.1.5 讨论

样品 YJ3511, YJ3611 和 KP111 均为低级变质岩, 绢云母含量较高, 发育镶嵌结构, 具有一定程度的定向排列 (图 4.2a-f)。样品 KP111 石英斑晶表面可见明显的熔蚀结构和炸裂纹, YJ3511 和 YJ3611 变质泥岩或粉砂岩中可见变余结构, 都说明经历了一定程度的重结晶作用, 并保留了部分原始矿物结构构造。相反, 位于海南岛西侧的 Y1 具有更明显的绿泥石、白云母和石英矿物定向排列结构, 经历更高程度的白云母改造或变质作用 (图 4.2g-h), 其 Th/U 比值相对更低。然而总体来看, 这些样品 Th/U 比值绝大多数大于 0.1, 说明南海北部地区变质作用还不足以产生变质锆石。

高场强元素 (HFSE, High Field Strength Elements) 通常具有大离子半径和较高的电荷密度, 在地质过程中相对不易迁移, 不受风化改造和变质作用的影响, 例如 Nb、Ta、Zr、Hf、Th 等, 可以有效保留原岩信息。图 4.3a 显示 Ba、Nb、Ti 和 P 元素负异常, Rb、K 和 Hf 元素正异常, 一些放射性产热元素如 Th 和 U 也表现一定程度正异常。需要注意的是, 本研究中同时出现的 Nb-Ti 负异常和 Rb 元素正异常不能简单地归因于岩石形成过程中的结晶分异作用。根据 Pearce (1983)^[213], 大离子亲石元素 (LILE, Large Ion Lithophile Elements) 富集和高场强元素亏损反映弧岩浆作用; 随着研究进一步深入, 学者们发现板块熔体或伴随俯冲作用形成的沉积物均可以产生 Nb-Ti 亏损和 Hf 元素富集。本研究中 Rb、Th 和轻稀土元素都表现为正异常, 说明基底岩石形成过程中存在大量流体和熔体物质。根据微量元素、稀土元素配分形式以及岩石薄片镜下观察结果, 可以初步判断洋壳俯冲过程中受到高温高压影响, 熔融和流体交换作用非常活跃, 导致俯冲板片中的岩石发生部分熔融, 产生俯冲岩浆; 同时, 板块中的水分和挥发性物质也会释放出来形成俯冲流体。这些熔融岩浆和俯冲流体很大程度上会对俯冲板片和上覆岩石成分和结构产生影响, 从而表现出南海北部基底岩石相应的元素地球化学特征。

正如第二章研究背景及争议热点所述,前人认为南海前新生代盆地基底主要由近北向或西北-东南向的构造断裂系统控制,表现为“东西分带、南北分块”的特征^[31, 106, 214-216]。然而这些假设均建立在邻区地质学(以岩相观察描述为主)和地震反射资料的基础之上,缺乏高精度的年代学分析^[31, 32, 95, 217, 218]。需要强调的是,根据基底钻井样品锆石 U-Pb 年代学结果, Zhu et al. (2017)揭示了西沙地区晚侏罗世至早白垩世经历了一定程度的变质作用(152.9–137 Ma),并在晚白垩世遭受花岗岩侵入(107.8±3.6 Ma),推翻了之前根据 Rb-Sr 等时线法得到的 627 Ma 前寒武年龄^[108]。

锆石年龄谱系显示,大多数基底样品表现为明显的晚中生代峰值(图 4.6a)。本研究首次针对南海北部西侧基底变质碎屑岩开展锆石 U-Pb 年代学研究,其最年轻年龄均为晚白垩世。一般认为,最年轻锆石 U-Pb 年龄代表最大沉积年龄。考虑到新生代与前新生代记录之间存在角度不整合界面,新生代时期南海北部开始沉积巨厚地层,覆盖于早期形成的基底之上,因此该地区晚中生代的确广泛发育沉积地层(图 4.8)。包括 KP111、CC111、WC1711 和 CC211 在内的变质凝灰岩和变质火山碎屑岩以早燕山期年龄峰值(大约集中在 150–140 Ma)为特征(图 4.6a),其余变质碎屑岩 BD2311、YJ3511 和 YJ3611 除了表现次要加里东期峰值,其燕山期年龄仍然占主导地位(图 4.6b)。简言之,燕山期主峰(集中于约 150–135 Ma)和加里东期次峰(集中于约 435–405 Ma)说明其源区物质同时包含古生代及中生代锆石,连同少量沉积再循环的前寒武锆石颗粒共同形成了南海北部西侧基底变质碎屑岩沉积。另外根据薄片镜下观察结果和 Th/U 比值,这些碎屑岩沉积均只遭受了低级变质作用,远低于形成变质锆石所需要的压力和温度条件。换句话说,较年轻的燕山期峰值并非早期古生代或前寒武锆石经历高级变质作用而形成的中生代锆石,而是由于俯冲作用引发岩浆活动重新形成的岩浆锆石。西沙地区 XK1 井钻遇的上白垩统(107.8±3.6 Ma)花岗岩岩体,与南海东部早期研究发现的大量晚中生代岩浆岩记录和华南陆缘陆上晚燕山期火成岩相互对应,证实了大规模岩浆活动的存在。

第 4 章 南海北部基底属性及其构造指示意义

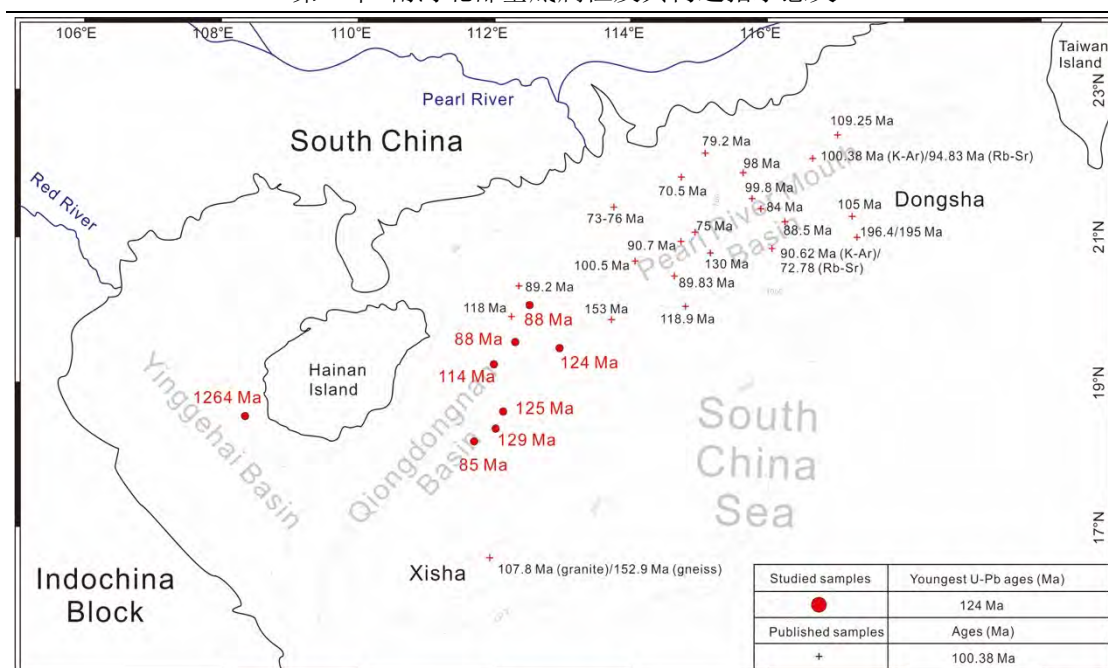


图 4.8 南海北部基底中生代地层最大沉积年龄（样品由红色实心圆点与红色字体表示）与岩浆岩年龄（样品由红色十字与黑色字体表示）分布图（据 Zhu et al. (2021)^[210]）

Fig. 4.8 Distribution map of the youngest ages dated by detrital zircon U-Pb ages for the studied meta-clastic rock samples, and K-Ar or Rb-Sr ages of previous researches for the northern SCS Basin basement (modified from Zhu et al. (2021)^[210]).

图 4.7a 和 b 共同显示，珠江口盆地西侧和琼东南盆地基底地球物理属性相似：二者表现为相似的 RTP 磁异常分布特征，范围在略负至略正之间，对广大的沉积地层区域，未能识别出明显的构造分界线。图 4.7b 显示，莺歌海盆地呈现出明显的负自由空气重力异常值，与海南岛东侧的南海北部基底表现的中等强度广泛分布的正异常值形成鲜明对比。结合岩相学和同位素年代学结果，二者地球物理性质确实存在一定差别。图 4.7e 前新生代二维地层厚度恢复图是通过将新生代沉积盖层（图 4.7c）从总体中（或更老）—新生代厚度（图 4.7d）除去得到的，显示位于海南岛东部的南海基底保留大规模中生代地层。就白云洼陷深水区而言，地层厚度明显减小，可能是由于地壳经历极度拉张减薄与特殊的盆地结构等因素造成的（图 4.7e）：在早期同伸展阶段，白云深水区以上地壳脆性伸展为主；而到了晚期同伸展阶段，该地区开始出现强烈的延展变形作用，产生碟状的流变学变形。上覆新生代沉积盖层对下部基底属性判断可能存在一定影响，在去除该潜在影响的前提下，本研究发现南海北部盆地基底和起伏莫霍面特征形态呈现一定镜像关系^[105, 219]。结合基底钻井样品更为准确的年代学结果，本研究认为南海基底整体以中生代地层和岩浆岩为主，受到空间上均匀应力场的影响（图 4.7f），并非是一个由南北断裂构造控制的、存在古老变质结晶基底的系统。

从晚三叠世（或更早）至早白垩世，南海地区可能持续受中特提斯和古太

平洋域的混合影响^[14, 17, 80, 91, 220] (图 4.9a): 从晚三叠世至早侏罗世, 中特提斯域可能自印支地块俯冲至华夏地块之下, 呈西北至东南向展布^[92, 221, 222] (图 4.9b), 海南岛(或“原海南岛”)基底可能作为单独的微陆块, 或与华夏地块之间存在构造亲缘属性, 在挤压环境下位于特提斯俯冲板片的前缘(图 4.9b)。

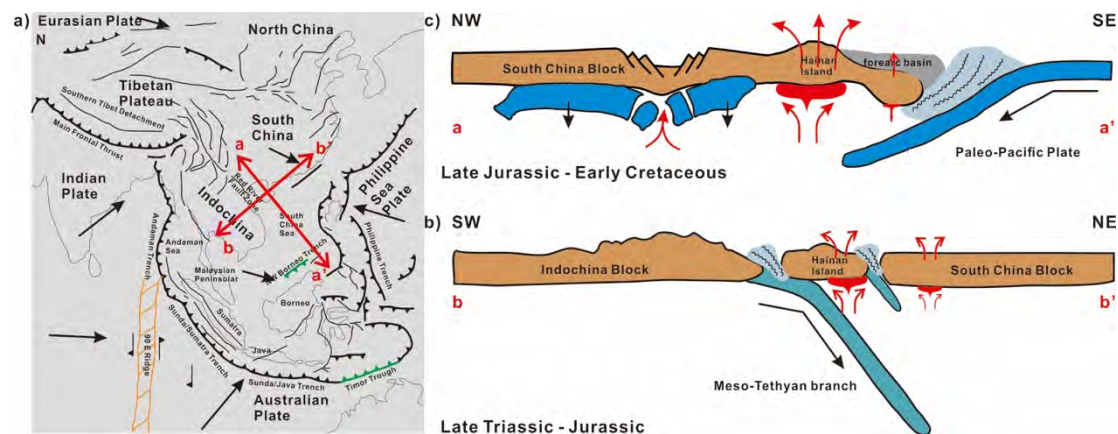


图 4.9a) 欧亚大陆边缘主要构造单元; b) 图 a 中 b-b'切面晚三叠-侏罗纪区域构造; c) 图 a 中 a-a'切面晚侏罗-早白垩纪区域构造示意图

Fig. 4.9 Sketch map showing the present topographic and active faults of the east Asia at the convergence zone of the Eurasian Plate, Philippine Sea Plate and Australian-Indian Plate (a) (modified from Metcalfe (1996, 2011)). A cartoon illustrating the switch-on and switch-off evolution of the Meso-Tethyan tectonic regime in the late Triassic-Jurassic (b) and the Paleo-Pacific regime in the late Jurassic-early Cretaceous (c).

印支地块在中生代时期可能持续与华夏地块发生强烈的碰撞挤压变形作用, 长时期的陆-陆板块相互作用无疑引发了程度更深的接触变质作用, 也与南海北部地区从东北至西南变质作用趋于强烈的变化规律相一致。从晚侏罗世至早白垩世, 古太平洋俯冲系统持续影响南海东部地区, 导致了安第斯型活动大陆边缘逐渐占主导地位, 华南大陆沿海及南海北部地区也在晚中生代发生一系列大规模岩浆活动和造山运动^[97, 123] (图 4.9c)。俯冲作用也产生了更广泛的弧岩浆记录, 并伴随一系列弧后伸展盆地的形成。整体来看, 晚侏罗-早白垩期间洋-陆碰撞导致南海东部基底变质作用相对较弱; 而海南岛以西地区, 远离古太平洋俯冲系统的控制, 则经历更复杂和强烈的变质作用(图 4.10)。

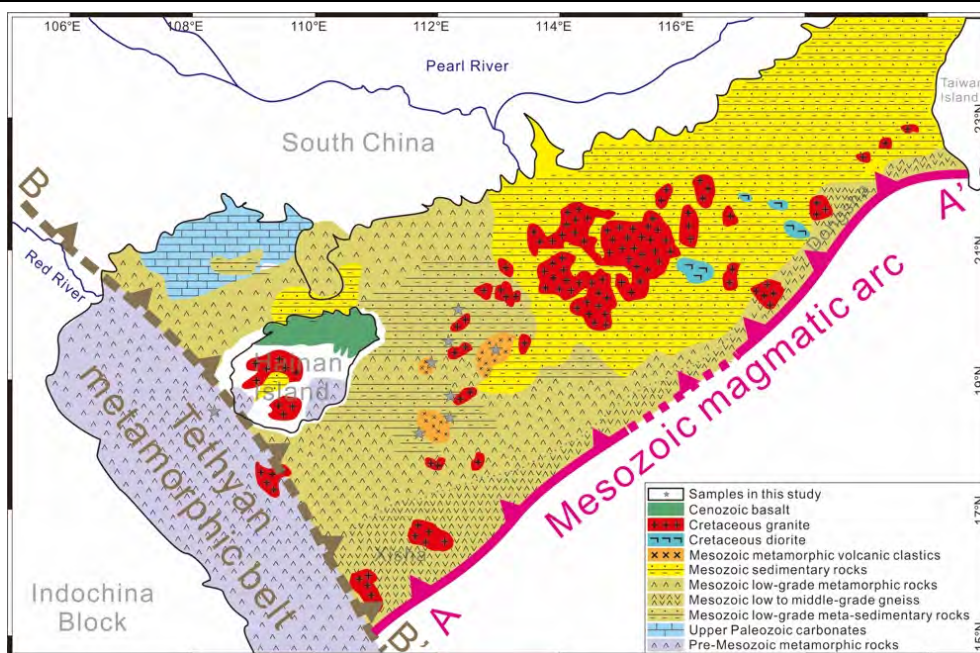


图 4.10 南海北部基底岩性分布新解释

Fig. 4.10 Systematic northern SCS pre-Cenozoic basement lithological map with an interpreted Mesozoic magmatic arc A-A' shown along the continental margin. This lithological pattern is constrained by the new ages, geochemical analysis, petrographic slice observation and gravity-magnetic-seismic joint inversion results reported in this study as well as other published data (Qiu et al., 1996; Li et al., 1999; Xu et al., 2017). A postulated Tethyan subduction direction is also shown to the west of Hainan Island. Section B-B' shows the possible active boundary of the pre-Cenozoic metamorphic belt along the present extension of the Red River Fault Zone (modified from Wang et al. (2002) and Sun et al. (2014)).

另外，从南至北空间上远离俯冲带，变质作用逐渐减弱。值得注意的是，由于可能处在特提斯域和太平洋俯冲体系交汇的地带，西沙地区很大程度上曾依次受到二者多阶段碰撞挤压的混合影响，因此也会形成更强烈、更宽广的变质带。

4.1.6 初步结论

本研究对南海北部前新生代基底钻井样品开展系统的元素地球化学分析、岩石学及矿物学鉴定、锆石 U-Pb 年代学分析以及重-磁-震联合反演地球物理约束，提出南海北部基底以广泛存在的中生代地层为主，并非前人认为的各项异性、分区分块的展布特征。同时，结合以前发表的南海北部东侧地区白垩系岩浆岩 U-Pb、K-Ar 及 Rb-Sr 年代学，环绕华南大陆边缘该时期的确大规模发育岩浆弧，处于古太平洋俯冲的控制之下。本研究首次取得来自南海西侧基底的凝灰岩、火山碎屑岩和沉积岩钻井样品，其大量存在的上侏罗统至白垩系碎屑锆石共同说明该地区是中生代活跃岩浆弧向西延伸的部分。位于海南岛东侧、南海西部的一系列变质碎屑岩样品同时表明中生代基底曾经发生低级变质作用。另外，部分样品呈现燕山期和加里东期的双峰年龄模式，指示附近存在包含中

生代和古生代锆石年龄的潜在物源。最后，位于海南岛西侧的变质花岗岩具有中元古代年龄（其构造指示意义详见本章第 4.3 节），可能一定程度反映印支地块和华夏板块之间存在的俯冲、碰撞、拼合与抬升过程，这些剧烈的板块交互作用保留了部分古老陆块物质。事实上，该地区在地理位置上恰好位于红河断裂带上，而红河断裂带可被视为新生代沿板块边界发育的古老缝合带的再活化作用。整体而言，南海北部盆地基底实际由陆-陆和洋-陆碰撞共同作用而成，新生代断陷盆地便是沿着碰撞-拼合-增生大陆边缘的一系列裂谷和断层发育而成的。

4.2 华南陆缘中生代安第斯型岩浆弧发育演化过程

华南大陆主要发育三个二叠/三叠-侏罗系造山带（图 4.11）：北侧是秦岭—大别—苏鲁造山带；西北缘是龙门山断裂带；华南褶皱带呈西南-东北向展布，几乎覆盖了华南板块东南地区的一半。推覆构造、变质作用以及同造山岩浆活动在华南褶皱带中呈现出从沿海地区向克拉通内部逐渐年轻化的趋势^[99]。内陆及沿海地区均发现了与俯冲有关的钙碱性 I-型花岗岩，年龄范围在 265 Ma 至 190 Ma 之间^[93, 99, 223]。华南褶皱带约 1300 公里，广泛发育侏罗-白垩年龄的后造山岩浆记录^[99, 102, 224-226]（图 4.11）。早期研究者强调 150 Ma 以后华南大陆发育的岩浆岩向海有逐渐变年轻的趋势^[97, 227]。部分学者认为，这些后造山岩浆活动与大陆岩浆弧逐渐向海后撤有关，推测古太平洋的俯冲倾角逐渐变陡^[97]。然而，研究者后来发现，这些后造山岩浆活动并非呈现上述简单的变化，其时空分布规律更加复杂：早中生代（年龄大约在 180 Ma 至 150 Ma 之间）岩浆岩呈放射状从内陆造山带中心向外幅散，且这些岩浆岩并非完全为大陆弧属性，很多为板内 A-型花岗岩^[99, 225]。因此，Li and Li (2007)曾提出平板俯冲模型来解释发生在 250 Ma 至 200 Ma 期间造山带向克拉通内陆发展的现象，推断板片会从中心开始下沉并最终沉没，从而诱发后造山岩浆活动，以此来解释复杂的时空分布规律^[99]。Li et al. (2012b)基于沿海地区大约 190 Ma 的 I-型花岗岩以及近源区的岩浆和沉积记录，进一步推测正常洋—陆俯冲可能于该时期重新启动^[102]。

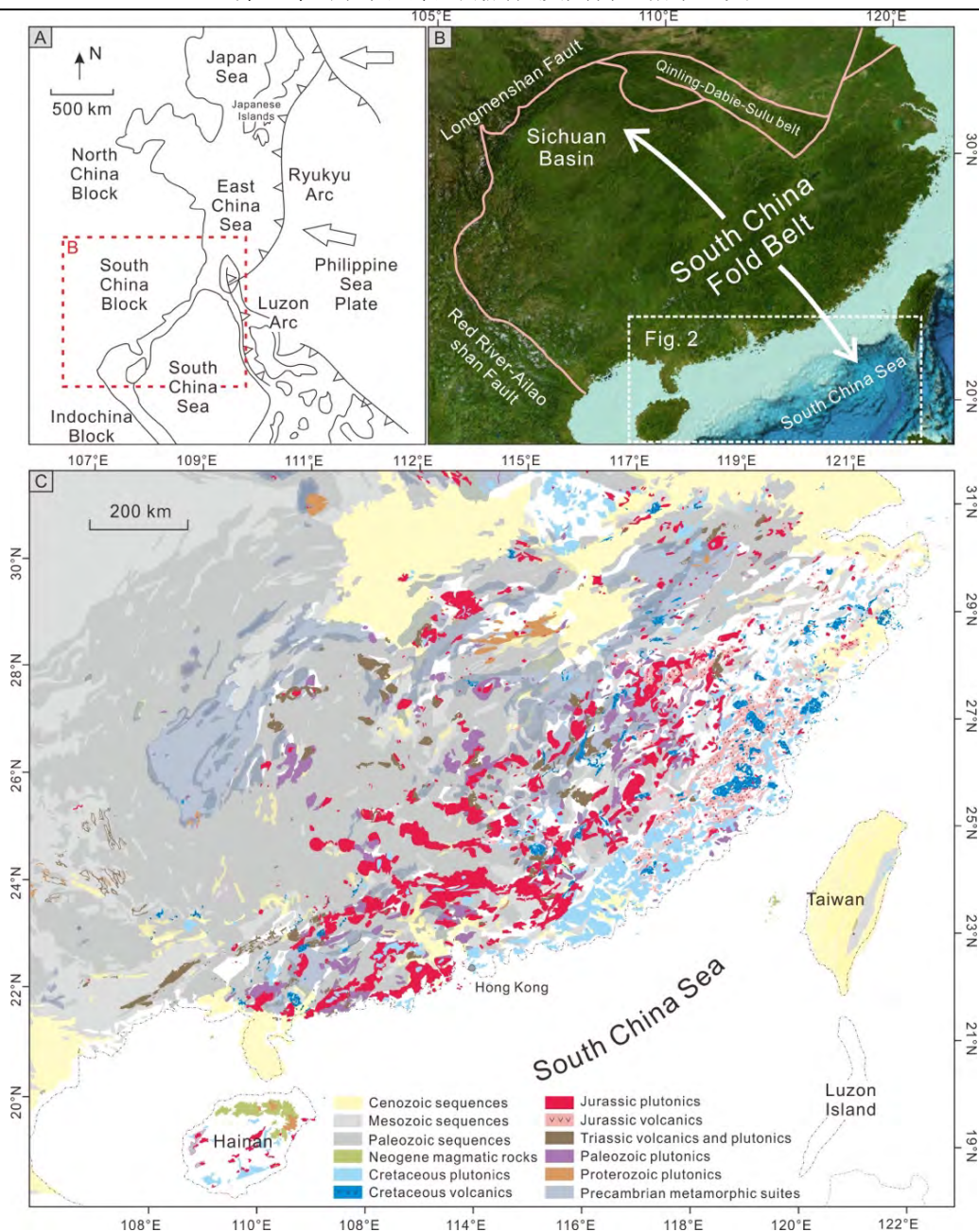


图 4.11a) 东南亚地区主要构造单元示意图; b) 华南大陆主要造山带及周缘断裂系统; c) 华南大陆岩性分布图 (据 Cui et al. (2021)^[228])

Fig. 4.11 A) Schematic map of Southeast Asia showing the major tectonic units; B) Digital topography of the South China Block (original data from the General Bathymetric Chart of the Oceans (GEBCO) [https://www.gebco.net/data_and_products/printable_maps/]) showing the width of the South China Fold Belt and major boundary faults; the position of our study area (see Fig. 4.12 for details) is also shown; C) A simplified geological map of South China (modified from Cui et al. (2021)^[228]).

华南大陆向南延伸进入南海北部盆地基底，陆壳经历强烈拉张减薄，厚度从约 6 公里至约 30 公里不等^[103]。结合前人发表资料和本研究取得的钻井样品数据，本论文在本章节第 4.1 节对南海北部基底岩石组成、年龄框架及地球物理特

征展开详细讨论, 这些地质资料对本节论述活动大陆边缘构造环境发育演化具有重要意义。另外, 台湾岛位于华南大陆东南缘, 与南海北部基底类似, 其中部和北部露头也显示出与华南大陆之间具有一定的构造亲缘关系(图 4.11)。其中, 南澳变质复合体是台湾岛出露的最古老岩体, 主要由片麻岩、大理岩和花岗岩组成。台湾岛可见大约 190 Ma 的 I-型花岗岩, 可能与洋壳俯冲至欧亚大陆边缘有关^[102, 229], 另外还发现了中生代末期大约 90–80 Ma 的花岗岩岩体^[230]。海南岛出露了大量三叠系岩浆岩, 其余包括侏罗至白垩系年龄: SHRIMP 定年结果显示, 海南岛发育 267–262 Ma 的碱性 I-型花岗岩, 推测来自晚二叠世的大陆弧环境^[93]; 另一方面, 也有学者认为, 海南岛形成于晚侏罗至白垩纪期间的侵入岩与火山岩可能来自俯冲作用改造的幔源混染岩浆, 整体处于伸展环境^[117, 231–234]。

在上述研究背景下, 本研究采集了南海北部和东海陆架盆地基底火成岩和变质碎屑岩样品, 开展地球化学、同位素年代学、Lu-Hf 同位素分析和物源判别研究(图 4.12 和图 4.13), 样品地理位置、岩性特征、钻井深度、测试方法、年龄等具体信息如表 4.3 和表 4.4 所示, 这些样品均来自中海油有限公司, 钻井均穿过了新生代沉积盆地之下的不整合面。为了更好的进行数据解释, 本节还重新整理与分析了华南大陆内陆和沿海地区、海南岛、台湾岛、盆地基底已发表研究成果。

第 4 章 南海北部基底属性及其构造指示意义

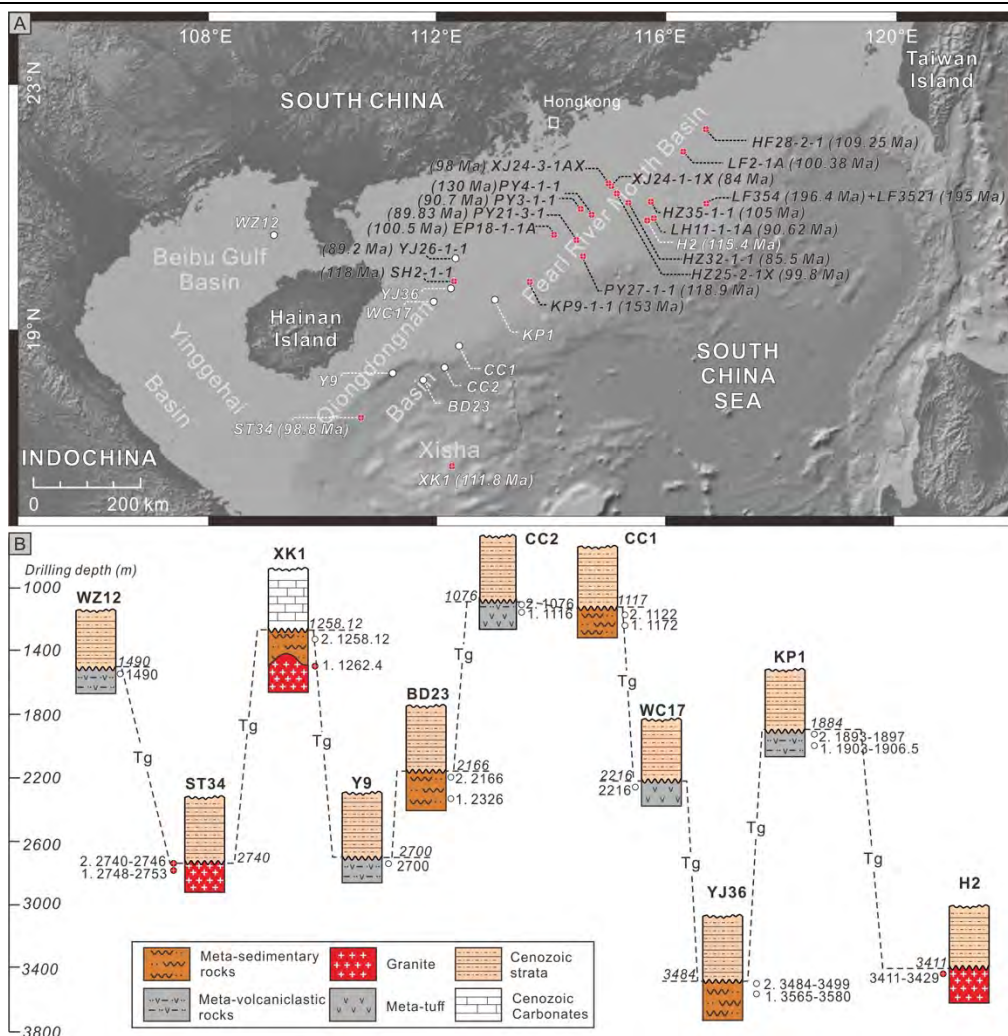


图 4.12A) 钻井样品示意图 (白色字体代表本研究钻井样品, 白色实心圆点代表沉积岩样品, 红色圆点代表岩浆岩样品; 黑色字体前人已发表年龄, 均为岩浆岩样品); B) 本研究钻井岩性柱状示意图 (虚线上方数字代表不整合面深度, 下方数字代表取样深度) (据 Cui et al. (2021)^[228])

Fig. 4.12. A) Topographic map of the northern South China Sea basin showing the locations of borehole samples analyzed in this study (white borehole names) and reported in previous studies (black borehole names from Li et al. (1999), Qiu et al. (1996), and Xu et al. (2017)). Boreholes that penetrated granites are shown by filled red circles with dated magmatic ages given following the borehole names. Refer to Table 4.3 for sampling and stratigraphic details, lithological characteristics, ages, analytical methods, and references of previously studied samples. B) Schematic stratigraphic columns of boreholes analyzed in this study; depth of the South China Sea basement (Tg) is shown in italic font. (For interpretation of the references to colour in this figure legend, the reader is referred to the web version of this article.)

表 4.3 本研究南海北部钻井样品信息

Table. 4.3 List of samples analyzed for Laser-ICP-MS detrital zircon U-Pb dating and trace element analyses.

第 4 章 南海北部基底属性及其构造指示意义

钻井名称	基底深度 (m)/Tg	样品名称	岩性	取样深度 (m)	结晶年龄或最大沉积年龄 (Ma)	锆石 U-Pb 定年及微量元素有效分析点/分析总数	锆石地化分析取样深度 (m)
ST34	2740	ST34-2	Granite	2740–2746	98.4±1.7	25/32	2740–2746
ST34	2740	ST34-1	Granite	2748–2753	98.6±2.1	39/51	2748–2753
XK1	1258.12	XK1-2	Amphibole plagiogneiss	1258.12	151.8±2.7	17/17	1258.12
XK1	1258.12	XK1-1	Granite	1262.4	111.8±3.3	13/16	1262.4
H2	3411	H2	Granodiorite	3411–3429	115.4±0.7	107/112	3411–3429
WC17	2216	WC17	Metatuff	2216	114.6±4.7	101/112	–
CC2	1076	CC2-2	Metavolcanic clastic rock	1076	91.9±8.2	111/112	–
CC2	1076	CC2-1	Metatuff	1116	138.3±2.6	110/112	–
WZ12	1490	WZ12	Metavolcanic clastic rock	1490	98±14	106/112	–
Y9	2700	Y9	Metavolcanic clastic rock	2700	111.9±6.2	104/112	–
KP1	1884	KP1-2	Metavolcanic clastic rock	1893–1897	122.0±7.5	228/252	–
KP1	1884	KP1-1	Metavolcanic clastic rock	1903–1906.5	103.9±9.0	106/120	–
BD23	2166	BD23-2	Meta-quartzose sandstone	2166	87.0±4.2	91/107	–
BD23	2166	BD23-1	Meta-quartzose sandstone	2326	122.7±2.8	92/117	–
CC1	1117	CC1-2	Metasandstone	1122	101±5	101/112	–
CC1	1117	CC1-1	Metasandstone	1172	112.8±7.5	95/105	–
YJ36	3484	YJ36-2	Metamudstone and metasilstone	3484–3499	88±2	128/140	–
YJ36	3484	YJ36-1	Metamudstone and metasilstone	3565–3580	112 ± 3	113/147	–

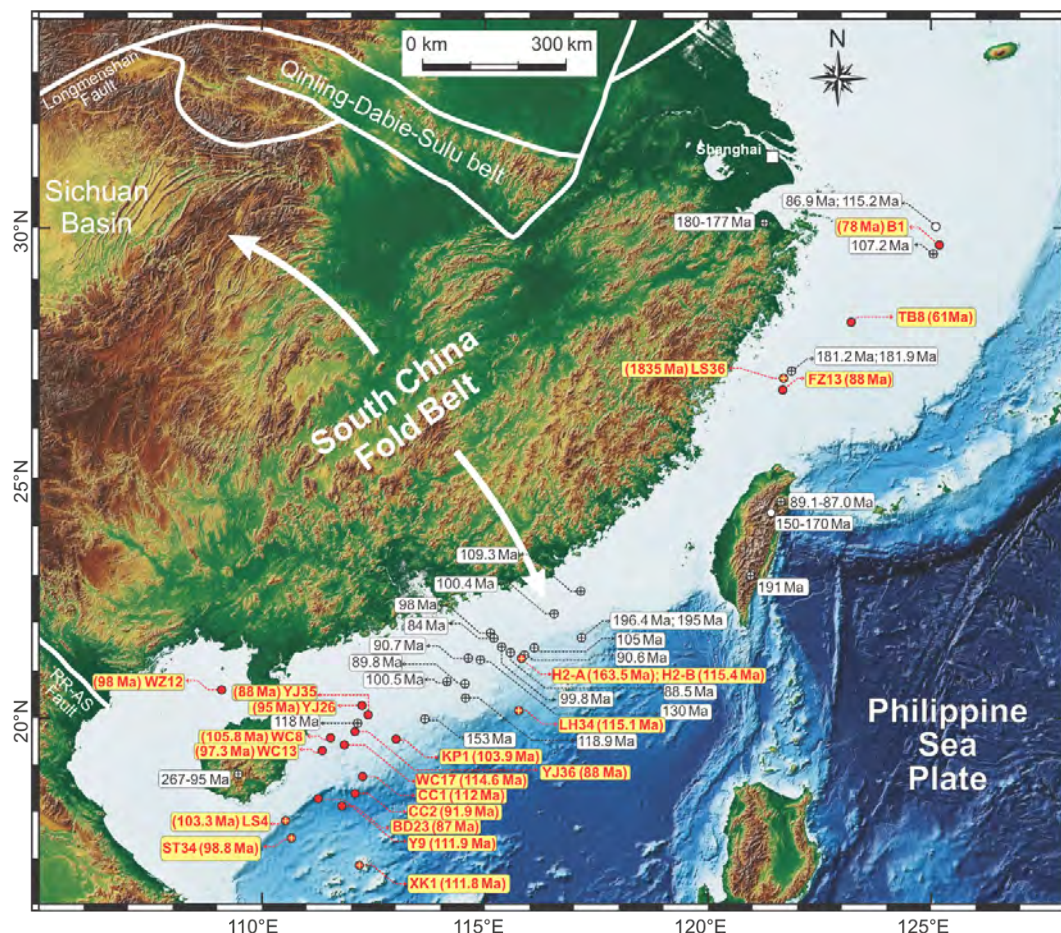


图 4.13 华南大陆边缘（南海北部及东海陆架盆地）钻井样品综合示意图（红色字体代表本研究样品，红色实心圆点为沉积岩最大沉积年龄，内部包含十字的红色圆点为岩浆岩结晶年龄；黑色字体代表前人已发表年龄）

Fig. 4.13 Digital topography of South China and marginal sea basins surrounding its continental margin (original data from the General Bathymetric Chart of the Oceans (GEBCO) [https://www.gebco.net/data_and_products/printable_maps/]), showing the extension of the South China Fold Belt and major boundary faults. Locations of drilling samples analyzed of this study (red sample names) and published ones of previous studies (black sample names). Boreholes penetrating or outcrops of granites are shown by crossed circles with dated magmatic ages beside sample names. Boreholes penetrating or outcrops of tuff, volcanoclastic or sedimentary rocks are shown by circles without crosses with maximum depositional ages along with sample names. Refer to Table 4.4 for geographic locations, sampling and stratigraphic information, lithology, igneous or maximum depositional ages, analytical methods and references.

表 4.4 华南大陆边缘（南海北部及东海陆架盆地）钻井样品信息（样品 H2-B 为 H2-A 顶部样品，取自 Cui et al. (2021)^[228]；FZ13-2 来自 CNOOC 未发表数据）

Table. 4.4 List of samples of the South China continental margin (the northern South China Sea and East China Sea Shelf Basin) analysed for Laser-ICP-MS zircon U-Pb dating, trace element and Lu-Hf isotopic geochemical analyses (sample H2-B was collected above H2-A from the same drill-hole (Cui et al. (2021)^[228]; sample FZ13-2 is unpublished data of CNOOC).

第 4 章 南海北部基底属性及其构造指示意义

钻井名称	样品名称	岩性	基底深度 (m)/Tg	取样深度 (m)	岩浆岩结晶年龄/最大沉积年龄 (Ma)	锆石 U-Pb 定年分析点数目	锆石微量元素分析取样深度 (m)	锆石 Lu-Hf 同位素分析取样深度 (m)
LS4	LS4-3	花岗岩	4500	4520-4522	103.3±1.1	75	-	4520-4522
LS4	LS4-2	花岗岩	4500	4702-4704	104±2	7	-	-
LS4	LS4-1	花岗岩	4500	4926-4928	105±3	3	-	-
LH34	LH34	花岗岩	3750	3750-3753	115.1±0.9	86	3750-3753	3750-3753
H2	*H2-B	花岗闪长岩	3411	3411-3429	115.4±0.7	50	3411-3429	-
H2	H2-A	花岗闪长岩	3411	4097-4107	163.5±2.1	73	4097-4107	4097-4107
WC8	WC8	火山角砾岩	2729	2729.03-2730	105.8±3.7	85	-	2729.03-2730
WC13	WC13	变质基底	1393	1393.5-1393.7	97.3±2.0	112	-	1393.5-1393.7
YJ26	YJ26	凝灰岩	1700	1700-1702	95±5	77	-	1700-1702
LS36	LS36	片麻岩	2496	2590.41	1835±11	101	-	2590.41
B1	B1	碎屑岩	4120	4200.7	57±2	71	-	4200.7
TB8	TB8	碎屑岩	2400	2643-2700	62.2±1.8	17	-	2643-2700
FZ13	*FZ13-2	变质碎屑岩	1636	1645-1670	99±1	10	-	-
FZ13	FZ13-1	变质碎屑岩	1636	1812.28	90.4±3.5	58	1812.28	1812.28
HJ	*HJ	变质碎屑岩	1400	1519	72±2	58	1519	-

4. 2. 1 薄片镜下观察与锆石 U-Pb 定年结果

ST34-1、ST34-2、XK-1 和 H2 样品均来自南海北部新生代盆地基底钻遇的花岗岩岩体 (表 4.3; 图 4.14)。井 ST34 位于海南岛东南侧的琼东南盆地, 钻遇中粒花岗岩。镜下薄片观察显示, ST 井花岗岩主要包括斜长石 (20%)、正长石 (45%)、石英 (30%) 和少量暗色矿物 (5%) 如黑云母组成。样品 ST34-1 的 Th 和 U 含量分别为 20.67–599.5 ppm 和 38.88–1069.61 ppm, 相应的 Th/U 范围在 0.18 至 1.93, 表明为岩浆锆石来源 (图 4.14), 阴极发光图像显示明显的振荡环带 (图 4.14)。该样品共取得 39 个有效分析点, $^{206}\text{Pb}/^{238}\text{U}$ 年龄介于 246 Ma 和 82 Ma 之间: 其中 35 个锆石年龄为 111–82 Ma, 加权平均年龄为 98.6 ± 2.1 Ma (MSWD = 1.8) (图 4.14A)。样品 ST34-2 为同一花岗岩岩体的重复样, Th 和 U 含量分别为 47.80 – 327.98 ppm 和 55.21 – 407.99 ppm, Th/U 比值为 0.65 至 1.46, 同样表明岩浆锆石来源 (图 4.15)。ST34-2 样品中获得 25 个有效锆石年龄, 均

来自具有振荡环带的锆石边缘或针状均质锆石，年龄范围在 107 Ma 至 93 Ma 之间，加权平均年龄为 98.4 ± 1.7 Ma (MSWD = 0.62) (图 4.14)。由于这两个样品的年龄在误差范围内无法明显区分，因此本研究将二者合并，得到整体加权平均年龄为 98.4 ± 1.1 Ma (MSWD = 1.06) (图 4.14)，并将其视为花岗岩结晶年龄。另外，样品 ST34-1 包含两个较老的锆石核部年龄，分别为 129 ± 5 Ma 和 155 ± 8 Ma，可能来自继承核锆石或在岩浆上升过程中从围岩中捕获的锆石；另一个较老的年龄 170 ± 8 Ma 可能由于激光剥蚀点位于锆石颗粒的裂隙处；唯一的三叠系年龄 246 ± 14 Ma 来自锆石边缘，可能代表从围岩中捕获的锆石颗粒。

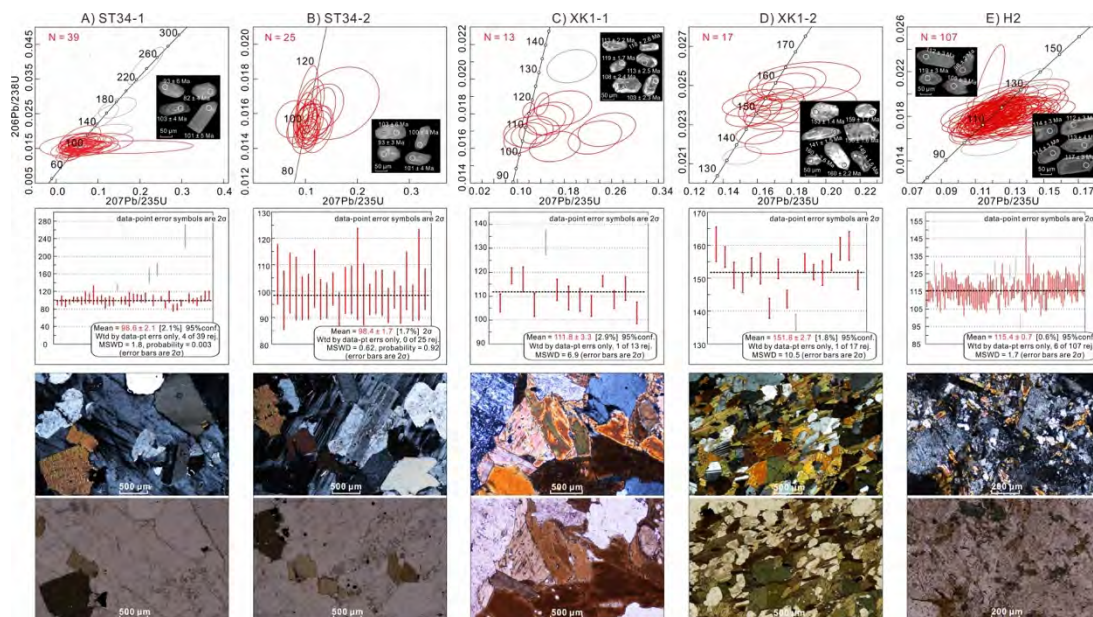


图 4.14 南海北部岩浆岩 ST34-1、ST34-2、XK1-1 和 H2 以及片麻岩 XK1-2 锆石 U-Pb 谐和图、代表性锆石阴极发光图像、锆石加权平均年龄以及正交偏光/单偏光镜下薄片

Fig. 4.14 LA-ICP-MS U-Pb concordia age plots, cathodoluminescence (CL) images of representative zircons, weighted mean ages and thin sections under cross/plane-polarized light of magmatic rocks. A) ST34-1: granite; B) ST34-2: granite; C) XK1-1: granite; D) XK1-2: amphibole plagiogneiss; E) H2: granodiorite. The term “N” denotes the total number of effective analyses for each sample. MSWD – mean square weighted deviations.

样品 XK-1 取自琼东南盆地最南端基底的中粒花岗岩岩体，镜下薄片观察结果显示其具有典型的花岗岩结构 (图 4.14C)。Th 和 U 含量分别为 72.73 - 1276.4 ppm 和 99.55 - 1847 ppm，Th/U 比值为 0.39 至 1.01，指示岩浆锆石来源 (图 4.15)。该样品共取得 13 个有效年龄点，介于 132 Ma 和 103 Ma 之间，其中下白垩统年龄 132 Ma 很大程度为继承性锆石，本次加权年龄计算中将其作为异常点去除后，得到的平均年龄为 111.8 ± 3.3 Ma (MSWD = 6.9) (图 4.14C)。样品 XK-2 取自 XK-1 上方 4 m 来自同一口钻井的角闪石片麻岩，主要矿物包括斜长石 (45%)、石英 (14%)、钾长石 (8%)、角闪石 (10%) 和黑云母 (20%) 以及少量副矿物，例如绿帘石、磷灰石、透辉石和锆石。矿物整体表现一定程度的

定向排列特征。薄片还显示角闪石和黑云母的绿泥石化现象，斜长石经历绢云母化作用（图 4.14D）。样品 XK-2 的 Th (81.61 ppm 至 1361.66 ppm) 和 U (214.78 ppm 至 2395.08 ppm) 含量变化相对较大，其 Th/U 比值在 0.37 至 0.88 之间变化，证实其岩浆锆石来源（图 4.15）。该样品共取得 17 个有效年龄，均在具有振荡环带的锆石边缘取得：其中一个下白垩统年龄 137 ± 1.2 Ma 被视作异常点去除，不参与加权平均年龄计算，剩余 16 个年龄点的平均年龄为 151.8 ± 2.7 Ma (MSWD = 10.5) (图 4.14D)。本研究认为 ST34-1 的 111.8 ± 3.3 Ma 代表了花岗岩结晶年龄，该花岗岩岩体侵入了侏罗系 151.8 ± 2.7 Ma 的角闪石片麻岩。

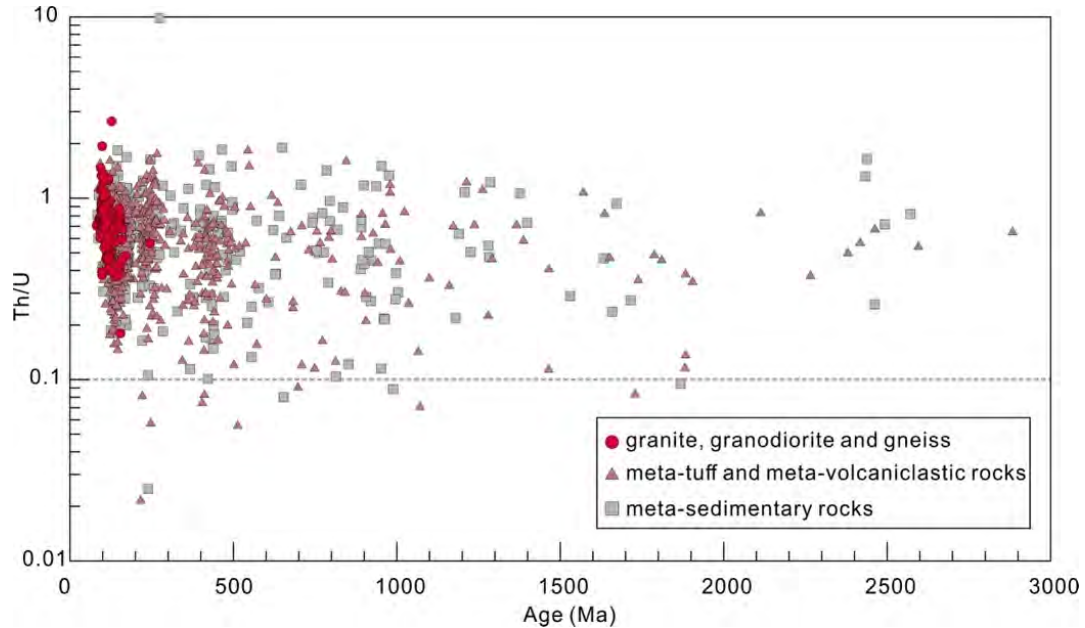


图 4.15 南海北部基底样品锆石 U-Pb 年龄 vs. Th/U

Fig. 4.15 Plots of Th/U ratios vs. U-Pb ages for all dated zircon grains.

样品 LS4-1、LS4-2、LS4-3、H2-A 和 LH34 也是来自南海北部新生代地层之下的基底花岗岩体（图 4.13；表 4.4）。样品 LS4-1、LS4-2、LS4-3 为细-中粒花岗岩，钻孔位于海南岛东南方向的琼东南盆地。钻孔 LS4 三件样品的 Th 和 U 含量分别为 56.72 ppm 至 2684.66 ppm，58.85 ppm 至 2689.33 ppm，相应的 Th/U 值在 0.11 至 1.65 之间，反映其来源是岩浆锆石（图 4.16A）。锆石颗粒表现为自形状，具有清晰的核-边结构或针状均质结构（图 4.17A）。最下部样品 LS4-1 取得三个谐和年龄，包含两个中生代年龄 105 ± 3 Ma 和 110 ± 3 Ma，一个古生代年龄 387 ± 11 Ma（可能是继承性锆石）。样品 LS4-2 取得 7 个谐和年龄，其中五个为中生代年龄，范围是 99 ± 2 Ma 到 250 ± 6 Ma，两个新元古代年龄为 800 ± 14 Ma 和 867 ± 16 Ma。最上部样品 LS4-3 总共获得 75 个谐和年龄，介于 93 ± 3 Ma 和 396 ± 8 Ma 之间（图 4.17A）：其中 69 个年龄位于 125–93 Ma 区间内，加权平均年龄为 103.3 ± 1.1 Ma (MSWD = 4.0)，本研究视作 LS4-3 花岗岩的结晶年龄；样品 LS4-3 还包含四个较老的三叠系年龄，分别为 231 ± 8 Ma、 234 ± 4 Ma、 240 ± 4

Ma 和 259 ± 4 Ma, 可能来自岩浆源区, 或是岩浆上升和结晶过程中从围岩中捕获的继承性锆石; 样品 LS4-3 的二叠系年龄 272 ± 8 Ma 可能是由于激光剥蚀点表面的裂缝造成的; 样品 LS4-3 的最老年龄 396 ± 8 Ma 可能代表了从围岩捕获的锆石颗粒。

样品 H2 取自珠江口盆地基底的中粒至细粒花岗闪长岩, 具有斑状结构, 斑晶直径大小为 0.5–5 mm, 包括斜长石 (35%)、钾长石 (10%)、石英 (20%)、角闪石 (10%) 和黑云母 (10%) (图 4.14E), 副矿物包括钛铁矿、磷灰石和锆石; 基质矿物直径大小为 0.02–5 mm, 主要为斜长石、钾长石、石英和少量角闪石、黑云母、锆石、磷灰石和磁铁矿。Th 和 U 含量分别为 65.42 ppm 至 3865.52 ppm, 117.29 ppm 至 1463.05 ppm (图 4.15), 相应的 Th/U 范围是 0.40 至 2.64, 锆石颗粒可见清晰的核边结构。该样品总共包含 117 个有效年龄: 其中下白垩统年龄 135 ± 3 Ma 为锆石核, 可能代表继承年龄; 另外 5 个明显偏离平均值的年龄最终也被去除 (图 4.14E); 剩下的 101 个有效锆石加权平均年龄为 115.4 ± 0.7 Ma (MSWD = 1.7), 为该花岗闪长岩的结晶年龄。

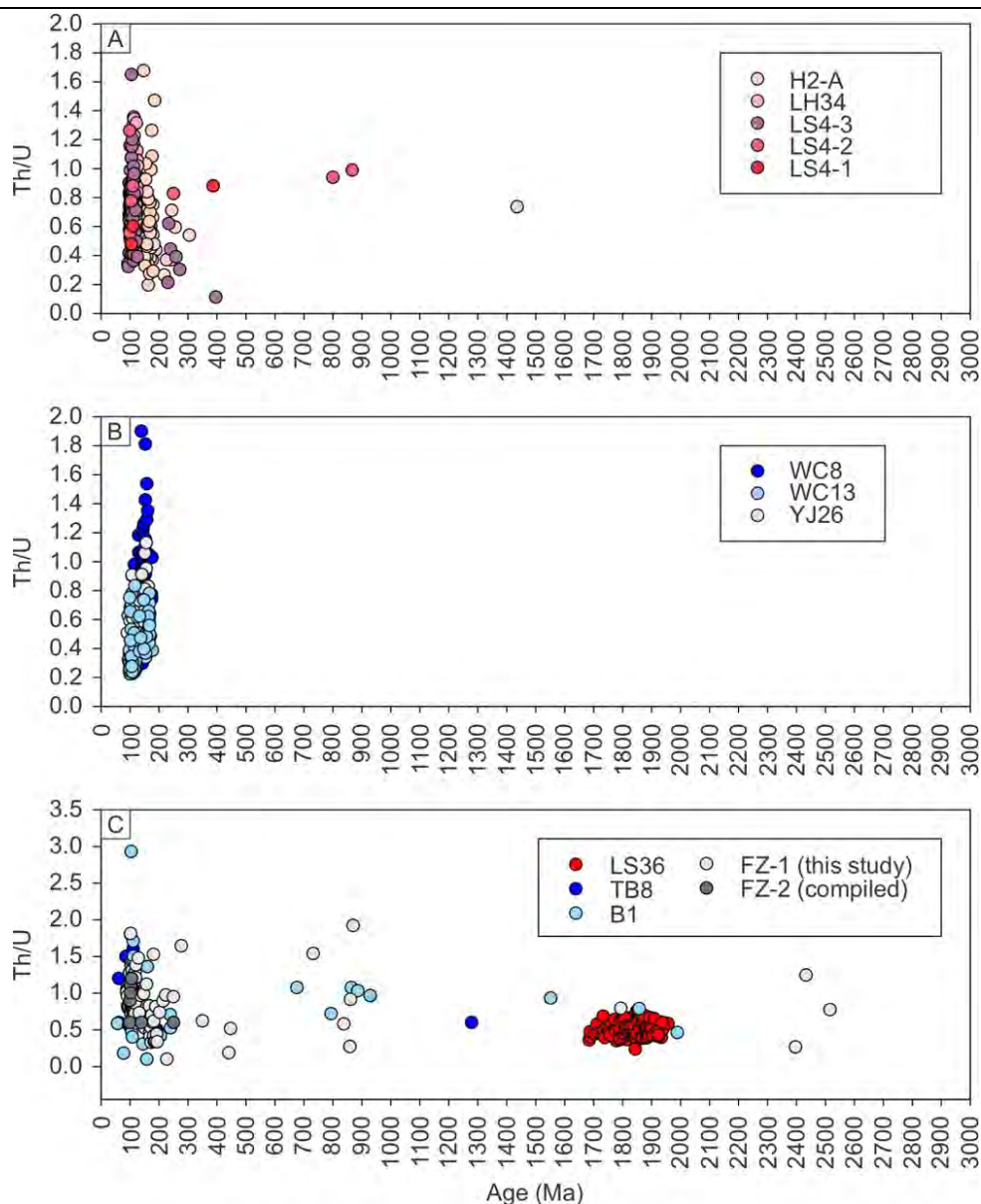


图 4.16 南海北部与东海陆架基底样品锆石 U-Pb 年龄 vs. Th/U 对比图

Fig. 4.16 Plots of Th/U ratios versus zircon U-Pb ages for (A) South China Sea igneous rock, (B) volcaniclastic or clastic rock and (C) East China Sea gneiss and clastic rock samples.

样品 H2-A 为中-细粒度花岗闪长岩，位于上述 H2（深度：3411–3429 m）下方深度 4097–4107 m 处，作为 H2 的补充样品（图 4.13）。H2-A 中锆石的 Th 和 U 含量变化明显，分别为 70.56 ppm 至 3478.19 ppm 和 95.99 ppm 至 8489.17 ppm，相应 Th/U 比值从 0.2 到 1.68 不等，锆石晶粒具有明显的振荡核-边结构，证实为岩浆锆石来源（4.16A）。总共分析 81 个锆石颗粒，共得到 73 个谐和年龄：其中 66 个锆石年龄介于 132 ± 3 Ma 和 189 ± 3 Ma 之间，加权平均年龄为 163.5 ± 2.1 Ma (MSWD = 5.4) (4.17C)。我们将这个年龄解释为 H2-A 样品的岩浆结晶年龄，比其上层样品 H2 的形成年龄 (115.4 ± 0.7 Ma) 要老；剩余的 7 个年龄包括 5 个三叠系年龄 (256–218 Ma)、一个晚古生代年龄 (305 Ma) 和一个

中元古代年龄 (1436 Ma)。这些年龄可能代表了在岩浆上升过程中从围岩中捕获的继承性锆石。

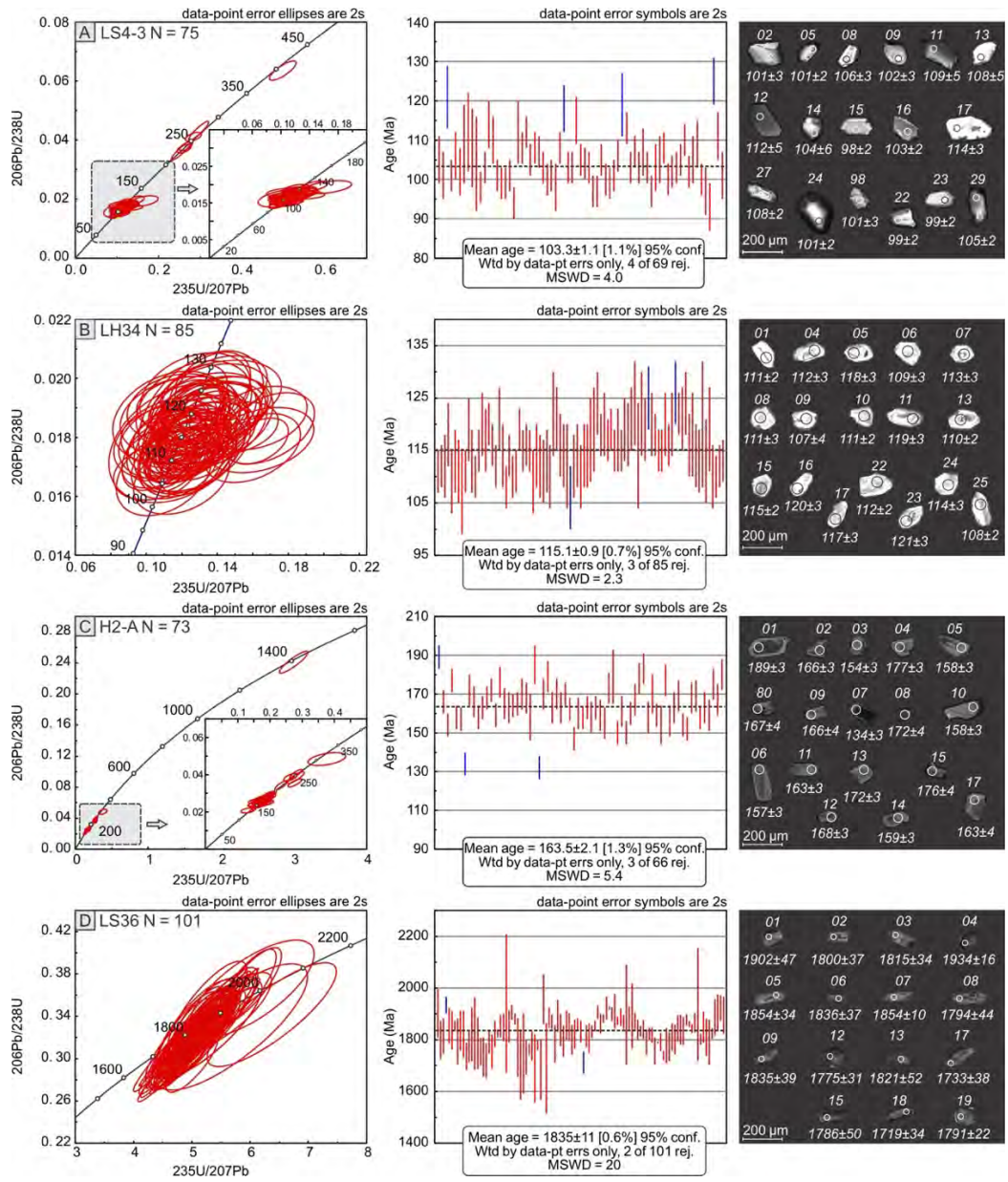


图 4.17 华南陆缘钻井样品 A) LS4-3; B) LH34; C) H2-A 及 D) LS36 锆石 U-Pb 年龄谐和图、加权平均年龄以及阴极发光图像

Fig. 4.17 LA-ICP-MS zircon U-Pb Concordia age plots, weighted mean ages, and cathodoluminescence (CL) images of representative zircon grains of igneous rock and gneiss samples in this study. (A) LS4-3: igneous rock; (B) LH34: granite; (C) H2-A: granodiorite; (D) LS36: gneiss. N = total number of effective analyses for each panel. MSWD – mean square weighted deviations. The number on the top of imaged zircon grain denotes analytical number while the bottom indicates its concordant age and error (1 sigma).

样品 LH34 为中等粒度花岗岩，来自南海北部珠江口盆地南缘的中生代基底 (图 4.13)。该样品 Th 和 U 含量范围分别为 65.76 ppm 至 486.41 ppm 和 116.96

ppm 至 560 ppm，相应的 Th/U 比值从 0.51 到 1.36 不等，表明岩浆锆石来源（图 4.16A）。总共得到 85 个谐和年龄，介于 126 ± 3 Ma 和 106 ± 3 Ma 之间。去除了三个偏离平均值的异常点后，剩余的 82 个谐和锆石的加权平均年龄为 115.1 ± 0.9 Ma (MSWD = 2.3) (4.17B)。

样品 WZ12、Y9、KP1-1、KP1-2 和 CC2-2 均为低级变质火山碎屑岩（图 4.12；表 4.3）。WZ12 井位于北部湾盆地，锆石颗粒大多呈自形状至半自形状，表现明显的振荡环带结构（图 4.18 和 4.19），Th (37–3048 ppm) 和 U (106–4642 ppm) 含量相对较高，大多数 Th/U 介于 0.11 至 1.57 之间（图 4.15）。其中六个有效年

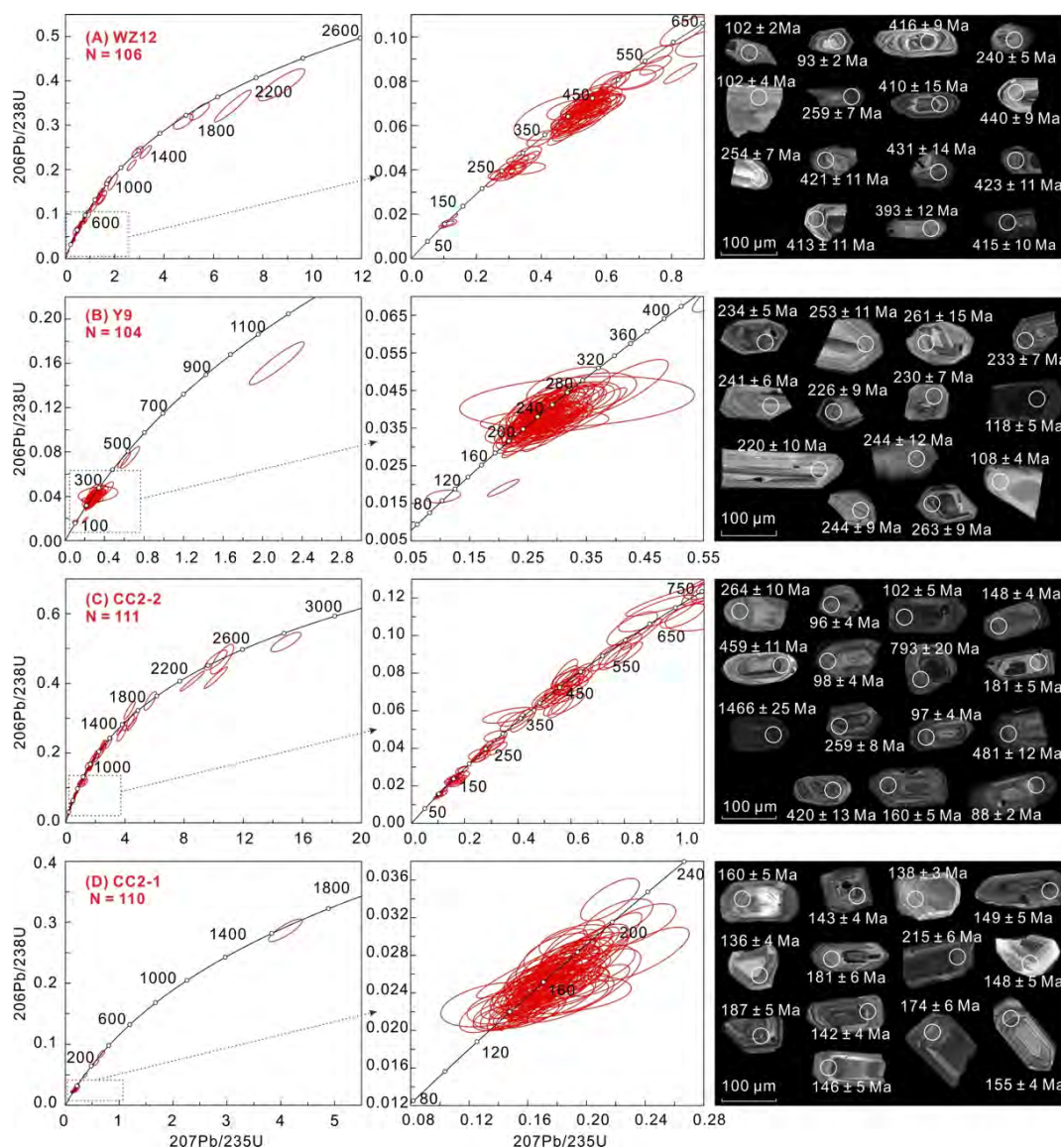


图 4.18 南海北部钻井样品 A) WZ12; B) Y9; C) CC2-2 及 D) CC2-1 锆石 U-Pb 年龄谐和图，主要年龄区间谐和放大图以及阴极发光图像

Fig. 4.18 LA-ICP-MS U-Pb concordia age plots and CL images of representative zircons from metatuffs and volcaniclastic rocks. (A) WC17; (B) KP1-2; (C) KP1-1. The term “N”

denotes the total number of effective analyses for each sample.

龄范围在 698 ± 17 Ma 至 217 ± 4 Ma 之间, Th/U 比值为 0.02–0.09, 可能为变质锆石。共取得 106 个有效年龄, 86 颗锆石年龄介于 567 ± 10 Ma 至 93 ± 2 Ma 之间; 其余年龄范围为 2114 ± 106 Ma 至 601 ± 16 Ma (图 4.20A)。最年轻的三个白垩系锆石年龄 (分别为 93 ± 2 Ma、 102 ± 2 Ma 和 102 ± 4 Ma) 的加权平均数给出了该样品的最年轻年龄 98 ± 14 Ma (MSWD = 5.6)。二叠–三叠系锆石年龄共同表现为次要峰值, 集中于大约 250 Ma 左右; 主要峰值集中于大约 420 Ma, 年龄范围在 567 ± 10 Ma 至 340 ± 9 Ma 之间; 剩余较老的年龄零星分布在 2114 Ma 至 601 Ma 之间 (图 4.20A)。

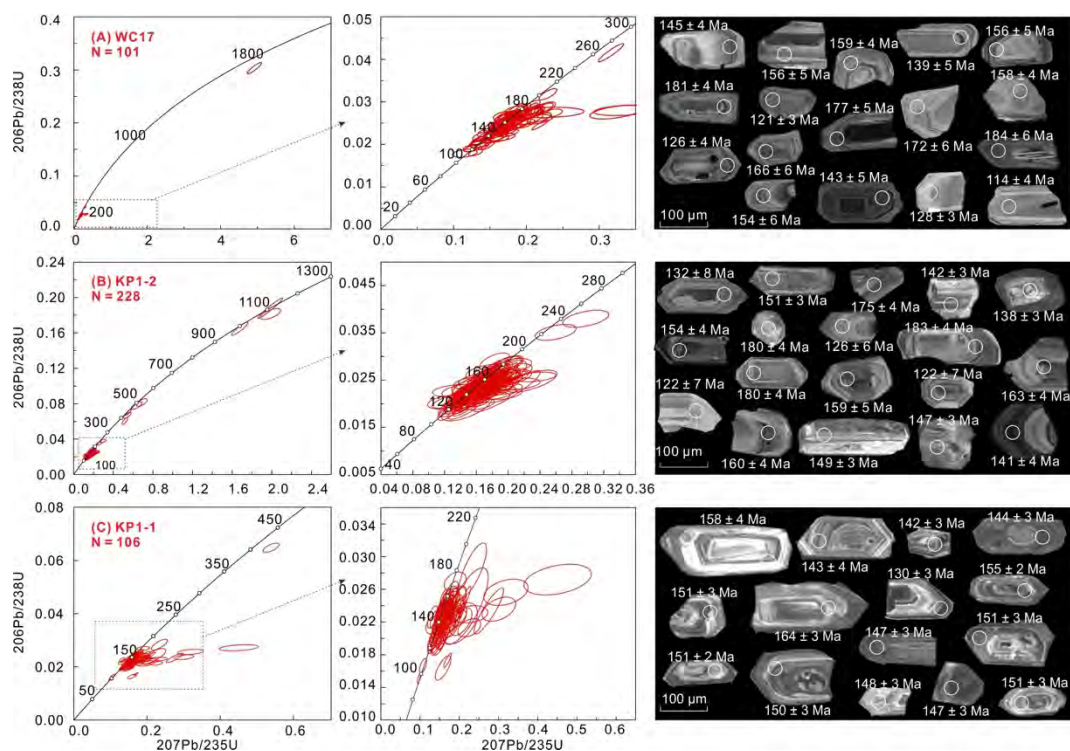


图 4.19 南海北部钻井样品 A) WC17; B) KP1-2 及 C) KP1-1 锆石 U-Pb 年龄谐和图, 主要年龄区间谐和和放大图以及阴极发光图像

样品 Y9 具有相对较高、变化范围相对较大的 Th 和 U 含量, 分别为 66–3314 ppm 和 149–9662 ppm, 相应的 Th/U 比值介于 0.30 至 1.78 之间 (图 4.15)。共取得 104 个有效年龄, 所有锆石均具有振荡环带 (图 4.18)。除了一个新元古代 (957 ± 44 Ma) 和两个早古生代 (467 ± 24 Ma 和 453 ± 17 Ma) 锆石颗粒外, 其余的 101 个年龄范围在 290 ± 13 Ma 至 108 ± 4 Ma 之间 (图 4.20)。该样品最年轻年龄由两个白垩系锆石 (108 ± 4 Ma 和 118 ± 5 Ma) 计算得出, 加权平均年龄为 111.9 ± 6.2 Ma, 作为该样品的最大沉积年龄。

样品 KP1-1 和 KP1-2 来自同一钻孔, 深度分别为 1903–1906.5 米和 1893–1897 米 (图 4.12; 表 4.3)。大多数锆石颗粒呈自形状至半自形状, 阴极发光图像显示清晰的核-边结构 (图 4.19)。样品 KP1-1 和 KP1-2 分别获得 106 个和 228

个有效年龄，其 Th/U 比值介于 0.08 和 1.63 之间。样品 KP1-2 包含一个 Th/U 值为 0.08 的三叠系年龄 222 ± 4 Ma (图 4.15)，可能代表变质锆石。这两个样品都以晚中生代年龄为主 (图 4.21)：样品 KP1-1 年龄介于 405 ± 7 Ma 和 97 ± 2 Ma 之间，只包含一个前中生代年龄，为 405 ± 7 Ma，其余 105 个分析点全部为侏罗-白垩系年龄 (图 4.21)，主要峰值集中在大约 140 Ma，最年轻四个锆石 (97 ± 2 Ma、 103 ± 4 Ma、 106 ± 2 Ma 和 109 ± 2 Ma)，加权平均年龄为 103.9 ± 9.0 Ma，为该样品最大沉积年龄；样品 KP1-2 中包含八个相对较老年龄的锆石，介于 1173 Ma 和 379 Ma 之间，但仅占全部 228 个分析点的 3.5%，其余包括两个三叠系年龄和 218 个侏罗/白垩系年龄 (图 4.21)。KP1-2 的年龄谱系特征与 KP1-1 相似，即表现为明显的燕山期主峰，集中在大约 145 Ma。由于样品 KP1-2 相对 KP1-1 地层较浅，假设未曾发生地层倒转，那么两个样品的实际沉积年龄都不应该比下部样品中的最年轻锆石年龄老，即 104 ± 9 Ma (图 4.21B 和 C)。

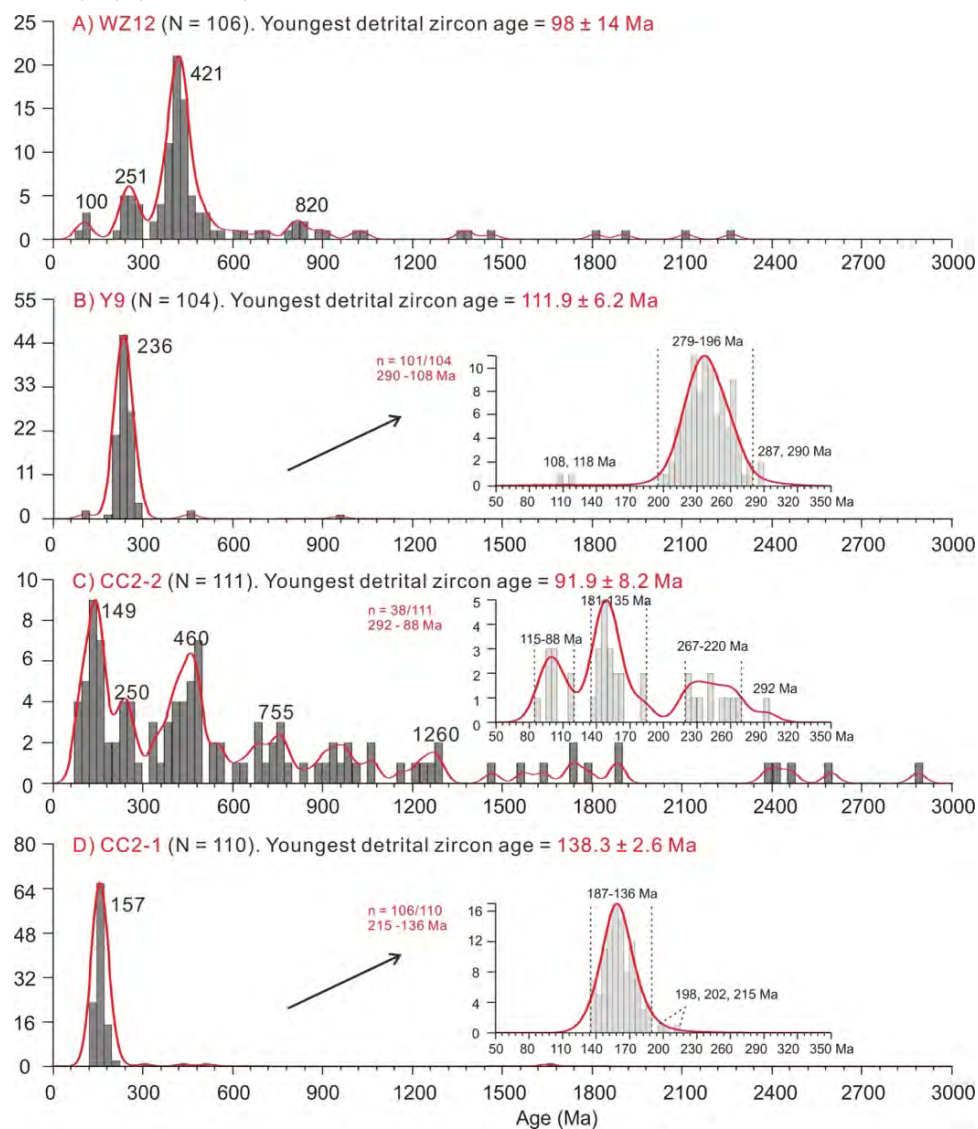


图 4.20 南海北部钻井样品 A) WZ12; B) Y9; C) CC2-2 及 D) CC2-1 锆石 U-Pb 年龄谱系图以及重点年龄区间放大图 (红色年龄代表各样品的最大沉积年龄)

Fig. 4.20 Zircon U-Pb age spectra of metatuffs and volcanoclastic rocks. (A) WZ12; (B) Y9; (C) CC2-2; (D) CC2-1. The term “N” denotes the total number of effective analyses for each sample. Centralized age groups are also enlarged for samples Y9, CC2-2 and CC2-1. The term “n” denotes the ratio between the analytical number of enlarged age group and the total effective number.

样品 CC2-1 和 WC17 为变质凝灰岩，来自海南岛东部的琼东南盆地基底钻井（图 4.12；表 4.3）。样品 CC2-1 共包含 110 个有效年龄（图 4.20D），其 Th 和 U 含量分别为 87.35–1354.50 ppm 和 129.38–2008.33 ppm，Th/U 比值介于 0.39 和 1.01 之间，为岩浆锆石来源。除了四个较老的年龄（1652–306 Ma），其余年龄都落在中生代约 215–136 Ma 范围内（图 4.20D）。最年轻九个锆石（ 140 ± 4 – 136 ± 4 Ma）加权平均年龄为 138.3 ± 2.6 Ma，是该样品的最大沉积年龄。样品 CC2-2 取自位于样品 CC2-1 上方 40 米处的变质火山碎屑岩，总共取得 111 个有效年龄（图 4.20C）。大多数 Th/U 比值介于 0.12 和 1.85 之间，只有两个较小值分别为 0.07 和 0.08。所有有效年龄组成了一个更为宽广的年龄谱系范围，介于 2884 Ma 和 88 Ma 之间（图 4.20C）。其中最年轻四个颗粒（ 88 ± 2 Ma、 96 ± 4 Ma、 97 ± 4 Ma 和 98 ± 4 Ma）的加权平均年龄为 91.9 ± 8.2 Ma，作为该样品的最大沉积年龄。样品 CC2-2 主要表现为燕山期主峰（149–99 Ma），次要年龄峰值聚集在 492–344 Ma、292–220 Ma 之间，以及一系列从 2463 Ma 到 545 Ma 之间的元古代锆石和少量太古代锆石。样品 WC17 中大多数锆石为自形状颗粒，具有岩浆生长环带，具有一定变化范围的 Th（56.70–2013.25 ppm）和 U（118.61–3115.30 ppm）含量，Th/U 比值大于 0.1（图 4.15）。总共包含 101 个有效年龄（图 4.21），两个年龄锆石（ 114 ± 4 Ma 和 115 ± 3 Ma）加权平均年龄为 114.6 ± 4.7 Ma（图 4.21A），是该样品最大的沉积年龄。除了一个古太古代 1884 ± 18 Ma 年龄外，样品 WC17 以中生代锆石为主，年龄介于约 184 Ma 和 114 Ma 之间，另外两个异常值为 202 ± 5 Ma 和 262 ± 9 Ma。

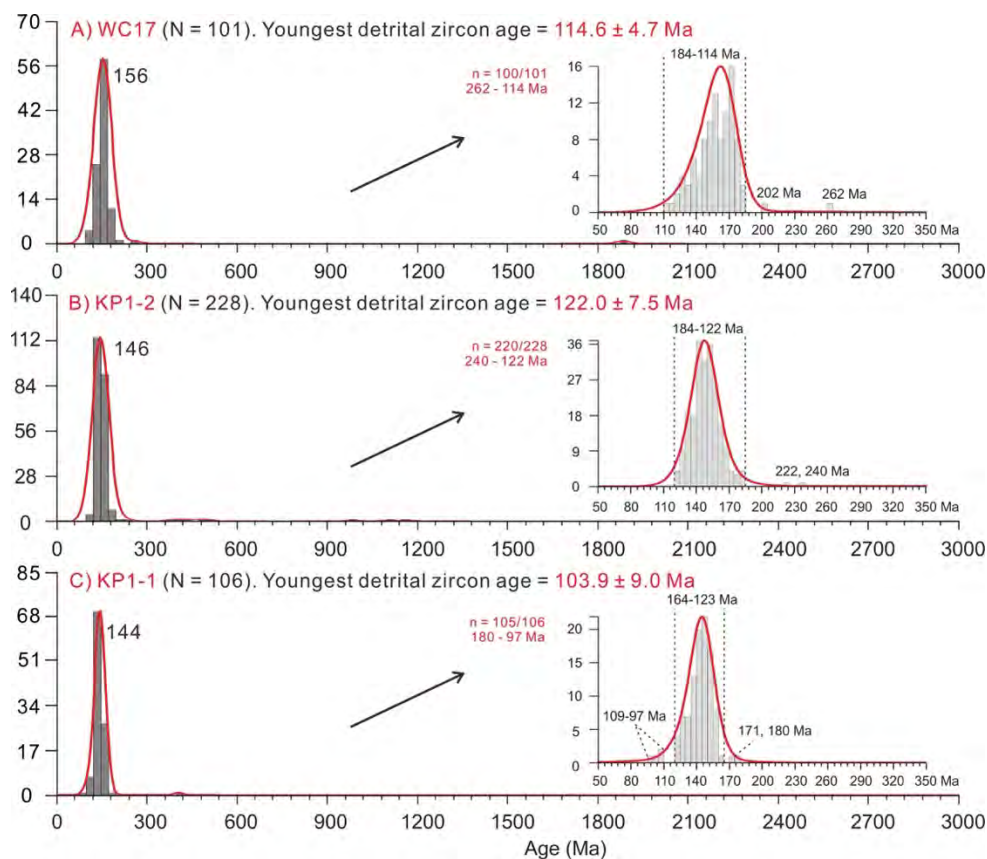


图 4.21 南海北部钻井样品 A) WC17; B) KP1-2 及 C) KP1-1 锆石 U-Pb 年龄谱系图以及重点年龄区间放大图（红色年龄代表各样品的最大沉积年龄）

Fig. 4.21 Zircon U-Pb age spectra of metavolcaniclastic samples. (A) WC17; (B) KP1-2; (C) KP1-1. The term “N” denotes the total number of effective analyses for each sample. Centralized age groups are also enlarged. The term “n” denotes the ratio between the analytical number of enlarged age group and the total effective number.

样品 WC8 和 WC13 分别为火山角砾岩和变质火山碎屑岩，均来自琼东南盆地中生代基底（图 4.13；表 4.4）。样品 WC8 的锆石晶粒主要为自形状，显示振荡环带结构（图 4.22 A）。该样品 Th（-15.4–1188 ppm）和 U（-32.7–1655 ppm）含量范围变化不大，Th/U 比值介于 0.25 到 1.9（图 4.16B）。样品 WC8 共包含 85 个谐和年龄，介于 104 ± 3 Ma 和 176 ± 5 Ma 之间。上白垩统的三个年龄（ 104 ± 3 Ma、 107 ± 3 Ma 和 107 ± 4 Ma）经加权平均得到 105.8 ± 3.7 Ma（MSWD = 0.3），为该样品的最大沉积年龄。WC8 整体表现为一个集中于侏罗系约 149 Ma 的主要峰值和集中于下白垩统约 118 Ma 的次要峰值（图 4.22A）。钻孔 WC13 也临近海南岛，位于 WC8 的西南方向。样品 WC13 的 Th 和 U 含量相对较高，分别为 182–3670 ppm 和 539–4889 ppm，其 Th/U 值在 0.22 到 0.83 之间，锆石颗粒发育振荡环带结构（图 4.16B），证实为岩浆锆石起源（图 4.22B）。总共获得 112 个谐和锆石年龄：其中四个锆石（一个 95 ± 2 Ma 年龄和三个 98 ± 2 Ma 年龄）的加权平均年龄为 97.3 ± 2.0 Ma（MSWD = 0.56），是该变质火山碎屑岩的最大沉积年龄；

整体年龄范围是 177–95 Ma，表现为一个集中于上白垩统 105 Ma 的主要峰值和集中于侏罗系 162 Ma 的次要峰值。

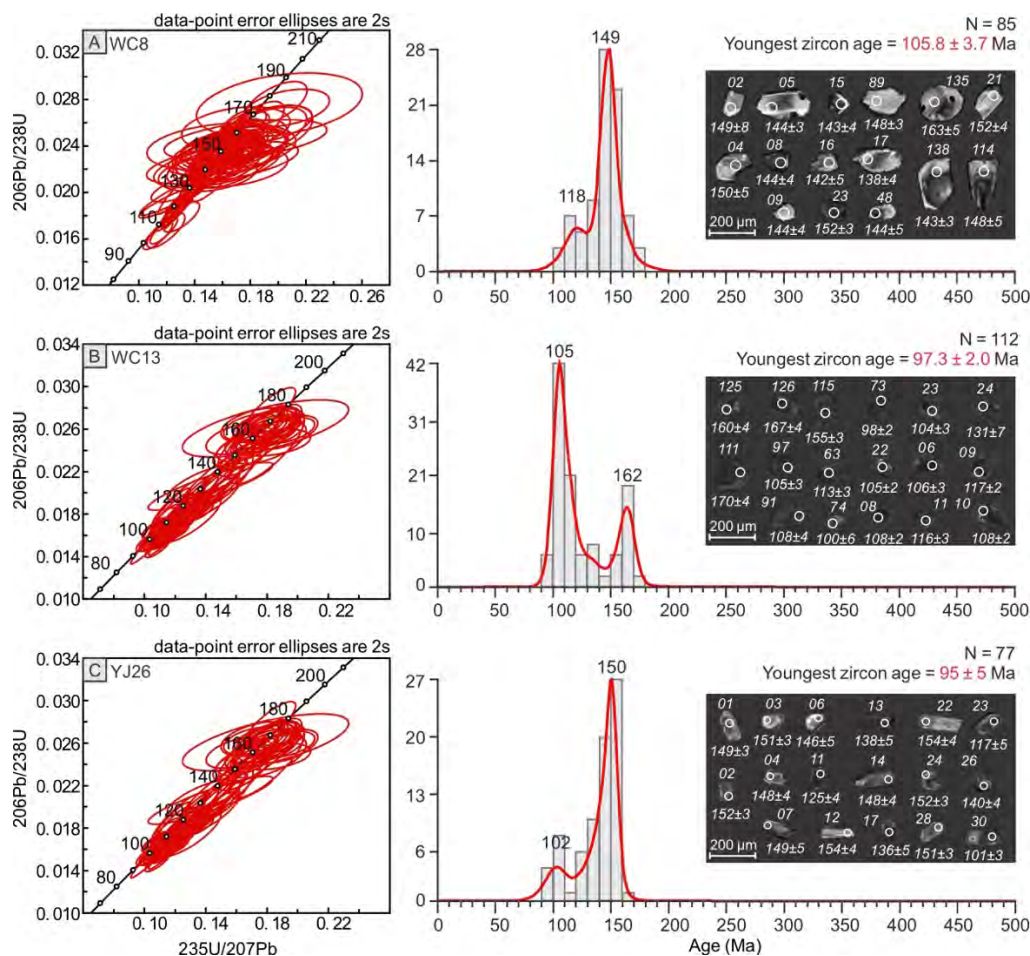


图 4.22 南海北部钻井样品 A) WC8; B) WC13 及 C) YJ26 锆石 U-Pb 年龄谐和图、年龄谱系图以及代表性锆石阴极发光图像（红色年龄代表各样品的最大沉积年龄）

Fig. 4.22 LA-ICP-MS zircon U-Pb Concordia age plots, U-Pb age spectra and CL images of representative zircon grains from volcanic breccia, tuff and metaclastic rocks from South China Sea and East China Sea. (A) WC8; (B) WC13; (C) YJ26. N = total number of effective analyses for each panel.

样品 YJ26 为凝灰岩，相对更靠近华南陆缘，位于珠江口盆地西部基底（图 4.13；表 4.4）。该样品中大多数锆石晶体呈自形状至半自形状，具有核-边结构或呈均质特征（图 4.22C）。总共获得 77 个谐和年龄，Th 和 U 含量变化较大，分别从 47 ppm 到 4961 ppm 以及从 92 ppm 到 7929 ppm，相应的 Th/U 比值介于 0.32 到 1.13（图 4.16B）。谐和年龄介于 163±4 Ma 和 91±2 Ma 之间，其中四个最年轻锆石（91±2 Ma、94±2 Ma、97±2 Ma 和 98±2 Ma）的加权平均年龄为 95±5 Ma（MSWD = 2.5），作为该样品的最大沉积年龄。与样品 WC8 类似，样品 YJ26 显示出一个集中于侏罗系约 150 Ma 的主要峰值，伴随一个集中于大约 102 Ma 的次要峰值（图 4.22C）。

样品 BD23-1、BD23-2、CC-1、CC-2、YJ36-1 和 YJ36-2 均为变质碎屑岩样品 (图 4.12; 表 4.3)。来自同一钻孔的变质石英岩样品 BD23-1 和 BD23-2 分别包含 92 和 91 个谐和年龄。大多数锆石呈现自形状至半自形状,但也有少数呈次圆状 (图 4.23A 和 B)。样品 BD23-1 包含一个年龄为 1869 Ma 的锆石,其 Th/U 比值较低 (0.09),说明可能为变质锆石;除此之外,这两个样品中剩余锆石的 Th/U 比值介于 0.10 和 1.85 之间 (图 4.15)。样品 BD23-1 表现明显的燕山期主峰,年龄范围在约 185 Ma 和 120 Ma 之间,除此之外仅有两个元古代年龄,分别为 1869 Ma 和 663 Ma (图 4.24A)。该样品最大沉积年龄是 122.7 ± 2.8 Ma,由六个最年轻年龄 (124 ± 4 – 119 ± 4 Ma) 的加权平均值来确定的。另一方面, BD23-2 主要年龄集中在 185 Ma 和 130 Ma 之间,次要年龄包括 130–85 Ma、250–200 Ma 和 510–270 Ma,以及六个零散的新元古代锆石颗粒 (图 4.24B)。两个最年轻锆石 (85 ± 3 Ma 和 89 ± 3 Ma) 的平均年龄为 87.0 ± 4.2 Ma,反映该样品的最大沉积年龄。

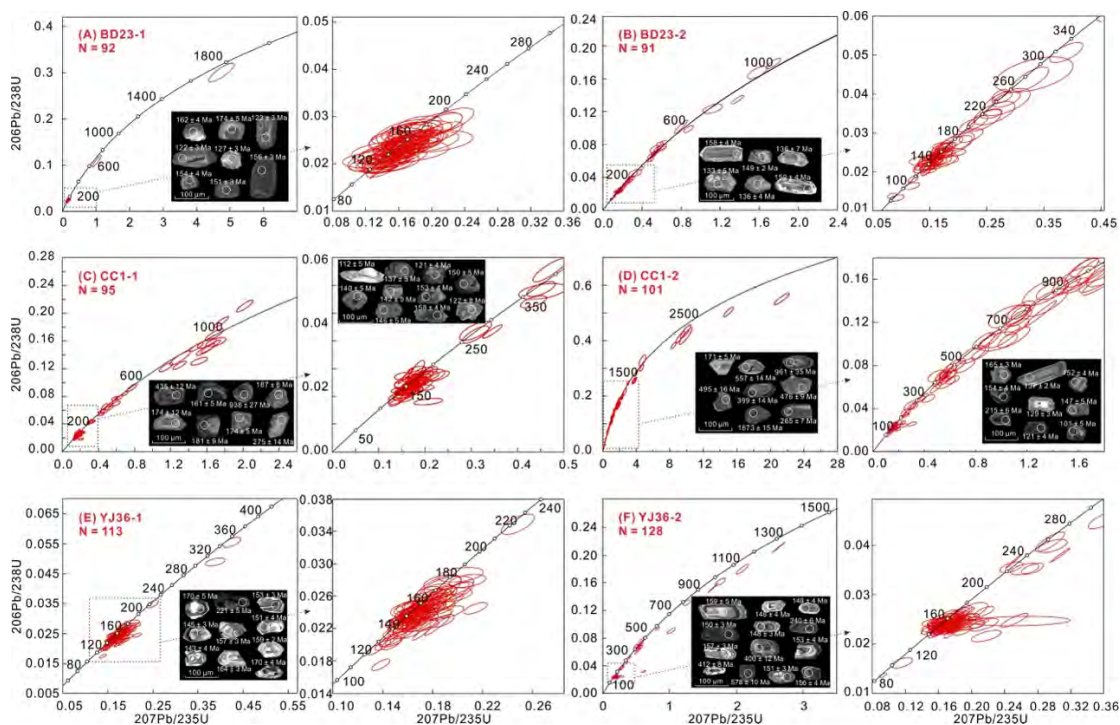


图 4.23 南海北部钻井样品 A) BD23-1; B) BD23-2; C) CC1-1; D) CC1-2; E) YJ36-1 及 F) YJ36-2 锆石 U-Pb 年龄谐和图、重点年龄区间谐和放大图和代表性锆石阴极发光图像

Fig. 4.23 LA-ICP-MS U-Pb concordia age plots and CL images of representative zircons from metasedimentary samples. (A) BD23-1; (B) BD23-2; (C) CC1-1; (D) CC1-2; (E) YJ36-1; (F) YJ36-2. The term “N” denotes the total number of effective analyses for each sample.

样品 CC1-1 和 CC1-2 为变质沉积岩,取自同一钻井,大多数锆石呈自形或半自形状 (图 4.23C 和 D),分别获得 93 和 101 个谐和锆石年龄。样品 CC1-1 的 Th 和 U 含量分别为 18.20–1926.05 ppm 和 105.08–3890 ppm,大多数 Th/U 比值

在 0.12 至 1.71 之间，仅存在一个 0.09 的较小值（图 4.15）。69 个锆石年龄介于 187 Ma 和 112 Ma 之间，主要峰值集中在约 150 Ma；13 个古生代和 13 个元古宙锆石（占总分析数目的 28.0%），分布在 250 Ma 至 990 Ma 之间（图 4.24C）。两个最年轻锆石年龄分别为 112 ± 5 Ma 和 114 ± 6 Ma，平均年龄为 112.8 ± 7.5 Ma，被视为该样品的最大沉积年龄。样品 CC1-2 的 Th 和 U 含量范围分别为 45.49 ppm 至 1630.02 ppm 和 71.97 ppm 至 2940.52 ppm，大多数 Th/U 比值超过 1，只有一个 Th/U 比值为 0.08，其锆石年龄为 654 ± 26 Ma（图 4.15）。与 CC1-1 相比，该样品 U-Pb 年龄谱更为宽广，其中 29 个谐和年龄组成最大的燕山期峰值，年龄范围介于 171 Ma 和 101 Ma 之间，最大沉积年龄为 101 ± 5 Ma（图 4.24D）。较老锆石年龄范围为 3323 Ma 到 208 Ma，占该样品总谐和年龄数目的 77.4%。

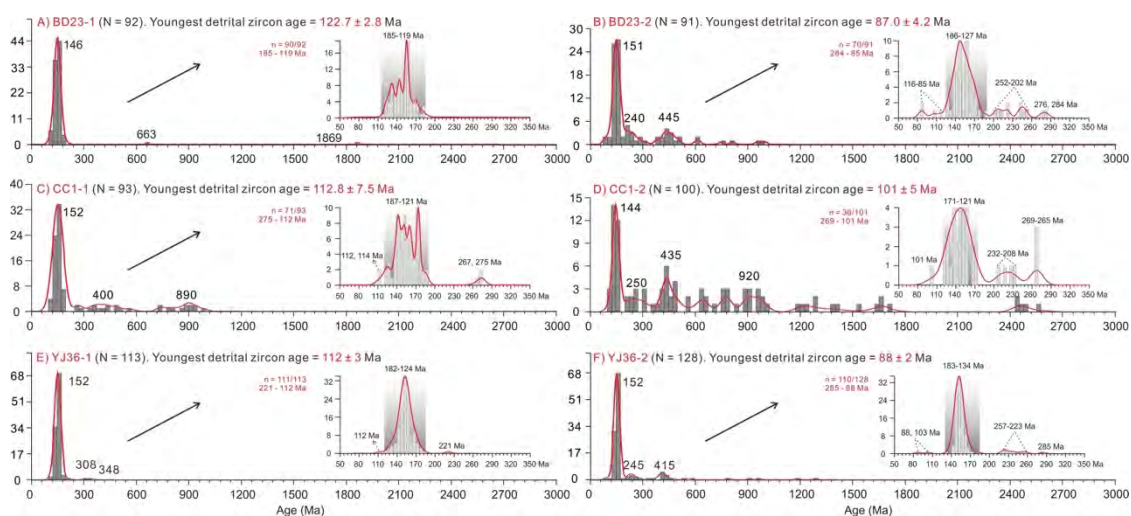


图 4.24 南海北部钻井样品 A) BD23-1; B) BD23-2; C) CC1-1; D) CC1-2; E) YJ36-1 及 F) YJ36-2 锆石 U-Pb 年龄谱系图及重点年龄区间放大图（红色年龄代表各样品的最大沉积年龄）

Fig. 4.24 Zircon U-Pb age spectra of metasedimentary samples. (A) BD23-1; (B) BD23-2; (C) CC1-1; (D) CC1-2; (E) YJ36-1; (F) YJ36-2. Centralized age groups are enlarged for all samples. The term “n” denotes the ratio between the analytical number of enlarged age group and the total effective number.

样品 YJ36-1 和 YJ36-2 为低级变质泥岩和变质粉砂岩，同样来自同一钻孔，锆石颗粒大多为自形至半自形（图 4.23E 和 F）。样品 YJ36-1 包含 113 个谐和年龄，YJ36-2 包含 128 个。这两个样品的 Th（122.73–8349.25 ppm）和 U（205.58–33224.03 ppm）浓度变化范围很大，仅有一个 240 ± 6 Ma 的锆石 Th/U 比值为 0.02，其余 Th/U 比值在 0.11 至 1.24 之间。两个样品均表现燕山期主峰，年龄范围在 170 Ma 至 110 Ma。样品 YJ36-1 最年轻颗粒为 112 ± 3 Ma，只有少数较老颗粒为 348 Ma（图 4.24E）。样品 YJ36-2 最年轻颗粒为 88 ± 2 Ma，另外存在若干较老锆石，最老为中元古代 1283 Ma（图 4.24F）。

本研究还包括四个来自东海陆架盆地基底的变质碎屑岩和片麻岩钻井样品，

样品 FZ13-1、B1、TB8 和 LS36 (图 4.13; 表 4.4)。样品 FZ13-1 总共获得了 58 个谐和年龄, 该钻孔位于本论文东海陆架盆地区域的最南端。大多数锆石晶体呈自形状, 显示岩浆生长的环带构造。Th 和 U 含量分别为 13–1146 ppm 和 92–1243 ppm, 相应的 Th/U 比值大多在 0.19 到 1.92 之间 (图 4.16C)。两个最年轻锆石 (88 ± 4 Ma 和 91 ± 2 Ma) 加权平均年龄为 90.4 ± 3.5 Ma (MSWD = 0.45), 代表最大沉积年龄。该样品年龄范围广泛, 从 2516 ± 50 Ma 到 91 ± 2 Ma, 包含一个集中于 157 Ma 的主要年龄峰值 (图 4.25D); 除此之外, 次要年龄组分包括 277–202 Ma、447–350 Ma 以及 2461–732 Ma。关于该样品侏罗–白垩的年龄组分, 表现一个集中在 116 Ma 的下白垩统主峰和 184 Ma、223 Ma 的次要年龄组分 (图 4.25D)。

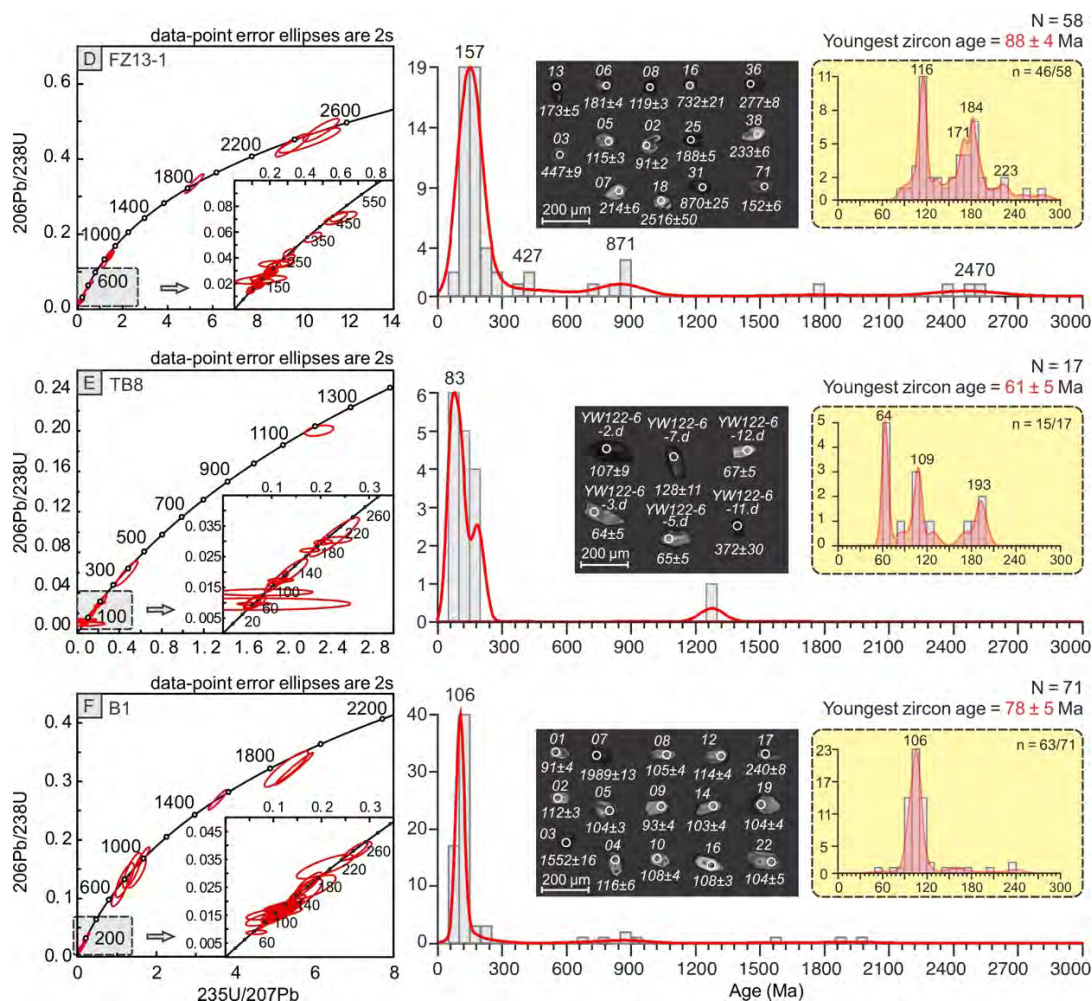


图 4.25 东海陆架盆地基底钻井样品 D) FZ13-1; E) TB8 及 F) B1 锆石 U-Pb 年龄谐和图、谱系图和代表性锆石阴极发光图像 (红色年龄代表各样品的最大沉积年龄)

Fig. 4.25 LA-ICP-MS zircon U-Pb Concordia age plots, U-Pb age spectra and CL images of representative zircon grains from volcanic breccia, tuff and metaclastic rocks from East China Sea. (D) FZ13-1; (E) TB8; (F) B1. N = total number of effective analyses for each panel; “n” of (D–F) = ratio between analytical number of enlarged age population and total effective number. The number on the top of imaged zircon grain denotes analytical number while the bottom indicates its

样品 B1 位置偏北, 共有 71 个谐和年龄。大多数锆石呈自形状或半自形状, 少数锆石有一定磨圆度 (图 4.25F)。Th 和 U 含量变化范围较大, 分别为 61–2570 ppm 和 103–14207 ppm, 只有一个年龄 158 Ma 的锆石 Th/U 较低, 为 0.1, 其余 Th/U 值介于 0.18 到 2.93 之间 (图 4.16C)。样品 B1 年龄范围宽广, 介于 1989 ± 13 Ma 到 57 ± 2 Ma (图 4.25F)。其中 63 个谐和年龄介于 171 Ma 到 57 Ma 之间, 大部分集中在 106 Ma, 另外还有三个三叠系年龄 (205 ± 11 Ma、 239 ± 8 Ma 和 240 ± 8 Ma)。样品 B1 还包含若干零散的元古代锆石, 年龄范围从 1989 Ma 到 676 Ma。值得注意的是, 样品 B1 仅产生了一个最早新生代 57 ± 2 Ma 的分析。在这里, 我们合理地将其解释为来自上层新生代中掉落的一个锆石晶粒。因此, 最年轻锆石 (78 ± 5 Ma) 被认为是该样品最大沉积年龄。

样品 TB8 也是东海陆架基底变质碎屑岩, 锆石晶体大多呈自形状, Th 和 U 含量变化范围不大, 分别为 170–2478 ppm 和 270–2739 ppm, Th/U 比值介于 0.4 和 1.8 之间 (图 4.16C)。共获得 17 个谐和年龄, 其中十五个介于 199 Ma 到 61 Ma 之间, 另外还有一个古生代 (372 Ma) 和一个元古代 (1279 Ma) 的年龄 (图 4.25E)。对于较年轻的年龄组分, 包含一个早新生代峰值, 集中于大约 64 Ma, 另外还有两个集中于 109 Ma 和 193 Ma 的次要峰值。最年轻的五个锆石加权平均年龄是 62.2 ± 1.8 Ma (MSWD = 0.28), 我们将其视为样品 TB8 的最大沉积年龄。

特别需要指出的, 样品 LS36 是本研究东海陆架基底唯一的片麻岩样品, 位于浙江省东部海域 (图 4.13)。锆石晶体主要呈长柱状至次长柱状, 无明显环带构造, 但呈现出较高的均质性。该样品 Th 和 U 含量分别在 116 ppm 至 401 ppm, 和 267 ppm 至 748 ppm 之间 (图 4.16C), Th/U 范围从 0.24 到 0.77, 表明为岩浆锆石来源。共取得 101 个谐和年龄, 去除两个异常点后, 剩余年龄的加权平均值为古元古代年龄 1835 ± 11 Ma (图 4.17D), 我们解释为样品 LS36 原岩的结晶年龄。

4.2.2 锆石微量元素结果

为了区分不同的构造环境, 本论文对南海北部及东海陆架盆地基底样品开展锆石微量元素含量分析, 花岗岩样品 ST34-1 (98.6 ± 2.1 Ma)、ST34-2 (98.4 ± 1.7 Ma)、XK-1 (111.8 ± 3.3 Ma)、LH34 (115.1 ± 0.9 Ma)、角闪斜长片麻岩 XK1-2 (151.8 ± 2.7 Ma)、花岗闪长岩 H2 (115.4 ± 0.7 Ma)、H2-A (163.5 ± 2.1 Ma) 锆石稀土配分曲线如图 4.26 和图 4.27 所示, 绝大多数锆石表现明显的 Ce 元素正异常和 Eu 元素负异常, 呈现左低右高、轻稀土变化幅度较大、重稀土极度富集的配分模式。然而, 样品 H2 中包含 17 个锆石颗粒展现出轻稀土元素平坦 ($(\text{Sm}/\text{La})_N < 1.45$)、重稀土急剧增加的配分模式, Ce 元素正异常值较小 ($\text{Ce}/\text{Ce}^* < 1.87$), 样品 XK1-2 中也包含一个呈类似稀土元素配分曲线的锆石

(图 4.26)。来自样品 LH34 的总共 125 个锆石中, 包含三个锆石显示出平坦的轻稀土元素模式 ($(\text{Sm}/\text{La})_N \leq 1.53$) 并产生较低的 Ce 正异常 ($\text{Ce}/\text{Ce}^* \leq 1.73$)

(图 4.27)。样品 H2-A 中存在更多产生类似 REE 配分模式的锆石, 其中 6 个表现为平坦的轻稀土 ($(\text{Sm}/\text{La})_N \leq 1.82$) 和较小 Ce 异常值 ($\text{Ce}/\text{Ce}^* \leq 1.62$) (图 4.27)。另外, 不同样品样品中 Eu 元素异常值存在一定变化, 样品 H2 的 Eu/Eu^* 为 0.04–0.55, H2-A 为 0.05–0.65, LH34 为 0.08–0.9, XK1-1 为 0.25–0.39, XK1-2 为 0.16–0.74, ST34-2 为 0.44–0.82; ST34-1 还包含两个 Eu 元素正异常值, 为 1.28 和 1.33, 其余锆石为 0.09 至 0.76; 样品 LH34 和 HJ 各含有一个 Eu 正异常, 分别为 1.04 和 1.03。此外, 由于仪器检测精确度限制, 部分锆石并未测得 Eu 元素含量。

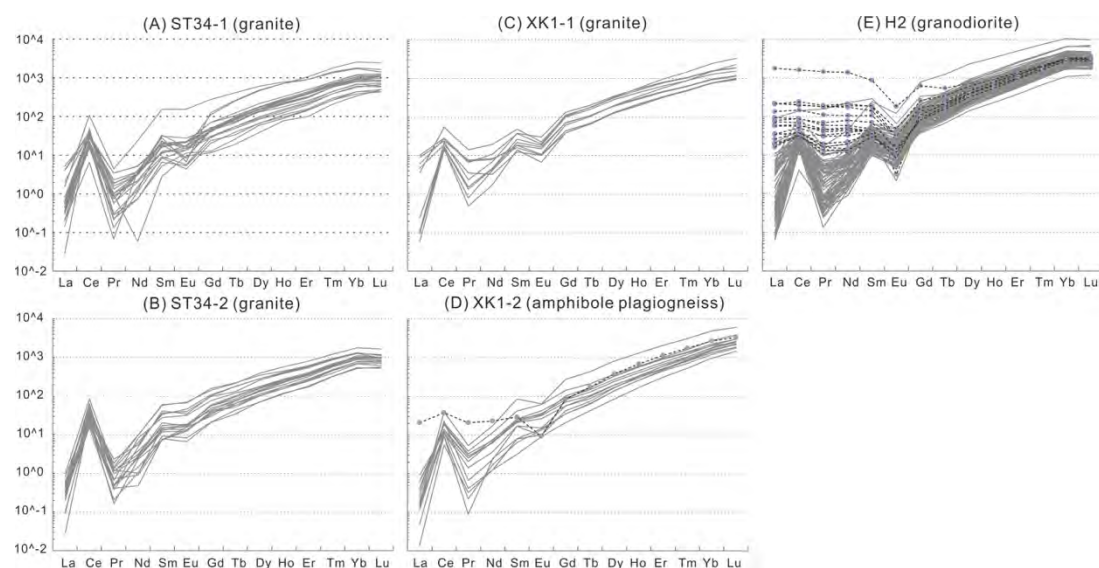


图 4.26 南海北部钻井样品 A) ST34-1; B) ST34-2; C) H2; D) XK1-1 及 E) XK1-2 锆石稀土元素配分曲线 (虚线代表部分锆石表现为轻稀土平缓、重稀土富集、Ce 元素正异常不明显的特点)

Fig. 4.26 Zircon rare earth element (REE) concentrations normalized to chondrites for igneous samples (A) ST34-1, (B) ST34-2, (C) XK1-1, (E) H2 and gneiss sample (D) XK1-2 from the northern South China Sea basin basement. Note that a few zircons from samples H2 and XK1-1 show flat LREE patterns (highlighted with purple dots and dashed lines).

东海陆架基底碎屑岩 (物源来自原位或附近的火成岩岩体) 样品锆石稀土元素配分模式对复杂 (图 4.27)。样品 FZ13-1 共获得 118 个有效数据, 其中 13 个表现为平坦的轻稀土元素模式, 其 $(\text{Sm}/\text{La})_N$ 低于 1.8, Ce 异常小于 2 (图 4.27C)。相比之下, 样品 HJ 包含二十颗稀土元素配分模式为平坦轻稀土 ($(\text{Sm}/\text{La})_N \leq 1.88$)、较小的 Ce 元素正异常 ($\text{Ce}/\text{Ce}^* \leq 1.82$) 的锆石 (总共 112 个有效值) (图 4.27D)。两个样品均呈现不同范围的 Eu 元素负异常, FZ13-1 和 HJ 分别为 0.004–0.84 和 0.01–0.92。

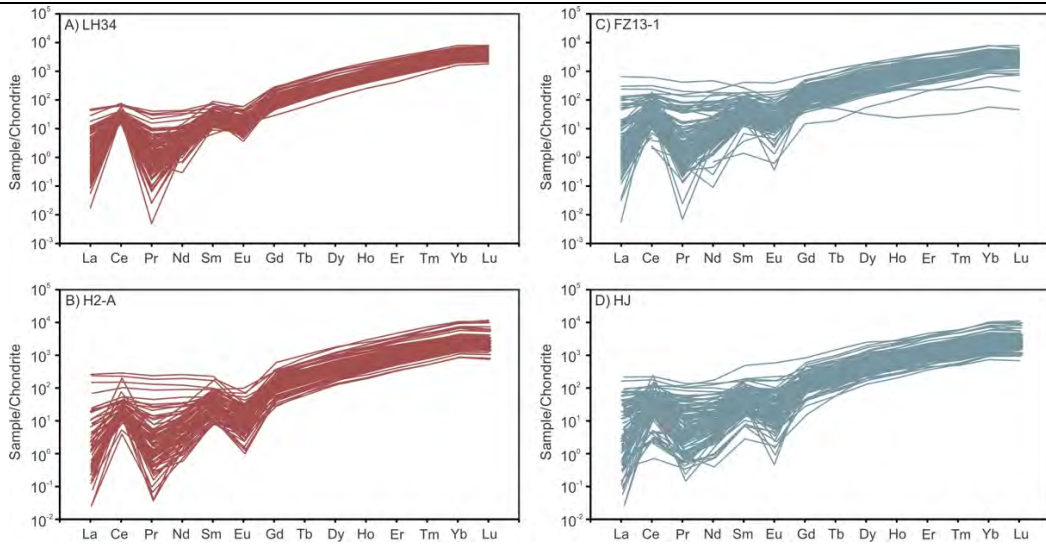


图 4.27 南海北部及东海陆架盆地基底钻井样品 A) LH34; B) H2-A; C) FZ13-1 及 D) HJ 锆石稀土元素配分曲线对比图

Fig. 4.27 Zircon rare earth element (REE) contents normalized to chondrites (McDonough and Sun, 1995) for samples (A) LH34 and (B) H2-A from South China Sea, (C) FZ13-1 and (D) HJ from East China Sea basin basement.

重要的锆石微量元素包括 Yb、Y、Hf 和 Nb 元素。其中，样品 H2 和 XK1-2 的 Yb 含量分别介于 243.34 ppm 和 2311.77 ppm 之间，203.44 ppm 和 1028.51 ppm 之间。样品 LH34 和 H2-A 含量分别介于 262.46 ppm 至 1289.96 ppm，135.98 ppm 至 1702.13 ppm。东海陆架基底碎屑岩样品 FZ13-1 和 HJ 的 Yb 含量具有相对类似的范围，分别为 9.19 ppm 至 1270.26 和 118.65 ppm 至 1670.16 ppm。样品 XK1-1、ST34-1 和 ST34-2 的 Yb 含量变化范围相对较窄，分别为 156.23–536.83 ppm、41.98–538.93 ppm 和 109.18–458.63 ppm。同样，样品 H2、XK1-2、LH34 和 H2-A 的 Y 含量范围较广，分别为 531.09–8413.27 ppm 和 440.63–3252.58 ppm，470.7 ppm 至 3220.74 ppm，375.21 ppm 至 4589.73 ppm；碎屑岩样品 FZ13-1 和 HJ 的变化范围分别为 50.66 ppm 至 4926.85 ppm，454.71 ppm 至 5781.05 ppm；而样品 XK1-1、ST34-1 和 ST34-2 的 Y 含量变化相对较小，分别为 475.63–1691.49 ppm、72.69–1748.14 ppm 和 272.95–1474.17 ppm。上述样品的 Hf 含量普遍较高，范围为 8114.13–14240.81 ppm（样品 H2）、9579.00–12617.61 ppm（样品 XK1-1）、6449.75–12005.61 ppm（样品 XK1-2）、8697.88–14476.86 ppm（样品 ST34-1）、8562.98–14395.66 ppm（样品 ST34-2）、7874.07–14167.26 ppm（LH34）、7756.35–15103.92 ppm（H2-A）、7200.4–16972.29 ppm（FZ13-1）和 7372.94–15572.52 ppm（HJ）。样品 H2、XK1-2、H2-A、FZ13-1 和 HJ 中锆石的 Nb 含量变化较大，分别为 0.65–24.06 ppm，0.53–18.17 ppm，0.72–55.36 ppm，0.66–55.96 ppm，0.72–153.22 ppm；而样品 XK1-1、ST34-1、ST34-2 和 LH34 的 Nb 含量变化较小，范围分别为 0.55–9.53 ppm、0.26–5.19 ppm、0.41–3.09 ppm、

0.6–7.64 ppm。

4.2.3 Lu-Hf 同位素分析结果

本论文对南海北部及东海陆架盆地基底火成岩样品 LS4-3 (103.3±1.1 Ma)、H2-A (163.5±2.1 Ma) 和 LH34 (115.1±0.9 Ma)、片麻岩样品 LS36 (1835±11 Ma) 以及六个凝灰岩、变质火山碎屑岩或变质沉积岩样品 WC8、WC13、YJ26、FZ13-1、B1 和 TB8 共计 598 颗定年锆石 Lu-Hf 同位素体系测试 (其中包括 473 个谐和年龄)。样品 H2-A 共得到 35 个 Hf 同位素结果, 其中 34 个具有谐和年龄, $\epsilon\text{Hf}(t)$ 值范围在 -14 至 +1.31 之间。其中, 大多数 $\epsilon\text{Hf}(t)$ 为负值, 介于 -14 和 -0.39 之间, 只有两个锆石为正 $\epsilon\text{Hf}(t)$ 值 (+0.48 和 +1.31)。所有谐和锆石的 $^{176}\text{Hf}/^{177}\text{Hf}$ 比值均在 0.282251 至 0.282737 之间, 其中大多数位于 CHUR 之下 (图 4.28A 和 B)。相比之下, 样品 LH34 共得到 67 个 Hf 同位素结果, 其中 52 个具有谐和年龄, $\epsilon\text{Hf}(t)$ 值均为正值, 变化范围为 1.04 至 5.66 (图 4.28A 和 B)。LH34 所有锆石 $\epsilon\text{Hf}(t)$ 值均位于 CHUR 和 DM 线之间。同样, 样品 LS4-3 共得到 65 个 Hf 同位素结果, 其中 54 个具有谐和年龄, 大多数锆石也为正 $\epsilon\text{Hf}(t)$ 值 (0.03–5.86), 只有一小部分 $\epsilon\text{Hf}(t)$ 值在 -10.29 至 -0.06 之间 (图 4.28A 和 B)。它们的 $^{176}\text{Hf}/^{177}\text{Hf}$ 比值范围为 0.282427 至 0.282886。

东海陆架盆地基底唯一的片麻岩样品 LS36, 共得到 63 个 Hf 同位素结果, 其中只有一个不谐和年龄。大多数锆石 $\epsilon\text{Hf}(t)$ 值为负值, 介于 -9.12 和 -0.05 之间, 只有八个正值 (+0.03–+3.91) (图 4.28E)。南海北部三个火山碎屑岩或凝灰岩样品 (WC8、WC13 和 YJ26) 以负 $\epsilon\text{Hf}(t)$ 值为主。样品 WC8 共取得 54 个 Hf 同位素结果, 其中有 47 个谐和年龄, $\epsilon\text{Hf}(t)$ 值介于 -4.8 至 -0.36 之间 (图 4.28A 和 B)。

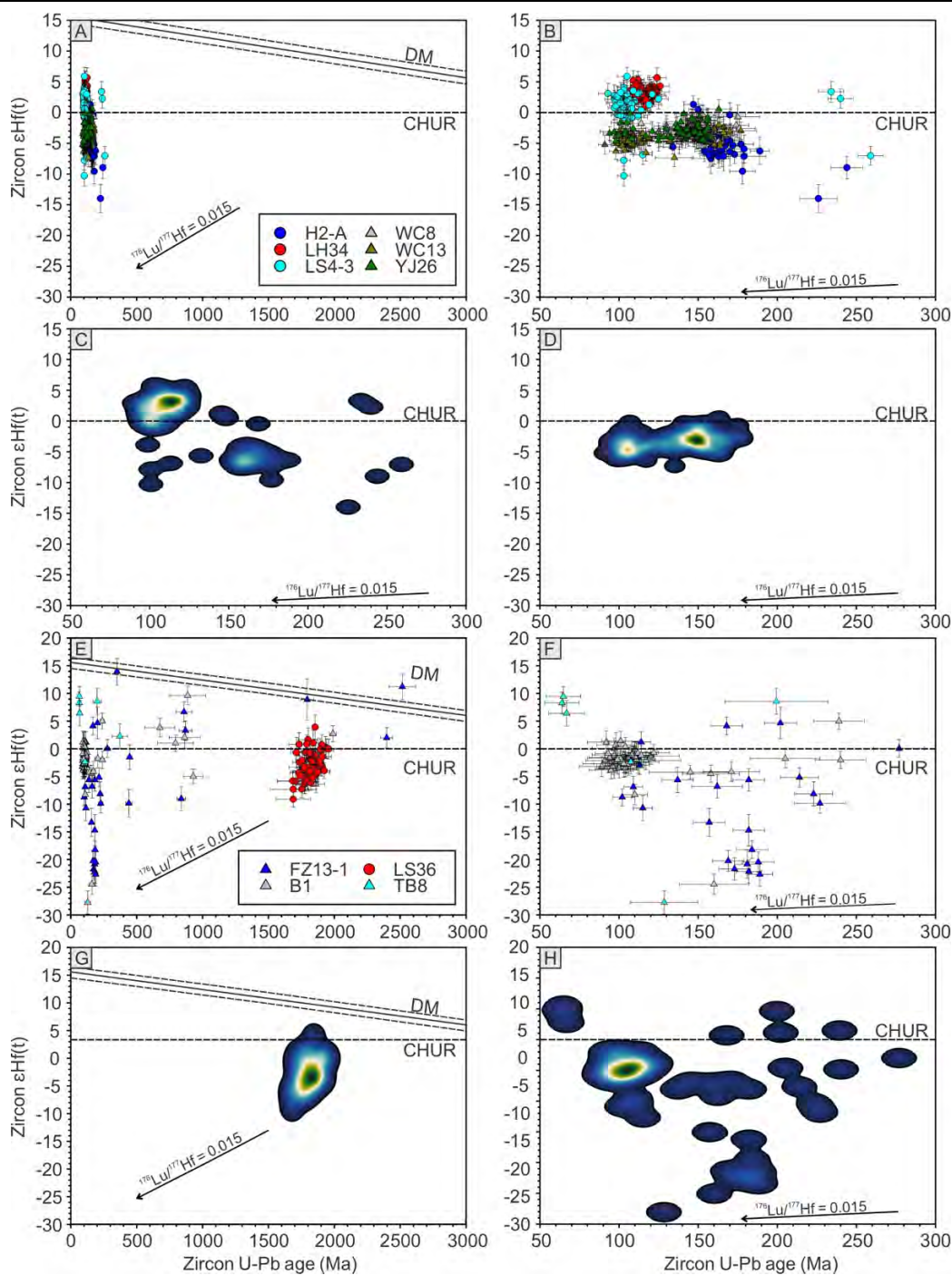


图 4.28 南海北部 (H2-A、LH34、LS4-3、WC8、WC13、YJ26) 及东海陆架盆地基底 (FZ13-1、B1、LS36、TB8) 钻井样品 (具体位置见图 4.13) 锆石 U-Pb 年龄 vs. $\epsilon\text{Hf}(t)$ 二元核密度分布

Fig. 4.28 Diagrams plotting zircon $\epsilon\text{Hf}(t)$ values vs. U-Pb ages of (A) drilling samples H2-A, LH34, L4-3, WC8, WC13 and YJ26 from South China Sea, and (E) samples FZ13-1, B1, LS36 and TB8 from East China Sea. $\epsilon\text{Hf}(t)$ values of enlarged age groups (0–300 Ma) are also shown in diagrams (B) and (F). Bivariate kernel density estimate plots of South China Sea igneous samples H2-A, LH34, LS4-3, and volcanoclastic or clastic samples WC8, WC13, YJ26 are shown in (C) and (D), separately; bivariate kernel density estimate plots of East China Sea gneiss sample LS36,

and clastic samples FZ13-1, B1, TB8 are shown in (G) and (H), separately.

同样, 样品 YJ26 大多数 $\epsilon\text{Hf}(t)$ 值为负值, 介于 -5.22 至 -0.13 之间, 其中只有一个略微为正 (+0.56)。相比之下, 样品 WC13 的 $\epsilon\text{Hf}(t)$ 值更偏负, 范围介于 -7.34 至 -0.21 之间 (图 4.28A 和 B)。然而, 来自东海陆架盆地基底的碎屑样品 Hf 同位素结果更加复杂和多变 (图 4.28E 和 F)。样品 FZ13-1 的 $\epsilon\text{Hf}(t)$ 值范围较大, 从 -22.68 至 13.94, 其中大多数为负值。有一个 $\epsilon\text{Hf}(t)$ 异常值 (+11.22) DM 线, 其锆石年龄为 2516 ± 50 Ma。样品 B1 分配模式类似, 其 $\epsilon\text{Hf}(t)$ 值变化范围在 -24.48 至 +9.63 之间。56 个 Hf 同位素分析结果中, 十一个 $\epsilon\text{Hf}(t)$ 值为正 (+0.08 至 +9.63), 其余均为负值。样品 TB8 只有七个具有谐和 U-Pb 年龄的 Hf 同位素结果, 其中五个 $\epsilon\text{Hf}(t)$ 值为正值 (+9.46 至 +2.27), 另外两个为负值, 包括一个极低值 (-27.76)。

花岗岩样品 H2-A 结晶年龄为 163.5 Ma, 其两阶段模式年龄 (T_{DM}^{C}) 范围在 904 Ma 至 1750 Ma 之间, 主要集中在约 1330 Ma 处 (图 4.29A)。然而, 样品 LH34 结晶年龄为 115.1 Ma, 模式年龄范围从 662 Ma 到 893 Ma, 显示出相对较年轻的年龄峰值, 约为 780 Ma (图 4.29A)。同样, 样品 LS4-3 结晶年龄为 103.3 Ma, 模式年龄在 635 Ma 至 1461 Ma 之间变化, 其中大多数集中在 800–900 Ma (图 4.29A)。碎屑岩样品 WC8 模式年龄处于 995–1217 Ma 的狭窄范围内, 与样品 YJ26 变化范围类似, 处于 945 Ma 至 1227 Ma 之间 (图 4.29A)。另一个碎屑岩样品 WC13 的模式年龄范围更窄, 介于 1073 Ma 至 1337 Ma 之间 (图 4.29B)。总体来看, 这三个样品的模式年龄大部分集中在约 950 Ma 至 1350 Ma 之间, 峰值集中在约 1130 Ma。

与南海北部相比, 来自东海陆架盆地基底的碎屑岩样品模式年龄分布特征更加复杂 (图 4.29C)。样品 FZ13-1 模式年龄范围较为宽广, 从 422 Ma 跨越至 2730 Ma, 其中大多数集中在约 1000–1500 Ma。样品 B1 的模式年龄特征类似, 其值在 790 Ma 至 2699 Ma 之间变化, 大多数集中在 1000–1100 Ma。同样, 样品 TB8 的模式年龄分散, 并在 416 Ma 至 2366 Ma 之间变化。特别注意的是, 具有古元古代结晶年龄 1835 Ma 的唯一片麻岩样品 LS36 表现为相对集中的模式年龄分布, 介于 2184 Ma 至 2695 Ma 之间, 其中大多数集中在 2500–2600 Ma 之间。

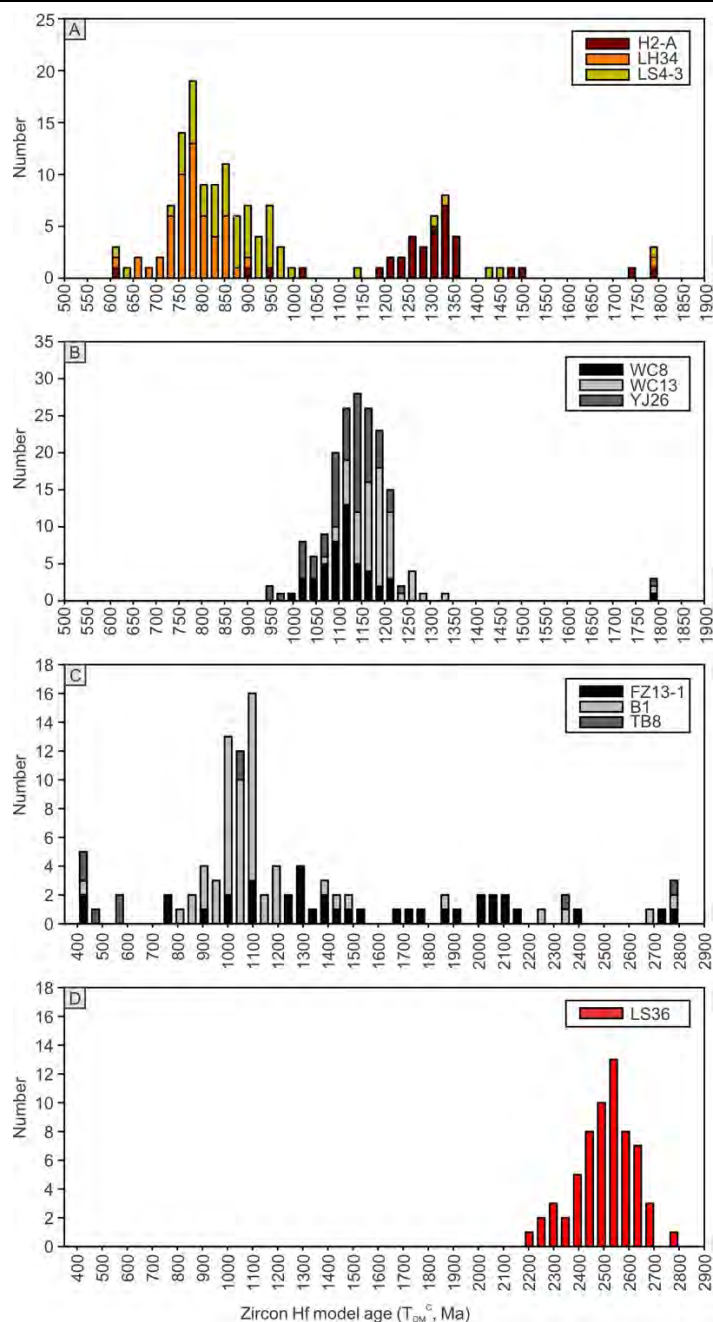


图 4.29 南海北部 (H2-A、LH34、LS4-3、WC8、WC13、YJ26) 及东海陆架盆地基底 (FZ13-1、B1、TB8、LS36) 钻井样品锆石两阶段模式年龄 (T_{DM}^C) 分布图

Fig. 4.29 Cumulative diagrams of zircon Hf model ages for South China Sea samples (A) H2-A, LH34, LS4-3; (B) WC8, WC13, YJ26; and (C) East China Sea samples FZ13-1, B1, TB8; (D) LS36.

4. 2. 4 讨论

1. 南海北部及东海陆架盆地基底变质凝灰岩、火山碎屑岩及沉积岩碎屑锆石年龄组成及物源指示意义

南海北部盆地基底的前新生代地层凝灰岩、火山碎屑岩以及其他变质碎屑

岩样品显示, 锆石 U-Pb 年龄谱系大都表现为单一的中生代峰值, 或表现以中生代峰为主、同时伴随更老年龄组分整体较宽广的谱系特征。部分样品年龄集中于大约 185 Ma 至约 120 Ma 之间 (图 4.20、4.21、4.22 和 4.24), 峰值年龄大约为 150–145 Ma: 例如 CC2-1 和 WC17 的碎屑锆石年龄聚集在大约 155 Ma 处, 而 KP1-1 和 KP1-2 则聚集在大约 145 Ma 附近。变质火山碎屑岩样品 CC2-2 位于 CC2-1 上方约 40 米处, 虽然显示多峰年龄组合模式, 但是该样品仍以明显的白垩系主峰 (集中于大约 150 Ma) 为特征。变质沉积岩样品 BD23-1、CC1-1 和 YJ36-1 都以集中在 150 Ma 的单一年龄峰为主 (范围在约 185 Ma 至约 120 Ma 之间)。与变质火山碎屑岩 CC2-2 类似, 上述钻井的较浅层样品 BD23-2、CC1-2 和 YJ36-2 也包含少量较老年龄的锆石组分含有较小的较老的锆石群体。它们主要表现为晚中生代年龄峰值 (大约 185–120 Ma)、保存相对良好的锆石晶形和地球化学特征上不成熟的岩石结构, 均指示原地或近源源区的影响。部分碎屑岩样品 U-Pb 年龄范围在 190 Ma 至 90 Ma 之间 (图 4.22), 例如 WC13 锆石年龄范围在大约 180–95 Ma 之间, 峰值年龄大约为 120 Ma。另外, 东海陆架盆地基底样品锆石年龄谱系也在 190–90 Ma 之间, 峰值年龄大约 115–120 Ma。值得注意的是, 井 FZ13 也表现为中生代主峰, 除包含一个大约集中在 118 Ma 的白垩年龄峰值, 还存在一个集中在 182 Ma 的下侏罗统次要峰值 (图 4.25)。需要强调的是, 东海陆架盆地基底碎屑岩钻井样品以及台湾露头样品的确曾发现下侏罗统碎屑锆石年龄组分。总体来看, 这些样品最年轻 U-Pb 年龄大多为 120–90 Ma, 其中 BD23-2 和 YJ36-2 最大沉积年龄约为 90–85 Ma。因此, 华南大陆边缘的原岩约在 145 Ma (或更晚) 开始沉积并逐渐延续至 120 Ma, 但极大可能在 85 Ma 左右结束大规模沉积, 这也是南海北部基底目前发现的最年轻岩浆岩年龄 (图 4.30B), 与东海地区发现的年轻岩浆岩年龄分布也一致 (图 4.30D)。

需要特别说明的是, 少数变质火山碎屑岩和变质沉积岩样品存在一定数量的较老锆石颗粒。一些古元古代 (约 1900–1800 Ma) 和太古代碎屑锆石仅在 WZ12、CC2-2 和 CC1-2 中出现, 表明在沉积南海北部基底地层时, 可能曾局部暴露华夏地块古元古代结晶基底^[235–237]。早古生代和新–中元古代锆石组分相对含量更高可能指示多个潜在内陆源区 1) 中元古代晚期–新元古代早期将扬子地块和华夏地块分隔开来的四堡造山带 (Sibao Orogen), 即约 960–890 Ma 的双溪坞岩浆弧和其他约 1000–890 Ma 的岩体^[238]和约 850–750 Ma 的大陆内部热点和/或裂谷岩浆^[239]以及 2) 早古生代的武夷-云开造山带^[240, 241]。根据同一钻孔中不同深度样品 (即 CC2、BD23、CC1 和 YJ36 井) 的物源变化, 本论文发现在同一地区沉积的白垩系地层中, 从原岩中剥蚀而来的元古代至早古生代基底物质随时间增加, 可能反映了晚中生代时期古老结晶基底暴露程度逐渐增加。

第 4 章 南海北部基底属性及其构造指示意义

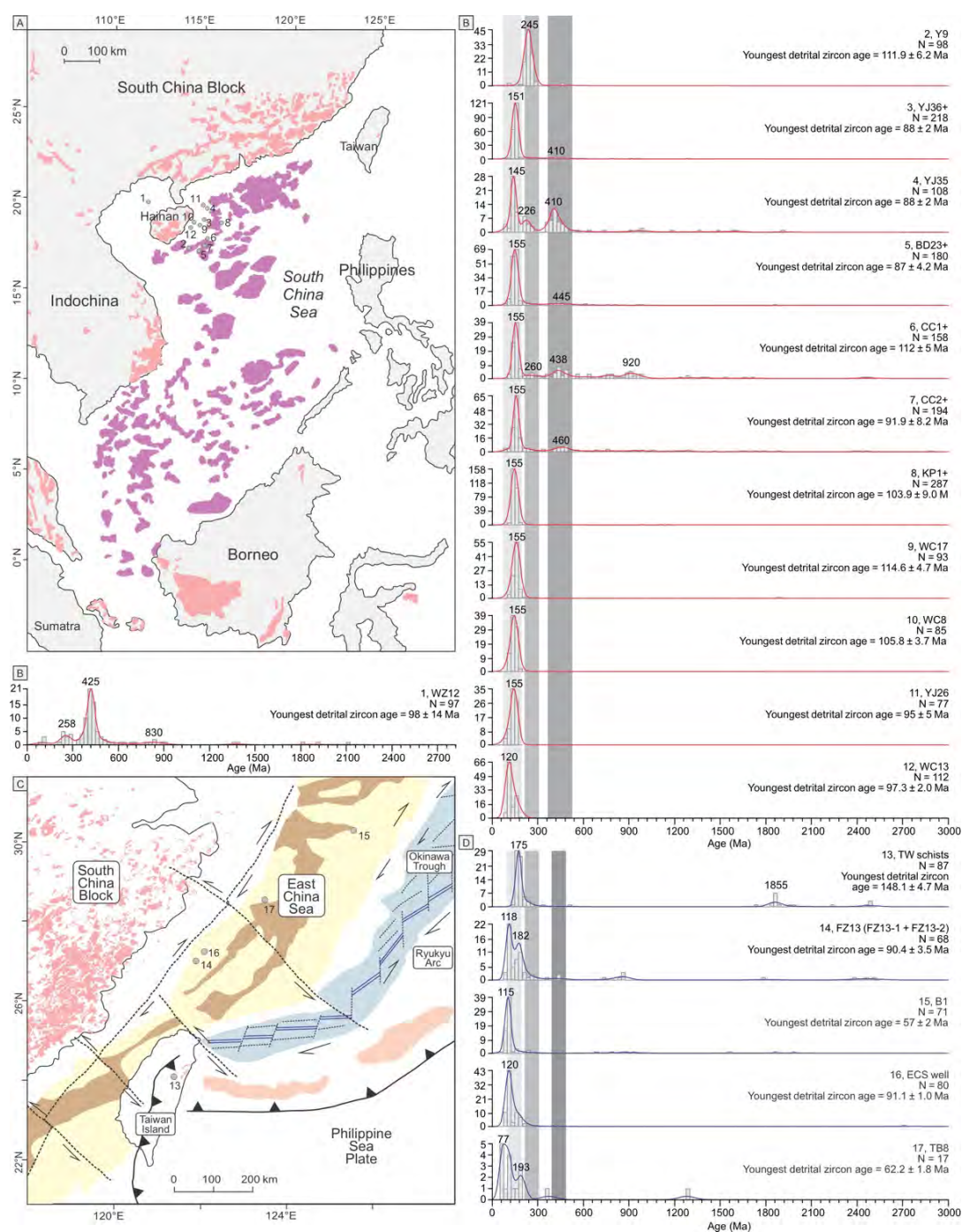


图 4.30A) 南海盆地及陆上岩浆记录分布图; B) 南海北部中生代基底钻井碎屑锆石 U-Pb 年龄谱系综合示意图 (钻井位置见图 A); C) 东海陆架盆地及周围构造单元示意图; D) 东海中生代基底钻井碎屑锆石 U-Pb 年龄谱系综合示意图 (钻井位置见图 C)

Fig. 4.30 (A) Simplified map showing distribution of onshore and offshore Mesozoic igneous rocks in the South China Sea and its surrounding areas based on compilation of published magmatic records and unpublished gravity-magnetic-seismic interpretation from commercial gas and petroleum corporation. U-Pb age spectra and youngest detrital zircon ages are shown in (B) and (D). (C) Simplified map showing onshore Mesozoic magmatic records and offshore tectonic divisions in the East China Sea area. Numbers of (A) and (C) denote boreholes in this

study and previous work, and their corresponding U-Pb ages are shown in (B) and (D). N = numbers of concordant ages in our compilation.

2. 锆石微量元素变化特征及构造环境判别

尽管本研究岩浆岩样品中只有少部分锆石呈现出平坦的轻稀土配分模式，表明它们可能受热液活动影响^[242]，但其中绝大多数显示出明显的 Ce 正异常和 Eu 负异常（图 4.26 和 4.27），进一步证实了这些锆石为岩浆锆石来源。前人提出，锆石微量元素可用于反映母岩岩浆的地球化学特征^[70]，并且它们的比值可以用来确定构造亲缘关系^[243]。根据火成岩和斜长角闪片麻岩样品的锆石微量元素数据，本研究得到 U/Yb vs. Y、U/Yb vs. Hf 和 $\log_{10}(U/Yb)$ vs. $\log_{10}(Nb/Yb)$ 的构造判别图解（图 4.31）。图 4.31A 和 B 中的虚线表示陆地和海洋锆石来源的分界线。

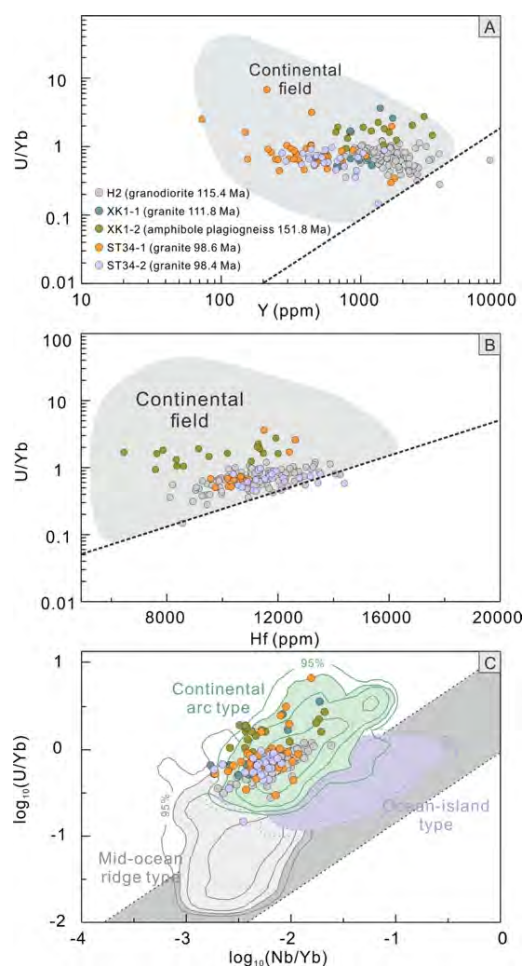


图 4.31 南海北部钻井样品 ST34-1、ST34-1、XK1-1、XK1-2 及 H2 锆石微量元素构造判别图解：A) U/Yb vs. Y; B) U/Yb vs. Hf; C) $\log_{10}(U/Yb)$ vs. $\log_{10}(Nb/Yb)$

Fig. 4.31 Tectonic discrimination diagrams based on zircon trace elements. A) U/Yb vs. Y; B) U/Yb vs. Hf; C) $\log_{10}(U/Yb)$ vs. $\log_{10}(Nb/Yb)$. The lower boundary of the continental field is plotted by the dashed line on diagrams A and B (Grimes et al., 2007). In diagram C, the gray shaded fields are overlapping two-dimensional kernel density distributions for compiled datasets

of “mid-ocean ridge-type”, “ocean island-type”, and “continental arc-type” zircons. The contours represent the density distribution of data from Grimes et al. (2015).

图 4.31 和 4.32 显示，本研究几乎所有数据都位于“陆壳岩石类型”区域内，较高 U/Yb 比值（图 4.31 平均为 0.87；4.32 平均为 0.74）也与整体陆壳的全岩 U/Yb 比值相一致（0.7^[211]），并非直接来自现代大洋中脊玄武岩源区^[203]。

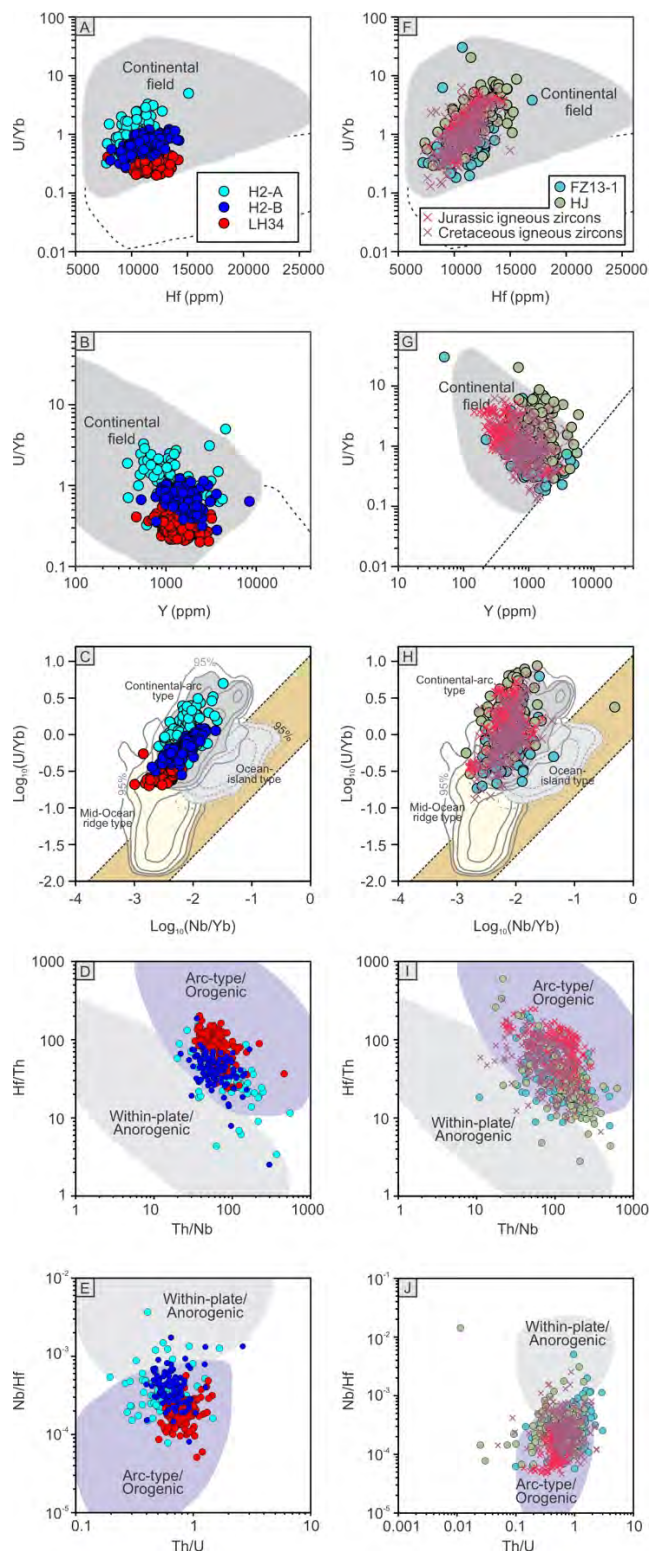


图 4.32 南海北部钻井样品 A-E) H2-A、H2-B、LH34 及 D-J) 东海钻井样品 FZ13-1、HJ 锆石微量元素 U/Yb vs. Y, U/Yb vs. Hf, $\log_{10}(\text{U}/\text{Yb})$ vs. $\log_{10}(\text{Nb}/\text{Yb})$, Hf/Th vs. Th/Nb 以及 Nb/Hf vs. Th/U 构造判别图解

Fig. 4.32 Tectonic discrimination diagrams based on zircon trace elemental contents or ratios. (A) U/Yb vs. Hf; (B) U/Yb vs. Y; (C) $\log_{10}(\text{U}/\text{Yb})$ vs. $\log_{10}(\text{Nb}/\text{Yb})$; (D) Hf/Th vs. Th/Nb and (E) Nb/Hf vs. Th/U of samples from South China Sea basin basement. (F-J) show tectonic discrimination for samples from East China Sea basin basement. The lower boundary of continental field is denoted by dashed line in panels A, B, F and G (Grimes et al., 2007). In panels C and H, the pale-yellow shades are overlapping 2D kernel density distributions for compiled data of “continental arc”, “mid-ocean ridge” and “ocean island” types of zircons. Contours indicate the density distribution of data from Grimes et al. (2015). In panels D, E, I and J, two separated fields of arc-related/orogenic and within-plate/anorogenic settings are after Hawkesworth and Kemp (2006) and Yang et al. (2012).

图 4.31C 和 4.32C 进一步显示，本研究岩浆岩的锆石通常位于大陆弧范围内；不过 4.32C 可见少量锆石处于 MORB-type 范围，说明位于更南端的 LH34 钻孔可能更易受海洋锆石源区的影响，同时该地区可能也代表了从大陆弧向洋壳逐渐过渡的区域。Hf/Th vs. Th/Nb 和 Nb/Hf vs. Th/U 判别图解指示（图 4.32 和图 4.33），这些锆石主要分布在大陆弧-造山带范围内^[244]；尽管来自 H2 钻孔的部分锆石位于非造山带构造判别区域内，可能代表来自板内环境的继承性锆石，但绝大多数还是来自大陆弧环境（样品 H2-A：163.5±2.1 Ma；样品 H2-B：115.4±0.7 Ma）。

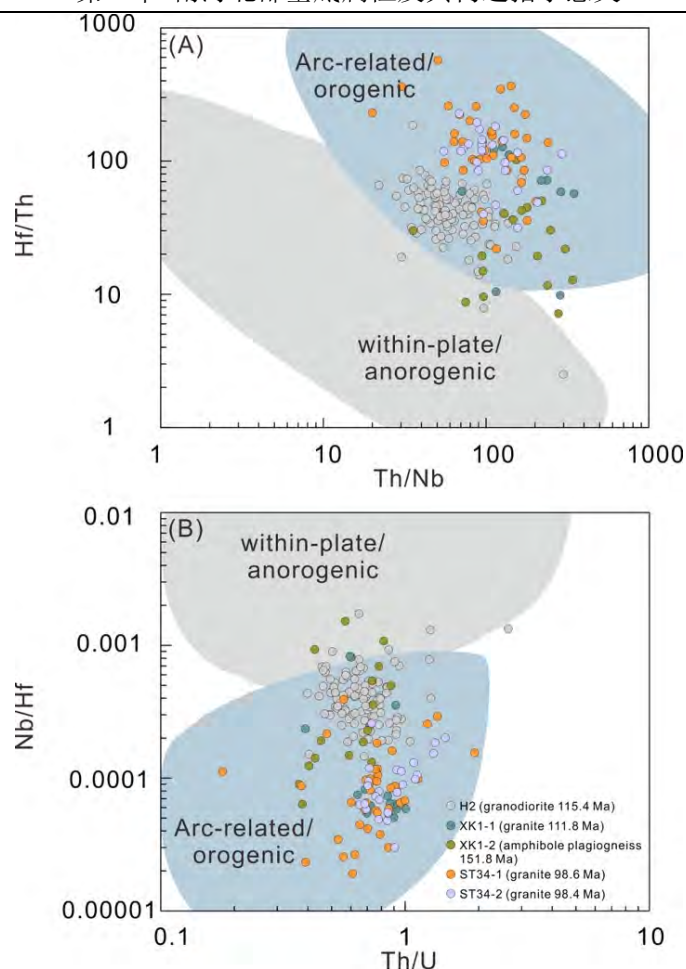


图 4.33 南海北部钻井样品 ST34-1、ST34-1、XK1-1、XK1-2 及 H2 锆石微量元素构造判别图解：A) Hf/Th vs. Th/Nb; B) Nb/Hf vs. Th/U

Fig. 4.33 Tectonic discrimination diagrams based on zircon trace elements. (A) Hf/Th vs. Th/Nb; (B) Nb/Hf vs. Th/U. The distinctly separated fields of the arc-related/orogenic environment and within-plate/anorogenic environment are from Hawkesworth and Kemp (2006) and Yang et al. (2012).

本研究还取得了东海陆架盆地基底样品的锆石微量元素数据，尽管来自碎屑锆石，但极大可能物源来自原地或近源区域，其微量元素含量与比值特征与前人有关侏罗–白垩岩浆锆石数据结果基本一致^[139]（图 4.32G 和 J），进一步证实样品 FZ13-1 和 HJ 的碎屑岩样品可能源自原位或附近造山带及岩浆弧^[245]。另外，岩浆和碎屑锆石的平均 U/Yb 比值分别为 1.5 和 2，高于整体陆壳的全岩值 0.7。很大程度上表明，与南海地区相比，大多数东海锆石由演化程度更深的岩浆组分而来。同样，在 Hf/Th vs. Th/Nb 和 Nb/Hf vs. Th/U 判别图解中，一小部分岩浆和碎屑锆石组分也处于非造山带或板内领域内。但大多数仍然显示与弧环境密切相关（图 4.32I 和 J）。

研究者在南海东北部地区曾发现 198–195 Ma 的花岗岩和闪长岩，反映该地区早侏罗世时期发育的大陆弧-造山岩浆活动^[101]。台湾南部和浙江东部的 I-型花

岗岩露头形成年龄大约在 190–180 Ma 和约 90 Ma^[102, 230]。本研究中, 南海北部中-西部地区 ST34、XK1 和 H2 钻孔以及前人研究的东部花岗岩^[101, 131, 154]共同说明南海北部曾在侏罗纪至晚白垩期间存在大陆弧岩浆岩带, 从约 195 Ma 活跃至至少约 90 Ma, 与华南大陆东南部陆上地区^[97, 99, 102]以及台湾岛和海南岛出露的花岗岩侵入体^[102, 230]在同一个构造环境控制之下。另外, 部分钻孔, 例如 Y9、YJ35、CC1 (图 4.30B) 还存在更明显的印支期峰值 (大约 250 Ma 至 230 Ma), 可能与大约 270 Ma (或更晚) 发生在海南岛的大陆弧型岩浆活动有关^[93], 该期岩浆活动在三叠纪期间持续活跃^[117], 并可能延续至晚白垩世^[117, 231, 234]。相比之下, 印支期锆石在东海地区的记录相对较少 (图 4.30D), 可能表明三叠纪大陆弧型岩浆活动更局限在南海北部的西侧地区, 华南陆缘的广大地区此时更可能受到平板俯冲的影响。

3. 锆石 Lu-Hf 同位素体系特征及岩浆来源

锆石 Hf 同位素组成是追溯岩浆来源和地壳-地幔相互作用的关键指标。本研究取得南海北部地区大陆弧属性的花岗岩岩体的 $\epsilon\text{Hf}(t)$ 值, 变化范围从 -14 到 +5.86。样品 H2-A (163.5±2.1 Ma) 的 $\epsilon\text{Hf}(t)$ 值在安第斯弧形成的早期阶段, 大部分锆石表现为负值, 介于 -14 到 -0.35 之间 (图 4.28B 和 C), 可能源自古老再循环陆壳的熔融作用。这些 $\epsilon\text{Hf}(t)$ 值也与同时期晚中生代分布在中国东南沿海地区的花岗岩的 $\epsilon\text{Hf}(t)$ 范围内。样品 H2-A 锆石的两阶段 Hf 模式年龄 (约 1.55–1.45 Ga) 与华夏地块结晶基底的陆壳物质具有密切联系 (图 4.29A)。对于相对年轻的花岗岩样品 (LH34 和 LS4-3), $\epsilon\text{Hf}(t)$ 值明显更趋向正值方向, 约为 +0.05 至 +5.9 (图 4.28B 和 C)。当然, 这些来源于幼年岩浆成分的锆石也有可能在整个构造环境为火山弧、局部表现为伸展构造的背景下形成的。火山弧中发育的伸展构造可能由于板块汇聚速度减小引起的^[246]。值得注意的是, 样品 LS4-3 的部分锆石具有负 $\epsilon\text{Hf}(t)$ 值 (-10.3–-0.6), 可能与地幔和岩石圈地幔来源的原始组分有关, 在一定深度与俯冲洋壳发生同化混染作用。另外, 研究表明, 原岩来自岩浆弧环境的碎屑锆石 U-Pb 年龄模式与原位岩浆岩年龄特征相似, 而本研究取得的凝灰岩和火山碎屑岩样品 Hf 同位素结果也为追溯活动陆缘岩浆弧的发育演化提供了更可靠的证据。南海北部碎屑锆石 $\epsilon\text{Hf}(t)$ 值在岩浆弧发育过程中, 整体趋势也是更加进化的特点 (-7.34 – -0.13) (图 4.28B 和 D), 可能由于在俯冲过程中, 古老陆壳遭受持续熔融和再循环作用。换句话说, 大陆边缘主要经历了持续的地壳挤压和增厚过程。

东海基底古元古代 (1835±11Ma) 片麻岩样品 LS36 锆石 Hf 同位素结果介于 -9.1 到 +3.9 之间 (图 4.28E 和 G), Hf 模式年龄集中大约 2.55 Ga (图 4.29D), 可能代表古老再循环地壳熔体与幼年地幔物质的混合作用。也有学者对东海西部具有类似结晶年龄的片麻岩样品 (约 1.85 Ga) 开展研究, $\epsilon\text{Hf}(t)$ 范围相对较窄 (-6–2.6), 认为完全来源于古老再循环、演化程度较高的陆壳成分^[139]。本

研究取得的东海古元古代碎屑锆石（约 2.55–1.8 Ga） $\epsilon\text{Hf}(t)$ 值显示出更大范围，从-13.4 到+7.2 不等。相比之下，华夏地块基底的古元古代片麻岩和花岗岩体（如巴都复合岩体）的 $\epsilon\text{Hf}(t)$ 值也呈现出变化范围较大的特征，主要在-14.4 到+8.9 之间，并且 Hf 模式年龄主要分布在 3.5 到 2.1 Ga 之间^[247]。这种来自华夏地壳原岩的演化程度更高的 Hf 同位素特征（古元古代时期华夏地块在南海和东海地区可能分布更广泛）在一定程度上决定了东海晚中生代岩浆的起源和属性。

前人研究表明，200–183 Ma 期间东海西部弧花岗岩 $\epsilon\text{Hf}(t)$ 为正值（+0.3–+6.7），主要由幔源熔体穿过厚度较薄的岩石圈而成^[139]。随后，180–155 Ma 期间随着弧岩浆活动的进行， $\epsilon\text{Hf}(t)$ 值呈现极低的特点（-26.7–14）。在 128–120 Ma 期间转变为相对较高的 $\epsilon\text{Hf}(t)$ 值，范围是-12.1–+1.7。先前模型表明，华夏地块古元古代基底经历了强烈地壳部分熔融和板块俯冲过程，导致早侏罗世末期至晚侏罗世岩浆弧的规模增大，而在早白垩期间，弧根被移除，导致地壳和幔源熔体之间的混合程度增加。晚白垩期间，来自华南沿海弧后区域的酸性岩 $\epsilon\text{Hf}(t)$ 值表现出略微升高的趋势（-10–+5），可能表明受亏损地幔的大规模改造。然而，本研究晚中生代东海基底碎屑锆石具有更广泛的 $\epsilon\text{Hf}(t)$ 值范围，大多数在-24.5 至+5 之间，与南海基底样品特征相反（图 4.28E-F 和 4.28H）。具有较大结晶年龄（> 300 Ma）的锆石以幼年岩浆来源为主，其 $\epsilon\text{Hf}(t)$ 范围从+0.1 到+13.9（图 4.28E）。而几乎所有相对较年轻的锆石（约 190–150 Ma），都表现为负 $\epsilon\text{Hf}(t)$ ，只存在一个异常值（图 4.28F）。这种 $\epsilon\text{Hf}(t)$ 记录特征表明，华南陆缘岩浆弧形成以来，地壳经历了强烈而持续的再循环过程。尽管在年轻锆石中发现了更高的 $\epsilon\text{Hf}(t)$ 结果，绝大多数负值表面此时初始地幔部分熔融作用可能仍相当有限（4.28H）。晚白垩期间，中国东南沿海地区和东海基底均存在 I 型和 A 型岩浆记录，可能由于俯冲板片或岩浆弧后撤导致。样品 TB8 的 $\epsilon\text{Hf}(t)$ 正值表明此时可能以伸展环境为主，幼年岩浆来源丰富。还应注意的是，南海和东海基底碎屑岩样品的两阶段 Hf 模式年龄大都集中在 1.2 Ga 至 1.0 Ga 之间（图 4.29B-C）。

4. 华南陆缘中生代构造发育演化过程：安第斯型大陆岩浆弧的形成、发育与终止

本研究取得的南海北部与东海陆架盆地基底样品为中生代华南大陆活动陆缘和安第斯弧的时空展布范围及发育演化规律提供了新认识。如图 4.34 所示，本论文在 Li and Li (2007)和 Li et al. (2012b)模型的基础上，认为安第斯型活动大陆边缘始于大约 280 Ma，并沿华南大陆东南缘分布（图 4.34D）。靠近海南东南部的样品 Y9 显示 270–205 Ma 的锆石年龄组分，也指示附近存在同时期的岩浆弧。类似的，钻井 YJ35、CC1、FZ13 也包含 270–205 Ma 的主要或次要年龄峰值。根据 Li and Li (2007)模型，该安第斯型活动大陆边缘在三叠纪时期（大约 250–200 Ma）很可能经历了平板俯冲，岩浆活动从沿海地区逐渐向克拉通内陆地区

推进, 使得香港到上海之间长达 1000 公里的展布范围内无大规模岩浆活动发生 (图 4.34D)。本研究取得的部分碎屑岩样品, 如 CC2-2、CC1-1 和 YJ36-2 在大约 200 Ma 前后明显缺失相应的锆石年龄。样品 BD23-2 和 CC1-2 中现象相对不明显, 可能与海南岛持续发生的岩浆活动有关, 而海南岛及其邻区位于平板俯冲的影响范围以外。

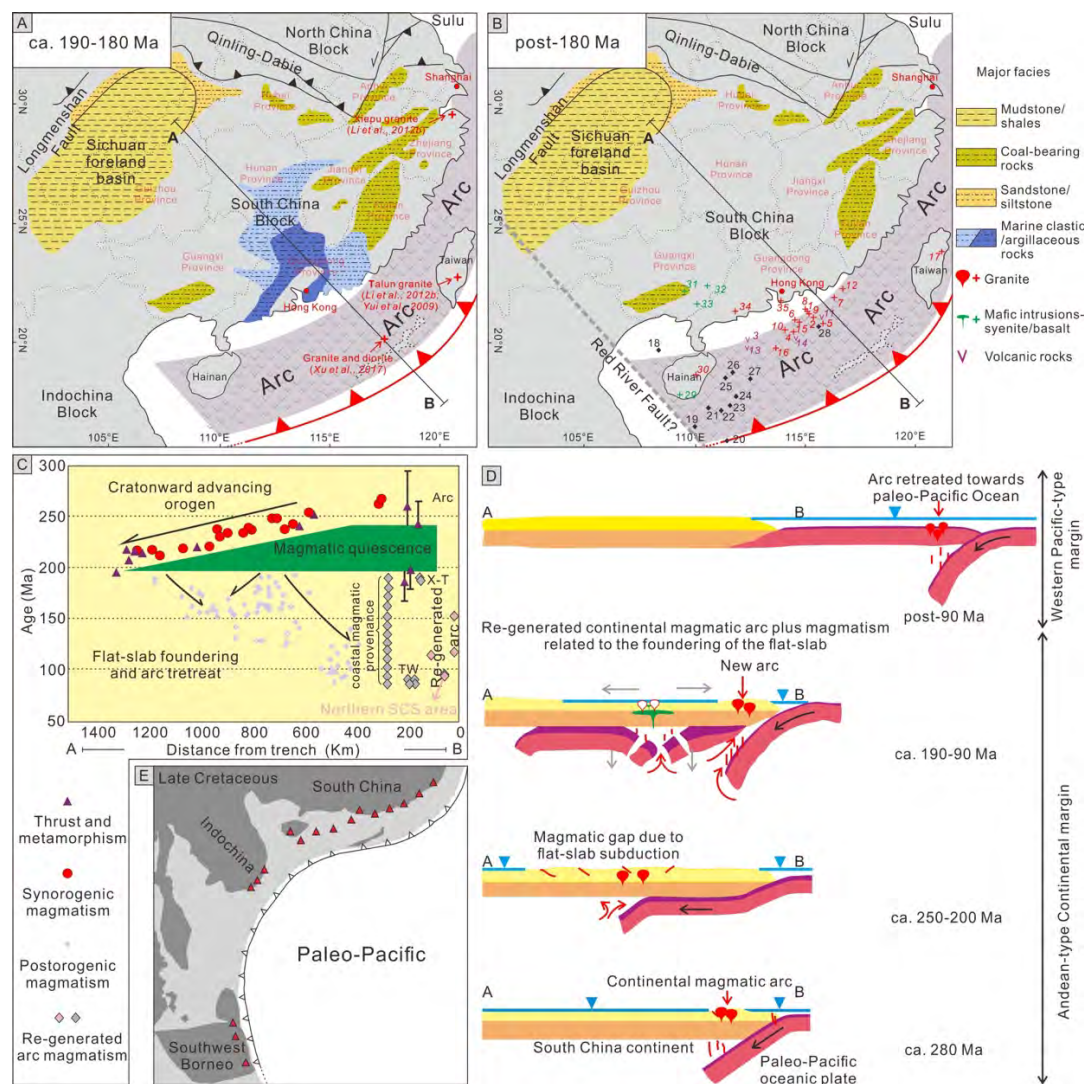


图 4.34A) 190-180 Ma 及 B) < 180 Ma 华南大陆及周缘地区区域构造示意图; C) 华南大陆及周缘地区岩浆记录时空分布规律; D) 华南大陆边缘构造属性转变规律 (A-B 剖面位置见图 A); E) 晚白垩纪欧亚大陆东南缘安第斯弧空间分布示意图

Fig. 4.34 A) Early Jurassic (ca. 190–180 Ma) paleogeography of the South China Block with a regenerated magmatic arc along the continental margin (after Li et al., 2012b). B) Post-180 Ma paleogeography of the South China Block (modified after Li et al., 2012b). Numbers in (B) mark the post-180 Ma magmatism within the South China Sea basin region, interpreted to represent the regenerated magmatic arc: 1–16 = granitoids and other igneous rocks in the South China Sea basement from Qiu et al. (1996) and Li et al. (1999); 17 = 89–87 Ma granitoids from Tailuko valley, Taiwan Island, from Li et al. (2012b); 18–28 = granites, metatuffs, metavolcaniclastic

rocks and metasedimentary samples in this study; 29 = basalt-andesite-rhyolite volcanic rocks on Hainan Island from Zhou et al. (2015); 30 = granodiorites and biotite granites on Hainan Island from Wang et al. (2012); 31–35 = mafic intrusions and granites within southern Guangxi and Guangdong Province from Li and Li (2007), and biotite granites therein. C) Time-space plot of magmatic rocks and thrust/metamorphic ages along cross-section A-B in A) and B), modified after Li and Li (2007) and Li et al. (2012b). “Coastal magmatic provenance” plotted as gray rhombuses = near-source provenance inferred from metatuff, volcanoclastic and metasedimentary rocks in this study and Tananao schist data from Li et al. (2012b). X-T = Xiepu and Talun granites that mark the onset of this regenerated arc (Yui et al., 2009; Li et al., 2012b). TW = ca. 89 Ma granites in eastern Taiwan Island from Li et al. (2012b). “Northern SCS basin” plotted as pink rhombuses = granites and granodiorites in the northern South China Sea basement. D) A cartoon illustrating the transformation from an active Andean-type continental margin to a passive Western Pacific-type continental margin, modified after Li et al. (2012b). E) A sketch of a reconstructed Late Cretaceous Andean-type arc along the South China and Sundaland margin, modified after Hall (2012).

平板俯冲阶段结束后，沿大陆边缘分布的弧岩浆活动似乎在大约 190 Ma 时重新启动，可能代表大陆边缘正常俯冲类型的恢复（图 4.34A-C）。本研究中，南海北部和东海陆架盆地基底小于 200 Ma 的碎屑锆石年龄组分占主要部分。这些样品中年龄为 180 Ma 至 120 Ma 的锆石持续出现，数量较多，以及表现几个突出的年龄峰值，集中于大约 150 Ma、120 Ma 等；但在大约 90 Ma 之后明显减少，说明至少从 180 Ma 至 90 Ma 之间，南海北部岩浆活动几乎持续进行，但在 120 Ma 后强度大大减弱。这种解释与台湾白垩碎屑岩的结果一致，表明在此期间大陆弧岩浆活动持续存在。

如图 4.34A-B 所示，在 190–90 Ma 大陆岩浆弧从海南岛经由南海北部向北延伸至台湾东侧。这一活跃在 90 Ma 以前的安第斯型板块边界的空间展布范围至少延伸至朝鲜半岛，以及向西南方向延伸的中南半岛和婆罗洲（图 4.34E）。

尽管南海北部基底很少 85 Ma 以后形成的侵入岩（本研究部分样品碎屑锆石显示存在 90–85 Ma 的年龄组分），但岩浆弧极大可能在 90 Ma 左右停止活动，或在 90 Ma 后活动急剧减弱。在 Li et al. (2012b) 模型的基础上，我们认为安第斯弧在 90 Ma 后向洋壳方向后撤（图 4.34D），标志着安第斯型板块边界结束；基于东亚地区和澳大利亚东部资料的整合，西太平洋型板块边界开始发育。此外，元素地球化学特征的变化，即从火山弧属性转变为板内环境（或火山弧与板内特征共存），也表明进入碰撞后环境，并非仅仅由洋壳俯冲后撤导致。

5. 90–70 Ma 南海北部基底与东海陆架盆地基底是否属于相同的构造环境？

台湾东缘发育了大约 90 Ma 的大陆弧岩浆岩和变质岩，其中花岗岩锆石 U-Pb 年龄集中在 90–85 Ma 之间，另外还发现一个相对较年轻的 79 Ma 的蓝闪片角闪岩，代表古太平洋向东亚大陆边缘俯冲并引发一系列构造热事件^[248]。尽管在南海北部基底中发现一些年龄小于 90 Ma 的侵入岩，但数量很少，大多数形成

于 90–87 Ma (图 4.30)。相比之下, 中国东南浙江-福建沿海地区发育一系列上白垩统岩浆岩 (> 86 Ma), 值得注意的是, 台湾变质带年龄 (86 Ma) 与琉球-石垣群岛和日本龙门-三泊川变质带年龄 (90 Ma) 基本一致^[141]。因此, 晚白垩世日本群岛和华南大陆东南缘可能主要发育一条沿古太平洋板块俯冲带延伸的连续岩浆弧。随后, 晚白垩世琉球和日本岛弧从东亚大陆分离, 向东漂移, 直至达到现今的位置^[141]。

研究表明, 古太平洋板块起初向北北西方向以平均 60-70 毫米/年的速率俯冲, 其俯冲角度逐渐从 10°增加至 80°。俯冲板块角度的增大和随后古太平洋板块回撤可能引发了上地幔的强烈上涌, 导致了陆壳的剧烈伸展、减薄和破裂。中国东南沿海地区大存在约 100–70 Ma 的 A 型花岗岩, 这些年龄与本研究东海基底碎屑岩样品中出现的少数上白垩统锆石一致 (图 4.30D)。Suo et al. (2014) 指出, 东海陆架盆地新生代岩浆岩年龄从西向东逐渐变年轻, 似乎在某种程度上继承了晚中生代构造运动东向迁移的构造模式^[249]。本研究中, 样品 TB8 显示明显的早新生代峰值 (约 70–65 Ma) (图 4.30D), 该年龄的碎屑锆石 $\epsilon\text{Hf}(t)$ 值大多为 +2.3 到 +9.5 之间的正值, 恰好可能是由于古太平洋板块一定程度后撤, 从相邻的走滑盆地输送而来或是来自该时期发育在华南陆缘的零星岩浆活动。

4.2.5 初步结论

本研究根据南海北部和东海陆架盆地基底钻井样品的 U-Pb 年代学、锆石元素地球化学和 Lu-Hf 同位素化学结果, 以及凝灰岩、火山碎屑岩和变质沉积岩的物源分析结果, 综合认为华南陆缘在白垩纪期间大约 145–140 Ma 至 85 Ma 广泛发育沉积地层; 尽管少数样品含有元古代和古生代碎屑锆石, 可能反映邻近华南大陆结晶基底的物质贡献。值得注意的是, 古老华夏地块结晶基底在古元古代可能具有更广泛的分布范围, 与其现在零星出露的分布特征形成对比, 正如本论文东海地区得到的约 1.84 Ga 片麻岩钻孔样品所示, 其锆石 $\epsilon\text{Hf}(t)$ 值变化范围从 -9.1 到 +3.9。虽然仍需进一步证实, 但可能一定程度上反映东海地区中-上侏罗统火成岩的岩浆来源和属性。大多数样品主要包含 190–90 Ma (主要在 180 Ma 至 120 Ma 之间的范围) 的锆石, 可见多个中生代年龄组分, 峰值年龄包括 175 Ma、155 Ma、150 Ma、145 Ma、120 Ma 等。锆石晶型相对完整且地球化学属性不成熟, 未经历远距离搬运, 表明了沿华南大陆海岸区域存在原地或相邻的岩浆岩源区。

变质沉积地层还受到花岗岩岩体的侵入, 锆石 U-Pb 年龄分别为 98.4±1.7 Ma、98.6±2.1 Ma、103.3±1.1 Ma、111.8±3.3 Ma、115.4±0.7 Ma、115.1±0.9 Ma 和 163.5±2.1 Ma。地球化学数据表明它们为大陆弧岩浆岩。南海样品 $\epsilon\text{Hf}(t)$ 值介于 -14 到 +5.9 之间, 东海样品 $\epsilon\text{Hf}(t)$ 值变化范围较大, 介于 -24.5 到 +13.9 之间。结合先前发现的东南沿海、海南和台湾岛 I 型花岗岩, 本论文研究结果证实了在 190 Ma 至 90 Ma 期间沿现今华南大陆边缘存在大型安第斯大陆岩浆弧。物源分析结

果表明, 此大陆弧在大约 280 Ma 之后开始发育, 约 250–200 Ma 期间进入平板俯冲过程; 大陆弧岩浆作用似乎在 90 Ma 之后强度迅速减弱并逐渐停止, 仅在南海东北部地区和东海局部地区发现年龄为 85–80 Ma 的岩浆岩和相应的碎屑锆石组分。本研究解释为俯冲带向洋壳方向跳跃, 并开始向如今西太平洋型板块边缘转变, 在经历大规模剧烈的裂谷作用之前, 只存在零星分散的岩浆活动 (70–60 Ma)。

4.3 海南岛前寒武基底组成及对超大陆循环的指示意义: 来自南海西部基底钻井 Y1 的新启示

如本章第 4.1 节所述, 位于海南岛西南部的盆地基底钻井 Y1 显示该地区并非发育中生代岩浆岩或沉积岩。为揭示中元古代海南岛基底构造属性, 并探讨其在超大陆循环中的古地理指示意义, 本研究对钻孔 Y1 的两个变质火成岩样品开展锆石 U-Pb 定年、锆石微量元素地球化学和 Lu-Hf 同位素分析。样品来自中国海洋石油总公司开展的油气勘探钻井, 钻孔穿过厚层的新生代莺歌海盆地 (主要勘探目标) 之下的不整合面。

4.3.1 镜下薄片观察及锆石 U-Pb 定年结果

样品 Y1_1 和 Y1_2 为中-细粒变质黑云母花岗岩, 来自南海西部基底钻孔 (图 4.35A, B)。镜下岩石薄片观察结果显示, 样品均具有典型的花岗结构, 主要由正长石、石英及少量斜长石及黑云母组成, 长石发生发生高岭土化、碳酸盐化和钠黝帘石化, 黑云母发生绿泥石化, 可见绿泥石、白云母及石英呈定向排列, 显示岩石遭受一定程度的变质作用 (图 4.36D 和 H)。

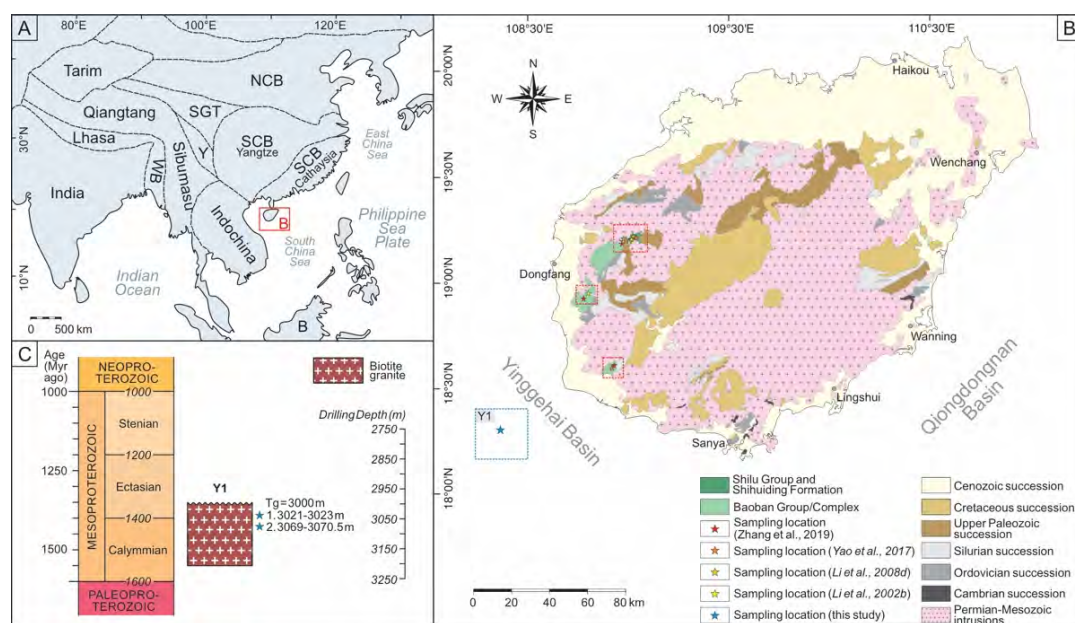


图 4.35A) 亚洲地区主要构造单元分布示意图; B) 海南岛岩性分布图与 C) 本研究钻井样品岩性柱状图

Fig. 4.35 (A) Present-day geographic sketch of major continental blocks or terranes of East Asia (modified after Metcalfe (1996)), in which: NCB – North China Block, SCB – South China Block (including Hainan Island which is enlarged in the geological map of Fig. 1B), SGT – Songpan-Garze Terrane, Y – Yidun Arc, WB – West Burma, B – Borneo. (B) Simplified geological map of Hainan Island showing Mesoproterozoic crystalline basement rocks and Phanerozoic rocks (modified from GDBGMR (1988) and Yao et al. (2017)). Borehole Y1 drilled within Yinggehai Basin (western South China Sea, off the southwest coast of Hainan Island) of this study and published outcrop samples from Li et al. (2002b, 2008b), Yao et al. (2017) and Zhang et al. (2019) are shown in the map. (C) Stratigraphic column of borehole analyzed in this study; depth of the South China Sea Cenozoic basement (Tg) is 3000 m; two drilling samples are shown by blue filled stars (refer to Table 1 for sampling and stratigraphic details, lithological features, ages and analytical methods).

两个钻井样品共得到 227 个锆石年龄, 大多数锆石晶体发育核-边结构, 指示岩浆锆石来源 (图 4.36C 和 G)。样品 Y1_1 锆石的 Th 和 U 含量分别在 51 ppm 至 638 ppm 之间, 151 ppm 至 4232 ppm 之间, Th/U 比值主要在 0.11 和 1.04 之间 (图 4.37B)。只有一个锆石 Th/U 值低于 0.1, 且谐和年龄为 1393 ± 22 Ma; 另外五个具有不谐和年龄的锆石 Th/U 值也低于 0.1, 可能由于铅丢失造成的。样品 Y1_2 的 Th/U 比值主要分布在 0.11 到 0.67 之间, Th 和 U 含量分别为 25–372 ppm 及 191–3362 ppm。

样品 Y1_1 共得到 132 个谐和年龄, 年龄范围在 1229 ± 68 Ma 到 2298 ± 25 Ma 之间 (图 4.36E), 其中 125 个年龄位于 1666–1229 Ma 区间内, 加权平均年龄为 1466 ± 11 Ma (MSWD = 4.1) (图 4.36F); Y1_2 共得到 49 个谐和年龄, 其中只有四个 Th/U 比值低于 0.1, 其 $^{206}\text{Pb}/^{207}\text{Pb}$ 年龄介于 1397 ± 26 Ma 和 1511 ± 19 Ma 之间 (图 4.36B)。Y1_1 的六个锆石核年龄较老, 分别为 2298 ± 25 Ma、 1807 ± 26 Ma、 1803 ± 70 Ma、 1772 ± 53 Ma、 1764 ± 22 Ma 和 1715 ± 34 Ma, 本研究认为来自源区或岩浆上升和结晶过程中捕获围岩的继承性锆石年龄。样品 Y1_2 来自同一钻孔, 共有 49 个谐和年龄, 范围在 1264 ± 83 Ma 到 1972 ± 23 Ma 之间 (图 4.36A)。去除一个最老的异常锆石年龄 1972 ± 23 Ma (可能代表自围岩的继承性锆石), 剩下 48 个锆石的加权平均年龄为 1427 ± 21 Ma (MSWD = 5.0) (图 4.36B)。由于这两个样品的年龄在分析误差内几乎完全一致, 综合所有分析数据后得到的总体加权平均年龄为 1454.8 ± 9.6 Ma (MSWD = 4.2), 本论文将其作为该变质花岗岩的结晶年龄。

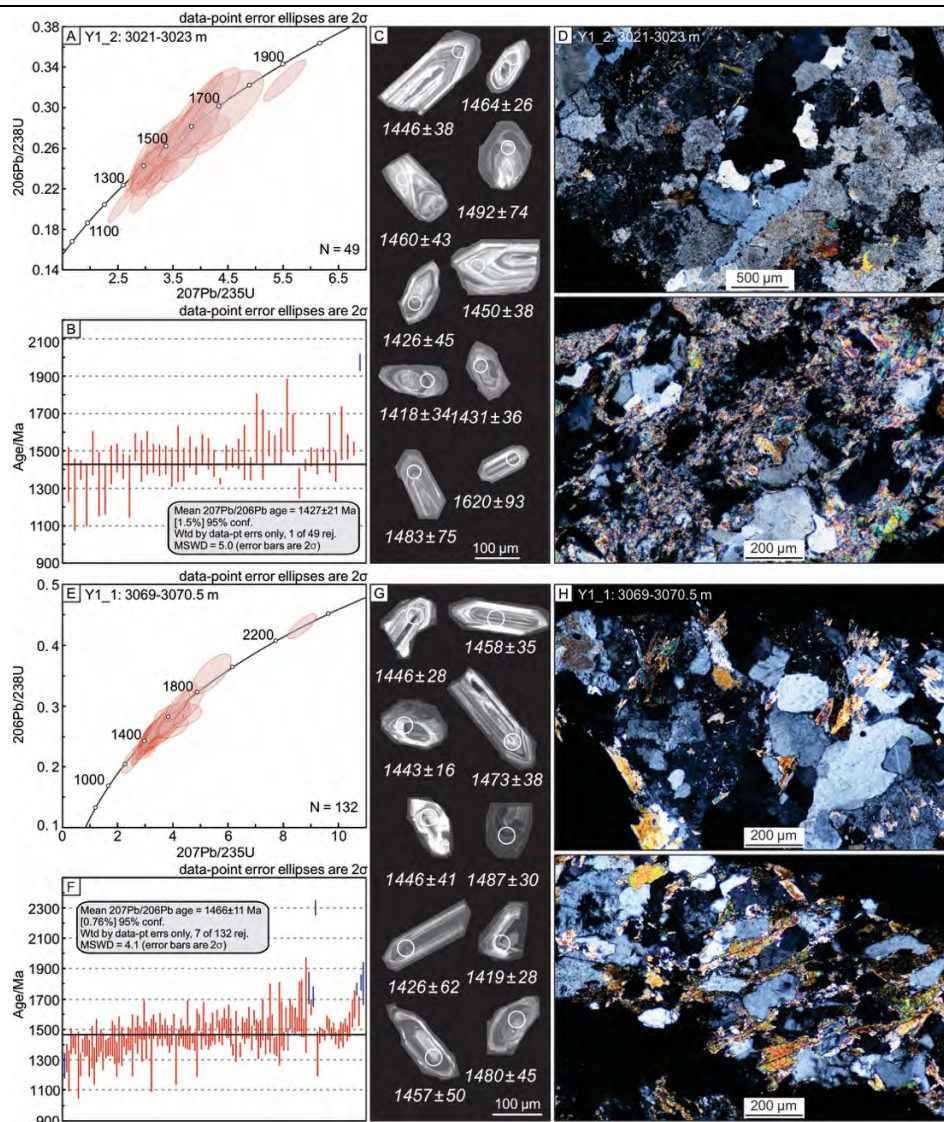


图 4.36 样品 Y1_2 和 Y1_1 锆石 A, E) U-Pb 年龄谐和图; B, F) 加权平均年龄; C, G) 代表性锆石阴极发光图像及 D, H) 正交镜下岩石薄片

Fig. 4.36 Zircon U-Pb Concordia diagrams of all analytical grains, weighted mean ages of all concordant spots (concordance is within 90-110%), CL images of representative grains with their ages and uncertainties (indicated as 1 sigma) and thin sections of the metamorphic biotite granite samples from borehole Y1.

4. 3. 2 锆石微量元素结果

本分析获得 Y1 井共计 50 颗锆石的微量元素含量，其中样品 Y1_1 (1466±11 Ma) 包含 31 组，样品 Y1_2 (1427±21 Ma) 包含 19 组。两个样品锆石稀土元素球粒陨石标准化配分曲线如图 4.38A 和 B 所示：大多数锆石显示从 La 到 Lu 稀土元素含量急剧增加，具有明显的 Ce 正异常和 Eu 负异常。具体而言，Y1_1 的 Eu/Eu* 比值为 0.03–0.38，Y1_2 为 0.04–0.35；Y1_1 的 Ce/Ce* 比值为 1.40–58.28，Y1_2 为 1.93–41.36。

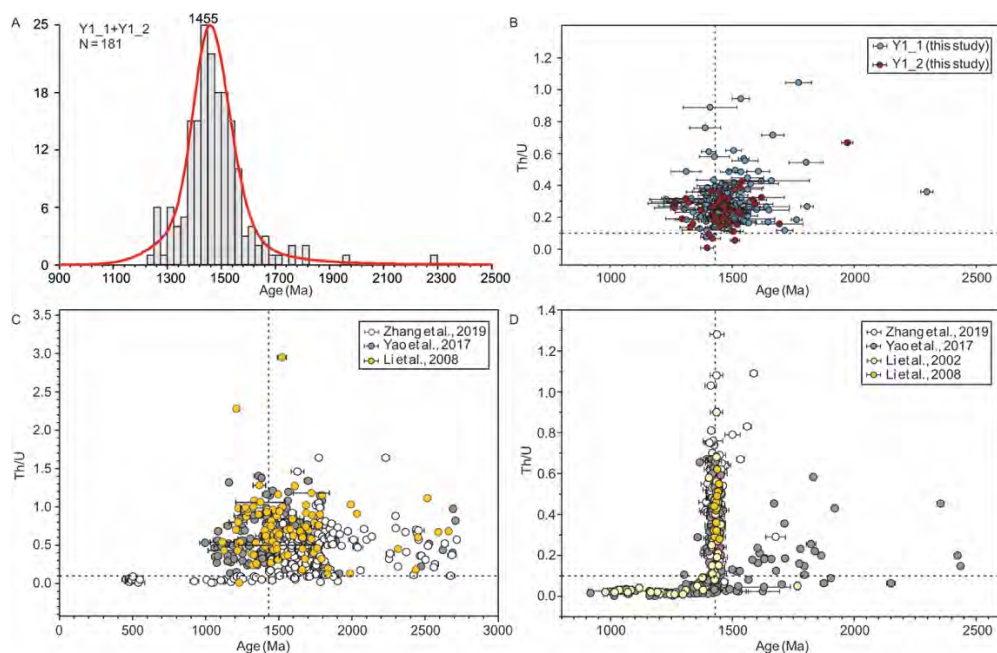


图 4.37A-B) Y1 井样品锆石 U-Pb 年龄谱系、U-Pb 年龄 vs. Th/U；海南岛元古代基底 C) 抱板群及年轻地层及 D) 抱板群岩浆岩锆石 U-Pb 年龄 vs. Th/U

Fig. 4.37 (A) Relative probability plot of zircon U-Pb spectra of drilling samples Y1_1 and Y1_2. Th/U ratios versus U-Pb age diagram for samples of (B) this study; (C) published clastic outcrop samples from Baoban and overlying sequences and (D) igneous outcrop samples from Baoban Complex of Li et al. (2002b, 2008b), Yao et al. (2017) and Zhang et al. (2019).

锆石微量元素原始地幔标准化配分曲线如图 4.38C 和 D 所示：样品 Y1_1 和 Y1_2 配分模式相似，U、Ta、Pb 和 Hf 元素富集，Th、Nb、La、Ce、Pr 和 Ti 元素亏损。具体而言，Y1_1 的 Gd 含量从 18.69 ppm 到 111.71 ppm 不等，而 Y1_2 的范围相对较窄，为 21–64.96 ppm。两个样品的 Hf 含量普遍较高，Y1_1 范围为 11032.85–23826.66 ppm，Y1_2 的范围为 8321.66–25388.00 ppm。样品 Y1_1 和 Y1_2 的 Lu 含量分别为 50.75–255.43 ppm 和 54.25–264.07 ppm，变化范围相似。Y1_1 的 Y 含量范围相对较广，为 1194.13–10873.08 ppm，而 Y1_2 的范围较窄，为 983.50–4229.89 ppm。样品 Y1_1 和 Y1_2 锆石的 Dy 含量分别为 101.78–672.41 ppm 和 96.39–368.35 ppm。样品 Y1_1 和 Y1_2 的 Yb 含量分别从 390.99 ppm 到 1553.49 ppm 和从 411.25 ppm 到 1560.49 ppm 不等。

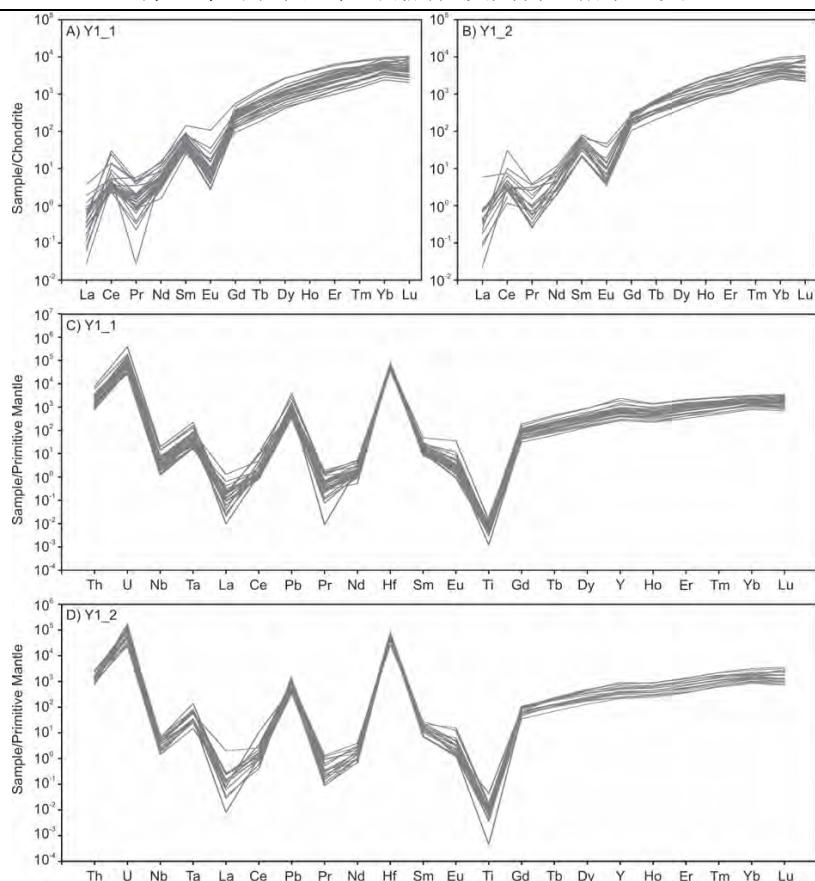


图 4.38A-B) Y1 井样品锆石稀土元素球粒陨石标准化配分曲线；C-D) 锆石微量元素原始地幔标准化配分曲线

Fig. 4.38 Zircon rare earth element (REE) concentrations normalized to chondrites (McDonough and Sun, 1995) and multi-elemental spidergrams normalized to primitive mantle (Sun and McDonough and Sun, 1989) for samples Y1_1 and Y1_2.

4.3.3 Lu-Hf 同位素结果

本研究对两个变质黑云母花岗岩样品 Y1_1 (1466±11 Ma) 和 Y1_2 (1427±21 Ma) 共进行了 156 颗锆石原位 Lu-Hf 同位素测试分析。样品 Y1_1 获得了 112 个 Hf 同位素分析结果，其中 92 个分析结果具有谐和锆石 U-Pb 年龄，其 $\varepsilon_{\text{Hf}}(t)$ 值范围介于 -3.49 到 +12.94 之间 (图 4.39A)， $^{176}\text{Hf}/^{177}\text{Hf}$ 比值为 0.281234–0.282247，大部分位于亏损地幔演化线和球粒陨石均一库 CHUR 线之间。

样品 Y1_2 获得了 44 个 Hf 同位素分析结果，其中 37 个锆石具有谐和 U-Pb 年龄，其 $\varepsilon_{\text{Hf}}(t)$ 值范围从 -1.07 到 +7.46 (图 4.39A)， $^{176}\text{Hf}/^{177}\text{Hf}$ 比值为 0.281870–0.282195。样品 Y1_1 (结晶年龄 1466 Ma) 的两阶段模式年龄 (T_{DM}^{C}) 呈现出 1458 Ma 到 2912 Ma 的年龄变化范围，主要峰值年龄为 1950 Ma (图 4.39D)。样品 Y1_2 (结晶年龄 1427 Ma) 的模式年龄从 1536 Ma 到 2148 Ma，主要峰值年龄为 1980 Ma (图 4.39D)。

4.3.4 讨论

研究认为，抱板混杂岩（Baoban Complex）是海南岛的一个重要地质单元，是海南岛最古老基底的组成部分，其成分复杂，片麻岩、角闪岩和花岗岩侵入变质沉积岩共同形成复合岩体。前人对这些中元古代岩体已经进行了大量同位素年代学和元素地球化学研究。本研究则根据重要的钻井样品新定年和同位素结果对海南中元古代基底的岩体年龄和构造亲缘关系，以及与其他元古代地质单元的关系开展系统对比分析。

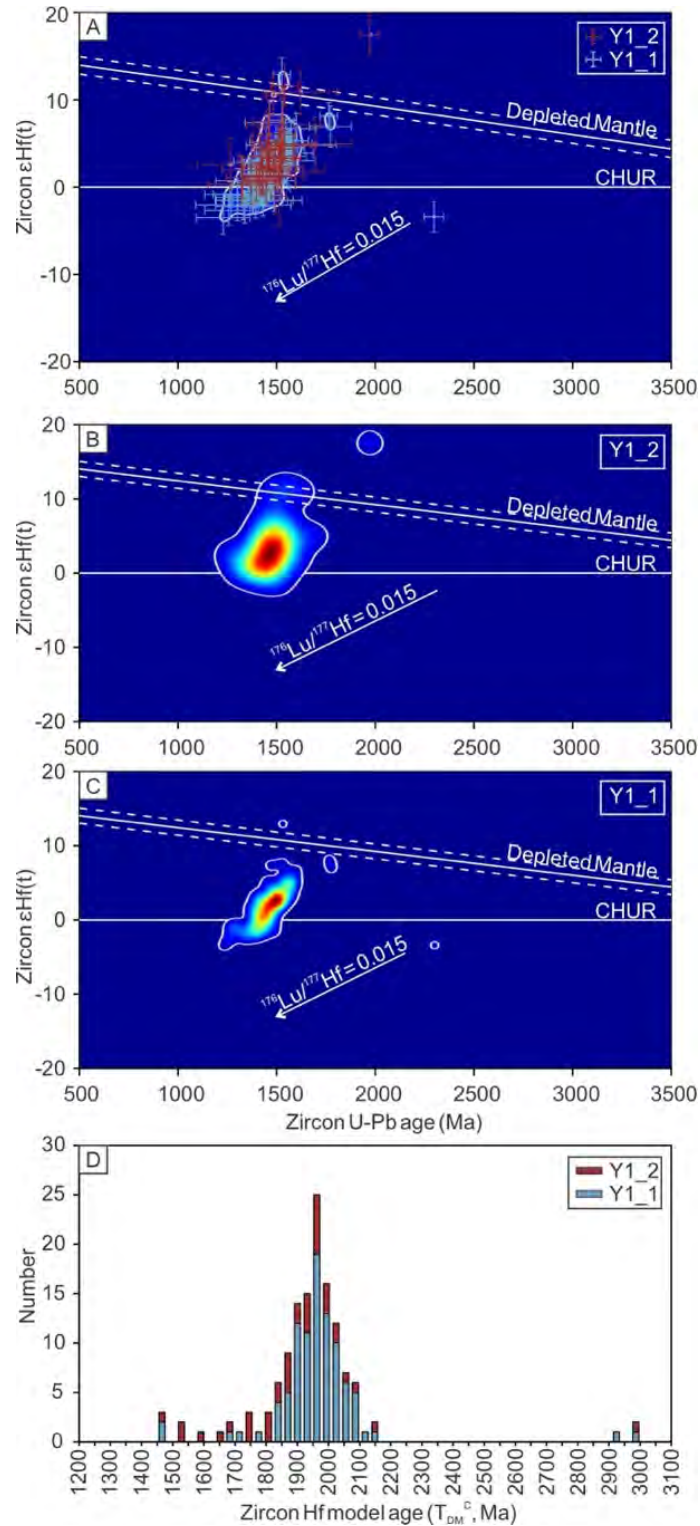


图 4.39A-C) Y1 井样品锆石 U-Pb 年龄 vs. $\epsilon\text{Hf}(t)$ 二元核密度分布; D) 锆石两阶段模式年龄 (T_{DM}^C) 分布图

Fig. 4.39 (A) Zircon $\epsilon\text{Hf}(t)$ values versus U-Pb ages; bivariate kernel density estimate plots of borehole sample (B) Y1_2 and (C) Y1_1 in this study, contours are calculated as a percentage from age peak density; (D) cumulative diagram of zircon Hf model ages.

首先, 本研究发现抱板混杂岩中的片麻状花岗岩、花岗闪长岩、火山岩^[250]以及流纹岩(约 1435–1430 Ma)^[116]和海南近岸基底中约 1455 Ma 的变质黑云母花岗岩之间存在 U-Pb 年龄的相似性(图 4.36 和 4.37)。这些年龄与抱板混杂岩副片麻岩的较宽广碎屑锆石年龄谱中的年轻年龄峰值(约 1430 Ma)也表现一致(Yao et al., 2017)。因此, 海南中元古代基底在约 1460–1430 Ma 时沉积相应地层, 并几乎同时被喷发岩和深成岩岩体侵入^[116]。

研究认为, 1.46–1.43 Ga 期间海南基底可能存在一定规模的岩浆活动, 然而关于此时构造环境究竟处于造山还是非造山的争论仍然存在: 一些学者根据抱板混杂岩中的片麻花岗岩地球化学特征, 认为海南岛此时以发育 A-型花岗岩为主, 受裂谷环境控制^[116, 250]; 然而, 也有人认为 S 型花岗岩的存在指示海南岛此时处于活动板块边界^[251]; 还有人指出中元古代花岗岩岩体可能形成于更复杂的构造环境, 该环境同时发育 I 型和 A 型花岗岩^[252]。本研究的锆石(结晶年龄 1455 Ma) $\epsilon\text{Hf}(t)$ 值变化范围从 -3.5 到 +12.9 (图 4.39A-C), 反映这些锆石来自混合岩浆来源, 其中大部分为正值可能表明以幼年岩浆为主, 地壳不断增厚, 负值的存在说明还包含少量古老陆壳再循环物质。 $\epsilon\text{Hf}(t)$ 正值逐渐增多很可能指示幔源岩浆的贡献进一步加强。理论上讲, 锆石高 Th/Nb 和 Hf/Th 值由大陆弧环境产生。然而, 在多个岩浆源强烈混合时, 正如本研究中 $\epsilon\text{Hf}(t)$ 值变化范围较大且含有多个负值, 部分可以反映构造环境属性的比值和判别图解可能出现一定偏差, 从而造成错误的判断, 因此需要谨慎选择合适指标。考虑到海南基底早期缺乏俯冲相关记录和镁铁质岩体, 并结合部分锆石微量元素构造判别图解(大部分数据处于板内范围), 该时期更可能为伸展环境, 而非挤压环境^[253](图 4.40A-C)。

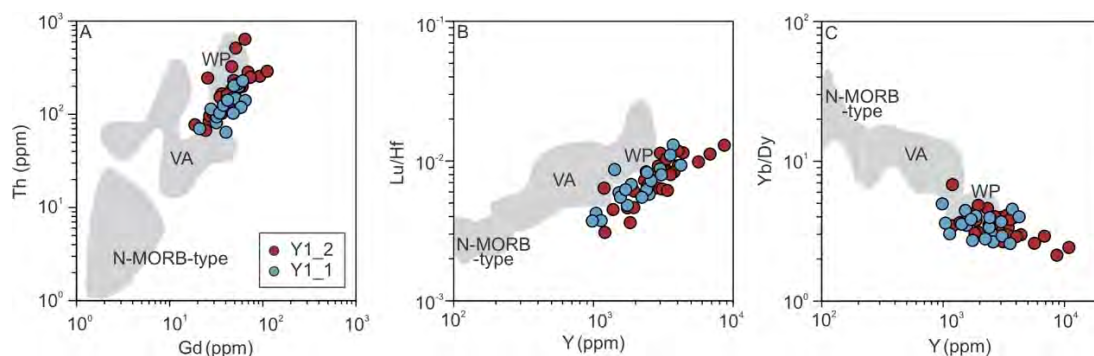


图 4.40 Y1 井样品锆石微量元素 A) Th vs. Gd; B) Lu/Hf vs. Y; C) Yb/Dy vs. Y 构造判别图解, 其中 VA (volcanic arc) 代表岩浆弧环境, WP (within plate) 代表板内环境

Fig. 4.40 Tectonic discrimination plots based on zircon trace elemental concentrations of samples Y1_1 and Y1_2. (A) Th vs. Gd; (B) Lu/Hf vs. Y; (C) Yb/Dy vs. Y. Geochemical features of zircon host rocks include: mid-ocean ridge basalt (N-MORB), volcanic arc (VA) and within-plate (WP), which are calculated from zircon trace elemental compositions and are denoted as three separated fields modified from Schulz et al. (2006).

前人还注意到 1.46–1.43 Ga 形成的沉积记录和火成岩锆石边部包含一组低 Th/U 比值, 这可能反映了约 1400–1300 Ma 的变质事件导致的铅损失。图 4.37C 和 D 显示 Th/U 在约 1.3–1.0 Ga 突然下降, 说明变质作用的持续进行。本研究花岗岩样品中的锆石 Th/U 值大多大于 0.1, 但它们仍然呈现出明显的下降趋势, 可能与后续变质事件中的铅损失相关 (图 4.37B)。因此, 学者们认为海南岛受到四堡造山运动 (约 13–9 Ga 的 Grenville 期造山运动) 的影响, 造成抱板混杂岩及其相关基底单元发生高级至中级变质作用和强烈变形, 上覆地层的褶皱和逆冲结构中也出现明显变形。Li et al. (2002b) 也认为该构造运动最终导致华南和扬子地块的拼合, 也影响至海南岛基底, 是四堡造山运动西南方向的延伸 (图 4.41)。

4.3.5 初步结论

海南岛位于华南大陆西南端, 包含古老的元古宙结晶基底, 被认为属于华夏地块基底的重要组成部分。在结合前人对海南岛中–新元古代露头进行的大量研究基础上, 本论文首次对海南岛西南部延伸至南海西部莺歌海盆地的钻孔样品开展分析, 结果显示其属于海南岛基底, 并针对其中的中元古代变质黑云母花岗岩开展锆石 U-Pb 定年、锆石元素地球化学、Lu-Hf 同位素测试分析。样品加权平均年龄为 1454.8 ± 9.6 Ma, 代表了 Y1 井花岗岩的结晶年龄。大多数锆石 $\epsilon_{\text{Hf}}(t)$ 值为正值, 范围从 -3.49 到 +12.94, 指示岩浆来源主要为幼年幔源岩浆, 但包含少量古老陆壳再循环组分。结合锆石元素地球化学判别图解和其他地区的年代学数据, 无论是海南岛陆上出露的抱板混杂岩 (主要由 1.43 Ga 火成岩和变质沉积岩组成) 还是位于海南岛西南的侵入岩, 主要形成于一个无造山的伸展环境, 并在大约 1.3 Ga 之后普遍经历了变质作用。

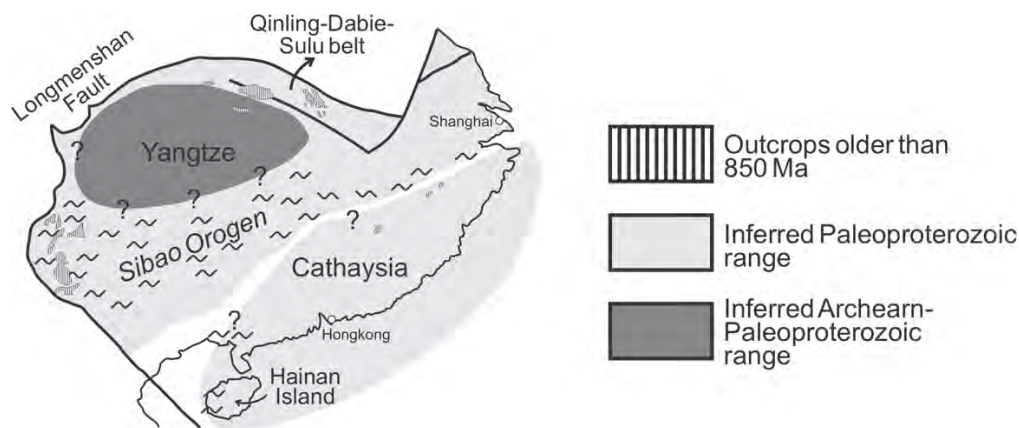


图 4.41 海南岛及华夏地块新元古代构造环境模式图

Fig. 4.41 Model showing inclusion of Hainan Island (also its potential southwest extension?) within the Cathaysia Block (Li et al., 2002b, 2008b).

第 5 章 南海北部早新生代岩浆活动

5.1 资料收集与样品来源

大约 90 Ma 以后, 古太平洋板块俯冲后撤, 华南大陆开始经历主动向被动陆缘的转换过程。但在南海扩张以前, 由于盆地地质资料匮乏, 早新生代岩浆活动发育演化特征大都依靠野外露头定性描述, 受早期技术限制, 测试结果仅局限于定年分析, 其年龄数据也相对粗糙。为进一步揭示因区域构造环境转变而引发的岩浆活动演化规律, 结合珠江口盆地珠一凹陷火成岩钻井样品早期年龄数据, 本研究对南海北部断陷期形成的凝灰岩、火山碎屑岩和沉积岩钻井样品开展锆石 U-Pb 定年、锆石微量元素地球化学和 Lu-Hf 同位素分析, 钻井位置如图 5.1 所示。测试样品均来自中国海洋石油总公司进行的油气勘探钻井。

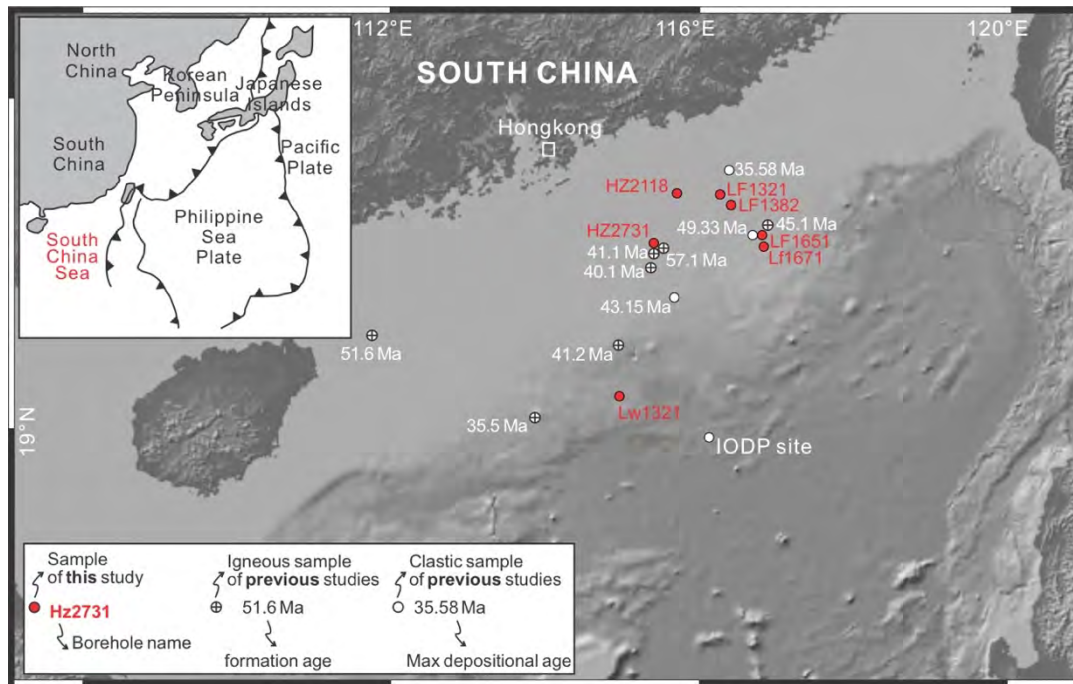


图 5.1 南海北部早新生代岩浆岩与沉积岩位置分布图 (红色字体表示本研究样品; 白色字体表示前人资料, 白色实心圆点代表碎屑岩样品, 包含十字的白色圆点代表岩浆岩样品 [132, 154])

Fig. 5.1 Locations of early Cenozoic igneous and sedimentary rock samples within the northern South China Sea (samples in this study are denoted in red; samples in previous studies are denoted in white; clastic rock samples are denoted in white filled circles; igneous rock samples are denoted in white crossed circles [132, 154])

5.2 锆石 U-Pb 年代学结果

本研究对南海北部一系列早新生代凝灰岩、火山碎屑岩和沉积岩钻井样品开展同位素年代学分析，锆石 U-Pb 定年结果详述如下。

样品 HZ27-3-1 为火山碎屑岩，取样深度为 2523-2541 m，锆石颗粒大多呈自形状，只有极少数呈一定磨圆度，具有明显的振荡环带结构。该样品 Th 和 U 含量变化较大，分别为 164–8184 ppm 和 200–3418 ppm，Th/U 比值全部大于 0.1，范围在 0.39 和 2.39 之间，说明为岩浆锆石来源。该样品共进行 125 次锆石 U-Pb 定年分析，取得 82 个谐和年龄，范围在 51 ± 2 Ma 到 1715 ± 30 Ma 之间，其中包含 70 颗新生代锆石，年龄为 63–51 Ma；9 颗上侏罗/下白垩统锆石，年龄为 146–107 Ma；一颗古生代锆石，年龄为 512 Ma；两颗前寒武继承性锆石，年龄分别为 940 Ma 和 1715 Ma。总体来看，其年龄谱系以早新生代峰为主，峰值年龄集中在大约 56 Ma，次要峰值年龄集中在大约 110 Ma（图 5.2）。另外，本研究对其新生代年龄组分计算加权平均年龄，除去两个异常点，剩余年龄加权平均值为 55.59 ± 0.53 (MSWD = 1.19)（图 5.3）。

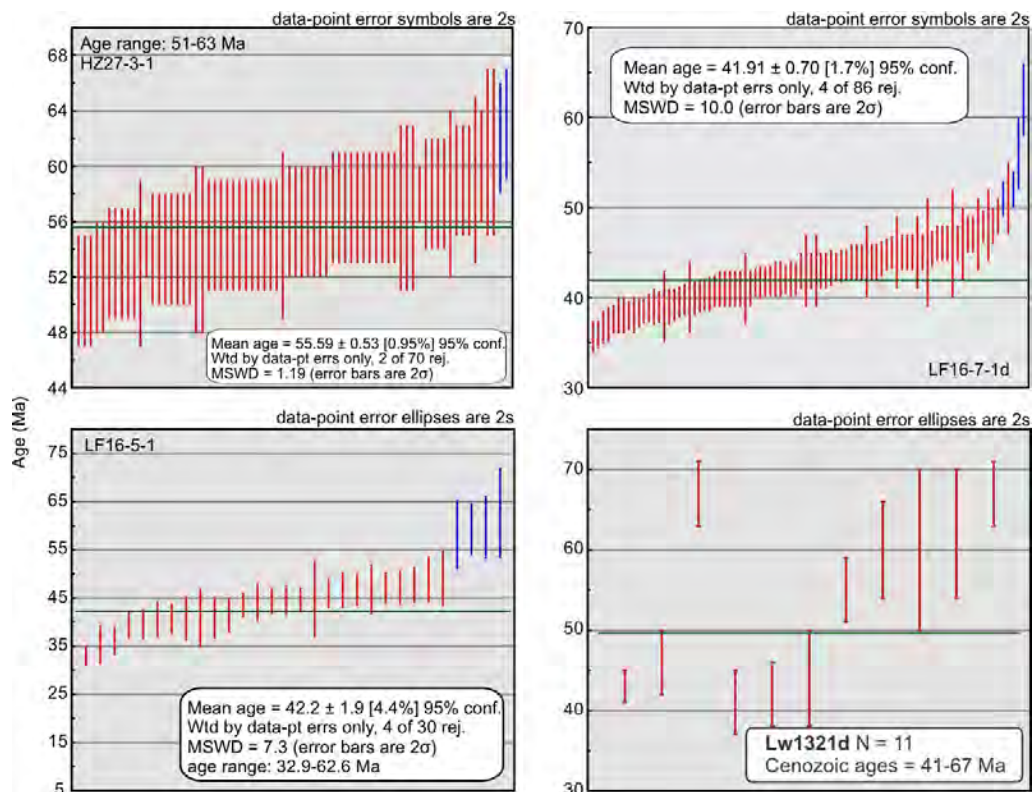


图 5.2 南海北部早新生代火山碎屑岩样品（HZ27-3-1、LF16-7-1d、LF16-5-1、LW13-2-1d）中包含的新生代锆石 U-Pb 年龄分布及加权平均值

Fig. 5.2 Zircon U-Pb Cenozoic age distribution patterns and weighted mean ages of early Cenozoic volcanoclastic rock samples (HZ27-3-1, LF16-7-1d, LF16-5-1 and LW13-2-1d) in the northern South China Sea.

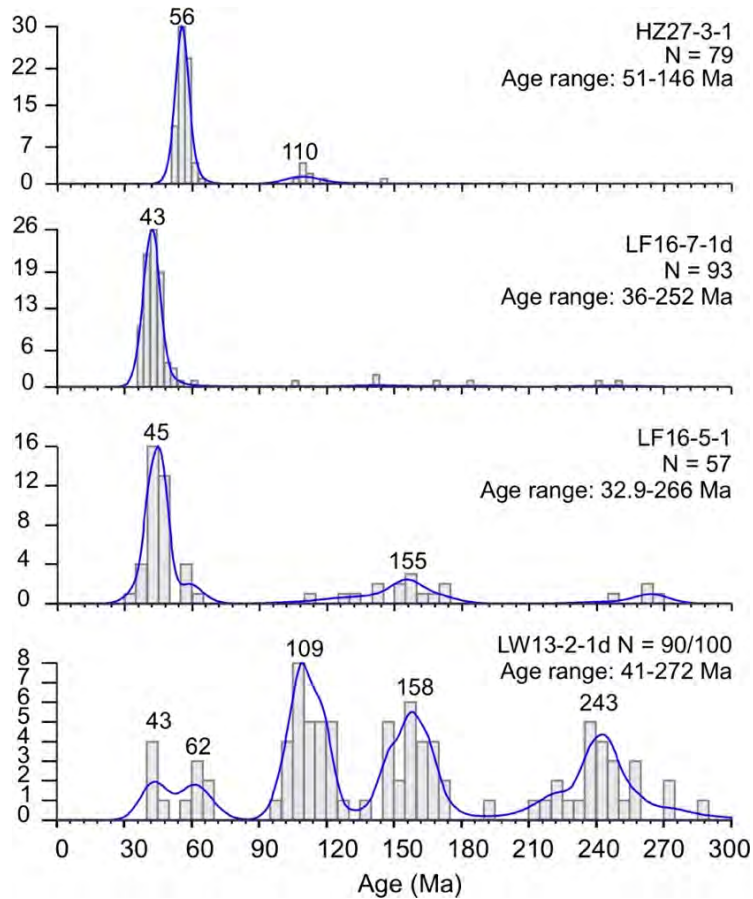


图 5.3 南海北部早新生代火山碎屑岩样品 (HZ27-3-1、LF16-7-1d、LF16-5-1、LW13-2-1d) 锆石 U-Pb 年龄谱系 (0–300 Ma)

Fig. 5.3 Zircon U-Pb age spectra (age ranges shown in this figure: 0–300 Ma) of the early Cenozoic volcanoclastic rocks samples (HZ27-3-1, LF16-7-1d, LF16-5-1 and LW13-2-1d) in the northern South China Sea.

钻井 HZ21-1-18 位于 HZ27-3-1 东北方向, 共取得两个 4437-4443 m 和 4386-4389 m 样品, 下部为火山碎屑岩, 上部为碎屑岩。这两个样品锆石颗粒具有一定磨圆度, 可见振荡环带结构。下部样品 Th 和 U 含量变化相对不大, 分别为 66–816 ppm 和 68–1007 ppm, Th/U 比值全部比值全部大于 0.1, 范围在 0.2 和 2.6 之间; 上部样品 Th 和 U 含量分别为 66–1686 ppm 和 101–996 ppm, Th/U 比值全部大于 0.1, 范围在 0.48 和 2.73 之间, 说明为岩浆锆石来源。下部样品共取得 38 个谐和年龄, 范围在 52 ± 4 Ma 到 131 ± 5 Ma 之间 (图 5.4), 其中包含 30 颗新生代锆石 (误差范围内), 年龄为 67–52 Ma; 8 颗白垩锆石, 年龄为 131–110 Ma (图 5.4)。总体来看, 其年龄谱系以早新生代峰为主, 峰值年龄集中在大约 58 Ma, 次要峰值年龄集中在大约 120 Ma (图 5.4)。另外, 本研究对其新生代年龄组分计算加权平均年龄, 除去 1 个异常点, 剩余年龄加权平均值为 58.8 ± 1.7 (MSWD = 2.1) (图 5.4)。上部样品共取得 50 个谐和年龄, 范围在 36 ± 2 Ma 到 886 ± 18 Ma 之间 (图 5.4), 其中包含 26 颗新生代锆石 (误差范围内), 年龄为

67–36 Ma; 19 颗白垩锆石, 年龄为 131–101 Ma; 3 颗古生代锆石, 年龄为 450–334 Ma; 两颗前寒武继承锆石, 年龄分别为 770 Ma 和 886 Ma (图 5.4)。总体来看, 其年龄谱系以早新生代峰为主, 峰值年龄集中在大约 56 Ma, 次要峰值年龄集中在大约 116 Ma (图 5.4)。另外, 本研究对其新生代年龄组分计算加权平均年龄, 除去 3 个异常点, 剩余年龄加权平均值为 57.1 ± 1.4 (MSWD = 3.1) (图 5.4)。

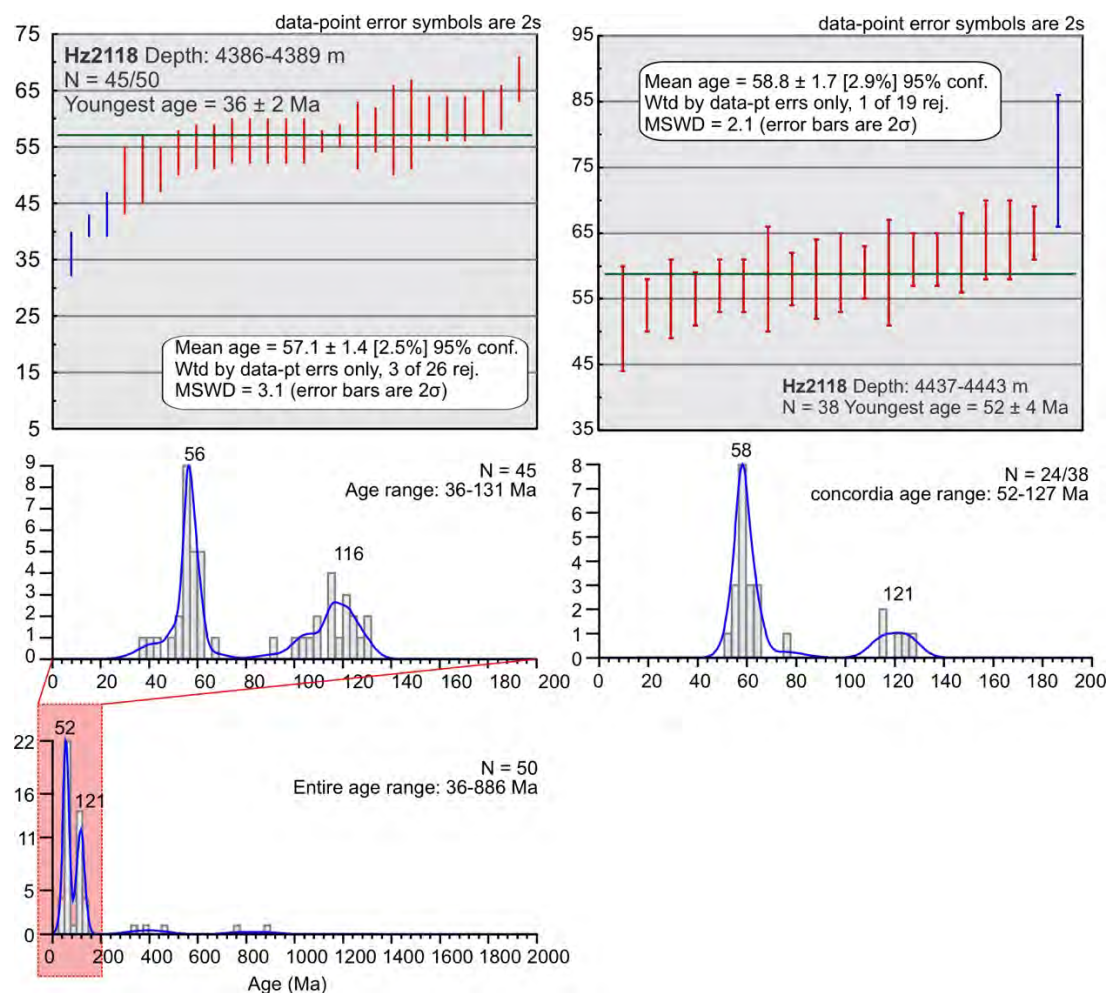


图 5.4 南海北部早新生代火山碎屑岩样品 (钻井 HZ21-1-18 取自 4386-4389 m 和 4437-4443 m 两个样品) 锆石 U-Pb 年龄谱系、主要年龄峰值放大图及包含的新生代锆石加权平均值

Fig. 5.4 Zircon U-Pb age spectra, zoom-in plots of major age clusters and weighted mean ages of Cenozoic zircons of the early Cenozoic volcanoclastic rock samples (two samples with the depths of 4386-4389 m and 4437-4443 m were extracted from borehole HZ21-1-18) in the northern South China Sea.

样品 LF13-2-1 为碎屑岩, 同样位于珠一凹陷 (图 5.1), 取样深度为 3232.5 m, 锆石颗粒呈自形状至半自形状, 具有一定磨圆度。该样品 Th 和 U 含量变化分别为 40–3310 ppm 和 79–1643 ppm, 绝大多数 Th/U 比值大于 0.1, 范围在 0.17 和 3.02 之间, 说明为岩浆锆石来源; 只有一颗锆石小于 0.1, 为 0.07, 年龄为

496±16 Ma, 可能由 Pb 丢失造成。该样品共进行 51 次锆石 U-Pb 定年分析, 取得 36 个谐和年龄, 范围在 33±2.5 Ma 到 1000±50 Ma 之间 (图 5.5), 其中包含 11 颗新生代锆石, 年龄为 60.7–33 Ma; 17 颗侏罗/白垩锆石, 年龄为 174–94 Ma; 7 颗古生代锆石, 年龄为 496–301 Ma; 1 颗前寒武继承性锆石, 年龄为 1000 Ma (图 5.5)。总体来看, 其年龄谱系包含多个年龄组分, 以早新生代和晚中生代峰为主, 峰值年龄集中在大约 38 Ma 和 137 Ma, 以及若干零星分散的古生代和前寒武锆石 (图 5.5)。

样品 LF13-8-2 为碎屑岩, 同样位于珠一凹陷 (图 5.1), 取样深度为 3835–3840 m, 锆石颗粒呈自形状至半自形状, 具有一定磨圆度。该样品 Th 和 U 含量变化分别为 30–1610 ppm 和 43–6091 ppm, Th/U 比值全部大于 0.1, 范围在 0.11 和 4.02 之间, 说明为岩浆锆石来源。该样品共进行 111 次锆石 U-Pb 定年分析, 取得 66 个谐和年龄, 范围在 34±2 Ma 到 2586±26 Ma 之间 (图 5.5), 其中包含 14 颗新生代锆石, 年龄为 64–34 Ma; 26 颗中生代锆石, 年龄为 250–94 Ma; 12 颗古生代锆石, 年龄为 467–260 Ma; 14 颗前寒武继承性锆石, 年龄为 2586–587 Ma (图 5.5)。总体来看, 其年龄谱系较为宽广, 包含多个年龄组分, 早新生代年龄峰值集中在大约 46 Ma, 中生代年龄峰值集中在大约 132 Ma, 以及若干零星分散的古生代和前寒武锆石 (图 5.5)。

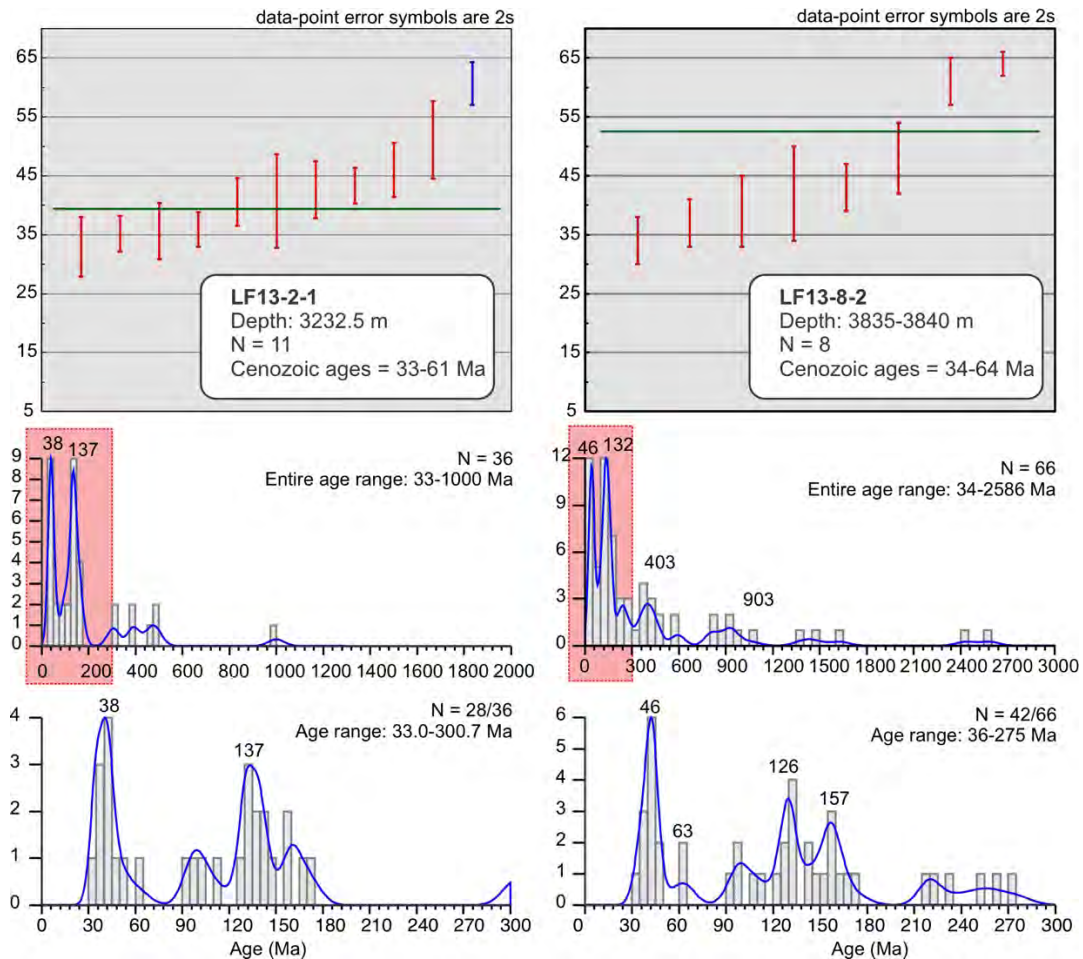


图 5.5 南海北部早新生代火山碎屑岩样品 (LF13-2-1、LF13-8-2) 锆石 U-Pb 年龄谱系、主

Fig. 5.5 Zircon U-Pb age spectra, zoom-in plots of major age clusters and weighted mean ages of Cenozoic zircons of the early Cenozoic volcanoclastic rock samples (LF13-2-1 and LF13-8-2) in the northern South China Sea.

样品 LF16-5-1 为火山碎屑岩，位于珠一凹陷的南侧区域（图 5.1），取样深度为 3783-3786 m，锆石颗粒呈自形状至半自形状，部分锆石具有一定磨圆度。该样品 Th 和 U 含量变化分别为 65-1888 ppm 和 123-2121 ppm，绝大多数 Th/U 比值大于 0.1，范围在 0.21 和 2.63 之间，说明为岩浆锆石来源。只有一颗锆石 Th/U 小于 0.1（为 0.09），年龄为 917 ± 29 Ma，可能代表一定程度铅丢失。该样品共取得 71 个谐和年龄，范围在 32.9 ± 1.07 Ma 到 1361 ± 69 Ma 之间，其中包含 39 颗新生代锆石，年龄为 62.6-32.9 Ma（图 5.2）；15 颗中生代锆石，年龄为 246-112 Ma；10 颗古生代锆石，年龄为 504-264 Ma；7 颗前寒武继承性锆石，年龄为 1361-548 Ma。总体来看，其年龄谱系包含多个年龄组分，但以早新生代年龄峰为主，峰值集中在大约 43 Ma，中生代年龄峰值集中在大约 155 Ma，以及若干零星分散的古生代和前寒武锆石。另外，本研究对其新生代年龄组分计算加权平均年龄，除去 4 个异常点，剩余年龄加权平均值为 42.2 ± 1.9 (MSWD = 7.3)（图 5.3）。

样品 LF16-7-1d 为凝灰岩，同样位于珠一凹陷的南侧区域，与样品 LF16-5-1 位置邻近（图 5.1），取样深度为 4164-4185 m，大部分锆石颗粒呈自形状。该样品 Th 和 U 含量变化分别为 55-3754 ppm 和 73-2725 ppm，Th/U 比值全部大于 0.1，范围在 0.17 和 2.29 之间，说明为岩浆锆石来源。该样品共取得 99 个谐和年龄，范围在 36 ± 1 Ma 到 689 ± 15 Ma 之间，其中包含 86 颗新生代锆石，年龄为 62-36 Ma；7 颗中生代锆石（误差范围内），年龄为 252-107 Ma；4 颗古生代锆石，年龄为 462-320 Ma；2 颗新元古代继承性锆石，年龄为 689 Ma 和 547 Ma（图 5.3）。总体来看，其年龄谱系以早新生代年龄峰为主，峰值集中在大约 42 Ma（图 5.2），本研究对其新生代年龄组分计算加权平均年龄，除去 4 个异常点，剩余年龄加权平均值为 41.9 ± 0.7 (MSWD = 10)（图 5.2）。

钻井 LW13-2-1d 位于珠江口盆地珠二凹陷南侧，共取得 4345-4350 m 和 4050-4055 m 两个样品，均为碎屑岩。这两个样品锆石颗粒具有一定磨圆度，可见振荡环带结构。下部样品 Th 和 U 含量变化相对不大，分别为 39-1842 ppm 和 72-1412 ppm，Th/U 比值全部比值全部大于 0.1，范围在 0.32 和 1.99 之间；上部样品 Th 和 U 含量分别为 18-1429 ppm 和 80-1154 ppm，绝大多数 Th/U 比值大于 0.1，范围在 0.12 和 1.90 之间，说明为岩浆锆石来源；只有两颗锆石小于 0.1（0.03 和 0.07），年龄分别为 272 Ma 和 456 Ma，可能因区域地质作用导致铅丢失。下部样品共取得 81 个谐和年龄，范围在 43 ± 2 Ma 到 1833 ± 30 Ma 之间，其中包含 6 颗新生代锆石，年龄为 65-43 Ma；61 颗中生代锆石（误差范围内），

年龄为 252–77 Ma; 10 颗古生代锆石, 年龄为 474–254 Ma; 4 颗元古代锆石, 年龄在 1833 Ma 至 826 Ma 之间。上部样品共取得 100 个谐和年龄, 范围在 41 ± 2 Ma 到 1850 ± 33 Ma 之间, 其中包含 11 颗新生代锆石 (误差年龄范围内), 年龄为 67–41 Ma (图 5.2); 73 颗中生代锆石, 年龄为 251–98 Ma; 13 颗古生代锆石, 年龄为 479–255 Ma; 3 颗元古代锆石, 年龄在 1850 Ma 至 745 Ma 之间。总体来看, 两个样品年龄谱系特征相似, 均表现为宽广而多峰的特点, 以中生代峰值为主: 下部样品年龄集中在大约 170 Ma 至 117 Ma 之间, 还具有 260 Ma 的印支期峰值, 可见大约 58 Ma 的早新生代年龄峰值; 上部样品年龄集中在 154 Ma 至 113 Ma 之间, 印支期峰值相对下部样品更明显, 集中在大约 244 Ma, 可见大约 52 Ma 的早新生代年龄峰值 (图 5.3)。

样品 LH34-6-1 为火山碎屑岩, 位于珠二凹陷, 取样深度为 3949–3955 m, 大部分锆石颗粒呈自形状至。该样品 Th 和 U 含量变化分别为 106–4766 ppm 和 130–6033 ppm, Th/U 比值全部大于 0.1, 范围在 0.36 和 1.03 之间, 说明为岩浆锆石来源。该样品共取得 26 个谐和年龄, 范围在 38 ± 1 Ma 到 188 ± 6 Ma 之间, 其中包含 13 颗新生代锆石, 年龄为 45–38 Ma; 13 颗中生代锆石, 年龄为 188–116 Ma。总体来看, 其年龄谱系以早新生代年龄峰为主, 峰值集中在大约 42 Ma, 还包含中生代次要年龄组分, 峰值年龄集中在大约 125 Ma。

5.3 锆石元素地球化学结果

本研究获得样品 HZ27-3-1、LF13-8-2、LF16-7-1d 以及 LW13-2-1d 的共计 553 颗锆石的微量元素含量: 其中 HZ27-3-1 包含 126 组, LF13-8-2 包含 111 组, LF16-7-1d 包含 112 组, LW13-2-1d 两个样品共计 204 组。样品锆石稀土元素球粒陨石标准化配分曲线显示: 大多数锆石显示从 La 到 Lu 稀土元素含量急剧增加, 重稀土元素富集, 具有明显的 Ce 正异常和一定程度的 Eu 负异常。部分样品, 例如 LF16-7-1d 以及 LW13-2-1d 某些锆石表现为轻稀土平坦、重稀土富集的配分模式。HZ27-3-1 的 Eu/Eu^* 比值为 0.05–0.85, LF13-8-2 为 0.02–1.72 (只有两个正异常, 为 1.16 和 1.71), LF16-7-1d 为 0.07–2.23 (只有一个正异常, 为 2.23), LW13-2-1d 上下两个样品为 0.005–0.927; 所测样品的 Ce/Ce^* 比值范围均极大, 分别为 1.13–489.68, 0.65–1764.05, 0.84–144.87, 0.65–1047.44。

本研究还取得其他用以判断构造环境的锆石微量元素含量, 如 Th、Gd、Yb、Dy 以及 Y 元素, 不同样品之间元素含量差别较大。样品 HZ27-3-1 的 Th 元素含量为 47–2960 ppm, Gd 为 4.7–126.7 ppm, Y 为 411–4188 ppm, Yb 为 219–1427 ppm, Dy 为 29–409 ppm; LF13-8-2 的 Gd 元素含量为 8.2–287.6 ppm, Y 为 217–11458 ppm, Dy 为 27–821 ppm, Yb 为 64–2524 ppm, Th 为 22.16–1610 ppm; LF16-7-1d 的 Th 元素含量为 55–3754 ppm, Gd 为 6.5–113.3 ppm, Y 为 389–2764 ppm, Yb 为 156–1093 ppm, Dy 为 33–335 ppm; LW13-2-1d 两个样品的 Th 元素

含量为 17.8–1841.9 ppm, Gd 为 1.6–97 ppm, Y 为 113–4860 ppm, Yb 为 49–1617 ppm, Dy 为 9.1–418.4 ppm。

5.4 锆石 Lu–Hf 同位素体系分析结果

本研究南海北部早新生代样品 HZ27-3-1、HZ21-1-8 (包括 4386–4389 m 和 4437–4443 m 两个深度)、LF13-8-2、LF16-7-1d 以及 LH34-6-1 开展原位 Lu–Hf 同位素含量测试, 具体数据结果详述如下。

样品 HZ27-3-1 共获得 82 个 Hf 同位素分析结果, 其中 81 个具有谐和锆石 U–Pb 年龄, 相应的 $\epsilon_{\text{Hf}}(t)$ 值范围介于 -0.19 到 +6.95 之间 (图 5.6), $^{176}\text{Hf}/^{177}\text{Hf}$ 比值在 0.281923 到 0.282897 之间, 大部分位于亏损地幔演化线和球粒陨石均一库 CHUR 线之间: 其中 10 个 $\epsilon_{\text{Hf}}(t)$ 负值, 范围是 -8 至 -0.19; 71 个 $\epsilon_{\text{Hf}}(t)$ 正值, 范围是 +0.75 至 +6.95。该样品的两阶段模式年龄 (T_{DM}^{C}) 呈现出 633 Ma 到 2027 Ma 的变化范围。

样品 HZ21-1-8 下部样品共获得 26 个 Hf 同位素分析结果, 均具有谐和锆石 U–Pb 年龄, 相应的 $\epsilon_{\text{Hf}}(t)$ 值范围介于 +1.50 至 +9.46 (图 5.6), $^{176}\text{Hf}/^{177}\text{Hf}$ 比值在 0.282794 到 0.283019 之间, 全部 $\epsilon_{\text{Hf}}(t)$ 值位于亏损地幔演化线和球粒陨石均一库 CHUR 线之间。该样品的两阶段模式年龄 (T_{DM}^{C}) 范围是 408 Ma 到 819 Ma。样品 HZ21-1-8 上部样品共获得 26 个 Hf 同位素分析结果, 均具有谐和锆石 U–Pb 年龄, 相应的 $\epsilon_{\text{Hf}}(t)$ 值范围介于 +1.69 至 +10.86 (图 5.6), $^{176}\text{Hf}/^{177}\text{Hf}$ 比值在 0.282800 到 0.283066 之间, 全部 $\epsilon_{\text{Hf}}(t)$ 值位于亏损地幔演化线和球粒陨石均一库 CHUR 线之间。该样品的两阶段模式年龄 (T_{DM}^{C}) 范围是 326 Ma 到 808 Ma。

样品 LF13-8-2 共获得 21 个 Hf 同位素分析结果, 相应的 $\epsilon_{\text{Hf}}(t)$ 值范围介于 -12.51 到 +8.73 之间 (图 5.6), $^{176}\text{Hf}/^{177}\text{Hf}$ 比值在 0.281586 到 0.283006 之间: 其中 9 个 $\epsilon_{\text{Hf}}(t)$ 负值, 范围是 -12.51 至 -0.96; 12 个 $\epsilon_{\text{Hf}}(t)$ 正值, 范围是 +1.24 至 +8.73。该样品的两阶段模式年龄 (T_{DM}^{C}) 呈现出 435 Ma 到 2827 Ma 较宽广的变化范围。

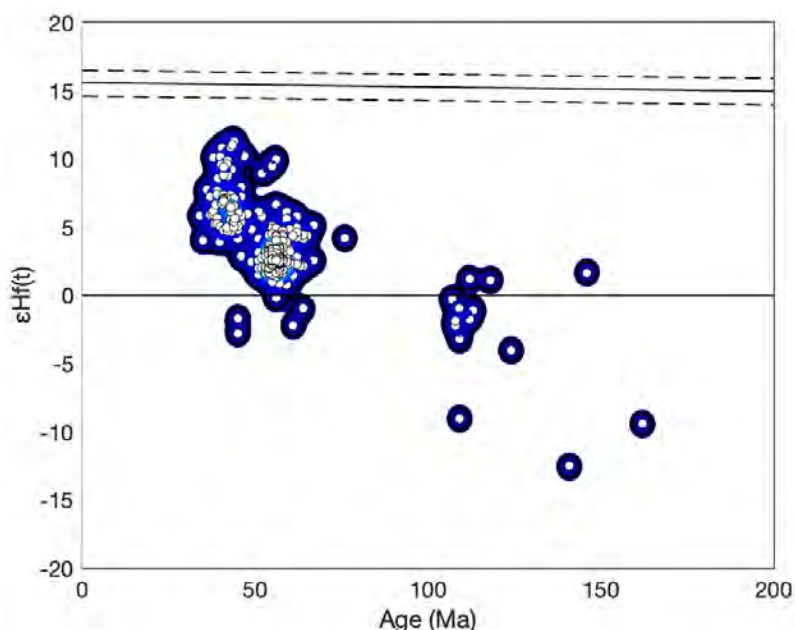


图 5.6 南海北部早新生代火山碎屑岩样品 (HZ27-3-1、HZ21-1-8 (包括深度 4386-4389 m 和 4437-4443 m 两个样品)、LF13-8-2、LF16-7-1d 以及 LH34-6-1) 锆石 U-Pb 年龄 vs. $\epsilon\text{Hf}(t)$ 二元核密度分布

Fig. 5.6 Zircon U-Pb ages vs. $\epsilon\text{Hf}(t)$ values (bivariate kernel density estimate plots of these samples also shown) of early Cenozoic volcanoclastic rock samples (HZ27-3-1 and HZ21-1-8 (including two samples with depths of 4386-4389 m and 4437-4443 m)) in the northern South China Sea.

样品 LF16-7-1d 共获得 49 个 Hf 同位素分析结果, 相应的 $\epsilon\text{Hf}(t)$ 值范围介于 -2.78 到 +11.25 之间 (图 5.6), $^{176}\text{Hf}/^{177}\text{Hf}$ 比值在 0.282679 到 0.283078 之间: 其中只有 1 个 $\epsilon\text{Hf}(t)$ 负值, 为 -2.78; 其余均为 $\epsilon\text{Hf}(t)$ 正值, 范围是 +2.89 至 +11.25。该样品的两阶段模式年龄 (T_{DM}^{C}) 呈现出 306 Ma 到 1030 Ma 的变化范围 (图 5.6)。

样品 LH34-6-1 共获得 8 个 Hf 同位素分析结果, 相应的 $\epsilon\text{Hf}(t)$ 值范围介于 +6.2 到 +8.83 之间 (图 5.6), 全部 $\epsilon\text{Hf}(t)$ 值位于亏损地幔演化线和球粒陨石均一库 CHUR 线之间, $^{176}\text{Hf}/^{177}\text{Hf}$ 比值在 0.282936 到 0.283009 之间。该样品的两阶段模式年龄 (T_{DM}^{C}) 呈现出 429 Ma 到 563 Ma 的变化范围。

5.5 南海北部早新生代岩浆活动时空分布特征

本研究对南海北部珠江口盆地珠一及珠二凹陷 (以珠一凹陷为主) 的早新生代钻井样品开展锆石 U-Pb 定年分析, 发现大量新生代锆石年龄组分。各样品最小年龄范围在 33 Ma 至 52 Ma, 而根据地层实际沉积年代应该晚于碎屑锆石中最年轻年龄, 说明南海北部早新生代地层年龄小于古新统, 因此证实神狐组古新统并不存在。

碎屑锆石 U-Pb 年龄谱系指示, 本研究大部分凝灰岩及火山碎屑岩以新生代年龄组为主, 主要集中于 63–50 Ma 和 45–35 Ma 两个范围, 这些锆石年龄与前人资料中的安山岩 (HZ2731: 57.1 Ma)、流纹岩 (YJ211: 51.6 Ma)、凝灰岩 (LF211: 49.3 Ma)、玄武岩 (LF1511: 45.1 Ma)、安山角砾岩 (LH411: 43.2 Ma)、玄武岩 (PY1611: 41.2 Ma; HZ3311: 40.1 Ma) 以及蚀变玄武岩 (BY711: 35.5 Ma) 这些火成岩年龄一致 (图 5.1), 进一步证实其来自原地或附近岩体剥蚀搬运而来的物质。

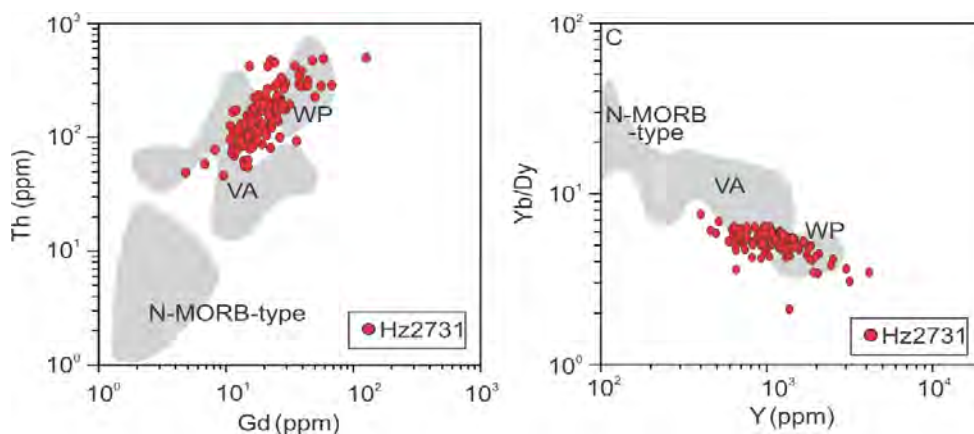


图 5.7 南海北部早新生代火山碎屑岩样品 HZ27-3-1 锆石微量元素判别图解

Fig. 5.7 Zircon trace elemental tectonic discrimination plots of early Cenozoic volcanoclastic rock sample HZ27-3-1 in the northern South China Sea.

除此之外, 碎屑岩样品还包含中生代年龄次峰, 集中在 170–100 Ma。需要注意的是, 在中生代和新生代之间几乎没有锆石年龄 (90–60 Ma), 说明此时火山活动极不活跃。另外, 锆石微量元素构造判别图解显示, 大部分新生代锆石形成于板内环境 (图 5.7), $\epsilon_{\text{Hf}}(t)$ 正值可能反映来自于幔源岩浆, 与中生代大陆弧活动陆缘的构造环境形成明显对比。本研究揭示的南海北部新生代岩浆活动规律恰好在某种程度上与最近完成的国际大洋钻探计划提出的独特岩浆演化模式相互印证, 即南海北缘在扩张过程中, 不完全符合经典大西洋被动陆缘的岩浆活动端元模式, 既非“富岩浆”型也非“贫岩浆”型。相反, 南海北部是超伸展边缘 (hyperextended margin) 的代表, 早期阶段经历了极度拉伸和薄化作用, 表现为贫岩浆型。部分地壳撕裂和拆解之后, 发生强烈的底侵作用, 转变为为富岩浆型。因此, 南海北部更倾向于被认为是“贫岩浆”向“富岩浆”过渡的陆缘类型^[35, 104, 105]。

第6章 南海物源演化特征及其指示意义

6.1 南海北部西侧物源与“崑-莺-琼”大型古河的发现

本论文对南海北部“源—汇”系统及古水系发育演化特征开展系统研究，钻井样品位置如图 2.3B 所示；样品具体信息如表 6.1、6.2 所示。

表 6.1 南海北部珠江口盆地钻井样品信息

Table. 6.1 List of samples (identified by borehole and stratigraphic age) analyzed for rare earth element (REE) geochemistry and detrital zircon U-Pb dating.

钻井名称	构造单元	年代	地化分析 取样深度 /m	资料来源	锆石 U-Pb 定 年取样深度 /m	资料来源
ZI-1	珠一凹陷	始新世	3048–3846	本研究	ZI-1-EO (3232.5–3834)	本研究
ZI-2	珠一凹陷	始新世	3098–3488	本研究	ZI-2-EO (3452–3464)	本研究
ZI-3	珠一凹陷	始新世	3378–4077	本研究	ZI-3-EO (3378–4074)	本研究
ZI-4	珠一凹陷	始新世	3705–3876	本研究	ZI-4-EO (3705–4506)	本研究
ZI-5	珠一凹陷	早中新世	1890–3087	本研究	ZI-5-LM (2392–2825)	本研究
ZI-5	珠一凹陷	晚渐新世	3114–4032	本研究	ZI-5-UO (3391–3425)	Compiled data from Shao et al. (2016) ^[181]
ZI-5	珠一凹陷	早渐新世	4050–4875	本研究	ZI-5-LO (3641–3672)	Compiled data from Shao et al. (2016)
ZI-6	珠一凹陷	晚渐新世	2470–2710	本研究	ZI-6-UO (2470–2710)	本研究
ZI-6	珠一凹陷	早渐新世	2750–2760	本研究	ZI-6-LO (2750–2760)	本研究
U-1	番禺低 突起	始新世	3294–3297	本研究	U-1-EO (3294–3297)	本研究
U-2	番禺低 突起	早中新世	2530–3495	本研究	U-1-LM (3430)	本研究
U-2	番禺低 突起	晚渐新世	3560–3950	本研究	U-1-UO (3815)	本研究
U-2	番禺低 突起	早渐新世	4010–5070	本研究	U-1-LO (4302)	本研究
ZII-1	珠二凹陷	晚渐新世	3346–3617	本研究	ZII-1-UO (3379–3536)	Compiled data from

第 6 章 南海北部物源演化特征及其指示意义

						Shao et al. (2016)
ZII-1	珠二凹陷	早渐新世	3622–3736	本研究	ZII-1-LO (3713–3726)	Compiled data from Shao et al. (2016)
ZII-1	珠二凹陷	始新世	3748–4036	本研究	ZII-1-EO (3766–3950)	Compiled data from Shao et al. (2016)
ZII-2	珠二凹陷	早中新世	2760–3040	本研究	–	–
ZII-2	珠二凹陷	晚渐新世	3050–4460	本研究	ZII-2-UO (3190–3200)	Compiled data from Shao et al. (2016)
ZII-2	珠二凹陷	早渐新世	4460–4580	本研究	ZII-2-LO (3730–3910)	Compiled data from Shao et al. (2016)
ZII-3	珠二凹陷	晚渐新世	1800–1860	本研究	ZII-3-UO (1850–1855)	Compiled data from Shao et al. (2016)
ZII-3	珠二凹陷	早渐新世	–	本研究	ZII-3-LO (1875–1880)	Compiled data from Shao et al. (2016)
ZII-4	珠二凹陷	中中新世	2088–2644	本研究	–	–
ZII-4	珠二凹陷	早中新世	2730–2910	本研究	ZII-4-LM (2926)	本研究
ZII-4	珠二凹陷	晚渐新世	2930–3170	本研究	ZII-4-UO (2946–2971)	本研究
ZII-4	珠二凹陷	始新世	3190–3525	本研究	–	–
ZII-5	珠二凹陷	早中新世	3440–3540	本研究	–	–
ZII-5	珠二凹陷	晚渐新世	3540–3955	本研究	ZII-5-UO (4040–4300)	本研究
ZII-6	珠二凹陷	早中新世	2472–2585	本研究	–	–
ZII-6	珠二凹陷	晚渐新世	2640–2750	本研究	–	–
ZII-6	珠二凹陷	早渐新世	2755–3205	本研究	–	–
ZII-6	珠二凹陷	始新世	3260–3320	本研究	–	–

表 6.2 南海北部琼东南盆地钻井样品信息

钻井名称	构造单元	年代	地化分析 取样深度 /m	资料来源	锆石 U-Pb 定 年取样深度 /m	资料来源
------	------	----	--------------------	------	--------------------------	------

第 6 章 南海北部物源演化特征及其指示意义

Y19	琼东南盆地	晚渐新世	-	-	3900-3920	Compiled data from Shao et al. (2016)
Y19	琼东南盆地	早渐新世	-	-	5061-5064	Compiled data from Shao et al. (2016)
YC19	琼东南盆地	早中新世	4241-4421	本研究	-	-
YC19	琼东南盆地	晚渐新世	4436-4780	本研究	-	-
YC19	琼东南盆地	早渐新世	4796-5067	本研究	-	-
LS33	琼东南盆地	早中新世	3405-3673	Li et al. (2014) ^[254]	-	-
LS33	琼东南盆地	晚渐新世	3691-3931	Li et al. (2014)	-	-
LS33	琼东南盆地	早渐新世	3940-4330	Li et al. (2014)	4030-4201	Xiu et al. (2017) ^[255]
QE	琼东南盆地	上新世	2510-3060	本研究	QE-P (2775)	本研究
QE	琼东南盆地	早中新世	3065-3630	本研究	QE-LM (3444)	本研究+compiled data
QE	琼东南盆地	晚渐新世	3636-4074	本研究	QE-UO (3870)	本研究
QE	琼东南盆地	早渐新世	4080-4110	本研究	-	-
QW	琼东南盆地	晚上新世	2205-3175	本研究	-	-
QW	琼东南盆地	早上新世	3180-3748	本研究	QW-P (2665-3666)	本研究
QW	琼东南盆地	早中新世	3750-4000	本研究	QW-LM (3766-3950)	本研究
LS4	琼东南盆地	晚渐新世	4444-4802	本研究	-	-
LS4	琼东南盆地	早渐新世	4826-4930	本研究	-	-
YC13	琼东南盆地	早中新世	3200-3448	本研究	-	-
YC13	琼东南盆地	晚渐新世	3634-3909	本研究	-	-
YC13	琼东南盆地	早渐新世	3936-4149	本研究	-	-
B1	神狐隆起	前新生代基底	3490-3530	本研究	3484-3580	本研究
B2	琼东南西侧基底	前新生代基底	2146-2326	本研究	2326	本研究
B3	西沙隆起	前新生代基底	1263	本研究	1263	Compiled data

6.1.1 南海北部潜在源区特征

古生代中期至早中生代，印支地块与华南大陆之间发生持续俯冲碰撞挤压过程，最终导致古特提斯洋闭合^[92, 220]。在此期间，印支运动造成了强烈的碰撞拼合现象，并保留大量岩浆和构造热事件记录。印支运动在早三叠世达到顶峰，广泛形成片理、韧性变形和变质剪切构造^[91]。残留下来的基性与超基性蛇绿岩套和混杂堆积可能反映古特提斯洋的存在^[256]，研究者曾在 Song Ma、Song Da、哀牢山及其他越南东部和北部褶皱带内发现相关地质记录^[257, 258]。此外，在此期间发生的挤压作用还引发了 Kontum Massif 高地的形成，该高地由大套高级变质岩和岩浆岩复合体组成^[259, 260]。之后些规模巨大的山脉经历剥蚀抬升过程，逐渐转变为相对平坦的地势。在渐新世至中新世时期，哀牢山—红河断裂带发生左行剪切走滑作用，也可能引发了特定岩石类型在空间上的重构现象^[261]。如今，越南北部—中部广泛分布古—中生代砂岩，灰岩，花岗岩和基性—超基性岩体（图 6.1A）。与流经印支地块与华南大陆板块边界的现代红河不同的是，其 U-Pb 年龄谱系以 260 Ma 和 430 Ma 为主要峰值，且这两个峰值比例几乎相同，以及一个集中在大约 945 Ma 的次要年龄峰值，特别是缺乏年轻的新生代年龄组分^[262]（图 6.1B）。

海南岛也发育了陡峭山坡和下切河道，并向南海北部输送了大量碎屑物质^[263]。海南岛母岩几乎全部由中-酸性侵入岩组成，仅在其北部地区出露有限的年轻年龄玄武岩（图 6.1A）。锆石 U-Pb 年龄谱系呈现出明显的双峰分布模式，集中在燕山期（约 100 Ma）和印支期（约 235 Ma）^[264-266]（图 6.1B）。除了来自周围大陆或岛屿的提供的沉积物之外，南海北部盆地基底也可能提供一定物质来源，从而影响整体沉积格局。基底钻孔 B1 和 B2 证实，锆石 U-Pb 年龄以燕山期峰值（约 145 Ma）为主，超过锆石颗粒总数的 90%（图 6.1B）；如今盆地内的局部隆起区已淹没在海底之下。

作为南海北部周缘地区重要的河流水系之一，研究证实珠江向南海北部盆地输入大量陆地沉积物（图 6.1A）。珠江起初从一个小规模河流开始发育，在晚渐新世至中新世，上游逐渐向西部内陆地区溯源侵蚀，开始搬运来自碳酸盐岩和其他类型沉积岩源区的碎屑物质^[169, 267]。现代珠江的西部支流以古元古代—中生代（2495–160 Ma）的锆石年龄为特征，具有印支期、加里东期和吕梁期的多个峰值^[235, 268]。相比之下，穿过华南大陆沿海花岗岩源区的的东北支流则以更年轻、范围更窄的锆石年龄为主（950–170 Ma），具有更明显的中生代峰值和较小的古生代年龄组分^[102]。

现代红河沿哀牢山-红河剪切带向东南方向延伸，流经复杂的母岩源区，其上游主要是中生代沉积岩，而下游则广泛出露片麻岩和片岩^[261]（图 6.1A）。由于青藏高原新生代经历剧烈隆升，红河在历史时期可能出现水系重组现象，因此从 2500 Ma 到 30 Ma 的宽广年龄范围只能代表现代地形格局下红河物源的特征^[269]（Fig. 6.1B）。值得注意的是，现代红河中独特的喜山期年龄峰值也非常明

显。

总的来说,珠江流域、现代红河、海南岛以及南海盆地内局部隆起区母岩都表现为相似的稀土元素右倾配分模式 (Fig. 6.1C)。尽管不同源区稀土元素总含量之间存在差别,但与澳大利亚后太古代页岩 (PAAS) 相比,轻稀土元素 (LREE) 富集,具有明显的 Eu 负异常,证实大多数源区为酸性或沉积岩特征。然而,对于越中地区的母岩特征,其稀土元素配分模式发生了显著变化。正如之前提到的,中南半岛在早三叠世经历了剧烈的挤压和变形过程,很大可能导致了大量玄武岩和其他超基性-基性岩的形成与出露,正如明显的 Eu 元素正异常所示。地震剖面显示,莺歌海盆地东方气田深水沉积发育大规模海底扇构造。本研究对靠近中南半岛大陆边缘的 DF 钻孔 (可代表由越中河流搬运而来的沉积物) 开展元素地球化学研究,也证实来自越南中部崑松高地的大量陆源物质,该钻孔发现的明显 Eu 元素富集与其他具有典型 Eu 元素亏损的源区具有显著差别。

第 6 章 南海北部物源演化特征及其指示意义

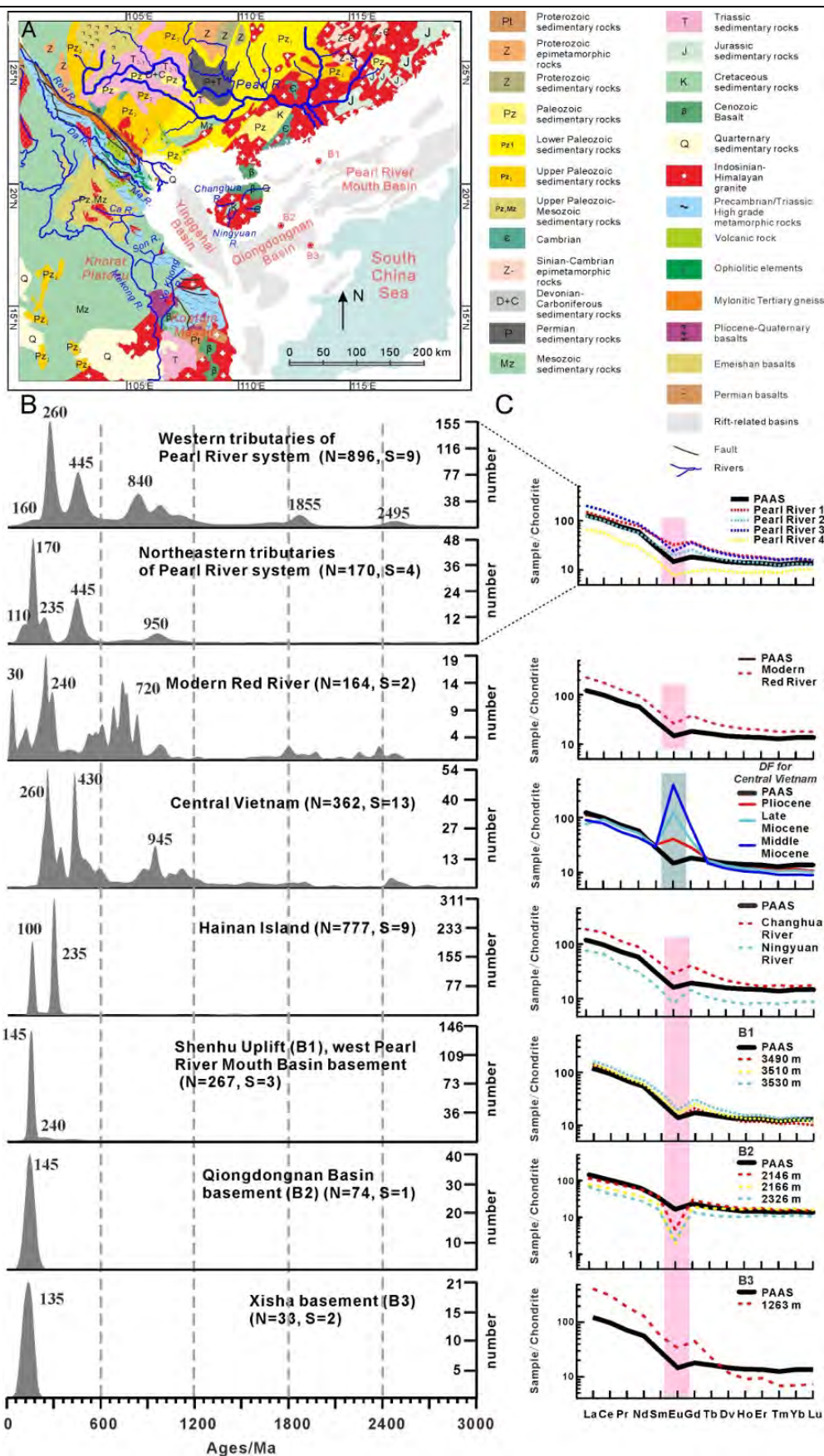


图 6.1 南海北部潜在源区 A) 岩性分布图; B) 碎屑锆石 U-Pb 年龄谱系; C) 稀土元素配分曲线

Fig. 6.1 (A) Simplified geological map of the potential source areas of the South China Sea basins, with tectonic units including the Pearl River Mouth Basin, Qiongdongnan Basin, Red River fault zone, Song Ma fault zone, Song Ca fault zone, Kontum Massif, and Khorat Plateau (based on the geological map of, Chinese Academy of Geological Sciences, 1975). Major drainage systems include the Pearl River, Red River, Mekong River, Changhua River, and Ningyuan River. (B) Compilations of published and unpublished detrital zircon U-Pb ages are displayed for different potential source areas. S—number of samples; N—number of concordant analyses. (C) Chondrite normalized rare earth element (REE) patterns for different sources including Pearl River tributaries (Zhang et al., 2012), modern Red River (Zhao et al., 2015a), Central Vietnam (well Dongfang [DF]), Hainan Island rivers (Shao et al., 2010), western Pearl River Mouth Basin (B1 for Shenhu Uplift), eastern Qiongdongnan Basin (B2), and Xisha basement (B3) are also shown. PAAS—post- Archean Australian shale.

6.1.2 南海北部盆地碎屑锆石 U-Pb 年龄结果

1. 珠江口盆地

始新统样品：本研究中大部分谐和锆石的 Th/U 值均大于 0.1，表明这些锆石为岩浆锆石。始新世盆地沉积记录仅局限于南海北部的东部凹陷（图 6.2），其碎屑锆石 U-Pb 年龄主要表现为燕山期峰值。然而，钻孔 ZI-1、ZI-2 和 ZI-3 始新统样品除具有中生代主峰外，还发现少数次要年龄，峰值集中在 435 Ma、725 Ma 或 2320 Ma，整体年龄谱系相对较宽广；相比之下，样品 ZI-4-EO、U-1-EO 和 ZII-1-EO 仅包含单一、明显的燕山期峰值。

下渐新统样品：靠近华南沿海地区的样品 ZI-6-LO 显示出一个狭窄的燕山期中生代峰值（110 Ma），而来自珠一凹陷西南部的样品 ZI-5-LO 则具有典型的燕山期、印支期、加里东期和若干零星分散的元古代锆石，整体表现为典型的多峰模式。特别的是，样品 ZI-5-LO 燕山期锆石几乎是其他年龄锆石数目的两倍。然而，位于更南部地区的样品 U-2-LO 显示出明显的双峰模式，包括燕山期（165 Ma）和加里东期（440 Ma）以及少量元古代锆石。尽管具有更多的年龄较老的锆石组分，以及明显的元古代峰值（955 Ma），样品 ZII-2-LO 仍然表现两个主要峰值，其中加里东期年龄峰值（410 Ma）占比较大，特征类似 U-2-LO。相比之下，样品 ZII-1-LO 和 ZII-3-LO 都只有单一的燕山期峰值，样品 ZII-1-LO 中还出现了少数三叠系甚至古生代-元古代锆石。

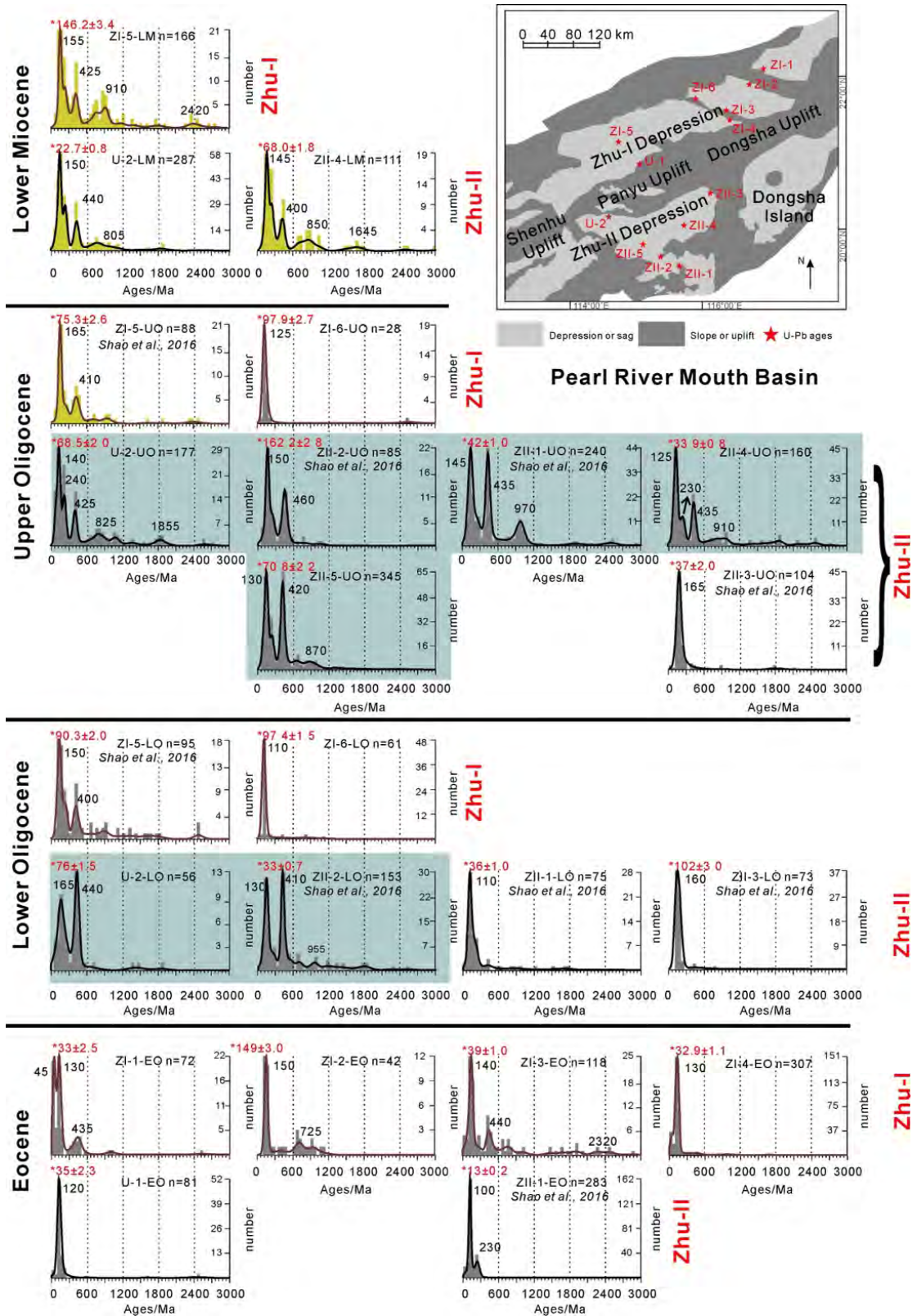


图 6.2 南海北部珠江口盆地（珠一和珠二凹陷）始新—早中新统样品碎屑锆石 U-Pb 年龄谱系^[181]

Fig. 6.2 Histograms and probability density distribution plots for detrital zircon U-Pb ages of the Pearl River Mouth Basin samples from Eocene to lower Miocene with characteristic age peaks

numbered (Ma). The youngest zircon U-Pb age (Ma) in red is marked with * in the upper left corner. “n” represents the number of concordant analyses relative to all grains. Data of wells ZI-5, ZII-1, ZII-2, and ZII-3 published by Shao et al. (2016) are included and re-analyzed for comparison. Different patterns of age spectra indicating different provenances are highlighted with yellow or bluish-gray shades. Locations of these boreholes are shown in the map in the upper right corner. The relationship of compiled wells and samples with original data are indicated in Table 6.1 [181].

上渐新统样品：样品 ZI-5-UO 主要为燕山期和加里东期峰值，几乎没有较老的年龄组分。值得注意的是，与 410 Ma 峰相比，165 Ma 峰更明显。样品 U-2-UO 具有多峰模式，主要为 140 Ma、240 Ma 和 425 Ma 峰，及次要的 825 Ma 和 1855 Ma 峰，燕山期是加里东期锆石数目的两倍。对于珠江口南部的珠二凹陷，ZII-1、ZII-2、ZII-4 和 ZII-5 井的上渐新统样品均以燕山期和加里东期主峰为特征。与北部同时代样品相比，这四口钻井的加里东期峰值显然更高，尤其对于 ZII-1、ZII-2 和 ZII-5 井。ZII-1 和 ZII-5 井还可见晋宁期峰值（970 Ma 和 870 Ma）。样品 ZII-1-UO 锆石年龄组合与其自身下渐新统的年龄谱系完全不同，特征更接近样品 ZII-2-UO 和 ZII-5-UO。样品 ZII-2-UO 中加里东期峰只有燕山期峰大小的一半，这与其下渐新统样品中的双峰模式不同。至于样品 ZII-3-UO，除了 155 Ma 的燕山期峰，还包含若干较老年龄的锆石颗粒，在较老地层中则缺失这类锆石年龄组分。

下中新统样品：珠江口盆地的所有样品都具有典型的多峰宽谱特征。每个样品中燕山期锆石的主导性明显。具体而言，在 ZI-5-LM 样品中，前寒武纪锆石颗粒的比例急剧增加。这也在南部井 U-2 和 ZII-4 中观察到，其中加里东期族群在比例上大幅减少。

2. 琼东南盆地

与珠江口盆地不同时代、不同凹陷样品之间明显的变化相比，琼东南盆地自早渐新世以来锆石 U-Pb 年龄变化并不显著（图 6.3）。位于西沙隆起附近的 Y19 井和 LS33 井下-上中新统地层样品普遍表现强烈的印支期峰值（220–250 Ma）和较弱的燕山期峰值（90–145 Ma）。另外，除样品 Y19-UO 以印支期峰为主，琼东南盆地中央凹陷还钻遇上渐新统样品 QE-UO，具有燕山期、印支期、加里东期和晋宁期峰值，以及少量吕梁期锆石，表现明显的多峰年龄模式。有趣的是，该样品与位于珠江口盆地中南部的样品 U-2-UO 在年龄组合上显示出一定的相似性。对于中新统至上新统样品，QW 井和 QE 井在一定程度上都类似于样品 QE-UO 的多峰模式。然而，需要详细说明的是：样品 QE-P 与样品 QE-LM 差别很大，QE-P 燕山期峰占比很大，而印支期、加里东期和晋宁期年龄占比均较小；位于越南中部附近的 QW 井在 U-Pb 年龄组合上变化不大，但其加里东期锆石数目在中新世至上新世仍显示出下降趋势；随着时间的推移，QE 和 QW 井的年龄谱系均呈现更宽广的趋势。

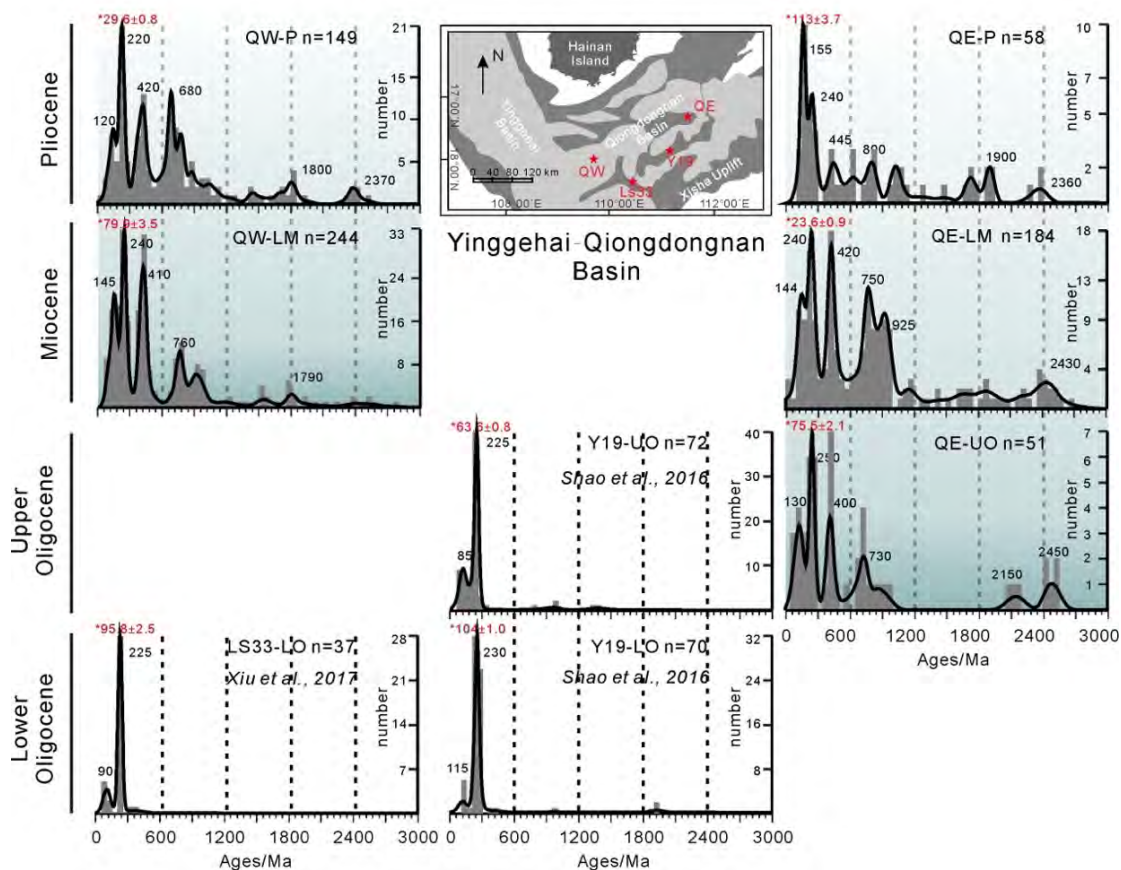


图 6.3 南海北部琼东南盆地渐新统-上新统样品碎屑锆石 U-Pb 年龄谱系^[181, 255]

Fig. 6.3 Histograms and probability density distribution plots for detrital zircon U-Pb ages and corresponding chondrite normalized rare earth element (REE) patterns of Qiongdongnan Basin, South China Sea, from lower Oligocene to Pliocene with typical age peaks numbered (Ma). The youngest zircon U-Pb age (Ma) in red color is marked with * in the upper left corner. “n” represents the number of concordant analyses relative to all grains. Samples QE-LM, well LS33, and Y19 are partially published by Cao et al. (2015), Xiu et al. (2017), and Shao et al. (2016). Locations of these boreholes are shown in the map at the top. The relationship of compiled wells and samples with original data are indicated in Table 6.1. Provenance-indicative multimodal age spectra are shaded^[181, 255].

6.1.3 南海北部盆地稀土元素含量及配分模式

1. 珠江口盆地

稀土元素球粒陨石标准化配分模式显示，从始新世到中新世，轻稀土元素普遍富集。在珠一凹陷东北部 ZI-1 至 ZI-4 井中，Eu 元素富集现象非常明显（图 6.4）。然而，更南部的 U-1 和 ZII-1 井则表现为强烈的 Eu 元素亏损特征。总体而言，珠江口盆地始新统样品的 Eu 元素异常现象在不同区域差异明显。ZI-5、ZI-6 和 U-2 井的下渐新统样品与 PAAS 配分模式相近，总稀土元素含量高度一致，具有明显的 Eu 元素负异常。相反，珠二凹陷绝大多数样品（除 ZII-1 井外）均

表现 Eu 元素正异常。特别需要注意的是，ZI-6 和 ZII-3 井的总稀土元素含量比 PAAS 低。晚渐新世期间，尤其是珠二凹陷中部至南部（ZII-2、ZII-4、ZII-5 井）可见更广泛、更明显的 Eu 元素正异常，这与珠一凹陷主要是 Eu 元素亏损的情况相反。此外，相较于 PAAS 的整体分布模式，仅 ZII-3 井显示出明显较低的总稀土元素含量。下中新统样品的 Eu 元素正异常现象不明显，仅限于 ZII-4 和 ZII-5 井，珠江口盆地大多数井该时期显示出一定程度的 Eu 元素负异常。

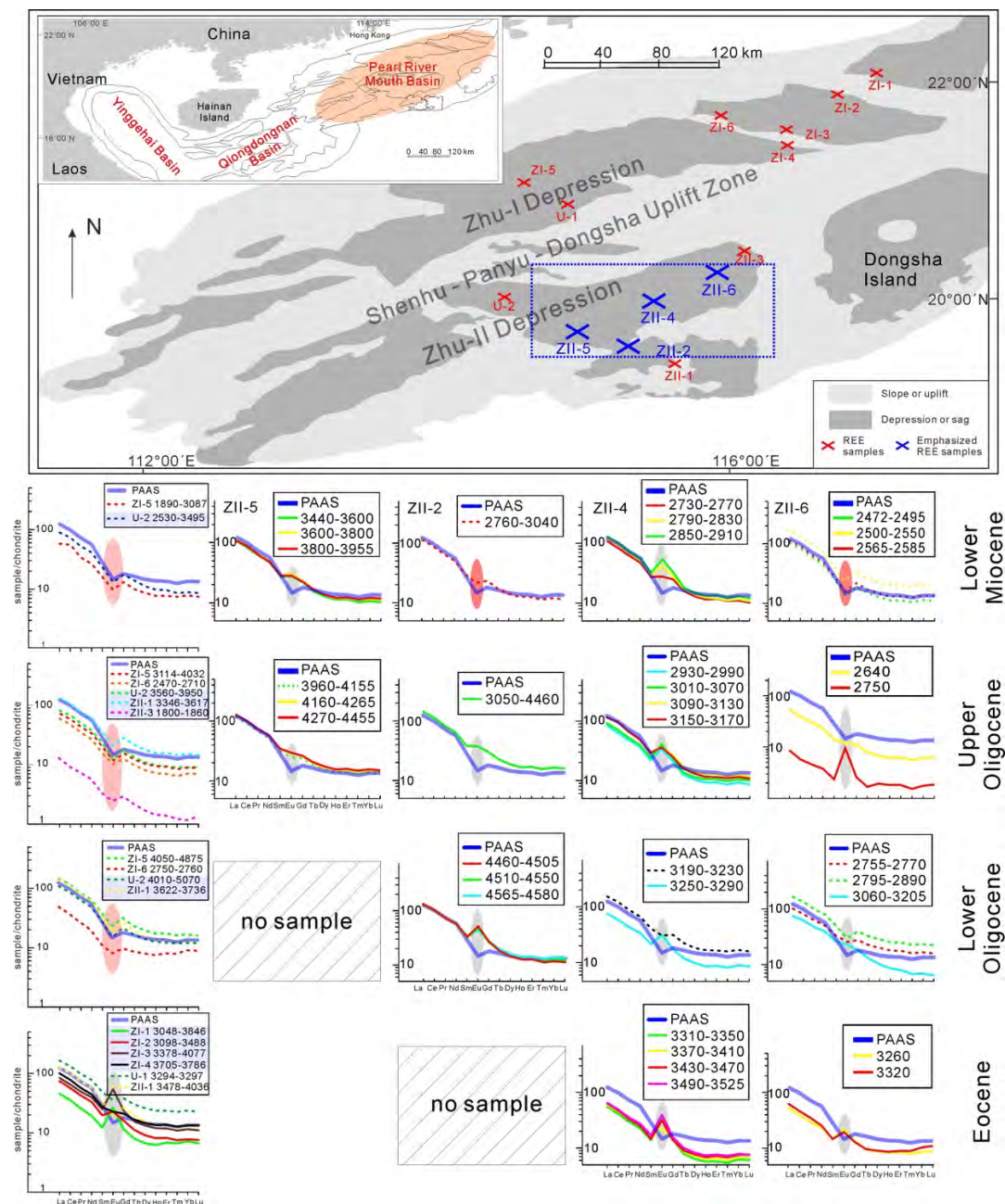


图 6.4 南海北部珠江口盆地始新–下中新统样品稀土元素配分曲线特征

Fig. 6.4 Chondrite normalized rare earth element (REE) patterns of Eocene–lower Miocene samples from the Pearl River Mouth Basin, South China Sea. Eu-anomaly values are highlighted on each plot with gray (positive) or red (negative) shades. The orange shaded Pearl River Mouth

Basin in the upper left map is zoomed to display the locations of studied boreholes. Analyses with red crosses are shown on the bottom left and analyses with blue crosses (ZII-2, ZII-4, ZII-5, and ZII-6) are more emphasized on the bottom right. Intervals in each REE pattern plot indicate the depth analyzed. PAAS— post-Archean Australian shale.

2. 莺歌海-琼东南盆地

前人研究显示, 靠近西沙隆起的 LS33 下渐新统样品显示出典型的轻稀土元素富集模式, 具有明显的 Eu 元素负异常。本研究中的井 QE、LS4、QW、YC19 和 YC13 位置如图 6.5 所示, 其稀土元素含量及配分模式结果显示, 从西到东, 除部分靠近盆地隆起或大陆边缘的钻孔 (如 LS33 和 QE (4080-4104 米)) 呈现 Eu 元素亏损, 正异常现象广泛存在。在上渐新统样品中, Eu 元素异常现象显示出一定区域性差异: 最西部的 YC13 井以较强的 Eu 富集为特征; 向东, YC19 井表现 Eu 亏损。在琼东南盆地的西部凹陷中, LS4 井不同地层样品变化不大。对于 QW 井, 除 3900-3948 米样品表现轻微的 Eu 负异常, 其他深度的样品均为正异常。QE 井位于最东部, 大多数样品 Eu 元素亏损, 但 3162-3168 米深度的样品出现较强的正异常值; 在 3636 和 4074 米之间也可见强烈的 Eu 元素亏损现象。对于莺歌海-琼东南盆地中新统样品, Eu 元素异常值分布特征也表现出明显的区域性差异。

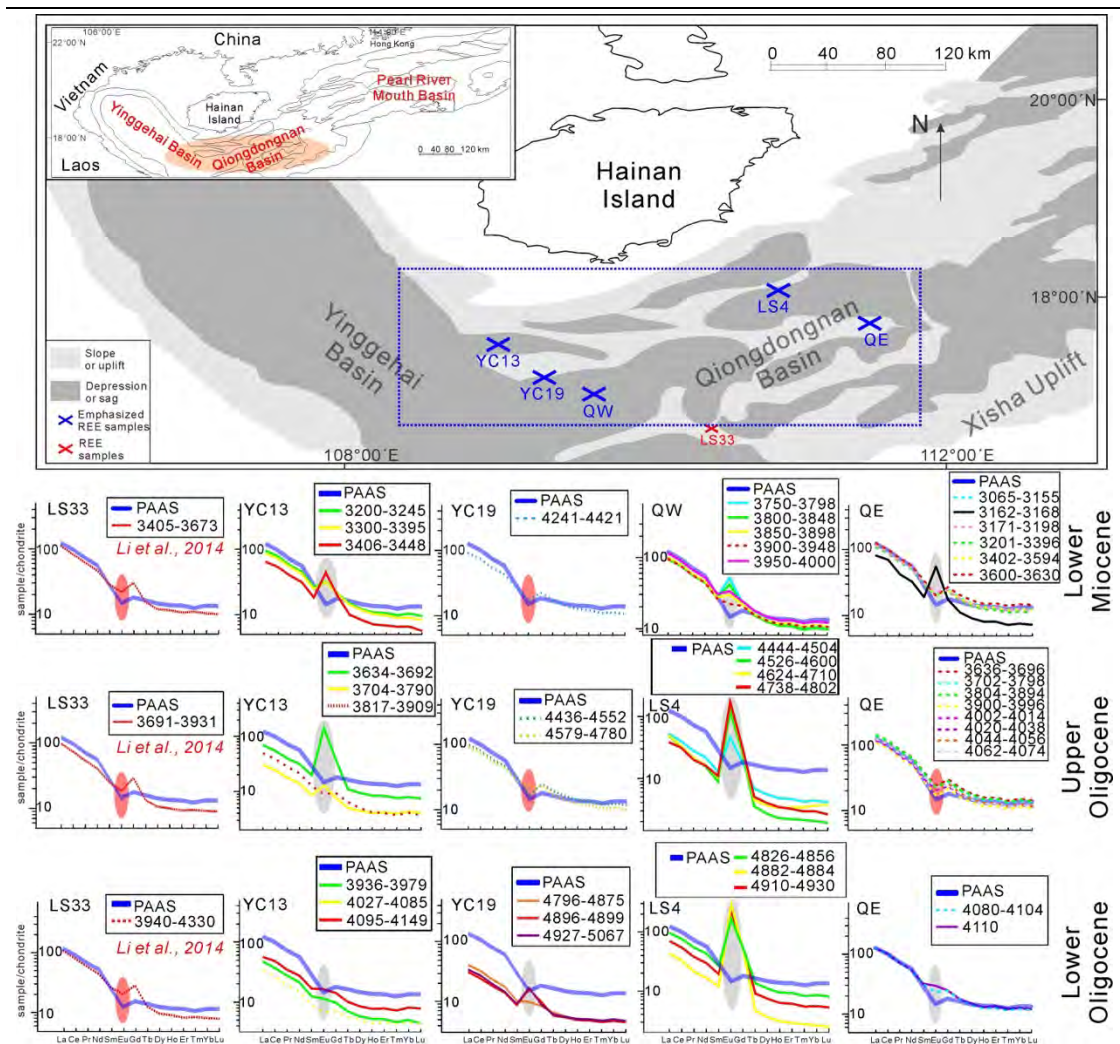


图 6.5 南海北部琼东南盆地中渐新统-下中新统样品稀土元素配分曲线特征^[254]

Fig. 6.5 Chondrite normalized rare earth element (REE) patterns of Eocene-lower Miocene samples from the Yinggehai-Qiongdongnan Basin, South China Sea. Eu-anomaly values are highlighted on each plot with gray (positive) or red (negative) shades. The orange shaded parts of the Yinggehai-Qiongdongnan Basin in the upper left map is zoomed to display the locations of studied boreholes. Analyses with red crosses (LS33; Li et al., 2014) are shown on the bottom left and analyses with blue crosses (YC13, YC19, QW, QE) are more emphasized on the bottom right. Intervals in each REE pattern plot indicate the depth analyzed. PAAS—post-Archean Australian shale^[254].

6.1.4 南海北部“源—汇”系统重建

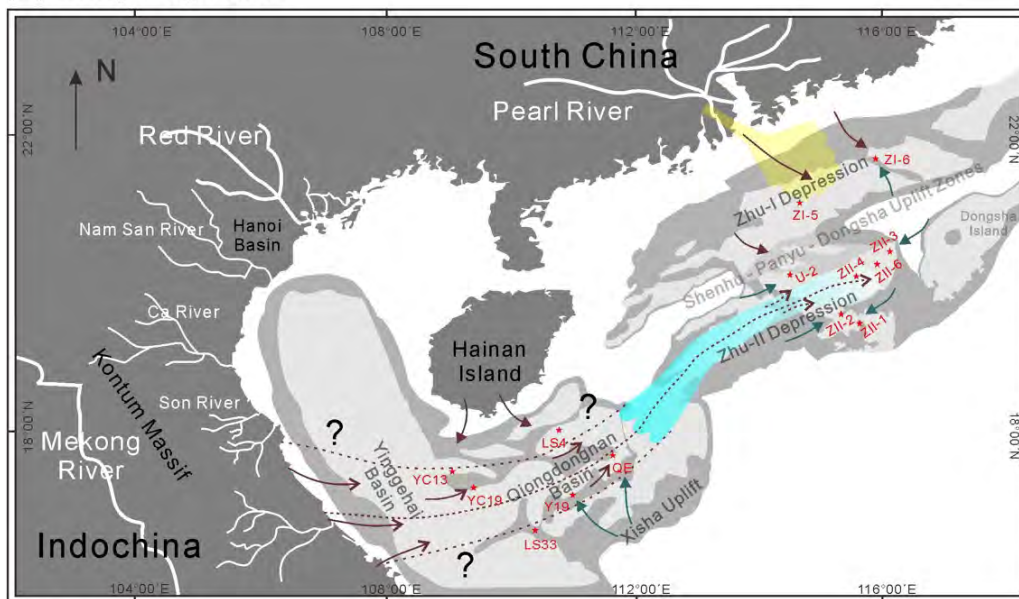
1. 始新世

将碎屑锆石 U-Pb 年龄谱系特征和稀土元素配分模式相结合的方法是一种重建“源—汇”系统的重要手段。珠一凹陷东北部始新世时期表现明显的燕山期峰值和较强烈的 Eu 元素正异常，说明受局部物源影响，比如盆地内部的古隆起，

东沙隆起带岩浆活动和新发现的镁铁质橄岩玄武岩可能是造成沉积物中 Eu 元素富集的重要原因之一。然而，部分样品中的加里东期和元古代锆石还说明该地区可能遭受镁铁质基底岩体和某些曾流经华南沿海地区的支流，如韩江这两种物源的共同影响。珠一凹陷始新世时期基本不受长距离搬运的影响（图 6.6A）。

位于珠江口盆地更南侧的样品 U-1-EO 和 ZII-1-EO 主要包含下白垩统锆石（伴随 230 Ma 的次要峰值），指示该时期受单一母岩源区的影响，以近距离快速搬运方式为主要特征。同时强烈的 Eu 负异常表明为酸性岩或沉积岩源区。然而，ZII-4 井始新统沉积物（样品深度 3310-3525 米）呈现强烈 Eu 正异常，可能曾受基性-超基性源区影响。前人研究表明，早新生代断陷期，南海西部地区可能曾与中南半岛越中地区相连，广泛发育剥蚀区。而作为一个潜在的基性-超基性源区，越中-南海西侧高地剥蚀下来的沉积物很有可能被搬运至珠二凹陷局部区域。但由于缺乏足够可靠的 U-Pb 年代学数据，西部物源仍需进一步地质资料证实。总体而言，南海北部在始新世以短距离快速搬运方式为主，陆上河流水系对盆地整体沉积格局影响有限（图 6.6A）。

(B) Early Oligocene



(A) Eocene

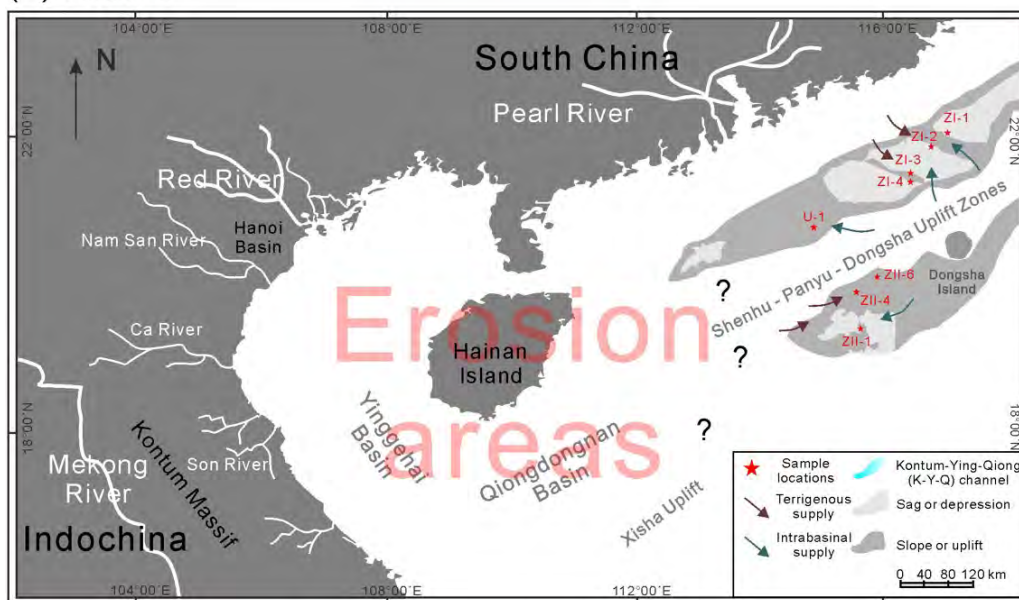


图 6.6 南海北部 A) 始新世; B) 早渐新世“源—汇”系统演化及搬运路径示意图

Fig. 6.6 Schematic source-to-sink evolution model for (A) Eocene and (B) early Oligocene in the northern South China Sea. Arrows show direction of sediment transport routes from different potential source areas to the studied locations. The zone of influence of the paleo-“Kontum-Ying-Qiong” river system is shaded in blue. Beginning influence of the Pearl River system is shaded in yellow.

2. 早渐新世

南海北部沉积物组成自早渐新世开始发生变化（图 6.6B）。与珠一凹陷东北部始新世时期出现的 Eu 元素富集现象相比，下渐新统地层可能开始受混合物源影响，ZI-5 和 ZI-6 井稀土元素配分模式更趋向与 PAAS 一致，Eu 元素正异常强

度减弱。特别指出的是,井 ZI-6 具有狭窄的燕山期峰和明显的 Eu 元素负异常,可能表明该地区受到了东沙地区火山活动或附近盆地内古隆起的共同影响。相比之下,井 ZI-5 表现较宽广的年龄谱,与 ZI-3 井始新统沉积物的年龄组成类似。然而,该样品具有明显的 Eu 元素亏损,可能揭示其遭受更强烈的酸性岩-沉积岩物源的影响,因此与 ZI-3 井有所区别(图 6.6)。早渐新世古珠江对珠江口盆地沉积格局的影响仍然相当有限,仅局限在珠一凹陷;然而地震剖面显示,珠二凹陷北部地区发育大规模向东的前积构造^[170]。本研究中的井 U-2 和 ZII-2 下渐新统样品表现典型的双峰模式,且加里东期峰和燕山期峰之间近乎相等的占比,与越中物源的 260 Ma、430 Ma 的主峰和 945 Ma 的次峰具有较高的一致性,强烈指示沉积物可能来自西侧地区。另外,ZII-2 井 Eu 正异常和 U-2 井 Eu 负异常在早渐新世同时存在,该现象也一定程度上支持了珠二凹陷西北部地区此时受北部和西部混合物源模式的影响:更南侧的 ZII-2 井更可能接受西部源区的碎屑物质,而受华南大陆沿海火成岩源区的影响较小。与此同时,样品 ZII-1-LO 和 ZII-3-LO 具有狭窄的燕山期峰,表明珠二凹陷东部和南部地区经历沉积物快速堆积,包含了大量中生代年龄的锆石。

相对珠江口盆地,西侧的莺歌海和琼东南盆地更大程度上受到钻井资料的制约。简单而言,越中地区、海南岛、西沙隆起和广大的盆地基底组成了多个潜在源区。海南岛双峰年龄模式表现为明显的燕山期和印支期峰,指示海南岛对井 Y19 和 LS33 物质贡献有限(图 6.6)。这些钻井以三叠系年龄峰为主,伴随 90 Ma 或 115 Ma 的较小年龄组分,而琼东南盆地北部基底仅显示单一的 145 Ma 燕山期峰,因此基底产生的影响相对较小。正如第 6.1.1 节所示,只有越中地区显示 Eu 富集特征,而其他物源区都表现明显的负异常。稀土元素地球化学结果显示,在莺歌海-琼东南盆地中,位于盆地中部的井 YC13、YC19、LS4 和 QE 普遍以 Eu 正异常为主,该现象与来自越中的镁铁质沉积物特征一致,而印支运动期间越中地区曾发生了强烈岩浆活动,也从区域构造的角度为该现象提供了一定合理性。而对于远离这一大规模 Eu 正异常带的区域,LS33 井可能受到附近隆起区的影响,正如西沙基底发育中生代片麻岩。此外,位于更东侧的 QE 井深度 4080-4110 米的样品表现 Eu 元素正负异常混合的特征,指示还受到其他酸性岩/沉积岩源区的影响,海南岛、西沙基底或东部的神狐隆起均可能为该地区提供碎屑物质。

3. 晚渐新世

晚渐新世时期,珠一凹陷东北部仍然受到邻近酸性岩物源(华南大陆东南沿海地区)以及东沙隆起火山活动(强度减弱)的影响(图 6.7A)。样品 U-2-UO 中多峰年龄组合模式显示,燕山期峰占比增加,而之前明显的加里东期信号急剧减弱。这种 U-Pb 年龄模式指示,来自珠江东北部支流对珠江口盆地沉积物的影响正逐渐取代来自西侧的越中源区的影响,表明珠二凹陷北部地区此时受

混合物源控制。尽管仍然具有较强烈的加里东期信号和部分前寒武年龄的锆石组分, 珠二凹陷大多数样品开始以燕山期峰为主, 且超过加里东期峰在整体年龄谱系所占的比例, 表明珠江流域已经开始越过番禺隆起, 向南输送大量陆源沉积物。然而, 珠二凹陷南部地区中的许多上渐新统样品仍然存在明显的 Eu 正异常现象, 例如 ZII-2, ZII-4 和 ZII-5 井, 代表大量基性-超基性物质经历远距离搬运过程, 最终沉积在该地区。特别强调的是, ZII-1 井该时期经历了从单峰到多峰的突变, 其与越中源区的 U-Pb 模式具有高度一致性, 强烈表明西部物源对其产生的影响。对于珠二凹陷东部地区, 本研究样品表现为 165 Ma 燕山期峰和明显的 Eu 负异常现象, 除华南大陆酸性火成岩源区之外, 也不能排除盆地内局部酸性岩物源的影响。

盆地内局部物源对琼东南盆地某些地区也产生了显著影响, 例如井 Y19, 其明显的 225 Ma 峰反映盆地内隆起区原地剥蚀而来的物质。位于东部的 QE 井上渐新统样品具有明显的印支期和加里东期峰, 与越中宽广的年龄组合特征一致, 表明该时期可能接收了大量来自西部镁铁质岩石源区的沉积物。然而, 位于越中的崑松地块 (Kontum Massif) 缺乏典型的燕山期峰, 而海南岛则显示出明显的印支期和燕山期双峰模式, 均不能完全解释 QE 井该时期样品的年龄谱系特征; 前人研究所示, 神狐隆起和西沙基底则一定程度上提供了部分物源^[270]。另外, 尽管显示出复杂的多峰年龄特征, 现代红河因其具有独特的 30 Ma 喜山期年龄组分, 因此基本不可能为其提供沉积物。综上所述, 越中地区、海南岛和局部隆起区可能共同影响琼东南盆地沉积格局。Eu 元素正异常独特的空间分布范围也恰好说明, 来自南海西侧越西地区的基性-超基性物质可能仅沿一定输送通道被搬运至东部地区; 而海南岛和西沙隆起作为酸性岩源区, 则对其他地区影响程度更大。

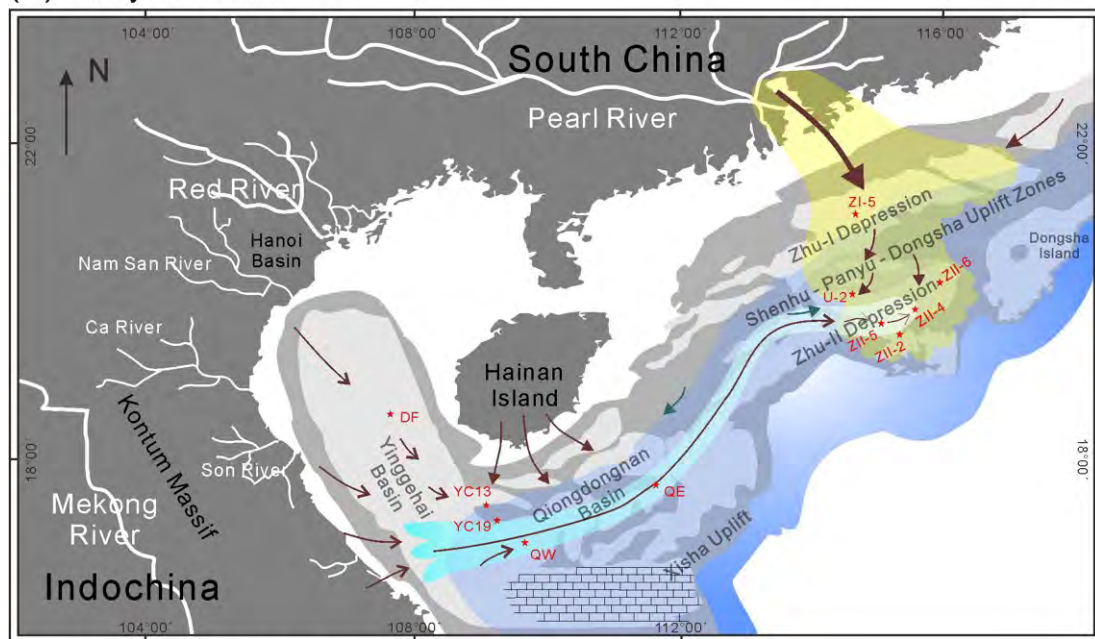
4. 中新世

早中新统样品 ZI-5-LM 中元古代锆石数目显著增加, 说明整个珠一凹陷自中新世以来持续受到远距离沉积搬运方式的影响 (图 6.7B), 珠江西部流域影响程度增加, 而来自华南沿海地区小规模河流的影响则显著降低。样品 U-2-LM 表现明显的燕山期信号, 更类似于珠江西部支流年龄特征, 说明与西部物源相比, 珠江物源影响更大。位于南部地区的样品 ZII-4-LM 显示典型多峰模式, 进一步说明珠江流域为珠二凹陷南部区域带来了大量沉积物。尽管 ZII-2 井表现 Eu 负异常, 但 ZII-4 和 ZII-5 井仍然在不同取样深度上具有 Eu 元素富集的特征, 表明仍持续接受镁铁质源区搬运而来的物质, 但影响逐渐减弱。

琼东南盆地早中新世后开始形成大量滨海-浅海沉积。琼东南盆地北部发育大规模深水浊积扇, 南部形成碳酸盐岩台地。西沙隆起不再是琼东南盆地南部区域的主要物源, 而是作为生物礁台地基底而发生沉降作用。QW 井表现为明显的印支期峰, 较高的加里东期和较小的晋宁期峰, 整体以 Eu 正异常为主, 表

明受到越中镁铁质物源的影响。相反，东部样品 QE-LM 中燕山期锆石比例增加，印支期峰为次要年龄信号，指示海南岛源区影响增强。Eu 正异常仅限于 YC13 井深度为 3200–3448 m、QW 井深度为 3750–4000 m 和 QE 井深度为 3162–3168 m 的样品，表明基性-超基性源区对盆地东部影响逐渐减弱。总体来看，越中基性物源区的影响从西向东逐渐减弱，并逐渐被其他酸性/沉积源区取代。

(B) Early Miocene



(A) Upper Oligocene

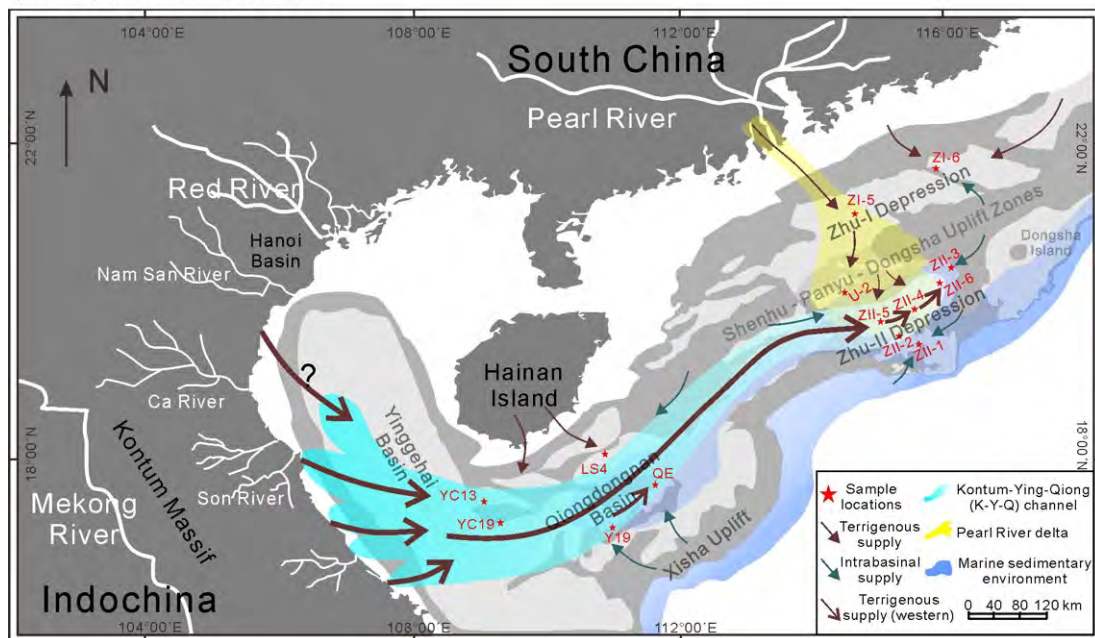


图 6.7 南海北部 A) 晚渐新世；B) 中新世“源—汇”系统演化及搬运路径示意图

Fig. 6.7 (A) Schematic source-to-sink evolution model for (A) late Oligocene and (B) early Miocene in the northern South China Sea. Arrows show direction of sediment transport routes from different potential source areas to the studied locations. The

“Kontum-Ying-Qiong” river system is shaded in blue. The influence of the Pearl River tributaries is shaded in yellow.

6.1.5 珠江流域与“崑一莺一琼”古河对南海北部沉积格局的影响

南海北部地区早新生代经历大规模裂谷阶段，南沙和巴拉望地块此时仍拼贴于华南大陆边缘。南海北部以沉积河流和湖沼相为主。印支半岛与华南大陆在早中生代可能曾发生剧烈的俯冲、碰撞、挤压、拼合与抬升作用，形成了越中地区广阔的造山带，包含大量的基性-超基性物质，很大程度上是古特提斯洋俯冲过程中的残留记录，具有独特的 Eu 元素正异常特征，与其他南海北部潜在源区在元素地球化学和锆石 U-Pb 年龄谱系上明显不同（图 6.1）。ZII-4 和 ZII-6 井始新沉积物可见强烈的 Eu 富集信号，指示珠二凹陷中-东部地区受到基性源区的影响；然而研究显示，盆地内局部物源以酸性岩为特征，表现为 Eu 负异常，如东沙隆起区。根据上述现象，本论文提出南海北部地区曾发育大型古河系统，在此命名为“崑-莺-琼”古河（图 6.6 和 6.7），与流经华南大陆火成岩源区的河流相比^[168]，这条沉积物输送系统可能长达上千公里，从西侧的越中地区一直延伸到东侧的巴拉湾和民都乐地区。

本论文首次揭示，下渐新统样品 ZII-2-LO 和 U-2-LO 显示强烈的加里东期年龄峰（410 Ma 和 440 Ma），证实了来自西部的基性岩源区。位于研究区最西侧的 YC13 井具有明显的 Eu 正异常信号，极大可能证实了越中地区为潜在的镁铁质物源区，为东部地区输送陆源沉积物。而这种强烈的 Eu 富集信号向东逐渐减弱，表现为 ZII-4（3190–3230 m）和 ZII-6（2755–2890 m）井中的 Eu 元素负异常现象。另一方面，琼东南盆地中则大规模出现轻微至显著的 Eu 正异常，进一步印证了基性-超基性物质搬运体系的存在。珠二凹陷中部的 ZII-2、ZII-4、ZII-5 和 ZII-6 井出现大量的 Eu 正异常，且表现与越中源区一致的 U-Pb 年龄谱系特征，显示西部物源的广泛影响。琼东南盆地 YC13 和 LS4 井上渐新统样品中 Eu 正异常现象更明显，比例和数量均大规模增加，说明受到“崑-莺-琼”古河搬运而来的沉积物的影响。但靠近海南岛的 YC19 和 QE 井也表现一定程度的 Eu 负异常，说明还可能受到酸性岩源区的影响。总的来说，这条搬运了大量基性物质的东西向古河很可能在晚渐新世到达了珠二凹陷东部地区，并与搬运大量酸性岩或沉积岩的珠江水系共同影响南海北部沉积格局。

珠江流域在早中新世进一步扩大了其对珠江口盆地南部凹陷的影响，Eu 元素正异常只出现在珠二凹陷的部分样品，包括样品 ZII-4（2730–2910 m）和 ZII-5（3440–3955 m）。此时，琼东南盆地中央凹陷 YC13、QW 和 QE 井可见 Eu 正异常。琼东南和珠江口盆地 U-Pb 年龄谱系显示，携带大量基性物质的“崑-莺-琼”古河在南海北部地区的影响已经大大降低：一方面，其东侧部分受到来自北部的珠江物源的干扰；另一方面，其西侧部分也受到酸性源区的混合作用，如海南岛。

珠二凹陷自中新世以来再也出现 Eu 富集现象，表明这条东西向古河已经严重萎缩并最终淹没至海下（图 6.8）。整个上新世期间，位于西侧的 QW 井包含 Eu 正异常信号，而东部 QE 井在都以负异常为主，指示基性物质仅局限于琼东南盆地西部。此外，上新世期间，样品 QE-P 开始出现大量的燕山期锆石，样品 QW-P 锆石 U-Pb 年龄谱系相对中新统样品则没有明显变化，表明酸性源区对琼东南东部地区影响较大。

早渐新世时期，只有珠一凹陷东北部地区受到流经华南大陆火成岩源区小规模古河的物源影响，而现代珠江在晚渐新世才开始形成。珠江影响起初可能仅局限于珠一凹陷西侧；与此同时，珠二凹陷接受了“崑-莺-琼”古河从西侧源区搬运而来的沉积物的影响。晚渐新世期间，珠二凹陷南部沉积物具有燕山期主峰和次要印支期、加里东期和晋宁期年龄组分，这些沉积物主要来自华南大陆沿海地区，经由古珠江搬运而来，表明珠江水系此时已经逐渐发展壮大至一定规模，越过番禺低隆起延伸至珠江口盆地南侧。自早中新世以来，珠江持续向整个珠一凹陷输送了大量沉积物，发育大规模深水扇，逐渐取代“崑-莺-琼”古河并在南海北部沉积格局中建立主导地位。

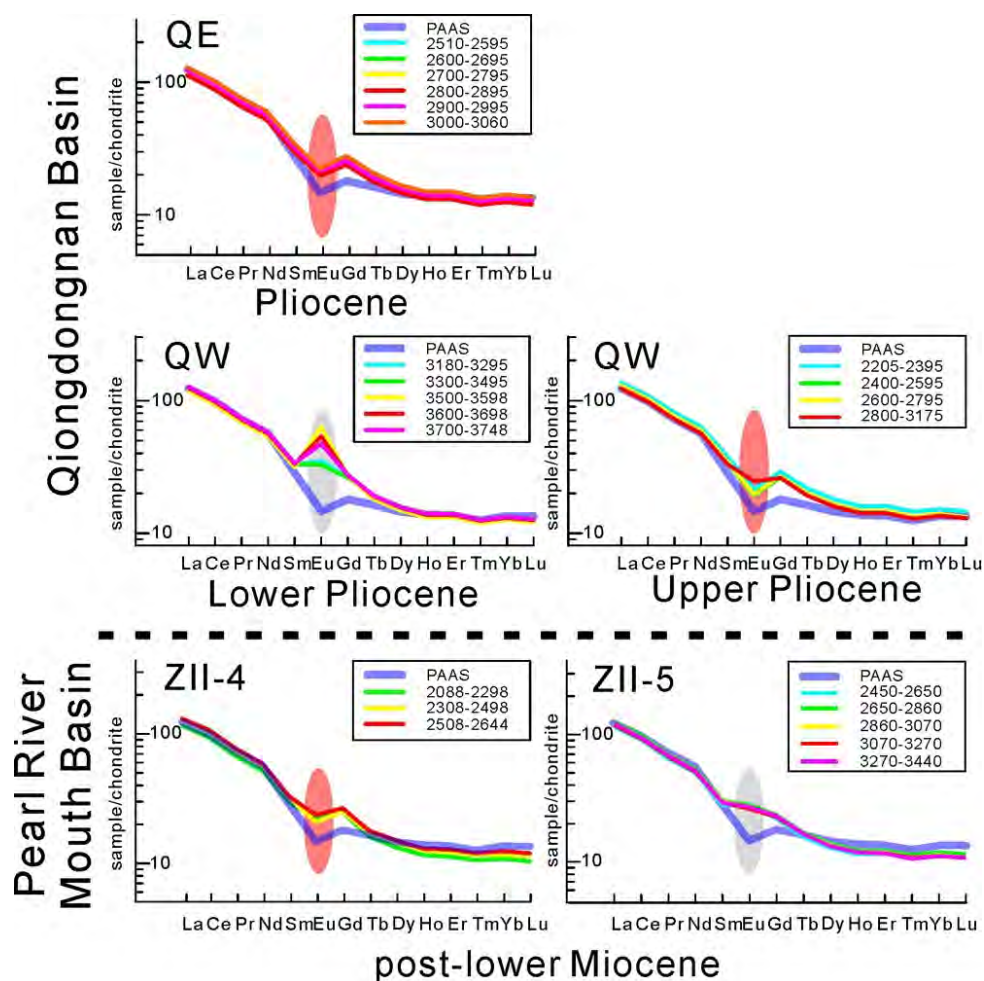


图 6.8 珠江口和琼东南盆地早中新世之后形成的沉积样品稀土元素球粒陨石标准化配分曲线特征

Fig. 6.8 Chondrite normalized rare earth element (REE) patterns of selected post-lower Miocene samples from the Pearl River Mouth (ZII-4 and ZII-5) and Qiongdongnan Basin (QW and QE), South China Sea. Eu-anomaly values are highlighted on each plot with gray (positive) or red (negative) shades. Intervals in each REE pattern plot indicate the depth analyzed. PAAS—post-Archean Australian shale.

6.2 中央峡谷晚中新世-上新世物源演变特征

本论文对南海北部晚中新世中央峡谷沉积物源演变特征开展研究，钻井位置如图 2.4B 所示；样品具体信息如表 6.3 所示。

表 6.3 南海北部琼东南盆地钻井样品信息

Table. 6.3 Stratigraphic position of analyzed samples in this study and published research (Wang et al. 2014; Cao et al. 2015)

钻井名称	构造单元	年代	样品名称	地化分析取样深度/m	资料来源	锆石 U-Pb 定年取样深度/m	资料来源
DF	莺歌海盆地	上新世	DF-1	900–2392	本研究	1105–2193	Wang et al. (2014)
DF	琼东南盆地	晚中新世	DF-2	2422–3234	本研究	2600–2898	Wang et al. (2014)
QW1	琼东南盆地	上新世	QW1-1	2205–3748	本研究	2665–3666	本研究
QW1	琼东南盆地	晚中新世	QW1-2	3750–4000	本研究	3766–3950	本研究
QW2	琼东南盆地	上新世	QW2-1	960–1810.5	本研究	-	-
QW2	琼东南盆地	晚中新世	QW2-2	1844–2020.8	本研究	-	-
QW3	琼东南盆地	上新世	QW3-1	1500–3610	本研究	-	-
QW3	琼东南盆地	晚中新世	QW3-2	3640–4124	本研究	-	-
QE	琼东南盆地	上新世	QE-1	2510–3065	本研究	-	-
QE	琼东南盆地	晚中新世	QE-2	3070–3630	本研究	3276	Cao et al. (2015) ^[264]
MW	琼东南盆地	中中新世	MW	3430–3616	本研究	-	-
MM	琼东南盆地	中中新世	MM	2910–3255	本研究	-	-
ME	琼东南盆地	中中新世	ME	2660	本研究	-	-
B1	北部湾盆地	前新生代基底	B1	1440–1490	本研究	1490	-
B2	琼东南盆地	前新生代基底	B2	2700	本研究	2700	-

B3	琼东南盆地	前新生代基底	B3	2146-2326	本研究	2166-2326	-
----	-------	--------	----	-----------	-----	-----------	---

6.2.1 上中新统-上新统样品碎屑锆石 U-Pb 年龄

本论文对莺歌海-琼东南晚中新统至上新统样品开展碎屑锆石 U-Pb 年龄谱系研究 (图 6.9)。位于研究区最西侧的样品 DF-1 和 DF-2 表现为相似的年龄组合特征, 其锆石频谱较为宽广, 包含燕山期、印支期、加里东期、晋宁期甚至吕梁期多个峰值。与 DF-1 相比, 上新统样品 DF-2 显示出比例更大的印支期峰 (~ 235 Ma)。对于琼东南盆地另外两口钻孔, 不同时代沉积的样品之间年龄组合差异更明显。QW1 井更靠近越中地区, 虽然从晚中新世到上新世均显示多个年龄峰值, 但样品 QW1-1 印支期 (240 Ma) 和加里东期 (410 Ma) 峰值比例几乎相同, 而 QW1-2 明显以印支期 (220 Ma) 为主, 加里东期 (420 Ma) 锆石数目急剧减少, 晋宁期 (680 Ma) 大幅增加。位于研究区最东侧的钻孔 QE 也在较年轻地层沉积物中发现较弱的加里东期信号 (445 Ma)。此外, QE-1 和 QE-2 都含有较高的燕山期峰。值得注意的是, QE-2 表现为明显的 155 Ma 和 240 Ma 年龄峰值, 而 445 Ma 和 800 Ma 年龄峰则缩小至次要成分。

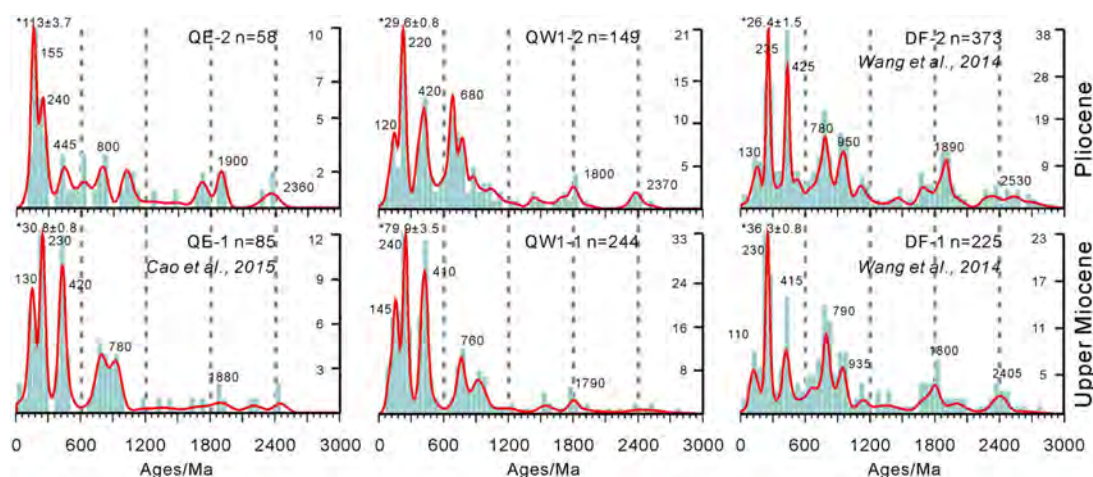


图 6.9 莺歌海和琼东南盆地上中新统-上新统样品碎屑锆石 U-Pb 年龄谱系^[165, 264]

Fig. 6.9 Histograms and probability density distribution plots for detrital zircon U-Pb ages of the Yinggehai-Qiongdongnan Basin samples from upper Miocene to Pliocene with typical age peaks numbered (Ma). The youngest zircon U-Pb age (Ma) is marked with * in the upper left corner. n represents the number of concordant analyses relative to all grains. Published data in Dongfang gas field of Yinggehai Basin from Wang et al. (2014) and data in Qiongdongnan Basin from Cao et al. (2015) have been renamed and displayed on plot for comparison^[165, 264].

6.2.2 上中新统-上新统样品稀土元素含量及配分模式

图 6.10 显示, 本研究所有钻孔样品均表现明显的轻稀土元素富集、右倾型配分模式。DF、QW3、QW1 和 QE 上中新统至上新统样品可见 Eu 正异常现象, 但自西向东该信号逐渐减弱。具体来说, 位于莺歌海盆地西北部的 DF 井中, 几

乎所有深度的样品都显示出明显的 Eu 正异常，只有 DF-2 在 1506–2030 米处 Eu 元素正异常不明显。向东，尽管 QW3-2 其它深度的样品都显示出明显的 Eu 正异常，但其上新统样品在 1500–1865 米处首次出现轻微的 Eu 负异常。对于 QW1，上新统样品与上中新统样品差异更明显：QW1-1 中没有发现 Eu 负异常，而 QW1-2 浅层的样品则以中等到明显的负异常为特征。琼东南盆地最东端，QE 钻井除了在 3070–3168 米处可见唯一轻微的 Eu 正异常外，几乎所有 QE 样品都以 Eu 负异常为特征。靠近海南岛的 QW2 稀土配分模式与 PAAS 差异较大，而其他钻孔均与 PAAS 特征类似。此外，样品 QW2-2 与 PAAS 相似程度更高，稀土元素总含量比下方 QW2-1 更高。然而，QW2 大多数样品都显示出强烈的 Eu 元素亏损现象，只在 960–1100 米处表现轻微的 Eu 正异常。此外，作为补充证据，包括 MW、MM 和 ME 在内的中中新统样品 Eu 元素异常值空间分布差别明显，位于最西端的 MW 正异常最显著，而位于东部的 ME 则表现为强烈的负异常。

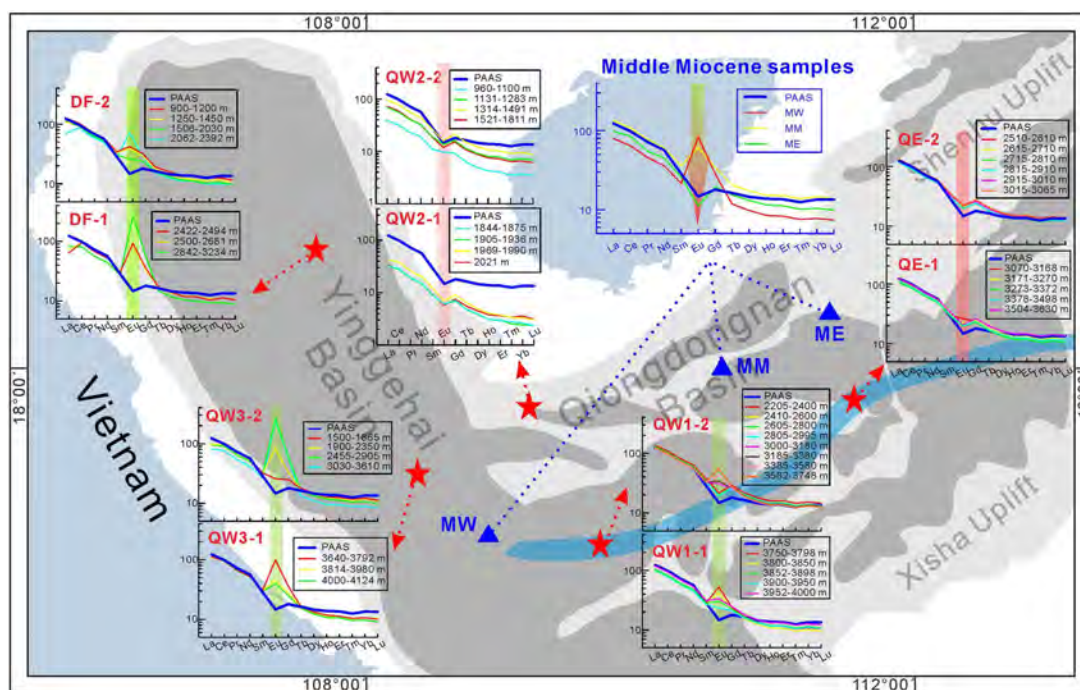


图 6.10 莺歌海和琼东南盆地中中新统–上新统样品稀土元素配分曲线及空间分布特征

Fig. 6.10 Chondrite normalized REE patterns of upper Miocene–Pliocene samples in the study area; Eu anomaly values are highlighted on the plot.

6.2.3 中央峡谷物源演变特征

前人研究表明，发生在印支半岛和华南大陆板块边界的印支造山运动是该地区重要的区域构造事件，不仅包括多阶段的俯冲和碰撞过程，还伴随强烈的岩浆活动及变质作用。特别的，崑松地块（Kontum Massif）位于越中地区，其规模巨大的蛇绿岩套可能代表了特提斯洋俯冲残留物质，随着挤压变形、抬升剥蚀过程而大规模暴露出来^[260, 271]，可能作为重要的基性-超基性岩源区，为南海

西部地区提供大量碎屑物质。沿中央峡谷分布的样品 MW、MM 和 ME 元素地球化学结果显示,晚中新世以前琼东南盆地沉积样品中的基性物质信号空间分布存在差异:最接近越南陆缘的样品 MW 相对于更靠近海南岛的另外两件样品受基性源区影响的程度更深,其稀土元素配分模式显示更明显的 Eu 正异常;而基性源区的影响可能自西向东逐渐减弱,或逐渐被酸性源区取代(图 6.10)。

锆石 U-Pb 年龄谱系显示,中新世至上新世中央峡谷西侧部分沉积物源一直处于稳定状态。其中 DF 井持续显示显著的印支期、加里东期和晋宁期多峰年龄组合特征,与越中物源的年龄谱系一致(图 6.9 和图 6.1)。与此同时,DF 井两个样品显著的 Eu 正异常也表明莺歌海盆地北部沉积物来自越中基性岩源区(图 6.1)。此外,尽管不是主要年龄组分,但上新统样品 DF-2 中的喜山期(约 30 Ma)和吕梁期(约 2500-1800 Ma)锆石数目比例相对早期样品增加,与现代红河特征在一定程度上相似。虽然越中地区崑松高地在物质贡献上仍占主导地位,但这种 U-Pb 年龄组合上的轻微变化可能表明,新生代区域构造运动,例如红河剪切带及其周围的构造热活动,一定程度上影响了其他次要物源。

QW1 和 QE 分别位于中央峡谷的西部和东部(图 6.9),其锆石 U-Pb 年龄谱系特征相似,均与越中地区一致,显示出印支期、加里东期和晋宁期宽广的年龄组合。与上述 DF 样品不同,这两个样品表现出清晰的燕山期峰值,表明其他重要物源的影响。由于海南岛具有独特的双峰模式,包含燕山期和印支期两个主要峰值,沉积物也可能从其中央高地被剥蚀搬运至中央峡谷通道的北部。尽管南海西北部盆地基底以单一或主要的燕山期峰值为主,但对中新世-上新世盆地沉积供源有限。位于琼东南盆地东侧的神狐隆起在该时期也因大规模海侵作用沉没于海面之下,不再提供沉积物源。

然而,上新统样品 QW1-2 和 QE-2 相对各自的中新统样品锆石年龄组合差别较大,表明物源在时间和空间上均有较大变化。燕山期和印支期年龄此时占主导地位,表明来自海南岛的陆源输入增加。相比之下,加里东期年龄在上新统样品中占比相对较小,表明自晚中新世以来越中地区对盆地影响趋于减弱。总的来说,这两个样品的年龄谱系更加宽广,吕梁期锆石含量增高。因此表明具有更多古元古代锆石的潜在物源也开始向中央峡谷提供沉积物。空间上从西到东, QE-2 与 QW1-2 在年龄组合完全不同,前者以燕山期和印支期锆石为主要峰值,进一步证实沿整个河道向东输送沉积物时,海南岛源区的影响远大于西侧越中地区。

整个中央峡谷基性-超基性沉积物稀土元素示踪信号在空间上具有明显变化。QW3-2 相对接近越南边缘,从晚中新世到上新世,该地区持续不断地获得了大量基性物源补给, Eu 元素正异常一直很明显。然而, QW1 井位置相对靠东,海南岛对样品 QW1-2 影响更大,搬运了更多酸性沉积物,因此造成轻微至中等强度的 Eu 正异常,甚至开始产生 Eu 负异常。QE 钻孔位于最东侧,基性物源信号已被途径的酸性源区稀释到较大的程度,在晚中新世只在深度为 3070-3168 m 处

观察到一个轻微的 Eu 正异常值。自上新世以来，样品 QE-2 主要受海南岛源区影响，已经全部被明显的 Eu 负异常所取代。位于琼东南盆地西部边缘，远离中央凹陷的 QW2 可能从晚中新世开始受到海南岛的影响，因其特殊的位置导致持续产生 Eu 负异常。基于这种 Eu 异常值的不均衡分布模式，可以进一步证实越中地区或海南岛作为中央峡谷沉积物主要的潜在物源，随时间和空间尺度的不断变化为其提供不同含量的基性/超基性或酸性陆源碎屑物质（图 6.11）。

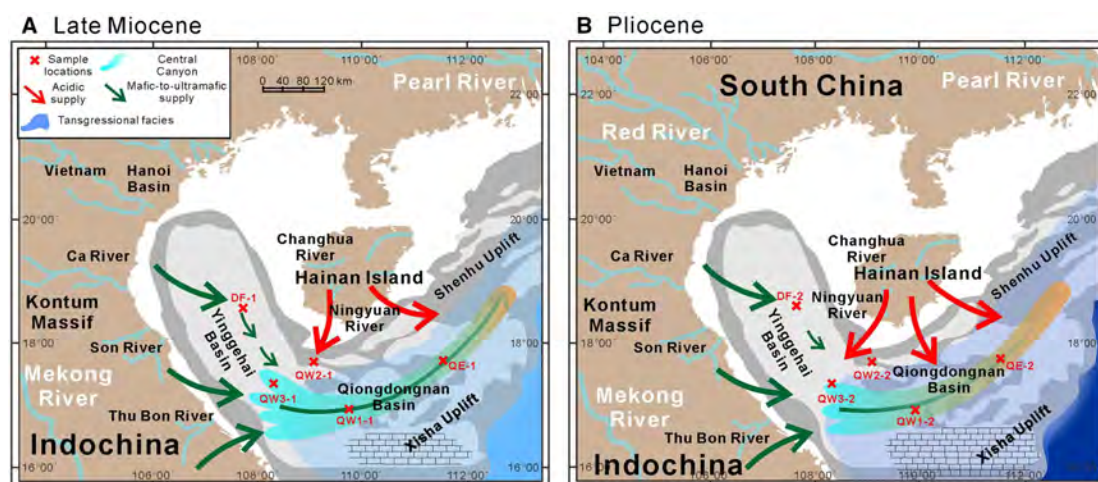


图 6.11 中央峡谷 A) 晚中新世；B) 上新世物源演化及搬运路径示意图

Fig. 6.11 Schematic source-to-sink evolution model for the late Miocene–Pliocene Yinggehai–Qiongdongnan Basin with Central Canyon highlighted. Arrows stand for sediment transportation routes from different potential source areas to the studied locations. Cyan—areas tend to be more influenced from basic rock sources; orange—areas tend to be more influenced from acidic or sedimentary rock sources.

6.3 恒春半岛增生楔浊积岩晚中新世形成发育演化过程及对南海北部深水搬运过程的启示

本文通过野外地质、地球化学及锆石 U-Pb 年龄谱系等方法，对恒春半岛发育的晚中新世深海浊积砂体开展系统“源—汇”对比研究。本研究样品位置如图 2.5 所示，样品具体信息如表 6.4 所示。

表 6.4 恒春半岛露头及南海北部盆地钻井样品信息

Table. 6.4 Sample data including sample names (outcrops and boreholes), locations, depths for boreholes, stratigraphic ages, methods (geochemistry or U–Pb), and lithological characteristics.

样品名称	位置	地层年代	取样深度(m)/露头	分析方法	岩性
S02	四重溪	-	露头	锆石 U-Pb 定年	辉长岩

K01	青蛙石	-	露头	锆石 U-Pb 定年	辉长岩
D01	大尖山	-	露头	锆石 U-Pb 定年	辉长岩
S01	四重溪	晚中新世	露头	锆石 U-Pb 定年	砂岩
J01	尖山	晚中新世	露头	锆石 U-Pb 定年	砂岩
Y01	Liangluanxi 溪	晚中新世	露头	锆石 U-Pb 定年	砂岩
W-1	琼东南盆地	早中新世	3500–3755	锆石 U-Pb 定年	砂岩
U1500B 22R	18°18.2707' N, 116°13.195 1' E	晚中新世	1039.3– 1049	锆石 U-Pb 定年	砂岩
U1500B 25R	18°18.2707' N, 116°13.195 1' E	晚中新世	1068.4– 1078.1	锆石 U-Pb 定年	砂岩
U1499B 33R	18°24.5750' N, 115°51.5990' E	晚渐新世	3758.1	锆石 U-Pb 定年	砂岩

6.3.1 恒春半岛地层格架

恒春半岛位于台湾岛的最南端，向北延伸至中央山脉，向南外延至海面之下的恒春海脊。在时间上，恒春半岛处在台湾岛构造演化中的初期碰撞隆升阶段，保存了大量洋壳基性砾岩层、深海浊积层序及后期浅海沉积，共同组成垦丁混杂堆积，是研究增生楔形成演化的天然实验室^[190, 194, 198]。恒春半岛发育中-上新统深海相浊积岩、上上新统-更新统浅海相两套沉积层序，共同组成垦丁混杂堆积（图 2.5B）。其中，牡丹层（Mutan Formation）是增生楔浊积砂体的主要沉积单元，石门砾岩（Shihmen Conglomerate）、乐水层（Loshui Sandstone）、里龙 layers（Lilungshan Sandstone）分别为牡丹组地层中的夹层。牡丹组厚度约 2000 米，以砂岩和粉砂岩互层为主，夹有大量透镜状砾石，浮游有孔虫化石指示其形成时间为 11.6–6.4 Ma，可能代表深海水道环境^[191, 198, 272]。砾岩分布较广泛，在四重溪、青蛙石等地区大量出露（图 2.6C），颗粒或杂基支撑，砾石成分包括玄武岩、辉长岩和辉绿岩，分选好，具有较高的磨圆度。乐水层主要分布于恒春半岛东部地区，厚度约 1000 米，以厚层细粒至中粒砂岩为主，浮游有孔虫化石指示其沉积年龄大约为 12 Ma，代表深水扇前缘环境。里龙 layers 主要分布于恒春半岛西侧，厚度约 2000 米，可见向上粒度变粗的反粒序沉积，形成时间为 11.6–6.4 Ma^[272]。

上新世至更新世时期，恒春半岛地区为浅海相沉积环境。其中，马鞍山组（Maanshan Formation）厚度约 800 米，为上上新统-下更新统浅海相沉积，时代为 3.7–1 Ma，与下部上新统深海相砾岩层呈不整合接触关系（图 2.5B），主要分布于恒春半岛西台地，海拔高度大约为 200–300 米，代表台湾弧-陆碰撞过程的开始。更新统地层沉积年龄小于 0.5 Ma，主要分布于恒春半岛西台地东侧斜坡，以浅海相生物礁灰岩和河流相沉积为主，反映该时期斜坡盆地开始隆升并出露于海平面之上。

6.3.2 野外观察结果

恒春半岛浊积砂体底部常包含基性岩砾石, 构成鲍玛层序 A 段, 砾石以玄武岩和辉长岩为主, 磨圆较好, 分选差, 变质岩碎屑含量较少。浊积砂层底部具有明显的冲刷槽模, 含有砾石, 向上发育平行层理及交错层理, 顶部为水平层理泥岩, 构成典型的鲍玛层序 (图 2.6a)。基性岩砾石分散分布在层序 A 段 (图 2.6b)。部分层段基性岩砾石含量极高, 构成厚度从 0.5 米至数米不等的砾岩层, 具基质或颗粒支撑结构 (图 2.6c), 枕状玄武岩砾石可见 (图 2.6f), 偶见叠瓦状构造, 指示古水流方向。地层层面上深水遗迹化石常见 (图 2.6d), 在层序砂层中常见碟状层理等泄水构造 (图 2.6e)。

可以认为, 基性岩砾石与厚层砂岩均为重力流沉积的产物。恒春半岛除了出露大量深海浊流沉积物外, 还出露大量碎屑流、泥石流等重力流沉积物, 包含大量基性-超基性岩砾石, 如枕状熔岩、辉长岩等砾石 (图 2.6b, f)。

6.3.3 锆石 U-Pb 定年及元素地球化学结果

恒春半岛增生楔辉长岩砾石样品锆石阴极发光图像显示, 绝大多数锆石颗粒发育明显的振荡环带结构, 且 Th/U 值高于 0.1, 为岩浆成因锆石^[212]。样品 K 01 锆石 U-Pb 协和年龄为 23.60 ± 0.20 Ma (MSWD = 0.11), 样品 S 02 的协和年龄为 23.78 ± 0.41 Ma (MSWD = 1.40), 样品 D 01 的协和年龄为 25.40 ± 0.24 Ma (MSWD = 0.99) (图 6.12), 代表辉长岩结晶年龄。

浊积砂岩碎屑锆石 U-Pb 年龄谱系特征显示, 样品 S 01、J 01、Y 01 均呈现宽广的多峰特征, 包括明显的燕山期 (150–65 Ma)、印支期 (260–200 Ma)、吕梁期 (2500–1800 Ma) 以及新生代峰值, 次要峰值包括加里东期 (550–350 Ma) 和晋宁期 (1000–800 Ma)。特别引人注目的是, 样品 S 01 和 J 01 都表现出非常显著的新生代年龄峰值, 主要集中在 -23 Ma; 样品 Y 01 的新生代峰值略低 (图 6.13A)。

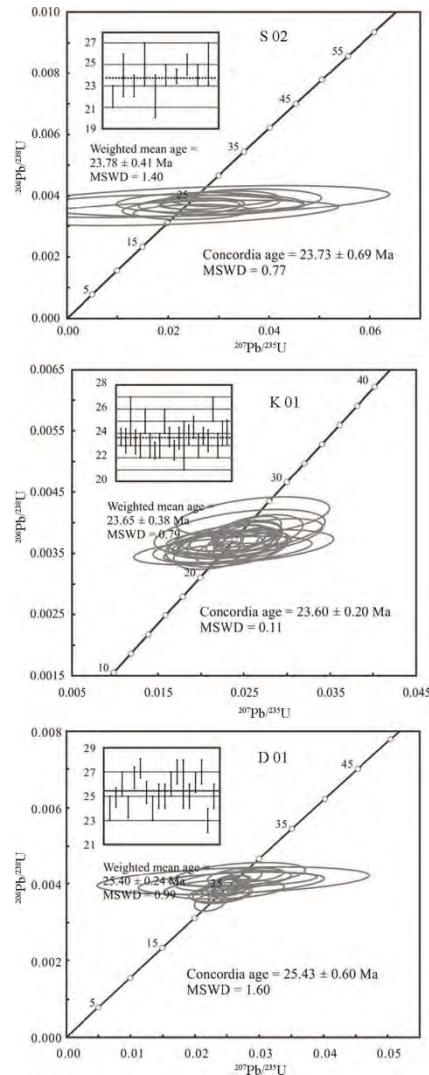


图 6.12 台湾恒春半岛增生楔浊积体基性砾石锆石 U-Pb 年龄谐和图及加权平均年龄

Fig. 6.12 Zircon U-Pb dating of the gabbro gravels within the Hengchun turbidite sequences. Both weighted mean ages and concordia ages are shown for samples S 02, K 01 and D 01.

样品 U1499 33R 来自 U1499B 站位，为上渐新统砂岩，其碎屑锆石 U-Pb 年龄以燕山期单峰（150 Ma）为特征。来自 U1500B 站位的两个上中新统浊积砂岩沉积物样品（U1500BB 22R 和 U1500B 25R）以深灰色富含长石-石英颗粒砂岩为主，碎屑锆石 U-Pb 年龄呈现非常宽广的谱系特征，以明显的燕山期、印支期和加里东期峰值为主，及晋宁期和太古代次峰（图 6.13B）。

样品 W-1 位于琼东南盆地中央峡谷内，其碎屑锆石 U-Pb 年龄谱系亦表现出宽广的多峰特征，其中燕山期峰值非常明显，印支期、加里东期和晋宁期为次要年龄峰，印支期和加里东期的锆石含量几乎相同（图 6.13B）。

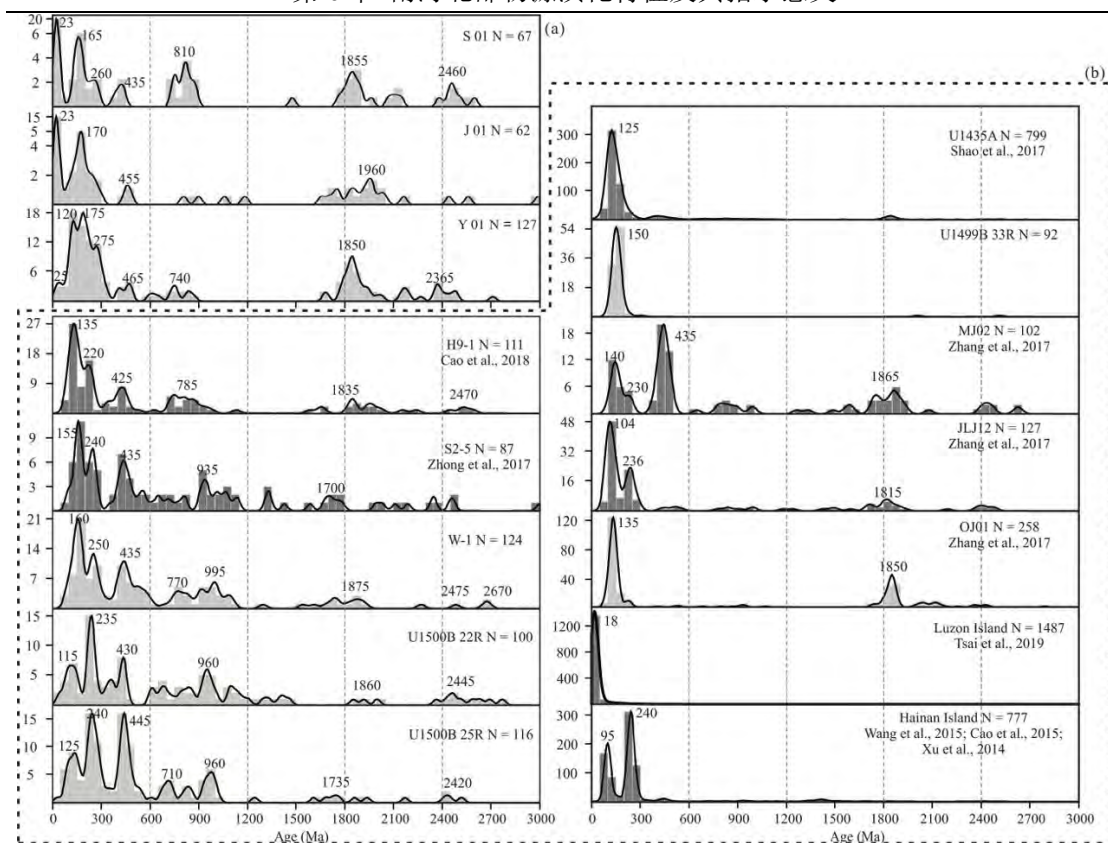


图 6.13 恒春半岛 A) 增生楔浊积砂岩及 B) 潜在源区碎屑锆石 U-Pb 年龄谱系特征^[168, 189, 200, 264-266, 273, 274]

Fig. 6.13 Detrital zircon U-Pb age spectra. (a) Hengchun turbidite sandstones; (b) samples within the northern South China Sea basin and surrounding provenance areas. Studied samples shaded light gray; published data shaded dark gray^[168, 189, 200, 264-266, 273, 274].

6.3.4 恒春半岛浊积岩基性砾石形成机制

前人对恒春半岛增生楔浊积岩中的基性岩砾石开展了大量的岩石地球化学研究，其岩性涵盖玄武岩、辉长岩、角闪岩，其元素和同位素地球化学特征类似于 N-MORB、E-MORB 和 OIB^[195, 275]。南海洋壳是恒春半岛增生楔的下伏板块，大洋钻探和拖网采样揭示，南海洋壳组成包括 N-MORB、E-MORB 和 OIB^[276]，与恒春半岛增生楔基性岩砾石具有完全相同的岩石组合，极可能是其重要的物源区。菲律宾海板块的西部边界，即花东海盆和吕宋岛，是马尼拉海沟的上覆板块，其中花东海盆洋壳为 E-MORB 型，吕宋岛弧出露晚中生代以来的蛇绿岩和岛弧，其物源成分相对复杂，二者在海沟前缘断离过程中也可以为增生楔提供物源。由于恒春半岛增生楔的砾石均为基性岩，显著区别于吕宋岛岛弧中酸性火山岩，因此吕宋岛对增生楔的贡献可能非常有限。对南海和花东海盆而言，二者最明显的区别在洋壳的年龄。南海洋壳年龄为 -33-16.5 Ma^[37]，花东海盆洋壳为早白垩世。本文基性岩砾石开展的锆石 U-Pb 定年结果均集中于上渐新统-下中新统 (23-25 Ma, 图 6.12)，与南海洋壳完全相同。结合恒春半岛

增生楔基性岩砾石已发表年龄数据^[195, 275]，可以认为，南海洋壳来源砾石在增生楔中占主导位置，而来自花东海盆洋壳的砾石甚少。

6.3.5 恒春半岛浊积砂岩物源及砂体形成演化过程

恒春半岛增生楔浊积砂体的碎屑锆石年龄谱系包含 - 23 Ma 峰值，与增生楔中的玄武岩、辉长岩砾石结晶年龄一致，而与吕宋岛 - 18 Ma 的锆石峰值明显不同（图 6.13），表明南海洋壳为恒春半岛增生楔浊积沙提供了物源。在南海洋壳的破碎及搬运磨蚀过程中，大量洋壳物质形成磨圆良好的玄武岩及辉长岩砾石，还有更多物质以更细的碎屑颗粒形式，通过重力流的方式搬运到马尼拉海沟中，形成增生楔中 - 23 Ma 的锆石年龄峰值。

前人认为，恒春半岛在晚中新世时期主要接受了来自华南大陆东南沿海地区由闽江或九龙江搬运而来的沉积物^[189]。闽江 U-Pb 锆石年龄谱系包含加里东期（-430 Ma）主峰和燕山期（-143 Ma）次峰，并含有一定数量的年龄较老的锆石颗粒，但与恒春半岛浊积砂岩的年龄谱系组合存在明显差别（图 6.13）。具体而言，恒春半岛浊积砂岩 U-Pb 锆石年龄谱系中包含了大量新生代，新元古代和中元古代的锆石，加里东期的峰值明显低于燕山期，而闽江沉积物完全不具备这样的特征。此外，九龙江和瓯江，甚至海南岛样品，在 MDS 相关性分析图上与恒春半岛样品也相距极远，它们在年龄谱系分布上均表现为较窄的双峰或单峰特征，元古代锆石含量极为有限（图 6.14）。恒春浊积砂岩年龄谱系特征与来自琼东南盆地 W-1 井的砂岩样品、珠江口盆地的 H9-1 砂岩样品和 U1500B 钻井的砂岩样品更为相似，在 MDS 相关性分析图上亲缘性更高（图 6.13 和图 6.14）。

南海西部地区经历过多期强烈的构造运动^[91, 92]，其源区特征近年来受到广泛关注^[277]，在锆石 U-Pb 年龄谱系中也表现为非常明显的印支期（-250-210 Ma）和加里东期（-470-400 Ma）峰值，以及相当数目的元古代等古老年龄锆石。近年来在琼东南盆地发现中央峡谷水道沉积，它在晚中新世时期搬运了大量来自中南半岛和海南岛的碎屑物质，以浊流的形式自西向东输送到南海西北次海盆^[167, 182, 278]。最新研究揭示，琼东南盆地中央峡谷水道的前身为昆莺琼古河，自西向东绵延上千公里，其开始活跃时间在晚始新世^[135]。随着南海海侵，昆莺琼古河被淹没在海下，形成中央峡谷继续自西向东搬运沉积物。图 6.13 显示来自 U1500 的砂岩样品与琼东南盆地 W-1 井的砂岩样品有非常相似的碎屑锆石组成，二者在 MDS 相关性分析图解上十分相近（图 6.14），推断昆莺琼古河的中央峡谷沉积物搬运到了 U1500B 站等深水区。

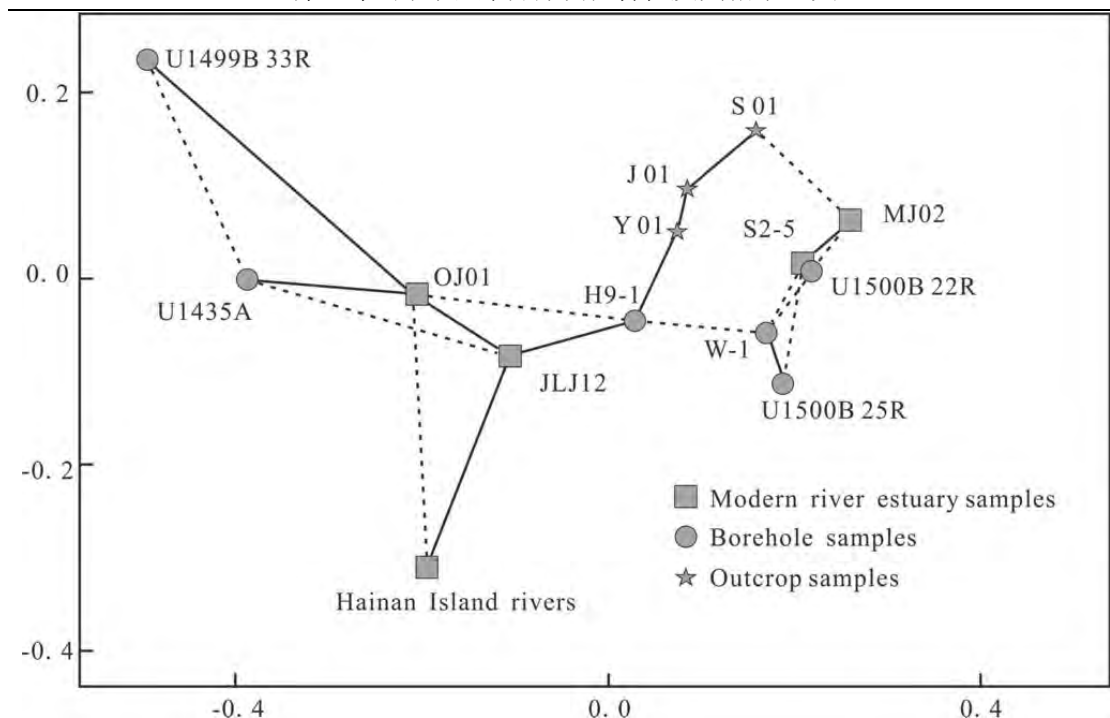


图 6.14 台湾恒春半岛增生楔浊积体及潜在源区 MDS 相关性分析

Fig. 6.14 Nonmetric multidimensional scaling (MDS) correlation analysis diagram for Hengchun turbidite sandstones and their surrounding potential provenances.

古珠江从渐新世发育以来，到中新世已经从区域性小河演变为流域面积较大的河流^[168]。由于自中中新世以来古珠江已基本接近现在的规模，其支流拓展到了广阔的华南内陆云贵高原，因此古珠江沉积物除了包含燕山-印支期碎屑锆石外，还包含较多加里东期以及元古代-太古代等古老锆石（图 6.13）。地震剖面揭示南海北部陆坡区发育大量从北向南的大型深水扇及峡谷水道，把珠江沉积物以重力流的形式输送到南海深水区^[170]。图 6.13 中 H9-1 样品为珠江三角洲中新统晚期沉积物，锆石年龄谱系以燕山期-印支期峰值为主，较低的加里东期和晋宁期等更老的年龄峰值，代表华夏内陆及扬子板块的特征。MDS 相关性分析图解显示，H9-1 与 U1500B 相关性同样较高，反映出除南海西部物源外，U1500B 钻位还接受了从南海北部珠江搬运来的沉积物。需要注意的是，来自 U1435A 和 U1499B 的砂岩碎屑锆石 U-Pb 年龄以白垩系单峰形式存在（图 6.13），与燕山期华南陆缘岛弧岩浆岩年龄一致，可能是局部隆升物源的产物^[134]。可以认为，南海北部深水区是南海西部昆莺琼古河、南海北部珠江以及盆地周边古隆起三方物源混合沉积的地区，造成该地区晚中新世发育了厚达数百米的浊流沉积。

恒春半岛发育的上中新统深海浊积砂体，包含大量磨圆度较好的洋壳砾石，辉长岩砾石成岩时间在 23.60–25.40 Ma，与浊积砂岩样品中的新生代年龄峰值范围 23–26 Ma 完全一致，反映南海洋壳的破碎风化作用为浊积砂体提供了部分物源。众所周知，南海洋壳的年龄从 -33 Ma 跨越至 -15 Ma，但是在恒春半岛

增生楔发现的新生代基性岩砾石仅局限于晚渐新世，表明只有晚渐新世磁异常条带 C8-C6_b (26.5 Ma-23.1 Ma) 的洋壳碎屑物进入到了增生楔 (图 6.15)。

据此推论，古珠江和“崑一莺一琼”古河两大水系携带大量陆源碎屑沉积物在 U1500 钻孔附近汇聚，之后继续自西向东奔涌而下，恰好途径磁异常条带 C8 - C6_b (-17°北) 的分布区域，强烈的重力流侵蚀下切南海晚渐新世洋壳，长途搬运的陆源碎屑沉积物和基性洋壳物质以浊流的形式一起向东搬运，最终在马尼拉海沟附近不断堆积。由于俯冲海沟负地型的增强效应，使海沟内同时沉积大量基性洋壳砾岩层、块体滑塌体等沉积体，与浊积体系一起共同构成俯冲海沟内的混杂堆积；伴随着菲律宾海板块向西北方向顺时针旋转漂移，这套混杂堆积最终被推挤、迁移并出露于恒春半岛地区。

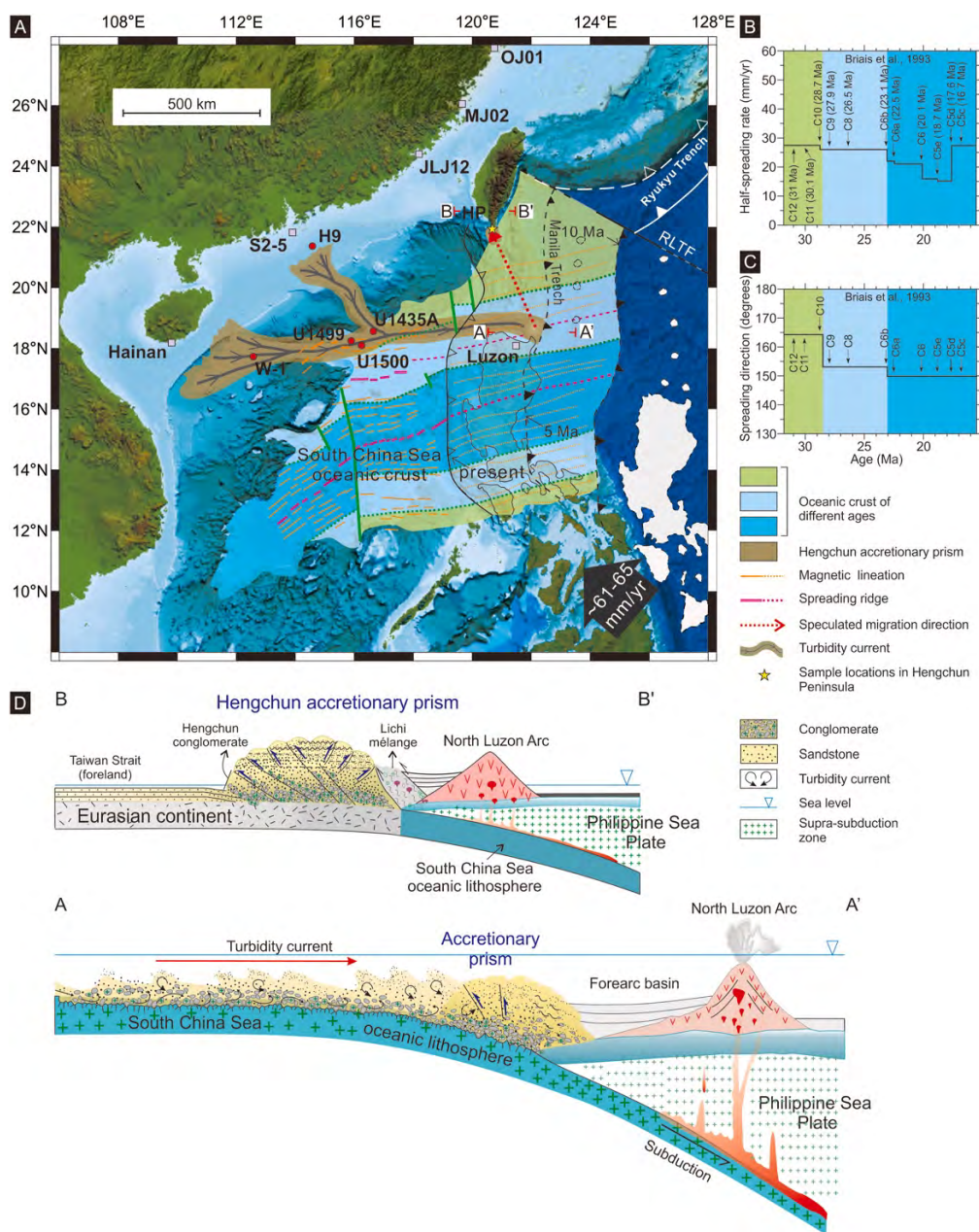


图 6.15A) 南海北部浊流体系平面展布图；B) 南海洋壳扩张速率变化曲线^[21]；C) 南海洋壳

扩张轴角度变化曲线^[21]；D) 台湾恒春半岛增生楔浊积体发育演化机制（剖面 A-A'和 B-B'如图 A 所示）

Fig. 6.15 (A) Schematic reconstruction map of the turbidity current across the northern SCS and the final deposition on the Hengchun Peninsula. Presumed paleogeographic locations of the Manila Trench and Luzon Arc are given in the figure (modified after Sibuet et al. (2016) and Wu et al. (2016)). Black dashed lines indicate the present Luzon Arc. Black solid lines indicate the Luzon Arc at approximately 10 and 5 Ma. Dark blue, light blue and green areas separated by green dashed lines mark oceanic domains formed during different kinematic phases, represented by changes in spreading rates, spreading directions or both parameters (Briais et al., 1993). Orange dashed lines show the magnetic anomalies during the SCS oceanic crust extension. Rose red dashed lines show the SCS mid-ocean spreading ridges. Red dots indicate studied or published boreholes representing different source areas. The black bold arrow shows the estimated average speed of the PSP movement relative to the Eurasian Plate. Red dashed lines indicate migration pathway of the accretionary prism (B) Half-spreading rates are calculated from chrons C12 to C5c using magnetic models from Briais et al. (1993)^[21]. (C) Spreading directions are calculated based on the assumption that they are perpendicular to the trends of magnetic lineations^[21]. (D) Two transects subduction zones in the geographic map (A) are illustrated by geological profiles AA' and BB'.

第7章 南海新生代古水系古地理重建

本论文基于钻井、露头以及地震资料综合考虑沉积岩相分布，针对南海北部地区开展系统的古地理地貌重建工作。除本研究取得的最新数据和认识之外，还参考了前人已发表的大量成果，中海油集团有限公司内部研究资料也为本节内容提供了重要的理论支撑。总体来看，伴随着南海北部西侧古隆起古高地的侵蚀和剥露，东西向“崑-莺-琼”古河道逐渐萎缩消亡，珠江流域随之扩大并开始向南海北部盆地搬运大量来自华南内陆的碎屑物质；除此之外，包括海南岛、盆地内局部隆起以及现代红河也作为次要物源区，影响南海北部及周缘地区的沉积格局。

7.1 晚中生代-古新世

早白垩世期间，华南大陆边缘持续经历古太平洋板块俯冲过程，形成了大规模典型的安第斯型岩浆弧。强烈的俯冲、碰撞和挤压作用导致华南东部古地形整体高于西部地区。在此期间，华南大陆东南地区发育了许多小型断陷盆地，东部岩浆活动也比西部更普遍。南海北部仅接受来自沿海地区距离短且流域范围有限的河流搬运而来的沉积物，缺乏古元古代或太古代的老锆石组分，基本不受华南内陆地区远源输送的影响。珠江口盆地西部地区和琼东南盆地基底钻井揭示了下白垩统沉积火山碎屑岩记录（图 7.1）。如今已漂移至南海南侧的南沙地块也在中生代被花岗岩岩体侵入。南海东部 LF35-1-1、CFC-10、CJA-1、CFC-16 等一系列下白垩统钻孔显示该时期发育海相沉积，包括东北向展布的滨岸相和浅海相沉积。同时，巴拉望地块仍然拼贴于华南陆缘，其钻孔记录 Penascosa-1、Catalat-1、Malajion-1 和 Destacado-A-1x 显示中部地区为半深海相，北部地区为海相到陆相沉积。

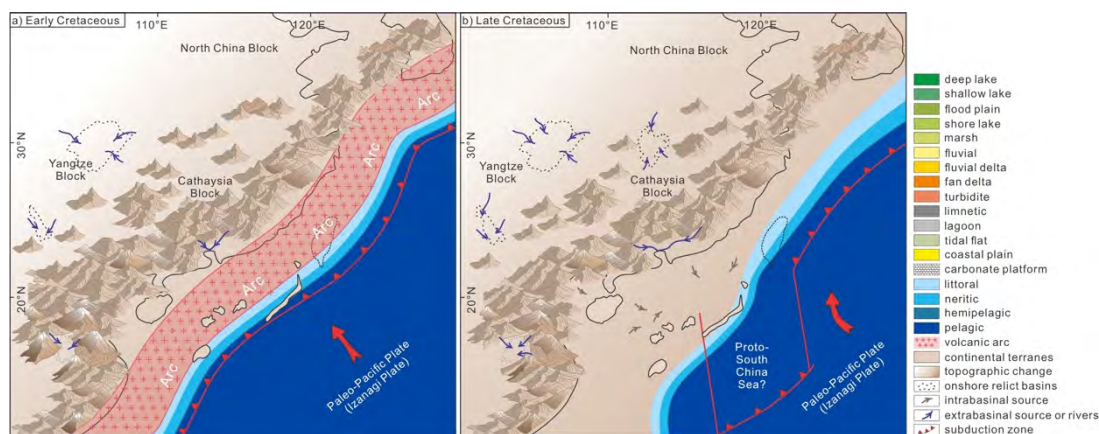


图 7.1 白垩纪南海古水系古地理演化示意图

Fig. 7.1 Sedimentary facies distribution patterns and paleogeographic reconstruction maps during the a) Early Cretaceous, b) Late Cretaceous.

晚白垩世，先前的安第斯型活动陆缘向西太平洋型被动陆缘转变（图 7.1）。伴随古太平洋板块向海洋方向撤退和华南大陆东部地区进入伸展环境，裂谷作用导致南海北部地区经历了多期早新生代岩浆活动，形成一系列断陷沉积盆地，早期拼合在大陆边缘的微陆块也开始向南漂移。钻孔资料显示台西南盆地此时发育过渡相，珠江口盆地东部地区受干旱陆相环境影响。北巴拉望上白垩统地层显示从三角洲相转变为深水相沉积。而此时北部湾盆地和莺歌海-琼东南盆地则主要沉积陆相地层。南海北部地区晚白垩世总体表现为向南水深逐渐增加的趋势，主要接受来自原地或临近大陆弧搬运的火山碎屑物质。伸展环境和地壳减薄可能导致华南大陆东部地区地形起伏程度增加。尽管东部古河流域向西出现轻微的拓展，但南海北部沉积仍表现单一的燕山期锆石 U-Pb 年龄，大约从 185 Ma 到 90 Ma，说明大陆岩浆弧和华南东南沿海造山带持续经历侵蚀作用和近距离输送过程。

南海北部地区在古新世持续经历断陷活动。尽管该时期华南东部地势逐渐降低，造山带遭到一定程度破坏，但由于中生代末持续存在的碰撞挤压作用，东部古地形整体上仍高于西部地区（图 7.2）。南海北部是否存在古新统沉积地层，学术界仍存在很大争议，长期以来未得到古生物或同位素年代学资料的证实。台湾西部和台湾海峡 THS-1 和 WG-1 钻孔发现中-上古新统微体化石，表明南海东北部地区此时为浅海至海湾相沉积。巴拉望此时发育陆架边缘沉积，礼乐地区则发育三角洲相沉积。整体来看，古新世古地理地貌特征大体继承了晚白垩时期的基本框架。古新世时期，华南大陆边缘的前新生代基底作为古隆起，可能经历广泛侵蚀剥露作用。北部湾盆地此时处于河流、三角洲和沼泽相环境，可能受到云开隆起向西南方向的延伸部分以及盆地基底物源的影响。古新世时期，陆上古河流域仍极为有限，华南陆缘古新世盆地主要发育冲积平原相，局部发育沼泽和浅湖相。

7.2 早-中始新世

相比稀少的古新统沉积记录，南海北部广泛沉积始新统裂陷期地层（图 7.2）。早-中始新世期间，南海西侧（即如今莺歌海-琼东南盆地地区）以及中南半岛东部大陆边缘以大规模古隆起为主要特征，并经历强烈的侵蚀搬运过程；南海东部在经历一系列拉张过程后，最终形成多个相互分隔、规模较小的分散洼地或凹陷。珠江口盆地珠三凹陷和琼东南盆地东部地区主要堆积山间粗粒碎屑沉积物；北部湾盆地和珠一凹陷则发育河流-冲积扇和湖泊相。

珠江口盆地南部的珠二凹陷此时主要发育半深湖或深湖相。与西部广泛高地不同的是，南海东部明显被中央隆起带分割成南北两个不同的构造单元。早-中始新世南海北部以短距离快速搬运沉积方式为主，具有一定规模的河流水系尚未形成。东西向展布的“崑-莺-琼”古河此时仍处于早期孕育阶段，其影响局限于琼东南盆地部分地区。珠二凹陷最南缘发育海陆过渡相，向南为坡度极陡的大陆斜坡。

钻孔 DP21-1-1 证实，台西南盆地早-中始新世发育浅海相沉积。相应地，台湾西部陆上下-中始新统地层发现有孔虫和钙质超微化石，也证实浅海相环境。还应该注意的，礼乐和巴拉望地块都紧邻华南大陆南部边缘：礼乐东南部主要以半深海相为特征，而其西北部分则以三角洲和浅海相为主。同样，南巴拉望发育深水浊积岩，表明处于上陆坡环境，与北巴拉望浅海环境形成对比。

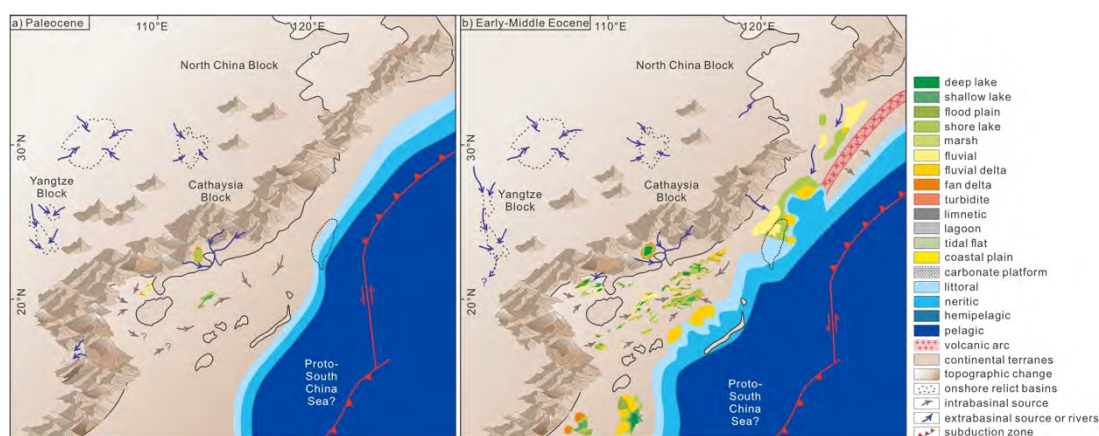


图 7.2 古新世一早/中始新世南海古水系古地理演化示意图

Fig. 7.2 Sedimentary facies distribution patterns and paleogeographic reconstruction maps during the a) Paleocene, b) Lower-Middle Eocene.

7.3 晚始新世

伴随着古南海持续俯冲至婆罗洲之下以及晚始新世新南海海洋壳的发育扩张，南海北部沉积环境此时开始发生明显变化（图 7.3）。台西南盆地和台湾西部海岸平原发育平原相及沙滩相沉积；珠江口盆地则广泛发育海陆过渡相，湖相、沼泽相范围减小。琼东南盆地直至早渐新世晚期才经历海侵过程，且海水从东侧开始影响琼东南盆地。北部湾盆地主要由河流、沼泽和浅湖环境组成，但湖泊规模减小。从晚始新世（或者更早），“崑-莺-琼”古河道开始沿南海西部古隆起带发育，从中南半岛东部及东北部地区，如崑松地块，剥蚀搬运了大量基性至超基性沉积物，并运输到了琼东南盆地东部、珠江口盆地珠二凹陷大部分地区以及仍然贴合在华南陆缘的礼乐地区。与此同时，珠江在南海北部影响有限，穿越华南沿海花岗岩源区的古珠江仅为珠一凹陷提供了一定酸性岩沉积物。

7.4 早渐新世

中央隆起带是珠江口盆地中的一个重要构造单元，由一系列断层和褶皱构成的复杂古突起，位于盆地的中心区域，贯穿整个盆地，将其分隔为南北两个主要沉积区。由于中央隆起带的存在，珠江口盆地在早渐新世受到不同源区的影响。一方面，珠一凹陷以陆相地层为主，主要发育河流相或湖泊相沉积，古珠江和古韩江形成了小规模浅水三角洲（图 7.3）。另一方面，珠二凹陷在早渐新世主要表现为海陆过渡相，特别是珠二凹陷最南端发育浅海相地层，与台西南盆地的外陆架环境一致。琼东南盆地在早渐新世开始经历海侵，普遍发育滨岸相和浅海相沉积。莺歌海盆地为浅海环境，其西北部地区发育河流三角洲和海岸平原，东部地区发育扇三角洲。只有北部湾盆地仍发育河流相、沼泽相以及湖泊相沉积。早渐新世晚期阶段，礼乐和巴拉望从大陆边缘裂离并向南海南部漂移，沉积环境整体也由之前浅水陆架边缘环境向上陆坡深水环境转变。

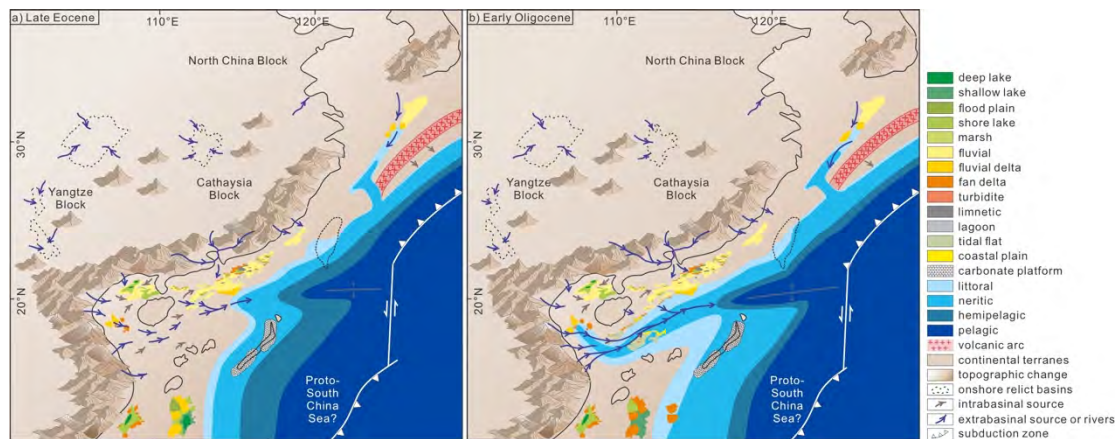


图 7.3 晚始新世—早渐新世南海古水系古地理演化示意图

Fig. 7.3 Sedimentary facies distribution patterns and paleogeographic reconstruction maps during the a) Late Eocene, b) Early Oligocene.

7.5 晚渐新世

晚渐新世东西向展布的“崑-莺-琼”古河规模达到鼎盛阶段（图 7.4）。由于发生大规模海侵现象，琼东南盆地广泛形成海陆过渡相、浅海相沉积；“崑-莺-琼”古河持续将大量基性-超基性碎屑物质搬运至琼东南盆地东部以及珠江口盆地的中-南部深水区。与此同时，珠江流域显著扩大，突入华南内陆云贵高原地带。珠江将大量来自华南大陆酸性岩和沉积岩源区的物质搬运至珠江口盆地，最终跨越中央隆起带进入珠二凹陷，此时这些位于盆地中部的构造高地已经历剥蚀削减。因此，晚渐新世南部凹陷表现为独特的混合物源特征：珠江流域作为纵向搬运方式，“崑-莺-琼”古河作为轴向搬运通道，共同影响该地区沉积格

局。渐新世末期，珠一和珠二凹陷完全连通，同时受到海陆过渡环境的影响，其中珠二凹陷发育广泛的滨海相沉积，最南端处于陆坡环境并发育深海沉积。更东部的台西南盆地此时为浅海甚至半深海环境。礼乐和巴拉望已完全脱离南海北部，普遍发育泻湖和生物礁碳酸盐岩台地。

7.6 早中新世

伴随持续的海底扩张过程，琼东南盆地早中新世以发育浅海到半深海相为主（图 7.4）。莺歌海盆地大部分地区此时转变成深海环境，北部湾盆地最终也经历东南方向海侵作用的影响，开始发育滨海沉积。多个微陆块如中沙和西沙古隆起，现在完全被淹没至海下，随后发育生物礁碳酸盐岩台地。“崑-莺-琼”古河逐渐萎缩至消亡，来自西侧基性源区的碎屑沉积物也随之减少。

早中新世珠江流域基本发展至现代水系的规模，珠江口盆地大量接受来自扬子地块、云贵高原以及其他华南内陆地区输送的陆源碎屑，包含显著增加的元古代碎屑锆石。在晚渐新世-早中新世期间，陆架坡折带从珠二凹陷南部的白云深水区迅速迁移至北侧。珠二凹陷也相应受大陆坡或半深海环境控制。海平面在早中新世后继续上升，台湾部分地区出现浅海和半深海相及碳酸盐沉积。此时礼乐和巴拉望已到达南海南部，持续发育浅海相、泻湖相和生物礁碳酸盐岩台地。

值得说明的是，琼东南盆地晚中新世发育的中央峡谷一直受到研究者的广泛关注，在某种程度上可以认为是“崑-莺-琼”古河的残余，仅局限于莺歌海-琼东南盆地的中央凹陷，仍有可能作为南海北部重要的轴向通道，在半深海环境中向东部地区运输基性碎屑物质。

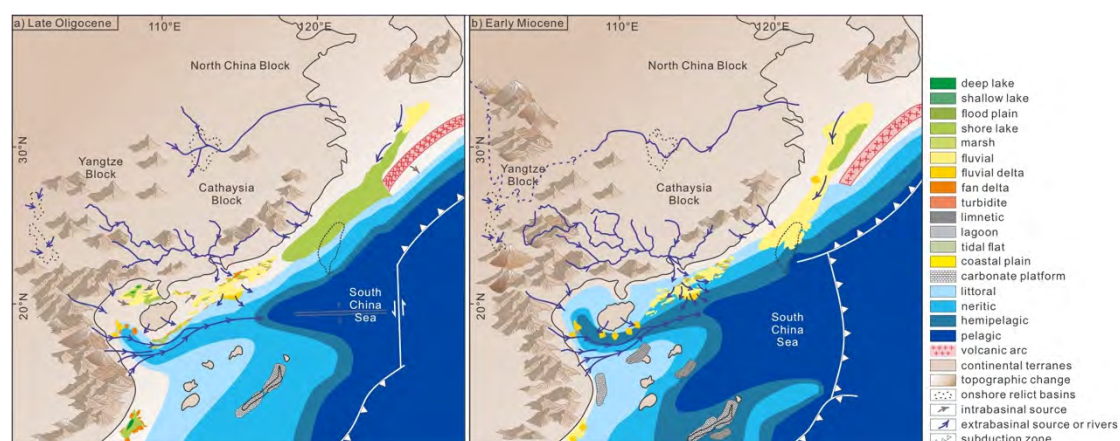


图 7.4 晚渐新世-早中新世南海古水系古地理演化示意图

Fig. 7.4 Sedimentary facies distribution patterns and paleogeographic reconstruction maps during the a) Late Oligocene, b) Early Miocene.

第8章 结论与展望

8.1 结论

本论文重建了南海地区中生代末至新生代以来“源—汇”系统、区域构造及古水系古地理的演化过程，基本结论及各阶段重建结果简述如下。

南海北部基底广泛存在中生代岩浆岩和沉积岩记录：东侧以大量白垩系岩浆岩和沉积岩为主，受古太平洋和华南大陆洋—陆碰撞的影响；西侧以上侏罗统至白垩系沉积岩和变质碎屑岩为主，也是东侧大陆岩浆弧的延伸；海南岛西侧变质花岗岩具有中元古代年龄，可能反映在印支和华夏地块相互作用过程中，古老陆块基底残余的出现。南海北部盆地基底实际受印支与华南陆—陆碰撞、古太平洋与华南洋—陆碰撞的共同作用。

综合物源分析及岩浆记录，华南大陆发育安第斯型活动大陆边缘，大约从280 Ma开始发育大陆岩浆弧，250–200 Ma进入平板俯冲过程，200–190 Ma进入岩浆活动静止期，大约190–90 Ma重新发育正常安第斯型火山弧，展布范围从海南岛南侧，经过南海北部地区及台湾岛东侧，向北延伸至东海地区。90 Ma后伴随着古太平洋板块俯冲后撤，岩浆活动迅速减弱，仅在南海东北部和东海局部地区发现少量85–80 Ma的岩浆岩。

南海北部早新生代地层年龄小于古新统，并不存在神狐组古新统。大部分新生代年龄组分主要集中于63–50 Ma以及45–35 Ma两个阶段。锆石微量元素构造判别图解显示，大部分新生代锆石形成于板内环境， $\epsilon_{\text{Hf}}(t)$ 正值可能反映来自于幔源岩浆，与之前中生代时期的大陆弧活动陆缘形成明显对比。南海早新生代岩浆作用相对中生代较不活跃，结合国际大洋钻探计划最新成果，本研究认为南海在经历极度拉伸和薄化作用之前，整体表现为贫岩浆型。

印支半岛与华南大陆在早中生代可能曾发生剧烈的俯冲、碰撞、挤压、拼合与抬升作用，形成了越中地区广阔的造山带，包含大量的基性-超基性物质，很大程度上是古特提斯洋俯冲过程中的残留记录，具有独特的Eu元素正异常特征，这个位于南海西侧的物源区与其他潜在源区在元素地球化学和锆石U-Pb年龄谱系上均存在明显差异。

由于中生代末太平洋板块俯冲拼合与安第斯型火山弧的发育，华南大陆边缘形成了近东西向展布、隆拗相间的地貌特征。南海北部地区早新生代开始经历大规模裂谷阶段，西侧靠近印支半岛的地区以隆升剥蚀区为主，东侧以河流相、湖泊相和沼泽相为主。再此构造古地理整体格局下，本论文发现南海西部自始新世发育一条东西向古河——“崑—莺—琼”古河，向南海东侧珠二凹陷输送了大量基性物；珠一凹陷仅在靠近华南沿海地区接受了来自流经华南东南

火成岩源区的河流搬运的碎屑物质。晚渐新世这条东西向古河的规模达到顶峰,北侧的珠江水系也已接近现在的规模,两大水系共同影响了南海北部的沉积格局。早中新世,珠江流域进一步扩大对珠江口盆地的影响,现代珠江基本形成,全面控制珠一与珠二凹陷;“崑一莺一琼”古河逐步萎缩至琼东南盆地,而晚中新世以来在琼东南深水区发育的中央峡谷便是该古河的残余。

中央峡谷上中新统一上新统西侧样品大都呈Eu元素正异常,东侧样品以Eu元素负异常为主,随着地层变年轻,呈现Eu元素亏损的样品数量增多。同时,碎屑锆石年龄谱系表现出一定的时空演变规律,西侧沉积物包含较多的古生代及元古代等古老锆石,东侧以燕山期和印支期峰值为主。中南半岛中北部印支期的板块拼合带是中央峡谷的重要源区,海南岛是另一重要源区,在中央峡谷西侧沉积物中为次要物源,但对于东侧沉积物则变为主要物源。

晚中新世,源自中南半岛的“崑一莺一琼”古河和华夏地块的珠江均向南海北部深水区提供了大量陆源物质,形成数百米厚的深海砂质沉积。这些砂质沉积物以浊流形式继续自西向东搬运,并下切侵蚀沿途洋壳基性物质,最终进入马尼拉海沟堆积下来,形成包含基性砾石的浊积体。伴随菲律宾海板块向西北方向顺时针旋转漂移,这些浊积体被推挤、迁移并最终增生楔的形式在中更新世出露于恒春半岛地区。

8.2 进一步工作的方向

本文的研究虽然取得了初步的成功,但依然任重道远,尚有许多有待进一步深入进行的研究工作,这里择其要者简要讨论如下:

古珠江作为南海北部沉积物的重要物源区,源汇对比研究比较深入,已经取得较多成果。相对来说,对南海北部深水区的沉积物源研究相对落后,其研究主要集中在对红河物源以及珠江深水扇的研究上。现有资料显示,南海东部与西部地区接受沉积的时间并不一致,存在东早西晚的特征。受中生代末板块俯冲拼合的影响,欧亚大陆东南缘在新生代初期总体呈现近东西向展布、隆坳相间的地貌形态。在这种古地理格局上,南海西侧在地形-沉积等方面如何与东侧海湾相连尚不清楚,沉积物在东西方向的轴向搬运值得关注。

南海北部沉积物主要由珠江和红河提供,现有研究已经系统揭示珠江形成与南海北部沉积充填之间的耦合关系。对于南海西部中央峡谷的研究也获得突破性进展。同时发现存在一条东西向古河,把南海西侧物质从西向东搬运进南海,晚中新世琼东南盆地的中央峡谷可能是该古河流的残余。但是,该河流搬运的碎屑物质是源自红河、越南中部,还是来自海南岛并不清楚,不同物源的贡献率也未研究。

欧亚大陆东南缘由一系列从东冈瓦纳大陆北部边缘裂离的陆块组成，在中-新生代构成了环太平洋俯冲带的重要一环。研究认为，该地区自中生代以来受到古太平洋板块俯冲的强烈影响，发育了安第斯型增生造山带的主动陆缘，在日本、东海及华南大陆沿海地区保留了大量的地质记录，并经南海进一步延伸至印支半岛东南部。进入新生代，南海地区转换为西太平洋型被动陆缘，经历断陷—拆离—拉张等过程形成了西太平洋面积最大的边缘海盆地。研究显示，南沙地块、礼乐盆地及巴拉望陆块中生代时期始终拼贴于华南大陆南缘，在构造上属于古太平洋俯冲体系的一部分，在南海断陷扩张之后才逐步裂离并漂移至南海南部地区。然而，学术界目前对古太平洋板块俯冲及其动力学过程的研究主要基于华南大陆东缘及东南缘中的岩浆—沉积记录，对南海南部的研究明显欠缺。

相对南海北部，有关南海南部地区的源汇对比、剥蚀-搬运-沉积过程、地形地貌演变及其构造控制因素等研究极为欠缺。婆罗洲出露的上白垩统一中新统沉积序列，主要包括古晋超级群、拉让群、克拉克扇以及新近系前陆沉积地层，是研究南海南部源-汇系统及沉积演变的最佳素材。其中对于巨厚的拉让群和克拉克扇沉积物来源一直存在很大争议：早期学者认为，伴随“古南海”持续俯冲，沉积物来自北部中南半岛或华南大陆，通过古湄公河、古巽他河等搬运而来。近年来，有学者提出婆罗洲北部可能主要接受来自西南婆罗洲斯赫瓦纳山剥蚀搬运的物质，且搬运距离相对较近；同时还可能受到西侧马来半岛源区的影响，搬运距离相对较远。由于婆罗洲自然条件恶劣，地层结构和演化过程复杂，缺少精准的古生物或同位素年代学资料，至今未能建立一套完整统一的地层框架。同时，该地区发生多期造山作用，构造改造强烈，一直没有发现确凿的新生代俯冲岛弧岩浆岩。相邻盆地内钻井基本仅钻至中新统，造成现有源-汇对比研究成果以局部认识为主，制约了对南海南部地区沉积充填过程及其控制因素的整体认识。

参考文献

- [1] Tamaki K., Honza E. Global tectonics and formation of marginal basins: Role of the western Pacific. *Episodes Journal of International Geoscience*, 1991, 14(3): 224–230.
- [2] Tatsumi Y., Otofujii Y.-I., Matsuda T., Nohda S. Opening of the Sea of Japan back-arc basin by asthenospheric injection. *Tectonophysics*, 1989, 166(4): 317–329.
- [3] Sleep N., Toksöz M.N. Evolution of marginal basins. *Nature*, 1971, 233(5321): 548–550.
- [4] Honza E. Spreading mode of backarc basins in the western Pacific. *Tectonophysics*, 1995, 251(1-4): 139–152.
- [5] 任建业, 李思田. 西太平洋边缘海盆地的扩张过程和动力学背景. *地学前缘*, 2000, 7(3): 203–213.
- [6] Karig D.E. Origin and development of marginal basins in the western Pacific. *Journal of geophysical research*, 1971, 76(11): 2542–2561.
- [7] Uyeda S., Kanamori H. Back-arc opening and the mode of subduction. *Journal of Geophysical Research: Solid Earth*, 1979, 84(B3): 1049–1061.
- [8] Carlson R., Melia P. Subduction hinge migration. *Tectonophysics*, 1984, 102(1-4): 399–411.
- [9] 张勇, 任治军, 葛海明, 王广哲, 李三忠, 郭玲莉, 王鹏程. 南海转换断层成因机制及对南海扩张的启示. *海洋地质与第四纪地质*, 2017, 37(4): 193–208.
- [10] Zhou D. Marginal Seas, in *Encyclopedia of Marine Geosciences*, J. Harff, et al., Editors. 2016, Springer Netherlands: Dordrecht. p. 423–427.
- [11] 王鹏程, 李三忠, 郭玲莉, 赵淑娟, 李玺瑶, 王永明, 惠格格, 王倩. 南海打开模式: 右行走滑拉分与古南海俯冲拖曳. *地学前缘*, 2017, 24(4): 294–319.
- [12] Tapponnier P., Lacassin R., Leloup P.H., Schärer U., Dalai Z., Haiwei W., Xiaohan L., Shaocheng J., Lianshang Z., Jiayou Z. The Ailao Shan/Red River metamorphic belt: tertiary left-lateral shear between Indochina and South China. *Nature*, 1990, 343(6257): 431–437.
- [13] Leloup P.H., Arnaud N., Lacassin R., Kienast J., Harrison T., Trong T.P., Replumaz A., Tapponnier P. New constraints on the structure, thermochronology, and timing of the Ailao Shan-Red River shear zone, SE Asia. *Journal of Geophysical Research: Solid Earth*, 2001, 106(B4): 6683–6732.
- [14] Hall R. Cenozoic geological and plate tectonic evolution of SE Asia and the SW Pacific: computer-based reconstructions, model and animations. *Journal of Asian earth sciences*, 2002, 20(4): 353–431.
- [15] 李三忠, 索艳慧, 刘鑫, 戴黎明, 余珊, 赵淑娟, 马云, 王霄飞, 程世秀, 安慧婷. 南海的盆地群与盆地动力学. *海洋地质与第四纪地质*, 2012, 32(6): 55–78.
- [16] Yin A. Cenozoic tectonic evolution of Asia: A preliminary synthesis. *Tectonophysics*, 2010, 488(1-4): 293–325.
- [17] Metcalfe I. Pre-Cretaceous evolution of SE Asian terranes. Geological Society, London, Special Publications, 1996, 106(1): 97–122.
- [18] Metcalfe I. Palaeozoic and Mesozoic tectonic evolution and palaeogeography of East Asian crustal fragments: the Korean Peninsula in context. *Gondwana Research*, 2006, 9(1-2): 24–46.
- [19] 林间, 李家彪, 徐义刚, 孙珍, 夏少红, 黄小龙, 解习农, 李春峰, 丁巍伟, 周志远.

- 南海大洋钻探及海洋地质与地球物理前沿研究新突破. 海洋学报, 2019, 41(10): 125–140.
- [20] 汪品先. 追踪边缘海的生命史: “南海深部计划” 的科学目标. 科学通报, 2012, 57(20): 1807–1826.
- [21] Briais A., Patriat P., Tapponnier P. Updated interpretation of magnetic anomalies and seafloor spreading stages in the South China Sea: Implications for the Tertiary tectonics of Southeast Asia. *Journal of Geophysical Research: Solid Earth*, 1993, 98(B4): 6299–6328.
- [22] Jian Z., Larsen H., Alvarez Zarikian C. Expedition 368 preliminary report: South China Sea rifted margin. Preliminary report, 2018, 368.
- [23] 解习农, 赵帅, 任建业, 杨允柳, 姚永坚. 南海后扩张期大陆边缘闭合过程及成因机制. 地球科学, 2022, 47(10): 3524–3542.
- [24] Sibuet J.-C., Yeh Y.-C., Lee C.-S. Geodynamics of the south China sea. *Tectonophysics*, 2016, 692: 98–119.
- [25] Morley C. A tectonic model for the Tertiary evolution of strike–slip faults and rift basins in SE Asia. *Tectonophysics*, 2002, 347(4): 189–215.
- [26] Pigott J.D., Ru K. Basin superposition on the northern margin of the South China Sea. *Tectonophysics*, 1994, 235(1-2): 27–50.
- [27] Nissen S.S., Hayes D.E., Bochu Y., Zeng W., Chen Y., Nu X. Gravity, heat flow, and seismic constraints on the processes of crustal extension: Northern margin of the South China Sea. *Journal of geophysical research: solid earth*, 1995, 100(B11): 22447–22483.
- [28] Nissen S.S., Hayes D.E., Buhl P., Diebold J., Bochu Y., Zeng W., Chen Y. Deep penetration seismic soundings across the northern margin of the South China Sea. *Journal of Geophysical Research: Solid Earth*, 1995, 100(B11): 22407–22433.
- [29] Braitenberg C., Wienecke S., Wang Y. Basement structures from satellite-derived gravity field: South China Sea ridge. *Journal of Geophysical Research: Solid Earth*, 2006, 111(B5).
- [30] Pichot T., Delescluse M., Chamot-Rooke N., Pubellier M., Qiu Y., Meresse F., Sun G., Savva D., Wong K.P., Watremez L. Deep crustal structure of the conjugate margins of the SW South China Sea from wide-angle refraction seismic data. *Marine and Petroleum Geology*, 2014, 58: 627–643.
- [31] Sun X., Zhang X., Zhang G., Lu B., Yue J., Zhang B. Texture and tectonic attribute of Cenozoic basin basement in the northern South China Sea. *Science China Earth Sciences*, 2014, 57: 1199–1211.
- [32] Nielsen L., Mathiesen A., Bidstrup T., Vejbæk O., Dien P., Tiem P. Modelling of hydrocarbon generation in the Cenozoic Song Hong Basin, Vietnam: a highly prospective basin. *Journal of Asian Earth Sciences*, 1999, 17(1-2): 269–294.
- [33] Yan Q., Shi X., Liu J., Wang K., Bu W. Petrology and geochemistry of Mesozoic granitic rocks from the Nansha micro-block, the South China Sea: Constraints on the basement nature. *Journal of Asian Earth Sciences*, 2010, 37(2): 130–139.
- [34] Barckhausen U. Engels M., Franke D., Ladage S., Pubellier M., Evolution of the South China Sea: Revised ages for breakup and seafloor spreading. *Marine and Petroleum Geology*, 2014, 58: 599–611.
- [35] Larsen H.C., Mohn G., Nirrengarten M., Sun Z., Stock J., Jian Z., Klaus A., Alvarez-Zarikian C., Boaga J., Bowden S. Rapid transition from continental breakup to igneous oceanic crust in

- the South China Sea. *Nature Geoscience*, 2018, 11(10): 782–789.
- [36] Huang C.-Y., Wang P., Yu M., You C.-F., Liu C.-S., Zhao X., Shao L., Zhong G., Yumul Jr G.P., Potential role of strike-slip faults in opening up the South China Sea. *National Science Review*, 2019, 6(5): 891–901.
- [37] Li C.F., Xu X., Lin J., Sun Z., Zhu J., Yao Y., Zhao X., Liu Q., Kulhanek D.K., Wang J. Ages and magnetic structures of the South China Sea constrained by deep tow magnetic surveys and IODP Expedition 349. *Geochemistry, Geophysics, Geosystems*, 2014, 15(12): 4958–4983.
- [38] Sun Z., Lin J., Qiu N., Jian Z., Wang P., Pang X., Zheng J., Zhu B. The role of magmatism in the thinning and breakup of the South China Sea continental margin: Special Topic: The South China Sea Ocean Drilling. *National Science Review*, 2019, 6(5): 871–876.
- [39] Pubellier M., Morley C. The basins of Sundaland (SE Asia): Evolution and boundary conditions. *Marine and Petroleum Geology*, 2014, 58: 555–578.
- [40] 孙珍, 赵中贤, 周蒂, 杨少坤, 林鹤鸣, 陈广浩. 南沙海域盆地的地层系统与沉积结构. *地球科学*, 2011, 36(5): 798–806.
- [41] 李铁刚, 曹奇原, 李安春, 秦蕴珊. 从源到汇: 大陆边缘的沉积作用. *地球科学进展*, 2003, 18(5): 713–721.
- [42] 操应长, 徐琦松, 王健. 沉积盆地“源-汇”系统研究进展. *地学前缘 (中国地质大学 (北京))*, 2018, 25(4): 116–131.
- [43] Allen P.A. From landscapes into geological history. *Nature*, 2008, 451(7176): 274–276.
- [44] 朱红涛, 徐长贵, 朱筱敏, 曾洪流, 姜在兴, 刘可禹. 陆相盆地源-汇系统要素耦合研究进展. *地球科学*, 2017, 42(11): 1851–1870.
- [45] Bhattacharya J.P., Copeland P., Lawton T.F., Holbrook J. Estimation of source area, river paleo-discharge, paleoslope, and sediment budgets of linked deep-time depositional systems and implications for hydrocarbon potential. *Earth-Science Reviews*, 2016, 153: 77–110.
- [46] Helland-Hansen W., Sømme T.O., Martinsen O.J., Lunt I., Thurmond J. Deciphering Earth's natural hourglasses: perspectives on source-to-sink analysis. *Journal of Sedimentary Research*, 2016, 86(9): 1008–1033.
- [47] Leeder M.R., Harris T., Kirkby M.J. Sediment supply and climate change: implications for basin stratigraphy. *Basin research*, 1998, 10(1): 7–18.
- [48] Densmore A.L., Allen P.A., Simpson G., Development and response of a coupled catchment fan system under changing tectonic and climatic forcing. *Journal of Geophysical Research: Earth Surface*, 2007, 112(F1): 1–16.
- [49] Allen P.A., Armitage J.J., Carter A., Duller R.A., Michael N.A., Sinclair H.D., Whittaker A.L., Whittaker A.C. The Qs problem: Sediment volumetric balance of proximal foreland basin systems. *Sedimentology*, 2013, 60(1): 102–130.
- [50] Densmore A.L., Hovius N., Topographic fingerprints of bedrock landslides. *Geology*, 2000, 28(4): 371–374.
- [51] Garzanti E. The maturity myth in sedimentology and provenance analysis. *Journal of Sedimentary Research*, 2017, 87(4): 353–365.
- [52] Johnsson M.J. The system controlling the composition of clastic sediments. 1993, 284: 1–19.
- [53] Weltje G.J. Quantitative models of sediment generation and provenance: state of the art and future developments. *Sedimentary Geology*, 2012, 280: 4–20.
- [54] Whittaker A.C., Duller R.A., Springett J., Smithells R.A., Whittaker A.L., Allen P.A.

- Decoding downstream trends in stratigraphic grain size as a function of tectonic subsidence and sediment supply. *Bulletin*, 2011, 123(7-8): 1363–1382.
- [55] Dickinson W.R., Suczek C.A. Plate tectonics and sandstone compositions. *Aapg Bulletin*, 1979, 63(12): 2164–2182.
- [56] Roser B.P., Korsch R.J. Provenance signatures of sandstone-mudstone suites determined using discriminant function analysis of major-element data. *Chemical geology*, 1988, 67(1-2): 119–139.
- [57] Rollinson H. A terrane interpretation of the Archaean Limpopo Belt. *Geological Magazine*, 1993, 130(6): 755–765.
- [58] McLennan S., Hemming S., McDaniel D., Hanson G. Geochemical approaches to sedimentation, provenance, and tectonics. 1993. p. 21–40.
- [59] Nesbitt H., Young G., McLennan S., Keays R. Effects of chemical weathering and sorting on the petrogenesis of siliciclastic sediments, with implications for provenance studies. *The journal of geology*, 1996, 104(5): 525–542.
- [60] Morton A.C., Hallsworth C. Identifying provenance-specific features of detrital heavy mineral assemblages in sandstones. *Sedimentary Geology*, 1994, 90(3-4): 241–256.
- [61] Gehrels G., Valencia V., Pullen A. Detrital zircon geochronology by laser-ablation multicollector ICPMS at the Arizona LaserChron Center. *The Paleontological Society Papers*, 2006, 12: 67–76.
- [62] Gehrels G. Detrital zircon U-Pb geochronology: Current methods and new opportunities. *Tectonics of sedimentary basins: Recent advances*, 2011: 45–62.
- [63] Vermeesch P. On the visualisation of detrital age distributions. *Chemical Geology*, 2012, 312: 190–194.
- [64] Vermeesch P. How many grains are needed for a provenance study? *Earth and Planetary Science Letters*, 2004, 224(3-4): 441–451.
- [65] 郭广慧, 钟世华, 李三忠, 丰成友, 戴黎明, 索艳慧, 刘嘉情, 牛警徽, 黄宇, 薛梓萌. 运用机器学习和锆石微量元素构建花岗岩成矿潜力判别图解: 以东昆仑祁漫塔格为例. *西北地质*, 2023, 56(6): 57–70.
- [66] Zhong S., Li S., Liu Y., Cawood P.A., Seltmann R. I-type and S-type granites in the Earth's earliest continental crust. *Communications Earth, Environment*, 2023, 4(1): 61.
- [67] 李继亮, 肖文交, 闫臻. 盆山耦合与沉积作用. *沉积学报*, 2003, 21(1): 52–60.
- [68] 张进, 马宗晋, 任文军. 对盆山耦合研究的新看法. *石油实验地质*, 2004, 26(2): 169–175.
- [69] Sharman G.R., Covault J.A., Stockli D.F., Wroblewski A.F.-J., Bush M.A. Early Cenozoic drainage reorganization of the United States Western Interior–Gulf of Mexico sediment routing system. *Geology*, 2017, 45(2): 187–190.
- [70] Grimes C., Wooden J., Cheadle M., John B. “Fingerprinting” tectono-magmatic provenance using trace elements in igneous zircon. *Contributions to Mineralogy and Petrology*, 2015, 170: 1–26.
- [71] McKenzie N.R., Smye A.J., Hegde V.S., Stockli D.F. Continental growth histories revealed by detrital zircon trace elements: A case study from India. *Geology*, 2018, 46(3): 275–278.
- [72] Müller R.D., Cannon J., Qin X., Watson R.J., Gurnis M., Williams S., Pfaffelmoser T., Seton M., Russell S.H., Zahirovic S. GPlates: Building a virtual Earth through deep time.

- Geochemistry, Geophysics, Geosystems, 2018, 19(7): 2243–2261.
- [73] Müller R.D., Royer J.-Y., Lawver L.A. Revised plate motions relative to the hotspots from combined Atlantic and Indian Ocean hotspot tracks. *Geology*, 1993, 21(3): 275–278.
- [74] Scotese C.R., Gahagan L.M., Larson R.L. Plate tectonic reconstructions of the Cretaceous and Cenozoic ocean basins. *Tectonophysics*, 1988, 155(1-4): 27–48.
- [75] Lee T.-Y., Lawver L.A. Cenozoic plate reconstruction of Southeast Asia. *Tectonophysics*, 1995, 251(1-4): 85–138.
- [76] Matthews K.J., Maloney K.T., Zahirovic S., Williams S.E., Seton M., Müller R.D. Global plate boundary evolution and kinematics since the late Paleozoic. *Global and Planetary Change*, 2016, 146: 226–250.
- [77] Seton M., Müller R.D., Zahirovic S., Gaina C., Torsvik T., Shephard G., Talsma A., Gurnis M., Turner M., Maus S. Global continental and ocean basin reconstructions since 200 Ma. *Earth-Science Reviews*, 2012, 113(3-4): 212–270.
- [78] Zahirovic S., Seton M., Müller R. The cretaceous and cenozoic tectonic evolution of Southeast Asia. *Solid Earth*, 2014, 5(1): 227–273.
- [79] Hall R. Reconstructing Cenozoic SE Asia. Geological Society, London, Special Publications, 1996, 106(1): 153–184.
- [80] Hall R. Late Jurassic–Cenozoic reconstructions of the Indonesian region and the Indian Ocean. *Tectonophysics*, 2012, 570: 1–41.
- [81] Hall R. Australia–SE Asia collision: plate tectonics and crustal flow. 2011.
- [82] 李三忠, 余珊, 赵淑娟, 张国伟, 刘鑫, 曹花花, 许立青, 戴黎明, 李涛. 超大陆与全球板块重建派别. *海洋地质与第四纪地质*, 2014, 34(6): 97–117.
- [83] Li Z.-X., Bogdanova S., Collins A., Davidson A., De Waele B., Ernst R., Fitzsimons I., Fuck R., Gladkochub D., Jacobs J. Assembly, configuration, and break-up history of Rodinia: a synthesis. *Precambrian research*, 2008, 160(1-2): 179–210.
- [84] Li Z.-X., Evans D.A. Late Neoproterozoic 40 intraplate rotation within Australia allows for a tighter-fitting and longer-lasting Rodinia. *Geology*, 2011, 39(1): 39–42.
- [85] Cawood P.A., Hawkesworth C., Dhuime B. Detrital zircon record and tectonic setting. *Geology*, 2012, 40(10): 875–878.
- [86] Zhao G., Cawood P.A., Wilde S.A., Sun M. Review of global 2.1–1.8 Ga orogens: implications for a pre-Rodinia supercontinent. *Earth-Science Reviews*, 2002, 59(1-4): 125–162.
- [87] Metcalfe I. Gondwana dispersion and Asian accretion: Tectonic and palaeogeographic evolution of eastern Tethys. *Journal of Asian Earth Sciences*, 2013, 66: 1–33.
- [88] Morley C. Late Cretaceous–early Palaeogene tectonic development of SE Asia. *Earth-Science Reviews*, 2012, 115(1-2): 37–75.
- [89] Collins A.S., Clark C., Plavsa D. Peninsular India in Gondwana: The tectonothermal evolution of the Southern Granulite Terrain and its Gondwanan counterparts. *Gondwana Research*, 2014, 25(1): 190–203.
- [90] Franke D., Barckhausen U., Baristean N., Engels M., Ladage S., Lutz R., Montano J., Pellejera N., Ramos E., Schnabel M. The continent-ocean transition at the southeastern margin of the South China Sea. *Marine and Petroleum Geology*, 2011, 28(6): 1187–1204.
- [91] Carter A., Roques D., Bristow C., Kinny P. Understanding Mesozoic accretion in Southeast Asia: significance of Triassic thermotectonism (Indosinian orogeny) in Vietnam. *Geology*,

- 2001, 29(3): 211–214.
- [92] Lepvrier C., Maluski H., Van Tich V., Leyreloup A., Thi P.T., Van Vuong N. The early Triassic Indosinian orogeny in Vietnam (Truong Son Belt and Kontum Massif); implications for the geodynamic evolution of Indochina. *Tectonophysics*, 2004, 393(1-4): 87–118.
- [93] Li X.-H., Li Z.-X., Li W.-X., Wang Y. Initiation of the Indosinian Orogeny in South China: evidence for a Permian magmatic arc on Hainan Island. *The Journal of geology*, 2006, 114(3): 341–353.
- [94] Hutchison C.S. *Geological evolution of South-east Asia*. 13. 1989: Clarendon Press Oxford.
- [95] Dien P., Nielsen L., Andersen C., Nhuan D. Late-Mesozoic and Cenozoic basin development along the northwest margin of Vietnam. in *American Association of Petroleum Geologists Annual Convention, Abstract*, Salt Lake City, Utah. 1998.
- [96] Fyhn M.B., Cuong T.D., Hoang B.H., Hovikoski J., Olivarius M., Tuan N.Q., Tung N.T., Huyen N.T., Cuong T.X., Nytoft H.P. Linking Paleogene rifting and inversion in the northern Song Hong and Beibuwan basins, Vietnam, with left-lateral motion on the Ailao Shan-Red River shear zone. *Tectonics*, 2018, 37(8): 2559–2585.
- [97] Zhou X., Li W. Origin of Late Mesozoic igneous rocks in Southeastern China: implications for lithosphere subduction and underplating of mafic magmas. *Tectonophysics*, 2000, 326(3-4): 269–287.
- [98] Yui T., Maki K., Lan C., Hirata T., Chu H., Kon Y., Yokoyama T., Jahn B., Ernst W. Detrital zircons from the Tananao metamorphic complex of Taiwan: Implications for sediment provenance and Mesozoic tectonics. *Tectonophysics*, 2012, 541: 31–42.
- [99] Li Z.-X., Li X.-H. Formation of the 1300-km-wide intracontinental orogen and postorogenic magmatic province in Mesozoic South China: A flat-slab subduction model. *Geology*, 2007, 35(2): 179–182.
- [100] Faure M., Lin W., Chu Y. Lepvrier C., Triassic tectonics of the southern margin of the South China Block. *Comptes Rendus. Géoscience*, 2016, 348(1): 5–14.
- [101] Xu C., Zhang L., Shi H., Brix M.R., Huhma H., Chen L., Zhang M., Zhou Z. Tracing an early Jurassic magmatic arc from South to East China Seas. *Tectonics*, 2017, 36(3): 466–492.
- [102] Li Z.-X., Li X.-H., Chung S.-L., Lo C.-H., Xu X., Li W.-X. Magmatic switch-on and switch-off along the South China continental margin since the Permian: Transition from an Andean-type to a Western Pacific-type plate boundary. *Tectonophysics*, 2012, 532: 271–290.
- [103] Hayes D.E., Nissen S.S., The South China sea margins: Implications for rifting contrasts. *Earth and Planetary Science Letters*, 2005, 237(3-4): 601–616
- [104] Lei C., Ren J. Hyper-extended rift systems in the Xisha Trough, northwestern South China Sea: Implications for extreme crustal thinning ahead of a propagating ocean. *Marine and Petroleum Geology*, 2016, 77: 846–864.
- [105] Lei C., Alves T.M., Ren J., Pang X., Yang L., Liu J. Depositional architecture and structural evolution of a region immediately inboard of the locus of continental breakup (Liwan Sub-basin, South China Sea). *GSA Bulletin*, 2019, 131(7-8): 1059–1074.
- [106] Wang J., Zhang X., Wu J., Chen B., Zhong H., Hao H. Integrated geophysical researches on base texture of Zhujiang River Mouth Basin. *Journal of Tropical Oceanography*, 2002, 21(2): 13–22.
- [107] 秦国权. 西沙群岛“西永一井”有孔虫组合及该群岛珊瑚礁成因初探. *热带海洋*,

- 1987, 6(3): 10–20.
- [108] Zhu W., Xie X., Wang Z., Zhang D., Zhang C., Cao L., Shao L. New insights on the origin of the basement of the Xisha Uplift, South China Sea. *Science China Earth Sciences*, 2017, 60: 2214–2222.
- [109] Ebbing J., Braitenberg C., Götze H.-J. The lithospheric density structure of the Eastern Alps. *Tectonophysics*, 2006, 414(1-4): 145–155.
- [110] Hsu S.-K., Yeh Y.-c., Doo W.-B., Tsai C.-H. New bathymetry and magnetic lineations identifications in the northernmost South China Sea and their tectonic implications. *Marine Geophysical Researches*, 2004, 25: 29–44.
- [111] Li C.-F., Zhou Z., Hao H., Chen H., Wang J., Chen B., Wu J. Late Mesozoic tectonic structure and evolution along the present-day northeastern South China Sea continental margin. *Journal of Asian Earth Sciences*, 2008, 31(4-6): 546–561.
- [112] Li C.-F., Zhou Z., Li J., Chen B., Geng J. Magnetic zoning and seismic structure of the South China Sea ocean basin. *Marine Geophysical Researches*, 2008, 29: 223–238.
- [113] Ebinger C., Hayward N. Soft plates and hot spots: Views from Afar. *Journal of Geophysical Research: Solid Earth*, 1996, 101(B10): 21859–21876.
- [114] Clift P., Lin J. Preferential mantle lithospheric extension under the South China margin. *Marine and Petroleum Geology*, 2001, 18(8): 929–945.
- [115] Qiu X., Ye S., Wu S., Shi X., Zhou D., Xia K., Flueh E.R. Crustal structure across the Xisha trough, northwestern South China Sea. *Tectonophysics*, 2001, 341(1-4): 179–193.
- [116] Yao W., Li Z.-X., Li W.-X., Li X.-H. Proterozoic tectonics of Hainan Island in supercontinent cycles: New insights from geochronological and isotopic results. *Precambrian Research*, 2017, 290: 86–100.
- [117] Jiang X.-Y., Li X.-H., Collins W., Huang H.-Q. U-Pb age and Hf-O isotopes of detrital zircons from Hainan Island: Implications for Mesozoic subduction models. *Lithos*, 2015, 239: 60–70.
- [118] Jahn B.-M., Chen P., Yen T. Rb-Sr ages of granitic rocks in southeastern China and their tectonic significance. *Geological Society of America Bulletin*, 1976, 87(5): 763–776.
- [119] Klimetz M.P. Speculations on the Mesozoic plate tectonic evolution of eastern China. *Tectonics*, 1983, 2(2): 139–166.
- [120] Lapierre H., Jahn B., Charvet J., Yu Y. Mesozoic felsic arc magmatism and continental olivine tholeiites in Zhejiang Province and their relationship with the tectonic activity in southeastern China. *Tectonophysics*, 1997, 274(4): 321–338.
- [121] Ramos V.A., Folguera A. Andean flat-slab subduction through time. *Geological Society, London, Special Publications*, 2009, 327(1): 31–54.
- [122] Kiminami K., Imaoka T. Spatiotemporal variations of Jurassic–Cretaceous magmatism in eastern Asia (Tan-Lu Fault to SW Japan): evidence for flat-slab subduction and slab rollback. *Terra Nova*, 2013, 25(5): 414–422.
- [123] Zhou X., Sun T., Shen W., Shu L., Niu Y. Petrogenesis of Mesozoic granitoids and volcanic rocks in South China: a response to tectonic evolution. *Episodes Journal of International Geoscience*, 2006, 29(1): 26–33.
- [124] Charvet J., Lapierre H., Yu Y. Geodynamic significance of the Mesozoic volcanism of southeastern China. *Journal of Southeast Asian Earth Sciences*, 1994, 9(4): 387–396.

- [125] Li X.-H., Li Z.-X., He B., Li W.-X., Li Q.-L., Gao Y., Wang X.-C. The Early Permian active continental margin and crustal growth of the Cathaysia Block: In situ U–Pb, Lu–Hf and O isotope analyses of detrital zircons. *Chemical Geology*, 2012, 328: 195–207.
- [126] Zhang F.-Q., Wu H.-X., Dilek Y., Zhang W., Zhu K.-Y., Chen H.-L. Guadalupian (Permian) onset of subduction zone volcanism and geodynamic turnover from passive-to active-margin tectonics in southeast China. *Bulletin*, 2020, 132(1-2): 130–148.
- [127] Isozaki Y., Aoki K., Nakama T., Yanai S. New insight into a subduction-related orogen: A reappraisal of the geotectonic framework and evolution of the Japanese Islands. *Gondwana Research*, 2010, 18(1): 82–105.
- [128] 崔盛芹, 李锦蓉. 试论中国滨太平洋带的印支运动. *地质学报*, 1983, 57(1): 51–61.
- [129] Hsü K.J., Li J., Chen H., Wang Q., Sun S., Şengör A. Tectonics of South China: key to understanding West Pacific geology. *Tectonophysics*, 1990, 183(1-4): 9–39.
- [130] Li Z.X. Tectonic history of the major east Asian lithospheric blocks since the mid-Proterozoic—a synthesis. *Mantle dynamics and plate interactions in East Asia*, 1998, 27: 221–243.
- [131] Qiu Y., Li P., Liang H. Late Cretaceous-Cenozoic tectonic evolution and nature of continental margin in the northern South China Sea and Taiwan Strait. *Guangdong Geology (in Chinese)*, 1996, 11(3): 10–16.
- [132] 李平鲁, 梁慧娴. 珠江口盆地新生代岩浆活动与盆地演化, 油气聚集的关系. *广东地质*, 1994, 9(2): 23–24.
- [133] Nguyen T.T.B., Satir M., Siebel W., Chen F. Granitoids in the Dalat zone, southern Vietnam: age constraints on magmatism and regional geological implications. *International Journal of Earth Sciences*, 2004, 93: 329–340.
- [134] Shao L., Cao L., Qiao P., Zhang X., Li Q., van Hinsbergen D.J. Cretaceous–Eocene provenance connections between the Palawan Continental Terrane and the northern South China Sea margin. *Earth and Planetary Science Letters*, 2017, 477: 97–107.
- [135] Shao L., Cui Y., Statterger K., Zhu W., Qiao P., Zhao Z. Drainage control of Eocene to Miocene sedimentary records in the southeastern margin of Eurasian Plate. *GSA Bulletin*, 2019, 131(3-4): 461–478.
- [136] Hennig J., Breitfeld H.T., Hall R., Nugraha A.S. The Mesozoic tectono-magmatic evolution at the Paleo-Pacific subduction zone in West Borneo. *Gondwana Research*, 2017, 48: 292–310.
- [137] Suggate S.M., Cottam M.A., Hall R., Sevastjanova I., Forster M.A., White L.T., Armstrong R.A., Carter A., Mojares E. South China continental margin signature for sandstones and granites from Palawan, Philippines. *Gondwana Research*, 2014, 26(2): 699–718.
- [138] Niu Y., Liu Y., Xue Q., Shao F., Chen S., Duan M., Guo P., Gong H., Hu Y., Hu Z. Exotic origin of the Chinese continental shelf: new insights into the tectonic evolution of the western Pacific and eastern China since the Mesozoic. *Science Bulletin*, 2015, 60(18): 1598–1616.
- [139] Xu C., Deng Y., Barnes C.G., Shi H., Pascal C., Li Y., Gao S., Jiang D., Xie J., Ma C. Offshore-onshore tectonomagmatic correlations: Towards a Late Mesozoic non-Andean-type Cathaysian continental margin. *Earth-Science Reviews*, 2023, 240: 104382.
- [140] Suo Y., Li S., Jin C., Zhang Y., Zhou J., Li X., Wang P., Liu Z., Wang X., Somerville I. Eastward tectonic migration and transition of the Jurassic-Cretaceous Andean-type continental

- margin along Southeast China. *Earth-Science Reviews*, 2019, 196: 102884.
- [141] Li S., Suo Y., Li X., Zhou J., Santosh M., Wang P., Wang G., Guo L., Yu S., Lan H. Mesozoic tectono-magmatic response in the East Asian ocean-continent connection zone to subduction of the Paleo-Pacific Plate. *Earth-Science Reviews*, 2019, 192: 91–137.
- [142] Zhang Q., Wu S., Dong D. Cenozoic magmatism in the northern continental margin of the South China Sea: Evidence from seismic profiles. *Marine Geophysical Research*, 2016, 37: 71–94.
- [143] White R., McKenzie D. Magmatism at rift zones: the generation of volcanic continental margins and flood basalts. *Journal of Geophysical Research: Solid Earth*, 1989, 94(B6): 7685–7729.
- [144] Planke S., Symonds P.A., Alvestad E., Skogseid J. Seismic volcanostratigraphy of large-volume basaltic extrusive complexes on rifted margins. *Journal of Geophysical Research: Solid Earth*, 2000, 105(B8): 19335–19351.
- [145] Franke D., Savva D., Pubellier M., Steuer S., Mouly B., Auxietre J.-L., Meresse F., Chamot-Rooke N. The final rifting evolution in the South China Sea. *Marine and Petroleum Geology*, 2014, 58: 704–720.
- [146] Dean S., Minshull T., Whitmarsh R., Louden K. Deep structure of the ocean-continent transition in the southern Iberia Abyssal Plain from seismic refraction profiles: The IAM-9 transect at 40°20' N. *Journal of Geophysical Research: Solid Earth*, 2000, 105(B3): 5859–5885.
- [147] Mohn G., Manatschal G., Beltrando M., Masini E., Kuszniir N. Necking of continental crust in magma-poor rifted margins: Evidence from the fossil Alpine Tethys margins. *Tectonics*, 2012, 31(1).
- [148] Péron-Pinvidic G., Manatschal G., Minshull T.A., Sawyer D.S. Tectonosedimentary evolution of the deep Iberia-Newfoundland margins: Evidence for a complex breakup history. *Tectonics*, 2007, 26(2).
- [149] Yan P., Deng H., Liu H., Zhang Z., Jiang Y. The temporal and spatial distribution of volcanism in the South China Sea region. *Journal of Asian Earth Sciences*, 2006, 27(5): 647–659.
- [150] 石学法, 鄢全树. 南海新生代岩浆活动的地球化学特征及其构造意义. *海洋地质与第四纪地质*, 2011, 31(2): 59–72.
- [151] Hui G., Li S., Li X., Guo L., Suo Y., Somerville I.D., Zhao S., Hu M., Lan H., Zhang J. Temporal and spatial distribution of Cenozoic igneous rocks in the South China Sea and its adjacent regions: Implications for tectono-magmatic evolution. *Geological Journal*, 2016, 51: 429–447.
- [152] Allain V., Kerandel J.-A., Andréfouët S., Magron F., Clark M., Kirby D.S., Muller-Karger F.E. Enhanced seamount location database for the western and central Pacific Ocean: Screening and cross-checking of 20 existing datasets. *Deep Sea Research Part I: Oceanographic Research Papers*, 2008, 55(8): 1035–1047.
- [153] Zhang B., Pujun W., Zhang G., Xiaomeng S., Baoliang L., Weiyi N. Cenozoic volcanic rocks in the Pearl River Mouth and Southeast Hainan Basins of South China Sea and their implications for petroleum geology. *Petroleum exploration and development*, 2013, 40(6): 704–713.
- [154] 李平鲁, 梁慧娴. 珠江口盆地燕山期岩浆岩的成因及构造环境. *广东地质*, 1999,

- 14(1): 1–8.
- [155] Chung S.-L., Cheng H., Jahn B.-m., O'Reilly S.Y., Zhu B. Major and trace element, and Sr-Nd isotope constraints on the origin of Paleogene volcanism in South China prior to the South China Sea opening. *Lithos*, 1997, 40(2-4): 203–220.
- [156] Ru K., PIGOTT J.D. Episodic rifting and subsidence in the South China Sea. *AAPG bulletin*, 1986, 70(9): 1136–1155.
- [157] Müller R.D., Seton M., Zahirovic S., Williams S.E., Matthews K.J., Wright N.M., Shephard G.E., Maloney K.T., Barnett-Moore N., Hosseinpour M. Ocean basin evolution and global-scale plate reorganization events since Pangea breakup. *Annual Review of Earth and Planetary Sciences*, 2016, 44: 107–138.
- [158] Milliman J.D., Farnsworth K.L. *River discharge to the coastal ocean: a global synthesis*. 2013: Cambridge University Press.
- [159] Zheng H., Clift P.D., Wang P., Tada R., Jia J., He M. Jourdan F., Pre-miocene birth of the Yangtze River. *Proceedings of the National Academy of Sciences*, 2013, 110(19): 7556–7561.
- [160] Clark M., Schoenbohm L., Royden L., Whipple K., Burchfiel B., Zhang X., Tang W., Wang E., Chen L. Surface uplift, tectonics, and erosion of eastern Tibet from large-scale drainage patterns. *Tectonics*, 2004, 23(1).
- [161] Clift P.D. Controls on the erosion of Cenozoic Asia and the flux of clastic sediment to the ocean. *Earth and Planetary Science Letters*, 2006, 241(3-4): 571–580.
- [162] Zhao M., Shao L., Liang J., Li Q. No Red River capture since the late Oligocene: Geochemical evidence from the northwestern South China Sea. *Deep Sea Research Part II: Topical Studies in Oceanography*, 2015, 122: 185–194.
- [163] Yan Y., Carter A., Palk C., Brichau S., Hu X. Understanding sedimentation in the Song Hong–Yinggehai Basin, South China Sea. *Geochemistry, Geophysics, Geosystems*, 2011, 12(6): 48–58.
- [164] 钟泽红, 刘景环, 张道军, 何小胡, 张迎朝, 刘小燕, 尤丽, 刘新宇. 莺歌海盆地东方区大型海底扇成因及沉积储层特征. *石油学报*, 2013, 34(S02): 102–111.
- [165] Wang C., Liang X., Xie Y., Tong C., Pei J., Zhou Y., Jiang Y., Fu J., Dong C., Liu P. Provenance of upper miocene to quaternary sediments in the Yinggehai-Song hong basin, south China sea: evidence from detrital zircon U–Pb ages. *Marine Geology*, 2014, 355: 202–217.
- [166] Yao G.-S., Yuan S.-Q., Wu S.-G., Zhong C. Double provenance depositional model and exploration prospect in the deep-water area of Qiongdongnan Basin. *Petroleum Exploration and Development*, 2008, 35(6): 685–691.
- [167] Cui Y., Shao L., Qiao P., Pei J., Zhang D., Tran H. Upper miocene–pliocene provenance evolution of the Central Canyon in northwestern South China Sea. *Marine Geophysical Research*, 2019, 40: 223–235.
- [168] Cao L., Shao L., Qiao P., Zhao Z., van Hinsbergen D.J. Early Miocene birth of modern Pearl River recorded low-relief, high-elevation surface formation of SE Tibetan Plateau. *Earth and Planetary Science Letters*, 2018, 496: 120–131.
- [169] Shao L., Qiao P., Zhao M., Li Q., Wu M., Pang X., Zhang H. Depositional characteristics of the northern South China Sea in response to the evolution of the Pearl River. *Geological Society, London, Special Publications*, 2016, 429(1): 31–44.
- [170] Pang X., Chen C., Wu M., He M., Wu X. The Pearl River Deep-water Fan Systems and

- Significant Geological Events. *Advances in Earth Science*, 2006, 21(8): 793–799.
- [171] Liu Q., Zhu H., Shu Y., Zhu X., Yang X., Chen L., Tan M., Geng M. Provenance identification and sedimentary analysis of the beach and bar systems in the Palaeogene of the Enping Sag, Pearl River Mouth Basin, South China Sea. *Marine and Petroleum Geology*, 2016, 70: 251–272.
- [172] He Y., Xie X., Kneller B.C., Wang Z., Li X. Architecture and controlling factors of canyon fills on the shelf margin in the Qiongdongnan Basin, northern South China Sea. *Marine and Petroleum Geology*, 2013, 41: 264–276.
- [173] Gong C., Wang Y., Zhu W., Li W., Xu Q., Zhang J. The Central Submarine Canyon in the Qiongdongnan Basin, northwestern South China Sea: architecture, sequence stratigraphy, and depositional processes. *Marine and petroleum Geology*, 2011, 28(9): 1690–1702.
- [174] Yuan S., Lü F., Wu S., Yao G., Ma Y., Fu Y. Seismic stratigraphy of the Qiongdongnan deep sea channel system, northwest South China Sea. *Chinese Journal of Oceanology and Limnology*, 2009, 27(2): 250–259.
- [175] Li C., Lv C., Chen G., Zhang G., Ma M., Shen H., Zhao Z., Guo S. Source and sink characteristics of the continental slope-parallel Central Canyon in the Qiongdongnan Basin on the northern margin of the South China Sea. *Journal of Asian Earth Sciences*, 2017, 134: 1–12.
- [176] Li C., Ma M., Lv C., Zhang G., Chen G., Yan Y., Bi G. Sedimentary differences between different segments of the continental slope-parallel Central Canyon in the Qiongdongnan Basin on the northern margin of the South China Sea. *Marine and Petroleum Geology*, 2017, 88: 127–140.
- [177] Su M., Xie X., Wang Z., Jiang T., Zhang C., He Y. Sedimentary evolution of the Central Canyon System in the Qiongdongnan Basin, northern South China Sea. *Petroleum Research*, 2016, 1(1): 81–92.
- [178] Clift P.D., Carter A., Campbell I.H., Pringle M.S., Van Lap N., Allen C.M., Hodges K.V., Tan M.T. Thermochronology of mineral grains in the Red and Mekong Rivers, Vietnam: Provenance and exhumation implications for Southeast Asia. *Geochemistry, Geophysics, Geosystems*, 2006, 7(10): 123–129.
- [179] Van Hoang L., Clift P.D., Schwab A.M., Huuse M., Nguyen D.A., Zhen S. Large-scale erosional response of SE Asia to monsoon evolution reconstructed from sedimentary records of the Song Hong-Yinggehai and Qiongdongnan basins, South China Sea. *Geological Society, London, Special Publications*, 2010, 342(1): 219–244.
- [180] Xie X., Müller R.D., Ren J., Jiang T., Zhang C. Stratigraphic architecture and evolution of the continental slope system in offshore Hainan, northern South China Sea. *Marine Geology*, 2008, 247(3-4): 129–144.
- [181] Shao L., Cao L., Pang X., Jiang T., Qiao P., Zhao M. Detrital zircon provenance of the Palaeogene syn-rift sediments in the northern South China Sea. *Geochemistry, Geophysics, Geosystems*, 2016, 17(2): 255–269.
- [182] Ma M., Li C., Lv C., Chen G., Yang F., Yan Y., Yin N., Zhang G. Geochemistry and provenance of a multiple-stage fan in the Upper Miocene to the Pliocene in the Yinggehai and Qiongdongnan basins, offshore South China Sea. *Marine and Petroleum Geology*, 2017, 79: 64–80.
- [183] Fyhn M.B., Boldreel L.O., Nielsen L.H. Geological development of the Central and South

- Vietnamese margin: Implications for the establishment of the South China Sea, Indochinese escape tectonics and Cenozoic volcanism. *Tectonophysics*, 2009, 478(3-4): 184–214.
- [184] Huang C.-Y., Yuan P.B., Tsao S.-J. Temporal and spatial records of active arc-continent collision in Taiwan: A synthesis. *Geological Society of America Bulletin*, 2006, 118(3-4): 274–288.
- [185] Cui Y., Shao L., Yu M., Huang C. Formation of Hengchun Accretionary Prism Turbidites and Implications for Deep-water Transport Processes in the Northern South China Sea. *Acta Geologica Sinica-English Edition*, 2021, 95(1): 55–65.
- [186] Lin A.T., Yao B., Hsu S.-K., Liu C.-S., Huang C.-Y. Tectonic features of the incipient arc-continent collision zone of Taiwan: Implications for seismicity. *Tectonophysics*, 2009, 479(1-2): 28–42.
- [187] Huang C.-Y., Wu W.-Y., Chang C.-P., Tsao S., Yuan P.B., Lin C.-W., Xia K.-Y. Tectonic evolution of accretionary prism in the arc-continent collision terrane of Taiwan. *Tectonophysics*, 1997, 281(1-2): 31–51.
- [188] Zhang X., Yan Y., Huang C.-Y., Chen D., Shan Y., Lan Q., Chen W., Yu M. Provenance analysis of the Miocene accretionary prism of the Hengchun Peninsula, southern Taiwan, and regional geological significance. *Journal of Asian Earth Sciences*, 2014, 85: 26–39.
- [189] Zhang X., Huang C., Wang Y., Clift P.D., Yan Y., Fu X., Chen D. Evolving Yangtze River reconstructed by detrital zircon U-Pb dating and petrographic analysis of Miocene marginal Sea sedimentary rocks of the Western Foothills and Hengchun Peninsula, Taiwan. *Tectonics*, 2017, 36(4): 634–651.
- [190] Lester R., McIntosh K., Van Avendonk H.J., Lavier L., Liu C.-S., Wang T.-K. Crustal accretion in the Manila trench accretionary wedge at the transition from subduction to mountain-building in Taiwan. *Earth and Planetary Science Letters*, 2013, 375: 430–440.
- [191] Cheng Y.-M., Huang C.-Y., Yeh J.-J., Chen W.-S. The Loshui Formation; deeper-water sandstones on the Hengchun Peninsula, southern Taiwan. *Acta Geologica Taiwanica*, 1984, 22: 100–117.
- [192] Page B., Lan C.-Y. The Kenting Mélange and its record of tectonic events. *Memoir of the Geological Society of China*, 1983, 5: 227–248.
- [193] Zhang X., Cawood P.A., Huang C.-Y., Wang Y., Yan Y., Santosh M., Chen W., Yu M. From convergent plate margin to arc-continent collision: Formation of the Kenting Mélange, Southern Taiwan. *Gondwana Research*, 2016, 38: 171–182.
- [194] Pelletier B., Stephan J.F. Middle miocene deduction and late miocene beginning of collision registered in the hengchun peninsula: Geodynamic implications for the evolution of Taiwan. *Tectonophysics*, 1986, 125(1-3): 133–160.
- [195] Tian Z.X., Yan Y., Huang C.Y., Zhang X.C., Liu H.Q., Yu M.M., Yao D., Dilek Y. Geochemistry and geochronology of the accreted mafic rocks from the Hengchun Peninsula, southern Taiwan: Origin and tectonic implications. *Journal of Geophysical Research: Solid Earth*, 2019, 124(3): 2469–2491.
- [196] Kirstein L.A., Carter A., Chen Y.G. Testing inferences from palaeocurrents: Application of zircon double-dating to Miocene sediments from the Hengchun Peninsula, Taiwan. *Terra Nova*, 2010, 22(6): 483–493.
- [197] Meng X., Shao L., Cui Y., Zhu W., Qiao P., Sun Z., Hou Y. Sedimentary Records from

- Hengchun accretionary prism turbidites on Taiwan Island: Implication on late Neogene migration rate of the Luzon subduction system. *Marine and Petroleum Geology*, 2021, 124: 104820.
- [198] Chang C.-P., Angelier J., Lee T.-Q., Huang C.-Y. From continental margin extension to collision orogen: structural development and tectonic rotation of the Hengchun peninsula, southern Taiwan. *Tectonophysics*, 2003, 361(1-2): 61–82.
- [199] Shan Y., Nie G., Yan Y., Huang C.Y. The transition from the passive to active continental margin: A case study of brittle fractures in the Miocene Loshui Sandstone on the Hengchun Peninsula, southern Taiwan. *Tectonics*, 2013, 32(1): 65–79.
- [200] Tsai C.-H., Shyu J.B.H., Chung S.-L., Ramos N.T., Lee H.-Y. Detrital zircon record from major rivers of Luzon Island: implications for Cenozoic continental growth in SE Asia. *Journal of the Geological Society*, 2019, 176(4): 727–735.
- [201] Wiedenbeck M., Alle P., Corfu F., Griffin W.L., Meier M., Oberli F.v., Quadt A.v., Roddick J., Spiegel W. Three natural zircon standards for U-Th-Pb, Lu-Hf, trace element and REE analyses. *Geostandards newsletter*, 1995, 19(1): 1–23.
- [202] Sláma J., Košler J., Condon D.J., Crowley J.L., Gerdes A., Hanchar J.M., Horstwood M.S., Morris G.A., Nasdala L., Norberg N. Plešovice zircon—a new natural reference material for U–Pb and Hf isotopic microanalysis. *Chemical geology*, 2008, 249(1-2): 1–35.
- [203] Liu Y., Gao S., Hu Z., Gao C., Zong K., Wang D. Continental and oceanic crust recycling-induced melt–peridotite interactions in the Trans-North China Orogen: U–Pb dating, Hf isotopes and trace elements in zircons from mantle xenoliths. *Journal of petrology*, 2010, 51(1-2): 537–571.
- [204] Compston W., Williams I., Kirschvink J., Zichao Z., Guogan M. Zircon U–Pb ages for the Early Cambrian time-scale. *Journal of the Geological Society*, 1992, 149(2): 171–184.
- [205] Ludwig K.R. User's manual for IsoPlot 3.0. A geochronological toolkit for Microsoft Excel, 2003, 71.
- [206] Olierook H.K., Rankenburg K., Ulrich S., Kirkland C.L., Evans N., Brown S., McInnes B.I., Prent A., Gillespie J., McDonald B. Resolving multiple geological events using in situ Rb–Sr geochronology: implications for metallogenesis at Tropicana, Western Australia. *Geochronology Discussions*, 2020, 2020: 1–31.
- [207] Paton C., Hellstrom J., Paul B., Woodhead J., Hergt J. Iolite: Freeware for the visualisation and processing of mass spectrometric data. *Journal of Analytical Atomic Spectrometry*, 2011, 26(12): 2508–2518.
- [208] Ickert R.B. Algorithms for estimating uncertainties in initial radiogenic isotope ratios and model ages. *Chemical Geology*, 2013, 340: 131–138.
- [209] Sundell K., Saylor J.E., Pecha M. Provenance and recycling of detrital zircons from Cenozoic Altiplano strata and the crustal evolution of western South America from combined U–Pb and Lu–Hf isotopic analysis, in *Andean tectonics*. 2019, Elsevier. p. 363–397.
- [210] Zhu W., Cui Y., Shao L., Qiao P., Yu P., Pei J., Liu X., Zhang H. Reinterpretation of the northern South China Sea pre-Cenozoic basement and geodynamic implications of the South China continent: constraints from combined geological and geophysical records. *Acta Oceanologica Sinica*, 2021, 40: 13–28.
- [211] Rudnick R.L. *The crust*. 3. 2005: Elsevier.

- [212] Hoskin P.W., Schaltegger U. The composition of zircon and igneous and metamorphic petrogenesis. *Reviews in mineralogy and geochemistry*, 2003, 53(1): 27–62.
- [213] Pearce J.A. Role of the sub-continental lithosphere in magma genesis at active continental margins. 1983.
- [214] Hailing L., Pin Y., Yingchun L., Hui D. Existence of Qiongnan suture zone on the north margin of South China Sea. *Chinese Science Bulletin*, 2006, 51: 107–120.
- [215] Liu H., Zheng H., Wang Y., Lin Q., Wu C., Zhao M., Du Y. Basement of the South China Sea area: tracing the Tethyan realm. *Acta Geologica Sinica-English Edition*, 2011, 85(3): 637–655.
- [216] 鲁宝亮, 孙晓猛, 张功成, 张斌, 郎元强, 王璞珺. 南海北部盆地基底岩性地震-重磁响应特征与识别. *地球物理学报*, 2011, 54(2): 563–572.
- [217] Ling W., Bo-chu Y., Wei-jun Z., Neng-you W., Bin X., Ben-duo Z. Lithospheric structure and petroleum distribution in the South China Sea. *Geology in China*, 2006, 33(4): 874–884.
- [218] Hao T.-Y., Xu Y., Sun F.-L., You Q.-Y., LV C.-C., Huang S., Qiu X.-L., Hu W.-J., Zhao M.-H. Integrated geophysical research on the tectonic attribute of conjugate continental margin of South China Sea. *Chinese Journal of Geophysics*, 2011, 54(12): 3098–3116.
- [219] Xiong P., Jianye R., Zheng J., Jun L., Peng Y., Baojun L. Petroleum geology controlled by extensive detachment thinning of continental margin crust: A case study of Baiyun sag in the deep-water area of northern South China Sea. *Petroleum Exploration and Development*, 2018, 45(1): 29–42.
- [220] Zhou D., Sun Z., Chen H.z., Xu H.h., Wang W.y., Pang X., Cai D.s., Hu D.k. Mesozoic paleogeography and tectonic evolution of South China Sea and adjacent areas in the context of Tethyan and Paleo-Pacific interconnections. *Island Arc*, 2008, 17(2): 186–207.
- [221] Roger F., Leloup P.H., Jolivet M., Lacassin R. Trinh P.T., Brunel M., Seward D., Long and complex thermal history of the Song Chay metamorphic dome (Northern Vietnam) by multi-system geochronology. *Tectonophysics*, 2000, 321(4): 449–466.
- [222] Sone M., Metcalfe I. Parallel Tethyan sutures in mainland Southeast Asia: new insights for Palaeo-Tethys closure and implications for the Indosinian orogeny. *Comptes Rendus Geoscience*, 2008, 340(2-3): 166–179.
- [223] Ding X., Chen P., Chen W., Huang H., Zhou X. Single zircon LA-ICPMS U-Pb dating of Weishan granite (Hunan, South China) and its petrogenetic significance. *Science in China Series D: Earth Sciences*, 2006, 49: 816–827.
- [224] Fu J. The determination of the formation ages of the Xishan volcanic-intrusive complex in southern Hunan province. *Acta Geoscientica Sinica*, 2004, 25: 303–308.
- [225] Li X.-H., Li Z.-X., Li W.-X., Liu Y., Yuan C., Wei G., Qi C. U-Pb zircon, geochemical and Sr-Nd-Hf isotopic constraints on age and origin of Jurassic I-and A-type granites from central Guangdong, SE China: a major igneous event in response to foundering of a subducted flat-slab? *Lithos*, 2007, 96(1-2): 186–204.
- [226] Martin H., Bonin B., Capdevila R., Jahn B., Lameyre J., Wang Y. The Kuiqi peralkaline granitic complex (SE China): petrology and geochemistry. *Journal of Petrology*, 1994, 35(4): 983–1015.
- [227] Chen J., Jahn B.-m. Crustal evolution of southeastern China: Nd and Sr isotopic evidence. *Tectonophysics*, 1998, 284(1-2): 101–133.

- [228] Cui Y., Shao L., Li Z.-X., Zhu W., Qiao P., Zhang X. A Mesozoic Andean-type active continental margin along coastal South China: New geological records from the basement of the northern South China Sea. *Gondwana Research*, 2021, 99: 36–52.
- [229] Jahn B., Martineau F., Peucat J., Cornichet J. Geochronology of the Tananao schist complex, Taiwan, and its regional tectonic significance. *Tectonophysics*, 1986, 125(1-3): 103–124.
- [230] Yui T., Okamoto K., Usuki T., Lan C., Chu H., Liou J. Late Triassic–Late Cretaceous accretion/subduction in the Taiwan region along the eastern margin of South China—evidence from zircon SHRIMP dating. *International Geology Review*, 2009, 51(4): 304–328.
- [231] Wang Q., Li X.-H., Jia X.-H., Wyman D., Tang G.-J., Li Z.-X., Ma L., Yang Y.-H., Jiang Z.-Q., Gou G.-N. Late Early Cretaceous adakitic granitoids and associated magnesian and potassium-rich mafic enclaves and dikes in the Tunchang–Fengmu area, Hainan Province (South China): Partial melting of lower crust and mantle, and magma hybridization. *Chemical Geology*, 2012, 328: 222–243.
- [232] Zhu K.-y., Li Z.-x., Xu X.-s., Wilde S.A. A Mesozoic Andean-type orogenic cycle in southeastern China as recorded by granitoid evolution. *American Journal of Science*, 2014, 314(1): 187–234.
- [233] Zhu K.-Y., Li Z.-X., Xia Q.-K., Xu X.-S., Wilde S.A., Chen H.-L. Revisiting Mesozoic felsic intrusions in eastern South China: spatial and temporal variations and tectonic significance. *Lithos*, 2017, 294: 147–163.
- [234] Zhou Y., Liang X., Kröner A., Cai Y., Shao T., Wen S., Jiang Y., Fu J., Wang C., Dong C. Late Cretaceous lithospheric extension in SE China: Constraints from volcanic rocks in Hainan Island. *Lithos*, 2015, 232: 100–110.
- [235] Xu X., O'Reilly S.Y., Griffin W., Wang X., Pearson N., He Z. The crust of Cathaysia: age, assembly and reworking of two terranes. *Precambrian Research*, 2007, 158(1-2): 51–78.
- [236] Yu J.-H., Wang L., O'reilly S., Griffin W., Zhang M., Li C., Shu L. A Paleoproterozoic orogeny recorded in a long-lived cratonic remnant (Wuyishan terrane), eastern Cathaysia Block, China. *Precambrian Research*, 2009, 174(3-4): 347–363.
- [237] Li X.-H., Li Z.-X., Li W.-X. Detrital zircon U–Pb age and Hf isotope constrains on the generation and reworking of Precambrian continental crust in the Cathaysia Block, South China: a synthesis. *Gondwana Research*, 2014, 25(3): 1202–1215.
- [238] Li X.-H., Li W.-X., Li Z.-X., Lo C.-H., Wang J., Ye M.-F., Yang Y.-H. Amalgamation between the Yangtze and Cathaysia Blocks in South China: constraints from SHRIMP U–Pb zircon ages, geochemistry and Nd–Hf isotopes of the Shuangxiwu volcanic rocks. *Precambrian Research*, 2009, 174(1-2): 117–128.
- [239] Li Z.-X., Li X.H., Kinny P.D., Wang J., Zhang S., Zhou H. Geochronology of Neoproterozoic syn-rift magmatism in the Yangtze Craton, South China and correlations with other continents: evidence for a mantle superplume that broke up Rodinia. *Precambrian Research*, 2003, 122(1-4): 85–109.
- [240] Li Z.-X., Li X.-H., Wartho J.-A., Clark C., Li W.-X., Zhang C.-L., Bao C. Magmatic and metamorphic events during the early Paleozoic Wuyi-Yunkai orogeny, southeastern South China: New age constraints and pressure-temperature conditions. *Bulletin*, 2010, 122(5-6): 772–793.
- [241] Wang Y., Zhang A., Fan W., Zhao G., Zhang G., Zhang Y., Zhang F., Li S. Kwangian

- crustal anatexis within the eastern South China Block: geochemical, zircon U–Pb geochronological and Hf isotopic fingerprints from the gneissoid granites of Wugong and Wuyi–Yunkai Domains. *Lithos*, 2011, 127(1-2): 239–260.
- [242] Hoskin P.W. Trace-element composition of hydrothermal zircon and the alteration of Hadean zircon from the Jack Hills, Australia. *Geochimica et Cosmochimica Acta*, 2005, 69(3): 637–648.
- [243] Grimes C.B., John B.E., Kelemen P., Mazdab F., Wooden J., Cheadle M.J., Hanghøj K., Schwartz J. Trace element chemistry of zircons from oceanic crust: A method for distinguishing detrital zircon provenance. *Geology*, 2007, 35(7): 643–646.
- [244] Hawkesworth C.J., Kemp A. Using hafnium and oxygen isotopes in zircons to unravel the record of crustal evolution. *Chemical Geology*, 2006, 226(3-4): 144–162.
- [245] Witt C., Poujol M., Chiaradia M., Villagomez D., Seyler M., Averbuch O., Bouden N. Geodynamic controls in the southernmost Northern Andes magmatic arc: Trace elements and Hf–O isotopic systematics in forearc detrital zircon. *Bulletin*, 2023, 135(7-8): 2141–2154.
- [246] Horton B.K. Sedimentary record of Andean mountain building. *Earth-Science Reviews*, 2018, 178: 279–309.
- [247] Yu J.-H., O'Reilly S.Y., Zhou M.-F., Griffin W., Wang L. U–Pb geochronology and Hf–Nd isotopic geochemistry of the Badu Complex, Southeastern China: implications for the Precambrian crustal evolution and paleogeography of the Cathaysia Block. *Precambrian Research*, 2012, 222: 424–449.
- [248] Huang Z. *Evolution of Plate Tectonics and Environment in Taiwan*. 1995: Beijing: Maritime Press, 1995. 1–210.
- [249] Suo Y., Li S., Yu S., Somerville I.D., Liu X., Zhao S., Dai L. Cenozoic tectonic jumping and implications for hydrocarbon accumulation in basins in the East Asia Continental Margin. *Journal of Asian Earth Sciences*, 2014, 88: 28–40.
- [250] Li Z.X., Li X.H., Li W.X., Ding S. Was Cathaysia part of Proterozoic Laurentia?—new data from Hainan Island, south China. *Terra Nova*, 2008, 20(2): 154–164.
- [251] 许德如, 马驰, 李鹏春, 夏斌, 张玉泉. 海南岛变碎屑沉积岩锆石 SHRIMP U–Pb 年龄及地质意义. *地质学报*, 2007, 81(3): 381–393.
- [252] Zhang Y., Wang Y. Early Neoproterozoic continental arc system at the central Jiangnan Orogen, South China: Geochronological and geochemical constraints on the key igneous rock-association. *GSA Bulletin*, 2020, 132(3-4): 638–654.
- [253] Schulz B., Klemm R., Brätz H. Host rock compositional controls on zircon trace element signatures in metabasites from the Austroalpine basement. *Geochimica et Cosmochimica Acta*, 2006, 70(3): 697–710.
- [254] Li N., Zhai S., Liu X., et al. The trace elements geochemistry and depositional environment changes recorded in the core of Well LS33-1-1 in deepwater area of Qiongdongnan Basin. *Marine Geology, Quaternary Geology*, 2014, 34(3): 1–12.
- [255] Xiu C., Sun Z., Zhai S., Liu X., Liu X., Chen K. U–Pb ages of detrital zircons from deep-water Well LS33A at Lingnan Low Uplift of the Qiongdongnan Basin and their geological significances. in *IOP Conference Series: Earth and Environmental Science*. 2017. IOP Publishing.
- [256] Hutchison C.S. Gondwana and Cathaysian blocks, Palaeotethys sutures and Cenozoic

- tectonics in South-east Asia. *Active Continental Margins—Present and Past*, 1994: 388–405.
- [257] Lepvrier C., Van Vuong N., Maluski H., Thi P.T., Van Vu T. Indosinian tectonics in Vietnam. *Comptes Rendus Geoscience*, 2008, 340(2-3): 94–111.
- [258] Vương N.V., Hansen B.T., Wemmer K., Lepvrier C., Tích V.V., Thăng T.T. U/Pb and Sm/Nd dating on ophiolitic rocks of the Song Ma suture zone (northern Vietnam): Evidence for upper paleozoic paleotethyan lithospheric remnants. *Journal of Geodynamics*, 2013, 69: 140–147.
- [259] Nakano N., Osanai Y., Owada M., Nam T.N., Toyoshima T., Binh P., Tsunogae T., Kagami H. Geologic and metamorphic evolution of the basement complexes in the Kontum Massif, central Vietnam. *Gondwana Research*, 2007, 12(4): 438–453.
- [260] Liu H., Wang Y., Cawood P.A., Fan W., Cai Y., Xing X. Record of Tethyan ocean closure and Indosinian collision along the Ailaoshan suture zone (SW China). *Gondwana Research*, 2015, 27(3): 1292–1306.
- [261] Leloup P.H., Lacassin R., Tapponnier P., Schärer U., Zhong D., Liu X., Zhang L., Ji S., Trinh P.T. The Ailao Shan-Red river shear zone (Yunnan, China), tertiary transform boundary of Indochina. *Tectonophysics*, 1995, 251(1-4): 3–84.
- [262] Burrett C., Zaw K., Meffre S., Lai C.K., Khositanont S., Chaodumrong P., Udchachon M., Ekins S., Halpin J., The configuration of Greater Gondwana—Evidence from LA ICPMS, U–Pb geochronology of detrital zircons from the Palaeozoic and Mesozoic of Southeast Asia and China. *Gondwana Research*, 2014, 26(1): 31–51.
- [263] Zeng Z., Zeng X. *Physical Geography of Hainan Island*, in *Science*, Beijing. 1989. p. 60–110.
- [264] Cao L., Jiang T., Wang Z., Zhang Y., Sun H. Provenance of Upper Miocene sediments in the Yinggehai and Qiongdongnan basins, northwestern South China Sea: Evidence from REE, heavy minerals and zircon U–Pb ages. *Marine Geology*, 2015, 361: 136–146.
- [265] Wang C., Liang X., Zhou Y., Fu J., Jiang Y., Dong C., Xie Y., Tong C., Pei J., Liu P. Construction of age frequencies of provenances on the eastern side of the Yinggehai Basin: Studies of LA-ICP-MS U–Pb ages of detrital zircons from six modern rivers, western Hainan, China. *Earth Science Frontiers*, 2015, 22(4): 277–289.
- [266] Xu Y., Sun Q., Cai G., Yin X., Chen J. The U–Pb ages and Hf isotopes of detrital zircons from Hainan Island, South China: implications for sediment provenance and the crustal evolution. *Environmental earth sciences*, 2014, 71: 1619–1628.
- [267] Clift P.D., Blusztajn J., Nguyen A.D. Large-scale drainage capture and surface uplift in eastern Tibet–SW China before 24 Ma inferred from sediments of the Hanoi Basin, Vietnam. *Geophysical Research Letters*, 2006, 33(19): L19403.
- [268] Zhao M., Shao L., Qiao P. Characteristics of detrital zircon U–Pb geochronology of the Pearl River Sands and its implication on provenances. *Journal of Tongji University*, 2015, 43: 915–923.
- [269] Van Hoang L., Wu F.Y., Clift P.D., Wysocka A., Swierczewska A., Evaluating the evolution of the Red River system based on in situ U–Pb dating and Hf isotope analysis of zircons. *Geochemistry, Geophysics, Geosystems*, 2009, 10(11): 292–310.
- [270] Cai G., Shao L., Qiao P., Liang J. Marine transgression and evolution of depositional environment in the Paleogene strata of Qiongdongnan Basin, South China Sea. *Acta Petrolei Sinica*, 2013, 34: 91.

- [271] Trung N.M., Tsujimori T., Itaya T. Honvong serpentinite body of the Song Ma fault zone, Northern Vietnam: A remnant of oceanic lithosphere within the Indochina–South China suture. *Gondwana Research*, 2006, 9(1-2): 225–230.
- [272] Chang L.-S. A biostratigraphic study of the tertiary in the Hengchun Peninsula, Taiwan, based on smaller foraminifera (II: Middle Part). in *Proc. Geol. Soc. China*. 1965.
- [273] Zhong L., Li G., Yan W., Xia B., Feng Y., Miao L., Zhao J. Using zircon U–Pb ages to constrain the provenance and transport of heavy minerals within the northwestern shelf of the South China Sea. *Journal of Asian Earth Sciences*, 2017, 134: 176–190.
- [274] Shao L., Meng A., Li Q., Qiao P., Cui Y., Cao L., Chen S. Detrital zircon ages and elemental characteristics of the Eocene sequence in IODP Hole U1435A: Implications for rifting and environmental changes before the opening of the South China Sea. *Marine Geology*, 2017, 394: 39–51.
- [275] Chen H.-Y., Yang H.-J., Liu Y.-H., Huang K.-F., Takazawa E. Tectonic affinities of the accreted basalts in southern Taiwan. *Journal of Asian Earth Sciences*, 2018, 158: 253–265.
- [276] Zhang G.-L., Luo Q., Zhao J., Jackson M.G., Guo L.-S., Zhong L.-F. Geochemical nature of sub-ridge mantle and opening dynamics of the South China Sea. *Earth and Planetary Science Letters*, 2018, 489: 145–155.
- [277] Fyhn M.B., Thomsen T.B., Keulen N., Knudsen C., Rizzi M., Bojesen-Koefoed J., Olivarius M., Tri T.V., Phach P.V., Minh N.Q. Detrital zircon ages and heavy mineral composition along the Gulf of Tonkin-implication for sand provenance in the Yinggehai-Song Hong and Qiongdongnan basins. *Marine and Petroleum Geology*, 2019, 101: 162–179.
- [278] Lei C., Alves T.M., Ren J., Tong C. Rift structure and sediment infill of hyperextended continental crust: insights from 3D seismic and well data (Xisha Trough, South China Sea). *Journal of Geophysical Research: Solid Earth*, 2020, 125(5): e2019JB018610.

致谢

自 2010 年本科入学以来，我在同济大学已经驻足了将近 14 个年头。时常跟人提起从呱呱坠地以来，在同济的时间甚至超过了在家的时间，所谓“母校”并非虚言，来的真是名副其实。回望过去的十几个春秋，从本科到硕士，从硕士到博士，我有幸见证了发生在它身上的巨大变化，从南北楼、图书馆、海洋楼、食堂、樱花大道、音乐广场……这种共同成长、相伴相随的经历让人感慨良多。在博士研究的六年漫长旅程中，我得到了许多人的支持和帮助，他们的关怀、指导和激励使我取得了各项成果并顺利完成了这篇博士学位论文。再此我向所有给予我支持的人们表达我最诚挚的谢意。

首先，我要特别感谢我的导师邵磊教授，他的智慧、耐心和无私的指导贯穿了我整个博士研究阶段。其实，他对我的支持和引导不仅限于博士阶段，从本科的创新项目和毕业论文，到硕士的第一篇英文 SCI，再到大大小小的野外地质考察和样品采集，点点滴滴我都铭记于心。他不仅在学术上为我提供了宝贵的意见和建议，并且在每个学生遇到困难和挫折时，都给予极大的鼓励和帮助。邵磊教授的学术严谨和热情投入深深地感染了我，使我在科研道路上不断进步。

感谢我的第二母校 Curtin University 导师，澳大利亚科学院院士李正祥教授。在澳学习期间，李正祥教授不仅在学术上为我提供了宝贵的指导和支持，还在日常生活中给予了我极大的帮助和关怀。他以极其渊博的学识和严谨的治学态度，为我的科研工作指明了方向。在我遇到科研瓶颈和困难时，他总是耐心倾听并细心指导，帮助我克服难关。李正祥教授的言传身教和亲身经历，也让我坚定了未来职业生涯的发展方向。

感谢我的论文答辩委员会成员朱伟林教授、刘传联教授、蔡进功教授、姚永坚教授、张成立教授、罗静兰教授以及两位匿名论文审稿人，他们在我论文的构思、研究和撰写过程中提出了很多宝贵建议，帮助我完善了论文结构和内容，并于百忙之中参与了最后的博士学位论文答辩。你们的专业知识和细致入微的批评指正使我受益匪浅。

还要感谢我的研究团队，尤其是负责实验室工作的顶梁柱乔培军老师。我们取得的大量成果离不开乔老师在实验过程中给予的大量帮助和支持。另外包括课题组的师兄、师姐、同门、师弟及师妹，他们是刘正华、曹立成、宋亚敏、董茜茜、张浩、孟宪博、夏东升、侯元立、周俊燊、陈心怡、李莉妮、杨逸凯、鲁毅、马琼、赵晓逸，我们一起度过了无数个加班加点的夜晚，这些回忆将永远是我人生道路的宝贵财富。

致谢

感谢 Curtin University 李老师领导的 EDRG 课题组的各位老师及兄弟姐妹，他们是刘也博、李江瑜、黄川、舒楚天、张亮、康健丽、王冲、包国栋、胡伟、Daniel Brennan、Piero Azevedo Berquo de Sampaio、Hamed Gamaleldien、Sergi Pisarevskiy、Josh Beardmore、Maelys Privat、Uwe Kirscher、Luc Doucet；感谢我的副导师 Katy Evans 教授、Chris Elders 教授以及 John De Laeter Center 实验中心的 Dr.Hugo Olierook，在我攻读 Curtin University 第二博士学位的过程中提供了极大的鼓励、支持和帮助。

当然，每个博士在求学过程中都会经历期待、迷茫、低落、纠结、挣扎、失意、兴奋、欢愉、释然和轻松一系列如同过山车一般的心情变化，再此真诚地感谢一路走来的朋友们，包括海洋学院 315 办公室“饭饭之辈”的刘晶晶、王星星、吴伟艳、张洪瑞、马岑玲、杨策、刘丰豪、杨莹、张靖雯、李科、党少华、陈越、殷雅倩等兄弟姐妹，感谢因地球系统科学大会小报组结缘并一路互相支持的挚友杜佳宗和曾治惟，感谢因同济大学学术先锋结缘并互相鼓励的挚友娜娜、小白杨和金兄，感谢一起吐槽、欢笑、支持和出行的挚友川哥、晓龙和志杰。

最后感谢在背后默默支持我的父母和先生，让我永远有底气说走就走，想做就做。

没有技术，全是感情，想感谢的人太多，无奈篇幅有限，但你们的付出我将永远铭记于心。

2024 年 5 月

个人简历、在读期间发表的学术成果

个人简历:

崔宇驰, 女, 1991年6月生。

2014年6月毕业于同济大学, 地质学专业, 获学士学位。

2015年9月入同济大学攻读硕士研究生, 海洋科学专业, 获硕士学位。

2018年9月入同济大学攻读博士研究生, 海洋科学专业。

2020年11月入澳大利亚科廷大学攻读博士研究生双学位, 应用地质学专业。

已发表论文:

[1] **Cui, Y.**, Shao, L., Tang, W., Qiao, P., Goh, T., Yao, Y. Late Eocene–early Miocene provenance evolution of the Crocker Fan in the southern South China Sea. *Acta Oceanologica Sinica*, 2023, 42(3): 215–226.

[2] Liu, J., Li, S., Liao, K., ***Cui, Y.**, Shao, L., Qiao, P., Lu, Y., Hou, Y., Goh, T.L., Yao, Y. New interpretation on the provenance changes of the upper Pinghu–lower Huagang Formation within Xihu Depression, East China Sea Shelf Basin. *Acta Oceanologica Sinica*, 2023, 42(3): 89–100.

[3] 崔宇驰, 赵志刚, 邵磊, 朱伟林, 乔培军, 唐武, 李莉妮. 南海南部 Crocker 扇物源特征及油气地质意义. *石油学报*, 2022, 43(10): 1427–1438.

[4] **Cui, Y.**, *Shao, L., Li, Z.-X., Zhu, W., Qiao, P., Zhang, X. A Mesozoic Andean-type active continental margin along coastal SouthChina: New geological records from the basement of the northern South China Sea. *Gondwana Research*, 2021, 99: 36–52.

[5] Zhu, W., ***Cui, Y.**, Shao, L., Qiao, P., Yu, P., Pei, J., Liu, X., Zhang, H. Reinterpretation of the northern South China Sea pre-Cenozoic basement and geodynamic implications of the South China continent: constraints from combined geological and geophysical records. *Acta Oceanologica Sinica*, 2021, 40(2): 13–28.

[6] Zhang, H., **Cui, Y.***, Qiao, P., Zhao, M., Xiang, X. Evolution of the Pearl River and its Implication for East Asian Continental Landscape Reversion. *Acta Geologica Sinica*, 2021, 95(1): 66–76.

[7] **Cui, Y.**, *Shao, L., Yu, M., Huang, C. Formation of Hengchun Accretionary Prism Turbidites and Implications for Deep-water Transport Processes in the Northern South China Sea. *Acta Geologica Sinica*, 2021, 95(1): 55–65.

[8] Meng, X., Shao, L.* , **Cui, Y.****, Zhu, W., Qiao, P., Sun, Z., Hou, Y. Sedimentary records from Hengchun accretionary prism turbidites on Taiwan Island: Implication on late Neogene migration rate of the Luzon subduction system. *Marine and Petroleum Geology*, 2021, 124: 104820.

[9] Shao, L., **Cui, Y.***, Statterger, K., Zhu, W., Qiao, P., Zhao, Z. Drainage control of Eocene to Miocene sedimentary records in the southeastern margin of Eurasian Plate. *GSA Bulletin*, 2019, 131(3/4): 461–478.

[10] **Cui, Y.**, Shao, L.* , Qiao, P., Pei, J., Zhang, D., Tran, H. Upper Miocene–Pliocene provenance evolution of the Central Canyon in northwestern South China Sea. *Marine Geophysical Research*, 2019, 40: 223–235.

[11] 崔宇驰, 曹立成, 乔培军, 陈淑慧, 庞雄, 邵磊. 南海北部古近纪沉积物碎屑锆石 U-

- Pb 年龄及物源演化. 地球科学, 2018, 43(11): 4169–4179.
- [12] 崔宇驰, 赵志刚, 邵磊, 朱伟林, 乔培军, 唐武, 李莉妮, 南海南部 Crocker 扇物源特征及油气地质意义. 石油学报, 2022, 43(10): 1427–1438.
- [13] Qiao, P., **Cui, Y.***, Ma, Q., Shao, L. Paleogene transgression process and environmental evolution in the deepwater area of the Baiyun Depression in the northern South China Sea. *Acta Oceanologica Sinica*, 2024, 43(5): 1–11.
- [14] Cao, L., *Shao, L., van Hinsbergen, D.J., Jiang, T., Xu, D., **Cui, Y.**. Provenance and evolution of East Asian large rivers recorded in the East and South China Seas: A review. *GSA Bulletin*, 2023, 135(11/12): 2723–2752.
- [15] *Li, R., Jones, B., Qiao, P., **Cui, Y.**, Pei, J., Liu, X., Shao, L. Genesis of island dolostones during rapid island subsidence: Example from the Xisha (Paracel) islands, South China Sea. *Sedimentology*, 2023, 70: 1785–1811.
- [16] *Hou, Y., Shao, L., **Cui, Y.**, Allen, M.B., Zhu, W., Qiao, P., Huang, C.Y., Yao, Y., Goh, T.L. Sediment features and provenance analysis of the late Mesozoic–early Cenozoic strata of the Ryukyu Islands: Implications for palaeogeography of East China Sea. *Marine Petroleum Geology*, 2022, 145: 105840.
- [17] 李莉妮, 赵志刚, 崔宇驰, 刘世翔, 唐武, 鲁毅, 乔培军. 南海南部上白垩统—始新统 Rajang 群浊流沉积物源-汇对比分析. 古地理学报, 2022, 24(01): 61–72.
- [18] 鲁毅, 崔宇驰, Si Si Thu, Kyaw Kyaw Khing, Myo Min Aung, 朱伟林, 邵磊. 东喜马拉雅构造结快速隆升时期: 来自缅甸中央盆地沉积学证据. 地球科学, 47(7): 2573–2585.
- [19] 张向涛, 向绪洪, 赵梦, 崔宇驰, 张浩. 珠江水系演化与东亚地形倒转的耦合关系. 地球科学, 2022, 47(7): 2410–2420.
- [20] 邵磊, 鲁毅, 乔培军, 崔宇驰, 任建业, 曹立成, 马琼. 弧陆碰撞背景下沉积物轴向与横向搬运转换. 古地理学报, 2022, 24(05): 894–907.
- [21] Cao, L., *Shao, L., Qiao, P., **Cui, Y.**, Zhang, G., Zhang, X. Formation and paleogeographic evolution of the Palawan continental terrane along the Southeast Asian margin revealed by detrital fingerprints. *GSA Bulletin*, 2021, 133(5–6): 1167–1193.
- [22] Zhao, Z., *Zhang, H., **Cui, Y.**, Tang, W., Qiao, P. Cenozoic Sea-land Transition and its Petroleum Geological Significance in the Northern South China Sea. *Acta Geologica Sinica*, 2021, 95(1): 41–54.
- [23] *Wu, F., Xie, X., Zhu, Y., Coletti, G., Betzler, C., **Cui, Y.**, Bai, H., Chen, B., Shang, Z. Early development of carbonate platform (Xisha Islands) in the northern South China Sea. *Marine Geology*, 2021, 441: 106629.
- [24] Hou, Y., *Zhu, W., Qiao, P., Huang, C.-Y., **Cui, Y.**, Meng, X. Sediment source and environment evolution in Taiwan Island during the Eocene–Miocene. *Acta Oceanologica Sinica*, 2021, 40(2): 114–122.
- [25] Zhang, H., *Shao, L., **Zhang, G., **Cui, Y.**, Zhao, Z., Hou, Y. The response of Cenozoic sedimentary evolution coupled with the formation of the South China Sea. *Geological Journal*, 2021, 55(10): 6989–7010.
- [26] Zhang, G., *Shao, L., Qiao, P., **Cao, L., Pang, X., Zhao, Z., Xiang, X., **Cui, Y.** Cretaceous–Palaeogene sedimentary evolution of the South China Sea region: A preliminary synthesis. *Geological Journal*, 2020, 55(4): 2662–2683.
- [27] Cao, L., Shao, L., Qiao, P., **Cui, Y.**, Zhang, G., Zhang, X. Formation and paleogeographic evolution of the Palawan continental terrane along the Southeast Asian margin revealed by detrital

- fingerprints, *GSA Bulletin*, 2020, 133(5/6): 1167–1193.
- [28] Zhang, H., Shao, L., Zhang, G., **Cui, Y.**, Zhao, Z., Hou, Y. The response of Cenozoic sedimentary evolution coupled with the formation of the South China Sea. *Geological Journal*, 2020, 55(10): 6989–7010.
- [29] 周俊燊, 邵磊, 乔培军, **崔宇驰**, 孙珍, 侯元立, 杨逸凯. 南海北部深海盆地晚中新世浊积砂体物质来源. *古地理学报*, 2020, 22(4): 775–784.
- [30] 邵磊, 乔培军, **崔宇驰**, 张浩. 新生代早期南海北部水系演变. *科技导报*, 2020, 38(18): 57–61.
- [31] 鲁毅, **崔宇驰**, 刘新宇, 邵磊, 乔培军. 中国南海西沙碳酸盐岩台地形成过程及控制因素:来自西科1井的地球化学证据. *古地理学报*, 2020, 22(6): 1197–1208.
- [32] 陈淑慧, 侯元立, 邵磊, 黄奇瑜, 乔培军, **崔宇驰**, 孟宪博. 台湾始新-中新统沉积物源与沉积环境. *沉积学报*, 2020, 38(2): 319–330.
- [33] Wu, F., *Xie, X., Li, X., Betzler, C., Shang, Z., **Cui, Y.** Carbonate factory turnovers influenced by the monsoon (Xisha Islands, South China Sea). *Journal of the Geological Society*, 2019, 176(5): 885–897.
- [34] *Huang, C.-Y., Shao, L., Wang, M., Xue, W., Qiao, P., **Cui, Y.**, Hou, Y. Benthic foraminiferal fauna and sediment provenance of Eocene syn-rift sequences in Taiwan: implication for onset of Asian epi-continental marginal seas off China coast. *Marine Geophysical Research*, 2019, 40: 111–127.
- [35] Zhang, G., Shao, L., Qiao, P., Cao, L., Pang, X., Zhao, Z., Xiang, X., **Cui, Y.** Cretaceous–Paleogene sedimentary evolution of the South China Sea region: a preliminary synthesis. *Geological Journal*, 2020, 55(4): 2662–2683.
- [36] Husnul, K., Shao, L., Goh, T.L., **Cui, Y.**, Batara, 2019. A new geological map for formation distribution on southern part of South China Sea: west Kalimantan, Indonesia. *International Journal of GEOMATE*, 2019, 17(63): 249–254.
- [37] 邵磊, **崔宇驰**, 乔培军, 朱伟林, 钟锴, 周俊燊. 南海北部古河流演变对欧亚大陆东南缘早新生代古地理再造的启示. *古地理学报*, 2019, 21(2): 216–231.
- [38] Li, R., *Qiao, P., **Cui, Y.**, Zhang, D., Liu, X., Shao, L. Composition and diagenesis of Pleistocene aeolianites at Shidao, Xisha Islands: Implications for palaeoceanography and palaeoclimate during the last glacial period. *Palaeogeography, Palaeoclimatology, Palaeoecology*, 2018, 490: 604–616.
- [39] Chen, S., *Qiao, P., Zhang, H., Xie, X., **Cui, Y.**, Shao, L. Geochemical characteristics of Oligocene-Miocene sediments from the deepwater area of the northern South China Sea and their provenance implications. *Acta Oceanologica Sinica*, 2018, 37: 35–43.
- [40] Huang, C.-Y., Shao, L., Wang, M.H., Xue, W.G., Qiao, P.J., **Cui, Y.C.**, Hou, Y.L. Benthic foraminiferal fauna and sediment provenance of Eocene synrift sequences in Taiwan: implication for onset of Asian epi-continental marginal seas off China coast, *Marine Geophysical Research*, 2019, 40: 111–127.